Transactions of the ASME

TRANSACTIONS OF THE AMERICAN SOCIETY OF MECHANICAL ENGINEERS

VOLUME 78 NOVEMBER 1956 NUMBER 8

Transactions

of The American Society of Mechanical Engineers

Published on the tenth of every month, except March, June, September, and December

Published monthly by The American Society of Mechanical Engineers. Publication office at 20th and Northampton Streets, Easton, Pa. The editorial department is located at the headquarters of the Society, 29 West Thirty-Ninth Street, New York 18, N. Y. Cable address, "Dynamic," New York. Price $1.50 a copy, $12.00 annually for Transactions and the *Journal of Applied Mechanics;* to members $1.00 a copy, $6.00 annually. Add $1.50 for postage to all countries outside the United States, Canada, and Pan-American Union. Changes of address must be received at Society headquarters seven weeks before they are to be effective on the mailing list. Please send old as well as new address. . . . By-Law: The Society shall not be responsible for statements or opinions advanced in papers or . . . printed in its publications (B13, Par. 4). . . . Entered as second-class matter March 2, 1928, at the Post Office at Easton, Pa., under the Act of August 24, 1912. . . .

Heat-Conduction Methods in Forced-Convection Flow

By S. LEVY,[1] SCHENECTADY, N. Y.

Transient heat-conduction solutions are used to determine the thermal characteristics of fluid flowing in circular conduits, annuli, and between parallel plates. Jaeger's method of deriving the time lag for heat conduction in composite slabs (herewith extended to include composite cylinders) reduces the problem to a series of arithmetical calculations. Numerical results are presented for flow between parallel plates with the following boundary conditions: Constant heat rate, linear wall-temperature variation, and constant wall temperature at one of the external surfaces with constant heat rate, no heat transfer, or zero temperature at the other surface. Some solutions are extended to account for external wall resistance, and thermal entry lengths are evaluated for fluids with high or low Prandtl numbers.

Introduction

BECAUSE heat-conduction equations lend themselves to exact mathematical treatment, the number and range of available solutions is very large. Reduction of a forced-convection problem to a corresponding one in heat conduction often means that the solution may be obtained readily from the book of Carslaw and Jaeger (1).[2] Such solutions have been presented before for forced-convection flow with constant-velocity profile. It is proposed here to make further application of the heat-conduction solutions to the case of arbitrary velocity and diffusivity distributions, utilizing a method developed by Jaeger (2) to deal with the conduction of heat in composite slabs; to apply solutions available in Carslaw and Jaeger (1) to the problem of thermal-entry length.

A thermal-entry length occurs whenever a fluid at constant temperature is subjected suddenly to heating or cooling. Theoretical solutions of this problem have been proposed for the case of constant wall temperature (3–7), and constant heat rate (6–9), and are described in reference (10). With the exception of Latzko's solution (11) for a Prandtl number of unity, all the results including the present, apply to established hydrodynamic conditions at the entrance of the heating or cooling section.

Differential Equations

Consider flow in the x-direction of a fluid with prescribed velocity and diffusivity profiles. The term α used in the present analysis includes the thermal diffusivity of the fluid and its eddy diffusivity for heat. The temperature T of the fluid is obtained in cylindrical co-ordinates from the following differential equation

$$u \frac{\partial T}{\partial x} = \frac{1}{r} \frac{\partial}{\partial r} \left(\alpha r \frac{\partial T}{\partial r} \right) \quad \ldots\ldots [1]$$

Assume that the velocity and diffusivity profiles are subdivided in a series of steps as shown in Fig. 1. The number of steps is chosen so that both distributions are represented adequately. The size of each step is arbitrary but the same for the two profiles. For values of the radius r between r_i and r_{i-1} the velocity u and diffusivity α may be assumed constant and equal to u_i, α_i.

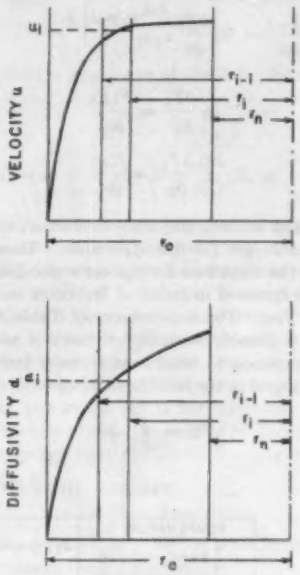

Fig. 1 Diffusivity and Velocity Profiles

The differential equations become

$$\left.\begin{aligned} u_i \frac{\partial T_i}{\partial x} &= \alpha_i \left\{ \frac{\partial^2 T_i}{\partial r^2} + \frac{1}{r} \frac{\partial T_i}{\partial r} \right\} \qquad r_{i-1} \leq r_i \leq r_i \\ & \qquad\qquad\qquad\quad i = 1, 2, \ldots\ldots, n \end{aligned}\right\}$$

with the following boundary conditions at $r = r_{i-1}$

$$\left.\begin{aligned} T_{i-1} &= T_i \\ \alpha_{i-1} \frac{\partial T_{i-1}}{\partial r} &= \alpha_i \frac{\partial T_i}{\partial r} \qquad i = 2, 3, \ldots\ldots, n \end{aligned}\right\} \quad \ldots [2]$$

The conditions at the surface may be written

$$T_1 = T_w(x) \quad \text{or} \quad \alpha_1 \frac{\partial T_1}{\partial r} = \frac{F(x)}{\rho c_p} \qquad r = r_1$$

$$T_n = t_w(x) \quad \text{or} \quad \alpha_n \frac{\partial T_n}{\partial r} = \frac{f(x)}{\rho c_p} \qquad r = r_n$$

the product ρc_p being equal to the thermal capacity of the fluid.

[1] Heat Transfer Equipment Unit, Atomic Power Equipment Engineering, Guided Missiles Department, General Electric Company.

[2] Numbers in parentheses refer to the Bibliography at the end of the paper.

Contributed by the Heat Transfer Division and presented at the Annual Meeting, New York, N. Y., November 28–December 3, 1954, of The American Society of Mechanical Engineers.

Note: Statements and opinions advanced in papers are to be understood as individual expressions of their authors and not those of the Society. Manuscript received at ASME Headquarters, August 26, 1954. Paper No. 54—A-142.

The energy equation for a fluid with arbitrary velocity and diffusivity distributions becomes identical to the transient heat-conduction equation in a series of composite sections. This problem is solved best by means of the Laplace transform and requires the evaluation of numerous residues. It appears, therefore, that no real simplification was introduced. In reality, the results are obtained readily using the method of Jaeger (2). The method of solution will be described in details for the case of flow between parallel plates.

Flow Between Parallel Plates

For parallel plates a distance $2h$ apart, the differential equations are

$$u_i \frac{\partial T_i}{\partial x} = \alpha_i \frac{\partial^2 T_i}{\partial y^2} \qquad l_1 + \ldots\ldots + l_{i-1} < y < l_1 + \ldots\ldots + l_i$$

with

$$T_{i-1} = T_i$$

$$\alpha_{i-1} \frac{\partial T_{i-1}}{\partial y} = \alpha_i \frac{\partial T_i}{\partial y} \qquad y = l_1 + \ldots\ldots + l_{i-1}$$

$$T_1 = T_w(x) \quad \text{or} \quad \alpha_1 \frac{\partial T_1}{\partial y} = \frac{F(x)}{\rho c_p} \qquad y = 0$$

$$T_n = t_w(x) \quad \text{or} \quad \alpha_n \frac{\partial T_n}{\partial y} = \frac{f(x)}{\rho c_p} \qquad y = l_1 + \ldots\ldots + l_n$$

If a single step is used, the heat-conduction results presented in Carslaw and Jaeger (1) are applicable. These are shown in Table 1 where the equations for the corresponding thermal characteristics are expressed in terms of Reynolds and Prandtl number, N_{RE} and N_{PR}. The first column of Table 1 shows quantities which vary linearly with the distance x as $x \to \infty$. The symbol Q corresponds to total heat transfer from 0 to x and is equal to the integral of the local heat flux q or

$$Q = \int_0^x q\,dx$$

Jaeger (2) was able to evaluate all the quantities shown in column 1 for the case of composite slabs. His results are shown in column 2. The symbols A_n, B_n, a_n, b_n, A_n', B_n', a_n', and b_n' are computed from

$$A_i = \frac{R_i'}{R_i}$$

$$B_i = \frac{R_{i-1}}{R_i} B_{i-1} + \frac{1}{2} R'_{i-1} H_i + \frac{1}{6} R_i H_i + B'_{i-1}$$

$$A_i' = 1$$

$$B_i' = R'_{i-1} H_i + \frac{1}{2} R_i H_i + B'_{i-1}$$

$$a_i = 1$$

$$a_i' = H_i'$$

$$b_i' = b'_{i-1} + b_{i-1} H_i + \frac{1}{6} R_i H_i^2 + \frac{1}{2} R_i H_i H'_{i-1}$$

$$b_i = b_{i-1} + \frac{1}{2} R_i H_i + R_i H'_{i-1}$$

where $R_i = \dfrac{l_i/h}{(\alpha/\nu)_i}$ $\qquad R'_i = \displaystyle\sum_{s=1}^{i} R_s$

$$H_i = \frac{l_i}{h} \frac{u_i^+}{u_m^+} \qquad H_i' = \sum_{s=1}^{i} H_i \qquad u^+ = u/\sqrt{\tau_w/\rho}$$

and $A_1 = 1$ $\qquad B_1 = \dfrac{1}{6} \dfrac{l_1/h}{(\alpha/\nu)_1} \dfrac{l_1}{h} \dfrac{u_1^+}{u_m^+}$

$$a_1 = 1 \qquad b_1 = \frac{1}{2} \frac{l_1/h}{(\alpha/\nu)_1} \frac{l_1}{h} \frac{u_1^+}{u_m^+}$$

$$A_1' = 1 \qquad B_1' = \frac{1}{2} \frac{l_1/h}{(\alpha/\nu)_1} \frac{l_1}{h} \frac{u_1^+}{u_m^+}$$

$$a_1' = H_1 \qquad b_1' = \frac{1}{6} R_1 H_1^2$$

TABLE 1 HEAT-CONDUCTION RESULTS BY CARSLAW AND JAEGER (1)

TEMPERATURE 0 $2h = l_1 + \cdots + l_n$ TEMPERATURE V	$Q_{2h} = \rho c_p u_m hV \left[\frac{4x}{hN_{RE}} - \frac{1}{6} N_{PR}\right]$ $Q_0 = \rho c_p u_m hV \left[\frac{4x}{hN_{RE}} + \frac{1}{3} N_{PR}\right]$	$Q_{2h} = \frac{\rho c_p u_m hV}{R_n'} \left[\frac{4x}{hN_{RE}} - \frac{B_n}{A_n}\right]$ $Q_0 = \frac{\rho c_p u_m hV}{R_n'} \left[\frac{4x}{hN_{RE}} - \frac{B_n}{A_n} + b_n\right]$	$Q_0 - Q_{2h} = \rho c_p u_m hV b_n$ $X = \frac{T_0 - T_m}{T_0 - T_{2h}} = 1 - b_n/2$
FLUX F $h = l_1 + \cdots + l_n$ FLUX F	$T_w = \frac{Fh}{\rho c_p \nu} \left[\frac{4x}{hN_{RE}} + \frac{1}{3} N_{PR}\right]$	$T_w = \frac{Fh}{\rho c_p \nu H_n'} \left[\frac{4x}{hN_{RE}} - \frac{b_n'}{a_n'} + B_n'\right]$	$\frac{H(4h)}{K} = \frac{4}{1/N_{PR}\left[B_n' - \frac{b_n'}{a_n'}\right]}$
INSULATED $2h = l_1 + \cdots + l_n$ $T_0 = 4Bx/hN_{RE}$	$T_{2h} = B\left[\frac{4x}{hN_{RE}} - \frac{1}{2} N_{PR}\right]$	$T_{2h} = B\left[\frac{4x}{hN_{RE}} - B_n'\right]$	$Y = \frac{T_0 - T_{2h}}{\frac{d\,T_0}{d\,4x/hN_{RE}}} = B_n'$
TEMPERATURE 0 $2h = l_1 + \ldots + l_n$ FLUX F	$Q_{2h} = \frac{FhN_{RE}}{4} \left[\frac{4x}{hN_{RE}} - \frac{1}{2} N_{PR}\right]$	$Q_{2h} = \frac{FhN_{RE}}{4} \left[\frac{4x}{hN_{RE}} - b_n\right]$	$T_m = \frac{Fh}{K} \frac{b_n}{2} \frac{1}{(N_{RE})^2 N_{PR}}$
INSULATED $2h = l_1 + \ldots + l_n$ FLUX F	$T_{2h} = \frac{Fh}{\rho c_p \nu} \left[\frac{4x}{hN_{RE}} - \frac{1}{6} N_{PR}\right]$ $T_0 = \frac{Fh}{\rho c_p \nu} \left[\frac{4x}{hN_{RE}} + \frac{1}{3} N_{PR}\right]$	$T_{2h} = \frac{Fh}{\rho c_p \nu H_n'} \left[\frac{4x}{hN_{RE}} - \frac{b_n'}{a_n'}\right]$ $T_0 = \frac{Fh}{\rho c_p \nu H_n'} \left[\frac{4x}{hN_{RE}} - \frac{b_n'}{a_n'} + B_n'\right]$	$X = \frac{T_0 - T_m}{T_0 - T_{2h}} = \frac{B_n' - \frac{b_n'}{a_n'} h/2}{B_n'}$
$T_{2h} = 4Bx/hN_{RE}$ $h = l_1 + \ldots + l_n$ $T_0 = 4Bx/hN_{RE}$	$T_h = B\left[\frac{4x}{hN_{RE}} - \frac{1}{2} N_{PR}\right]$	$T_h = B\left[\frac{4x}{hN_{RE}} - B_n'\right]$	$Y = \frac{T_0 - T_h}{\frac{d\,T_0}{d\,4x/hN_{RE}}} = B_n'$

the kinematic viscosity of the fluid being represented by ν and the superscript + meaning that the velocity has been made nondimensional by dividing by $\sqrt{\tau_w/\rho}$, where τ_w is the wall shear stress and ρ the fluid density. The mean flow velocity is equal to u_m.

These equations were derived by Jaeger (2) and only have been modified to account for the velocity profile. In a later section similar equations will be derived for flow in circular conduits and may be referred to if it becomes necessary to know how these recurrence formulas were obtained.

The thermal characteristics of the fully developed flow are computed directly from the equations shown in column 2 of Table 1. For instance, in the case of constant heat flux at both surfaces the mean fluid temperature T_m is obtained from a heat balance or

$$T_m = \frac{Fx}{\rho c_p u_m h}$$

and

$$T_w - T_m = \frac{Fh}{\rho c_p \nu}\left[B_n' - \frac{b_n'}{a_n'}\right]$$

The local heat-transfer coefficient defined as

$$H = F/(T_w - T_m)$$

is given by

$$\frac{H(4h)}{K} = \frac{4}{\frac{1}{N_{PR}}[B_n' - b_n'/a_n']}$$

with

$$h = l_1 + \ldots\ldots + l_n$$

In column 3 of Table 1 are shown similar equations for the heat-transfer coefficient, mean fluid temperature, or other important property of the fully developed state for each boundary condition considered. Confirmation of these equations will be discussed in a later section where some numerical results are presented.

It may be added that the boundary conditions need not be limited to those shown in Table 1. Similar solutions are possible whenever the total heat rate or temperature at the wall varies linearly with x as $x \to \infty$. The important case of external wall resistance may be accounted for partially.

Effect of External Resistance

When heat is transferred by a second fluid maintained at constant temperature, the boundary condition at the wall becomes

$$\alpha_1 \frac{\partial T_1}{\partial y} = \frac{H}{\rho c_p}(T_1 - V) \qquad y = 0 \ldots\ldots\ldots\ldots [3]$$

where V represents the second fluid bulk temperature and H corresponds to its heat-transfer coefficient. Such an effect is encountered in most heat exchangers and solutions dealing with constant (4) or parabolic (12) velocity profiles are available. The present method applies to arbitrary velocity and diffusivity profiles.

The Laplace transform of Equation [3] is

$$\frac{\partial \bar{T}_1}{\partial y/h} = \frac{Hh}{\rho c_p \nu}\frac{1}{(\alpha/\nu)_1}\left(\bar{T}_1 - \frac{V}{p}\right) \qquad y = 0$$

The total heat flow Q_0 is when the surface at $y = 2h$ is maintained at zero temperature

$$\bar{Q}_0 = -\left(\frac{\alpha}{\nu}\right)_1 \rho c_p u_m h \frac{1}{p}\left.\frac{\partial \bar{T}_1}{\partial y/h}\right|_{y=0}$$

and the use of series expansions and determinants as prescribed by Jaeger (2) leads to

$$Q_0 = \frac{Hh^2 u_m V}{\nu\left[1 + \frac{Hh}{\rho c_p \nu} R_n'\right]}\left[\frac{4\,x/h}{N_{RE}} + \frac{Hh}{\rho c_p \nu} R_n'\left(b_n - \frac{B_n}{A_n}\right)\right]$$

The corresponding total flux at $y = 2h$

$$Q_{2h} = \frac{Hh^2 u_m V}{\nu\left[1 + \frac{Hh}{\rho c_p \nu} R_n'\right]}\left[\frac{4\,x/h}{N_{RE}} - \frac{b_n + \frac{Hh}{\rho c_p \nu} R_n' \frac{B_n}{A_n}}{1 + \frac{Hh}{\rho c_p \nu} R_n'}\right]$$

The net heat flow is

$$Q_0 - Q_{2h} = \frac{Hh^2 u_m V}{\nu\left[1 + \frac{Hh}{\rho c_p \nu} R_n'\right]} = 2h\rho c_p u_m T_m$$

and the mean fluid temperature of the fully developed flow becomes

$$T_m = \frac{V}{2} b_n \frac{Hh/\rho c_p \nu}{1 + \frac{Hh}{\rho c_p \nu} R_n'}$$

When the temperature at $y = 2h$ varies linearly, superposition of the previous solution with the third case treated in Table 1 becomes possible. Such a superposition technique is valid for all the results given in Table 1 and may be used through proper application to account for various combinations of the boundary conditions shown in Table 1.[3] As mentioned previously, not all types of boundary conditions may be considered. The method of solution fails for constant wall temperature or equal external resistance at the two surfaces. If the latter two cases could be solved, their superposition to the results of Table 1 would yield solutions of the energy equation for all the most important engineering problems.

Flow in Annuli

Thermal characteristics may be derived from the flat-plate equations by means of the transformation

$$\zeta = \ln r$$

The energy equation becomes

$$ur^2 \frac{\partial T}{\partial x} = \frac{\partial}{\partial \zeta}\left(\alpha \frac{\partial T}{\partial \zeta}\right)$$

and subdividing the annulus in a series of cylinders of radius r_i yields

$$U_i \frac{\partial T_i}{\partial x} = \alpha_i \frac{\partial^2 T_i}{\partial \zeta^2} \qquad \ln r_i \leq \zeta_i \leq \ln r_{i-1}$$

where

$$\alpha_i = \frac{1}{\ln r_i/r_{i-1}} \int_{\ln r_{i-1}}^{\ln r_i} \alpha\, d(\ln r)$$

$$U_i = \frac{1}{\ln r_i/r_{i-1}} \int_{\ln r_{i-1}}^{\ln r_i} ur^2 d(\ln r) = \frac{1}{\ln r_i/r_{i-1}} \int_{r_{i-1}}^{r_i} ur\, dr$$

[3] Convection at both surfaces to two fluids at different temperature, and other boundary conditions of this type may be handled with small additional complication.

The flat-plate equations are valid if u_i is replaced by U_i and l_i by $\ln r_i/r_{i-1}$. The velocity and diffusivity distributions are not, however, identical to those for flat-plate flow and may be obtained from equations proposed by Bailey (13).

Flow in Circular Conduits

Equations [2] are the governing differential equations and their corresponding Laplace transforms are

$$\frac{d^2T_i}{dr^2} + \frac{1}{r}\frac{dT_i}{dr} - q_i^2 T_i = 0 \qquad r_{i-1} \leqq r \leqq r_i$$

$$T_{i-1} = T_i$$

$$\alpha_{i-1}\frac{dT_{i-1}}{dr} = \alpha_i \frac{dT_i}{dr} \qquad r = r_{i-1} \qquad i = 2, \ldots\ldots, n-1$$

where

$$q_i = \frac{p^{1/2}}{\alpha_i^{1/2}} u_i^{1/2} \qquad \bar{T}_i = \int_0^\infty e^{-px} T_i dx$$

The outer boundary conditions are

$$\alpha_1 \frac{dT_1}{dr} = \frac{F_0}{\rho c_p}\frac{1}{p} \qquad r = r_0$$

$$\frac{dT_n}{dr} = 0 \qquad r = r_n = 0$$

The present conditions of constant heat rate at the outer surface and no heat transfer at the center line may be modified to include other types of boundary conditions discussed in the previous sections.

Solutions to Equations [3] are of the Bessel form and may be written

$$\bar{T}_i = C_i I_0(q_i r) + D_i K_0(q_i r)$$

The $2n$ boundary conditions become

$$C_1 I_1(q_1 r_0) - D_1 K_1(q_1 r_0) = \frac{F_0}{\rho c_p}\frac{1}{q_1 p}$$

$$C_i I_0(q_i r_i) + D_i K_0(q_i r_i) = C_{i+1} I_0(q_{i+1} r_i) + D_{i+1} K_0(q_{i+1} r_i)$$

$$i = 1, \ldots, n-1$$

$$C_i I_1(q_i r_i) - D_i K_1(q_i r_i) = C_{i+1}\sigma_{i+1} I_1(q_{i+1} r_i) - D_{i+1}\sigma_{i+1} K_1(q_{i+1} r_i)$$

$$D_n = 0$$

Next, consider the determinant Δ_i (shown in square brackets).

$$\Delta_i = \begin{bmatrix}
I_0(q_1r_0) & K_0(q_1r_0) & 0 & 0 & 0 & 0 & \cdots \\
I_0(q_1r_1) & K_0(q_1r_1) & -I_0(q_2r_1) & -K_0(q_2r_1) & 0 & 0 & \cdots \\
I_1(q_1r_1) & -K_1(q_1r_1) & -\sigma_2 I_1(q_2r_1) & \sigma_2 K_1(q_2r_1) & 0 & 0 & \cdots \\
0 & 0 & I_0(q_2r_2) & K_0(q_2r_2) & -I_0(q_3r_2) & -K_0(q_3r_2) & \cdots \\
0 & 0 & I_1(q_2r_2) & -K_1(q_2r_2) & -\sigma_3 I_1(q_3r_2) & \sigma_3 K_1(q_3r_2) & \cdots \\
 & & \cdots & \cdots & \cdots & \cdots & \\
 & & \cdots & \cdots & \cdots & \cdots & \\
\cdots & I_0(q_{i-2}r_{i-2}) & K_0(q_{i-2}r_{i-2}) & -I_0(q_{i-1}r_{i-2}) & -K_0(q_{i-1}r_{i-2}) & 0 & 0 \\
\cdots & I_1(q_{i-2}r_{i-2}) & -K_1(q_{i-2}r_{i-2}) & -\sigma_{i-1} I_1(q_{i-1}r_{i-2}) & \sigma_{i-1} K_1(q_{i-1}r_{i-2}) & 0 & 0 \\
\cdots & 0 & 0 & I_0(q_{i-1}r_{i-1}) & K_0(q_{i-1}r_{i-1}) & -I_0(q_ir_{i-1}) & -K_0(q_ir_{i-1}) \\
\cdots & 0 & 0 & I_1(q_{i-1}r_{i-1}) & -K_1(q_{i-1}r_{i-1}) & -\sigma_i I_1(q_ir_{i-1}) & \sigma_i K_1(q_ir_{i-1}) \\
\cdots & 0 & 0 & 0 & 0 & I_0(q_ir_i) & K_0(q_ir_i)
\end{bmatrix}$$

If in the last row $I_0(q_ir_i)$, $K_0(q_ir_i)$ are replaced by $I_1(q_ir_i)$ and $-K_1(q_ir_i)$ the determinant will be referred to as Ω_i. If in the first row $I_0(q_1r_0)$ becomes $I_1(q_1r_0)$ and $K_0(q_1r_0)$ becomes $-K_1(q_1r_0)$ the determinant will be denoted by δ_i. If both changes are made simultaneously, the determinant will be called ω_i.

All the solutions can be expressed in terms of the four determinants Δ_i, Ω_i, δ_i, and ω_i. The determinants are evaluated by means of Laplace's development of the last two columns

$$\Delta_i = \sigma_i D_{0,1}(q_ir_i, q_ir_{i-1})\Delta_{i-1} - D(q_ir_i, q_ir_{i-1})\,\Omega_{i-1}$$

$$\Omega_i = \sigma_i D_{1,1}(q_ir_i, q_ir_{i-1})\,\Delta_{i-1} - D_{1,0}(q_ir_i, q_ir_{i-1})\Omega_{i-1}$$

where

$$D(q_ir_i, q_ir_{i-1}) = I_0(q_ir_i)K_0(q_ir_{i-1}) - K_0(q_ir_i)\,I_0(q_ir_{i-1})$$

$$D_{r,s}(q_ir_i, q_ir_{i-1}) = \frac{\partial^{r+s} D(q_ir_i, q_ir_{i-1})}{\partial(q_ir_i)^r\,\partial(q_ir_{i-1})^s}$$

and

$$\Delta_1 = -D(q_1r_1, q_1r_0)$$

$$\Omega_1 = -D_{1,0}(q_1r_1, q_1r_0)$$

$$\delta_1 = -D_{0,1}(q_1r_1, q_1r_0)$$

$$\omega_1 = -D_{1,1}(q_1r_1, q_1r_0)$$

The determinants δ_i and ω_i satisfy the same recurrence relations as Δ_i and Ω_i. To obtain the required results, the explicit expressions for these determinants are not needed. Only the first two terms of their expansions in ascending powers of p are necessary. The expansions

$$\Delta_i = (-1)^{i-1}(A_i + B_ip)\frac{1}{\eta_i(p^{1/2})^{i-1}}$$

$$\Omega_i = (-1)^i \frac{1}{\eta_i(p^{1/2})^i}(A_i' + B_i'p)$$

$$\delta_i = (-1)^i (a_i + b_ip)\frac{1}{\eta_i(p^{1/2})^i}$$

$$\omega_i = (-1)^{i-1}\frac{1}{\eta_i(p^{1/2})^{i-1}}(a_i' + b_i'p)$$

where

$$\eta_i = \frac{u_i^{1/2}r_i}{\alpha_i^{1/2}}$$

with

$$\Delta_1 = -\ln\frac{r_1}{r_0}\left[1+\left(\frac{q_1r_0}{2}\right)^2+\left(\frac{q_1r_1}{2}\right)^2\right]+2\left(\frac{q_1r_1}{2}\right)^2-2\left(\frac{q_1r_0}{2}\right)^2$$

$$\Omega_1 = -\frac{1}{q_1r_1}\left[1+\left(\frac{q_1r_1}{2}\right)^2\ln\frac{r_1}{r_0}-(q_1r_1)^2+\left(\frac{q_1r_0}{2}\right)^2\right]$$

$$\delta_1 = \frac{1}{q_1r_0}\left[1+\frac{(q_1r_0)^2}{2}\ln\frac{r_0}{r_1}+\left(\frac{q_1r_1}{2}\right)^2-(q_1r_0)^2\right]$$

$$\omega_1 = \frac{1}{2}\frac{r_1}{r_0}-\frac{1}{2}\frac{r_0}{r_1}-\frac{q_1^2}{4}r_0r_1\ln\frac{r_1}{r_0}$$

are used for this purpose. The results are

$$A_i = (u_i/u_{i-1})(r_i/r_{i-1})^2\left[\frac{\alpha_i^{1/3}}{u_i^{1/3}r_i}A_{i-1}+A'_{i-1}\frac{\alpha_{i-1}^{1/3}}{\alpha_i^{1/3}}\ln\frac{r_{i-1}}{r_i}\right]$$

$$B_i = \frac{u_i}{u_{i-1}}\left(\frac{r_i}{r_{i-1}}\right)^2\left[\frac{\alpha_i^{1/3}}{u_i^{1/3}r_i}B_{i-1}+B'_{i-1}\frac{\alpha_{i-1}^{1/3}}{\alpha_i^{1/3}}\ln\frac{r_{i-1}}{r_i}\right]$$
$$+\frac{u_i^{1/3}r_i}{\alpha_i^{1/3}}A_i\left[\frac{1}{4}\frac{u_i}{u_{i-1}}\left(\frac{r_i}{r_{i-1}}\right)^2+\frac{1}{4}\frac{u_i}{u_{i-1}}\ln\frac{r_{i-1}}{r_i}-\frac{u_i}{u_{i-1}}\right]$$
$$+\frac{u_ir_i^2}{\alpha_i}A'_{i-1}\frac{\alpha_{i-1}^{1/3}}{\alpha_i^{1/3}}\frac{u_i^{1/3}}{u_{i-1}^{1/3}}\frac{r_i}{r_{i-1}}\left[\left(\ln\frac{r_{i-1}}{r_i}\right)\left\{\frac{1}{4}\left(\frac{r_{i-1}}{r_i}\right)^2+\frac{1}{4}\right\}+\frac{1}{2}-\frac{1}{2}\left(\frac{r_{i-1}}{r_i}\right)^2\right]$$

$$A_i' = A'_{i-1}\frac{\alpha_{i-1}}{u_{i-1}^{1/3}r_{i-1}}$$

$$B_i' = \frac{1}{2}A_{i-1}\frac{u_i}{u_{i-1}}\left(\frac{r_i}{r_{i-1}}\right)^2\left[\left(\frac{r_{i-1}}{r_i}\right)^2-1\right]+B'_{i-1}\frac{\alpha_{i-1}^{1/3}}{u_{i-1}^{1/3}r_{i-1}}$$
$$-A'_{i-1}\frac{\alpha_{i-1}^{1/3}}{u_{i-1}^{1/3}r_{i-1}}\left[1-\frac{1}{4}\left(\frac{r_{i-1}}{r_i}\right)^2+\frac{1}{4}\ln\frac{r_{i-1}}{r_i}\right]\frac{u_i}{\alpha_i}r_i^2.$$

The terms a_i, b_i, a_i', b_i' satisfy similar relations

$$a_i = a_{i-1}\frac{\alpha_i^{1/3}u_i^{1/3}}{u_{i-1}\,r_{i-1}}$$

$$b_i = b_{i-1}\frac{\alpha_i^{1/3}u_i^{1/3}}{u_{i-1}\,r_{i-1}}+a_{i-1}\frac{\alpha_i^{1/3}u_i^{1/3}}{u_{i-1}\,r_{i-1}}\left[\frac{1}{4}\frac{r_{i-1}}{r_i}\ln\frac{r_{i-1}}{r_i}\right.$$
$$\left.+\frac{1}{4}-\left(\frac{r_{i-1}}{r_i}\right)^2\right]\frac{u_i}{\alpha_i}r_i^2+a'_{i-1}\frac{u_i^{2/3}}{u_{i-1}^{1/3}}\frac{\alpha_{i-1}^{1/3}}{\alpha_i^{1/3}}\frac{r_i}{r_{i-1}}\ln\frac{r_{i-1}}{r_i}$$

$$a_i' = a_{i-1}\frac{u_i}{u_{i-1}}\left[\frac{1}{2}-\left(\frac{r_i}{r_{i-1}}\right)^2\right]+a'_{i-1}\frac{\alpha_{i-1}^{1/3}}{u_{i-1}^{1/3}r_{i-1}}$$

$$b_i' = b_{i-1}\frac{u_i}{u_{i-1}}\left[\frac{1}{2}-\left(\frac{r_i}{r_{i-1}}\right)^2\right]-a_{i-1}\frac{u_i}{u_{i-1}}\frac{r_i}{r_{i-1}}\frac{u_i}{\alpha_i}r_i^2\frac{r_{i-1}}{r_i}\ln\frac{r_{i-1}}{r_i}$$
$$+a'_{i-1}\frac{\alpha_{i-1}^{1/3}}{u_{i-1}^{1/3}r_{i-1}}\left[\frac{1}{4}\frac{u_i}{\alpha_i}r_i^2\ln\frac{r_i}{r_{i-1}}-\frac{u_i}{\alpha_i}r_i^2\right.$$
$$\left.+\frac{1}{4}\frac{u_i}{\alpha_i}r_{i-1}^2\right]+b'_{i-1}\frac{\alpha_{i-1}^{1/3}}{u_{i-1}^{1/3}r_{i-1}}$$

The starting values for $i = 1$ are determined from the expansions of $\Delta_1, \Omega_1, \delta_1$ and ω_1. The relations are valid from $i = 1$ to $i = n$ if r_0 differs from zero. When r_n equals zero the relations are valid from $i = 1$ to $i = n-1$. The values corresponding to the center interval are computed from

$$A_n = A'_{n-1} \qquad B_n = \left(\frac{u_n}{u_{n-1}}\right)^{1/3}\left(\frac{\alpha_n}{\alpha_{n-1}}\right)^{1/3}\frac{u_n^{1/3}}{\alpha_n^{1/3}}r_{n-1}\frac{A_{n-1}}{2}$$
$$+B'_{n-1}+A'_{n-1}\frac{u_n}{\alpha_n}\frac{r_{n-1}^2}{4}$$

$$a_n = 0$$

$$b_n = \left(\frac{u_n}{u_{n-1}}\right)^{1/3}\left(\frac{\alpha_n}{\alpha_{n-1}}\right)^{1/3}\frac{r_{n-1}}{2}a_{n-1}+b'_{n-1}$$

where for only $i = n$, η_n has been replaced by η_{n-1} in the definitions of Δ_n and δ_n in order to avoid any limiting process as $r_n \to 0$. The wall temperature is given by

$$T_w = \frac{F_0}{\rho c_p}\frac{\alpha_1^{1/3}}{u_1^{1/3}p^{1/3}}\frac{\Delta_n}{\delta_n} = -\frac{F_0}{\rho c_p}\frac{\alpha_1^{1/3}}{u_1^{1/3}}\frac{A_n+B_np}{b_np^2}$$

and its inverse transform is

$$T_w = -\frac{F_0}{\rho c_p u_1^{1/3}}\alpha_1^{1/3}\frac{A_n}{b_n}\left[x+\frac{B_n}{A_n}\right]$$

which compares with the corresponding value of a single cylinder of diameter D and thermal conductivity K

$$T_w = -\frac{F_0D}{2K}\left[\frac{8\,x/D}{N_{RE}N_{PR}}+\frac{1}{4}\right]$$

The mean fluid temperature is obtained from

$$T_m = \frac{4\,F_0x}{\rho c_p u_m D}$$

and the local heat-transfer coefficient becomes

$$H = \frac{F_0}{T_w-T_m} = \frac{\rho c_p u_m D}{4}\frac{A_n}{B_n}$$

Similar expressions may be derived for other types of boundary conditions. The results may be used also to determine the time lag in composite cylinders. Practical problems where the time lag plays an important role are discussed in reference (2).

Numerical Calculations

The numerical steps will be described briefly for flow between parallel plates. Utilizing the usual velocity and diffusivity distributions (5) the following expressions are obtained if the channel between the two plates is subdivided into twelve sections

$$u_1^+/u_m^+ = 2.5/u_m^+ \qquad l_1/h = 5/h^+$$

$$u_2^+/u_m^+ = 1/u_m^+\,[7.5\ln 15 - 2.5\ln 5 - 8.05] \qquad l_2/h = 10/h^+$$

$$u_3^+/u_m^+ = 1/u_m^+\,[10\ln 30 - 5\ln 15 - 8.05] \qquad l_3/h = 15/h^+$$

$$u_4^+/u_m^+ = 1/u_m^+\left[5.5+\frac{10}{h^+-120}\left(\frac{h^+}{4}\ln\frac{h^+}{4}-\frac{h^+}{4}-30\ln 30+30\right)\right] \qquad l_4/h = \frac{h^+-120}{4h^+}$$

$$u_5^+/u_m^+ = 1/u_m^+\left[5.5+10\left(\frac{1}{2}\ln\frac{h^+}{2}-\frac{1}{4}\ln\frac{h^+}{4}-\frac{1}{4}\right)\right] \qquad l_5/h = 1/4$$

$$u_6^+/u_m^+ = 1/u_m^+\left[5.5+5\left(\ln h^+-\frac{1}{2}\ln\frac{h^+}{2}-\frac{1}{2}\right)\right] \qquad l_6/h = 1/8$$

$$(\alpha/\nu)_1 = 1/N_{PR}$$

$$(\alpha/\nu)_2 = 1/N_{PR} + 1 - (22.5 - 5/6)/h^+$$

$$\left(\frac{\alpha}{\nu}\right)_3 = \frac{21}{6} + \frac{1}{N_{PR}} - 105/h^+$$

$$\left(\frac{\alpha}{\nu}\right)_4 = \frac{1}{N_{PR}} - 1 + \frac{4}{2.5(h^+ - 120)}\left[\frac{5h^{+2}}{192} - 450 + \frac{9000}{h^+}\right]$$

$$\left(\frac{\alpha}{\nu}\right)_5 = \frac{1}{N_{PR}} - 1 + 11h^+/120$$

$$\left(\frac{\alpha}{\nu}\right)_6 = \frac{1}{N_{PR}} - 1 + h^+/10$$

where

$$h^+ = \frac{u_m\sqrt{f/8}\,h}{\nu} = \frac{4u_m h}{\nu}\frac{1}{4}\sqrt{f/8}$$

$$u_m^+ = u_m/\sqrt{\tau_w/\rho} = 1/\sqrt{f/8}$$

The half-channel width is denoted by h, and f and u_m represent, respectively, the friction factor and mean velocity. The friction factors were calculated from

$$f = 0.316\left(\frac{4u_m h}{\nu}\right)^{-0.25} \qquad 10^4 \leqq 4u_m h/\nu \leqq 10^5$$

$$f = 0.0032 + 0.221\left(\frac{4u_m h}{\nu}\right)^{-0.237} \qquad 4u_m h/\nu > 10^5$$

The values of a_n, b_n, a_n', b_n', A_n, B_n, A_n', B_n' are obtained readily from Jaeger's equations for a given value of $N_{RE} = 4u_m h/\nu$ and N_{PR}. They have been tabulated in Table 2 for $N_{RE} = 10^4$ and $N_{PR} = 0.01, 0.1, 1, 10$. Excellent agreement between the present results and the values of Martinelli (14) and Seban (15) is noted in Figs. 2 and 3 for the only two types of boundary conditions considered previously. All other results are shown in Fig. 4. Values of Prandtl number larger than 10 or smaller than 0.01 were not considered because more general solutions covering these ranges are derived in the next two sections.

High Prandtl Number Fluids

When the Prandtl number is large $N_{PR} \geqq 100$ the diffusivity distribution consists of a thin laminar layer with high thermal resistance $\alpha/\nu = 0.01$ and of a buffer and turbulent layer where the thermal resistance is very small (for $N_{RE} = 10^4$ (α/ν) is on the average equal to 2 and 13 in the buffer and turbulent layer respectively). An approximate but accurate solution may be obtained, therefore, by subdividing the distance $0 < x < h$ in two sections: A laminar sublayer of width l_1 with diffusivity α_1 and velocity u_1, and a much larger layer $l_1 < x < l_1 + l_2$ with diffusivity α_2 and velocity u_2. For all practical purposes it may be assumed that $u_2 = u_m$ and $l_2 = h$.

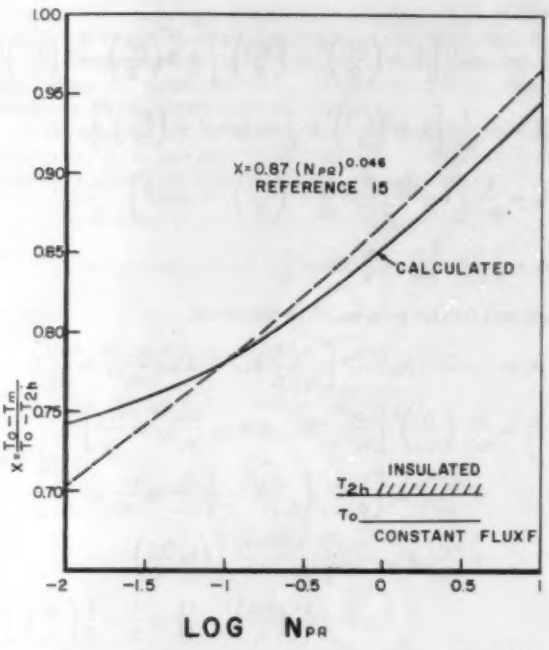

Fig. 2 Forced Convection for Parallel Plates With Heat Through One Side Only

The energy equation for high Prandtl number flow becomes identical with the transient heat-conduction equation across two composite sections. Several such solutions are available in the literature and these results may be simplified considerably by means of the relation $\alpha_2/\alpha_1 \gg 1$. Because $\alpha_2/\alpha_1 \gg 1$ it is possible to utilize equations shown in Carslaw and Jaeger (1) for a slab of thickness l_1 in contact with a well-stirred fluid at the edge of the laminar sublayer. There result

$$\frac{H(4h)}{K} = \frac{4h}{l_1}\frac{e^{-\frac{\alpha_1}{u_m}\frac{x}{l_1 h}} + 2e^{-\frac{\alpha_1}{u_1}\frac{\pi^2}{l_1^2}x} + \cdots}{e^{-\frac{\alpha_1}{u_m}\frac{x}{l_1 h}} + \frac{2}{\pi}e^{-\frac{\alpha_1}{u_1}\frac{\pi^2}{l_1^2}x} + \cdots} \quad \ldots\ldots [4]$$

and

$$\frac{H(4h)}{K} = \frac{4h}{l_1}\frac{1}{1 - \frac{8}{\pi^2}e^{-\frac{\alpha_1}{u_1}\frac{\pi^2}{4}\frac{x}{l_1^2}} - \cdots\cdots} \quad \ldots\ldots [5]$$

TABLE 2 VALUES OF a_n, b_n, ETC.

N_{PR}	A_6	B_6	A'_6	B'_6	a_6	b_6	a'_6	b'_6	A_{12}	B_{12}	A'_{12}	B'_{12}	a_{12}	b_{12}	a'_{12}	b'_{12}
0.01	2.0600	.00337	1	.00538	1	.00396	1.03987	.00147	56.4632	.45544	1	.01867	1	.01867	2.07974	.01000
0.10	2.4903	.02292	1	.03350	1	.01888	1.03987	.00605	31.8740	1.35250	1	.10475	1	.10475	2.07974	.04747
1.00	4.5749	.09717	1	.11974	1	.03154	1.03987	.01319	9.1498	1.28991	1	.30256	1	.30256	2.07974	.09198
10.0	14.0774	.42788	1	.45849	1	.03533	1.03987	.01586	2.9965	1.46005	1	.98763	1	.98763	2.07974	.10518

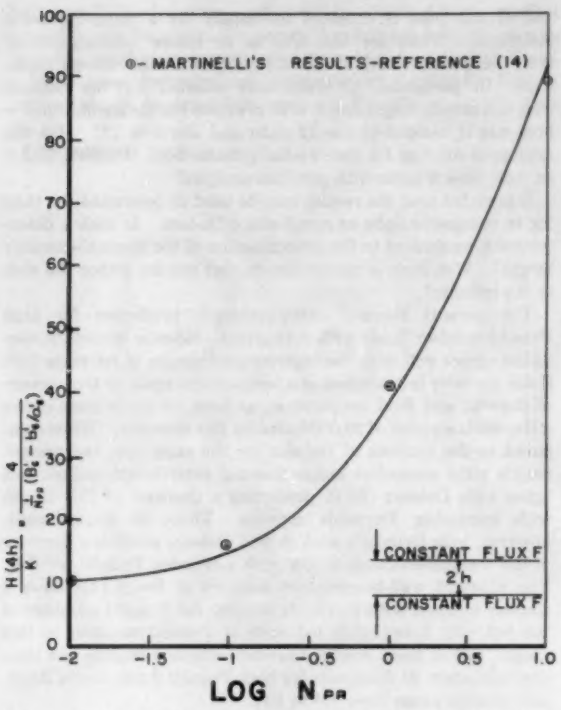

FIG. 3 FORCED CONVECTION FOR PARALLEL PLATES WITH CONSTANT HEAT RATE

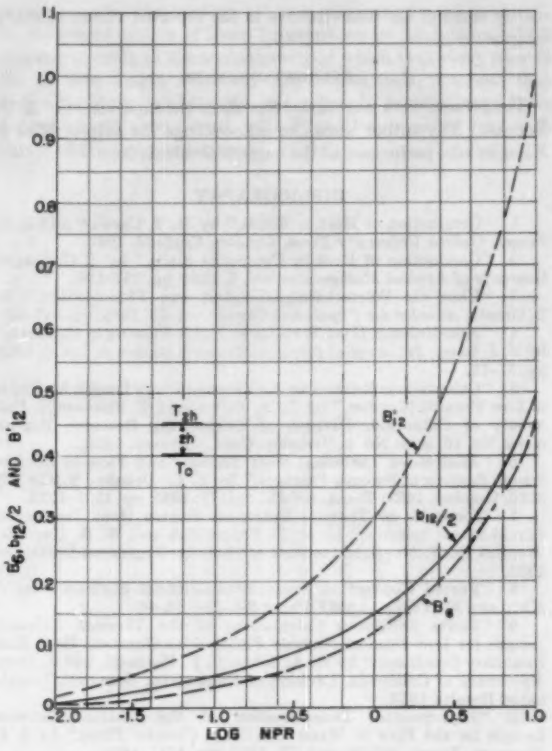

FIG. 4 RESULTS OF CALCULATIONS

for constant wall temperature and constant heat rate, respectively. The corresponding values of the thermal entry length L_e measured in the direction from the start of heating or cooling are equal to

$$\frac{L_e}{4h} = 31.2 \frac{N_{PR}}{N_{RE}\sqrt{f/8}}$$

$$\frac{L_e}{4h} = 112 \frac{N_{PR}}{N_{RE}\sqrt{f/8}}$$

The entry length L_e is defined herewith as the point where the local heat-transfer coefficient is equal to 1.01 times its fully developed value. Also note that l_1^+ was taken equal to 5 in Equations [4] and [5]. When the property variation becomes large, the value of the laminar sublayer l_1^+ depends on the ratio of the viscosity at wall temperature to the viscosity at bulk-fluid temperature. This sublayer thickness was computed by Boelter, Martinelli, and Jonassen (16).

Equations [4] and [5] reveal that the entry length decreases with Reynolds number for high Prandtl-number fluids, which verifies a trend observed by Hartnett (10) and Aladyev (17) in their 5 per cent entry-length values. Also, the entry lengths computed from Equation [5] fall within the range of test results presented by Hartnett after proper correction for the ratio of wall viscosity to bulk viscosity. While the present equations disagree with Berry's statement (4) that the entry length reaches a constant value independently of the Reynolds number, both solutions indicate that eddy diffusivity in the core reduces the values predicted by the slug flow relations and that the entry length does not increase with Reynolds number for high Prandtl number fluids.

Examination of Equations [4] and [5] shows that the value of entry length is dependent upon the type of surface boundary condition while the heat-transfer coefficient approaches the same value

$$\frac{H(4h)}{K} = \frac{4h}{l_1} = \frac{N_{RE}\sqrt{f/8}}{5} \qquad l_1^+ = 5$$

for constant wall temperature or heat flux.

LOW PRANDTL NUMBER FLUIDS

At low Prandtl numbers the eddy diffusivity across the cross section is constant and it becomes necessary only to account for the velocity distribution. Because the effect of velocity profile upon entry length is negligible (7), (18) the use of slug equations has been recommended. The results obtained in the preceding section demonstrate that the slug equations would give values slightly too large, and therefore conservative. The heat-transfer coefficients for very low Prandtl may be calculated from the relations derived in the first sections of this paper.

The following simplification is noted

$$R_i = \frac{l_i/h}{\alpha_i/\nu} = N_{PR}\frac{l_i}{h}$$

Entry lengths for Prandtl number values between 1 and 100 may be calculated by subdividing the flow system into a laminar sublayer and a buffer layer in contact with a well-stirred fluid at the edge of the buffer layer. For $0.01 < N_{PR} < 0.1$ the following two sections may be utilized: A joint laminar and buffer layer, and a layer corresponding to the turbulent core. While such solutions are expected to be approximate, they may help to

clarify some of the discrepancies in the reported values of entry lengths.

Acknowledgments

The present work was carried out under the supervision of R. D. Brooks. The author wishes to acknowledge the help of Miss J. Klingler who performed all the numerical calculations.

BIBLIOGRAPHY

1 "Conduction of Heat in Solids," by H. S. Carslaw and J. C. Jaeger, Oxford University Press, London, England, 1947.

2 "Conduction of Heat in Composite Slabs," by J. C. Jaeger, *Quarterly of Applied Mathematics*, vol. 8, 1950, pp. 187–198.

3 "Über die Wärmeleitungsfähigkeit von Flüssigkeiten," by L. Graetz, *Annalen der Physik und Chemie*, vol. 25, 1885, pp. 337–357.

4 "Non-Uniform Heat Transfer to Fluids Flowing in Conduits," by V. J. Berry, Jr., *Applied Scientific Research*, section A, vol. 4, 1953, pp. 61–75.

5 "Calculations Relative to the Thermal Entry Length for Fluids of Low Prandtl Number," by R. A. Seban and T. Shimazaki, University of California, Division of Engineering Research Report, series No. 16, issue No. 4, Berkeley, Calif., January, 1950.

6 "Analysis of Turbulent Heat Transfer and Flow in the Entrance Regions of Smooth Passages," by R. G. Deissler, NACA TN 3016, October, 1953; Trans. ASME, vol. 77, 1955, pp. 1221–1233.

7 "Remarks on Thermal Entrance—Region Heat Transfer in Liquid-Metal Systems," by H. F. Poppendiek and W. B. Harrison, Preprint No. 7, American Institute of Chemical Engineers, December, 1953.

8 "Forced Convection From Nonisothermal Surfaces," by J. Klein and M. Tribus, ASME Paper No. 53—SA-46.

9 "Finite Difference Calculations of the Thermal Entrance Length for Low Prandtl Number Fluids With Constant Heat Rate Boundary Condition," by R. A. Seban, J. P. Hartnett, and S. Levy, University of California, Division of Engineering Research, Unpublished Results, 1953.

10 "Experimental Determination of the Thermal-Entrance Length for the Flow of Water and Oil in Circular Pipes," by J. P. Hartnett, Trans. ASME, vol. 77, 1955, pp. 1211–1220.

11 "Der Wärmeübergang an einen turbulenten Flüssigkeits-oder Gasstrom," by H. Latzko, *Zeitschrift für angewandte Mathematik und Mechanik*, vol. 1, 1921, pp. 268–290.

12 "Heat Transfer in Laminary Flow Between Parallel Plates," by J. A. Prins, J. Mulder, and J. Schenk, *Applied Scientific Research*, vol. A2, 1950, pp. 431–438.

13 "Heat Transfer to Liquid Metals in Concentric Annuli," by R. V. Bailey, Oak Ridge National Laboratory Report, No. 521, 1950.

14 "Heat Transfer to Molten Metals," by R. C. Martinelli, Trans. ASME, vol. 69, 1947, pp. 947–959.

15 "Heat Transfer to a Fluid Flowing Turbulently Between Parallel Walls With Asymmetric Wall Temperatures," by R. A. Seban, Trans. ASME, vol. 72, 1950, pp. 789–795.

16 "Remarks on the Analogy Between Heat Transfer and Momentum Transfer," by L. M. K. Boelter, R. C. Martinelli, and F. Jonassen, Trans. ASME, vol. 63, 1941, pp. 447–455.

17 "Experimental Determination of Local and Mean Coefficients of Heat Transfer for Turbulent Flow in Pipes," by I. T. Aladyev, NACA TM 1356, February, 1954.

18 "Heat Transfer to Constant-Property Laminar Boundary-Layer Wedge Flows With Stepwise and Arbitrary Wall-Temperature Variation," by S. Scesa and S. Levy, Trans. ASME, vol. 76, 1954, pp. 279–286.

Discussion

J. P. Hartnett.[4] The author is to be commended for having undertaken the formidable task of solving the problem of composite cylinders and also for pointing out how additional useful convection solutions may be obtained from the text of Carslaw and Jaeger (1).[5]

The solution of the energy equation in the case of the channel and of the pipe is obtained essentially by a finite-difference technique. What are the criteria to insure convergence of the "composite solution" to the solution of the energy equation? In particular, 12 slabs were selected for the channel case and excellent agreement with previous results are obtained—how was it decided to use 12 slabs and not 6 or 18? Has the analogous solution for the circular cylinder been obtained, and if so, how does it agree with previous analysis?

It is stated that the results may be used to determine the time lag in composite slabs or composite cylinders. Is such a determination equivalent to the determination of the thermal-entrance length? Was such a calculation carried out for either the slab or the cylinder?

The present thermal entrance-length prediction for high Prandtl-number fluids with a constant heat-rate boundary condition agrees well with the experimental results of reference (10) if the viscosity is evaluated at a temperature equal to the average of the wall and fluid temperature, at least for those cases above a Reynolds number of 20,000 based on this viscosity. When compared to the analysis of Deissler for the same case the present results yield somewhat longer thermal entry-length values, but agree with Deissler (6) in predicting a decrease of this length with increasing Reynolds number. There is disagreement, however, with Deissler's work in that Deissler predicts a decrease of the thermal-entrance length with increasing Prandtl number. The constant wall-temperature analysis of Berry (4) shows a marked increase with Reynolds number for Prandtl numbers of 100 but only a negligible influence of Prandtl numbers in this range. All of these analyses predict entrance lengths less than approximately 20 diameters for high Prandtl fluids over a Reynolds number range from 10^3 to 10^5.

The asymptotic Nusselt value predicted by Levy for the high Prandtl case appears questionable in that it is independent of the Prandtl modulus and in addition yields values which are considerably lower than obtained experimentally for Reynolds values of the order of 10^5.

Herbert Saunders.[6] The author has continued the trend of applying finite-difference methods to heat-transfer problems involving varied boundary conditions which either cannot be solved or solved with difficulty by analytical means. The important thing to be considered in all finite-difference approaches is the stability of the system equation. Many authors have given necessary solutions for stability and convergence of the heat-flow equation. In applying Jaeger's method, the author has not shown the stability limits of the solutions. This is extremely important because these limits convey the necessary information concerning the allowable mesh size and, in addition, the numerical errors in "rounding-off" procedure. Has the author done any further work on this problem concerning its stability?

Author's Closure

The author wishes to thank Professor Hartnett and Mr. Saunders for their comments. He agrees with their statement that the method presented is essentially one of finite difference and that stability of the equations needs further condideration. The complexity of the equations, however, eliminates the possibility of a simple stability criterion and a logical substitute would be to try various numbers of steps and ascertain that the choice is satisfactory by comparison with available results or between each set of calculations.

In order to determine the thermal-entry length it is necessary to find the zero of the determinant Δ_4. As Jaeger points out in

[4] Assistant Professor of Mechanical Engineering, University of Minnesota, Minneapolis, Minn. Assoc. Mem. ASME.

[5] Numbers in parentheses refer to the references in the Bibliography at the end of the paper.

[6] Research Engineer, Grumman Aircraft Engineering Corporation, Bethpage, L. I., N. Y. · Assoc. Mem. ASME.

his paper,[7] a crude approximation can be obtained to the smallest zero of Δ_i and its application shows that it is not accurate enough to yield a satisfactory answer to the thermal-entry-length problem.

Dr. Hartnett indicates that the asymptotic value of the Nusselt number should be dependent upon the Prandtl modulus. This is not true for the analogy solution as demonstrated by fig. 74 in the second edition of Heat Transmission by McAdams. This is a shortcoming of the analogy method which may carry over in the entrance-length solution. The author feels, however, that Deissler's work exhibits the same trend, namely, very little dependence of entry length with Prandtl number at very high values of the latter parameter.

[7] See reference (2) in paper

Effect of Vapor Velocity on Laminar and Turbulent-Film Condensation

By W. M. ROHSENOW,[1] J. H. WEBBER,[2] and A. T. LING,[3] CAMBRIDGE, MASS.

The liquid condensate layer (film) on vertical plates or tubes under the influence of the gravity force flows downward in essentially laminar flow over the upper part of the surface but may change to turbulent flow over the lower part if the condensation rate is sufficiently high. Colburn (1)[4] reviewed the results of Kirkbride and developed a correlation equation based on a very elementary description of the condensate layer which was considered to be composed of a laminar sublayer and a turbulent outer region. The laminar layer was considered to have the sole resistance to heat transfer. This type of analysis was extended by Carpenter and Colburn (2, 3) to include the effect of vapor shear stress. Seban (4) performed an analysis of the turbulent condensate film assuming the existence of the "universal velocity distribution" of Prandtl-Nikuradse. The calculated results extend over a wide range of Prandtl numbers and agree well with the empirical results of Colburn (1) in the range $N_{Pr} = 2$ to 5. This paper presents analyses showing the effect on rates of condensation of vapor shear stress at the liquid-vapor interface. Both laminar and turbulent films are considered and are combined to give analytical results for the case of laminar flow on the upper portion of a plate and turbulent flow on the lower portion. The analysis of the turbulent film is essentially an extension of the one presented by Seban (4). The system considered is a vertical flat plate, Fig. 1, with pure saturated vapor condensing on the plate whose temperature is uniform. Flow acceleration and momentum changes are neglected in the analysis. The physical properties are assumed to be constant.

Nomenclature

The following nomenclature is used in the paper:

a = thermal diffusivity, $k/\rho c$, sq ft per hr
c = specific heat, Btu/lb$_m$ deg F
$F_1 \equiv 5.5 + 2.5 \ln x_0^+$, Equation [17]
F_2 = right-hand side of Equation [23]
g = acceleration of gravity, ft/hr^2
g_0 = conversion factor, 4.16×10^8 lb$_m$ ft/lb$_f$ hr^2
G = mass velocity, lb$_m$/hr sq ft
h = heat-transfer coefficient, Btu/hr sq ft deg F
h_{fg} = latent heat of vaporization, Btu/lb$_m$
$h'_{fg} = h_{fg} + (3/8)c(\Delta t)$
k = thermal conductivity, Btu/hr ft deg F
L = height of plate or tube
$M \equiv 1/(1 + \tau_v^*/x_0^*)$, Equation [24]
q = heat-transfer rate, Btu/hr
t = temperature, deg F
Δt = temperature difference across condensate film, deg F
t_{sat} = saturation temperature, deg F
v_z = velocity in z-direction, fph
w = flow rate, lb$_m$/hr
x, x_0, Y, z = linear distances defined in Fig. 1, ft
x^+, v^+ = defined in Equation [17]
z^*, x_0^*, τ_v^* = defined in Equation [7]
ρ = density, lb$_m$/cu ft
μ = viscosity, lb$_m$/ft hr
ν = kinematic viscosity, sq ft per hr
τ = shear stress
$\Gamma = w/Y$, flow rate per unit perimeter or width, lb$_m$/hr ft
ϵ_h, ϵ_m = eddy diffusivity of heat and momentum

Subscripts

m = mean value over $z = 0$ to L
t = transition point
v = vapor (properties without subscript refer to liquid)
z = local value at z
L = total length

Laminar Film

A force balance on the element of liquid between x and x_0, Fig. 1, is

$$\tau = \frac{g}{g_0}(\rho - \rho_v)(x_0 - x) + \tau_v \quad \ldots\ldots [1]$$

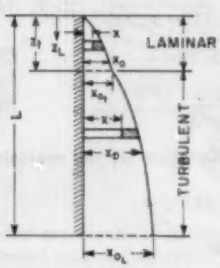

Fig. 1(a)

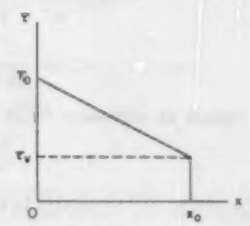

Fig. 1(b)

which is a linear distribution of τ as shown in Fig. 1. Since $\tau = \tau_0$ at $x = 0$

$$\tau_0 = \frac{g}{g_0}(\rho - \rho_v)x_0 + \tau_v \quad \ldots\ldots [2]$$

Actually, Equation [1] should include terms representing the z-direction momentum flow across each of the faces of the element. (The effect of these terms is usually quite small.) The effect of the momentum crossing the element faces within the liquid is

[1] Associate Professor of Mechanical Engineering, Massachusetts Institute of Technology. Mem. ASME.
[2] Lieutenant, USN; Research Assistant, Department of Mechanical Engineering, Massachusetts Institute of Technology.
[3] Research Assistant, Department of Mechanical Engineering, Massachusetts Institute of Technology. Assoc. Mem. ASME.
[4] Numbers in parentheses refer to the Bibliography at the end of the paper.

Contributed by the Heat Transfer Division and presented at the Annual Meeting, New York, N. Y., November 28–December 3, 1954, of The American Society of Mechanical Engineers.
Note: Statements and opinions advanced in papers are to be understood as individual expressions of their authors and not those of the Society. Manuscript received at ASME Headquarters, August 27, 1954. Paper No. 54—A-145.

quite small. To include the effect at the liquid-vapor interface the momentum term which should be added to Equation [1] is $(1/g_0)v_{s,x0}d\Gamma$. This represents the z-direction velocity of the vapor crossing at the liquid-vapor interface which is very nearly equal to the liquid surface velocity $v_{s,x0}$ and not the velocity of the vapor flow in the main vapor stream. This momentum term also is usually quite small.

In laminar flow $\tau = (\mu/g_0)dv_x/dx$. Replacing τ by this in Equation [1] and integrating with τ_v constant

$$v_x = \frac{g(\rho - \rho_v)}{\mu}\left(x_0 x - \frac{x^2}{2}\right) + \frac{g_0\tau_v}{\mu}x \quad \ldots\ldots [3]$$

Defining

$$\Gamma \equiv \int_0^x \rho v_x dx$$

Then

$$\Gamma = g\frac{(\rho - \rho_v)}{\nu}\frac{x_0^3}{3} + \frac{g_0\tau_v}{\nu}\frac{x_0^2}{2} \quad \ldots\ldots [4]$$

$$\frac{d\Gamma}{dx_0} = g\frac{\rho - \rho_v}{\nu}x_0^2 + \frac{g_0\tau_v}{\nu}x_0 \quad \ldots\ldots [5]$$

On the basis of the assumptions made thus far, the temperature distribution in the liquid film will be linear (5). Then an energy balance on the control element, Fig. 1, assuming a linear temperature distribution (5) across the film, is

$$\frac{k\Delta t}{x_0}dx = h'_{fg}d\Gamma = h\Delta t\,dx \quad \ldots\ldots [6]$$

where $h'_{fg} = h_{fg} + (3/8)c_p(\Delta t)$ which is the enthalpy change per pound in condensing from saturated vapor to liquid at the mean temperature of the liquid film.

Equating expressions for $d\Gamma$ from Equations [5] and [6] and integrating from $x_0 = 0$ at $x = 0$

$$x^* = (x_0^*)^4 + \frac{4}{3}\tau_v^*(x_0^*)^3 \quad \ldots\ldots [7]$$

where

$$x^* = \frac{4x\Delta t}{N_{Pr}}\frac{c_p}{h'_{fg}}\left(\frac{g}{\nu^2}\right)^{1/3}\frac{1}{(1 - \rho_v/\rho)} \quad \ldots\ldots [7a]$$

$$x_0^* = [x_0/(\nu^2/g)^{1/3}] \quad \ldots\ldots [7b]$$

$$\tau_v^* \equiv \frac{g_0\tau_v}{g(\rho - \rho_v)(\nu^2/g)^{1/3}} \quad \ldots\ldots [7c]$$

Obtain an expression for dx from Equation [7] and evaluate

$$h_m = (1/x_L)\int_0^{x_L}(k/x_0)dx$$

The result may be written in the form

$$\frac{h_m}{k}\left(\frac{\nu^2}{g}\right)^{1/3} = \frac{4}{3}\frac{(x_{0L}^*)^3}{x_L^*} + 2\tau_v^*\frac{(x_{0L}^*)^2}{x_L^*} \quad \ldots\ldots [8]$$

where $x_0 = x_{0L}$ at $x = x_L$. Equation [4] may be rewritten in the form

$$\frac{4\Gamma}{\mu}\frac{1}{(1 - \rho_v/\rho)} = \frac{4}{3}(x_{0L}^*)^3 + 2\tau_v^*(x_{0L}^*)^2 \quad \ldots\ldots [9]$$

The results plotted for the laminar region in Figs. 3, 5, and 7 are obtained by eliminating x_{0L}^* between Equations [7] and [8]. Similarly, x_{0L}^* may be eliminated between Equations [8] and [9] with the laminar-zone results as shown in Figs. 4, 6, and 8.

Figs. 3, 5, 7 relate the dimensionless heat-transfer coefficient with a dimensionless plate height. In Figs. 4, 6, 8 it is shown as a function of the liquid-film Reynolds number at the bottom.

Transition, Laminar to Turbulent Film

In the absence of the effect of vapor shear stress, McAdams (6) suggests the transition from laminar to turbulent films occurs when $4\Gamma/\mu = 1800$. When the vapor shear stress is significant, it is reasonable to expect transition to occur with much thinner films and hence at lower values of $4\Gamma/\mu$. Indeed, at high values of vapor shear stress Carpenter and Colburn (2) found transition to occur at values of $4\Gamma/\mu$ as low as 200 or 300.

The transition Reynolds number for flow in a pipe filled with a single-phase fluid is $(DV/\nu)_{trans} = 2000$. This may be rewritten with $\tau_0 = f\rho V^2/2g_0$ and $f = 0.046/(DV/\nu)^{0.2}$ in the form

$$\left(\frac{D}{\nu}\sqrt{\frac{g_0\tau_0}{\rho}}\right)_{trans} = 140 \quad \ldots\ldots [10]$$

where $\sqrt{g_0\tau_0/\rho}$ has the dimensions of velocity and has been called the "friction velocity."

Carpenter (7) has suggested that Equation [10] be considered the criterion for transition in a liquid film of a partially filled pipe. For a particular size pipe and set of conditions of the liquid (physical properties ν and ρ) this implies that transition will occur at a particular value of τ_0 which is independent of τ_v.

This same type of criterion, τ_0 at transition independent of τ_v, may be applied to the flat-plate case. From Equation [4] the expression for Γ with $\tau_v = 0$ may be inserted in the equation for the transition Reynolds number when $\tau_v = 0$ which is $(4\Gamma/\mu) = 1800$. The results solved for x_0 is

$$x_{0t} = \left[\frac{1350(\nu^2/g)}{(1 - \rho_v/\rho)}\right]^{1/3} \quad \ldots\ldots [11]$$

or from Equation [2] with $\tau_v = 0$

$$\tau_{0t} = \frac{g}{g_0}(\rho - \rho_v)\left[\frac{1350(\nu^2/g)}{(1 - \rho_v/\rho)}\right]^{1/3} \quad \ldots\ldots [12]$$

This then is also the expression for τ_{0t} when $\tau_v \neq 0$. Equating the expressions for τ_0 from Equations [2] and [12]

$$\frac{g}{g_0}(\rho - \rho_v)(x_0)_{trans} + \tau_v = \frac{g}{g_0}(\rho - \rho_v)\left[\frac{1350(\nu^2/g)}{(1 - \rho_v/\rho)}\right]^{1/3}$$

which may be rearranged and written as

$$x_{0t}^* = \frac{11.05}{(1 - \rho_v/\rho)^{1/3}} - \tau_v^* \quad \ldots\ldots [13]$$

This may be substituted for x_{0t}^* in the expression for Reynolds number, Equation [9]. Then

$$\left(\frac{4\Gamma}{\mu}\right)_{trans} = 1800 - 246(1 - \rho_v/\rho)^{1/3}\tau_v^* + 0.667(1 - \rho_v/\rho)(\tau_v^*)^3 \quad \ldots\ldots [14]$$

These equations for the transition condition have only a limited applicability to the region of low and moderate values of τ_v^* because when $\tau_v^* > 11.05/(1 - \rho_v/\rho)^{1/3}$ Equation [13] requires x_{0t}^* to be negative.

For very high values of τ_v^* it is quite probable that x_0 approaches a limiting value, perhaps that of the laminar sublayer thickness which exists in ordinary full pipe flow. Carpenter (7) suggests the following magnitude for this thickness

$$x_{0t}^+ = \frac{x_0}{\nu}\sqrt{\frac{g_0\tau_0}{\rho}} = 6 \quad \ldots\ldots [15]$$

Ordinarily a magnitude of 5 expresses the laminar sublayer thickness. Actually an appropriate value is somewhere between 5 and perhaps 10. The 6 is arbitrarily chosen. Substitute into Equation [15] the expression for τ_s from Equation [2] and rearrange to get

$$(x_{0t}^*)^3 + (x_{0t}^*)^2\tau_v^* = \frac{36}{1 - \rho_v/\rho} \quad \ldots\ldots\ldots [16]$$

This result will apply for high values of τ_v^*. When the resulting (x_{0t}^*) calculated from Equation [13] is less than its value calculated from Equation [16], the latter value is used. The transition condition Equation [16] may be expressed in terms of $(4\Gamma/\mu)_{trans}$ by a trial-and-error calculation eliminating x_{0t}^* between Equations [9] and [16]. These results are plotted in Fig. 2.

There are very few good data available to establish the conditions under which transition occurs when there is a significant vapor shear stress. A single point can be obtained from the ethanol data of Carpenter (7). In terms of the present analysis these data are at $\tau_v^* = 110$ and $(4\Gamma/\mu)_{trans} = 96.5$, which agrees very well with $(4\Gamma/\mu)_{trans} = 71.8$ from Equations [16] and [9] or from extended Fig. 5. In terms of x_{0t}^+ the extrapolated data have the value of 6.9, which is close to the 6 of Equation [15].

Although the criterion for transition as portrayed by Fig. 2 has not been adequately substantiated, the results are nevertheless quite reasonable and are probably not seriously in error. This entire phenomenon of transition as affected by vapor shear stress must be investigated by obtaining much more experimental data. In spite of lack of adequate substantiation it seems reasonable to select the transition criterion as shown in Fig. 2 for use in the present analysis.

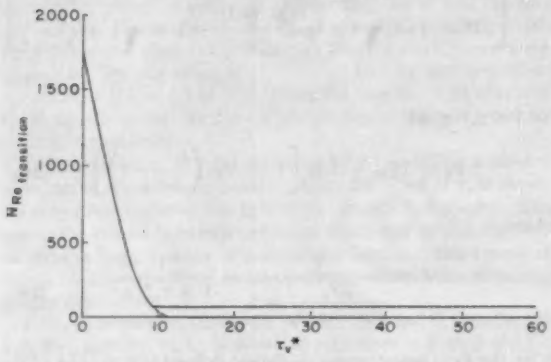

Fig. 2

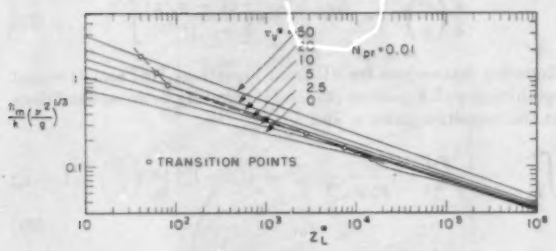

Fig. 3

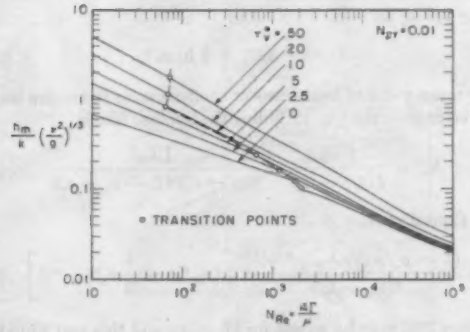

Fig. 4

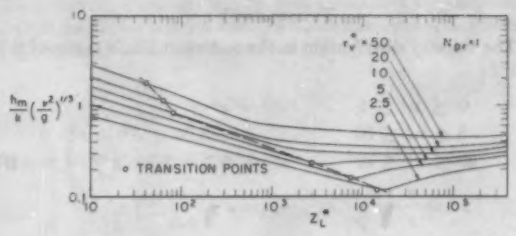

Fig. 5

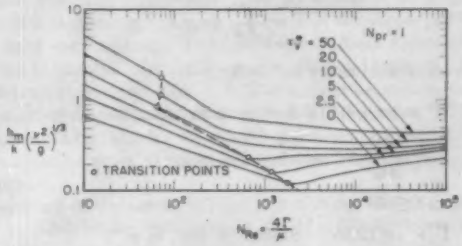

Fig. 6

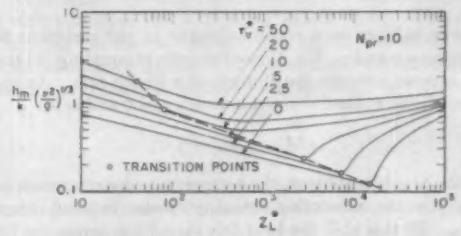

Fig. 7

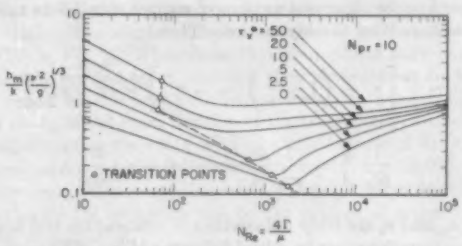

Fig. 8

Turbulent Film

The velocity distribution in the turbulent film is assumed to be (8)

$$\left.\begin{array}{ll} 0 \le x^+ \le 5 & v^+ = x^+ \\ 5 \le x^+ \le 30 & v^+ = -3.05 + 5.0 \ln x^+ \\ 30 \le x^+ \le x_0^+ & v^+ = 5.5 + 2.5 \ln x^+ \\ x^+ \equiv \dfrac{x}{\nu}\sqrt{\dfrac{g_0\tau_0}{\rho}} & v^+ \equiv v\sqrt{\dfrac{\rho}{g_0\tau_0}} \end{array}\right\} \quad [17]$$

From this distribution the flow rate

$$\Gamma = \int_0^{x_0} \rho v_x \, dx$$

may be evaluated as for $x_0^+ > 30$

$$\left.\begin{array}{l} \Gamma = \rho\nu(-64 + 3x_0^+ + 2.5x_0^+ \ln x_0^+) \\ \dfrac{d\Gamma}{dx_0^+} = \rho\nu(5.5 + 2.5 \ln x_0^+) \\ \text{for } 5 < x_0^+ \le 30 \\ \Gamma = \rho\nu(12.55 - 8.05x_0^+ + 5x_0^+ \ln x_0^+) \\ \dfrac{d\Gamma}{dx_0^+} = \rho\nu(-3.05 + 5 \ln x_0^+) \end{array}\right\} \quad [18]$$

A force balance on a control element in the turbulent liquid film between x and x_0, Fig. 1, results again in equating [1] and [2] which express a linear distribution of τ in the film. An energy balance for the control element between $x = 0$ and x_0 is

$$(q/A)_0 = h_{fg}(d\Gamma/dz) \quad [19]$$

Since the film is turbulent, the temperature distribution is nearly uniform; so the subcooling enthalpy change is small compared with h_{fg}. In this case the heat flux is uniform across the film or $q = q_0$.

The heat-transfer and momentum-transfer processes in turbulent flow may be expressed as sums of components due to molecular motion and due to eddy motion. Then

$$\frac{g_0\tau}{\rho} = \frac{g_0}{\rho}\left[\tau_v + \left(1 - \frac{x}{x_0}\right)(\tau_0 - \tau_v)\right] = (\nu + \epsilon_m)\frac{dv}{dx} \quad [20]$$

$$\frac{1}{\rho c_p}\frac{q}{A} = \frac{1}{\rho c_p}\frac{q_0}{A} = -(a + \epsilon_h)\frac{dt}{dx} \quad [21]$$

where ϵ_m and ϵ_h are eddy diffusivities of momentum and heat.

These equations may be solved following Martinelli's procedure (9) for a fluid flowing turbulently in a full pipe. As in that solution ν may be neglected compared with ϵ_m in the region $x^+ > 30$ and $(1 - x/x_0) \cong 1$ in the region $x^+ < 30$. Also it has been found that experimental determinations of the ratio of ϵ_h/ϵ_m for flow in full pipes have resulted in values ranging from 1.0 to 1.7. The assumption of $\epsilon_h = \epsilon_m$ is found to lead to results which are in agreement with heat-transfer data. This assumption will be made here.

Equations [20] and [21] may be solved for ϵ/ν with τ_0 given by Equation [2] with the result

$$\frac{\epsilon}{\nu} = \frac{\dfrac{g_0\tau_v}{\rho\nu} + \dfrac{g}{\nu}\left(1 - \dfrac{\rho_v}{\rho}\right)(x_0 - x)}{dv/dx} \quad [22]$$

The expressions for dv/dx in the three regions of flow are obtained by differentiating Equations [9]. Then with ϵ/ν given by Equation [22], Equation [21] may be integrated in the three flow regions to obtain the temperature distribution. The results for the temperature difference between the liquid-vapor interface and the wall surface is

$$\frac{(t_{x0} - t_w)}{(q/A)_0}\rho c_p\sqrt{\frac{g(1 - \rho_v/\rho)x_0}{M}} = F_2 \quad [23]$$

for $x_0^+ > 30$

$$F_2 \equiv 5N_{Pr} + 5\ln(1 + 5N_{Pr}) + \frac{2.5}{\sqrt{1 + \dfrac{10M}{N_{Pr}x_0^+}}} \ln\left[\frac{2M - 1 + \sqrt{1 + \dfrac{10M}{N_{Pr}x_0^+}}\,\dfrac{60M}{x_0^+} - 1 - \sqrt{1 + \dfrac{10M}{N_{Pr}x_0^+}}}{2M - 1 - \sqrt{1 + \dfrac{10M}{N_{Pr}x_0^+}}\,\dfrac{60M}{x_0^+} - 1 + \sqrt{1 + \dfrac{10M}{N_{Pr}x_0^+}}}\right] \quad [24a]$$

for $5 < x_0^+ \le 30$

$$F_2 \equiv 5N_{Pr} + 5\ln\left[1 + N_{Pr}\left(\frac{x_0^+}{5} - 1\right)\right] \quad [24b]$$

where

$$M \equiv \frac{1}{\dfrac{g_0\tau_v}{g(\rho - \rho_v)x_0} + 1} = \frac{1}{1 + \tau_v^*/x_0^*} \quad [24c]$$

With the local heat-transfer coefficient defined as $h \equiv (q/A)_0/(t_{x0} - t_w)$, Equation [23] may be rearranged in the form

$$\frac{h}{k}\left(\frac{\nu^2}{g}\right)^{1/3} = \frac{N_{Pr}(x_0^+)^{1/3}}{F_2}\left[\frac{(1 - \rho_v/\rho)}{M}\right]^{1/3} \quad [25]$$

Equating expressions for $d\Gamma$ from Equations [18] and [19] and combining with Equation [25] and integrating between conditions at the transition point z_t and L

$$\int_{x_{0t}^+}^{x_{0L}^+} \frac{F_1F_2M^{1/3}}{(x_0^+)^{1/3}(1 - \rho_v/\rho)^{1/3}}\,dx_0^+ = (t_{x0} - t_w)\frac{c_p}{h_{fg}}\left(\frac{g}{\nu^2}\right)^{1/3}(L - z_t) \quad [26]$$

where for $x_0^+ > 30$

$$F_1 \equiv 5.5 + 2.5 \ln x_0^+ \quad [27a]$$

for $5 < x_0^+ \le 30$

$$F_1 \equiv -3.05 + 5 \ln x_0^+ \quad [27b]$$

The mean value of heat-transfer coefficient for the entire length of the layer from the top, including the laminar film is

$$h_m = \frac{\Gamma h_{fg}}{L(t_{x0} - t_w)} = \frac{\Gamma h_{fg}}{(t_{x0} - t_w)(L - z_t + z_t)} \quad [28]$$

From Equation [7]

$$z_t = \frac{(1 - \rho_v/\rho)N_{Pr}h_{fg}'(\nu^2/g)^{1/3}}{4(t_{x0} - t_w)c_p}\left[(x_{0t}^*)^4 + \frac{4}{3}\tau_v^*(x_{0t}^*)^3\right] \quad [29]$$

Equation [26] may be solved for $(L - z_t)$ and this and Equation [29] substituted into Equation [28] with the result

$$\frac{h_m}{k}\left(\frac{\nu^2}{g}\right)^{1/3} = \frac{\dfrac{\Gamma}{\rho\nu}N_{Pr}}{\displaystyle\int_{x_{0t}^+}^{x_{0L}^+}\frac{F_1F_2}{(x_0^+)^{1/3}}\left[\frac{M}{(1-\rho_v/\rho)}\right]^{1/3}dx_0 + \left(1-\frac{\rho_v}{\rho}\right)N_{Pr}\left[\frac{1}{4}(x_{0t}^*)^4 + \frac{\tau_v^*}{3}(x_{0t}^*)^3\right]} \quad [30]$$

Evaluations of Equation [30] at various values of τ_v^* and N_{Pr} have been made by calculating the integral numerically and the results plotted in Figs. 3 through 8. The value of x_{0t}^* at transition is taken from either Equation [13] or [16] whichever is the larger.

Discussion of Results

In all of these calculations for Figs. 3 through 8 the quantity $(1 - \rho_v/\rho)$ was taken as unity; e.g., ρ_v/ρ small. This is a good assumption except at pressures approaching the critical pressure of the fluid. It was also assumed that τ_v and $(t_{s0} - t_w)$ were uniform along the plate. Equation [3] may be readily evaluated accounting for any value of $(1 - \rho_v/\rho)$ and for any prescribed variation of $(t_{s0} - t_w)$ or of τ_v along the length. The effects of these variations are functions of the particular geometry and are difficult to generalize.

The results for $\tau_v = 0$ are presented by Seban (4) for a number of values of N_{Pr} between 0 and 5. Here the effect of τ_v is shown for only a few values of N_{Pr} to limit the quantity of graphs. The value $N_{Pr} = 0.01$ is representative of liquid metals and $N_{Pr} = 1$ to 10 of a large number of nonmetallic liquids. The curves of Seban for $\tau_v = 0$ will aid in interpolating between the three N_{Pr} graphs drawn here.

From cross plots of the results in Figs. 4, 6, and 8, the effect of τ_v^*, N_{Re}, and N_{Pr} on h_m is shown as solid lines in Figs. 9 and 10.

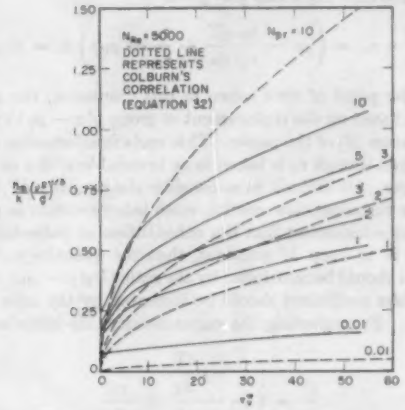

Fig. 9

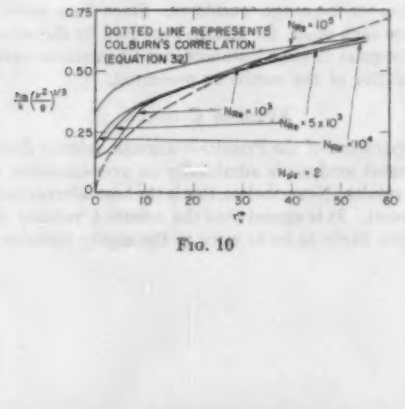

Fig. 10

The following empirical equation was obtained by Carpenter and Colburn (2) for condensation of fluids having N_{Pr} in a range of 2 to 5 with τ_v^* in a range 5 to about 150

$$\frac{h_m\mu}{k\rho^{1/3}} = 0.065 N_{Re,l}^{1/3}\tau_v^{1/3} \quad [31]$$

This may be readily converted to the dimensionless form

$$\frac{h_m}{k}\left(\frac{\nu^2}{g}\right)^{1/3} = 0.065 N_{Pr,l}^{1/3}(\tau_v^*)^{1/3} \quad [32]$$

This empirical relation is shown as dotted lines in Figs. 9 and 10. It agrees very well with results of the present analysis in the N_{Pr} range of 2 to 3 and τ_v^* range 5 to 50 where the larger portion of their data was obtained. The Carpenter-Colburn Equation [32] does not include an effect of Reynolds number; however, results of the present analysis, Figs. 4, 6, and 8, show a significant effect. The effect of Prandtl number as included in Equation [32] does not appear to be valid for N_{Pr} outside the range of 1 to 5, which is beyond the range of validity recommended by Carpenter and Colburn.

Inspection of the curves in Figs. 3 to 8 shows that the effect of τ_v on h_m is less at the higher values of $4\Gamma/\mu$. At the lower values of N_{Pr} the curves in the turbulent range do not deviate significantly from extensions of the curves for the laminar region. However, at the higher Prandtl numbers there is a marked change in slope with accompanying increasing values of h_m. The dotted lines crossing the curves represent the loci of transition points. The discontinuity in the slope of these dotted curves represents the location of change in transition criterion at $\tau_v^* = 9.2$ as shown in Fig. 2.

Conclusions

The present results are based on a rational analysis to show the effect of vapor shear stress on heat transfer in laminar and turbulent film condensation for a wide range of $4\Gamma/\mu$ and N_{Pr}. In the turbulent film it was assumed that the "universal velocity distribution," Equations [17], exists. The average values of heat-transfer coefficients are based on assumed conditions at transition from laminar to turbulent flow as represented by Equations [13] and [16] or Fig. 2. While these two assumptions have not been extensively verified by experiment, they nevertheless are logical ones based on the best information currently available. The effect on h_m of the exact location of the transition point becomes less significant as the value of $4\Gamma/\mu$ at the bottom of the surface increases and is practically insignificant for $4\Gamma/\mu > 10{,}000$. Both of these assumptions regarding velocity distribution in the film and the criterion for transition will be the subject of future experimental investigation.

In applying the results to a piece of apparatus it is necessary to know the magnitude of τ_v, which actually varies along the length. There is available some experimental information for shear stresses in co-current gas-liquid flow (10). With increasing values of τ_v there will ultimately exist a condition under which parts of the liquid film will be torn away from the surface and entrained in the vapor. Such conditions are obviously not included in the present analysis. Carpenter and Colburn (2) suggest obtaining an average value of τ_v in a tube from $\tau_v = fG_{vm}^2/2g_c\rho_v$ by evaluating f at a $G_{vm}^2 = (1/3)(G_{top}^2 + G_{top}G_{bottom} + G_{bottom}^2)$. If all of the vapor is condensed, $G_{bottom} = 0$ and $G_{vm} = 0.58\,G_{top}$.

For condensation of a particular fluid on a vertical surface of a given geometry and magnitudes of t_v and t_w, the values of N_{Pr} and z_L^* are readily calculated. Interpolation in Figs. 3, 5, and 7 will give a value of $(h_m/k)(\nu^2/g)^{1/3}$ from which h_m is obtained and $(q/A)_{avg}$ is calculated. This value of h_m includes the effect of a

laminar film on the upper part of the surface and, if present, the effect of a turbulent film on the remainder of the surface.

BIBLIOGRAPHY

1 "Note on the Calculation of Condensation When a Portion of Condensate Layer Is in Turbulent Motion," by A. P. Colburn, Transactions of the Institute of Chemical Engineers, vol. 30, 1933–1934, pp. 187–193.

2 "The Effect of Vapor Velocity on Condensation Inside Tubes," by F. S. Carpenter and A. P. Colburn, Proceedings of the General Discussion of Heat Transfer, The Institution of Mechanical Engineers and The American Society of Mechanical Engineers, July, 1951, pp. 20–26.

3 "Problems in Design and Research on Condensation of Vapours and Vapour Mixtures," by A. P. Colburn, Clayton Lecture, Proceedings of the General Discussion of Heat Transfer, The Institution of Mechanical Engineers and The American Society of Mechanical Engineers, July, 1951, pp. 1–11.

4 "Remarks on Film Condensation With Turbulent Flow," by R. A. Seban, Trans. ASME, vol. 76, 1954, pp. 299–303.

5 "Heat Transfer and Temperature Distribution in Laminar-Film Condensation," by W. M. Rohsenow, published in this issue, pp. 1645–1648.

6 "Heat Transmission," by W. H. McAdams, McGraw-Hill Book Company, Inc., New York, N. Y., third edition, 1954, p. 334.

7 "Pressure Drop and Heat Transfer for Condensation in Tubes With High Vapor Velocities," by F. G. Carpenter, PhD thesis, Chemical Engineering Department, University of Delaware, 1948.

8 Loc. cit., reference (6), p. 110.

9 "Heat Transferred to Molten Metals," by R. C. Martinelli, Trans. ASME, vol. 69, 1947, pp. 947–955.

10 "Co-Current Gas-Liquid Flow in Vertical Tubes," by O. P. Bergelin, P. K. Kegel, F. G. Carpenter, and Carl Gayley, Heat Transfer and Fluid Mechanics Institute, Berkeley, Calif., published by The American Society of Mechanical Engineers, 1949, pp. 19–28.

Discussion

R. A. Seban.[8] The authors have achieved plausible results in the calculation by means of analogy methods of the effect of vapor velocity on turbulent film condensation. This is an area in which the writer in an earlier work was reticent to enter, since it seemed that the suitability of the Prandtl-Nikuradse distribution would be diminished as the traction on the external surface of the layer became greater than zero. Certainly the velocity distribution in the region near the liquid-vapor interface must depend on the character of the turbulence in the liquid as that region is approached, and some diminution is expected, so that the eddy transport assumed in the analysis of the paper may be expected to be perhaps larger than what actually exists.

The primary point of this discussion is, however, the application of the equations of motion as made in the present analysis. Equation [1] is the basic equation for the liquid, and it neglects pressure variation in the direction of vapor flow. While such a situation may be possible, it does not exist in condensation within a tube, the case in which vapor-velocity effects are most important and the case to which the present results are indirectly compared. Considering a pressure variation, and taking co-ordinates as in Fig. 1 of the paper, the momentum equation can be written as follows if the change in the liquid momentum rate is neglected

$$0 = -\frac{\partial p}{\partial z} + g\rho + \frac{\partial \tau}{\partial x}$$

Of the changes in momentum rate that actually occur, that due to the addition of condensed vapor is probably the largest, and its significance has been considered by Carpenter and Colburn.[6] It seems, however, assuming no slip at the vapor-liquid interface, that the velocity of the vapor which is condensed is not much different from that of the liquid, and hence its momentum cannot be much different from that of the liquid already in the layer, for which the change in momentum rate is neglected. Omitting all changes in momentum rate then, and assuming the pressure to be constant across the liquid layer, the shear distribution is found to be

$$\tau - \tau_V = \left(\frac{dp}{dz} - g\rho\right)(x - x_0)$$

from which

$$\tau_0 - \tau_V = \left(g\rho - \frac{dp}{dz}\right)x_0 \quad \ldots\ldots\ldots\ldots [33]$$

The pressure gradient is found from the momentum equation for the vapor flow, which can be written as follows in a unidimensional and therefore approximate form

$$\frac{dp}{dz} + \rho_V u\frac{du}{dz} - \rho_V g + \frac{\tau_V}{r_H} = 0$$

where r_H is the hydraulic radius of the vapor flow cross section.

If the vapor is considered almost incompressible, then the change in its momentum rate is due to change in the flow cross section and to removal of vapor due to condensation. Then since

$$\frac{d\rho u A_s}{dz} = -P\frac{d\Gamma}{dz}$$

(where A_s is the vapor flow cross section and P its perimeter) if the change in flow cross section is neglected, the pressure drop can be approximated as

$$\frac{dp}{dz} = \frac{u_V}{r_H}\frac{d\Gamma}{dz} - \frac{\tau_V}{r_H} + \rho_V g$$

Substitution into Equation [33] gives

$$\tau_0 - \tau_V = \left(g\rho - \frac{u_V}{r_H}\frac{d\Gamma}{dz} + \frac{\tau_V}{r_H} - \rho_V g\right)x_0 = Gx_0$$

From the point of view taken in this discussion, the analysis should be based on the replacement of group $g(\rho - \rho_V)$ by group G in Equation [2] of the paper. This leads to substantial difficulties, for even though τ_V is taken to be invariable with z as is done in the paper, it is difficult to so consider the quantity $d\Gamma/dz$.

For the turbulent-flow results, some interpretation is perhaps possible by considering that if a substitution as indicated in the foregoing is to keep M constant, then the quantity τ_V used in the results should be multiplied by the ratio $G/g(\rho - \rho_V)$, and the heat-transfer coefficient should be increased by the cube root of this ratio. By neglecting the vapor density, the ratio becomes

$$\frac{G}{g\rho} = 1 - \frac{u_V\dfrac{d\Gamma}{dz}}{r_H g\rho} + \frac{\tau_V}{g\rho r_H}$$

where τ_V and $u_V(d\Gamma/dz)$ are interpreted as some kind of suitable mean values for the range considered. Since these terms tend to compensate each other, the change produced by the substitution may not be great in some instances, but its existence casts doubt on the validity of the results as presented.

Authors' Closure

The application of the Prandtl-Nikuradse velocity distribution in the present analysis is admittedly an over-extension of these empirical results. Nevertheless, this is the best information available at present. It is agreed that the assumed velocity distribution is quite likely to be in error in the highly turbulent region

[8] Lecturer in Mechanical Engineering, University of California, Berkeley, Calif. Mem. ASME.

[6] Reference (2) of the authors' bibliography.

near the liquid-vapor interface. On the other hand, it seems that this velocity formulation should predict actual conditions quite closely in the remainder of the condensate film. Realizing that the region of expected error is also a region of very small resistance to heat flow when compared to that of the "buffer" layer and the laminar sublayer, it is felt that deviations in this area will have but little effect on the predicted values of heat-transfer coefficient for the entire film.

Professor Seban's comments on the momentum terms are in agreement with the comments following Equation [2] of the paper. This is in disagreement with the Colburn (2) treatment of the momentum term.

The derivation in the paper is for a flat plate in an infinite atmosphere and the only pressure gradient is that due to the height of the vapor. This pressure gradient appears as the vapor density in the force balance. For the case of a vertical tube condenser, additional terms will enter into the pressure gradient which are dependent on the particular geometry under consideration. It is apparent that if these terms are to be included, the results, as presented in the dimensionless curves in the article, will lose their universal applicability and must include the additional parameter of system geometry. Rather than re-evaluate the equations for each specific case confronting the designer, it is more convenient to derive a fictitious vapor density, which will include the additional pressure gradient terms for a vertical tube condenser. This new vapor density ρ_v' can then be substituted for ρ_v in the equations and curves presented in the article. Here

$$\rho_v' = \rho_v + \frac{v_{v,z_0}}{g_0 r_h}\frac{d\Gamma}{dz} - \frac{g\tau_v}{g_0 r_h}$$

It should be noted that in the foregoing equation and in those in the body of the paper ρ is lb_m/ft^3 and v represents velocity. In Professor Seban's discussion ρ is in slugs/ft^3 and u represents velocity.

In terms of the local coefficient h

$$\frac{d\Gamma}{dz} = \frac{h(\Delta t)}{h_{fg}}$$

The calculation including the pressure drop and decreasing vapor flow with length follows in similar stepwise fashion. The results would be difficult to generalize. This is the subject of a current ScD thesis.[7] Until more positive suggestions appear, it is suggested that the curves of Figs. 3 through 8 be used with an average value of τ_v evaluated at a mean vapor mass velocity defined by

$$G_{vm} = \sqrt{\left[\frac{1}{3}\left(G_{top}^2 + G_{top}G_{bottom} + G_{bottom}^2\right)\right]}$$

which is suggested by Colburn (2).

[7] "Film Condensation in a Vertical Tube Subject to Varying Vapor Velocity," by J. Lehtinen, ScD thesis, Dept. of Mechanical Engineering, M.I.T., Cambridge, Mass. To be finished in June, 1957.

Heat Transfer and Temperature Distribution in Laminar-Film Condensation

By W. M. ROHSENOW,[1] CAMBRIDGE, MASS.

Most of the analyses of laminar-film condensation since Nusselt's[2] pioneer paper have assumed a linear-temperature distribution within the film. Bromley[3] performed an analysis allowing for a nonlinear temperature distribution but omitting the effect of cross flow within the film. His result is in variance with the result obtained here.

Nomenclature

The following nomenclature is used in the paper:

c = specific heat, Btu/lb$_m$ F
g = acceleration of gravity, ft/hr^2
g_0 = conversion factor, 4.16×10^8 lb$_m$ ft/lb$_f$ hr^2
h = heat-transfer coefficient, Btu/hr sq ft deg F
h_{fg} = latent heat of vaporization, Btu/lb$_m$
h_{fg}' = $h_{fg} + (3/8)c(\Delta t)$
k = thermal conductivity, Btu/hr ft deg F
q = heat-transfer rate, Btu/hr
t = temperature, deg F
Δt = temperature difference across condensate film, deg F
t_{sat} = saturation temperature, deg F
v_z = velocity in z-direction, ft/hr
w = flow ratio, lb$_m$/hr
x, x_0, Y, z = linear distances defined in Fig. 1, ft
L = height of plate or tube, ft
ρ = density, lb$_m$/ft^3
μ = viscosity, lb$_m$/ft hr
ν = kinematic viscosity, ft^2/hr
τ = shear stress, lb$_f$/ft^2
Γ = w/Y, flow rate per unit perimeter or width, lb$_m$/hr ft

Subscripts

v = vapor (properties without subscript refer to liquid)
z = local value at z
m = mean value over $z = 0$ to L

Analysis

The analysis presented here attempts to obtain the correct nonlinear temperature distribution and heat-transfer rates in a liquid condensate film which under the influence of gravity flows downward in essentially laminar flow on vertical plates or tubes. In the analysis, it is assumed that the vapor is saturated with no noncondensable gas present, the wall surface temperature is uniform, there is no appreciable vapor shear stress existing at the liquid-vapor interface, and the physical properties of the fluid are constant and uniform.

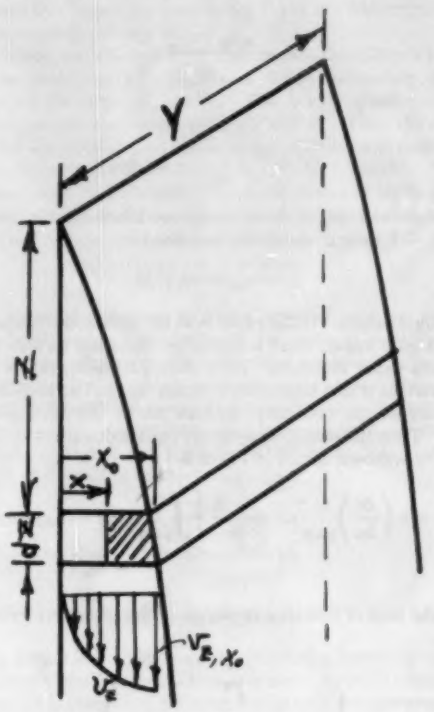

Fig. 1

Force Balance. Neglecting momentum changes the force balance for the shaded element, Fig. 1, of dimensions Y, $(x_0 - x)$, dz is

$$\tau\, Y\, dz = \frac{\mu}{g_0}\frac{dv_z}{dx}\, Y\, dz = \frac{g}{g_0}\,\rho(x_0 - x)Y\, dz - \frac{g}{g_0}\,\rho_v\,(x_0 - x)Y\, dz \quad [1]$$

Integrating from 0 to x and 0 to v_z

$$v_z = \frac{g(\rho - \rho_v)}{\mu}\left(x_0 x - \frac{x^2}{2}\right) \quad [2a]$$

$$v_{z,x0} = \frac{g(\rho - \rho_v)}{\mu}\,\frac{x_0^2}{2} \quad [2b]$$

$$v_{z,m} = \frac{1}{x_0}\int_0^{x_0} v_z dx = \frac{g(\rho - \rho_v)}{\mu_f}\,\frac{x_0^2}{3} \quad [2c]$$

---

[1] Associate Professor of Mechanical Engineering, Massachusetts Institute of Technology. Mem. ASME.

[2] "Die Oberflächenkondensation des Wasserdampfes," by W. Nusselt, *Zeitschrift des Vereines Deutscher Ingenieure*, vol. 60, 1916, pp. 541 and 569.

[3] "Effect of Heat Capacity of Condensate in Condensing," by L. A. Bromley, *Industrial and Engineering Chemistry*, vol. 44, 1952, pp. 2966–2969.

Contributed by the Heat Transfer Division and presented at the Annual Meeting, New York, N. Y., November 28–December 3, 1954, of The American Society of Mechanical Engineers.

Note: Statements and opinions advanced in papers are to be understood as individual expressions of their authors and not those of the Society. Manuscript received at ASME Headquarters, August 27, 1954. Paper No. 54—A-144.

Comparing Equations [2b] and [2c]

$$v_{z,m} = \frac{2}{3} v_{z x_0}$$

The mass rate of flow per unit width at any z is

$$\Gamma = w/Y = \rho v_{z,m} x_0$$

or

$$\Gamma = \frac{g\rho(\rho - \rho_v)}{\mu_f} \frac{x_0^3}{3} \quad \ldots\ldots [3]$$

and

$$d\Gamma = \frac{g\rho(\rho - \rho_v)}{\mu_f} x_0^2 \, dx_0 \quad \ldots\ldots [4]$$

Drew showed that if the temperature distribution is linear and if $(1/\mu) \sim t$, then μ_f should be evaluated at

$$t_f = t_{sat} - (3/4)\Delta t$$

Energy Analysis. If the vapor is at the saturation temperature and is a pure vapor, there is negligible resistance to flow toward the liquid-vapor interface. Then the liquid temperature at the liquid surface is also saturation temperature and no heat is transferred across the boundary through which the condensate dw passes. Then the steady flow-energy equation applied to the control surface shown dotted in Fig. 2 is

$$-\frac{dq}{Y} = k\left(\frac{\partial t}{\partial x}\right)_{x=0} dz = \frac{-\partial}{\partial x_0}\left[\int_{x=0}^{x_0} \rho c(t - t_{sat})\, v_x dx\right] dx_0 + h_{fg}\, d\Gamma \quad \ldots\ldots [5a]$$

where the zero of enthalpy is placed at the saturated liquid conditions.

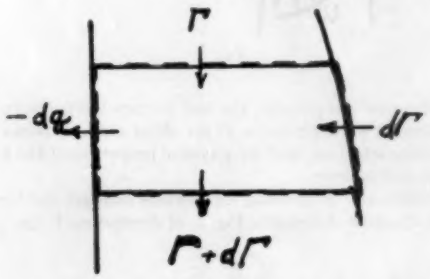

FIG. 2

ubstituting from Equations [2a] and [4] into [5a] and solving

$$\frac{dx_0}{dz} = \frac{\mu k (\partial t/\partial x)_{x=0}}{g\rho(\rho - \rho_v)\left\{h_{fg} x_0^2 - c\,\dfrac{\partial}{\partial x_0}\left[\displaystyle\int_{x=0}^{x_0} (t - t_{sat})(x_0\, x - x^2/2)dx\right]\right\}} \quad \ldots\ldots [5b]$$

As a first approximation, the temperature distribution in the laminar film may be assumed to be linear; then with $\Delta t \equiv (t_{sat} - t_w)$

$$(t - t_{sat}) = \Delta t\left(\frac{x}{x_0} - 1\right) \quad \ldots\ldots [6]$$

Then Equation [5a] becomes with Equation [4]

$$k\,\frac{\Delta t}{x_0}\, dz = h_{fg}'\, d\Gamma = h(t_{sat} - t_w)dz \quad \ldots\ldots [7]$$

where

$$h_{fg}' \equiv h_{fg} + \frac{3}{8} c(t_{sat} - t_w)$$

which is the enthalpy change per pound of steam condensed from saturated vapor to liquid at the mean temperature of the liquid film. Equation [5b] may be integrated with Equations [2], [4], and [6] with the result

$$x_0 = \sqrt[4]{\frac{4k\Delta t\, \mu z}{g\rho(\rho - \rho_v)h_{fg}\left(1 + \dfrac{3}{8}\,\dfrac{c\Delta t}{h_{fg}}\right)}} \quad \ldots\ldots [8]$$

Since $dq/Y\, dz = h_x \Delta t$

$$h_x = -\frac{k}{\Delta t}\left(\frac{\partial t}{\partial x}\right)_{x=0} \quad \ldots\ldots [9]$$

For this case then

$$h_x = \frac{k}{x_0} = \sqrt[4]{\frac{\frac{1}{4}g\rho(\rho - \rho_v)h_{fg}\left(1 + \dfrac{3}{8}\,\dfrac{c\Delta t}{h_{fg}}\right)}{4\mu\Delta t z}} \quad \ldots [10a]$$

This is the local coefficient at a particular z. The average coefficient between $z = 0$ and L is

$$h_m = \frac{1}{L}\int_0^L h_x dz = 0.943\sqrt[4]{\frac{g\rho(\rho - \rho_v)k^3 h_{fg}\left(1 + \dfrac{3}{8}\,\dfrac{c\Delta t}{h_{fg}}\right)}{\mu L \Delta t}} \quad \ldots\ldots [10b]$$

or a Nusselt number is

$$N_{Nu} = \frac{h_m L}{k} = 0.943\sqrt[4]{\frac{g\rho(\rho - \rho_v)L^3 h_{fg}\left(1 + \dfrac{3}{8}\,\dfrac{c\Delta t}{h_{fg}}\right)}{\mu k \Delta t}} \quad \ldots\ldots [10c]$$

This is the type of analysis and result obtained by Nusselt (1916) utilizing an assumed linear temperature distribution. The analysis may be improved by determining the actual temperature distribution which is not linear, Fig. 3, because of the addition of liquid at t_{sat} to the outer edge of the film. For the control volume fixed in space shown shaded in Fig. 3, there is a flow of liquid $d\Gamma_{0x}$ across the face at x which with Equation [2] equals

$$d\Gamma_{0x} = \frac{\partial}{\partial x_0}\left[\int_0^x \rho v_x dx\right] dx_0 = \frac{g\rho(\rho - \rho_v)}{\mu}\,\frac{x^3}{2}\, dx_0 \quad \ldots [11]$$

An energy balance equating the heat transferred at the face at x with the net enthalpy change of the fluid crossing the control surface is

$$k\,\frac{dt}{dx}\, dz = -\frac{\partial}{\partial x_0}\left[\int_x^{x_0} \rho c(t - t_{sat}) v_x dx\right] dx_0 - c(t - t_{sat})d\Gamma_{0x} + h_{fg} d\Gamma \quad \ldots\ldots [12]$$

Expressions for v_x, $d\Gamma_{0x}$, $d\Gamma$ and dx_0/dz are given in Equations [2], [11], [4], and [5b]. Substitute these in Equation [12] which

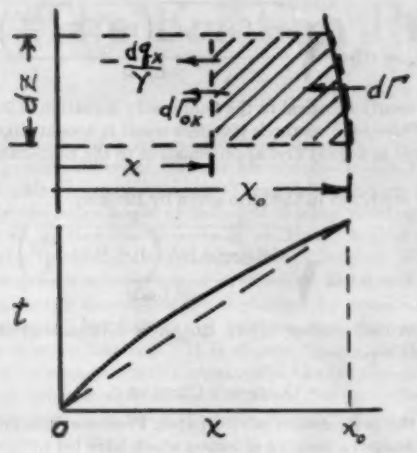

FIG. 3

may be solved by successive approximations for t as a function of x. The right side of Equation [12] is evaluated for an assumed relation of t versus x and then is integrated to determine a new t versus x relation. The process is then successively repeated with each new relationship. Actually, the results converge rapidly and only one or two repetitions are needed for a satisfactory answer. If the linear temperature distribution is assumed initially the first integration of Equation [12] is

$$(t - t_w) = \Delta t \left\{ \left(\frac{x}{x_0}\right) + \frac{c\Delta t}{h_{fg}'} \left[-\frac{1}{8}\left(\frac{x}{x_0}\right)^4 + \frac{1}{40}\left(\frac{x}{x_0}\right)^5 \right] \right\} \quad \ldots\ldots [13a]$$

and at $x = x_0$, $t = t_{sat}$ so

$$(t_{sat} - t_w) = \Delta t \left(1 - \frac{1}{10}\frac{c\Delta t}{h_{fg}'}\right) \quad \ldots\ldots [13b]$$

or dividing one equation by the other

$$\frac{t - t_w}{t_{sat} - t_w} = \frac{\left(\frac{x}{x_0}\right) + \frac{c\Delta t}{h_{fg}'}\left[-\frac{1}{8}\left(\frac{x}{x_0}\right)^4 + \frac{1}{40}\left(\frac{x}{x_0}\right)^5 \right]}{1 - \frac{1}{10}\frac{c\Delta t}{h_{fg}'}} \quad \ldots [13c]$$

This is a temperature distribution having a shape as shown in Fig. 3. Using this temperature distribution in Equation [5b] to evaluate dx_0/dz and integrating

$$x_0 = \sqrt[4]{\frac{4k_e\Delta t\,\mu z}{g\rho(\rho - \rho_v)h_{fg}'\left[1 - \frac{1}{10}\frac{c\Delta t}{h_{fg}'} - 0.0328\left(\frac{c\Delta t}{h_{fg}'}\right)^2\right]}} \quad \ldots [14]$$

From Equation [9] the average h_m may be calculated

$$h_m = 0.943 \sqrt[4]{\frac{k_e^3 g\rho(\rho - \rho_v)h_{fg}'\left[1 - \frac{1}{10}\frac{c\Delta t}{h_{fg}'} - 0.0328\left(\frac{c\Delta t}{h_{fg}'}\right)^2\right]}{\mu\Delta t L\left(1 - \frac{1}{10}\frac{c\Delta t}{h_{fg}'}\right)^4}} \quad \ldots\ldots [15a]$$

For a range $0 < (c\Delta t/h_{fg}) < 1.0$ this equation is very closely approximated by

$$h_m = 0.943 \sqrt[4]{\frac{k_e^3 g\rho(\rho - \rho_v)h_{fg}\left(1 + 0.68\frac{c\Delta t}{h_{fg}}\right)}{\mu\Delta t L}} \quad \ldots [15b]$$

Comparison of Equations [14] and [15b] with Equations [8] and [10b] shows that the more correct values of h and x_0 are larger than the ones obtained with the assumed linear temperature distribution. These results are compatible because a larger h will result in a larger condensate flow Γ at any z which from Equation [3] requires a larger x_0.

Obviously, the effect of this refinement in the analysis becomes more important at high values of liquid subcooling or more precisely high values of $c\Delta t/h_{fg}$. For a very great number of applications $c\Delta t/h_{fg}$ is quite small (0 to 0.2). Then the analysis with the assumed linear temperature distribution resulting in the simpler energy balance Equation [7] may be used.

Similar analyses for laminar film condensation on inclined plates and on the outside of horizontal tubes[4] result in the same type correction factor as in Equation [15b], e.g.

$$\sqrt[4]{1 + 0.68(c\Delta t/h_{fg})}$$

Experimental data are usually compared with an equation similar to Equation [15b] but with the term $(1 + 0.68c\Delta t/h_{fg})$ omitted. In such a comparison the data[5] are found to be around 10 to 20 per cent higher than the calculated values. This discrepancy is usually ascribed to such things as ripples in the condensate layer. These departures from the idealized conditions surely do contribute greatly to the discrepancy; however, it is quite obvious that the omission of the factor

$$\sqrt[4]{1 + 0.68(c\Delta t/h_{fg})}$$

contributes to a part of the disagreement.

Discussion

L. A. BROMLEY.[6] The author's derivation correctly includes the effect of cross flow on the heat transfer. As the method of approximation is somewhat different and as only one approximation is included it will be of interest to compare the result with that which would be obtained by correcting Bromley's derivation. The latter derivation is here corrected for the cross-flow term and the result compared with that given by the author.

Using as a basis the enthalpy of the liquid at the boiling point, the heat flow by conduction at a given point y in the condensate film is equal to the decrease in enthalpy of the material between y and y_0 plus the heat liberated by the condensate minus the heat carried by cross flow.

These items are, respectively, using nomenclature of Bromley[7]

$$-dH = \frac{c_p\rho(\rho - \rho_v)g\Delta t}{\mu}\left(\frac{3y_0^2}{8} - \frac{y^2}{2} + \frac{y^4}{8y_0^2}\right)dy_0 \quad \ldots [16]$$

$$\lambda d\Gamma = \frac{\lambda\rho(\rho - \rho_v)g}{\mu}\,y_0^2 dy_0 \quad \ldots\ldots [17]$$

$$-dH_{cf} = \frac{c_p\rho(\rho - \rho_v)g\Delta t}{\mu}\left[-\frac{y^2}{2} + \frac{y^3}{2y_0}\right]dy_0 \quad \ldots [18]$$

[4] "Heat Transfer," by M. Jakob, John Wiley & Sons, Inc., New York, N. Y., vol. 1, 1949, eq. (30–53).

[5] "Heat Transmission," by W. H. McAdams, McGraw-Hill Book Company, Inc., New York, N. Y., third edition, 1954, p. 340, Table 13-4.

[6] Associate Professor of Chemical Engineering, University of California, Berkeley, Calif.

[7] See footnote 3 of the paper.

But the sum of these as written must equal the heat flow due to conduction; hence

$$-dH + \lambda d\Gamma - dH_{ef} = k dL \frac{dt}{dy} \quad \ldots\ldots [19]$$

Substituting Equations [16], [17], and [18] into Equation [4] of the paper and rearranging and integrating between $y = 0$ and $y = y_0$ we obtain

$$k \frac{dL}{dy_0} \frac{\Delta t}{y_0} = \frac{\rho(\rho - \rho_v) g y_0}{\mu} \left[\lambda + \frac{11}{40} c_p \Delta t\right] \quad \ldots\ldots [20]$$

If we now refer to the original derivation of Bromley[7] it is apparent that

$$h = 0.943 \frac{\left(1 + \frac{3}{8} \frac{\Delta t c_p}{\lambda}\right)}{\left(1 + \frac{11}{40} \frac{\Delta t c_p}{\lambda}\right)^{3/4}} \sqrt[4]{\frac{k^3 \rho(\rho - \rho_v) g \lambda}{L \mu \Delta t}} \quad \ldots\ldots [21]$$

If this approximate equation is expanded in series form for small values of $\Delta t c_p/\lambda$ it may be written (using the author's nomenclature)

$$h_m = 0.943 \sqrt[4]{\frac{k^3 \rho(\rho - \rho_v) g h_{fg} \left(1 + 0.675 \frac{c \Delta t}{h_{fg}}\right)}{L \mu \Delta t}} \quad \ldots\ldots [22]$$

which is nearly identical to the final result, Equation [15*b*] of the paper. Since both methods give this result it appears likely that the answer is a good first approximation to the heat-transfer coefficient.

If this is written in the form given by Bromley

$$h = 0.943 \sqrt[4]{\frac{k^3 \rho(\rho - \rho_v) g \lambda \left(1 + 0.34 \frac{\Delta t c_p}{\lambda}\right)^3}{L \mu \Delta t}} \quad \ldots\ldots [23]$$

Note that the number before $\Delta t c_p/\lambda$ is 0.34 instead of 0.4 as previously reported.

Author's Closure

Since the presentation of this paper, Professor Bromley and I have exchanged a number of letters which have led to corrections in our respective arithmetic. A comparison of Equations [15*b*] and [22] shows that we are in agreement. I am grateful to Professor Bromley for engaging in these written "conversations."

The Friction Process in Metal Cutting

By IAIN FINNIE[1] and M. C. SHAW[2]

Coefficients of friction obtained in metal cutting are often greatly different from those obtained with the same metal pair in conventional sliding-friction experiments. If only the rake angle is changed during cutting, a wide range of friction coefficients is obtained, and it is noted that the tendency toward complete adhesion of chip to tool increases as coefficient of friction decreases. These two apparent anomalies are explained by considering the fundamental mechanism of friction and the conditions which exist in cutting. It is shown that a coefficient of friction is inadequate to characterize the friction process in cutting, being mainly an indication of the normal stress on the tool face, and thus strongly dependent on the shear process in cutting.

Introduction

IN THE cutting of ductile metals it can be seen from photomicrographs such as Fig. 1, that two major processes occur, shear along a fairly sharply defined shear plane and friction at the tool-chip interface. The shear process has already been treated in some detail (1)[3] and in this paper the friction process will be discussed. It was pointed out in previous papers (1, 2) that the shear and friction processes are not independent, a fact which will be shown to be important in the following analysis of the friction process.

Although friction in cutting is of interest as a potential test for fundamental studies of wear, friction, and chemical reaction under conditions of high temperature, high pressure, and a nascent surface, use of a coefficient of tool-face friction has been limited by lack of an explanation for the wide range of coefficients which are obtained when only the rake angle is varied. Such coefficients of friction may be greater and are often less than those obtained with the same metal combination in conventional sliding. Another disturbing feature of the coefficient of friction is the increasing tendency for complete adhesion and formation of a built-up edge with decreased rake angle, while the coefficient of friction is decreasing.

This behavior is in strong contrast to that of clean, dry, smooth surfaces sliding in air where the rules of Amontons (3) as originally stated in 1699 and given below are still satisfactory.

1 The coefficient of friction is independent of applied load N.

2 The coefficient of friction is independent of apparent area of contact A.

Other empirical rules for ordinary bodies in dry sliding contact include:

Fig. 1 Typical Photomicrograph Showing Shear and Friction Processes

(The friction coefficient calculated from measured force components F_P and F_Q is equal to $\tan^{-1}\beta$.)

3 The coefficient of friction is independent of the ambient temperature of the metals θ_0.

4 The coefficient of friction is independent of the sliding speed V.

While these rules represent good approximations under usual conditions for bodies in sliding contact, they may fail completely if test conditions are sufficiently abnormal.

Typical data are given in Table 1 for the orthogonal cutting of copper and steel in air with sharp tools, the tools being of high-speed steel. The stresses were calculated from the measured forces and observed contact areas on the tool face. These stresses (τ_a, σ_a) are based on the apparent area of contact as opposed to those based on the real area of contact (τ^*, σ^*) to be considered presently.

TABLE 1 REPRESENTATIVE LOW-SPEED CUTTING DATA

	Rake angle α, deg	Average stresses at tool-chip interface, psi: Shear stress τ_a	Normal stress σ_a	Friction coefficient f
Electrolytic tough pitch copper; cutting speed V, 0.3 fpm; depth of cut t, 0.002 in.	30	35600	43300	0.82
	45	34700	30000	1.15
	60	36700	16000	2.3
SAE B1112 steel; cutting speed V, 0.04 fpm; depth of cut t, 0.003 in.	16	46000	70000	0.66
	30	49300	57000	0.86
	45	51700	43200	1.20

According to the empirical rules of sliding contacts, we should not expect the coefficient of friction to change with rake angle. To explain the wide range of friction coefficients obtained and the other anomalies already mentioned, we need to consider the fundamental mechanism of dry friction.

Mechanism of Dry Friction

At the present time the most generally accepted theory of dry friction is a composite of contributions due to Holm (4), Ernst and Merchant (5), and Bowden and his associates at Cambridge University (6). According to this picture of friction, sliding resistance is viewed as being composed of three factors:

1 A mechanical interlocking of surface asperities.

---

[1] Shell Development Company, Emeryville, Calif.

[2] Professor of Mechanical Engineering, Massachusetts Institute of Technology, Cambridge, Mass. Mem. ASME.

[3] Numbers in parentheses refer to the Bibliography at the end of the paper.

Contributed by the Research Committee on Lubrication under the auspices of the Lubrication Activity and presented at a joint session of the Lubrication Activity and Research Committee on Metal Processing at the Annual Meeting, New York, N. Y., November 28–December 3, 1954, of The American Society of Mechanical Engineers.

Note: Statements and opinions advanced in papers are to be understood as individual expressions of their authors and not those of the Society. Manuscript received at ASME Headquarters, August 6, 1954. Paper No. 54—A-108.

2 A plowing of the surface asperities of the harder of the two metals through the softer.

3 A welding of the surface asperities of the one metal to the other, resulting in metallic junctions.

For relatively smooth surfaces, such as we have in metal cutting, experimental evidence (6, 7) would indicate that frictional resistance is primarily due to the shearing of asperities, factors 1 and 2 being negligible. Feng (8) recently suggested that the third factor involves mechanical interlocking in its mechanism, but this will not substantially alter the discussion that follows.

When two clean surfaces are brought together under load, a real area of contact A_r is developed by plastic flow of asperities present on all engineering surfaces, this flow being just sufficient to support the load. It has been shown experimentally (6), for example, that two smoothly ground gage blocks with an apparent contact area A of 1 sq in. under a normal load of 10 lb will have a real area of contact of only 10^{-4} sq in. If the hardness of the asperities of the softer metal is σ^*, then the applied load N will be

$$N = \sigma^* A_r \quad [1]$$

The friction force F will be

$$F = K\tau^* A_r \quad [2]$$

where τ^* is the surface shear stress required to rupture the welds and KA_r is the fraction of the real area of contact over which welding has occurred. Then the coefficient of friction f is

$$f = \tau^* KA_r/\sigma^* A_r = K\tau^*/\sigma^* \quad [3]$$

For relatively light loads per unit apparent contact area, this picture explains the independence of coefficient of friction on normal load and apparent contact area (Amontons' rules). The small dependence of f on heat-treatment, or ambient temperature, is also consistent with Equation [3], since τ^* and σ^* change in approximately the same ratio in these cases. The reason for the reduction in f when low shear-strength films are used on a hard backing is further evident from Equation [3].

The rule pertaining to speed does not hold for very high values of speed (above about 2000 fpm for an ordinary slider) nor for very low values of speed (below about 1 fpm for an ordinary slider). At very low values of speed the time required for welds to be established plays an important role. As the speed of a slider increases so will the temperature at the surface. Also, this rise in surface temperature becomes more superficial as the speed increases, there being less time for heat to flow away from the surface at high speeds. At speeds below about 2000 fpm, for an ordinary steel slider, the depth of the heated layer is about equal to the depth of the layer that flows plastically when surface A_r is developed. Hence both τ^* and σ^* in Equation [3] are influenced in about the same way and there is no change in f. However, at higher speeds, τ^* is decreased more than σ^* because of its more superficial nature and the coefficient of friction will begin to drop. There is nothing universal about the 2000 fpm just mentioned.

The value at which f begins to decrease with speed depends on other properties of the system than just the velocity of the slider. Quantities of importance include length of the surface of contact in the direction of motion, thermal conductivity, and volume specific heat of the metals in sliding contact, and the amount of the friction energy per unit area converted into heat at the sliding surface. In metal cutting a decrease in the coefficient of friction on the tool face with chip speed is normally observed at speeds above a few feet per minute due to the short length in the direction of motion and the large amount of friction energy that is dissipated per unit area. Rule 4 is thus seen to be very approximate indeed.

An extreme pressure lubricant decreases K by reacting chemically with the chip to form low shear-strength nonmetallic solids at the chip-tool interface and thus reduces the real area of metallic contact. K may vary with velocity due to the time required to form welds and also with normal pressure due to the rupture of protective layers, such as oxides, at higher pressures.

From the plastic behavior of metals in other tests we should not expect τ^* and σ^* to be independent material constants for surface asperities. As Burwell and Rabinowicz (9) have pointed out, we should expect τ^* and σ^* to be connected by a plasticity condition such as

$$\psi(\tau^*, \sigma^*) = Y \quad [4]$$

where Y is the stress required to produce a given plastic flow in a stress state such as torsion or tension and ψ denotes some function.

Parker and Hatch (10) and McFarlane and Tabor (11) showed that the area of contact between bodies in contact increased when shear stress was applied which shows experimentally that a relationship between τ^* and σ^* must exist. The expressions for normal load, friction force, and Equation [4] do not yield a determinate solution for the friction force and, as there is apparently no additional plasticity condition, it appears that the friction force is an independent quantity.

Experiments on indium, by Burwell and Rabinowicz (9), showed that this was indeed the case and that different tangential loads resulted in different speeds of sliding.

Bowden (12) has stated that the more sophisticated theory implied by Equation [4] works only if the surfaces are so clean that they form strong metallic junctions and then combined stresses lead to an increase in junction area. For this to occur the surfaces must have no oxide layer or other contaminant film.

The experiments cited in references (9 to 11) have been made with steel sliding on indium or lead; that is, soft metals in which the normal stresses have produced considerable flattening of the asperities and a larger ratio (A_r/A) of real to apparent area of contact than obtained in most sliding experiments. Under these conditions the oxide layers will have ruptured and the relationship of Equation [4] will have led to even greater real areas of contact.

Usually in sliding-friction experiments the ratio A_r/A will be small and the picture of friction leading to Equation [3] will hold. As normal load is increased the real area of contact may increase by a deformation of the asperities; i.e., an increasing A_r/A, or by a flow in bulk by one or both of the metals; i.e., an increasing A with A_r/A fairly constant.

Friction in Cutting

In cutting it can be seen from data such as Table 1 that friction takes place under high normal stresses which should result in higher ratios of A_r/A than are obtained in conventional sliding. Furthermore, the second method of area increase with high loads, as given in the foregoing for conventional sliding, a flow in bulk of the chip, is apparently not possible in cutting. Due to the mechanism of chip formation and chip curl the apparent area of contact at the chip-tool interface bears no direct relation to the normal forces. For example, when a good cutting fluid is used the forces will decrease and for reasons which are yet to be explained, the chip will curl away more rapidly from the tool, resulting in average normal stresses for the friction process which are actually higher than when cutting without a fluid.

The comparatively nascent surfaces in cutting should, as already pointed out, lead to strong metallic junctions and hence an additional increase in the real area of contact due to the action of the combined stresses.

The implications of this increased A_r/A ratio in cutting will now be examined.

The shear that takes place on the shear plane in cutting may be regarded as a special case of the friction process where $A_r/A = 1$. The friction coefficient is then equal to the shear stress on the shear plane divided by the normal stress on the shear plane. It is well established that hydrostatic pressure does not significantly influence the shear process and hence for a given shear stress the coefficient of friction is inversely proportional to the normal stress for this special case. The rule of Amontons regarding the constancy of the coefficient of friction with variation of normal load is only a good approximation as long as the real area of contact represents a small percentage of the apparent area of contact ($A_r/A << 1$). Fig. 2 shows the relations between shear and normal stresses based on the apparent area for the ordinary friction slider ($A_r/A << 1$) and for internal shear flow ($A_r/A = 1$). As the load on the friction slider becomes more intense we should expect the slope of the curve to change gradually from the one extreme at A to the other at B, somewhat as shown by the dotted curve.

FIG. 2 RELATIONSHIP BETWEEN SHEAR STRESS AND NORMAL STRESS FOR SURFACE ASPERITIES AS REAL AREA OF CONTACT A_r INCREASES RELATIVE TO APPARENT AREA OF CONTACT A

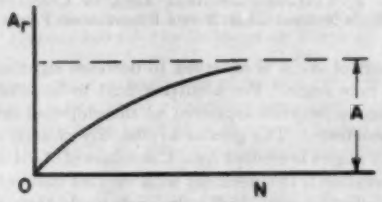

FIG. 3 RELATION BETWEEN REAL AREA OF CONTACT A_r AND NORMAL LOAD N CORRESPONDING TO FIG. 2

This picture also may be presented as in Fig. 3 where A_r is plotted against normal load N for a constant apparent area of contact A. For light loads A_r is seen to be proportional to N, Equation [1], while the required load is seen to increase without limit when A_r approaches A asymptotically. The reason for this behavior lies in the tendency for asperities to offer greater resistance to flattening as flow occurs owing to strain-hardening and the increasing material restraint to flow introduced by adjacent deformed peaks.

The behavior of Fig. 3 may be represented analytically by the following expression

$$A_r/A = 1 - e^{-BN} \quad [5]$$

where B is a constant. This equation is seen to satisfy the end conditions of Fig. 3 ($A_r = 0$ when $N = 0$, and $A_r = A$ when $N = \infty$), and if it is to be useful should reduce to Equation [1] when the applied load N is small. The latter property of Equation [5] may be demonstrated as follows:

Differentiating Equation [5] with respect to N

$$\frac{1}{A}\frac{dA_r}{dN} = Be^{-BN} \quad [6]$$

or

$$\frac{dN}{dA_r} = \frac{e^{BN}}{AB} \quad [7]$$

When Equation [1] is differentiated with respect to A_r we have

$$\frac{dN}{dA_r} = A_r\frac{d\sigma^*}{dA_r} + \sigma^* \quad [8]$$

If N is small, σ^* will be constant, $(d\sigma^*)/(dA_r)$ will be zero, e^{BN} will approach 1, and thus from Equation [7] and [8]

$$\sigma^* = 1/AB \text{ (for small } N) \quad [9]$$

Likewise, when N is small, e^{-BN} may be written as $(1-BN)$ to a good approximation. From Equation [5] we have

$$e^{-BN} = 1 - \frac{A_r}{A} = 1 - BN \text{ (for small } N) \quad [10]$$

or

$$\frac{A_r}{A} = BN \text{ (for small } N) \quad [11]$$

which reduces to Equation [1] when σ^* is substituted for $1/AB$ from Equation [9].

Equation [5] is thus seen to be in agreement with known performance at extremes of load and to reduce to Amontons' rule for light values of load. It should prove useful for situations in which the load is somewhat beyond values for which Equation [1] represents a good approximation.

Stress-strain data for the friction process such as given in Table 1 confirm the picture presented in Figs. 2 and 3. The shear stress is remarkably constant, most of the change in friction coefficient being due to the change in normal stress. And if a trend exists it is for the shear stress to decrease as normal stress increases, possibly because of a combined stress condition as represented in Equation [4] or the action of the size effect to be discussed. This relative constancy of the friction force while normal force changes has been recognized earlier by Kronenberg (13, 14). The larger normal stresses on the tool face that result as rake angle decreases are largely a consequence of the decreasing shear angle and greater shear-plane forces. Hence the coefficient of friction in cutting bears little relation to the ordinary friction process, but depends on the shear process in cutting and how this is influenced by rake angle.

At lower rake angles the higher normal loads give larger values of A_r/A and lower values of f. As A_r/A increases it becomes increasingly likely that shear will occur on an internal shear plane rather than on the almost completely welded chip-tool interface. The chip metal making contact with the tool face is stronger than comparable metal in bulk as a result of the restraint imposed by the stronger metal in the tool face. Progressively more metal flow takes place at the chip surface as rake angle is decreased, and eventually internal shear occurs with the formation of a built-up edge, although this may not happen if shear fracture occurs first on the shear plane as a result of the large strains imposed by small rake angles. This is the situation met in discontinuous chip formation (15).

Other evidence that a coefficient of friction is inadequate to characterize the sliding between chip and tool can be found in a study made of the metal transferred from radioactive copper to a steel tool by Finnie and Rabinowicz (16). It was found that the metal transferred varied very little with rake angle although the friction coefficient changed greatly. In sliding experiments the wear is approximately proportional to the normal load as apparently the volume of asperities being sheared is proportional to the load. In cutting we have apparently reached a limiting value of metal transfer.

Quantitative Example

In order to illustrate the use of Equation [5] we might consider some two-dimensional cutting data published by Crawford and Merchant (17). The results of Table 2 were obtained at a cutting speed of 272 fpm. If τ^* and A are considered constant[4] in these tests, then from Equations [2] and [5] we have

$$F = K\tau^* A_r = K\tau^* A(1 - e^{-BN}) \quad [12]$$

However, in metal cutting the loads are sufficiently intense so that K may be taken as unity for reasons previously stated and hence

$$\frac{F}{A\tau^*} = 1 - e^{-BN} \quad [13]$$

We may choose the constants $(A\tau^*)$ and B such that Equation [13] is in good agreement with the observed data of Table 2. When this is done it is found that

$$A\tau^* = 1300$$
$$B = 0.001$$

The observed data correspond to the points in Fig. 4 while the curve shown corresponds to Equation [13] using the foregoing values of $(A\tau^*)$ and B. All points except the last one at a rake angle of 50 deg are seen to be in good agreement with the fitted curve.

TABLE 2 CUTTING FORCES OBTAINED WITH TOOLS OF DIFFERENT RAKE ANGLE (17)

Work material, 1020 steel; tool material, 18-4-1 HSS; width of cut, 0.25 in.; feed, 0.0063 ipr; cutting speed, 272 fpm; cutting fluid, water-based fluid

α, deg	F_P, lb	F_Q, lb	F, lb	N, lb	f	A_r/A
0	885	775	775	885	0.88	0.57
10	670	420	532	587	0.90	0.44
20	550	290	460	418	1.09	0.34
30	460	150	360	323	1.12	0.28
40	365	60	281	241	1.17	0.21
50	340	70	305	165	1.85	0.15

where α = rake angle
F_P = cutting-force component in direction o resultant velocity (power component of force)
F_Q = cutting force at right angles to F_P
F = friction force on tool face = $F_P \sin \alpha + F_Q \cos \alpha$
N = normal force on tool face = $F_P \sin \alpha - F_Q \cos \alpha$
f = coefficient of friction on tool face = F/N
A_r = real area of contact
A = apparent area of contact

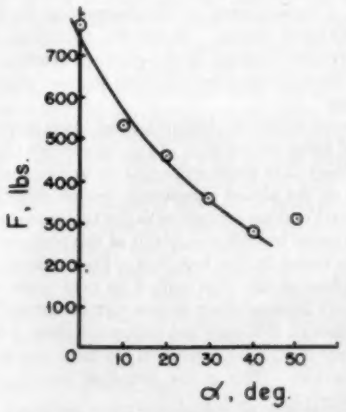

Fig. 4 Variation of Friction Force F With Rake Angle α

If a reasonable value is assumed for the apparent area of chip-tool contact we may plot A_r versus N as in Fig. 3, for this example. Taking the length of contact along the tool face as twice the depth of layer removed we have

$$A = 2bt = 2(0.25)(0.0063) = 0.00315 \text{ sq in.}$$

When values of A_r from Equation [5] are plotted against the normal force on the tool N, Fig. 5 is obtained. Here it is evident that over the entire range of the cutting tests A_r is not proportional to N as for lightly loaded sliders (Amontons' rule). The value of A that is approached asymptotically is shown dotted in Fig. 5. The values of A_r/A given in Table 2 are seen to be much larger than values for ordinary sliding contacts.

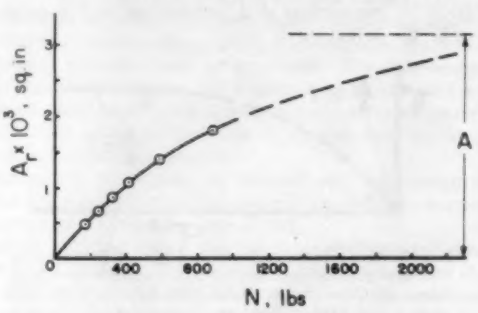

Fig. 5 Variation of Real Area of Contact A_r With Normal Load N for Example of Table 2

The value of A_r/A is observed to decrease significantly with increased rake angle. For a cutting fluid to be effective there must be space between asperities at the chip-tool interface for fluid to penetrate. The greater availability of such space with larger rake angles is evident from the values of A_r/A in Table 2. This observation is in agreement with the fact that cutting fluids are more effective with high rake-angle tools than with those having low or negative rake angles.

In obtaining Fig. 5, A was assumed to be constant. Actually, A should decrease somewhat with increased α, but this will only result in the curve of Fig. 5 deviating even farther from proportionality, and all the conclusions presented will be the more true.

The value of τ^* that was assumed constant in the foregoing calculation may be estimated by dividing the value for $A\tau^*$ by A. When this is done

$$\tau^* = 1300/0.00315 = 413{,}000 \text{ psi}$$

At first glance a shear stress of this magnitude, which is within a factor of 5 of the value corresponding to a perfect iron lattice, (based on $\tau_{\text{theoretical}}$ = shear modulus/2π) may seem unreasonably high. However, when the smallness of the contact areas of individual asperities is considered, it is to be expected that such a high value of shear stress should obtain by virtue of the size effect associated with the flow of metals (18).

The value of σ^* may be similarly estimated for small values of N from Equation [9]

$$\sigma^* = \frac{1}{AB} = \frac{1}{(0.00315)(0.001)} = 318{,}000 \text{ psi}$$

Again, this stress which may appear unusually high is influenced by the size effect. The fact that τ^* is of a more superficial nature and hence more strongly influenced by size effect than σ^* can be

[4] The tips of the asperities will always be severely strain-hardened and to such an extent that τ^* may be considered to be independent of load. While the apparent area of contact may be constant to a first approximation it probably will increase somewhat with rake angle. The influence of assuming A to be constant with α will be discussed later.

seen by comparing these two quantities. In making this comparison normal stress σ^* should be reduced by a factor of 2 by virtue of the maximum-shear theory and by an additional factor between 2 and 3 to account for the difference in flow stress of a cone and a member in simple shear. The net result is that for the same size effect to be operative σ^* should be from 4 to 6 times τ^*.

As previously stated, the value of σ^* should be expected to increase with increased load N, due to strain hardening and the mutual restraint of adjacent asperities. The manner in which σ^* changes with N in the foregoing example may be seen by dividing observed values of N by calculated values of A_r at each point in accordance with Equation [1]. When this is done, Fig. 6 results. It is evident that σ^* is not constant as for ordinary sliders but increases with N.

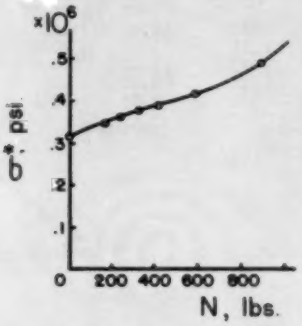

FIG. 6 VARIATION OF ASPERITY HARDNESS σ^* WITH NORMAL LOAD N FOR EXAMPLE OF TABLE 2

The large increase in coefficient of friction (τ^*/σ^*) with rake angle is due to the fact that τ^* remains essentially constant with N (since even for light loads τ^* is at a much higher stress level than σ^* is for relatively heavy loads and consequently τ^* is saturated with regard to strain hardening) while σ^* increases with increased N.[8] The reason for the increase in N with decreased rake angle α is obviously due primarily to the decreased shear angle that accompanies a decrease in α.

For ordinary sliders the value of N/A usually amounts to 500 psi or less. If $A = 0.00315$ sq in. then N would be 1.57 lb. When A_r/A is computed from Equation [5] using the value of B from the foregoing example, we obtain

$$A_r/A = 1 - e^{-0.601(1.57)} = 0.00157$$

This is the order of magnitude of values of A_r/A measured by Bowden and his associates (6) with ordinary steel sliders. Values of τ^* and σ^* for such a slider may be taken approximately as follows from the foregoing example when the normal load N is light

$$\tau^* = 413{,}000 \text{ psi}$$
$$\sigma^* = 318{,}000 \text{ psi}$$

The corresponding coefficient of friction would be 1.3 from Equation [2] if K were taken equal to 1. While K will approach 1 in cutting it undoubtedly will be less than 1 for an ordinary dry slider and the expected value of f would be reduced to 0.9 to 1 for steel sliding on steel in dry air.

BIBLIOGRAPHY

1 "The Shear Stress in Metal Cutting," by M. C. Shaw and Iain Finnie, Trans. ASME, vol. 77, 1955, p. 115.

2 "The Shear-Angle Relationship in Metal Cutting," by M. C. Shaw, N. H. Cook, and Iain Finnie, Trans. ASME, vol. 75, 1953, p. 273.

3 "De la Resistance Causeó dans les Machines," by G. Amontons, Mèmoires Académie Royale Science, 1699, p. 206; 1704, p. 96.

4 "Electric Contacts," by R. Holm, Hugo Gebers, Forläg. Stockholm, Sweden, 1946.

5 "Surface Friction of Clean Metals," by H. Ernst and M. E. Merchant, Proceedings of the Special Summer Conference on Friction and Surface Finish, M.I.T., Cambridge, Mass., 1940, p. 76.

6 "The Friction and Lubrication of Solids," by F. P. Bowden and D. Tabor, Oxford University Press, Oxford, England, 1950.

7 "Analysis and Lubrication of Bearings," by M. C. Shaw and E. F. Macks, McGraw-Hill Book Company, Inc., New York, N. Y., 1949.

8 "Metal Transfer and Wear," by I. M. Feng, *Journal of Applied Physics*, vol. 23, 1952, p. 1011.

9 "Nature of the Coefficient of Friction," by J. T. Burwell and E. Rabinowicz, *Journal of Applied Physics*, vol. 24, 1953, p. 136.

10 "The Static Coefficient of Friction and the Area of Contact," by R. C. Parker and D. Hatch, Proceedings of the Physical Society, vol. 63B, 1950, p. 185.

11 "Relation Between Friction and Adhesion," by J. S. McFarlane and D. Tabor, Proceedings of the Royal Society, London, England, series A, vol. 202, 1950, p. 244.

12 "Structure and Properties of Solid Surfaces," edited by R. Gomer and G. S. Smith, University of Chicago Press, Chicago, Ill., 1953.

13 "Grundzouge der Zerspannungslehre," by M. Kronenberg, Julius Springer, Verlag, Berlin, Germany, 1927; vol. 1, 1954, second edition.

14 "Metal Cutting Friction Coefficient Needs Reinterpretation," by M. Kronenberg, *Tool Engineer*, vol. 32, 1953, p. 49.

15 "Discontinuous Chip Formation," by N. H. Cook, Iain Finnie, and M. C. Shaw, Trans. ASME, vol. 76, 1954, p. 153.

16 "A Radioactive Study of the Wear Process," by Iain Finnie and E. Rabinowicz, *Lubrication Engineering*, vol. 12, 1956, p. 29.

17 "The Influence of Higher Rake Angles on Performance in Milling," by J. H. Crawford and M. E. Merchant, Trans. ASME, vol. 75, 1953, p. 561.

18 "Plastic Flow in the Cutting and Grinding of Materials," by M. C. Shaw, Proceedings of the National Academy of Sciences, vol. 40, 1954, pp. 394–401.

Discussion

B. T. CHAO[6] AND K. J. TRIGGER.[7] The authors are to be congratulated for their new and useful treatment of the friction process, the calculation of the real area of contact, and the local stresses at the tool chip interface. This analysis clarifies certain aspects of metal-cutting phenomena which have heretofore been obscure. Our experience is in accord with the authors' contention that the subrupture dynamic flow stress along the shear zone is unaffected by the normal stress[8] and, in a general way, we agree with the τ^* versus σ^* relationship as depicted in Fig. 2.

In calculating the numerical values of τ^* and σ^* (which are for small values of N) the authors assume that the length of contact along the tool face is twice the depth (feed) of layer removed. The writers have not found this to be the case in the machining of steel. Table 3 of this discussion compares the apparent tool-chip

[8] In the discussion presented here the increase in σ^* that is observed with increase in N is considered to be due to strain hardening and mutual interaction of flowing asperities. As pointed out in a previous paper (2), part of this increase in σ^* with increased N could be due to a restraining action associated with the presence of the shear plane. By this latter mechanism, σ^* would increase when the angle between shear plane and tool face decreased, and hence σ^* would increase when N increased as a result of an increase in α. While it is not known how much of the increase in σ^* with N is due to strain hardening and how much is due to shear-plane restraint, it is now thought that the influence of strain hardening is the greater of the two.

[6] Associate Professor of Mechanical Engineering, University of Illinois, Urbana, Ill.

[7] Professor of Mechanical Engineering, University of Illinois, Urbana, Ill. Mem. ASME.

[8] "Thermophysical Aspects of Metal Cutting," by B. T. Chao, K. J. Trigger, and L. B. Zylstra, Trans. ASME, vol. 74, 1952, pp. 1039–1054.

TABLE 3 COMPARISON OF MEASURED APPARENT AREA OF TOOL-CHIP CONTACT WITH CALCULATED VALUES BASED ON AUTHORS' ASSUMPTION

Work material: SAE 52100 steel, annealed
Tool material: Steel-cutting-grade carbide
Width of cut: 0.102 in.

Cutting speed V_c, fpm	Feed t, in.	Tool rake, deg	Apparent area of tool-chip contact, A 10^{-3} in. As measured[a]	As calculated[b]
200	0.01265	−2	7.22	2.58
		10	6.82	2.58
	0.00736	−2	5.21	1.50
		10	5.00	1.50
	0.00492	−2	4.23	1.00
		10	4.04	1.00
320	0.01265	−2	6.05	2.58
		10	5.94	2.58
	0.00736	−2	4.50	1.50
		10	4.35	1.50
	0.00492	−2	3.64	1.00
		10	3.44	1.00

[a] All area measurements were determined from photographic records, enlarged to several hundred diameters.
[b] Based on authors' assumed relationship $A = 2bt$.

contact area as measured with that as calculated according to the authors' assumption when annealed SAE 52100 steel is turned with a steel-cutting-grade carbide tool. For HSS tools, the discrepancy will be of the same order under comparable conditions.

It is evident that the measured apparent area of contact is 2 to 4 times the value used by the authors in the calculation of τ^* and σ^*. With HSS tools, even at such high rake angles as 30 or 40 deg, it seems very unlikely that the area could be estimated from the assumed relation $A = 2bt$. Consequently, the writers believe that the values of τ^* and σ^* as reported in this paper are in error.

Also, from Table 3, a definite and noticeable decrease of the apparent area of contact is observed when the rake angle is increased. Hence the relationship between σ^* and N, as shown in Fig. 6 of the paper, should be modified accordingly. The trend is to increase the relative magnitude of σ^* at small values of N or to decrease σ^* at high values of N.

Fig. 5 of the paper also should be modified for the same reason. Evidently, when the variation of the apparent area of contact with changes in tool rake is taken into account, the relationship between A_r and N will tend to become linear, at least within the range of the experimental data used by the authors.

MAX KRONENBERG.[9] This paper has the particular merit of offering plausible explanations for the conclusions in which the authors and the writer concur with regard to the coefficient of friction in metal cutting.

The two most significant sentences of the paper are as follows:

"A coefficient of friction is inadequate to characterize the sliding between chip and tool."

"The coefficient of friction in metal cutting bears little relationship to the ordinary friction process."

The writer came to the same conclusions several years ago[10] and suggested at that time going even a step further than the authors do in this paper, by recommending to discontinue the use of the concept of coefficient of friction in metal cutting.

The reasons for this recommendation are based not only on scientific considerations but also on a practical point of view. In the writer's opinion it is necessary to keep in mind the effect which our findings in metal-cutting research may have on the men in the shop and on productivity in general. A tool engineer who is busy in his daily work has but little time to analyze the reasons for a high or low value of the so-called coefficient of friction and must come to entirely wrong conclusions unless we discontinue the use of this concept. His conclusions may affect his work substantially and also his actions, say, in the application of cutting fluids, purchasing of tools, selection of work materials, and other such items on which the efficiency of production depends.

Let us assume that our tool engineer learns about a new metal and that he finds from cutting tests the coefficient of friction to be higher when machining this new metal than in the case of his older metal. What would be your conclusion? Supposedly, it would be the same as that of the tool engineer. He would continue to use the older metal with the lower coefficient of friction, assuming that he would get better conditions than with the new metal with the higher coefficient of friction.

Analysis of table 2 of paper by Finnie & Shaw

True Rake α	Friction Force F	Normal Force N	Socalled Coeff. of Friction	Angle ω (Conclusion	Angle γ Kronenb[9]
0°	775 lbs	885 lbs	0.88	48.5°	36.5°
10	532	587	0.99	48.0	27.0
20	460	418	1.09	42.5	22.5
30	360	323	1.12	41.8	13.2
40	281	241	1.17	40.5	4.5
50	305	165	1.85	28.5	9.5
	both decrease		increase		

FIG. 7

He would be wrong, as will be seen from the data of Fig. 7 of this discussion, which represents an analysis of Table 2 presented in the paper. Consider columns 2 and 3 for the friction force F and the normal force N, respectively. You will notice, when following from top to bottom, that they both decrease when the true rake angle α in column 1 increases from 0 to +50 deg. The friction force F drops from 775 to 305 lb and the normal force drops likewise, namely, from 885 to 165 lb. Such drop is certainly a desirable feature.

However, let us consider now what the coefficient of friction reveals. It will be seen from column 4 that the coefficient of friction increases from top to bottom—in spite of the decrease of the two forces, namely, from 0.88 to 1.85. Hence our tool engineer comes to the conclusion that something undesirable has happened, because the coefficient of friction has increased, although the contrary is true. It follows that the concept of a coefficient of friction is misleading in metal cutting and should be discarded.

Discarding the coefficient of friction, however, does not mean that we should discontinue to investigate the friction process altogether; to the contrary. Investigations as presented in this paper should be continued because we can obtain from such research useful data when using a different concept than the friction coefficient.

It is suggested that the inverse value of the coefficient of friction be used. This inverse value is the tangent of the angle of direction of the resultant cutting force R, indicated by angle ω in Fig. 7 ($tg\omega = N/F$).

This angle has been calculated from the data of the paper under discussion and also the angle γ which indicates the direction of the resultant cutting force with respect to the flank of the tool. The two angles are tabulated in columns 5 and 6. You may ask why these two angles are of interest in metal cutting. If you follow the change in angle γ in column 6, you will see that the resultant cutting force acts considerably closer to the tool flank when the true rake is 50 deg than when it is 0 deg, and tension and com-

[9] Consulting Engineer, Cincinnati, Ohio. Mem. ASME.
[10] "On the Analysis of Cutting-Tool Temperatures," by E. G. Loewen and M. C. Shaw, Trans. ASME, vol. 76, 1954, p. 229. See also *Tool Engineer*, October 1953, pp. 49–50.

pression in the tool face depend on angle ω. It also will be noted from the two sketches at the bottom of Fig. 7, that the cutting forces in the left-hand sketch are large, and small in the right-hand sketch in spite of the inverse values for the so-called coefficient of friction. This graphic representation is a good indication for the misleading concept as discussed.

When recently publishing a book on the "Fundamentals of Metal Cutting Science" the writer came to the conclusion that the difference between a coefficient of friction in metal cutting and in ordinary friction results from the fact that the gliding body (chip) is plastically deformed in metal cutting, a deformation that does not occur in ordinary friction.

The authors differ somewhat in their explanation from that of the writer and attribute the difference in the behavior of a coefficient of friction in metal cutting to the change in the ratio of the real to the apparent area of contact between chip and tool that takes place as the normal force changes. This hypothesis is very interesting and the authors should be commended for developing it.

They indicate also that the number of capillaries would change with a change in the contact-area ratio, concluding that cutting fluids become less effective as the ratio approaches unity. Hence, in the case of negative rakes, cutting fluids would be least effective. In the writer's opinion, however, cutting fluids also could be used in the case of negative rakes and carbides.

To explain this, Fig. 8 has been prepared to show the practical significance of the angles ω and γ for the resultant cutting force in conjunction with the appearance of compression and tension in the tool face.

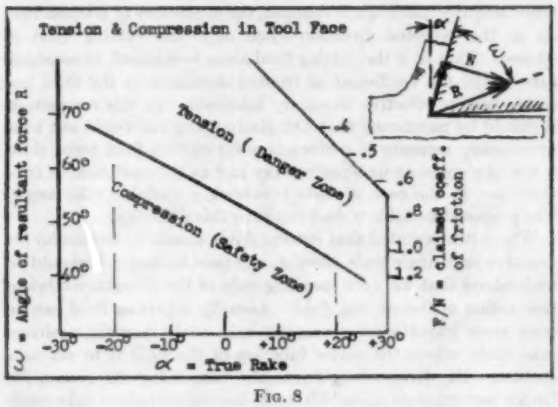

FIG. 8

The angle ω is plotted at the left-hand scale, the so-called coefficient of friction of the right-hand scale, running in opposite direction.

Tension in the tool face is indicated by the field marked "Tension (Danger Zone);" compression in the tool face exists for combinations of α and ω represented by the lower field marked "Compression (Safety Zone)."

It will be seen that the compression zone increases as the true rake α becomes smaller and even more so as the true rake enters the negative field.

Example. When $\alpha = +20$ deg, compression in the tool face exists only for small angle ω (or for large coefficients of friction —greater than 1.2). Hence compression exists only when the resultant cutting force R is relatively close to the tool face.

Using a cutting fluid and reducing the friction force would make the conditions worse, because we would reduce the so-called coefficient of friction to, say, 0.8 or increase angle ω and thereby cause tension (and perhaps cracks) in the tool face. (If we go still higher than the inclined line, conditions change, but this cannot be discussed here.)

However, when a negative true rake of $\alpha = -20$ deg is used it would be possible to employ a cutting fluid without entering the danger zone of tension, unless the angle of direction of the cutting force exceeds about $\omega = 65$ deg.

Cutting without a coolant is the rule in the case of carbides with positive rakes because a high coefficient of friction is required to keep out of the tension range. Fig. 8, however, indicates that new avenues for application of cutting fluids may be opened in connection with carbide tools when investigations on tension and compression produced in the tool face are carried out for various cutting fluids. Thus it may be realized why the paper presented by the authors is a valuable contribution toward explanation of these problems.

ERNEST RABINOWICZ.[11] This interesting paper introduces two quantities that are relatively new to friction theory, namely, A_r/A and K. The authors point out that for the case of sliding surfaces, A_r/A will be small; however, this is not necessarily so. When concentrated contact occurs, e.g., a hemisphere on a flat surface, high normal pressures are produced, and we may estimate values of A_r/A of $^1/_2$, using taper section methods of (cf. Moore[12]), and $^1/_4$, using a comparison of friction and wear data.[13] These values are of the same order of magnitude as those given by the authors.

In regard to K, the fraction of the surfaces that has formed welds, it should first be pointed out that Equation [2] given by the authors is not in the form customarily used in friction calculations, allowance being made in the latter for a friction force produced by the shearing of nonwelded junctions. In other respects, the constant K is similar to that given by Archard,[14] who calculated the fraction of junctions that produce metal-transfer fragments during sliding. Comparing Archard's values with those in the paper, it is necessary to multiply his results by a factor of 3 for an assumed A_r/A ratio of 1:3 and by a factor of 2, since metal transfer was measured in one direction only. The recalculated values of K for unlike metal combinations range from 0.9 to 0.06 per cent. It is likely, but by no means certain, that K during metal cutting is larger.

A complication that the authors have not considered is the effect of the difference in sliding conditions for points away from the cutting edge, which will lead to systematic variations in both A_r/A and K.

It is felt that the stimulating treatment by the authors is definitely in the right direction but that an additional factor may have to be introduced to bring out fully the difference between the cutting and sliding situations.

A. O. SCHMIDT.[15] The authors present again a thorough analysis of a significant sector in the metal-cutting field. The importance of their findings is expressed in their statements that the "coefficient of friction" in metal cutting is not the same as thought of in the ordinary friction process. The experimental data and

[11] Assistant Professor of Mechanical Engineering, Massachusetts Institute of Technology, Cambridge, Mass.

[12] "Deformation of Metals in Static and in Sliding Contact," by A. J. W. Moore, Proceedings of the Royal Society, London, England, series A, vol. 195, 1948, pp. 231-244.

[13] "The Importance of Wear Fragments During Sliding," by E. Rabinowicz, pp. 165–178, "Fundamentals of Friction and Lubrication in Engineering:" The American Society of Lubrication Engineers, Chicago, Ill., 1954.

[14] "Contact and Rubbing of Flat Surfaces," by J. F. Archard, *Journal of Applied Physics*, vol. 24, 1953, pp. 981–988.

[15] Research Engineer, Kearney & Trecker Corporation, Milwaukee, Wis. Mem. ASME.

those given in Table 2 show the effect of different rake angles. This table could be extended into the range of negative rake angles and also include average chip temperatures as well as tool-tip interface temperatures.

Average chip temperatures have been determined by thermal balance from calorimeter measurements of heat in the chips during milling tests with SAE 1020: as 1280 F for $\alpha = 30$ deg negative and only 600 F for $\alpha = 30$ deg positive (cutting speeds, 200–1200 fpm.; feed, 0.006 in. per tooth).

It can be stated that the relationship F/N is definitely influenced by temperatures occurring in and between chip, tool, and workpiece.

Another temperature value which can be obtained is that of the tool-chip interface which would vary in cuts of this type between a high temperature of 1650 F for the tool with 30-deg negative rake angle, to a low temperature of 800 F for the 30-deg positive rake angle.

Measuring and considering such temperature values will help to explain that F/N must vary because positive rake angles will entail lower temperatures in chips and at the tool-chip interface.

There is such an intimate contact between the chip and tool that we can speak of a weld. This weld will be broken more easily at higher temperature, i.e., when using negative rake angles, and that will make the relation $F/N < 1$. However, it should be borne in mind that with negative rake angles there are always higher cutting forces first, which next bring about higher temperatures in the cutting region.

We hope that the authors will bring this investigation to a conclusion which will benefit all of us interested in these problems.

B. F. V. Turkovich.[16] The authors present another of their fine papers which definitely provide many fruitful thoughts. Some of their assumptions and conclusions deserve a rather thorough discussion. The mechanism of dry friction between metals has been a field of investigation for quite some time. Although several of its aspects are well known, the intimate process is still obscure in its essence. This is probably due to the fact that our knowledge in physics of metallic surfaces in intimate contacts is not sufficiently complete to permit a broad all-embracing theory of friction. It is therefore more than gratifying to study the paper of the authors because it takes so many factors into consideration, offering a plausible interpretation of the friction process in metal cutting.

Let us analyze Equation [1] of the paper. There is an implication of uniform distribution of the normal load. Although this may be true in the case of an ordinary slide, even with extremely high pressure it is questionable that it would also happen necessarily in the cutting of metals. If uniform load distribution is not the case, then the friction force would vary somehow along the chip-tool interface. Our measurements, however, would indicate only some sort of average value. It is also important to emphasize the influence of the temperature distribution as shown in a recent paper by Chao and Trigger.[17]

Authors' Closure

The authors wish to thank the several discussers for their valued comments.

Professors Chao and Trigger question the assumption that the area between chip and tool is given by $A = 2bt$ and present data in support of their comment. It would appear from these data that a better assumption might have been $A = 7bt$ for the range of speed, rake angle, and undeformed chip thickess of Table 2. Substitution of this relation would change none of the conclusions, but would result in the following changes in detail:

1 The value of A for the cutting tests considered would be 3.5 times the value given or 0.01103 sq in.

2 The value of τ^* would be $^1/_{3.5}$, the value given or 118,000 psi, which is still a very high value of flow shear stress for mild steel.

3 The value of σ^* would be $^1/_{3.5}$, the value given or 91,000 psi.

4 The ordinates of Fig. 5 would be multiplied by 3.5, while those of Fig. 6 would be divided by 3.5.

5 The value of N in the slider discussion would be 3.5 times the value given and consequently the value of A_r/A for the slider would be 3.5 times the value given or 0.0055. The values of τ^* and σ^* for the slider would each be divided by 3.5.

The measurement of the apparent area of contact between chip and tool is very difficult to make and, in view of the approximate nature of the results obtained, it does not seem justified to use an expression for this area more complex than the one used here. However, it would appear that the observations of Professors Chao and Trigger to the effect that the value of the constant 7 in the foregoing expression for area will decrease somewhat with increase in rake angle are correct. A sthey point out, this would tend to make the curves of Figs. 5 and 6 somewhat more linear.

Dr. Kronenberg suggests that use of a coefficient of friction in cutting be discontinued since it can be misleading. While this is true when we observe what happens to the coefficient of friction when only the rake angle is changed, the coefficient of friction varies in the expected direction when only the cutting fluid is altered. That is, if the cutting fluid alone is changed, at constant rake angle, the coefficient of friction decreases as the fluid becomes a more effective boundary lubricant. In this connection it should be mentioned that Dr. Kronenberg's ω would not be a satisfactory measure of performance for cutting-fluid tests, since it would vary in an unexpected way just as the coefficient of friction does in the case of tests involving a variable rake angle. The proposed variable γ does not have this difficulty.

Where it was stated that cutting fluids should be less useful for negative rake-angle tools, since A_r will then be larger, it should be understood that we were speaking only of the boundary-lubrication action of the cutting fluid. Actually a cutting fluid can be even more important for negative-rake tools than for positive-rake tools, where the major function of the fluid is to act as a coolant. Dr. Kronenberg's remarks concerning the reason for better performance of carbide tools having a positive rake angle when used dry are very interesting.

Professor Rabinowicz is correct in stating that A_r/A need not be small for ordinary slider experiments. Where ordinary sliders were referred to we had in mind a block sliding on a flat plate rather than a heavily loaded ball. The value of K in Archard's treatment of wear is different from that used here. Archard's K is the probability of a weld breaking in one surface or the other, while our K is the fraction of the real area that is actually welded. The stress to shear tbe unwelded portion of the area was not included in our discussion, since it was assumed to be relatively small. The variation in stress and area of contact along the tool face was not considered in this discussion. Actually it would appear that the real area is distributed more densely near the cutting point than near the region where the chip leaves the tool. While this refinement is apparently important in some calculations, as noted later, no attempt was made to include it in this paper.

As Dr. Schmidt points out, a change of chip-tool-interface

[16] Research Engineer, Kearney & Trecker Corporation, Milwaukee, Wis.

[17] "Temperature Disribution at the Tool-Chip Interface in Metal Cutting," by B. T. Chao and K. J. Trigger, Trans. ASME, vol. 77, 1955, pp. 1107–1121.

temperature will accompany a change in rake angle and this could be responsible for part of the change in coefficient of friction observed. This change in temperature would be in the right direction to cause a decrease in friction with decrease in rake angle. However, the main change in coefficient of friction is not thought to be due to this cause, since about the same change in coefficient of friction with rake angle is observed when cutting at the slowest of speeds where temperature could have no influence. The reason the coefficient of friction is thought to change slowly with change of surface temperature lies in the fact that both τ and σ for surface asperities are influenced by temperature in about the same way. The change in temperature with rake angle that is observed is due to the more superficial nature of τ than α. A more refined analysis than that presented here should include the effect of chip-tool temperature on the coefficient of friction.

Mr. Turkovich raises the question of force distribution along the tool face, as did Professor Rabinowicz. It is only to gain a first approximation that we assume the normal stress to be uniformly distributed. Actually a better second approximation would involve a linear variation in normal and tangential force from a maximum at the tool point to zero at the point where the chip leaves the tool face. In the reference,[17] cited by Mr. Turkovich, the authors compute the temperature variation based upon a uniform face distribution and find the chip-tool-interface temperature to be maximum not at the tool point, but at the point where the chip leaves contact with the tool. However, this is not where the crater first develops and we have reason to question this calculation on the same grounds on which Mr. Turkovich discusses the present calculation. We recently have repeated the temperature-distribution calculation with gradually varying forces instead of uniform ones and have found the maximum temperature now to come close to the center of the chip-tool contact length, which is also the point where the crater has its maximum depth. It would appear that the solutions to both the problem discussed here and the temperature-distribution problem will benefit from a nonuniform force distribution.

Scoring Characteristics of Thirty-Eight Different Elemental Metals in High-Speed Sliding Contact With Steel

By A. E. ROACH,[1] C. L. GOODZEIT,[2] and R. P. HUNNICUTT,[3] DETROIT, MICH.

A study has been made of the "score resistance" of 38 elemental metals tested as slider bearings against 1045 steel disks. It was found that the metals which have the best score resistance against steel are the B-subgroup metals which are either insoluble with iron or else form intermetallic compounds with iron.

Introduction

THIS paper is concerned with the score resistance of elemental substances, chiefly metals, in high-speed sliding contact with steel. By score resistance is meant the ability of materials to slide against each other without welding or otherwise sticking together. The terms "galling," "seizing," and "metal transfer and pickup" are sometimes used in technical literature as synonyms for scoring.

Score resistance is a property of great practical importance in bearings, piston rings, shaft seals, gears, and indeed all parts that rub together. Although it is a property that has been studied for many years (1)[4] very little is actually known about it, and what is known is entirely empirical and frequently contradictory.

The motivation for the present study was the belief that certain developments in the field of solid-state physics may now offer at least a partial explanation for the scoring and nonscoring behavior of various metals.

The first step was to carry out a systematic series of bearing tests with various metallic elements. There are 92 naturally occuring elements of which 70 may be described as metallic. Not all of these are suitable for testing. Certain metals are not available in sufficient quantity—metals such as radium, polonium, protoactinium, and various rare earths. Some quite common metals—mercury, gallium, sodium, and potassium—have melting points so low that running them as solid bearings is not possible in our tests. For these and similar reasons, a number of metals were struck off the list of those to be tested. In the end, tests were carried out with 38 different elements ranging from beryllium (atomic No. 4) to uranium (atomic No. 92).

Apparatus

Fig. 1 shows the bearing test machine used in the experiments. The various metallic elements were tested in the form of slider bearings, measuring $^5/_8 \times {}^5/_8$ in., pressed at an angle of $^1/_2$ deg against the face of a 1045 steel disk, as shown in Fig. 2.

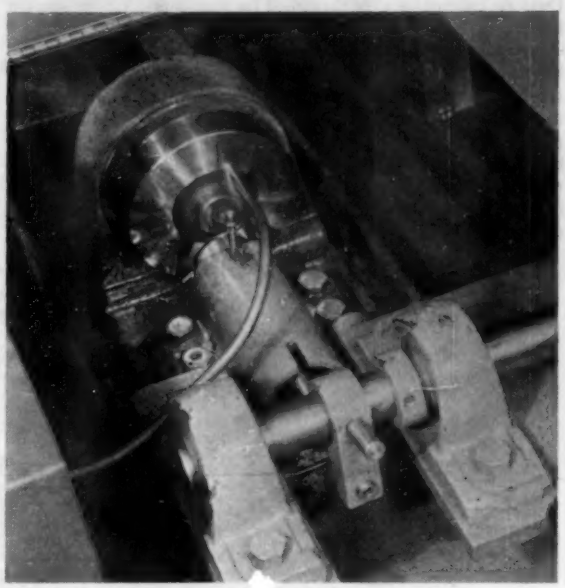

Fig. 1 Slider-Bearing Test Machine

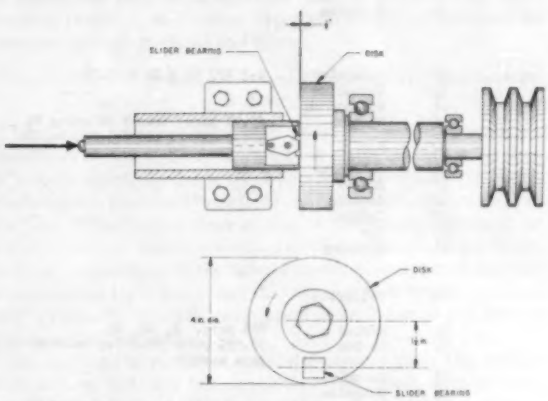

Fig. 2 Schematic of Slider-Bearing Test Machine

Disk speed was 5400 rpm, giving an average sliding velocity of 4640 fpm. The load was applied by means of weights which acted through a beam not shown in the figure. The load was variable between zero and 1200 lb.

---

[1] Supervisor of Bearing Development, Research Staff, General Motors Corporation. Deceased, July, 1955.

[2] Research and Development Engineer, Research Staff, General Motors Corporation. Assoc. Mem. ASME.

[3] Research Metallurgist, Research Staff, General Motors Corporation.

[4] Numbers in parentheses refer to Bibliography at end of paper.

Contributed by the Research Committee on Lubrication under the auspices of the Lubrication Activity and presented at a joint session with the Research Committee on Metal Processing at the Annual Meeting, New York, N. Y., November 28–December 3, 1954, of The American Society of Mechanical Engineers.

Note: Statements and opinions advanced in papers are to be understood as individual expressions of their authors and not those of the Society. Manuscript received at ASME Headquarters, August 3, 1954. Paper No. 54—A-61.

Lubrication was provided by a fine stream of kerosene (2.7 cc per sec) sprayed upon the hub of the disk. The lubrication was partial at best; electrical resistance measurements made across the kerosene film indicated that metal-to-metal contact occurred at all loads.

Preparation of Slider Bearings and Disks

Thirty-eight different elemental metals were tested as slider bearings against 1045 steel disks. Table 1 is a list of the elements tested, their known impurities, and pertinent physical properties. Data on impurities were furnished by suppliers. Where specific impurities are not listed, the element is described as "commercially pure." The hardness given in the table is the indentation hardness of the finished slider bearing, measured at room temperature with a Tukon microhardness tester, using a diamond pyramid indenter. The solubility is the per cent solubility of solid iron in molten bearing metal at the melting-point temperature of the bearing metal. If the bearing metal has a higher melting point than iron, the solubility is that of solid bearing metal in molten iron at the melting-point temperature of iron. Solubility data are taken from the "Metals Handbook," Hansen's "Der Aufbau der Zweistofflegierungen," and other sources. "Periodic Group" indicates the position of the element in the Periodic Table. The symbol "A" denotes a "true" metal of the alkali or alkaline earth groups. "T" denotes a true metal of the transition metal group. "IB" . . . "VIB" denote the various B-subgroups.

The slider bearings of various metallic elements were faced off by turning in a lathe. They were washed in solvent and air-dried. A new slider bearing was used for each test.

The disks were of 1045 steel hardened to 50 R_c or greater to a depth of $^1/_{16}$ in. and then tempered to 28–30 R_c. This steel was selected for its low alloy content and satisfactory hardenability; an additional reason for its selection is that it is widely used as a crankshaft steel in automotive engines. The faces of the disks were ground in a special fixture which rotated the disks about an axis at right angles to the axis of rotation of the grinding wheel. This produced a very flat surface with concentric grinding marks, the roughness of which was maintained between 5 and 8 microinches. Squareness of the faces with the bores was within 0.0005 in. total indicated runout. Each disk was inspected under the microscope for uniformity of surface texture, freedom from embedded abrasive particles, nicks, skippers, and other surface defects. A newly ground disk was used for each test.

TABLE 1 ELEMENTAL METALS TESTED AS SLIDER BEARINGS

Atomic Number	Name	Known Impurities	Melting Point Degrees C	Hardness DPH	Solubility Per Cent	Periodic Group	Remarks
4	Beryllium	Less than 1% Fe, Si, Al, Ca	1280	314	>0.05	A	
6	Carbon		--		1.7	-	Delanium Graphite
12	Magnesium	99.99% pure	651	38.4	0.026	A	
13	Aluminum	99.99% pure	660	31.1	0.03	A	
14	Silicon		1420		(4-5)?	-	
20	Calcium	99.9% pure	810	24.6	Insoluble	A	
22	Titanium	99.5% pure; 0.1-0.3 Fe, 0.02-0.08 N, 0.1 C, trace O	1800	277	6.5	T	
24	Chromium		1615	910	100	T	Electroplated on steel
26	Iron		1535	105.5	100	T	
27	Cobalt		1480	339	100	T	
28	Nickel		1455	644	100	T	Electroplated on steel
29	Copper		1083	101.4	4	IB	
30	Zinc		419	35.4	0.0009-0.0028	IIB	
32	Germanium	Less than 5 ppm of Si, Mg, Cu, Pb	958.5	798	(Compound)?	IVB	Bearing fractured during test but did not damage disk
34	Selenium		220	39.2	Compound	VIB	Clad to Delanium Graphite back; Se extruded under test
40	Zirconium	2-3 Hf, Hf + Zr = 99.7%	1900	121		T	
41	Columbium		1950	73.5	12	T	
42	Molybdenum		2620	186	34	T	
45	Rhodium	99.9% pure; traces of other Pt group metals and Ag, Au, Cu, Ca	1985	517	100	T	0.015 inch thick; brazed to silver-clad steel back
46	Palladium	Same	1553	71.3	100	T	Same
47	Silver		960	31.2	0.0004-0.0006	IB	Clad on steel
48	Cadmium		320.9	22	0.0002-0.0004	IIB	Puddled on steel
49	Indium		155	1.6	Insoluble	IIIB	Same
50	Tin		231.9	17.7	Compound	IVB	Same
51	Antimony		630.5	106.8	Compound	VB	Electroplated on steel; columnar structure
52	Tellurium		452		Compound	VIB	
56	Barium	98% pure. N, Ca, Mg	850		Insoluble	A	
58	Cerium	98.05% pure. 0.8 Fe, balance rare earths	640	54.8	Soluble	T	
73	Tantalum		2850	106	7	T	
74	Tungsten		3370	484	32.5	T	Sintered
77	Iridium	99.9% pure; traces of other Pt group metals and Ag, Au, Cu, Ca	2350	722	37.8	T	0.015 inch thick; brazed to silver-clad steel back
78	Platinum	99.99% pure; traces of other Pt group metals and Ag, Au, Cu, Ca	1773	91.4	100	T	Same
79	Gold		1063	73.7	34	IB	Electroplated on nickel
81	Thallium		303.5	3.5	Insoluble	IIIB	Puddled on steel
82	Lead		327.4	7.0	Insoluble	IVB	Same
83	Bismuth		271.3	25.9	0.0002-0.0004	VB	Same
90	Thorium	98.5% pure. 0.04 Ca, 0.05 Fe, 0.5-1.5 thorium oxide	1845	111.3		T	
92	Uranium		1130	454		T	

Procedure

In testing various metallic elements as slider bearings, it was found that elements (such as lead and tin) which are known to have good score resistance against steel are able to carry heavy loads without seizing, while other elements (such as iron) which are known to have poor score resistance against steel seize at very light loads. Accordingly, it was decided to adopt load-carrying ability as a criterion for score resistance.

Four different score-resistance classifications were then defined on the basis of an elimination procedure involving testing at three different load conditions of increasing severity. These four classifications are as follows:

Very Poor Score Resistance Against Steel. The class comprises all elements that fail the first or least severe test in which the load is increased uniformly from zero to 300 lb at a rate of 4.35 lb per sec.

Poor Score Resistance Against Steel. This class comprises all elements that pass the first test but fail the second test in which the load is maintained constant at 300 lb for 1 min.

Fair Score Resistance Against Steel. This class comprises all elements that pass the first two tests but fail the third test in which the load is maintained constant at 500 lb for 1 min.

Good Score Resistance Against Steel. This class comprises all elements that pass the 500-lb constant-load test.

Results

Table 2 summarizes the principal results of the tests.

In most instances at least four different tests were made with each metal, a new slider bearing and disk being used in each test. The exceptions were the precious metals—rhodium, palladium, platinum, and iridium—for which only two runs each were made.

TABLE 2 SCORE RESISTANCE OF ELEMENTS AGAINST 1045 STEEL

Good	Fair	Poor	Very Poor
Germanium	Carbon	Magnesium	Beryllium
Silver	Copper	Aluminum	Silicon
Cadmium	Selenium	Copper	Calcium
Indium	Cadmium	Zinc	Titanium
Tin	Tellurium	Barium	Chromium
Antimony		Tungsten	Iron
Thallium			Cobalt
Lead			Nickel
Bismuth			Zirconium
			Columbium
			Molybdenum
			Rhodium
			Palladium
			Cerium
			Tantalum
			Iridium
			Platinum
			Gold
			Thorium
			Uranium

The results of the separate tests made with slider bearings of the same metal were generally in excellent agreement. A few metals exhibited erratic or marginal behavior, successive tests placing them in two adjacent classes as indicated by Table 2. These were cadmium and copper. In no case did the variation exceed two adjacent classes. The widest variation was exhibited by copper which in some tests rated high in the "fair" class and in other tests rated low in the "poor" class.

Fig. 3 shows the appearance (after testing) of a slider bearing and disk which have "good" score resistance. The only evidence of sliding contact is the polishing of the edge of the slider bearing where it has been in contact with the disk and a corresponding polishing of the disk along the circumferential track of contact with the slider bearing. Examination of the slider bearing and disk under the microscope shows no evidence of metal transfer either from the slider bearing to the disk or vice versa.

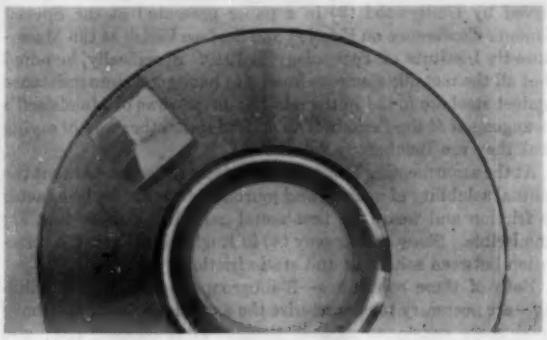

Fig. 3 Antimony Slider Bearing With 1045 Steel Disk—Typical of Good Metal Combination

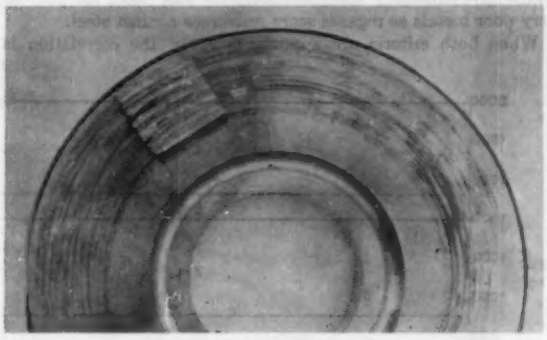

Fig. 4 Zirconium Slider Bearing With 1045 Steel Disk—Typical of Very Poor Metal Combination

Fig. 4 shows the appearance (after testing) of a slider bearing and disk which have "very poor" score resistance together. Both have suffered extensive grooving, tearing, and metal transfer. With such materials failure is manifested by sudden stoppage of the disk due to seizure of the bearing or by the sudden appearance of transferred bearing metal to the disk, accompanied by rapid heating, evolution of kerosene vapor and smoke, and in some instances, showers of sparks and flames.

Correlation of Score Resistance With Other Properties of Metals

Numerous attempts have been made to relate the score resistance of metals to other more readily definable properties such as melting point, hardness, oxide-forming activity, specific heat, conductivity, modulus of elasticity, metallographic structure, and the like. These correlations appear to have been suggested, for the most part, by experience with a small number of metals. When they are re-examined in the light of the more complete data of the slider-bearing tests, it is found that they provide what is, at best, only a partially successful description of the behavior of metals in high-speed sliding contact.

In studying the results of the slider-bearing tests, the authors were able to find only one correlation that agreed with all their experimental findings. This correlation may be stated as follows:

The only elemental metals that had satisfactory score resistance against steel in the slider-bearing tests were the B-subgroup metals that are immiscible with iron or that form intermetallic compounds with iron. All other metals had unsatisfactory score resistance against steel.

The fact that the score resistance of metals sliding against steel is related to their position in the Periodic Table was first ob-

served by Underwood (2) in a paper presented at the Special Summer Conference on Friction and Surface Finish at the Massachusetts Institute of Technology in 1940. Specifically, he noted that all the metallic elements known to have good score resistance against steel are found in the odd-numbered rows of Mendeleeff's arrangement of the Periodic Table. This is another way of saying that they are B-subgroup metals.

At the same meeting Ernst and Merchant (3) suggested that the mutual solubility of bearing and journal metals should be a factor in friction and wear, the best metal pairs being those that are immiscible. Shaw and Leavey (4) in England had found a correlation between solubility and static friction even earlier.

Both of these conditions—B-subgroupedness and immiscibility—are necessary to characterize the metallic elements that have good score resistance against steel. Thus copper, zinc, and gold, which are B-subgroup metals, have poor to very poor score resistance against steel. Likewise calcium and barium which have extremely small solubility for solid iron, are poor to very poor metals as regards score resistance against steel.

When both criteria are applied, however, the correlation is excellent. In fact, there are no exceptions among the elements tested as slider bearings. All metals that rated good against steel satisfied both conditions. Conversely, all metals that satisfied both conditions rated good against steel.

Solubility of Iron in B-Subgroup Metals

The constitution diagrams of binary systems containing iron and a B-subgroup metal may be divided into three general categories; namely, (*a*) systems of metals that are insoluble, (*b*) systems of metals that form solutions without intermediate phases, and (*c*) systems of metals that form solutions with intermediate phases. The last category may be further subdivided, as will be shown later.

Systems of Insoluble Metals. This category comprises binary systems in which the elements are immiscible in both solid and liquid states. There are no intermediate phases. The constitution diagrams consist of series of horizontal straight lines, as shown in Fig. 5.

Some systems in this category are bismuth-iron (reference 5). cadmium-iron (all known diagrams incomplete), indium-iron (reference 6), lead-iron (reference 7), silver-iron (all known diagrams incomplete), and thallium-iron (all known diagrams incomplete).

Although these metals are called "insoluble," there is undoubtedly some solubility, and in a few cases it has been measured. Liquid bismuth, for example, will dissolve 0.0002–0.0004 per cent of solid iron. For cadmium and silver the solubilities are 0.0002–0.0004 and 0.0004–0.0006 per cent, respectively. The solubility of solid iron in liquid indium, thallium, or lead is not known.

All B-subgroup metals in this category had good score resistance against steel in the slider-bearing tests.

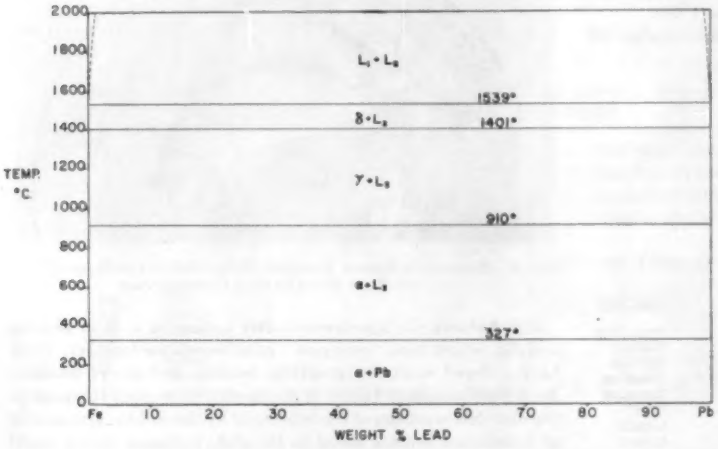

Fig. 5 Phase Diagram of Lead-Iron System

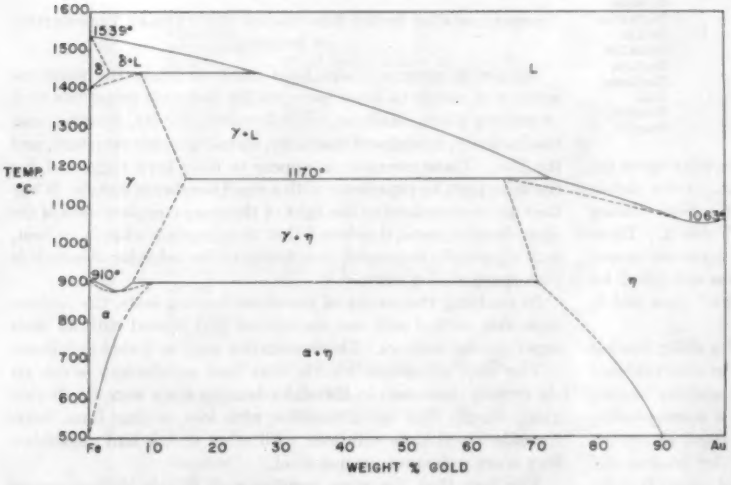

Fig. 6 Phase Diagram of Gold-Iron System

Systems of Metals Forming Solutions Without Intermediate Phases. This category comprises binary systems in which the elements form alloys with extended terminal solubility but without intermediate phases. A typical constitution diagram is shown in Fig. 6.

Systems in this category are gold-iron (reference 8), and copper-iron (reference 9).

The score resistance of gold was very poor in the slider-bearing tests, while that of copper ranged from fair to poor.

Systems of Metals Forming Solutions With Intermediate Phases. Metal pairs in this category differ widely as regards score resistance. The observed differences may be correlated with the constitution diagrams which are of two different types:

(*a*) Those containing intermediate phases composed of intermetallic compounds of definite stoichiometric composition.

(*b*) Those containing intermediate phases composed of solid solutions with a range of compositions.

All B-subgroup metals forming well-defined intermetallic compounds with iron

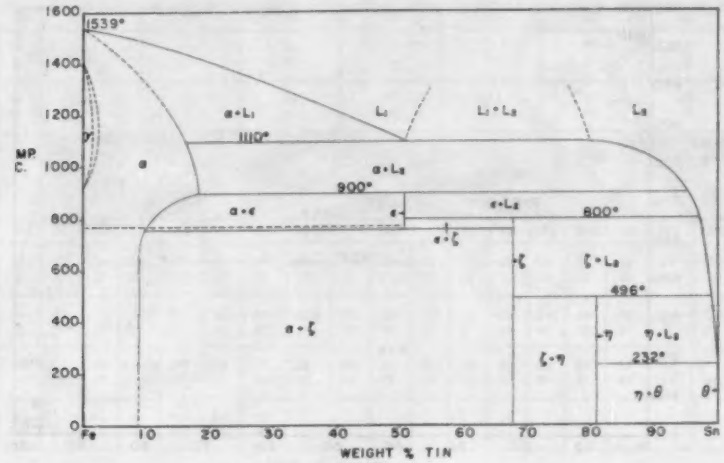

FIG. 7 PHASE DIAGRAM OF TIN-IRON SYSTEM

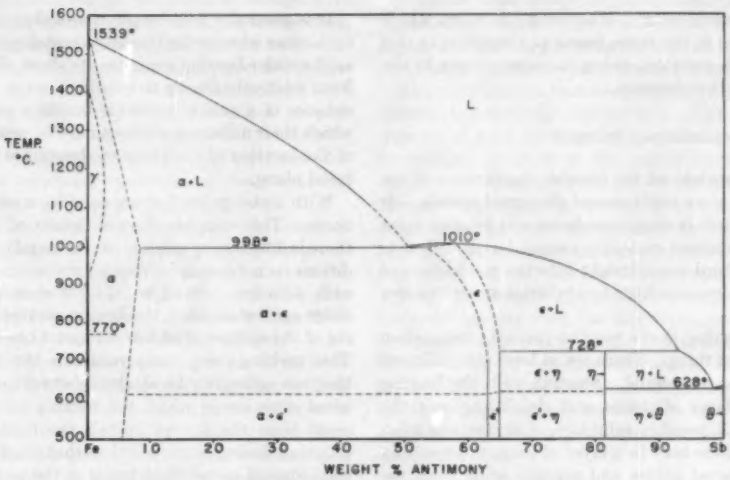

FIG. 8 PHASE DIAGRAM OF ANTIMONY-IRON SYSTEM

rated fair to good in the slider-bearing tests. These metals were as follows:

Tin (references 10 and 11). Tin and iron form a series of intermetallic compounds corresponding to the compositions Fe_2Sn, FeSn, and $FeSn_2$. These are indicated on the constitution diagram Fig. 7, by vertical lines.

Antimony (reference 12). Antimony and iron form an intermetallic compound of composition $FeSb_2$ which is represented by a vertical line at 33⅓ atomic per cent iron on the constitution diagram, Fig. 8.

Selenium and Tellurium (reference 13). Selenium and tellurium are reported to form intermediate compounds of composition FeSe and FeTe.

Germanium (reference 14). Many features of the germanium-iron diagram are unknown. The system is reported to contain two intermediate phases which are believed to be intermetallic compounds. Some sources indicate that the phase occurring on the low iron side is suppressed by rapid cooling and is replaced by a eutectic transformation at about 800–850 deg.

Of the B-subgroup metals tested in the slider-bearing tests, only zinc forms a series of intermediate solid solutions with iron (references 15 and 16). These are shown as areas on the constitution diagram, Fig. 9. Zinc had poor score resistance in the slider-bearing tests.

We may now summarize the correlation between the score resistance of the B-subgroup metals and their constitution diagrams:

1 B-subgroup metals that are immiscible with iron in both the solid and the liquid states had good score resistance in the slider-bearing tests.

2 B-subgroup metals that have extended solid solubility for iron had poor to very poor score resistance in the tests. Copper, which generally rated poor, rated fair in some tests.

3 B-subgroup metals that form intermediate phases with iron had either good to fair or poor score resistance, depending upon the character of the intermediate phases. When the intermediate phase is a definite intermetallic compound, the score resistance is good to fair. When the intermediate phase is a solid

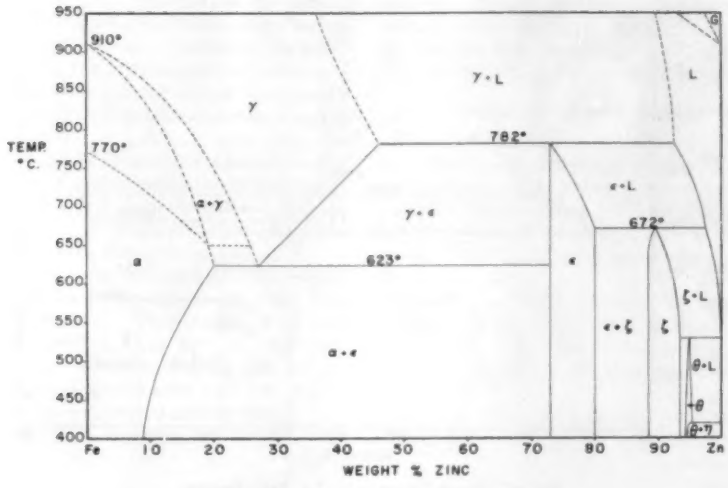

FIG. 9 PHASE DIAGRAM OF ZINC-IRON SYSTEM

solution the score resistance is poor. Whether germanium, which had good score resistance in the tests, forms an exception to this generalization is an open question, owing to uncertainties in the germanium-iron constitution diagram.

MECHANISM OF SCORING

It is interesting to speculate on the possible significance of the correlation between the score resistance of elemental metals sliding against steel and their B-subgroupedness and solubility for iron. While such speculations certainly cannot be proved, it is hoped that they may afford some insight into the mechanism of bearing failure and thereby contribute to a rational understanding of bearing metals.

We may start by observing that a bearing-journal combination is an exceedingly complex thing. There are at least nine different layers of materials to be considered. Starting with the bearing metal, we have first a layer of oxides and, depending upon the character of the lubricant, possibly sulphides, chlorides, and other materials. Over these there may be a layer of soap, produced by reaction between the metal oxides and organic acids from the lubricant. Over this there may be an adsorbed layer of oriented polar molecules from the lubricant. Finally, we have the lubricant itself.

The thickness of these various layers is extremely small. The oxides and soap layers may each be on the order of a hundred Ångstrom units, while the layer of oriented polar molecules is at most only a few molecules thick. The thickness of the lubricant layer may range from as large as a few thousandths of an inch to as small as a few millionths of an inch or less.

As we move on toward the journal, we encounter the same layers in reverse order—first the oriented polar molecules, then the soap film, then the oxide layer, and finally the steel of the journal itself.

Although a complete description of the events involved in the scoring failure of a bearing would take account of each of these layers, the most important aspect of the problem is what happens when bare metal slides against bare metal, because the layers of oriented polar molecules and soap films offer only weak resistance to penetration, while the oxide layer is undoubtedly broken up and stirred about, exposing areas of bare metal, when the bearing and journal slide against each other at high speed and under heavy load.

It is generally held by physicists that all metals will adhere to each other when actual metal-to-metal contact occurs. However, as the slider-bearing experiments show, this adhesion may range from relatively strong to relatively weak. In fact, the score resistance of a pair of metals is simply a measure of the ease with which their adhering surfaces may be separated by shearing and of the location of the plane of shearing with respect to the interfacial plane.

With metal pairs that are soluble, scoring and welding readily occur. This suggests that at points of metal-to-metal contact there is diffusion or solution of one metal into the other. The conditions in a bearing-journal combination are very favorable for such diffusion. Bowden (17) has shown that when one metal slides against another, the heat generated by friction causes melting of the surface of whichever metal has the lower melting point. This melting-point temperature is the maximum temperature that can ordinarily be attained between sliding metals. For the usual situation in which the bearing metal has a lower melting point than the journal metal, the limiting condition between points of sliding contact is thus that of molten bearing metal and solid journal metal, both being at the melting-point temperature of the bearing metal.

If the solid journal metal is soluble in the molten bearing metal, the resulting junction, when solidification occurs, will be an alloy of the two metals, and this will tend to give a strong weld. On the other hand, if the solid journal metal is not soluble in the molten bearing metal, diffusion of journal atoms into the molten bearing metal will be on a greatly reduced scale. Such a junction will be weaker, all other things being equal, than the junction between miscible metals.

This argument is supported by the behavior of the B-subgroup metals tested in the slider-bearing tests. Without exception, the B-subgroup metals that are immiscible with iron had excellent score resistance against steel. However, certain other metals, not B-subgroup metals, such as magnesium, barium, and calcium, which are also immiscible with iron, did not have good score resistance. The question then arises—What is the special characteristic of the immiscible B-subgroup metals that sets them apart from other immiscible metals as regards score resistance against steel?

An answer to this question is suggested by the nature of the binding forces that hold the atoms of the various metals in their crystal lattices.

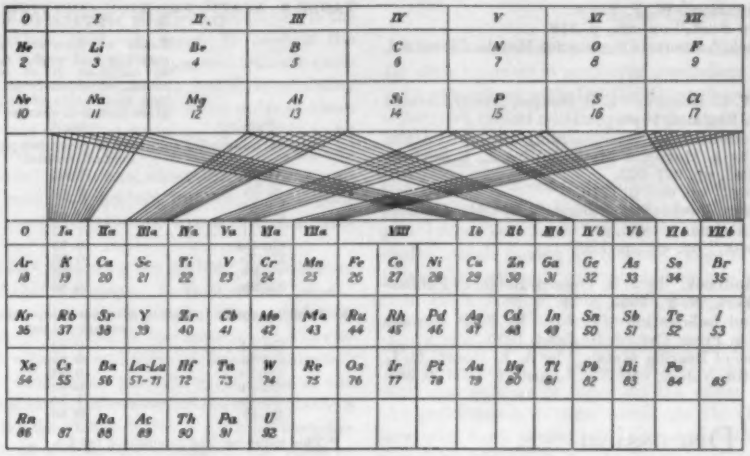

FIG. 10 PERIODIC TABLE OF THE ELEMENTS

Many solid-state physicists regard the metallic elements as being of two more or less distinct types—first, the true metals, and second, the B-subgroup metals. The true metals comprise the alkali metals, the alkaline-earth metals, and the transition metals. These are the elements in columns Ia through VIII of the Periodic Table, Fig. 10. They are characterized by pronounced metallic properties—strong electropositivity, metallic luster, ductility and malleability, good thermal and electrical conductivity. Close-packed structures predominate—body-centered cubic, face-centered cubic, and close-packed hexagonal.

The B-subgroup elements, on the other hand, are characterized by a diminution of metallic properties. In any row of B-subgroup elements—for example, copper, zinc, gallium, germanium, arsenic, selenium, and bromine—there is a steady transition from highly metallic to highly nonmetallic properties. At the same time, these elements tend to have rather complex crystal structures.

These changes in metal properties are thought to result from changes in the forces that bind metal crystals together. True metals are held together by a so-called metallic bond. This bond is characterized by the mobility of certain loosely held electrons—which accounts for the good electrical and thermal conductivity of true metals and for their ductility and malleability. The B-subgroup elements, on the other hand, are thought to possess both metallic and covalent bonding. The earlier B-subgroup metals, such as copper, silver, and gold, are thought to be principally metallic with regard to bonding while the latter B-subgroup metals, such as indium, bismuth, and lead, are thought to be more highly covalent. This covalent or shared-electron bond is characterized by great rigidity; it is a highly brittle bond.

It is this concept of mobility versus brittleness that has been most suggestive of an explanation for the superiority of the B-subgroup metals as regards score resistance against steel. Thus the solubility of a pair of metals determines the number of junctions that will be formed on an atomic scale when the metals slide against each other. The periodic grouping, whether the metal is B-subgroup or true metal, determines the character of these junctions.

Even though a true metal such as calcium or barium, for example, is immiscible with iron and therefore forms few junctions on an atomic scale, it may be that the bonding of these junctions is largely metallic. Because of the mobility of such bonding, it gives a junction which tends to wipe and smear rather than break cleanly, and in this way it is conducive to the formation of still more junctions.

With the B-subgroup metals the bond to iron may not be wholly metallic. It may be appreciably covalent, and if so, this may be significant in giving a more brittle and more easily broken junction, and hence better score resistance against steel.

The same general reasoning applies to metal pairs forming well-defined intermetallic compounds. The good to fair score resistance of such metal pairs is a consequence of this compound formation. Because of the purely covalent bonding of these compounds, the junctions are brittle and hence easily broken. Damage is confined to the immediate interface, and damage in depth is minimized. As we have already seen, the metal pairs falling in this category are iron-tin, iron-antimony, iron-selenium, iron-tellurium, and possibly iron-germanium.

While the foregoing hypothesis is consistent with the results of the slider-bearing tests, the supporting evidence is circumstantial, and material proof is lacking. It is probable that such proof may be obtained by electron-diffraction studies of the surfaces produced by scoring and nonscoring metal pairs. In so far as we have been able to learn, such studies have not been made. In our opinion, they offer a promising field for future research on this subject.

ACKNOWLEDGMENT

The support and encouragement of Messrs. A. F. Underwood and B. J. Bidwell are gratefully acknowledged. Thanks are due to Dr. Cyril S. Smith and his colleagues at the Institute for the Study of Metals (University of Chicago), for helpful criticism. Mr. Paul A. Totta, now serving in the U. S. Air Force, assisted with the preparation of the slider bearings and collaborated in the preparation of a preliminary communication (18).

BIBLIOGRAPHY

1 "Some Experiments With Sleeve Bearing Materials," by B. Lunn, Trans. of the Danish Academy of Technical Sciences, vol. 2, 1952, gives an up-to-date review of the literature on score resistance. There are 123 references.

2 "Some General Aspects of Rubbing Surfaces," by A. F. Underwood, Proceedings of the Special Summer Conference on Friction and Surface Finish, Massachusetts Institute of Technology, Cambridge, Mass., 1940, pp. 5–12.

3 "Surface Friction of Clean Metals—A Basic Factor in the Metal Cutting Process," by H. Ernst and M. E. Merchant, op. cit., pp. 76–101.

4 "Friction of Dry Solids in Vacuo," by P. E. Shaw and E. W. L. Leavey, *Philosophical Magazine*, series 7, vol. 10, 1930, pp. 809–822.

5 "Metal Reference Book," by C. J. Smithells, Interscience Publisher, Inc., New York, N. Y., 1949, p. 295.

6 Private communication—W. F. Ehret.
7 "Metal Reference Book," op. cit., p. 319.
8 "Metals Handbook," American Society for Metals, Cleveland, Ohio, 1948, p. 1171.
9 Ibid., p. 1196.
10 "Tinplate," by W. E. Hoare and E. S. Hedges, Edward Arnold and Company, London, England, 1946, pp. 143–146.
11 "The Rate of Formation of Tin-Iron Alloy During Hot Dip Tinning as Measured by a Magnetic Method," by A. I. Seybolt, Trans. ASM, vol. 29, 1941, pp. 937–952.
12 "Metals Handbook," op. cit., p. 1216.
13 "Der Aufbau der Zweistoffiegierungen," by M. Hansen, Julius Springer, Berlin, Germany, 1936, p. 748.
14 "Metals Handbook," op. cit., p. 1207.
15 Ibid., p. 1220.
16 "Galvanizing Handbook," by J. R. Daesen, Reinhold Publishing Corporation, New York, N. Y., 1946, p. 24.
17 "The Friction and Lubrication of Solids," by F. P. Bowden and D. Tabor, Clarendon Press, Oxford, England, 1950.
18 "Score Resistance of Bearing Metals," by A. E. Roach, C. L. Goodzeit, and P. A. Totta, *Nature*, vol. 172, August 15, 1953, p. 301.

Discussion

A. T. Gwathmey.[5] This seems to me to be the first comprehensive paper on scoring. The results are striking, and the interpretation is an interesting one. It is hoped that the authors plan further measurements.

The writer is surprised that the oxide layer does not play a more important part than the interpretation of the authors indicates. It would be interesting to find out how the good metals would behave if oxygen were excluded and the experiments were carried out in an atmosphere of hydrogen. There is no obvious connection between the properties of the oxides and the position of the B-group in the Periodic Table, but results obtained when the oxide was largely eliminated would strengthen the proposed interpretation of scoring. The influence of crystal face on scoring of a pure iron crystal with some good and poor metals would be interesting. For example, the bonding of polycrystalline tin or copper with an iron crystal (or steel crystal if such were available) might depend on the structural arrangement of the iron atoms on the different faces. This paper is considered to be outstanding.

M. E. Merchant.[6] The results of the authors' studies on the scoring characteristics of metals in sliding contact are of considerable practical importance and the general principles evolved should prove most helpful to all concerned with the choice of pairs of metals for service conditions where inherent antiscoring properties are needed. The authors and their company are to be congratulated on the thorough investigation carried out to test the basic principles.

It is of interest to note the extent to which the principles developed correlate with predictions made by Mr. Hans Ernst and the writer in their earlier publications on the static friction and scoring properties of clean metals, one of which (publications) is referred to by the authors. It was there pointed out that mutual solid insolubility of pairs of metals is a necessary condition for such pairs to have inherent antiscoring properties. To quote from a later publication than that referred to by the authors,[7] "Bearing metals which exhibit quite complete mutual insolubility at the temperatures existing at their points of contact, ordinarily have inherent antiscoring properties, even when dry! This knowledge should be of use wherever problems involving scoring and non-abrasive wear of rubbing surfaces arise." This conclusion was reached by study of the data and related theory obtained from measurements of static friction on unlike pairs of clean metals in vacuum. It is illustrated by the data of Table 3 of this discussion, originally published in the paper referred to by the authors in their reference (3). However, the authors have found that, for metals in sliding contact (kinetic friction conditions), a second necessary requirement for inherent antiscoring properties is that at least one of the metals of the pair be from the B-subgroup in the periodic table. In addition, they have found that formation of an intermetallic compound can be substituted for the requirement of immiscibility. This latter finding does not seem to apply in the case of static-friction conditions, as may be seen from the data on the pair copper-cadmium (Cu-Cd) in Table 3 of this discussion. Both copper and cadmium are B-subgroup metals and, although they are soluble, are known to form the two intermetallic compounds Cu_2Cd and $CuCd_3$. Thus, according to the principles developed by the authors, this pair should be "antiscoring." Nevertheless, the static-friction value observed shows no reduction in interface shear strength S, for this pair, over that for cadmium on cadmium (the softer, weaker metal of the pair), as evidenced by the fact that the observed friction coefficient for the pair is identical with the ratio of the shear strength to the hardness of cadmium alone. Thus scoring of these metals occurred when initial slip took place, under the conditions of the test. It would appear that either (1) both Cu_2Cd and $CuCd_3$ are stronger in shear than cadmium itself, or (2) what is more likely, these compounds do not form in sufficient amount under static conditions at the contact interface to lower the strength of that interface. Under kinetic conditions this situation would be changed and a copper-cadmium pair might well show good score resistance.

Another point of difference which may be noted between the authors' results and those of the writer summarized in Table 3 of this discussion is the behavior of the pair copper-iron (Cu-Fe). The authors find this combination to have fair to poor score resistance, while the writer's data show a value of interface shear strength S for this pair considerably less than that for copper on copper (the softer, weaker metal of the pair), as evidenced by the low value of observed friction coefficient for the pair relative to the ratio to the shear strength to the hardness of copper alone.

TABLE 3 STATIC FRICTION COEFFICIENTS OF MIXED PAIRS OF CLEAN METALS IN VACUUM

Pair	Ratio of interface shear strength S of weaker metal to hardness H of softer metal, obtained from friction coefficients of each of given metals in contact with itself	Observed value of friction coefficient of pair
(a) Pairs forming solid solutions at room temperature (scoring occurred at contact points)		
Al-Fe	1.05	1.05
Al-Zn	0.85	0.82
Co-Fe	...	0.54[a]
Co-Cu	0.90	0.89
Co-Al	1.05	1.01
Cu-Cd	0.83	0.85
Cu-Zn	0.85	0.86
Zn-Fe	0.85	0.85
Zn-Sb	0.85	0.85
(b) Pairs mutually insoluble at room temperature (no scoring occurred at contact points)		
Cd-Al	0.83	0.57
Cd-Bi	0.83	0.79
Cd-Fe	0.83	0.64
Cd-Zn	0.83	0.62
Cu-Fe	1.35	1.05
Zn-Bi	0.86	0.70

[a] This value used to calculate S for Co.

Note: For clean metals, $\mu = S'/H$
where μ = coefficient of friction
H = surface hardness of softer metal of pair
S' = actual shear strength of metal junctions at contact interface between pair—equal to or less than shear strength S of weaker metal of pair

[5] Department of Chemistry, University of Virginia, Charlottesville, Va.
[6] Assistant Director of Research, The Cincinnati Milling Machine Company, Cincinnati, Ohio. Mem. ASME.
[7] "Chip Formation, Friction and High-Quality Machined Surfaces," by H. Ernst and M. E. Merchant, Surface Treatment of Metals, Trans. ASM, vol. 29, 1941, pp. 299–378.

Thus no scoring occurred between the members of this pair in the writer's tests. Nevertheless, this only serves to confirm the authors' principles, for it is known that copper and iron are quite mutually insoluble at room temperature, but that their solubility becomes very considerable at temperatures of the order of those occurring at contact points of sliding surfaces. Thus it is to be expected that a copper-iron pair would be inherently antiscoring under static (or near static) conditions, where the interface temperature is at (or near) room temperature, but would show poor score resistance under kinetic conditions, where interface temperatures are high.

One other interesting fact regarding the authors' findings may be seen from Table 3 of this discussion. In their second paper,[8] they draw the conclusion, "there is no simple direct correlation between the surface damage suffered by the various metallic elements in sliding contact with iron and their friction coefficients." This is certainly true as long as the absolute value, only, of the friction coefficient is considered. However, as shown by Table 3 of this discussion, there is a direct correlation possible between the value of friction coefficient and surface damage if the value of friction coefficient of the mixed pair is compared with the ratio of interface shear strength to interface hardness obtained from the friction coefficient of each member of the pair in contact with itself. Whenever the friction coefficient of the pair is approximately equal to this ratio, scoring will occur; whenever it is considerably less than this ratio, the pair is inherently antiscoring.

[8] "Frictional Characteristics and Surface Damage of Thirty-Nine Different Elemental Metals in Sliding Contact With Iron," by C. L. Goodzeit, A. E. Roach, and R. P. Hunnicutt, published in this issue, pp. 1669–1676.

Authors' Closure

The authors wish to thank Dr. Gwathmey and Dr. Merchant for their kindness in preparing discussions for this paper.

In connection with Dr. Gwathmey's point on the oxide films it may be remarked that the tests reported in this paper were carried out at high speed and load under boundary lubrication conditions where the oxide film may not have such a profound effect as in low-speed tests without lubrication. This is evidenced by the list of metals that comprise the group that had "very poor" score resistance with steel. It is noted that this list includes metals having an extreme range of oxide-film characteristics. For example calcium and cerium are very reactive and form thick nonprotective oxide films; titanium and zirconium are also reactive but form thin protective films. Furthermore, the platinum group metals and gold are passive toward oxygen. The fact that all of these metals (except calcium) alloy easily with iron appears to dominate the effect of the oxide films in the performance in these tests. As Dr. Gwathmey points out, however, tests performed under oxygen-free conditions would certainly add much to the theoretical speculations and it is hoped that the results of such work may soon appear in the literature.

The comments of Dr. Merchant are welcomed, especially his correlation of some of the test results with friction and surface-damage data that he obtained. It is unfortunate that the copper-cadmium pair is a poor example of metals that react to form intermetallic compounds. As Dr. Merchant has mentioned, the compounds in this particular case may represent equilibrium phases which do not form fast enough to effect the strength of junctions formed at the interface of the sliding metals.

Frictional Characteristics and Surface Damage of Thirty-Nine Different Elemental Metals in Sliding Contact With Iron

By C. L. GOODZEIT,[1] R. P. HUNNICUTT,[2] AND A. E. ROACH,[3] DETROIT, MICH.

This paper describes an experimental investigation of the friction and surface-damage characteristics of iron in sliding contact with various elemental metals without lubrication. No simple, direct relationship was found between the value of the coefficient of sliding friction and the characteristics of the material transfer between metals. It was found that the surface-damage characteristics are related to the relative hardness of the metals in sliding contact, their mutual solubility, and their ability to form intermetallic compounds.

Introduction

IT IS well known that the value of the friction coefficient of a pair of metals is greatly affected by the condition of their surfaces. For example, Campbell (1)[4] measured the friction coefficients of such metal pairs as steel and speculum metal, steel and steel, brass and brass, and copper and copper, with the surfaces untreated and with the surfaces treated with various chemicals. His conclusion was that surface condition is a most important factor in such studies. Likewise, Bowden and Hughes (2) concluded that surface films have a profound influence on the friction of metals.

Not only is the friction coefficient affected by surface condition, but experience has shown that surface condition (in both physical and chemical senses) is an exceedingly difficult quantity to reproduce. The method of surface preparation adopted by many investigators has been that of generating a fresh surface by abrasion. Even so, there is usually found to be considerable disagreement between independent experimental determinations of the friction coefficients of various metal pairs. This is illustrated by Table 1 which gives the values found by several different investigators working with the same metals. As a result, there is frequently some uncertainty in utilizing such values in engineering analysis and design.

Moreover, in many technical applications, such as oil-film bearings and bushings, ball-bearing separators, and piston rings, the basis for selecting metals is usually not friction coefficient but surface-damage characteristics. Such parts are designed to operate ordinarily with lubrication, and the friction of the parts is, under this condition, virtually independent of the friction coefficients of the metals used. It is rather during periods of momentary distress involving insufficient lubrication, or excessive speed, or overload, that the use of suitable metals becomes of great importance, and then the desideratum is metals that will not score or gall or otherwise suffer surface damage.

TABLE 1 EXPERIMENTAL DETERMINATIONS OF FRICTION COEFFICIENTS OF VARIOUS METAL PAIRS

Metal	Shaw, Leavey[a] (against iron)	Tomlinson[b] (against mild steel)	Ernst, Merchant[c] (against iron)	Goodzeit, Hunnicutt, Roach[d] (against iron)
Aluminum	1.28	0.605	1.05	0.82
Cadmium	...	...	0.64	0.71
Cobalt	...	...	0.54	0.45
Copper	0.69	0.533	...	0.63
Iron	0.80	...	...	0.52
Lead	...	1.93	...	0.52
Nickel	0.69	0.429	1.05	0.58
Platinum	...	0.427	...	0.56
Silver	0.30	...	...	0.32
Tin	...	0.786	...	0.29
Zinc	...	...	0.85	0.52

[a] Shaw and Leavey's measurements (3) were carried out in 0.01-mm vacuum. Specimens were abraded dry on sandpaper or scraped with a clean blade.

[b] Tomlinson's measurements (4) were carried out in air at room temperature. Specimens were abraded on blue-black emery paper and polished on wet chamois with chromium oxide. The surface was washed with an alcohol-ether-ammonia cleaning fluid and scrubbed with cotton.

[c] Merchant's measurements (5) were carried out on freshly cut, chemically clean surfaces in a high vacuum.

[d] Goodzeit, Hunnicutt, and Roach's measurements (11) were carried out in air at room temperature. Specimens were washed with acetone and abraded dry in one direction on No. 1 emery paper.

Accordingly, the purpose of this paper is not merely to present another table of friction coefficients but to present also such information on surface-damage characteristics as may be useful to engineers and designers. Specifically, the paper will attempt to answer the following questions:

What is the character of the surface damage suffered by various elemental metals when they slide against iron?

Does the friction coefficient between metals in sliding contact give any indication of the surface damage suffered by them?

Is such surface damage associated with any more easily definable physical or chemical properties of metals?

[1] Research Engineer, Research Staff, General Motors Corporation. Assoc. Mem. ASME.

[2] Research Metallurgist, Research Staff, General Motors Corp.

[3] Supervisor of Bearing Development, Research Staff, General Motors Corporation. Deceased, July, 1955.

[4] Numbers in parentheses refer to Bibliography at end of paper.

Contributed by the Research Committee on Lubrication under the auspices of the Lubrication Activity and presented at a joint session with the Research Committee on Metal Processing at the Annual Meeting, New York, N. Y., November 28–December 3, 1954, of THE AMERICAN SOCIETY OF MECHANICAL ENGINEERS.

NOTE: Statements and opinions advanced in papers are to be understood as individual expressions of their authors and not those of the Society. Manuscript received at ASME Headquarters, August 3, 1954. Paper No. 54—A-53.

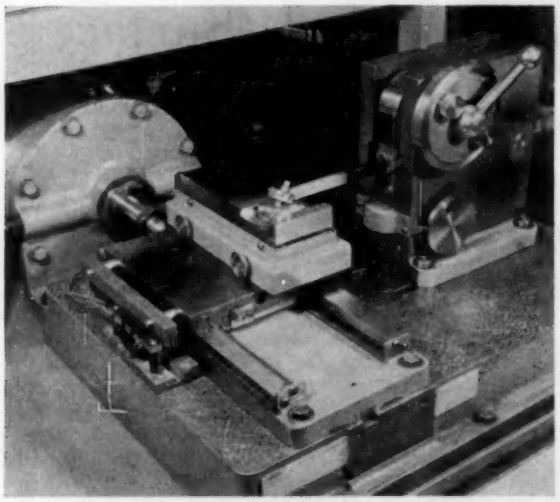

FIG. 1 VIEW OF FRICTION TEST MACHINE

APPARATUS

Fig. 1 shows the general appearance of the apparatus used in the experiments. This apparatus, which is modeled after the well-known Bowden-Leben (6) apparatus, is simply a convenient means of holding, loading, and providing relative motion between two test specimens. One specimen (called the plate specimen) is in the form of a flat plate; the other (called the rider) is in the form of a cylinder with a hemispherical end. The plate specimen is mounted on a carriage which moves at a uniform slow velocity along horizontal ways. The rider is attached to a cantilever beam in such a way that its hemispherical end contacts the plate specimen. Fig. 2 shows the arrangement of the apparatus in greater detail. For further information concerning this type of apparatus consult references (6, 7).

TEST SPECIMENS AND THEIR PREPARATION

Thirty-nine different elements were tested in sliding contact with iron. Table 2 is a list of these elements, their known impurities, and pertinent physical properties. The hardness given in this table is the indentation hardness of the finished plate specimen, measured at room temperature, with a Tukon microhardness tester using a diamond pyramid indenter. The solubility is the weight per cent solubility of solid iron in molten plate-specimen metal at the melting-point temperature of the plate-specimen metal. If the plate-specimen metal has a higher melting point than iron, the solubility is that of solid plate-specimen metal in molten iron at the melting-point temperature of iron. Solubility data are taken from the "Metals Handbook" and other standard sources.

Plate specimens of various elemental metals measured approximately $^5/_8 \times {}^6/_8 \times {}^1/_8$ in.

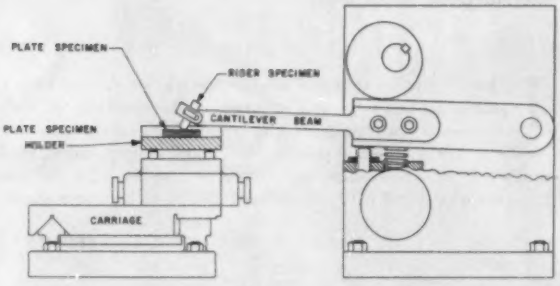

FIG. 2 SCHEMATIC DIAGRAM OF FRICTION TEST MACHINE

TABLE 2 CHARACTERISTICS OF METALS TESTED

Atomic number	Name	Known impurities	Hardness	Solubility	Remarks
4	Beryllium	Less than 1% Fe, Si, Al, Cu	314	>0.05	
6	Carbon		...	1.7	Delanium graphite
12	Magnesium	99.99% pure	38.4	0.026	
13	Aluminum	99.99% pure	37.1	0.03	
14	Silicon		...	(4–5)?	
20	Calcium	99.9% pure	24.6	Insoluble	
22	Titanium	99.5% pure; 0.1–0.3 Fe, 0.02–0.08 N, 0.1 C, trace O	277	6.5	
24	Chromium		910	100	Electroplated on steel
25	Manganese				Electroformed
26	Iron		105.5	100	
27	Cobalt		339	100	
28	Nickel		644	100	Electroplated on steel
29	Copper		101.4	4	
30	Zinc		35.4	0.0009–0.0028	
32	Germanium	Less than 5 ppm of Si, Mg, Cu, Pb	798	(Compound)?	
34	Selenium		39.2	Compound	Clad to delanium graphite
40	Zirconium	2–3 Hf, Hf + Zr = 99.7%, 0.1 Fe, 0.1 Ti	121	6–7	
41	Columbium		73.5	12	
42	Molybdenum		188	34	
45	Rhodium	99.9% pure; traces of other Pt group metals and Ag, Au, Cu, Ca	517	100	0.015 in. thick; brazed to silver-clad steel back
46	Palladium	Same	71.3	100	Same
47	Silver		31.2	0.0004–0.0006	Clad on steel; high purity silver rolled with steel ingot
48	Cadmium		22	0.0002–0.0004	Puddled on lightly tinned sheet iron
49	Indium		1.6	Insoluble	Same
50	Tin		17.7	Compound	Same
51	Antimony		106.8	Compound	Electroplated on steel
52	Tellurium			Compound	
56	Barium	98% pure; N, Ca, Mg present		Insoluble	
58	Cerium	98.05% pure; 0.8 Fe, balance rare earths	54.8	Insoluble	
73	Tantalum		106	7	
74	Tungsten		484	32.5	Sintered
77	Iridium	99.99% pure; traces of Pt group metals and Ag, Au, Cu, Ca	722	37.8	0.015 in. thick; brazed to silver-clad steel back
78	Platinum	99.99% pure; traces of Pt group metals and Ag, Au, Cu, Ca	91.4	100	Same
79	Gold		73.7	34	
81	Thallium		3.5	Insoluble	Puddled on sheet iron
82	Lead		7.0	Insoluble	Puddled on lightly tinned sheet iron
83	Bismuth		25.9	0.0002–0.0004	Same
90	Thorium	98.5% pure; 0.04 Ca, 0.05 Fe, 0.5–1.5 thorium salts	111.3	...	
92	Uranium		454	...	

Riders were made of Armco iron, machined in cylindrical form, $1^1/_4$ in. long and $^1/_4$ in. diam, with hemispherical end.

Preparation of the specimens was as follows:

Plate specimens were cleaned in acetone and abraded in one direction on No. 1 emery paper. The mounting of the plate specimens in the friction apparatus was such that the direction of travel was perpendicular to the scratches produced by abrasion.

Riders were polished before each test by turning first against grade 1/0 emergy paper and then against grade 2/0 emery paper.

Procedure

Each element was tested under two different normal loads. In the first test condition (referred to as Test I) the normal load was always 0.6 lb. In the second test condition (referred to as Test II) the normal load was proportional to the indentation hardness of the plate-specimen metals. For plate-specimen metals whose indentation hardness is equal to, or greater than, the hardness of Armco iron, the normal load was 1.0 lb. Thus the normal load varied over a range of from 0.1 lb for indium (the softest element tested) to 1.0 lb for all elements as hard as or harder than Armco iron. The purpose of varying the normal load in Test II was to equalize the ploughing effect of the rider through the soft plate-specimen elements.

In both Test I and Test II the velocity of sliding was 0.002 ips, and the duration of the run was two minutes. The track made by the rider on the surface of the plate specimen was therefore about $^1/_4$ in. long.

Surface damage was evaluated in two ways. The first was by comparing photomicrographs of the surfaces of the riders and plate specimens before and after testing. The second was by analyzing the surface of the plate specimens for the presence of iron along the track made by the rider. The technique employed in these analyses was electrographic spot testing (8) performed as follows:

A piece of gelatin-coated paper is moistened with a reagent solution containing potassium ferricyanide and placed in contact with the surface of the plate specimen to be tested. A piece of aluminum foil is placed over the paper. The resulting sandwich is then clamped together under light pressure and an electric current passed through it, the plate specimen being made anodic. The presence of even a very small trace of iron on the surface of the plate specimen is then indicated by a Prussian blue reaction on the gelatin-coated paper.

Results

Table 3 summarizes the principal results of the paper.

At least one run was made with each element under Test I and Test II conditions. Where more than one run was made, the friction coefficient is recorded separately for each run. The difference between the values of the frictional coefficients between

TABLE 3 PRINCIPAL RESULTS OF TESTS

Element	Test I		Test II		Evidence of metal transfer	
	Coefficient	Normal load	Coefficient	Normal load	Photomicrograph	Spot test
Beryllium	0.43	0.60	0.48	1.00	Fe on plate	Fe on plate
Carbon	0.15	0.60	(Note 1)	(Note 1)	None	Inconclusive (Note 2)
Magnesium	0.53, 0.46 S 0.35, 0.32 K	0.60	0.46, 0.46 S 0.38, 0.35 K	0.46	Mg on rider	None
Aluminum	0.81, 0.84, 0.81	0.60	0.85, 0.72, 0.63	0.42	Al on rider	None
Silicon	0.58	0.60	0.58, 0.58	1.00	Fe on plate	Fe on plate
Calcium	0.67	0.60	0.75	0.33	Ca on rider	(Note 3)
Titanium	0.59, 0.59	0.60	0.59	1.00	Fe on plate Ti on rider	Fe on plate
Chromium	0.53	0.60	0.54	1.00	Fe on plate	Fe on plate
Manganese	0.57, 0.57	0.60	0.54	1.00	Fe on plate	...
Iron	0.47, 0.56	0.60	0.57, 0.58	1.00	Fe on plate Fe on rider	...
Cobalt	0.45, 0.46	0.60	0.43	1.00	Fe on plate	(Note 4)
Nickel	0.59, 0.56	0.60	0.61	1.00	Fe on plate	Fe on plate
Copper	0.46	0.60	0.69	0.58	Cu on rider	None
Zinc	0.50	0.60	0.52, 0.55	0.42	Zn on rider	None
Germanium	0.66	0.60	0.65	1.00	Fe on plate	Fe on plate
Selenium	0.43	0.60	0.52	0.46	None	None
Zirconium	0.55	0.60	0.55	1.00	Zr on rider	Fe on plate
Columbium	0.58, 0.55	0.60	0.55, 0.51	0.75	Nb on rider Fe on plate	Fe on plate
Molybdenum	0.47, 0.46	0.60	0.47	1.00	Fe on plate	Fe on plate
Rhodium	0.54	0.60	0.46, 0.49	1.00	Fe on plate	Fe on plate
Palladium	0.65	0.60	0.72, 0.66	0.73	Pd on rider	Fe on plate
Silver	0.33, 0.32, 0.31	0.60	0.33, 0.30	0.36	None	None
Cadmium	0.67	0.60	0.75	0.30	Cd on rider	None
Indium	1.38, 1.26	0.60	0.87, 0.75	0.10	(Note 5)	None
Tin	0.30, 0.28	0.60	0.40, 0.19	0.26	None	None
Antimony	0.25, 0.26, 0.27	0.60	0.25, 0.28	1.00	None	Trace Fe on plate
Tellurium	0.31, 0.39	0.60	0.39, 0.43	0.20	None	None
Barium	0.89	0.60	0.88	0.20	Ba on rider	(Note 6)
Cerium	0.50	0.60	0.53	0.60	Ce on rider	None
Tantalum	0.58	0.60	0.57	1.00	Ta on rider Fe on plate	Fe on plate
Tungsten	0.47	0.60	0.49	1.00	Fe on plate	Fe on plate
Iridium	0.51	0.60	0.52	1.00	Fe on plate	Fe on plate
Platinum	0.52, 0.60	0.60	0.64, 0.74	0.71	Pt on rider Fe on plate	Fe on plate
Gold	0.54	0.60	0.57	0.77	Au on rider	None
Thallium	0.68	0.60	0.56	0.11	Tl on rider	None
Lead	0.82, 0.62 S 0.53, 0.50 K	0.60	0.76, 0.46	0.15	(Note 7)	None
Bismuth	0.67 S 0.40 K	0.60	0.64 S 0.43 K	0.33	Bi on rider	None
Thorium	0.82	0.60	0.86	1.00	Th on rider	None
Uranium	0.50	0.60	0.50	1.00	(Note 8)	Fe on plate

Notes:

1 Indentation hardness could not be evaluated satisfactorily for determination of normal load in Test II.
2 Electrographic spot test obscured by black carbon film transferred to surface of test paper.
3 Material too reactive for electrographic spot testing.
4 Electrographic spot test obscured by reaction between plate specimen and spot-test reagent.
5 Large blob of indium plastered on tip of rider under Test I conditions; little, if any, indium transferred to rider under Test II conditions.
6 Material too reactive for electrographic spot testing.
7 Little, if any, lead transferred to rider under Test I conditions; little, if any, lead transferred to rider under Test II conditions except in run giving 0.46 friction coefficient in which there was visual evidence of lead on tip of rider.
8 Iron transferred from rider to plate under Test I conditions; both iron transferred from rider to plate and uranium transferred from plate to rider under Test II conditions.

Test I and Test II conditions was significant only in the cases of indium and thallium, the two softest materials tested. The lower coefficients for Test II conditions are attributed to the reduced ploughing effect of the rider through these soft metals.

All elements exhibited smooth frictional behavior except magnesium, lead, and bismuth, which exhibited stick-slip behavior. For these three elements, therefore, both the static (S) and kinetic (K) coefficients are reported. For all other elements, the reported friction coefficients are the kinetic coefficients.

Surface Damage From Sliding Contact

In examining the plate specimens of the thirty-nine different metals, we found that the surface damage in the rider track was of four distinctly different types. Fig. 3 shows these four types of plate-specimen surface damage which may be described as follows:

Type 1P. The track is well defined but discontinuous. The ridges of the asperities are leveled off and displaced in the direction of rider travel. There is no evidence of rider metal welded to the plate specimen.

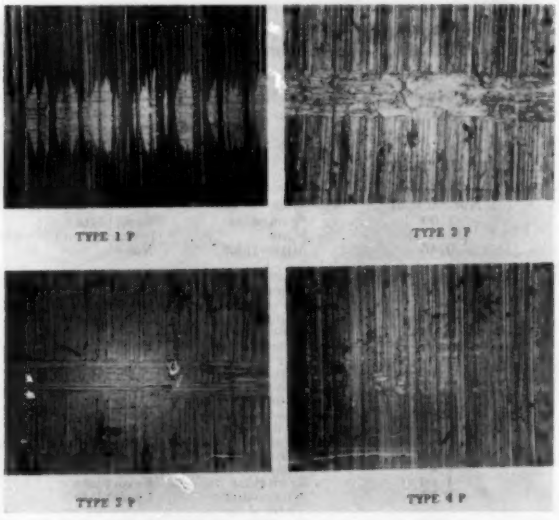

Fig. 3 Plate-Specimen Damage Classification

Type 2P. The track is well defined and continuous. There is no evidence of rider metal welded to the plate specimen.

Type 3P. The track is poorly defined. In some areas the original asperities are still distinguishable; in others they are smeared away. Pieces of rider metal are welded to the plate specimen, and these are often displaced in the direction of rider travel.

Type 4P. The track is poorly defined. The original asperities are still intact. Pieces of rider metal are welded to them.

TABLE 4 SURFACE-DAMAGE CHARACTERISTICS OF PLATE SPECIMENS

Type 1P	Type 2P	Type 3P	Type 4P
Magnesium	Carbon	Titanium	Beryllium
Selenium	Aluminum	Iron	Silicon
Silver	Calcium	Columbium	Chromium
Tin	Copper		Manganese
Antimony	Zinc	Tantalum	Cobalt
Tellurium	Zirconium	Uranium	Nickel
Gold	Palladium		Germanium
Lead	Cadmium		Molybdenum
Bismuth	Indium		Rhodium
	Barium		Tungsten
	Cerium		Iridium
	Platinum		
	Thallium		
	Thorium		

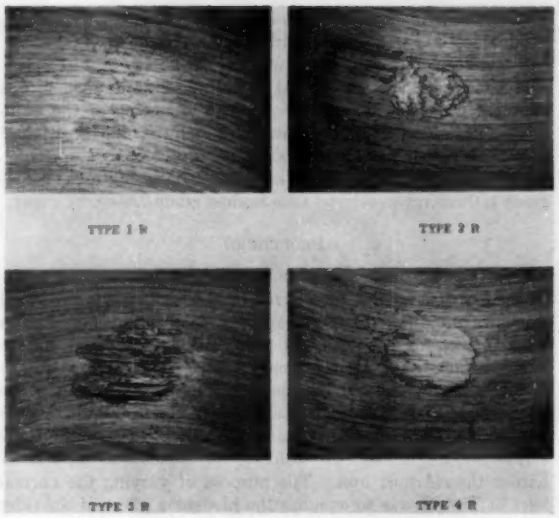

Fig. 4 Rider-Damage Classification

Table 4 classifies the various plate-specimen metals according to the type of surface damage that they suffer when in sliding contact with an iron rider.

In like manner, four distinctly different types of surface damage may be distinguished in the contact areas of the iron riders. These are illustrated in Fig. 4 and are as follows:

Type 1R. The contact area is poorly defined. The original asperities are still visible. There is no evidence of plate-specimen metal welded to the rider.

Type 2R. The contact area is well defined. There is evidence of plate-specimen metal, frequently in the form of a definite blob, transferred to the rider.

Type 3R. The contact area is well defined. Pieces of plate-specimen metal may be distinguished in some portions of the contact area. In other portions of the contact area there is evidence of removal of rider metal.

Type 4R. The contact area is well defined. The original asperities are leveled off and displaced toward the trailing edge of contact. There appears to be no plate-specimen metal welded to the rider.

Table 5 classifies the iron riders according to the type of surface damage which they suffer when in sliding contact with various plate-specimen metals.

By comparing Tables 4 and 5 it may be seen that rider damage Type 1R is found only with plate-specimen damage Types 1P

TABLE 5 SURFACE-DAMAGE CHARACTERISTICS OF IRON RIDERS IN SLIDING CONTACT WITH INDICATED PLATE SPECIMEN METALS

Type 1R	Type 2R	Type 3R	Type 4R
Carbon	Magnesium	Titanium	Beryllium
Selenium	Aluminum	Iron	Silicon
Silver	Calcium	Columbium	Chromium
Tin	Copper		Manganese
Antimony	Zinc	Tantalum	Cobalt
Tellurium	Zirconium	Uranium	Nickel
Lead	Palladium		Germanium
	Cadmium		Molybdenum
	Indium		Rhodium
	Barium		Tungsten
	Cerium		Iridium
	Platinum		
	Gold		
	Thallium		
	Bismuth		
	Thorium		

or 2P. These combinations of damage types indicate little, if any, plate-specimen material transferred to the rider and no rider material transferred to the plate specimen.

Rider damage Type 2R is also found only with plate-specimen damage Types 1P and 2P. With these combinations of damage types, material is transferred from the plate specimen to the rider, but there is no transference of material from the rider to the plate specimen.

Rider damage Type 3R is found only with plate-specimen damage Type 3P. Material is transferred both from the rider to the plate specimen and from the plate specimen to the rider.

Rider damage Type 4R is found only with plate-specimen damage Type 4P. Material is transferred from the rider to the plate specimen but not from the plate specimen to the rider.

Correlation of Friction Coefficients With Surface-Damage Characteristics

Table 3 shows that there is no simple direct correlation between the surface damage suffered by the various metallic elements in sliding contact with iron and their friction coefficients. Thus, while the metals (silver, tin, antimony, and tellurium) which have the lowest friction coefficients with iron invariably suffer little or no damage (Type 1P or 2P) and cause little or no rider damage (Type 1R), certain other metals (indium and lead) with the same damage characteristics have the highest friction coefficients.

Metals giving Type 2R rider damage with Type 1P or 2P plate-specimen damage tend to exhibit erratic frictional characteristics. Magnesium and bismuth, for example, give stick-slip motion, while aluminum, indium, barium, and thorium have the highest friction coefficients of any of the metallic elements tested against iron.

Metals giving Type 3R rider damage with Type 3P plate-specimen damage or Type 4R rider damage with Type 4P plate-specimen damage have relatively uniform friction coefficients. With the exception of germanium all these metals have coefficients close to $^1/_2$.

Correlation of Surface Damage With Physical Properties of Metals

Bowden (7), Holm (9), and others have shown that the true area of contact between contacting solids is extremely small, and therefore the contact pressures are large, approaching the yield point of the weaker material as a limit. As a consequence of these high pressures, very high local temperatures are generated between sliding solids; in the case of metals, these temperatures may approach the melting point of the lower-melting metal. Such conditions of high pressure and high temperature favor the formation of local welds between sliding metals. The making and breaking of these local welds are thought by many workers in this field to be a major part of metallic friction.

Examination of the plate specimens of the various metals tested by the present authors shows that a number of them (specifically those with Type 3P and 4P damage) have particles of iron adhering to their surfaces. The fact that these particles are iron is established by the electrographic spot tests. The experiments, therefore, tend to substantiate, for metals showing Type 3P and 4P damage, the mechanism of metallic friction outlined in the foregoing.

The surface damage suffered by metals in sliding contact is likewise a consequence of the formation and shearing of welded junctions. In particular, surface damage is greatly affected by the location of the plane of shearing with respect to the interface of the metal pairs.

Metal pairs giving Type 1R rider damage with Type 1P or 2P plate-specimen damage are those for which the shearing process occurs at the interface of the iron rider and metal-plate specimen. With these metal pairs there is little if any evidence of plate-specimen metal transferred to the rider and no evidence of rider iron transferred to the plate specimen.

Metal pairs giving Type 2R rider damage with Type 1P or 2P plate-specimen damage are those for which the shearing process occurs only within the plate-specimen metal. Consequently, there is plate-specimen metal visible on the tip of the rider.

Metal pairs giving Type 3R rider damage with Type 3P plate-specimen damage are those for which the shearing process occurs indiscriminatively in the rider metal and the plate-specimen metal.

Finally, metal pairs giving Type 4R rider damage with Type 4P plate-specimen damage are those for which the shearing process occurs only within the rider metal. Plate-specimen metals in this class give a positive electrographic spot test for iron.

In a study of the "score resistance" of elemental metals in high-speed sliding contact with steel it was found by the authors (10, 11) that the ability of metallic elements to resist scoring and seizing against steel is related to (*a*) their position in the periodic grouping of the elements and (*b*) their solubility for iron or their ability to form intermetallic compounds with iron. Specifically, it was found that metals having the greatest resistance to scoring are those that are immiscible with iron or that form stable intermetallic compounds with iron. The same general correlation was found in the present friction and surface-damage tests. Thus there were no soluble metal pairs that gave shearing at the interface. With all soluble metal pairs shearing occurred in the plate-specimen metal and/or in the rider metal. This may be seen by comparing the solubility and hardness data of Table 2 with the surface damage ratings of Tables 4 and 5.

Furthermore, the location of the plane of shearing with respect to the interface for soluble metal pairs is determined by the relative hardnesses of the metals. Metals giving Type 1P or 2P plate specimen damage with Type 2R rider damage (metal transferred from the plate specimen to the rider but little, if any, metal transferred from the rider to the plate specimen) all have indentation hardnesses less than that of iron at room temperature.

Metals giving Type 3P plate-specimen damage with Type 3R damage to the iron rider are all soluble with iron and all harder than iron at room temperature. With such metals the shearing process occurs both in the rider metal and in the plate specimen metal.

Metals giving Type 4P plate-specimen damage with Type 4R damage to the iron rider are all very much harder than iron. All such metals (excepting possibly germanium) are also soluble with iron. When such metals slide against iron, the shearing process occurs in the iron. These observations suggest that the shear strength of the metallic junctions between two soluble metals in sliding contact is greater that that of either of the metals themselves.

With metal pairs giving Type 1R rider damage with Type 1P or 2P plate-specimen damage (little, if any, metal transferred from the plate specimen to the rider, and no metal transferred from the rider to the plate specimen) shearing occurs at the interface of metallic contact. Such metals are either immiscible with iron or else form well-defined intermetallic compounds with iron. Thus silver and lead at their respective melting points each dissolve less than 0.001 per cent of solid iron. Tin, antimony, selenium, and tellurium form well-defined stable compounds with iron.

These observations suggest that with insoluble metal pairs the number of atomic bonds in the junction is limited and hence the junction is weak, while with metal pairs forming intermetallic compounds the junction is composed of such compounds and

hence is brittle. In either case, the junction tends to shear more easily than either of the uncombined metals. The shearing process therefore occurs in the interface, and damage in depth is minimized.

Correlation of Experiments With Engineering Experience

Only a few engineering applications involve elemental metals in sliding contact with iron or steel. Experience with these applications, although limited, is in good agreement with the results of the experiments.

It would be expected that metals giving Type 1P or 2P plate-specimen damage with Type 1R rider damage (no metal transfer) should perform extremely well in service. This is confirmed by experience. Silver, for example, is successfully used as a coating to reduce surface damage on such parts as separators for high-speed rolling-contact bearings. Lead and tin are used on such parts as pistons for internal-combustion engines; with such soft metals it is essential that the coating be very thin to prevent smearing. There is little or no experience with elemental antimony, selenium, and tellurium.

Metals giving Type 1P or 2P plate-specimen damage with Type 2R rider damage (plate-specimen metal adhered to top of rider but no rider metal adhered to plate specimen) include those with both good and bad service histories. Cadmium, indium, thallium, and bismuth are known to provide protection against surface damage when applied in very thin films. When used in thick coatings, they tend to smear. This is doubtless what happens in the friction apparatus—the rider pushes a blob of plate-specimen metal ahead of it, and this blob of metal is found plastered to the rider tip at the end of the run. In marked contrast, magnesium, aluminum, copper, and zinc have a generally unsatisfactory record as regards surface damage; these metals tend to pluck and tear when rubbed against iron or steel at high speed. Practically no engineering experience is available concerning calcium, zirconium, palladium, barium, cerium, platinum, or thorium.

Of the metals giving Type 3P plate-specimen damage with Type 3R rider damage (transfer of metal from both specimens) only iron and titanium are engineering metals. Both are sensitive to surface damage when rubbed against iron or steel.

Several of the metals giving Type 4P plate-specimen damage with Type 4R rider damage (transfer of rider metal to plate specimen but no transfer of plate-specimen metal to rider) are used as hard coatings to prevent surface damage. These are notably chromium, tungsten, cobalt, and nickel. These metals tend to "file" away the part against which they slide; hence they should be made as smooth as possible to minimize surface damage. Likewise, they should mate with parts of equal hardness. An example of the use of such materials is a hardened alloy-steel gear running in mesh with another hardened alloy-steel gear. Here surface finish and hardness are crucial in minimizing surface damage at high speeds.

Acknowledgment

The support and encouragement of Messrs. A. F. Underwood and J. B. Bidwell are gratefully acknowledged. Thanks are due to Dr. Cyril S. Smith and his colleagues at the Institute for the Study of Metals of the University of Chicago for helpful criticism in connection with the interpretation of the experiments.

BIBLIOGRAPHY

1 "Studies in Boundary Lubrication," by W. E. Campbell. Trans. ASME, vol. 61, 1939, pp. 633–641.

2 "The Friction of Clean Metals and the Influence of Absorbed Gases. The Temperature Coefficient of Friction," by F. P. Bowden and T. P. Hughes, Proceedings of the Royal Society of London, England, series A, vol. 172, 1939, p. 263.

3 "Friction of Dry Solids in Vacuo," by P. E. Shaw and E. W. L. Leavey, *Philosophical Magazine*, series 7, vol. 10, 1930, pp. 809–822.

4 "A Molecular Theory of Friction," by G. A. Tomlinson, *Philosophical Magazine*, series 7, vol. 7, 1929, p. 905.

5 "Surface Friction of Clean Metals—A Basic Factor in the Metal Cutting Process," by H. Ernst and M. E. Merchant, Proceedings of the Special Summer Conference on Friction and Surface Finish, Massachusetts Institute of Technology, Cambridge, Mass., June, 1940, p. 76.

6 "Apparatus for Measuring Friction," by F. P. Bowden and L. Leben, Proceedings of the Royal Society of London, England, series A, vol. 169, 1939, p. 371.

7 "The Friction and Lubrication of Solids," by F. P. Bowden and D. Tabor, Clarendon Press, Oxford, England, 1950.

8 "Electrographic Spot Testing of Bearing Surfaces," by A. E. Roach and A. O. DeHart, *Lubrication Engineering*, vol. 9, 1953, pp. 302–306.

9 "Electrical Contacts," by R. Holm, Almquist and Wiksells, Uppsala, 1946.

10 "Score Resistance of Bearing Metals," by A. E. Roach, C. L. Goodzeit, and P. A. Totta, *Nature*, vol. 172, 1953, p. 301.

11 "Scoring Characteristics of Thirty-Eight Elemental Metals in High-Speed Sliding Contact With Steel," by A. E. Roach, C. L. Goodzeit, and R. P. Hunnicutt, published in this issue, pp. 1659–1667.

Discussion

F. P. Bowden[8] and D. Tabor.[8] The authors have made a valuable attempt to correlate the friction and wear behavior of metals with their relative physical properties. All workers in the field will recognize the value of the systematic and extensive experimental work carried out. They may perhaps not agree with some of the details quoted. For example, in our experience it is difficult to prevent the transfer of indium to harder metals under any conditions of clean sliding.

The authors show that the coefficient of friction between metals provides little indication of the amount of wear and surface damage. This is a conclusion well supported by work in our laboratory and arises from the fact that the friction is determined by the over-all strength of the interfacial junctions; i.e., the specific shear strength multiplied by the area of real contact. This does not vary greatly from one metal to another so that for most metallic combinations μ, the coefficient of friction, is between $\mu = 0.5$ to $\mu = 1.5$. On the other hand, the surface damage depends on whether shearing occurs exactly at the interface (negligible wear) or a short distance away from it. Thus in an investigation using radioactive tracers it was shown that for clean sliding between various metal combinations the surface transfer could vary by a factor of a hundred or more without any corresponding systematic variation in μ.

The authors suggest that the primary factor determining the extent of the surface damage is the mutual solubility of one metal in the other. We agree that at high speeds of sliding, where frictional heating may be sufficient to produce surface melting, mutual solubility of the sliding materials will influence the friction and surface damage. However, at the extremely low speeds of sliding used in the authors' work the temperature rise produced by frictional heating can only be of the order of a few degrees C. It is difficult, therefore, to see how melting can take place or why mutual solubility in the ordinary sense of the phrase can be of importance at these very low speeds. It is true that the final classification of the wear damage appears to support the authors' hypothesis but many other physical and chemical properties provide similar classifications. In our experience the sliding process between unlubricated metals depends in a critical and complex way on a number of physical properties such as the hardness of the metal, its ductility, and on the thickness

[8] Research Laboratory on the Physics & Chemistry of Surfaces, Department of Physical Chemistry, University of Cambridge, Cambridge, England.

and nature of the oxide film present on the metal surface. The behavior also depends on the conditions under which sliding occurs, such as the load, the speed, the type of deformation of the surface asperities, and the temperatures generated at the sliding interface. For these reasons it seems to us somewhat unreal to attempt to pin down the frictional and wear characteristics of metals to any one single parameter.

L. Grunberg.[6] The correlation of the type of damage occurring in frictional contact and the physical characteristics of metals proposed by the authors is very ingenious. It is, however, doubtful whether a time-dependent process such as the formation of intermetallic junctions can properly be assessed in terms of a time-independent physical constant such as equilibrium solubility. Although the apparent contact between rider and plate at the velocity employed in the experiment may have been of the order of 10 sec, the actual contact at individual junctions and the time for which the junctions were at the melting temperature could at best have been of the order of 10^{-3} sec. Even if it were assumed that sufficient metal diffused at the point of contact, then the basis of the correlation should be diffusivity and not solubility. It would be interesting to know whether the authors have attempted a correlation of the friction results with diffusion constants, for which some data are available.

Also, while it is agreed that oxide films may disintegrate in frictional contact, the residual material must remain in the contact zone and may become intermingled with the metal. The mechanical properties of the mixture of metal and oxide which result from this process may be of greater importance than the small amount of metal diffusing across the junction in the brief periods of contact and high temperature.

While the paper quite rightly directs attention to the physical processes which are involved in frictional contact, the conclusion that solubility is the main factor involved cannot easily be accepted.

E. Rabinowicz.[7] The authors have collected a large number of data obtained with a Bowden-Leben type apparatus. Having worked with such an apparatus and some of the same metals, the writer can confirm both the general accuracy of the observations and the value in assembling them. There is, however, one point in the paper which can be clarified.

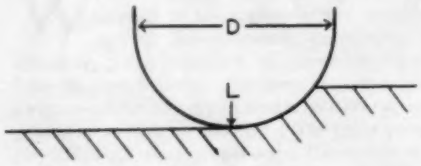

Fig. 5

The authors obtained a great difference in friction coefficients with the metal indium at the two loads 0.6 and 0.1 lb, and attribute the difference to ploughing. Now, from the work of Bowden and Tabor[8] we can readily calculate the importance of the ploughing term and find that the friction coefficient f_p produced by ploughing as shown in Fig. 5 of this discussion, may be written as

$$f_p = \frac{4}{3\pi^{1/2}} \frac{p'}{p} \frac{L^{1/2}}{p^{1/2}D} \quad [1]$$

where p'/p is a geometrical ratio and signifies the different resistances of the metal to penetration in the horizontal and vertical directions. Bowden and Tabor found an experimental value of 1.5 and hence

$$f_p = \frac{0.36L^{1/2}}{p^{1/2}D} \quad [2]$$

Substituting values given in the paper, $D = 6.2$ mm, $p = 1.6$ kg/mm^2, $L = 0.27$, and 0.045 kg, we obtain f_p values of 0.024 and 0.010 at the two loads, their difference being 0.014. This is nearly two orders of magnitude smaller than the difference observed, 0.51 (1.32 — 0.81); hence the change in friction coefficient with load must be due to some factor other than ploughing.

Probably the different friction coefficients were produced by different degrees of metal transfer. A recent treatment[9] demonstrates that changes in load can alter markedly the percentage of one metal covered during sliding by fragments of another, and it seems likely that at the higher load the sliding was largely indium on indium ($f = 2.0$), at the smaller load, steel on indium ($f = 0.5$). Note 5 to Table 3 in the paper confirms this supposition.

The practical importance of this metal-transfer phenomenon is that valid friction readings for metal pairs, one of which is soft, cannot be obtained in a sliding distance as great as $^1/_4$ in., unless very small loads are used. At high loads we might expect the friction coefficient to rise steadily during the run as metal transfer increased. Was this behavior observed by the authors?

Authors' Closure

The authors wish to express their gratitude to Messrs. Bowden and Tabor, Grunberg, and Rabinowicz for their kindness in preparing discussions for this paper.

Friction and surface damage, as Messrs. Bowden and Tabor point out, is such a complex process that it cannot be interpreted in terms of a single parameter. The authors did not wish to convey the idea that mutual solubility and compound formation between sliding metals explains friction and surface damage, but merely wished to emphasize these factors which have received so little attention in the literature.

The authors also wish to clarify the point concerning mutual solubility mentioned by Messrs. Bowden and Tabor:

Basically, friction and surface damage is related to two fundamental factors, the true area of metal-to-metal contact between a pair of sliding metals and also the relative strength of the junctions at areas of metal-to-metal contact to the strength of the base metals. Oxide films, boundary lubricants, surface geometry, and relative hardness affect the area of metal-to-metal contact. Mutual solubility, on the other hand, appears to affect the strength of the junctions. The experiments reported in this paper were carried out in order to try and determine what properties of metals affect the strength of the welded junctions rather than the amount of the area of metal-to-metal contact. In the true sense, this is a question of alloying ability or diffusivity rather than mutual solubility, and, in addition, the type of binding forces that hold the atoms of the metals in their crystal lattices. Therefore the best way to interpret the experiments would be in terms of diffusion data or data on the alloying tendency of different pairs of metals. However, such data were not available for many of the pairs of metals tested. Solubility data were then used as a guide to the alloying ability of the various metal pairs. Thus the authors have used the term, "mutual solubility"

[6] Department of Scientific and Industrial Research, Mechanical Engineering Research Laboratory, Lubrication and Wear Division, Thorntonhall, Glasgow, Scotland.

[7] Massachusetts Institute of Technology, Cambridge, Mass.

[8] See authors' Bibliography (7).

[9] "The Importance of Wear Fragments During Sliding," by E. Rabinowicz, Fundamentals of Friction and Lubrication in Engineering, The American Society of Lubrication Engineers, Chicago, Ill., 1954.

rather than alloying ability of diffusivity only as a matter of convenience. Therefore, in very slow sliding where frictional heating is of such a low order that localized melting does not take place, the friction and surface damage should really be looked at in terms of alloying ability or the ability of the two metals to diffuse at areas of metal-to-metal contact even though they are not in the liquid state. The authors feel that the low-speed experiments reported in the paper show the effects of strong and weak junction formation at the areas of metal-to-metal contact. Metals, with pronounced alloying tendencies, tend to form strong junctions and the only metals that formed relatively weak junctions were those pairs with low alloying tendency or those that tend to form brittle and friable intermetallic compounds with iron.

The comments of Mr. Grunberg are pertinent to the foregoing discussion and the authors are in agreement that diffusivity is a more realistic approach to the interpretation of the test results. Sufficient diffusivity data were not found at the time of the writinge to interpret the experiments. However, solubility data give a good qualitative idea of the alloying tendency of metal pairs.

Dr. Rabinowicz's observations on the effect of ploughing and metal transfer on the friction coefficient is evidenced by the results of the tests reported in the paper. The rider specimens for the soft metals such as indium, lead, and thallium showed blobs of metal transferred to the contact areas when tested at high load. An examination of the corresponding friction traces shows that the friction increased as the rider moved across the plate specimen and received the transferred metal. The high friction values for these soft metals therefore appear to be caused by the metal sliding against itself.

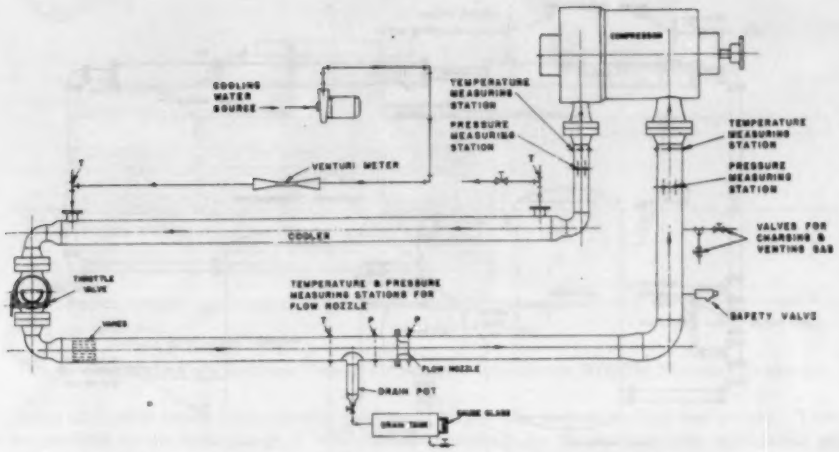

FIG. 1 DIAGRAM OF THE CLOSED SYSTEM FOR TESTING CENTRIFUGAL COMPRESSORS

Closed Systems for Testing Compressors

BY R. M. JOHNSON,[1] PHILLIPSBURG, N. J.

The closed system is discussed in its broad applications to the shop testing of centrifugal and displacement compressors. The essential requirements for the design and operation of test systems to use various gases are reviewed. Instrumentation and procedures necessary to meet the ASME Power Test Code standards of accuracy are considered in detail. Suggestions are made for code revisions needed to bring closed-system testing more fully within the scope of the test codes.

INTRODUCTION

WITHIN the past ten years there has been a phenomenal increase in the applications of centrifugal compressors serving the chemical, petroleum, and natural-gas industries. The extremes of operating conditions seem to have no fixed bounds. Machines have been built for inlet pressures ranging from a high vacuum to 1000 psi, and with discharge pressures as high as 2000 psi. The gases pumped have widely diversified physical properties. The k-values range from 1.1 to 1.64, and the mole weights vary from 4 to 140. From the viewpoint of factory testing, these machines cannot be treated as simple air compressors. Many of them cannot be operated safely with open intakes. Of necessity, the closed system has become commonplace for development and performance testing.

It is the object of this paper to describe the closed system and the associated apparatus as applied to the performance testing of centrifugal compressors. An attempt will be made to summarize practical experience with closed-system testing using air, natural gas, helium, steam, and Freon, in which the working pressures have varied from a vacuum to more than 2000 psi. Particular attention will be given to the merits and limitations of the system, as related to ASME Power Test Code procedures.

THE CLOSED-SYSTEM TEST LOOP

Fig. 1 shows the schematic arrangement of apparatus for testing a multistage centrifugal compressor. The pipe forms a closed loop, connecting the discharge to the inlet. The essential elements are the cooler, the throttle valve, the flow nozzle, and the measuring stations for pressures and temperatures. External facilities, not shown, include compressors and receivers for handling the gas with which the system is charged.

Fig. 2 shows a similar arrangement as applied to displacement compressors. It differs from Fig. 1 primarily in the use of receivers and pipe arrangements for the control of pulsation. The merits of this system will be discussed later.

Use of the closed system for testing rotating machines is probably as old as the flow nozzle. After the development of tight shaft seals, it was a simple step to build setups for testing with any dry gas. Owing to high cost, closed-loop tests have been generally restricted to research work. It is the relatively recent increase in applications of centrifugal compressors for gases other than air, that has forced the use of closed systems for commercial factory testing.

Unlike the open system, the closed loop provides great flexibility in the manipulation of inlet pressure and inlet temperature. This, in turn, controls the inlet density and the power requirement of a given machine. The control of these variables is precise, equilibrium of pressures and temperatures is more quickly established, and there is less fluctuation to contend with. Such features improve the accuracy of measurements and extend the scope of useful testing far beyond that of the open system which can be used only with atmospheric air.

The volume of a closed system is surprisingly small in relation

[1] Engineer in Charge, Engineering Test Department, Ingersoll-Rand Company. Mem. ASME.

Contributed by the Hydraulic Division and presented at a joint session of the Hydraulic and Gas Turbine Power Divisions at the Diamond Jubilee Annual Meeting, Chicago, Ill., November 13–18, 1955, of THE AMERICAN SOCIETY OF MECHANICAL ENGINEERS.

NOTE: Statements and opinions advanced in papers are to be understood as individual expressions of their authors and not those of the Society. Manuscript received at ASME Headquarters, August 29, 1955. Paper No. 55—A-157.

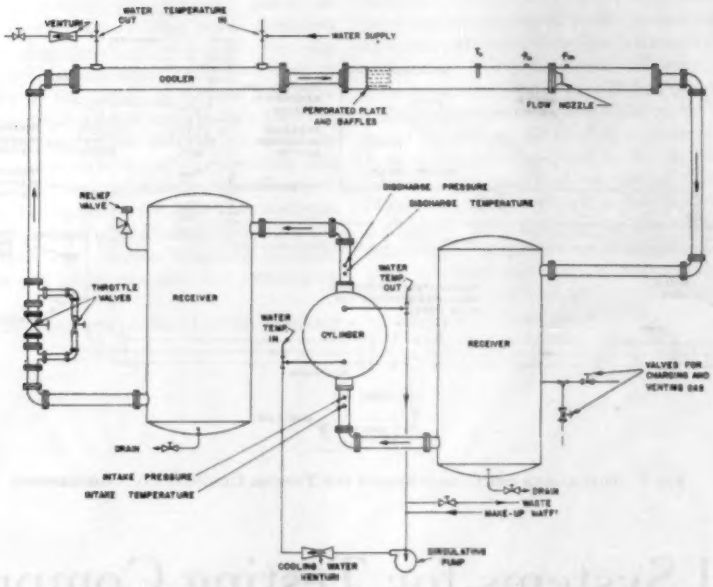

FIG. 2 DIAGRAM OF THE CLOSED SYSTEM FOR TESTING DISPLACEMENT COMPRESSORS

to the rated capacity of the compressor. For example, the total loop volume of a setup used to test a 5000-hp unit discharging at 2000 psi was less than 100 cu ft. This fact is of great commercial significance in view of the wide variety of gases which can be transported in steel cylinders at reasonable cost.

There are other important advantages. The heat exchanger provides another method of measuring the power input to the compressor. Unlike the heat-balance method (described in PTC 10),[1] it is completely independent of the gas properties.

Closed systems have become a useful adjunct to manufacturing operations. With these systems it is possible to operate the compressor at design loads, pressures, and temperatures, to check shaft seals, eliminate leaks, and to prove the over-all mechanical condition of the unit. If the machines have labyrinth-type shaft seals, the leakage can be measured accurately. As the gas is not necessarily wasted, it becomes economically feasible to measure over-all performance with a gas of physical properties for which the machine was designed.

TEST-LOOP DESIGN FOR CENTRIFUGAL COMPRESSORS

The essential dimensions of a test loop are governed by the sizes of the compressor connections and the pipe lengths necessary to accommodate the flow nozzle and heat exchanger. The pipe diameters must match at the compressor flanges. At the flow nozzle, they must not be less than two times the nozzle throat diameter to meet code requirements. The wall thickness of the pipe also must be sufficient to withstand the operating pressures.

The design of the heat exchanger and the flow nozzle requires a careful estimate of the compressor characteristics, such as the volume rate, the power input, the inlet temperature, the inlet pressure, and the discharge pressure. The range of these variables to be covered for a complete test is likely to develop critical situations (design problems).

The pressure loss of the circuit cannot exceed the available pressure rise of the compressor at any volume rate. The cooler capacity must handle the maximum heat load when the temperature difference between the gas and the cooling water is minimum. For the centrifugal compressor, it is important to note that maximum volume and maximum power coincide approximately with minimum pressure rise and minimum temperature rise. Control of friction loss of the cooler is often the key to a successful loop design.

A test loop to meet pressure-drop limitations is likely to be more difficult to design and more expensive to build for machines of low pressure rises, and especially so when the inlet-gas densities are also low. The pipe sizes will be large relative to the power input, and cooler designs must be chosen for minimum pressure loss. For this purpose, solid-core, extended-surface elements, similar to the familiar automobile radiator, have been used. Less expensive, and slightly higher in pressure loss, are the finned-tube arrangements. Smooth tubes with baffles and crossflow design, as conventionally used for compressor intercoolers and aftercoolers, are suitable and most economical where 5 to 10-psi pressure loss is tolerable. Shell stresses limit the use of these coolers for high gas pressures.

Where large pressure drops are available, it is good economy to use "gas-through-the-tube" cooler designs. For these coolers the tubes can be long and of small bore. The shell is not subjected to the stress of gas pressure. Fig. 3 illustrates the cooler design used for a 5000-hp compressor working at 1000 psi inlet pressure and 2000 psi discharge pressure. The tube sheets are welded to a heavy-wall pipe section; the water shell is welded outside. The tube bundle contains 200 tubes, $^1/_2$ in. OD, 18 BWG, 20 ft long.

The throttle valve should be as small as possible within the limits of available pressure rise. Plug-type valves are best suited to high pressure. Too large a valve is unnecessarily more expensive and makes flow regulation more difficult. On the other hand, too small a valve may limit the range of the test. Valve-loss data at high velocities are not usually available, and selections must be tempered with judgment.

For gas pressures above 125 psig, all-welded joints are preferred for reasons of low cost, and for the prevention of leaks. Flanged joints are necessary only at the compressor nozzles, at the flow nozzle, and at the throttle valve.

[1] ASME Power Test Code 10, Centrifugal, Mixed Flow, and Axial Flow Compressors and Exhausters, 1949.

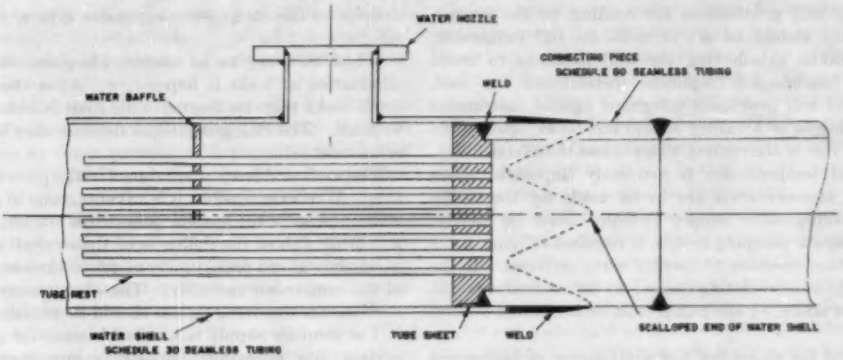

FIG. 3 SECTIONAL VIEW SHOWING DESIGN DETAIL OF A COOLER FOR 2000-PSI WORKING PRESSURE

Facilities for draining off liquids which inadvertently get into the system must be provided in the basic design. Where possible, the pipe should be pitched to a single low point and a drip connection of generous size installed. The upstream side of the flow nozzle forms a natural separator when the pipe is horizontal and is an effective location for a drain connection to remove liquids while the system is in operation. If the gas cannot be wasted, this drain must be piped into a collecting tank. To function properly the drain connection must be located in regions of relatively low velocity.

In addition, the pipe system must contain numerous small tapped connections for charging the gas, for purging, and for instruments to indicate pressures and temperatures. These will be discussed in detail.

INSTRUMENTATION

The measurements usually required for determining over-all performance are the pressures and temperatures of the gas, the flow rate, the speed, the power input, and the physical properties of the gas. Instrumentation for these measurements will be discussed from the viewpoint of ASME Power Test Code procedures. Specific reference is made to PTC 10, the Code for Centrifugal and Axial Flow Compressors, 1949, to indicate which of its provisions applies and to point out wherein they might be improved for closed-system testing.

The location of measuring stations for pressure and temperatures, prescribed for the inlet and the discharge in PTC 10, are believed to be adequate and practical for the closed circuit where the gas-velocity pressure does not exceed 5 per cent of the total pressure. It should be noted that traverses with delicate pitot-tubes are not practical at high pressures and can be avoided by selecting pipe sizes to hold the gas velocity below 125 fps.

The code specifies thermocouples or thermometers in wells for temperature measurements. Here a word of caution is in order. The wells must be designed to withstand the prevailing pressure and velocity without vibration. A broken well can be particularly hazardous in the closed system.

Pressures may be measured with calibrated Bourdon-tube gages, dead-weight gages, or U-tube manometers. The range of these instruments must be suitable for the prevailing pressure. The selection of manometers for the differential pressure across the flow nozzle becomes a problem at high pressures. The practical safe limits for $^3/_8$-in-bore manometer tubing is around 500 psig. For higher pressures, the differential must be measured with dead-weight gages. These should have not less than $^1/_{10}$ psi sensitivity.

Where the working pressure is above the safe range of glass manometers, the inconvenience of dead-weight gages prolongs unduly the task of setting test points. This situation can be corrected by the syphon-type differential gage. These gages are available for very high static pressures and a wide selection of differential-pressure ranges. They are particularly useful for indicating changes in flow. These gages are recommended only to supplement, not to replace, the dead-weight gage.

The ASME long-radius flow nozzle is recommended as the preferred device for measuring flow rates in the closed system. It is adaptable to systems for high pressure and the pipe diameter need not be larger than two times the nozzle throat. The code specifies a minimum pipe length of 10 D upstream, and 5 D downstream where D is the internal diameter of the pipe. Pressure taps are located 1 D upstream and $^1/_2$ D downstream. The temperature station is 3 D upstream. Straightener vanes are required. The code rules for manufacture and installation of the flow nozzle have been proved by experience, and strict adherence will insure the most reliable measurements.

Where high heads are available, it is good economy to select the flow-nozzle diameter for the maximum pressure differential consistent with the instrument to be used for its measurement. Contrary to some current opinions, there is no improvement in accuracy due to a low differential pressure. Discharge coefficients are likely to be more reliable at critical flow and are particularly unreliable at low values of Reynolds number.

For the measurement of shaft power, several methods are described in the current Code, PTC 10. These include the calibrated electric motor, the cradled dynamometer, the Amsler type torsion dynamometer, and the heat-balance method. In view of high speeds now common to centrifugal compressors, only the heat-balance method is of much use. Another method, already mentioned, is available in the cooler circuit of the closed system.

With few exceptions, the cooling-water circuit of a test loop can be arranged to measure the shaft power with high accuracy. After equilibrium is established, the power input to the cooler must equal the energy input to the gas. The shaft input is accounted for by the energy transfer from the gas to the cooling water, plus radiation and bearing losses. The radiation loss, normally less than 2 per cent, can be computed by the usual methods, or for practical purposes, eliminated with glass-wool insulation. The bearing losses, normally less than $^1/_2$ per cent, can be computed from oil-cooler measurements.

For accurate measurement of the heat input to the cooling water, special precautions are required for determination of the quantity and temperature rise. The venturi, or the flow nozzle, used for measurement of the flow rate, must be calibrated integrally with the pipe run with which it is used. The thermometers must be of laboratory grade, with scales selected to suit the

operating range, and graduations for reading to the nearest $^1/_{10}$ deg F. They should be set in wells for full immersion. Care must be taken in selecting the well locations to avoid stratified flow conditions. Duplicate instruments for each measuring station will provide a safeguard against instrument error. A high degree of accuracy should not be expected when the temperature rise of the cooling water is less than 20 deg F.

Equilibrium of temperatures is extremely important when accurate power measurements are to be made by the cooler circuit. The cooling-water supply pressure must be steady. Sometimes a separate pumping system is required to remove the pressure fluctuation common to factory water systems. If the cooler is too large, a recirculating pump may be necessary, and in this case the heat added by the pump must be accounted for and subtracted.

A third method for measuring the shaft power of high-speed compressors is the strain-gage torque meter. It has been used successfully for about 10 years in the range of 8000 to 10,000 rpm. It is particularly applicable for factory testing where turbine drivers are used in permanent test stands. Its convenience, sensitivity, and readability are excellent. When used in circumstances where the power measurement can be checked simultaneously with another method, this torque meter is considered reliable. It deserves a proper recognition in the test codes.

Speed measurements have a greater significance when the compressor is operated on a closed system. Owing to the small volume, normal fluctuation in speed may produce unacceptable disturbance of pressures and temperatures. For control purposes, a tachometer capable of indicating 0.2 per cent changes in speed is essential. If the torque meter is used, average speed should be measured with counters accurate within 0.1 per cent. In these respects, the prevailing code tolerances appear inadequate.

In closed-circuit testing, instruments for frequent measurement of the gas gravity are necessary. When air is used, the dew-point apparatus may be employed to indicate accurately the amount of water vapor present. Dew-point apparatus is available in two types. In one type the dew point is measured directly by adjusting the refrigeration on a metal mirror; in the other type, a fog is produced by adjusting the pressure. Both are reliable. For other gases, the specific weight may be compared directly to dry air with the gravity balance. Test engineers are indebted to the natural-gas industry for the development of a portable, precise, and reliable instrument known as the Acme gas gravity balance. Its use is limited to dry gases and the technique for its proper use should be described in the codes.

It is also necessary to know the k-value of a gas mixture for computing flow rates and the theoretical power. If the pressures are high, it is likewise necessary to take into account supercompressibility. Unfortunately, there are no instruments available for measuring these properties directly on the test floor. They must be computed from the laboratory analysis of a sample and they are therefore dependent upon the reliability of the sample. The lack of on-the-spot measurements for k and supercompressibility is probably the most pressing instrumentation problem related to closed-circuit testing. Detailed procedures for the taking of samples, the analysis of the sample, and the computation of k and supercompressibility should be incorporated in the test codes.

Operating Procedure for Centrifugal Compressors

The importance of scrupulous cleanliness during the assembly of a closed-system test loop cannot be overemphasized. Pipe scale, welding beads, bits of gasket material, and other loose foreign materials inadvertently left in the pipe, can cause serious damage to the compressor, expensive delays, and worthless test results.

When tests are to be made with gases other than air, the elimination of leaks is imperative. After the usual hydrotest, small leaks may be located with soap bubbles by pressurizing with air. The Halogen gas-leak detector may be used for further refinement.

The shaft seal is an integral part in the process of leak elimination. Wherever feasible, it is advantageous to make preliminary trial runs with the system pressurized on air. This procedure will usually show the tightness of the over-all system and at the same time afford opportunity to prove the mechanical functions of the compressor assembly. The effectiveness of the drain connections for removing liquids should be tested at this time.

The shop air supply is a valuable asset for getting the closed system into operation. Booster compressors will be needed where the system is above that of the shop supply. Suitable precautions must be taken to eliminate water and oil which are likely to be present in shop air lines. Good aftercoolers and separators are indispensable. If the air charge is to be used for performance, the presence of either water or oil may spoil the test.

The removal of air before charging with the test gas is often necessary. Two common methods are used, evacuation and dilution, the choice depending upon the cost and the degree of air removal desired. If the supply of gas will permit, the residual-air component can be reduced to any desired value by repeated charging and blowing down. Evacuation will require mechanical pumps. Vacuum pumps of the displacement type are available for exhausting down to the micron range (less than 1 mm Hg abs.). Three or four-stage steam jets will do a better job and much faster. The use of the evacuation method may be limited by the type of shaft seals used on the compressor. With the oil types, there is the problem of removing a small internal oil flow.

During a normal test operation, it is usual practice to hold speed and inlet pressure constant, and to vary the volume rate for a series of test points. To do this, the gas charge must be adjusted for each volume point. This procedure requires facilities for charging and removing gas during the test. If the gas is too expensive to waste, suitable storage tanks and a compressor will be needed.

Not to be overlooked are some minimum precautions for safety. A relief valve should be provided to prevent accidental overpressure beyond the safe limits of the system. Depending upon the type of gases, there may be other safety precautions, for the prevention of fire, explosion, or a build-up of a toxic atmosphere. For example, the accumulation of oil in a system charged with air may, under certain conditions, become a source of fire and overpressure. A temperature-actuated device for automatic shutdown in the event of cooling-water failure can be justified in many circumstances. The proper use of the rupture disk as a safety device should not be neglected.

Gases for Factory Testing of Centrifugal Compressors

There is a considerable variety of gases which have been used successfully in closed systems for shop testing. These include air, steam, carbon dioxide, nitrogen, helium, natural gas, hydrogen, and a number of the common refrigerants. There are many others that might be used, the choice usually being limited by cost, availability, and the prevailing safety requirements. Where it has been impractical to use the specified gas, substitutes have been employed with much success.

The ideal substitute gas should have the same physical properties as the specified gas. In practice, any combination of k and mole weight which will produce the design volume ratio with

specified speed is usually accepted as commercially satisfactory. In the closed circuit, it is the adjustment of inlet density that controls the power input, and permits some leeway in the values of k and mole weight.

The term "volume ratio" as used here, means the inlet-volume rate divided by the discharge-volume rate. Although there are other factors, such as vapor pressure and viscosity, which may affect performance in some degree, they are generally of minor importance.

From the viewpoint of Power Test Code standards of accuracy, the permissible deviation of k and mole weight should be re-examined for closed-circuit testing. With open-inlet testing on air, the engineer is accustomed to dealing with a considerable variation of inlet density due to normal fluctuation of atmospheric pressure, temperature, and humidity. The present code, PTC 10, permits a deviation of 10 per cent in inlet specific weight or mole weight and 5 per cent in k. Although these limits actually exclude a considerable portion of commercial testing, they tend to favor the use of substitute gases in closed systems.

Air can be used in the closed system as a useful substitute for a considerable range of gases. Within present code limitations, the k-values can vary between 1.33 and 1.47, and mole weights between 26.0 and 31.8. This range of properties might even be extended where the pressure ratio is low, providing a correct speed and volume ratio are held. However, air fails conspicuously as a substitute for machines of high pressure ratios when the needed k-values are in the range of 1.6 and the mole weights are around 10.

In certain cases mixtures of gases will provide the needed substitute. By adjusting the proportions of air and helium, it was possible to produce the specified volume ratio with rated speed for a compressor designed to compress refinery gas where the mol weight was 6.0, and the k-value 1.40. The prevailing values of k and mole weight for the test mixture were computed from gravity-balance measurements.

Mixtures of air and Freon, F115, have been used where gas of a high mole weight was needed to determine performance at Mach numbers above 1. In this instance a small portion of air was tolerated to avoid elaborate purging, and the properties of the mixture were calculated from gravity-balance measurements.

Steam also has served as a substitute gas for proving the mechanical operation at high pressures and temperatures. There is no basic reason, however, to prevent its use for performance testing, provided precautions are taken to prevent condensation. High temperatures would call for more elaborate insulation. The torque meter would solve the power-measuring problem if radiation loss became too high for reliable use of the heat-balance methods.

Supercompressibility should be given consideration in the selecting of gases for loop testing. The deviation from Boyle's law will vary with the kind of gas, the pressure ratio, and the inlet pressure. With natural gas, for example, the deviation is a matter of 8 to 9 per cent between 14.6 and 1000 psia. It is unwise to attempt performance testing with gases for which the compressibility factors are not well established. The Displacement Compressor Code, PTC 9,[3] 1954, gives a method for approximating these factors from a chemical analysis.

Closed Circuits for Displacement Compressors

There are several features of the closed circuit which permit improved accuracy in the testing of displacement compressors. Essential arrangement of the apparatus has already been mentioned in connection with Fig. 2.

The power consumption of displacement compressors is particularly sensitive to cooling-water fluctuations and the differential between the inlet-air and the inlet cooling-water temperatures is of considerable importance. The control of this differential has for a long time been considered subject to the prevailing weather, a matter quite beyond engineering effort. This is the viewpoint of the 1954 ASME code, PTC 9, for displacement compressors, and it is justified primarily by the limitations considered unavoidable in the field testing of air compressors. These limitations do not prevail in shop testing.

The closed circuit provides complete control of the temperature difference between inlet gas and inlet cooling water and thereby eliminates a troublesome situation. As specific weight has no effect on power, the inlet-gas temperature can be set at any convenient value to suit prevailing temperatures of the cooling water and a specified value of temperature difference maintained. In addition, the inlet pressure is easily controlled. By measuring the amount of charging gas, the total external leakage can be evaluated continuously throughout the test.

The pulsating-flow characteristic, inherent with displacement compressors, calls for special precautions in the design and instrumentation of the system. If resonance occurs at either the inlet or the discharge of the compressor, pressure waves of abnormal amplitude are likely to appear. These waves can upset normal performance and defeat the test effort. To avoid resonance, the receiver volumes and the pipe dimensions must be selected carefully. The completed setup must be checked for wave amplitudes before the test is attempted. Small receivers are required in the gage lines used for pressure measurements. The procedure for dealing with these problems is covered adequately in the 1954 Test Code, PTC 9.

When the compression ratio is above 2.5 it is practical to use critical-flow nozzles to measure capacity. This permits much smaller nozzles which are more easily calibrated, and eliminates the need of the downstream pressure measurement. Flow coefficients are likely to be considerably more reliable with critical flow owing to the higher Reynolds number.

The closed system has been used successfully for shop tests on air compressors. It is adaptable to other gases. It provides a precise control of the cooling problem and eliminates the need for intercooling corrections. The variable effects of water vapor in air can be either controlled or eliminated. Accuracy of the inlet-temperature measurement is appreciably improved. The potential error from uncertain external leakage is automatically eliminated. Inlet pressure can be adjusted to any specified value, a feature useful for the testing of boosters as well as for eliminating the effects of barometric fluctuation.

Summary

From the foregoing discussions it is evident that some knotty problems face the Power Test Code Committee in their attempt to revise the Centrifugal Compressor Code for testing with gases other than air. There is a need of general formulas for expressing performance of the centrifugal machine. These must be suitable for evaluating changes in head and efficiency when the gas properties deviate from those specified.

In this effort, it appears desirable to set up parameters for each of the essential variables likely to be dealt with in the course of practical testing. These will include such items as speed, volume, inlet specific weight, mole weight, k, volume ratio, supercompressibility, etc. The effect of each of these variables on performance requires careful analysis from the viewpoint of closed-loop testing. In the final code, acceptable commercial limits for each of the variables must be agreed upon.

The use of substitute gases for commercial testing calls for a rigorous study of the physical properties. When mixtures of gases are used it appears necessary to measure mole weight and k

[3] ASME Power Test Code 9, Displacement Compressors, Vacuum Pumps and Blowers, 1954.

value during the test. For many gas mixtures these measurements may not be possible with available instruments.

Discussion

C. F. Koenig, 3rd.[4] This seems to be an excellent paper and we have little to offer except compliments. It is certainly true that PTC 10 is inadequate for testing of this nature, and prompt revision thereof will be of tremendous value to the industry. It also will tend to clear up some misconceptions which appear to exist in certain quarters, mostly because of incomplete evaluation of the gas dynamics involved.

The author makes the point that gas properties must be selected for the test which will result in the design volume ratio through the machine. We believe that a further consideration is important—that of Mach number or the ratio of gas velocity to the local sonic velocity at various points within the compressor. The performance of a compressor varies considerably with the Mach number, particularly when tip speeds and/or Mach numbers are high at the design point.

We try to select a gas such that both the design density ratio (= volume ratio) through the machine and the design Mach numbers are simulated as closely as possible. The test speed is usually not the design speed, unless the test gas is similar to the design gas.

It is usually found that, for gases lighter than air, tests can be run on air at reduced speed and the proper volume ratio and Mach number can be simulated closely. For gases heavier than air, it is almost always necessary to use a special test gas, e.g., Freon.

Where the test speed as calculated from the foregoing considerations is different from the design speed, we would run mechanical tests at full speed to check seals, thrust bearings, case deflections, and so on. In extreme cases, it may be necessary to use different gases in the loop for performance tests and mechanical tests. On "platforming" compressors, for example, where the molecular weight is about 6.0 and the k-value about 1.39, performance tests are run on air at about 50 per cent of rated speed. The pressure level is not vital for performance tests, except that efficiency usually improves 1 or 2 points at the high pressures. For mechanical tests at rated pressure, air would require far too much horsepower, so a mixture of helium and air—mostly helium—is used. Note that the helium-air mixture would not be suitable for performance tests because of the high k-value of helium.

This paper should do much toward encouraging the industry to look with favor on testing of this nature. For a relatively small cost per machine it furnishes valuable data on the machine being tested. It also provides valuable information for future development which otherwise would probably not be obtained for a long time and which will pay off in better compressors for the future.

T. O. Kuivinen.[5] The writer was very ably aided by Messrs. B. C. Thiel and John Fullemann in reviewing the author's paper on "closed systems," and the following is a consolidated discussion:

We feel that this is an excellent paper revealing a wealth of experience obtained by the author. He is to be congratulated on this presentation. We fully agree with him on the wisdom of using closed loops, not only for research, but for production tests too.

One of the merits of closed systems (implied by the author but not spelled out in detail) is the evaluation of Reynolds-number effect (i.e., scale effect) on performance, which can be done easily by changing pressure levels. The author also mentions the need to consider supercompressibility and the fact that testing should not be attempted on gases where the compressibility effects are not well established. It is our belief that equipment is now available from instrument manufacturers whereby a simple method, originated by Dr. Burnnett of the Bureau of Mines, may be used to determine compressibility factors for the gas under consideration.

The present test code requires long straight runs after turns to insure accuracy. For large pipe sizes this becomes bulky and expensive. Does the author know if there is any activity considering relaxing the code toward shorter straight runs if turning-vane cascades are used instead of standard tube turns? Cascades provide better flow-energy distribution downstream than plain turns in the piping.

Author's Closure

The remarks by Mr. Koenig are well taken. They summarize the variables involved and emphasize the complexity of the problem.

Among these variables he mentions Mach number, which the author failed to include in the paper. When testing with substitute gases it is easy to get into serious trouble if velocities within the impellers approach the speed of sound. To avoid this pitfall it is necessary to examine the impeller design before a substitute gas is chosen.

A reference was made to the use of test speeds as low as 50 per cent of the rated speed. Although this is consistent with current theories of fluid dynamics, there is strong hesitancy on the part of some designers to accept tests where the speeds vary widely from the design value. For this reason the code limitations on the speed deviation must remain conservative.

Mr. Kuivinen, quite correctly, calls attention to the possibility of investigating the Reynolds-number effect by the simple expedient of changing the pressure level. It is to be expected that the experience with closed-system testing will produce some good papers on this subject in the near future.

Regarding the economic limitations of long pipe lengths specified in the present code, it will be observed that the code rules are of necessity conservative. The author has successfully used short pipe lengths by fitting elbows with turning vanes. It should be remembered, however, that short pipes cannot be safely used without investigating the prevailing velocity distributions with a pitot-tube traverse. These investigations are in themselves time-consuming and expensive and it may be cheaper to use longer pipe.

The comments by Mr. Koenig and Mr. Kuivinen are all constructive and contribute substantially to the development of the subject.

---

[4] Assistant Chief Engineer, Compressor Department, De Laval Steam Turbine Company, Trenton, N. J. Mem. ASME.

[5] The Cooper-Bessemer Corporation, Mt. Vernon, Ohio.

The Slotted-Blade Axial-Flow Blower

By H. E. SHEETS,[1] GROTON, CONN.

The slotted blade applies boundary-layer control to the blades of axial-flow blowers. This offers a means to design axial-flow blowers for higher efficiencies, or higher pressure coefficient, or possibly a combination of both. Test data of an experimental blower are presented, indicating blower efficiencies to 94 per cent and stage efficiencies to 96 per cent with high-pressure coefficients corresponding to a maximum flow deflection of about 52 deg.

Nomenclature

The following nomenclature is used in the paper:

- c = blade chord
- D = impeller tip diameter, ft
- D_H = impeller hub diameter, ft
- H = total head, ft
- n = revolutions per sec
- n_s = specific speed
- Q = volume of flow, cfs
- t = blade pitch
- v = absolute velocity, fps
- u = circumferential velocity of impeller tip, fps
- w = relative velocity, fps
- ϕ = flow coefficient
- ψ = pressure coefficient
- η = total efficiency
- ρ = density of air
- ν = hub ratio

Other symbols will be defined in the text.

Introduction

The slotted blade applies boundary-layer control to the blades of an axial-flow blower. The subject of boundary-layer control has attracted considerable attention in respect to the isolated airfoil (1),[2] but few data exist for its application to the blades of turbomachinery. The object of boundary-layer control is to delay the transition from a laminar to a turbulent boundary layer, thereby reducing skin friction, or to prevent boundary-layer separation, thus increasing permissible blade loading.

Boundary-layer control has been accomplished by the application of either suction or pressure to the boundary layer. One system uses an independent source of suction, or pressure, to remove or add fluid to the boundary layer; whereas another system uses slots or auxiliary airfoils, and accomplishes the same effect by using the pressure difference between the upper and lower surfaces of the airfoil for boundary-layer control. In the form of slotted flaps, boundary-layer systems are used on standard airplane wings, and a number of experimental airplanes have been flown with various types of suction and ejection systems operated from an independent pressure source.

The advantages of boundary-layer control systems for blades of compressors have been recognized (2), but experimental data have been disappointing. Tests using suction slots energized by an independent pressure source, as well as tests with slotted blades energizing the boundary layer by flow from the lower to the upper blade surface indicate about 75 per cent efficiency, a lower efficiency than for standard blades (3). The low efficiencies are ascribed to the increased profile drag caused by the slots and to the blade arrangement which produces large secondary flows, causing, in turn, high losses. A higher pressure coefficient and higher turning angles have been achieved.

The application of boundary-layer control to the blades of turbomachinery is considerably more complex than its application to the isolated airfoil because of the added problems of secondary flow (2), of three-dimensional effects due to the twisted blades, of radial distribution of flow, and of the effects of centrifugal force and pressure distribution on the boundary layer.

An analysis of boundary-layer control applied to the blades of a blower is presented herein. The slotted-blade construction is used, producing boundary-layer control by means of the flow from the lower to the upper surface in cascades of airfoils. Variables for the geometry of the slot are analyzed, and test data are submitted for one blower, resulting in both high efficiency and pressure coefficient.

Analysis

Boundary Layer. The boundary layer is the film of fluid immediately adjacent to the blades moving the fluid through the impeller. In this boundary layer, viscous forces predominate, whereas, outside the boundary layer, viscosity is unimportant because the velocity gradient is small. There are two types of boundary layer, namely laminar and turbulent. In the laminar layer, the flow is smooth and without eddies. In the turbulent layer a large number of relatively small eddies exist. These eddies in the turbulent boundary layer induce transfer of momentum from the outer parts of the fluid, moving with high velocity, to the fluid film close to the surface, resulting in a velocity distribution having a higher velocity near the surface. Because of this mechanism of fluid flow, skin friction of the turbulent boundary layer is higher than for the laminar flow.

For ideal fluid flow, the flow analysis on airfoils is represented by pressure and velocity distribution as a function of airfoil chord. The boundary-layer flow at its outer limit equals the ideal flow, but, due to the viscous forces, the flow within the boundary-layer is more complex. In the areas of flow deceleration, the loss of speed is greater for the particles of fluid in the boundary layer than for those in the outer flow because of the reduced kinetic energy in the boundary layer, thus limiting boundary-layer flow against adverse pressure gradients. The particles of the fluid within the boundary layer actually may reverse their motion if the rise in pressure exceeds a critical value, and then the flow is separated from the airfoil.

Turbulent boundary layers are less inclined to separation than laminar layers because of the increased interchange in momentum. If laminar-flow separation occurs, the flow may leave the surface permanently or reattach itself in the turbulent boundary layer. If turbulent-flow separation occurs, it can affect the flow through the guide vanes or the next row of blades.

---

[1] Chief Research and Development Engineer, Electric Boat Division, General Dynamics Corporation. Mem. ASME.

[2] Numbers in parentheses refer to Bibliography at end of paper.

Contributed by the Compressor Committee of the Hydraulic Division and presented at a joint session of the Hydraulic and Gas Turbine Power Divisions at the Diamond Jubilee Annual Meeting, Chicago, Ill., November 13–18, 1955, of The American Society of Mechanical Engineers.

 Manuscript received at ASME Headquarters, September 7, 1955. Paper No. 55—A-156.

Flow through airfoils displays a region of laminar flow beginning at the leading edge. Further downstream, at approximately the location of the minimum pressure, there is a transitional region in which the distribution of the mean boundary-layer velocity changes, and finally, there is a region of fully developed turbulent motion. As the fluid moves over the airfoil, the boundary layer is initially thin in the laminar-flow section, and thickens as the flow progresses along the surface and changes to a transitional and turbulent boundary layer. The extent of the laminar, transitional, and turbulent boundary layer along the airfoil is a function of the blade geometry, blade loading, Reynolds number, and turbulence in the general flow stream. In addition, irregularities on the surface may cause an earlier transition to turbulent flow. Thickness, and increase in thickness, of the boundary layer are a function of the local pressure gradients, Reynolds number, and surface conditions. If no separation occurs, the airfoil drag is primarily caused by skin friction and the value of the drag depends mainly on the relative amounts of laminar and turbulent boundary-layer flow. For further analysis of the drag, the relationship between pressure distribution and frictional intensity is of particular interest.

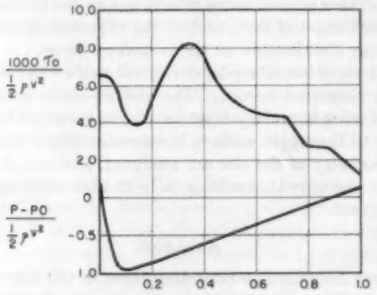

Fig. 1 Frictional Intensity and Pressure on the Upper Surface Versus Airfoil Chord

The total drag of the airfoils in cascade consists of form drag which is a function of the normal pressure and skin-friction drag which is associated with the tangential stress acting on the surface of the airfoil or frictional intensity (4). Frictional intensity is also defined by multiplying the velocity gradient in the boundary layer at the airfoil surface with the viscosity of the air (5). Thus frictional intensity can be determined experimentally. Fig. 1 shows data of pressure distribution and frictional intensity both in dimensionless form by dividing their corresponding values by the value of free-stream energy $^1/_2\rho v^2$ for the upper surface of an airfoil. On the upper surface, frictional intensity has one maximum value near the forward section, and a second and larger maximum value a certain distance downstream on the airfoil chord. The transition from laminar to turbulent flow in the boundary layer takes place in the region between these two maximums. Usually the transitional region moves toward the forward section as the blade loading increases. Distribution of normal pressures indicates that the transitional region is situated just downstream of the point of lowest absolute pressure. The distribution of frictional intensity on the lower surface resembles that on the upper surface, but the maximum values are smaller. It appears that the frictional intensity reduces toward the trailing edge, provided that no separation of flow occurs on either the upper or lower surface. It must be remembered that the values for frictional intensity will vary just like the values for pressure distribution with airfoil parameters like camber, thickness, cascade solidity, and stagger angle, and for the same airfoil it will vary with blade loading or angle of attack. Attempts to prevent the boundary layer from becoming turbulent, or separating from the body, by means of suction or blowing systems, are termed "boundary-layer control."

The National Advisory Committee of Aeronautics, NACA (6), has developed laminar-flow airfoils by designing airfoils of such a configuration as to give a slowly decreasing pressure distribution over a predetermined extension of the chord of the airfoil. The theory has been developed (7, 8) so that it can supply the shape of an airfoil to give a calculated velocity and pressure distribution, including consideration of the boundary layer in cascades (9). The laminar-flow airfoils have a laminar boundary layer over a certain extension of the chord, with sudden change in pressure gradient and transition to turbulent boundary layer. Airfoils have been designed with laminar flow to about 60 per cent of the blade-chord length. There are distinctive advantages of low drag when these airfoils are used within the range of optimum conditions for which they are designed. However, these airfoils are sensitive to proper blade loading. Fig. 2 shows the lift and drag coefficients for one conventional and two laminar-flow airfoils. Outside the normal range of blade loading, the laminar-flow airfoil can have a higher drag coefficient than conventional airfoils.

In cascades of airfoils for blowers, there is a pressure gradient between the inlet and the exit of the blade row resulting in higher local values of deceleration and pressure increase on the airfoil, as shown in Fig. 3. In this figure it is apparent that the pressure rise along the low-pressure side of the airfoil in cascade is considerably steeper than the equivalent rise in the case of the iso-

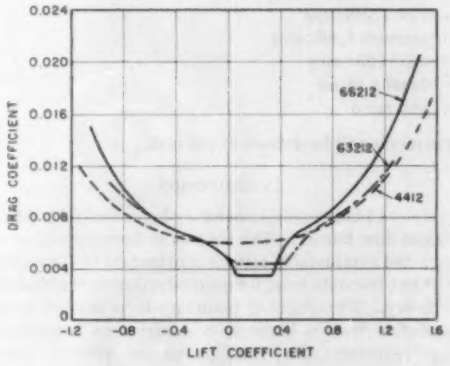

Fig. 2 Drag Versus Lift Coefficient

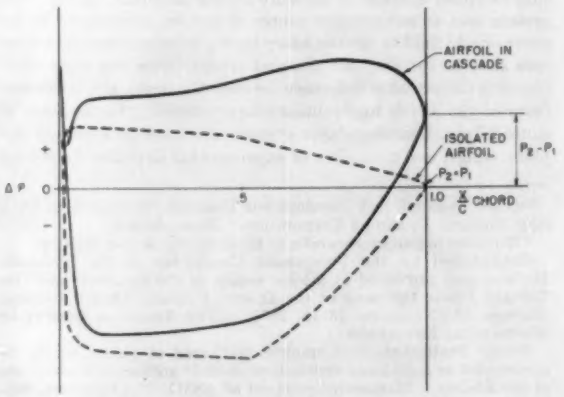

Fig. 3 Pressure Distribution of Airfoils

lated airfoil. Cascades of blowers become considerably more sensitive in their transition from laminar to turbulent boundary layer and to separation as the pressure increase per row of blades is increased.

The Slotted Blade. The slotted blade establishes a flow from the lower to the upper side of the airfoil for the purpose of boundary-layer control. This results in a sink and boundary-layer removal on the lower side of the airfoil, and a source with ejection of fluid on the upper side of the airfoil. In order to achieve a minimum drag, a dropping pressure is desirable over the initial part of the airfoil surface upstream of the slot location, using the principle of the NACA laminar-flow airfoils. On the upper blade surface, a laminar boundary layer is maintained to a predetermined point along the blade chord where ejection of fluid occurs, resulting in addition of energy to the boundary layer and simultaneously in a pressure change. This establishes quick transition to a turbulent boundary layer.

The formation of a turbulent boundary layer at this point on the upper airfoil surface is really advantageous, because the air is thereby given more momentum to follow the rest of the airfoil surface. If the transition to a turbulent boundary layer is delayed so much that the laminar boundary layer separates, and stays separated, then the result is an increased drag coefficient. The location and amount of fluid ejection producing energy addition can be controlled, thus permitting flow without separation against the necessary steep pressure gradient.

The slotted blade permits the design of airfoils with favorable pressure distribution and laminar flow over great portions of the chord even for highly cambered airfoils. The lower blade surface has a flow sink and removal of the boundary layer, thereby extending the range of laminar flow to approximately the trailing edge under design conditions. This reduces frictional drag by reducing frictional intensity. A pronounced reduction in drag is obtained by the reduction of the skin friction through increasing the relative extent of the laminar boundary layer on the lower airfoil surface. The slotted blade is designed to have a greater extent of laminar flow over the lower airfoil surface than over the upper surface and the relative extent of total laminar flow is increased.

The theory of stability of the laminar boundary layer indicates that transition to turbulence may be induced by the presence of disturbances and by surface roughness. Therefore the flow in the vicinity of the slot must be analyzed carefully and the slot be designed accordingly.

It should be noted that the characteristics of a slotted laminar-flow airfoil may show the typical narrow range of low drag followed by a higher drag outside the design range. This, in turn, requires for maximum efficiency careful analysis of the blades from hub to tip, so that at the point of maximum efficiency all airfoil sections operate within the optimum range. The entire flow problem is three-dimensional and considerable attention has to be given to secondary flows and movement of the boundary layer, requiring analysis of flow and pressure at the slot location, as well as at the trailing edge, between hub and tip. The importance of proper radial distribution of pressures has led to a change in the respective slot location and configuration. The pressure difference between the upper and lower side of the airfoil determines the amount of fluid flow through the slot and this quantity of flow and the relative pressure change at the slot are varied between hub and tip. The same type of airfoils are used, having a higher cambered profile at the hub, a lower cambered profile at the tip, and a variable degree of laminar flow due to the change in slot location.

Much greater increase in blade loading and stage-pressure ratio should be possible through the use of boundary-layer control on the rotor and stator blades. There should be no difficulty in doubling the loading obtainable without boundary-layer control. It is less easy to evaluate the effect of boundary-layer control on the efficiency of the stage in the entire blower. The profile lift-drag ratio should be increased because larger lift coefficients and corresponding flow deflections are possible. In addition, there is a decrease of profile drag and the stage efficiency should, therefore, be higher than for conventional blades, provided the secondary blade losses are not increased. The principle should be particularly beneficial for small Reynolds numbers. Boundary-layer control offers a means to design blowers for either higher efficiencies or higher pressure ratios, or possibly, a combination of both.

Design of Blower

The following dimensionless coefficients (10, 11) are used for the design and presentation of the performance data:

Flow coefficient

$$\phi = \frac{v_m}{u} = \frac{Q}{D^3 n} \frac{4}{\pi^2(1 - \nu^2)}$$

Pressure coefficient

$$\psi = \frac{2gH}{u^2} = \frac{2gH}{D^2 n^2 \pi^2}$$

Specific speed

$$n_s = \frac{nQ^{1/2}}{g^{3/4}H^{3/4}}$$

Hub ratio

$$\nu = \frac{D_H}{D}$$

An experimental blower was designed to meet the following specifications:

$Q = 40$ cfs	$\phi = 0.580$	$\nu = 0.744$
$p = 2.80$ in. water	$\psi = 0.900$	
$n = 1750$ rpm	$n_s = 0.262$	

This blower has a pressure coefficient which is beyond the range of ordinary blading requiring a deflection of the air of 52 deg at the hub of the rotor and stator. Therefore a design with slotted blades was undertaken. A casing diameter of 15.5 in. and a hub diameter of 11.5 in. were selected. The Reynolds number is $\mathbf{R}_c = 252{,}000$ based on the impeller-blade chord and $\mathbf{R}_a = 142{,}000$ based on the inlet area of the flow passage.

It was desirable to extend the range of capacity and pressure for this blower and still maintain the same physical configuration. Therefore the blower was designed to permit adjustment of the angle of incidence of the impeller blades, and to increase the speed to 3500 rpm by exchanging motors. The motor is supported within a cylindrical housing of the same diameter as the hub of the blower, as shown in Fig. 4. Therefore the selection of the hub diameter was limited by the physical size of the motors which drive the blower. A provision was made for an axial diffuser although for the standard unit no diffuser will be used owing to the limitation in axial length.

The blower was designed according to the free-vortex type of flow, which requires a larger amount of twist of the blading between hub and tip, and therefore is probably more critical with regard to disturbance by secondary flow. Fig. 5 shows the vector diagrams for the experimental unit, revealing a requirement of a deflection of 22.1 deg at the tip and 52 deg at the hub for the impeller. For the stator, the deflection varies from 43.6 deg at the tip to 52 deg at the hub. It should be noted that the vector dia-

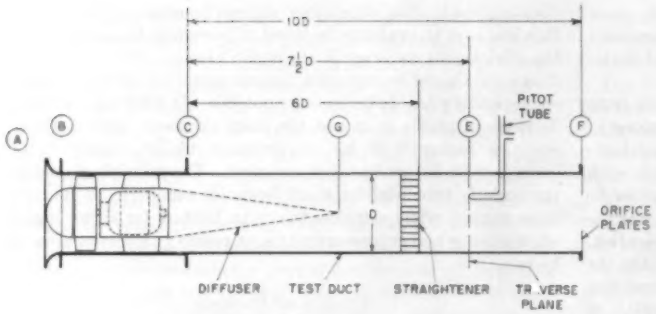

FIG. 4 TEST ARRANGEMENT

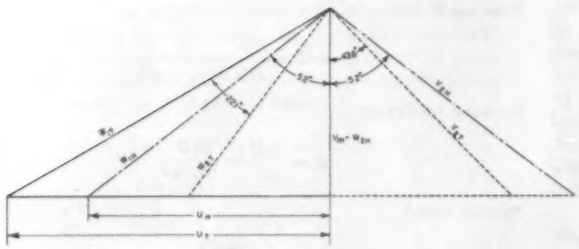

FIG. 5 VELOCITY-VECTOR DIAGRAM

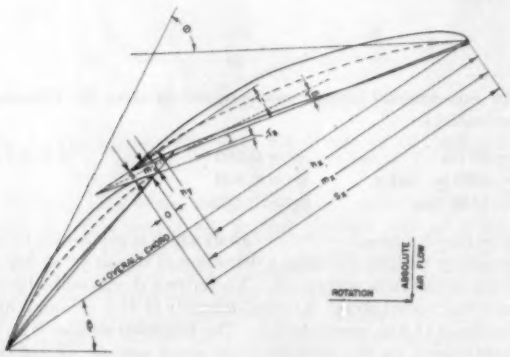

FIG. 6 SLOTTED BLADE

gram at the hub is a symmetrical diagram. The design of the blade is shown in Fig. 6. The combined blade consists of two individual airfoil-type blades, so positioned relative to each other that the larger front blade and the smaller rear blade are arranged in such a configuration that a slot is formed between the trailing edge of the front blade and the leading part of the rear blade. The combined airfoil is designed to give a nearly constant pressure distribution over about half of the blade chord on the upper surface at the design point.

The design of the blower permits variation of the blade angle of incidence to four positions. In addition to the design angle of incidence, designated as 0 deg, the combined blade can be turned to incidences of —10, +10, and +20 deg from the design condition. In addition, the blades were designed to permit the angle of deflection between the chord of front and rear blades to be varied ±5 deg from its mean value. This type of variation results in a considerable modification of the slot geometry; and, correspondingly, the amount of flow through the slot is changed. It should be noted that the free-vortex type of flow can be expected only for the design condition designated at 0 deg. For all other conditions, the blower will operate under slightly different flow conditions. Pressure and secondary flow have been analyzed for the stated blade modifications. The experimental unit was designed for easy exchange of blades and a separate set of blades was manufactured for each of the previously mentioned blade modifications.

The guide vanes for this blower were designed both as solid vanes and slotted vanes. In the case of the slotted guide vanes, a configuration equivalent to the blade at the root of the impeller was selected. This was possible because the blower was designed to have a symmetrical vector diagram at the root. The design of the blower permits for the slotted blade the use of the same airfoil in the stator by selecting the stator solidity and its variation from root to tip to give the required deflection from hub to tip. A higher value of solidity was used for the solid guide vanes in order to get the required flow deflection in the stator.

The geometry and the configuration of the slot presented a complex problem, introducing many new variables into the blade design. Table 1 and Fig. 6 show the detailed data relating to the slot configuration. The cascade of airfoils is defined by the blade solidity c/t and the impeller blade stagger angle β. Solidity

TABLE 1

		c/t	β	δ	θ	h_x/c	h_y/c	m_x/c	s_x/c	s/c	o/c	s/m	T_1	T_3	T_m
TIP	-5°	1.034	44.08	16.09	49.50	0.559	0.100	0.615	0.641	0.0255	0.0269	0.639	14.6	-5.7	4.5
	0°	1.030	45.50	21.50	53.25	0.575	0.114	0.617	0.641	0.0196	0.0250	0.628	14.6	-1.4	6.6
	+5°	1.025	46.75	24.75	57.50	0.587	0.129	0.621	0.641	0.0137	0.0197	0.578	14.6	3.6	9.1
MEAN	-5°	1.186	58.83	23.42	66.25	0.556	0.136	0.604	0.634	0.0258	0.0298	0.632	18.9	3.75	11.3
	0°	1.178	55.00	30.02	71.00	0.568	0.151	0.606	0.634	0.0200	0.0280	0.606	18.9	7.8	13.3
	+5°	1.168	56.83	34.83	75.75	0.581	0.168	0.610	0.634	0.0131	0.0228	0.560	18.9	12.2	15.6
ROOT	-5°	1.405	68.00	33.25	83.75	0.556	0.176	0.592	0.618	0.0284	0.0266	0.616	22.4	5.8	14.1
	0°	1.385	69.75	37.83	89.00	0.564	0.193	0.595	0.625	0.0200	0.0300	0.555	22.4	9.25	15.9
	+5°	1.367	71.75	42.25	92.50	0.576	0.210	0.601	0.627	0.0112	0.0264	0.454	22.4	13.2	17.8

varies from about 1.0 at the tip to 1.38 at the hub. The combined blade is characterized by the magnitude of the camber angle θ, and the physical location of the maximum of the mean camber line along the chord designated by the dimensionless values for the abscissa h_x/c and the ordinate h_y/c. For the selected configuration, the maximum camber is located near the rear part of the mean camber line of the forward airfoil. The slotted blade is further defined by the deflection angle δ between the chords of forward and rear airfoil. This deflection angle δ varies from 21.5 deg at the tip to 37.8 deg at the hub for the standard conditions. The location of the slot on the lower airfoil surface, representing the flow sink, is defined by the distance m_x. Term m represents the width of the slot inlet, and s represents the width at the slot exit. Term o represents the distance of the slot overlap between the forward and rear airfoils On the upper side of the blade, fluid is ejected at the location s_x for the purpose of energizing the boundary layer to avoid separation. In this analysis, the slot locations s_x and m_x, as well as the slot dimensions s and o, are all divided by the combined chord length c, and the values are presented in Table 1, together with the ratio of slot exit to inlet s/m for the design condition as well as for the modification in deflection of the rear airfoil chord. It should be pointed out that the location of the flow sink m_x/c on the lower side of the airfoil varies and moves farther forward for the higher-cambered airfoil. The same is true for the location of flow ejection s_x/c on the upper side of the combined airfoil. In addition, the amount of overlap is increased with the higher camber for the airfoil required at the root of the blades. In this particular application, the slot opening remains about constant. The larger pressure difference for the higher-cambered airfoil will result in a larger amount of flow through the slot if both the slot opening and overlap remain the same. The angle τ_1 of the lower-surface trailing edge of the forward airfoil and the angle τ_2 of the forward part of the upper surface of the rear airfoil at the slot exit have to be carefully selected to permit the flow moving through the slot to properly energize the boundary layer of the combined profile without causing undue drag. The angles τ_1 and τ_2, together with the angle τ_m of the mean direction of flow at the slot exit, are presented in Table 1. All angles τ are measured with regard to the direction of the chord line of the forward airfoil.

There are many variables in this blade configuration which can be modified without substantially changing the concept of the slotted blade. Time did not permit analysis of all the possible modifications, and thus the selected configuration may not represent the optimum solution of the problem.

Test Data

The tests with the experimental blower were made over a wide range of pressures and capacities and according to the ASME, Navy, and ASHVE test codes. The test setup is shown in Fig. 4. The standard blower extends from the intake A to the blower exit C, and is tested by measuring total pressure, static pressure, and dynamic pressure at the specified location E. Owing to the large hub-tip ratio, there is a sudden change in flow area and a loss in energy between the end of the blower at location C and the instrumentation. Therefore additional tests were made with a diffuser attached to the blower, to analyze pressure recovery. For the tests with diffuser, the blower extends from the inlet A to the diffuser exit at G. The tests with the diffuser meet all code requirements except that the pitot-tube location is not $7^1/_2$ diameters downstream of the end of the blower, now located at G, and this is taken into consideration by allowing duct friction only from the location of the pitot tube at E to the diffuser exit at G. In addition, a flow survey was made near the guide-vane exit, location C, to determine the stage efficiency of the blower. For this purpose a small pitot tube and a special yaw tube, shown in Fig. 7, were used. The energy input of the blower was determined by two wattmeters, while operating the motor with controlled voltage. The efficiency of the electric motors was determined by two independent brake tests which agreed with each other to within less than 1 per cent of accuracy.

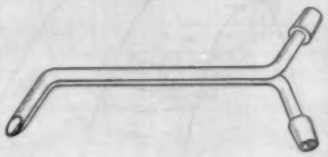

Fig. 7 Yaw Tube

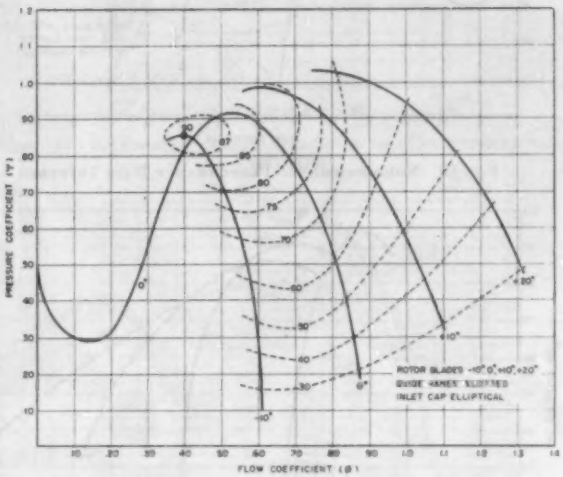

Fig. 8 Nondimensional Performance Without Diffuser

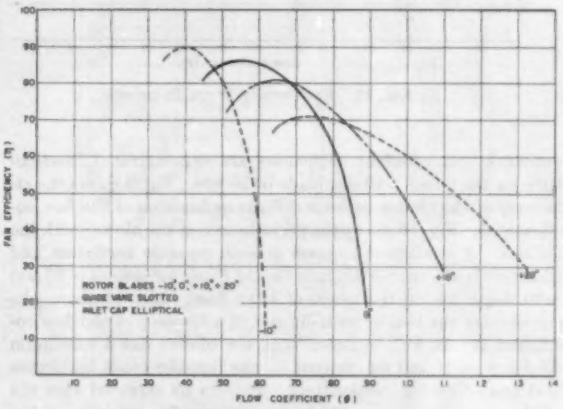

Fig. 9 Efficiency Without Diffuser

Fig. 8 shows the performance of the blower without diffuser, with both slotted impeller and slotted guide vanes. The performance of the blower is presented in terms of dimensionless coefficients ψ over ϕ with the efficiency η as independent variable over a range of impeller-blade incidence from —10 to +20 deg. The test data indicate that the blower meets the required per-

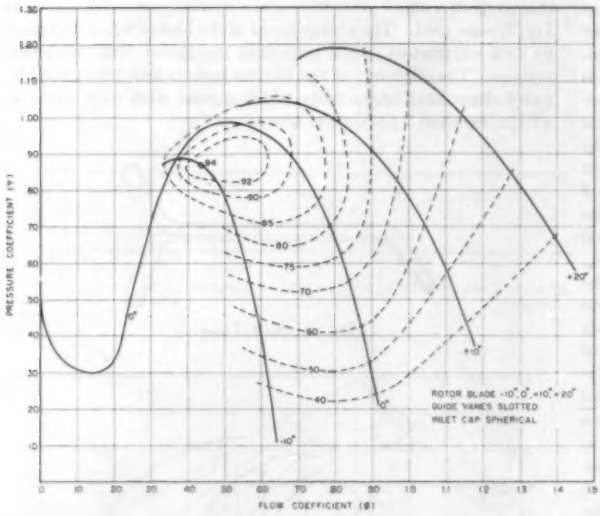

FIG. 10 NONDIMENSIONAL PERFORMANCE WITH DIFFUSER

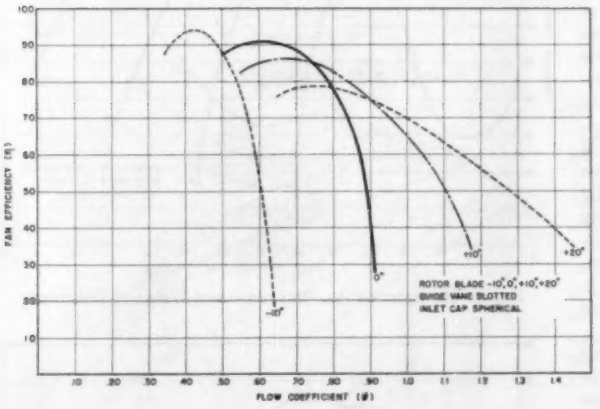

FIG. 11 EFFICIENCY WITH DIFFUSER

formance and excellent efficiencies are demonstrated, particularly for the 0 and —10 deg blade incidence. Fig. 9 shows the efficiency of the blower without diffuser as function of the flow coefficient ϕ. Fig. 10 shows the performance of the blower with the diffuser. A significant increase in both pressure coefficient and efficiency is shown, particularly for the blade incidences +10 and +20 deg covering the range of large flow. Fig. 11 shows the efficiency of the blower with diffuser as a function of the flow coefficient ϕ. It will be noted that the blower has a maximum efficiency of 91 and 94 per cent for the impeller-blade incidences of 0 and —10 deg, respectively. It is to be expected that the efficiency of this blower will be lower when the incidence of the impeller blades is turned to the +20-deg position and no adjustment of the guide vanes is made. Fig. 12 shows the performance for solid versus slotted guide vanes and diffuser effect of the blower in terms of pressure coefficient ψ and efficiency η over the flow coefficient ϕ for the 0-deg blade incidence. As expected, the pressure coefficient and efficiency improve by adding the diffuser and replacing solid with slotted guide vanes.

The stage efficiency of the blower near the point of maximum efficiency was measured at location *C* for slotted guide vanes with a small pitot and yaw tube. This survey of total pressure, static pressure, velocity pressure, and flow angle was made in both the radial and circumferential direction, and the values were integrated in both directions. An efficiency of about 96 per cent is shown in Fig. 12 at *A*. The stage efficiency also was determined from the test without diffuser by calculating the energy losses resulting from the sudden expansion of flow, and is indicated at *B* with a maximum efficiency of about 96 per cent. Fig. 13 shows near the design point the axial-velocity distribution from hub to tip downstream of the guide vanes, indicating a slightly larger velocity at the hub and good agreement with the calculated data. Fig. 14 shows the integrated values of velocity in the circumferential direction. The measured values of flow deflection with the yaw tube as shown in Fig. 15 indicate nearly axial flow in the vicinity of the design point. Fig. 16 shows the blower performance as it is affected by changing the chord of the rear airfoil ±5 deg with respect to the forward airfoil chord, resulting in a change of slot geometry, total blade camber, and type of flow. It is noted that the —5-deg position results in a maximum blower efficiency of 94 per cent.

Fig. 17 shows the conventional performance of the blower, according to the ASME Test Code, without diffuser for the 0-deg blade setting. Horsepower, static and total pressure in inches of water, as well as total and static efficiency, are plotted as ordinates over volume in cfm as abscissa. It should be noted that the values of both

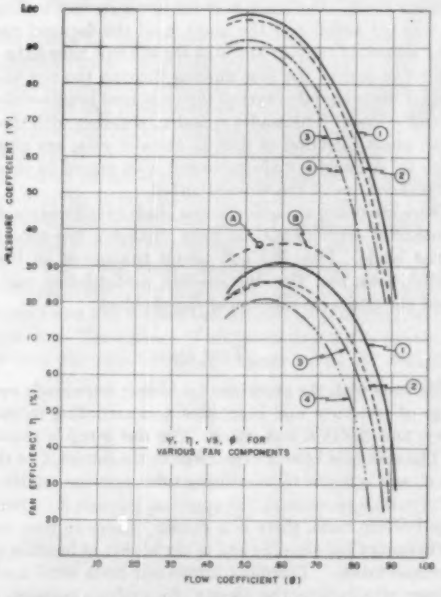

(1) Rotor 0°, Slotted Vane, Diffuser, Spherical Cap.
(2) Rotor 0°, Solid Vane, Diffuser, Spherical Cap.
(3) Rotor 0°, Slotted Vane, ..., Elliptical Cap.
(4) Rotor 0°, Solid Vane, ..., Elliptical Cap.
(A) Rotor 0°, Slotted Vane, Diffuser, Spherical Cap, Stage Efficiency Measured.
(B) Rotor 0°, Slotted Vane, Diffuser, Spherical Cap, Stage Efficiency Calculated.

FIG. 12 EFFECTS OF COMPONENT MODIFICATION ON PERFORMANCE

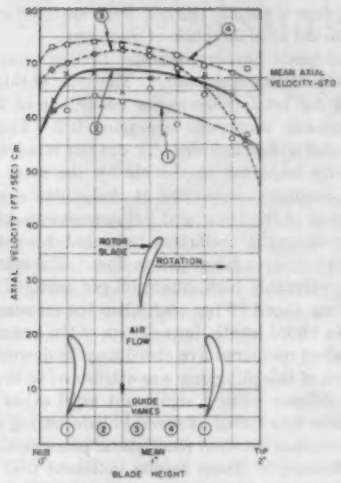

FIG. 13 AXIAL VELOCITY VERSUS BLADE HEIGHT

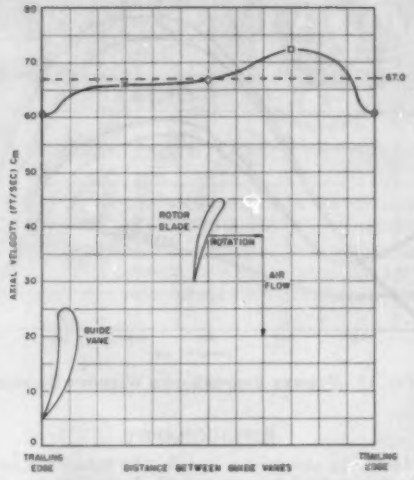

FIG. 14 INTEGRATED AXIAL VELOCITY IN CIRCUMFERENTIAL DIRECTION

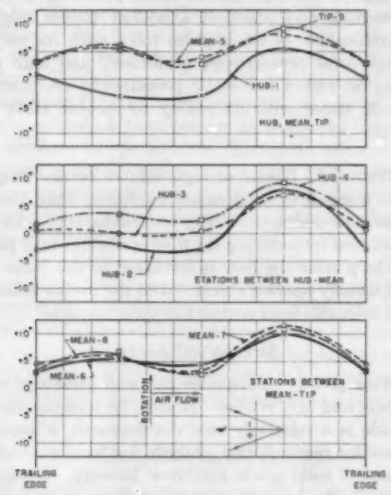

FIG. 15 YAW-TUBE MEASUREMENTS

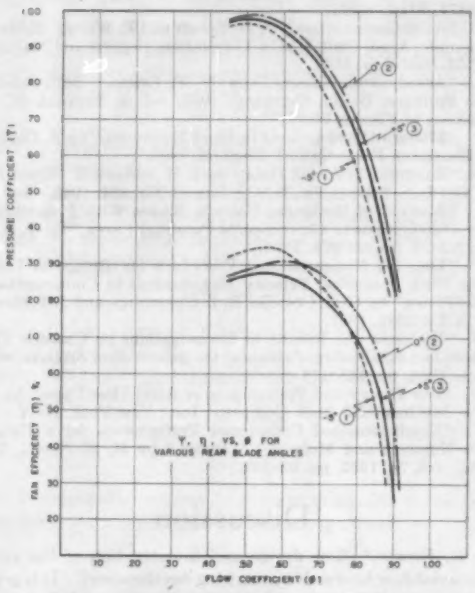

(1) Rear Blade —5°, Slotted Vanes, Diffuser, Spherical Cap.
(2) Rear Blade 0°, Slotted Vanes, Diffuser, Spherical Cap.
(3) Rear Blade +5°, Slotted Vanes, Diffuser, Spherical Cap.

FIG. 16 NONDIMENSIONAL PERFORMANCE—REAR BLADE VARIATIONS

static and total pressure are considerably reduced in the region of flow below maximum pressure. The power curve is characterized by low values in the region of low flow and highest values just beyond the point of maximum blower efficiency.

CONCLUSIONS

An analysis has been made for the application of boundary-layer control to the blades of axial-flow blowers. The design of the slotted blade extends laminar flow over a larger portion of the blade chord and simultaneously permits large flow deflections. Thus blowers with slotted blades offer the possibility to design for higher efficiency or higher pressure ratio, or possibly a combination of both. The slotted blade permits a considerable increase in pressure coefficient or corresponding operation at lower tip speed for a given pressure increase. Design data for the slot geometry are discussed. Test data of an experimental blower are presented demonstrating efficiencies to 94 per cent with flow deflection of about 52 deg at the hub. The effect of solid or slotted guide vanes and the diffuser on blower performance is shown. A variation in slot geometry is tested. The blower has a maximum stage efficiency of about 96 per cent.

ACKNOWLEDGMENT

The author wishes to thank the Electric Boat Division, General Dynamics Corporation, Groton, Conn., for permission to publish this paper. The author is indebted to members of the Research and Development Dept. of the Electric Boat Div. for the execution of all tests and the calculation of all test data.

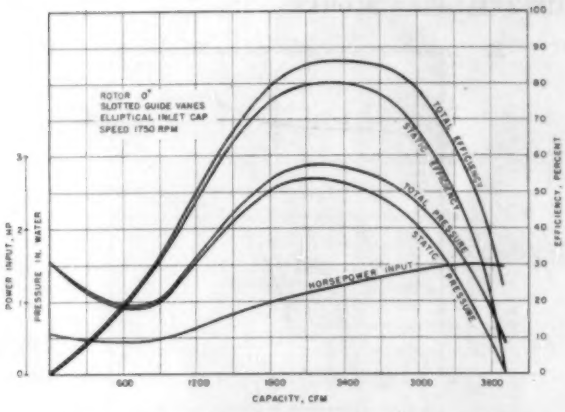

FIG. 17 BLOWER PERFORMANCE WITHOUT DIFFUSER

BIBLIOGRAPHY

1 "Low-Drag and Suction Airfoils," by Sidney Goldstein, *Journal of the Aeronautical Sciences*, vol. 15, April, 1948, pp. 189–214.

2 "Possible Application of Blade Boundary-Layer Control to Improvement of Design and Off-Design Performance of Axial-Flow Turbomachines," by J. T. Sinnette, Jr., and G. R. Costello, NACA TN 2371, May, 1951.

3 "Axial Compressors," by B. Eckert and F. Weinig, M.O.S. (A) Volkenrode, April, 1946, NACA Translation, Reports and Translation No. 353, February, 1947.

4 "Aerodynamic Theory," by W. F. Durand, Editor-in-Chief, Julius Springer, Berlin, Germany, 1935, vol. 3, Division G, "The Mechanics of Viscous Fluids."

5 "Modern Developments in Fluid Dynamics," by S. Goldstein, The Clarendon Press, Oxford, England, 1938.

6 "Summary of Airfoil Data," by I. H. Abbott, A. E. von Doenhoff, and L. S. Stivers, Jr., NACA Report No. 824, 1945.

7 "Method of Designing Cascade Blades With Prescribed Velocity Distributions in Compressible Potential Flows," by G. R. Costello, NACA Report 978, 1950.

8 "Detailed Computational Procedure for Design of Cascade Blades With Prescribed Velocity Distributions in Compressible Potential Flows," by G. R. Costello, R. L. Cummings, and J. T. Sinnette, NACA TR 2281, 1951.

9 "Problems and Results of Investigations on Cascade Flow," by Hermann Schlichting, *Journal of the Aeronautical Sciences*, vol. 21, March, 1954, pp. 163–178.

10 "The Theory and Performance of Axial-Flow Fans," by Kurt Keller, McGraw-Hill Book Company, Inc., New York, N. Y., 1937.

11 "Nondimensional Compressor Performance for a Range of Mach Numbers and Molecular Weights," by H. E. Sheets, Trans. ASME, vol. 74, 1952, pp. 93–102.

Discussion

J. R. ERWIN.[8] The design and investigation of the slotted-blade axial-flow blower is a promising development. It is gratifying to see that a very satisfactory performance of the test unit was obtained, particularly so in comparison with earlier attempts which were not successful. The question always arises as to whether the inner and outer case boundary layers will be able to undergo the static-pressure rise produced since they do not experience the boundary-layer control which is applied to the blades. This question seems to have been answered in the affirmative by the present investigation.

It would be of interest for the author to explain why the slotted-blade arrangement is better than two essentially separate blade rows so spaced that there would be little interference between the blade rows. Arrangements like this have been used previously, although the only applications which come to mind at present are the stator which was used with our first supersonic compressor and the double or triple-blade rows which are common at the exit from compressors used with axial-flow jet engines. In these applications, flow is usually turned from an inlet angle of from 50 to 60 deg to the axial direction at discharge.

The slotted-blade blower naturally invites comparison with the impulse axial-flow compressor.[4] The rotor of this compressor was designed for total pressure-rise coefficient of 2.5 with the static pressure-rise coefficient averaging 0.2. This rotor was tested alone and with a stator which did not remove all the tangential velocity imparted to the air by the rotor. The total pressure-rise coefficient measured at design-flow coefficient was 2.3 downstream of the rotor and 2.0 downstream of the stator. The static pressure-rise coefficient measured downstream of the stator was slightly over 1.2 at design flow. The efficiency of the rotor was unbelievably high, about 98 per cent. The efficiency of the stage was about 90 per cent when the measurements were taken within a chord length downstream of the stator, and about 83 per cent when measured five chord lengths downstream of the stator. Much of this difference was attributed to the inefficiency of a conical diffuser when a significant swirl exists in the flow. This same rotor was tested at several blade-setting angles to determine the relation between rotor static pressure-rise coefficient and rotor efficiency.[5] These results indicated that a rotor efficiency of about 94 per cent could be obtained with static pressure-rise coefficients of 0.4. However, subsequent tests of a symmetrical stage of this type showed rather poor stage performance.

An interesting and practical axial-flow blower might result from a combination of an impulse rotor with its very rugged blades, high total pressure-rise coefficient, and high efficiency when operated with a low static pressure-rise coefficient, and a slotted-blade stator with its ability to recover static pressure efficiently.

D. G. WILSON.[6] Blades of high camber or low stagger even working at a much lower pressure coefficient than those of the paper often show undue sensitivity to rotating stall. In addition, the stall induced by reducing the flow coefficient may persist in a hysteresis loop after the flow is increased to the value at which the blades usually operate stably. Did the author's blades show an equally dramatic improvement in these respects?

AUTHOR'S CLOSURE

The author greatly appreciates the well presented comments of Mr. Erwin and Mr. Wilson. It must be remembered that the slotted blade is a relatively new development, whereas a great deal of time for research and analysis has been expended in the development of solid blade axial-flow blowers. Because of the discrepancy in the amount of data available, a comparison between the slotted blade and two, essentially separate, blade rows is difficult. Preliminary analysis has indicated that the slotted blades do have the potential of lower drag due to the extension of the laminar flow region. In addition, the slotted blade offers the possibility of space and weight saving when compared with separate blade rows.

The author is in complete agreement with Mr. Erwin's comment that the slotted blade would be ideally suited to a stator in combination with an impulse-type axial-flow rotor.

Mr. Wilson proposes the interesting question of rotating stall and hysteresis. The slotted blades of high camber showed no hysteresis within the range of stagger tested. However, tests at low stagger angles have not yet been performed. It should be noted, as shown in Fig. 17, that the stalling characteristics of the slotted blade are quite different from those of the standard axial-flow blower.

---

[8] Aeronautical Research Scientist, National Advisory Committee for Aeronautics, Langley Aeronautical Laboratory, Langley Field, Va.

[4] NACA RM L9J05a, 1949.

[5] NACA RM L50F27a, 1950.

[6] Visiting Fellow, Commonwealth Fund, Gas Turbine Department, Massachusetts Institute of Technology, Cambridge, Mass.

Thermodynamic Aspects of Cavitation in Centrifugal Pumps

By H. A. STAHL[1] and A. J. STEPANOFF,[2] PHILLIPSBURG, N. J.

The effect of liquid properties on centrifugal-pump behavior under cavitation conditions is examined on the basis of a given pump handling various liquids. A criterion in terms of physical properties of the liquid is established which can be used to indicate cavitation effects on pump performance for various liquids. Test results and numerical illustrations are presented.

Introduction

THE boiling of liquid in the process of cavitation is a thermal process and is dependent on the liquid properties: pressure, temperature, latent heat of vaporization, and specific heat. During cavitation conditions damage to the pump performance (head-capacity and efficiency) is caused by the appearance and disappearance of vapor cavities in the low-pressure zone which disrupt the dynamic conditions existing during normal pump operation when the flow is all solid liquid. To make the boiling possible the latent heat of vaporization must be derived from the liquid flow. This necessary flow of heat from the liquid can only take place when the liquid temperature is above that corresponding to the saturation temperature at the prevailing pressure in the low-pressure cavitation zone. This is the same as to say that the pressure in the cavitation region must fall below the saturation pressure corresponding to the liquid temperature.

The extent of damage to the head-capacity characteristics of a pump depends upon the amount of liquid vaporized and the vapor specific volume at the existing pressure in the cavitation zone. The effect of the liquid properties on cavitation will be observed by comparing the performance of a given pump, at a given speed, handling water at various temperatures. In this way identical dynamic conditions are assured inside the impeller passages. The performance of a centrifugal pump when it is not affected by cavitation is independent of the fluid properties, be it liquid, vapor, or gas.

Thermal Cavitation Criterion

The effect of properties of liquids on the behavior of a centrifugal pump under cavitation conditions can be studied analytically as follows:

In Fig. 1, curve *A-B-C-D* is the normal *H-Q* characteristic established under ample NPSH so that no cavitation occurs. Curve *A-B-C'-E* is a typical *H-Q* curve under limited NPSH. The NPSH curve shown represents minimum values for incipient cavitation as determined by such points as *B* on the curve *A-B-C'-E*. Suppose now that the NPSH value for capacity Q_C is reduced by Δh and sufficient to produce a measurable effect on the performance (point *C'*). The saturation temperature corresponding to the new reduced pressure in the low-pressure zone of the impeller will be lower than the original temperature by ΔT. If a sufficient time is allowed, Δh_f Btu per lb of liquid passing through the low-pressure zone will be available for vaporization of liquid. The value of Δh_f is the difference between the

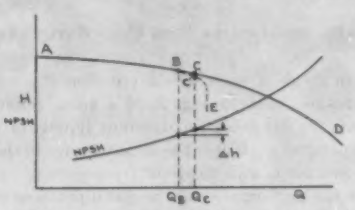

Fig. 1 Definition of the Depression Δh

enthalpy of the liquid at original conditions of thermal equilibrium and the new conditions at a pressure Δh less than original. This increment of enthalpy can be expressed as

$$\Delta h_f = C_L \Delta T \quad [1]$$

where C_L is the specific heat of the liquid.

If it is assumed that thermal equilibrium is restored, the following heat-balance equation can be written for each pound of liquid passing through the low-pressure zone. The liquid not passing through the low-pressure zone need not be considered as it takes no part in the cavitation process

$$1 \times \Delta h_f = r_v L \quad [2]$$

where $r_v < 1$ is a fraction of 1 lb of liquid boiled per each pound of liquid and L is the latent heat at vaporization. Introducing specific volumes of liquid and vapor instead of their weights, Equation [2] becomes after arrangement

$$\frac{V_v}{V_L} = \frac{v_v}{v_L} \times \frac{\Delta h_f}{L} = B \quad [3]$$

Here V represents volumes, v represents specific volumes, and subscript L is for liquid, subscript v for vapor, and

$$V_L = 1 \times v_L; \quad V_v = r_v v_v \quad [4]$$

For a given pump operated at the same speed and capacity when pumping two different liquids, the same value of V_v/V_L would mean the same extent of cavitation and the same damage to the performance. Thus this ratio may serve as a criterion of the pump behavior under cavitation conditions when handling different liquids. It will be given a symbol B. The value of the liquid thermal criterion B can be calculated from Equation [3] repeated as follows

$$B = \frac{v_v}{v_L} \frac{\Delta h_f}{L} \quad [5]$$

in terms of properties of the liquid for an assumed value of the depression Δh. When a comparison is made of the behavior of a pump under cavitation conditions pumping two different liquids the value of the thermal criterion B should be calculated for the same assumed value of the depression Δh.

[1] Engineer, Cameron Engineering Department, Ingersoll-Rand Company.

[2] Development Engineer, Cameron Engineering Department, Ingersoll-Rand Company.

Contributed by the Hydraulic Division and presented at the Diamond Jubilee Annual Meeting, Chicago, Ill., November 13–18, 1955, of The American Society of Mechanical Engineers.

Note: Statements and opinions advanced in papers are to be understood as individual expressions of their authors and not those of the Society. Manuscript received at ASME Headquarters, September 6, 1955. Paper No. 55—A-136.

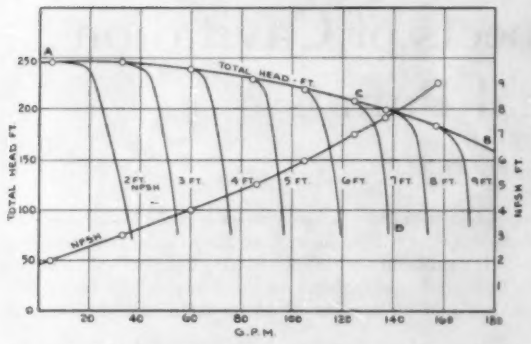

FIG. 2 1¹/₂-IN. SINGLE-STAGE PUMP COLD-WATER TEST—3470 RPM

For practical use of the thermal criterion B complete cavitation performance, such as Fig. 2, of a given pump (or similar pump) should be available for different liquids or for water at various temperatures. Water has an advantage in that its properties are known for a wide range of temperatures and pressures. To estimate the performance of the given pump or similar pump when pumping a different liquid under limited NPSH the value of B is first calculated for an assumed value of Δh. Then the available test of the pump which gives the same or approximately the same value of B for the same Δh will apply to the new liquid.

When the criterion B is applied in this manner its absolute value is not important. The value of B depends upon the value of Δh used for its calculation. The value of the depression Δh does not have to conform to the definition used for the development of the expression for B. The absolute value of $B = V_v/V_L$, or the fraction of vapor volume to liquid volume passing through the low-pressure cavitation zone, is probably of the order of 1–2 per cent based on tests on water with suspended air. However, the absolute value at B does not enter into consideration when B is used as proposed here.

Remarks. (*a*) The heat-balance Equation [2] is based on the assumption that the thermal equilibrium under the reduced pressure (Δh) is restored. This theoretically would require infinite time. However, when comparing the performance of the same or similar pump handling two different liquids at the same value of the criterion B, the effect of time will be the same in both cases. Equation [3] really means that for the same value of B the rate of increase of the volume of flow through the low-pressure zone (or the impeller channel) is the same for two liquids and hence the damage to the head-capacity characteristics is the same.

(*b*) A similar method of attack on the same problem was presented by R. C. Fisher[3] and also by E. E. Breault of Ingersoll-Rand Company in private correspondence with the authors in 1947.

TEST RESULTS AND NUMERICAL ILLUSTRATIONS

Fig. 3 shows the performance of a 1¹/₂-in. pump at 3470 rpm pumping deaerated water of different temperatures under the same net positive suction head (NPSH) of 4 ft. These curves were compiled from a series of tests with water at stated temperatures and different NPSH values. Fig. 2 is one of such tests with water at 70 F. For a given pump operated at the same speed with an ample suction head (no cavitation) the dynamic conditions within the impeller are identical at the same rate of flow. With a limited NPSH identical dynamic conditions will prevail at the point of incipient cavitation for all liquids (point B in Fig. 3). A given dynamic depression below the pressure prevailing at the low-pressure zone for point B will produce different amounts of vapor for different liquids. The difference in the form of the head-capacity and efficiency curves at capacities higher than that corresponding to the point B depends on the physical properties of liquids.

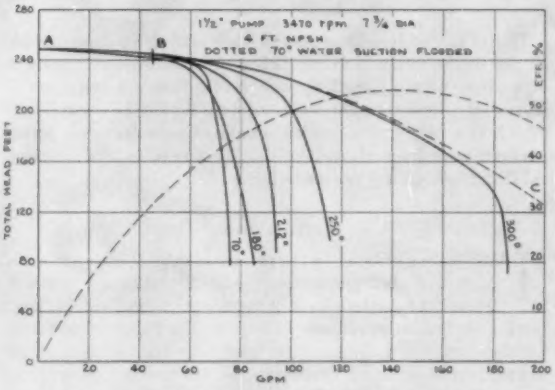

FIG. 3 PUMP PERFORMANCE PUMPING HOT WATER

The properties of water and its vapor are tabulated in Table 1 for several temperatures. The following observations can be made from an inspection of this table:

TABLE 1 PHYSICAL PROPERTIES OF WATER AND VAPOR

Temp, deg F	Press, psia	Vapor specific vol, cu ft/lb	Latent heat, Btu/lb	Enthalpy of liquid, Btu/lb
65	0.3056	1021.4	1057.1	33.05
70	0.3631	867.9	1054.3	38.04
180	7.510	50.23	990.2	147.92
212	14.696	26.80	970.3	180.07
250	29.825	13.82	945.5	218.48
300	67.013	6.466	910.1	269.59

1 The specific volume of vapor decreases rapidly as pressures and temperatures are increased. At the critical pressure and temperature the specific volume of liquid and saturated vapor are the same; thus it would appear that no cavitation can occur under these conditions.

2 A depression of only 0.0575 psia at 70 F (equivalent to a head of 1.6 in.) results in a temperature differential ΔT of 5 deg F; but for 300 F water the same depression corresponds to a temperature difference of only 0.0533 deg F. The difference in enthalpy of water per degree F is essentially the same at 70 F and at 300 F. Thus for the same depression of 1.6 in. of water more heat is available for vaporization at 70 F than at 300 F. At the same time the specific volume of vapor at 70 F is 134 times greater than that of vapor at 300 F; thus the difference in behavior under cavitation conditions for water at 70 F and at 300 F is easy to visualize.

Table 2 shows calculations of the thermal cavitation criterion B for water at five different temperatures. The last column gives the same variables for butane at 70 F. The value of the criterion B for butane is essentially the same as that for water at 300 F (slightly lower), thus it is expected that the pump performance on water at 300 F will apply to butane.

Since the criterion B by definition, Equation [3], represents the ratio of volume of vapor to the volume of liquid per pound of the liquid (V_v/V_L), for the same depression Δh lower values of B mean less pronounced effects of cavitation. High values of B shown in Table 2 at low temperatures ($B = 253$ at 70 F) merely mean that the assumed value of $\Delta h = 1.6$ in. was too high for this

[3] Discussion by R. C. Fisher, pp. 305–306, of "A Survey of Modern Centrifugal Pump Practice for Oilfield and Oil Refining Services," by N. Tetlow, Proceedings of The Institution of Mechanical Engineers, London, England, vol. 152, 1945.

TABLE 2 CALCULATION OF THERMAL CAVITATION CRITERION B FOR SEVERAL LIQUIDS FOR ΔA = 1.6 IN.

Liquid properties		Water, 70 F	Water, 180 F	Water, 212 F	Water, 250 F	Water, 300 F	Butane 70 F
1	Temp. difference, ΔT, deg F	5.0	0.34	0.194	0.1058	0.0533	0.0645
2	Spec. vol. of vapor, v_v, cu ft/lb	867.9	50.53	26.80	13.82	6.466	2.88
3	Spec. vol. of liquid, v_L, cu ft/lb	0.01606	0.01651	0.01672	0.01700	0.01745	0.02773
4	v_v/v_L = (2)/(3)	54000	3050	1603	812	369	103.5
5	v_L/v_v = (3)/(2)	0.0000185	0.000328	0.000625	0.00123	0.00272	0.00967
6	Enthalpy diff, h_f, Btu/lb	4.99	0.340	0.196	0.1065	0.055	0.0322
7	Latent heat, Δ, Btu/lb	1054.1	990.2	970.3	945.5	910.1	157.5
8	$\Delta h_f/L = r_v$ = (6)/(7)	0.00468	0.000344	0.000204	0.000115	0.000080	0.000198
9	B = (4) × (8)	253	1.048	0.324	0.0915	0.0223	0.0202

liquid, and the value of the temperature differential (5 deg F at 70 F) is not realistic under actual operating conditions. Considering the very short time it takes for the liquid to traverse the impeller channel (0.025 sec in the test pump) only a small fraction of the available heat is utilized for vaporization, the liquid passing the low-pressure zone in a superheated state. The fraction of liquid in a vapor state given by Equation [2] $r_v = \Delta h_f/L$ is never realized in actual pumps for that reason.

When pumping petroleum products which are mixtures of various hydrocarbons, under limited NPSH, it is expected that the lightest fraction will determine the cavitation behavior of the mixture. This follows from the fact that even in the case of water at 70 F under the exaggerated conditions assumed in Table 2, the amount of vapor is less than $^1/_2$ per cent of the weight of the liquid. The actual amounts of the vapor produced in the low-pressure zone may be a fraction of those tabulated if the effect of time is allowed. The values of r_v as small as they appear in the Table 2 are not unreasonable as can be seen from dynamic considerations. The head-capacity characteristic of a pump at a given speed does not depend upon the nature of the fluid, and is the same for liquids and vapors or gases. Assume that the pump will handle vapor only without any liquid. Then the weight of the vapor handled will be only a small fraction of the weight of the solid liquid. The ratio of the two is equal to the ratio of specific volumes (v_L/v_v) and is given in Table 2, item 5. It is interesting to note that the figures are of the same order as those in item 8 of the same table.

The effect of time on the extent of cavitation can be seen from Figs. 4 and 5, obtained by Krisam.[4] The values of NPSH for the best efficiency points at higher speeds (solid lines) are considerably lower than those given by the dynamic considerations σ = const (dash-and-dot lines). To state it differently, the values of the cavitation constant sigma are lower for the same pump at higher speeds.

Summary

1 Cavitation effects when pumping various liquids are similar for dynamically similar conditions if the thermal cavitation criteria, calculated for the same depression, are equal.

[4] "Neue Erkenntnisse im Kreiselpumpenbau," by F. Krisam, *Zeit. VDI*, vol. 95, 1953, p. 320.

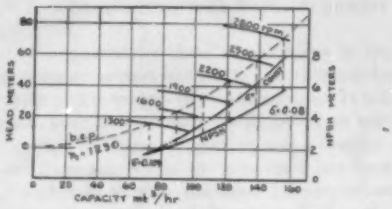

FIG. 4 CAVITATION TEST BY KRISAM—LARGER PUMP

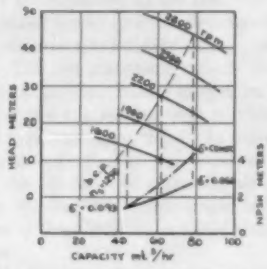

FIG. 5 CAVITATION TEST BY KRISAM—SMALLER PUMP

2 Owing to thermal and dynamic limitations only a small fraction of 1 per cent by weight of the liquid is vaporized under cavitation conditions. For liquid mixtures, such as some petroleum products, the lightest fraction of the mixture will determine the behavior of the mixture as to cavitation.

3 Under incipient cavitation conditions extension of test data to other conditions or to other sizes of units by the dynamic similarity requirements sigma = const is approximate only. Thus a given pump operated at various speeds will require less NPSH (sigma lower) at higher speeds than indicated by extension of data from tests at the lower speeds as the amount of boiling liquid is limited, among other factors, by the time.

4 The absolute value of the cavitation thermal criterion B is not important as long as it is used for a comparison of pump behavior under cavitation conditions when handling liquids of different physical properties.

Turbulence and Boundary-Layer Effects on Cavitation Inception From Gas Nuclei

By J. W. DAILY[1] and V. E. JOHNSON, JR.[2]

The inception of cavitation in a liquid medium is dependent on a variety of hydrodynamic and nonhydrodynamic effects which complicate the problem of scaling. Cavitation occurs in zones of low pressure hydrodynamically produced by flow relative to the boundaries. It is well known that changes in flow rate and size will modify the local hydrodynamic conditions, although the exact role of boundary-layer growth and associated turbulence on local pressures is not understood completely. In addition, it has been observed that cavitation inception is not always reproduced at the same hydrodynamic conditions, but seems to depend in some way on the physical properties and states of the liquid, the solid boundaries, and the entrained solid and gaseous matter. The investigation in progress at the M.I.T. Hydrodynamics Laboratory is directed at the general problem of scale effects in cavitation inception. The initial experiments have been concerned with the influence of boundary layers and turbulence on the pressure of cavitation inception and the location of inception relative to the solid boundary. The study necessarily has involved the role of gas bubbles as nuclei for cavitation and the interrelation of the stability of small gas bubbles, their size and space distribution, and the velocity and pressure variations in the turbulent boundary layer. This paper is a discussion of this combination of factors.

Experimental Variables and Test Equipment

FOR potential flow of a pure liquid the minimum pressure will occur on the boundary, can be predicted for any boundary configuration, and will be described for all scales and velocities by a constant value of the ratio

$$\frac{p_0 - p_{min}}{{}^1/_2\rho U_0^2}$$

where p_0 and U_0 are the reference pressure and velocity and p_{min} is the minimum boundary pressure. If the ability of a liquid to support a tension is ignored, cavitation will be incipient when the minimum pressure equals the vapor pressure and this ratio can be defined as the cavitation number for the body, or

$$K_i = \frac{p_0 - p_v}{{}^1/_2\rho U_0^2} \quad \ldots\ldots\ldots\ldots\ldots\ldots [1]$$

where p_v is the vapor pressure. It has been found for real liquids in states usually encountered that this parameter is inadequate as a scaling law and that effects exist that depend on size and velocity, but are not correlated entirely with Reynolds number (1, 2, 3).[3]

One possibility suggested by these observations is that the local minimum pressure is associated with the characteristics of the boundary layer and boundary-layer turbulence. It is known that the minimum boundary-pressure coefficient of an immersed body is some function of Reynolds number, and a possible effect of local pressure fluctuations due to turbulence has been considered (4). Another suggestion discussed by several authors (5, 6, 7) is that inception depends on the presence of undissolved gas nuclei trapped on foreign particles in the liquid. The so-called scale effects are explained as the result of the relation between size of entrained nuclei and the time available for growth of these nuclei to macroscopic bubbles as they pass through low-pressure regions. The last statement reflects the growing practice of making cavitation experiments in systems where resorbers (8) cause solution of free gas, leaving only microscopic nuclei presumably attached to entrained particles. In most practical situations the liquid is air-saturated or nearly so, so that conditions are favorable for the existence of entrained air dispersed in the liquid in the form of small but macroscopic bubbles. In these cases, the behavior of these bubbles as nuclei should influence the onset of cavitation.

An interest in the boundary-layer and turbulence effects leads to an experimental setup in which the only significant dynamic pressure gradients would be due to these factors. Using a small water tunnel, essentially two-dimensional flow was established along the flat boundary wall of a horizontal transparent test section. With this arrangement the test-section pressure at inception conditions was always less than the gas-saturation pressure and favorable to formation of gas bubbles as nuclei for cavitation. In addition, the tunnel had no resorber so that water entering the test section contained a dispersion of such nuclei. The experiments consequently involved the relation between gas-nuclei size and stability and the hydrodynamic pressure field.

The test section has the nominal dimensions of 6 in. width × 1¼ in. depth. The roof was employed as the test surface because the hydrostatic pressure is minimum there. The bottom surface was contoured to cause the minimum pressure to occur within the transparent working range. The test section follows a flow-nozzle reduction from a 6 in. × 6 in. square section. The sides of the nozzle are plane and the top and bottom surfaces contoured to give a monotonically increasing velocity along the wall. The test section and pressure-drop coefficient along the test-section roof are shown in Fig. 1. The pressure-coefficient data were obtained from piezometers in the roof, all of which were plugged except for a reference tap during cavitation tests. It will be noted that the pressure gradient in the flow direction is small giving a pressure near the minimum along the entire test length.

A percentage of the tunnel water is continuously by-passed and filtered through a diatomaceous-earth-type filter which removes particles down to less than 1 micron. The air content can be reduced to approximately 15 per cent of the saturation content at atmospheric pressure. This is equivalent to a deaeration pres-

[1] Professor of Hydraulics, Hydrodynamics Laboratory, Massachusetts Institute of Technology, Cambridge, Mass. Mem. ASME.

[2] Aeronautical Research Scientist, Hydrodynamics Division, National Advisory Committee for Aeronautics, Langley Field, Va.

Contributed by the Hydraulic Division and presented at the Diamond Jubilee Annual Meeting, Chicago, Ill., November 13–18, 1955, of The American Society of Mechanical Engineers.

Note. Statements and opinions advanced in papers are to be understood as individual expressions of their authors and not those of the Society. Manuscript received at ASME Headquarters, August 25, 1955. Paper No. 55—A-142.

[3] Numbers in parentheses refer to the Bibliography at the end of the paper.

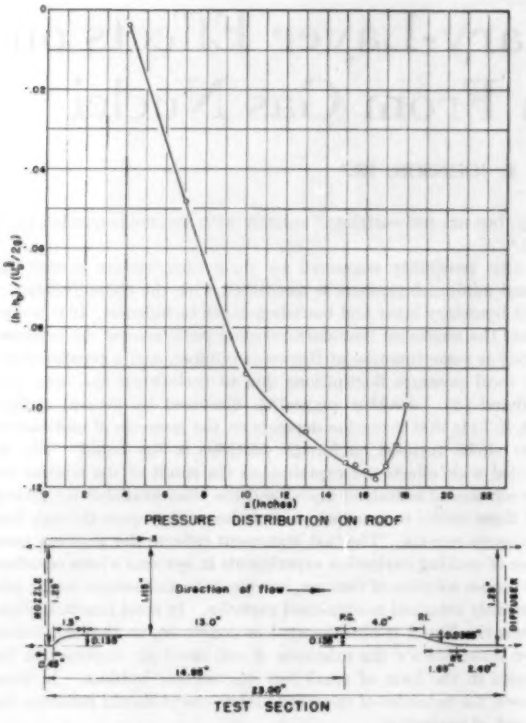

FIG. 1 TEST SECTION AND PRESSURE-DROP COEFFICIENT ALONG TEST-SECTION ROOF

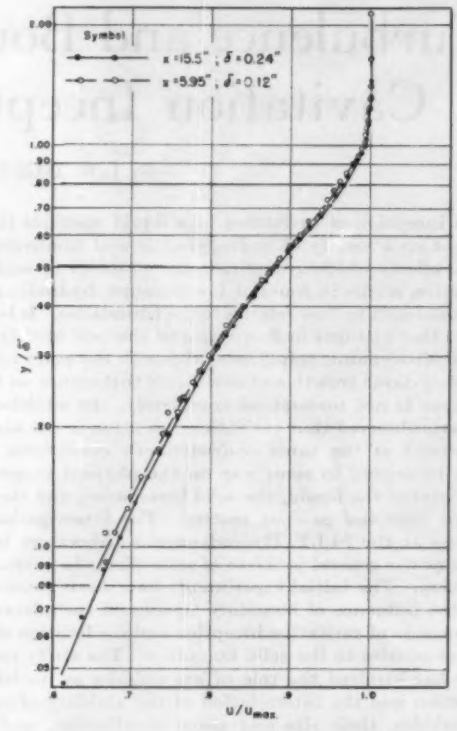

FIG. 2 VELOCITY DISTRIBUTION IN BOUNDARY LAYER

sure of 5 ft of water absolute. To reduce the free-stream turbulence caused by the circulating pump, bends, and the like, to a minimum, a series of screens is located upstream of the test section.

During the cavitation process, high-speed motion pictures were taken at various longitudinal positions along the test section. In order to confine the observations to the essentially two-dimensional flow in the center portion of the test section, the lens system of the 35-mm movie camera was chosen so as to have a depth of field less than $^1/_8$ in., and focused at a point near the center line. The light source was a high-speed stroboscope with a light-flash duration time of about 1 microsec and capable of producing about 6000 such flashes per sec.

EXPERIMENTAL OBSERVATIONS

The free-stream velocity for all the experimental observations reported here was 27.5 fps. The extent and character of the resulting boundary layer are shown by the velocity distributions in Fig. 2 for station $x = 15.5$ in. just ahead of the minimum pressure point, and for the upstream station $x = 5.95$ in. These distributions were obtained using a hypodermic needle of 0.021 in. OD as a stagnation tube. The boundary-layer thickness δ is 0.24 in. at $x = 15.5$ in. The Reynolds number based on δ is 60,000 at the average test temperature. Note that the velocity distribution is not described by a semilog equation but is more nearly given by a power law. Note also that the boundary layer grows stably without separation.

Approximately 30,000 high-speed motion-picture frames were taken of cavitation near the minimum pressure region ($x = 15.5$ in. in Fig. 1) and at stations upstream of this zone. These pictures were obtained at rates ranging from 2000 to 3000 frames per sec. In most cases the magnification ranged from 3 to 10 for which the camera and optical system permitted detection with certainty of bubbles smaller than 0.001 in. diam. In order to widen the field of view some pictures were taken with a reduction of 2 (magnification of $^1/_2$) for which the definition became poor for bubbles smaller than about 0.006 in.

Observations were made for conditions ranging from total absence of audible or visible cavitation to severe well-developed cavitation. At boundary pressures below about 3 ft of water, but above the onset of cavitation, small and apparently spherical gas bubbles appeared in the boundary layer ranging in size from 0.002 to 0.02 in. diam. As the boundary pressure was reduced, the larger individual bubbles became unstable, and expanded rapidly, and collapsed with the noise and appearance typical of cavitation. Simultaneously, however, bubbles of smaller diameter passed through the minimum-pressure region without detectable change in size. At successively lower pressures smaller and smaller bubbles became unstable and exploded. In Fig. 3(*a*) is an example (denoted by the arrows) showing a bubble of nearly constant diameter suddenly growing as it reaches a critical condition.

Of all the cavities observed, the majority were located in the central portion of the boundary layer with only $1^1/_2$ per cent located in the 10 per cent of the boundary layer nearest the wall, Fig. 4. Similarly, the distribution of the expanding cavities peaked in the central portion of the boundary layer, although none of the expanding cavities was observed in the 10 per cent of the boundary layer nearest the wall, Fig. 5. It was anticipated that cavitation inception would occur at a slight distance from the roof, but the apparent inception so far from the boundary was entirely unexpected.

As already mentioned, the boundary-layer development was stable so that the observed bubble distribution is not attributed to flow separation or other boundary-layer abnormalities.

The displacement of an individual bubble from frame to frame was not uniform, indicating some velocity fluctuation. Assuming the bubbles observed moved with the fluid, the "instantaneous" velocity components u and v were calculated from the frame-to-frame displacements. For the longitudinal direction the turbulent component $u' = u - \bar{u}$ was determined by obtaining $\bar{u}$ from the mean velocity traverse of Fig. 2. For the normal direction $v' \equiv v$. As shown in Fig. 6, these data indicate a nearly constant value of $\sqrt{\overline{u'^2}}/U_0$ over the inner 0.6 of the boundary layer ($y/\delta = 0.6$) with decreasing intensity in the outer portion. The magnitude of $\sqrt{\overline{v'^2}}/U_0$ appears to have a maximum in the central portion of the boundary layer. Only approximate values were expected from this method because of inherent inaccuracies in evaluating u and v and because the sample of bubbles at each y was relatively small. Laufer's measurements in air (9), shown for comparison, give comparable values of $\sqrt{\overline{u'^2}}/U_0$ near the wall

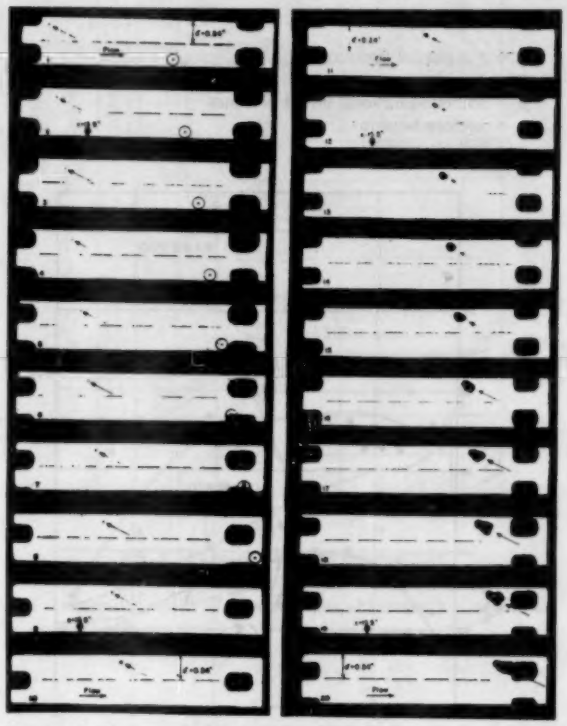

FIG. 3(a) HIGH-SPEED MOTION PICTURES OF INCEPTION OF CAVITATION FROM A GAS NUCLEUS

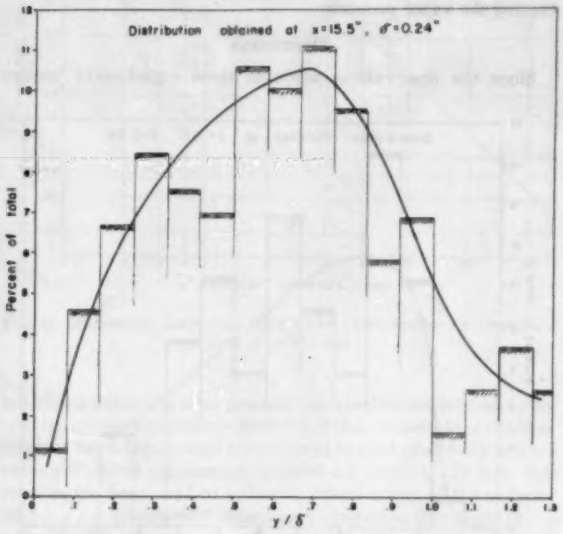

FIG. 4 DISTRIBUTION OF ALL BUBBLES IN BOUNDARY LAYER

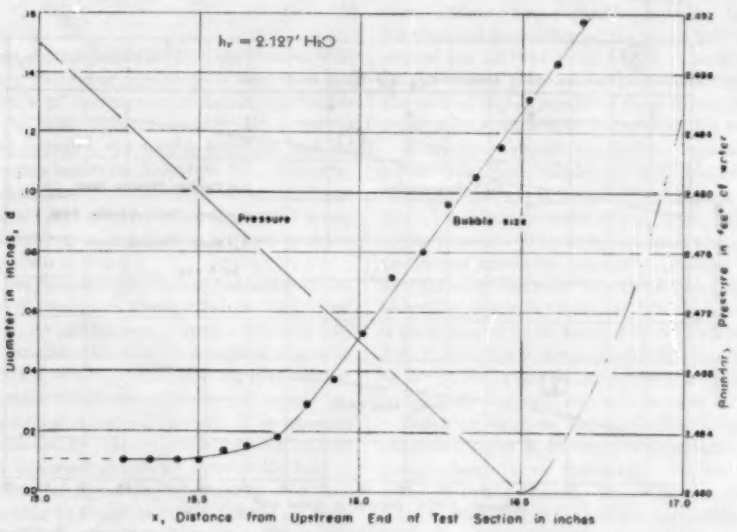

FIG. 3(b) PRESSURE AND SIZE OF CAVITY SHOWN IN FIG. 3(a)

with decreasing intensity away from the wall. The agreement of $\sqrt{v'^2}/U_0$ values is good.

The boundary pressure was found to be greater than the vapor pressure even when relatively severe cavitation was occurring in the zone of observation. The threshold at which the larger gas nuclei (0.02 in. diam) became unstable was about 0.5 ft of water above the vapor pressure. The critical diameter at which successively smaller bubbles became unstable was estimated for each of several boundary pressures and, as shown by the line marked 1 in Fig. 7, was found to decrease with decrease of pressure but not below the vapor pressure. As generally encountered with turbulent flow in hydraulic systems, some fluctuations in the boundary pressure were present during the experiments. It is estimated that an outside limit of the possible error from this effect would be about 0.15 ft of water, and would not account for the wall pressure exceeding the vapor pressure.

Discussion

Since the observations made in these experiments involve macroscopic gas nuclei, it is of value at this point to review the relation between mechanical stability and bubble size (6). The equation of static mechanical equilibrium for spherical bubbles is

$$p_g + p_v - p = 2\frac{\sigma}{r} \quad \ldots\ldots\ldots\ldots\ldots\ldots [2]$$

where

p_g = gas partial pressure
p_v = liquid vapor pressure
p = surrounding local liquid pressure
σ = surface tension
r = bubble radius

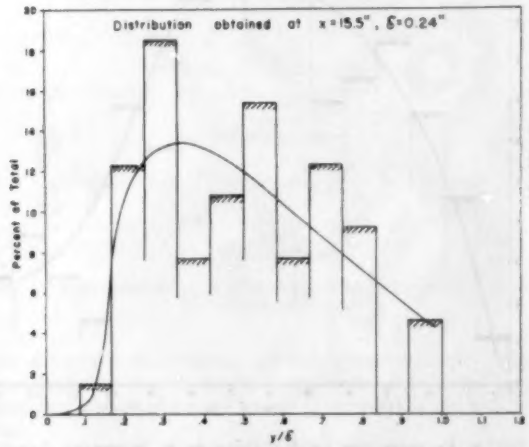

Fig. 5 Distribution of Expanding Bubbles in Boundary Layer

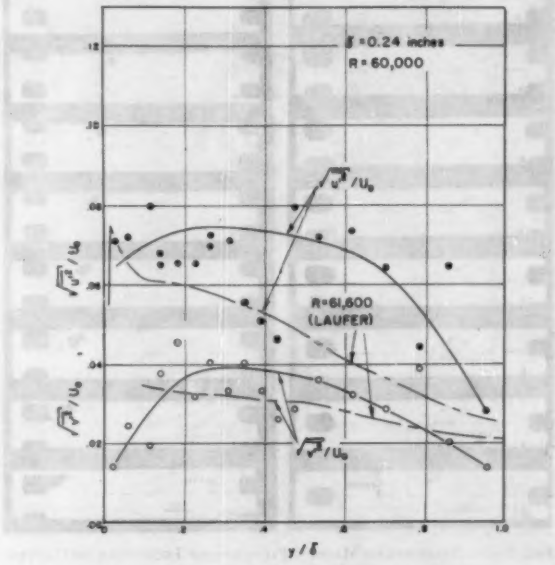

Fig. 6 Absolute Turbulence Intensity Distribution in Boundary Layer

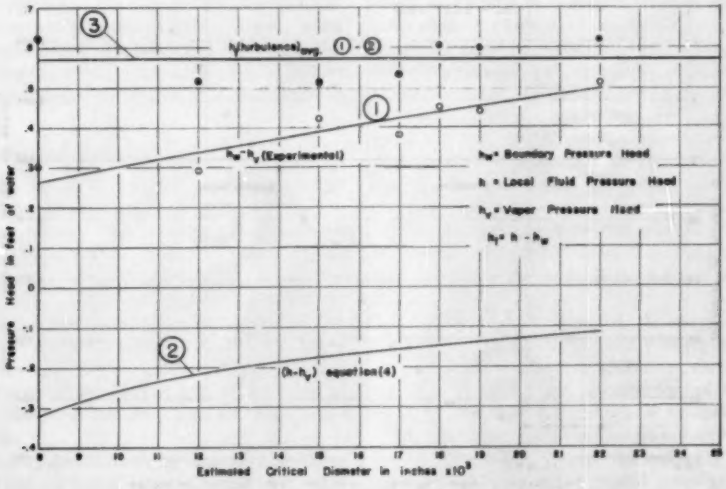

Fig. 7 Effect of Boundary Pressure on Critical Diameter of Gas Nuclei and Semi-Experimental Determination of Pressure Reduction Due to Turbulence

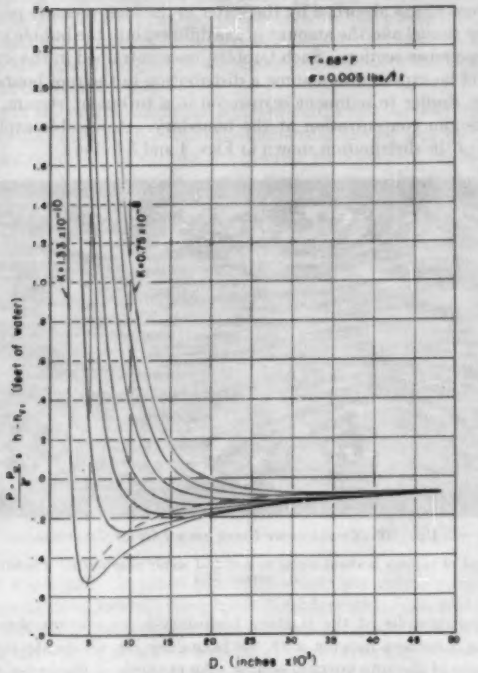

FIG. 8 PRESSURE VERSUS BUBBLE SIZE

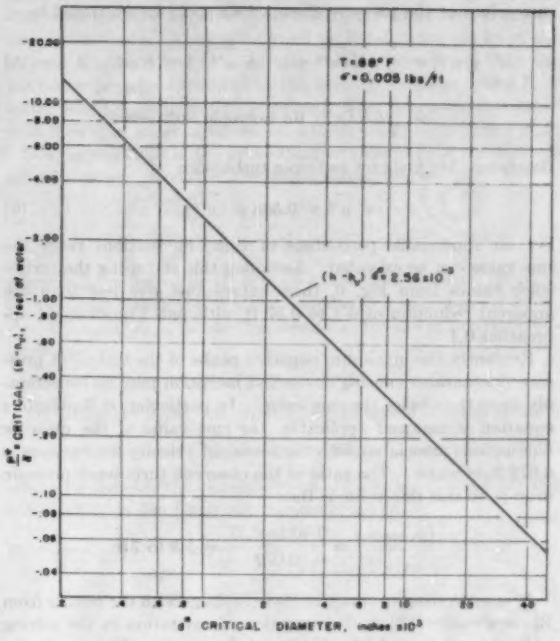

FIG. 9 PRESSURE REQUIRED TO CAUSE INSTABILITY OF CRITICAL-SIZE GAS NUCLEI

For a constant weight of a perfect gas at constant temperature $p_g = K/r^3$ so that

$$p - p_v = \frac{K}{r^3} - 2\frac{\sigma}{r} \quad \ldots\ldots [3]$$

From Equation [3] is found the minimum of $p - p_v = p^*$ where $r = r^* = (3K/2\sigma)^{1/2}$, or

$$r^* = \frac{-4\sigma}{3(p - p_v)} \quad \ldots\ldots [4]$$

In this relation the negative sign indicates that the critical fluid pressure is actually below the vapor pressure. If now from the condition $r = r^*$ at $p - p_v = p^*$, p is decreased slightly, the bubble is unstable and tends to grow without bound. At pressures greater than the critical pressure, the bubble is stable and assumes an equilibrium radius satisfying Equation [2]. The relations between $p - p_v$ and diameter for different values of K and assuming a surface-tension value of 0.005 lb per ft for 68 F water are shown in Fig. 8. The corresponding relation between pressure and critical diameter is shown in Fig. 9.

Fig. 8 does show that very rapid expansions of bubbles containing large masses of gas (K large) are possible before the critical size is reached. However, for gas masses yielding bubbles of 0.02 in. critical diameter or smaller, the rate of change of size with pressure drop is small until $d = d^*$. The former might be termed pseudo-cavitation as distinct from true cavitation, the rapid expansion expected on reaching critical diameter. The example shown in Fig. 3(a) is cavitation by this definition. As can be seen in Fig. 3(b), the bubble traversed about one third of the field of view at a constant diameter of approximately 0.01 in. and then suddenly expanded, reaching 13 times its initial size for an additional head drop of only 0.02 ft. It can be seen from Fig. 8 that such an expansion could not have taken place for a bubble of its initial size unless the local pressure had reached the critical value.

It is important to observe from Fig. 9 that, to initiate cavitation, tensions much higher than encountered in most practical cases are necessary unless macroscopic bubbles are present. In fact, this relation has been used to estimate critical nuclei of the order of 10^{-5} cm for acoustically determined cavitation thresholds in degassed water (6).

Of course, the preceding arguments in addition to assuming that temperature and gas mass are constant do not consider dynamic effects on an expanding bubble. In these experiments the longitudinal pressure gradient in the test section is relatively flat, only about 1.5 ft of water per ft. Therefore, the dynamic effects on the bubble prior to reaching instability should be small, and the critical size as predicted from Equation [4] should be a first-order approximation of the critical size to be expected.

From these simple equilibrium arguments, the observed decrease in critical bubble size with boundary pressure would be expected. However, the observed growth would be expected only if the local fluid pressure acting on the bubble dropped below the vapor pressure. The difference observed at critical conditions between the measured boundary pressure and the critical pressure given by Equation [4] can only be attributed to local pressure reduction due to turbulence. This difference for the test conditions appeared to be about 0.57 ft of water as shown by line 3 in Fig. 7, although it is recognized that the actual difference may be as low as 0.4 ft due to the possible error in wall pressure already mentioned.

Referring again to Fig. 3(a), the circled bubble illustrates the combined effect of turbulence and nuclei size. This bubble, although larger than the nucleus which becomes unstable and grows, does not expand. However, the circled cavity is well outside the boundary layer and thus not subject to the intense turbulence of the boundary layer.

Taylor (10) found for a theoretical model of turbulence that the

rms values of the pressure fluctuations could be expressed by

$$\sqrt{\overline{p'^2}} = \frac{1}{2}\rho K\left(\overline{u'^2} + \overline{v'^2} + \overline{w'^2}\right) \quad 1 < K < \sqrt{2} \quad \ldots\ldots [5]$$

$$= \frac{3}{2}\rho K\left(\overline{u'^2}\right) \text{ for isotropic turbulence}$$

Batchelor (11) finds for isotropic turbulence

$$\sqrt{\overline{p'^2}} = 0.583\,\rho\left(\overline{u'^2}\right) \quad \ldots\ldots [6]$$

For an appreciable percentage of time, fluctuations twice the rms value can be expected. Assuming this and using the turbulence values from Fig. 6, these expressions give less than the apparent reduction of 0.4 to 0.57 ft, although Equation [5] approaches 0.4.

Evidently the maximum negative peaks of the turbulent pressure fluctuations causing cavitation inception may be considerably more than twice the rms value. In particular, if Batchelor's equation is assumed applicable, the rms value of the pressure fluctuations associated with the observed velocity fluctuations is 0.072 ft of water. The ratio of the observed turbulence pressure drop p_i to this rms value is then

$$\frac{(p_i)_{\text{observed}}}{\sqrt{\overline{p'^2}}} = \frac{0.40 \text{ to } 0.57}{0.072} = 5.5 \text{ to } 7.9$$

It is interesting to compare these findings with the results from Rouse's study (12) of the inception of cavitation in the mixing zone of a submerged jet. He found the pressure drop due to the vorticity in this zone to be 10 to 13 times the rms of the pressure fluctuations, depending on the definition of inception, i.e.

$$\frac{p_i}{\sqrt{\overline{p'^2}}} = 10 \text{ to } 13$$

This value was obtained by measuring the pressure fluctuations with a specially designed instrument in air, and comparing with the ambient pressure necessary to cause cavitation inception in water.

Assume that Equation [5] is applicable for the determination of the turbulent pressure fluctuations in the boundary layer. If it is also assumed that $v' = w'$ (as found by Laufer, reference 9) and the bubble-turbulence distribution of Fig. 6 is used, Equation [5] shows that $\sqrt{\overline{p'^2}}$ is maximum in the center portion of the boundary layer. This may be sufficient explanation of the similar expanding cavity distribution found in Fig. 5. However, the fact remains that turbulence measurements by more reliable methods indicate maximum turbulence intensity (and from Equation [5] maximum pressure fluctuations) very near the wall where absolutely no expanding cavities were found.

Turn now to the entrained bubble nuclei and their distribution in the boundary layer. As will be discussed further, it seems probable that the gas nuclei in this experiment originated initially at boundary cracks and crevices. Such bubbles emerging in the presence of the high-velocity gradient near the wall would experience hydrodynamic lift until the drag force accelerated them to the fluid velocity. This point was verified by admitting air bubbles ranging in size up to 0.04 in. diam through a small hole in the roof at station $x = 7.0$ in. These bubbles were immediately lifted out into the boundary layer and assumed a distribution peaking at about 35 per cent of the boundary-layer thickness from the wall at station $x = 14.4$ in. The almost total absence of bubbles near the boundary, as shown in Fig. 4, might be attributed to this lift. But these bubbles are not resorbed after passing through the test section and must continually circulate and grow until they reach some equilibrium size depending on the amount of gas absorbed by the water in the high-pressure portion of the tunnel and the amount of gas diffused into the bubble in the low-pressure section. Such bubbles, once entrained in the water, would be expected to assume a distribution in the roof boundary layer similar to sediment suspension in a turbulent stream, i.e., maximum concentration at the boundary. A possible explanation of the distribution shown in Figs. 4 and 5 follows.

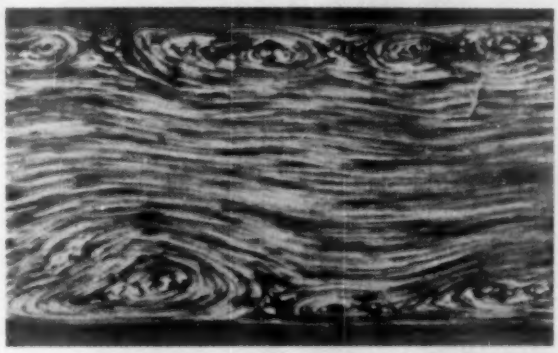

FIG. 10 TURBULENT FLOW IN AN OPEN CHANNEL

(Speed of camera is about equal to speed of water near walls. Prandtl, reference 13.)

Photographs of the relative boundary-layer motion obtained using a camera moving with the boundary layer indicate the existence of discrete vortical eddies. An example of the free-surface conditions in an open channel is reproduced from Prandtl (13) in Fig. 10. There are discrete vortical eddies in this photograph, elliptical in shape, with major axis in the direction of mean flow and minor dimension about equal to the boundary-layer thickness. Townsend (14) in an analysis of apparent eddy viscosity and local turbulence intensity found the length scales to be comparable with distance from the wall and concluded from his and Laufer's (9) experiments that the typical large eddy in the boundary layer is very elongated to about three times the boundary-layer thickness in the direction of flow, and of the same order of magnitude as the boundary-layer thickness normal to the wall. Bakhmeteff (15) concluded from an energy-balance analysis that only a small percentage of the energy obtained from the main flow is dissipated in the central region of the boundary layer, the majority being transmitted with little loss through this region to be spent in viscous friction at the boundary. Thus a simplified model of the boundary layer consists of a series of large elliptical-shaped eddies obtaining energy from the free stream, converting only a small portion of this to creation of smaller vortexes, and spending the majority in viscous shear at the boundary. The center of such eddies would be in the center portion of the boundary layer and moving at a velocity less than the main stream velocity.

The majority of free-gas nuclei, in the presence of such a turbulent boundary layer, would be transported toward the center of the large vortical eddies, if the vortex pressure gradient is sufficient to overcome hydrostatic forces on the bubble. The nucleus after reaching the center of the eddy is then subjected not to rapidly fluctuating pressures, as might be obtained from an instantaneous pressure-measuring tube which records the passage of such eddies, but to a more nearly constant pressure less than the free-stream pressure by an amount depending on the vortex strength. Thus this qualitative picture of the boundary layer offers a possible explanation of why only a few of the smaller gas nuclei were observed close to the boundary. Also, while it should be expected that the distribution of cavitating bubbles might

follow the distribution of all the nuclei present, this picture of the boundary-layer structure is consistent with the possibility that the optimum local pressure environment for cavitation is away from the boundary even if the maximum turbulent fluctuations are at the boundary.

As to the magnitude of the eddy strengths and vortex pressure gradients, note that a velocity-measuring device located in a stream composed of various size discrete eddies would record the passage of these eddies as velocity fluctuations. The magnitude of the velocity recorded would depend on the location of the measuring probe relative to the center of the eddy, with maximum fluctuations appearing when the periphery of an eddy reached the instrument. The maximum fluctuations in velocity recorded would be expected to be higher than the rms value, say, $c\sqrt{u'^2}$. Assuming the eddies are forced vortexes of peripheral velocity $c\sqrt{u'^2}$, the data of Figs. 6 and 7 give c as approximately 3. If the actual pressure reduction is only 0.4, c is 2.5. About 3 per cent of the bubble velocity fluctuations recorded in the inner region of the boundary layer were as high as $2.4\sqrt{u'^2}$. Using Rouse's (12) data, mentioned earlier, c is found to be about 3.5. Nothing is proved by these figures, yet the order of magnitudes involved does not appear impossible to realize. If the mean eddy size is about equal to the boundary-layer thickness, the foregoing strengths will produce vortex pressure gradients considerably higher than the hydrostatic gradient.

It is generally accepted that microscopic gas volumes may be trapped in crevices of hydrophobic boundary or foreign particles. At sufficiently low pressures these microscopic gas nuclei can grow from the crevice either as a result of their becoming unstable or by the diffusion of gas from the supersaturated surrounding fluid. The forces tending to expand these nuclei then are greatest in the minimum pressure region of the flow. The fact that the gas nuclei in crevices of the boundary are subject to low pressure for infinitely greater time than those trapped on foreign particles leads to the selection of boundary crevices as the most probable source of macroscopic bubbles. It is interesting to speculate on the role this source of nuclei plays in the cavitation process. As bubbles grow from the boundary, they become subject to the lift and drag of the high-velocity flow past the boundary and are swept off. Some gas remains in the crevice to repeat the process. The maximum size that these gas bubbles can reach before the lift and drag overcome the surface-tension force holding the bubble on the boundary must depend on the velocity, surface tension, and the characteristics of the boundary layer.

It was observed during deaeration as the water was slowly circulated that air bubbles formed at fine scratches in the plexiglas test-section walls and from select points on the machined surface of the bronze entrance nozzle. As the bubbles emerged into the boundary-layer flow, they were swept away after reaching diameters between 0.01 and 0.02 in. The size at detachment decreased with increased velocities. Although their formation was not actually observed, the smallest bubbles found in the boundary layer were about 0.002 in. diam, which suggests this may be the limiting size at the test velocity. Those bubbles created farthest upstream of the minimum-pressure zone are most apt to cause inception of cavitation because they may increase in size before reaching the minimum-pressure region. It is believed that gas nuclei from entrained foreign particles are not necessary to explain most cases of the observed phenomena.

In the case of immersed bodies, nuclei from the body surface will influence inception. Kermeen, et al. (2) cite observations of small cavities growing on the boundary upstream of the intermittent macroscopic cavitation associated with inception. These cavities, called microscale cavitation by the authors, grew on the boundary until they reached a size about equal to the displacement thickness (about 0.001 in.) and were then lifted up and carried with the flow apparently to "feed" the macroscopic cavitation downstream. They were in all probability gas nuclei in the process of formation at a crevice. It is interesting that the boundary pressure measured at the time of inception was 3 ft of water less than the vapor pressure. This compares favorably with 2.56 ft of water obtained for a 0.001-in. nucleus from Fig. 9.

The implications of the previous observations as to scale effects are of interest. Consider the dimensionless parameter

$$\frac{p_0 - p_{min}}{{}^1/_2\rho U_0^2}$$

where p_{min} = lowest local pressure in the flow system. If $p_{w_{min}}$ is the lowest pressure along the boundary of an immersed body, p_{min} will equal $p_{w_{min}}$ minus the pressure difference p_t due to turbulence, or

$$p_{min} = p_{w_{min}} - p_t \quad \ldots\ldots\ldots\ldots\ldots\ldots [7]$$

On the other hand, the onset of cavitation will occur when

$$p_{min} = p_v - |p^*| \quad \ldots\ldots\ldots\ldots\ldots\ldots [8]$$

where $|\ |$ denotes the absolute value. Equating [7] and [8] and substituting in the foregoing parameter gives

$$\frac{p_0 - p_{min}}{{}^1/_2\rho U_0^2} = \frac{p_0 - p_{w_{min}}}{{}^1/_2\rho U_0^2} + \frac{p_t}{{}^1/_2\rho U_0^2} = \frac{p_0 - p_v}{{}^1/_2\rho U_0^2} + \frac{|p^*|}{{}^1/_2\rho U_0^2}$$

$$= C_p + K_t = K_i + \frac{|p^*|}{{}^1/_2\rho U_0^2}$$

or

$$K_i = C_p + K_t - \frac{|p^*|}{{}^1/_2\rho U_0^2} \quad \ldots\ldots\ldots\ldots\ldots\ldots [9]$$

where

K_i = incipient cavitation index
C_p = boundary pressure-drop coefficient
K_t = pressure-drop coefficient due to turbulence

C_p is a function of the boundary layer-surface friction relation. For cavitation occurring on the walls of a conduit, the build-up of the displacement thickness constricts the flow and results in an increase in C_p with decreasing velocity. On the other hand, for immersed bodies, where the pressure drop is primarily due to boundary curvature, the displacement thickness decreases the curvature of the body and therefore C_p is less than predicted from potential-flow theory. At high velocities, where the displacement thickness becomes negligible, C_p is known to become nearly constant, approaching the potential value as the velocity increases.

Both Laufer and Lawrence (16) have found that the dimensionless absolute turbulence intensity $\sqrt{u'^2}/U_0$, in a fully developed boundary layer, decreases with increase in the Reynolds number. Since it has been shown that cavitation inception is dependent on the boundary-layer turbulence level, some change in the index K_t with the Reynolds number is to be expected. On curved streamlined surfaces, where the pressure gradients normal to the boundary may exceed the pressure reduction due to turbulence, the influence of boundary-layer turbulence on cavitation inception is probably reduced.

The value of the parameter

$$\frac{p^*}{{}^1/_2\rho U_0^2}$$

depends on surface tension and the size of nuclei present. The size of a nucleus originating at a model boundary would depend primarily on surface tension, fluid density, velocity, model size,

and characteristics of the boundary layer. In terms of dimensionless parameters, then, the value p^* is dependent on

$$\frac{VD}{\nu} \text{ and } \frac{V\sqrt{D}}{\sqrt{(\sigma/\rho)}}$$

the Reynolds and Weber numbers. It is interesting that Parkin and Holl (3) report reasonably good correlation of the data obtained on the various size bodies of revolution with the parameter $V\sqrt{D}$.

The dependency of the size of nuclei created at the boundary surface on some characteristic of the boundary layer is confirmed in reference (2) where these bubbles apparently grew to a size about equal to the displacement thickness before being swept off. The boundary-layer thickness, in general, is inversely proportional to U_0^n where n is less than 1. Correspondingly, p^* can be written proportional to U_0^n or

$$\frac{p^*}{\frac{1}{2}\rho U_0^2} = \frac{AU_0^n}{\frac{1}{2}\rho U_0^2} = \frac{B}{U_0^m} \; (m > 1) \quad \ldots\ldots\ldots [10]$$

Therefore, at high velocities, the effect of the parameter

$$\frac{p^*}{\frac{1}{2}\rho U_0^2}$$

becomes less important. In tests of small-scale models, the elimination or reduction of the factor

$$\frac{p^*}{\frac{1}{2}\rho U_0^2}$$

should greatly reduce the scale effects on the parameter K_i. As long as the source of nuclei is the boundary itself, the value of

$$\frac{p^*}{\frac{1}{2}\rho U_0^2}$$

can be reduced only by operating at very high velocities. References (2) and (3) indicate velocities greater than 100 fps may be required. The most obvious means of reducing the effect of boundary nuclei size is to introduce nuclei large enough to make p^*/γ very small (say, 0.1 ft of water), and to operate at a high velocity (say, greater than 30 fps). The problem here is to avoid entraining bubbles of such a large size that pseudo-cavitation occurs. While a resorber eliminates the troublesome recirculation of large masses of undissolved gas bubbles and allows a standardization of test conditions, the use of a resorber can actually increase the effect of

$$\frac{p^*}{\frac{1}{2}\rho U_0^2}$$

This is due to the very fact that relatively large nuclei from the main stream are nearly eliminated, leaving the boundary crevices as the main source of nuclei.

If the inception of cavitation depends on the supply of nuclei from boundary crevices, some speculation on the effect of gas content is also possible. Assuming that the growth of bubbles from boundary crevices is at least partly a process of diffusion from the supersaturated liquid, the pressure and location of the formation of macroscopic nuclei will depend on the air content of the test liquid. As previously mentioned, those bubbles which form and are swept off farthest upstream will be the largest in size upon reaching the minimum pressure region since they contain more weight of gas and have a longer time to grow. Decreasing the dissolved gas content of the liquid will move the upstream boundary of the macroscopic nuclei nearer to the minimum pressure location. Therefore decreasing the gas content should result in decreasing the size of nuclei at the minimum pressure region and thus a decrease in the incipient cavitation index. Based on this reasoning, the effect of variation in gas content on the inception of cavitation should be most pronounced on tests of large shapes, having flat pressure gradients and tested at low velocities. Conversely, on small bodies with steep gradients, tested at high velocities, little or no variation in K_i with dissolved gas content should be expected.

The latter case was confirmed experimentally by determining K_i for a 0.04-in. blunt-ended cylinder. This cylinder protruded $\frac{1}{4}$ in. into the flow through the floor piezometer hole at $x = 4\frac{3}{32}$ in. in Fig. 1. The air content was varied from the minimum value attainable (0.3 per cent by volume at STP) to complete saturation at atmospheric pressure (2.1 per cent by volume at STP). For a test velocity of 45 fps the ambient pressure upstream of the body at the time of inception was greater than atmospheric. Therefore the gas in the water should remain in solution. At this test velocity, only a very slight increase in K_i with increase in gas content was observed.

Summary of Conclusions and Observations

For the experiments considered here, the following conclusions may be stated:

1 Cavitation starts from gas bubbles in the fluid. Neglecting dynamic and heat-transfer effects, these gas bubbles will become unstable if their radius exceeds the critical radius

$$r^* = \frac{-4\sigma}{3(p - p_v)}$$

Thus the pressure required to cause instability of these gas nuclei must be less than the vapor pressure by an amount depending on the nuclei size.

2 If incipient cavitation occurs at or near the vapor pressure, as is usually the case in mechanical equipment and engineering structures, there must be relatively large gas nuclei present in the fluid.

3 The boundary pressure at inception exceeds the critical pressure required to cause instability given in item 1. This is attributed to the pressure drop associated with the vortical eddies composing the turbulent boundary layer.

4 Cavitation is incipient in the turbulent boundary layer (developed on a flat surface) near the center of the boundary layer. It is suggested that this phenomenon is also caused by the large vortical eddies of the turbulent boundary layer which pull gas nuclei to their centers and there subject them to sustained pressures less than the boundary pressure.

5 It is believed that the main source of macroscopic gas nuclei is the crevices of the hydrophobic boundary material. Undissolved gas volumes trapped in boundary crevices will grow from the boundary at sufficiently low pressures to be swept away as small gas bubbles by the passing flow. Upon reaching critical pressure downstream, these bubbles will become unstable and grow rapidly. Foreign particles entrained in the water also may contain such undissolved gas volumes. However, these particles are in the low-pressure region for much less time than gas trapped in boundary crevices. This leads to the selection of the boundary crevices as the most probable source of macroscopic bubbles.

6 The incipient-cavitation index is dependent on three factors expressed as follows

$$K_i = C_p + K_i - \frac{p^*}{\frac{1}{2}\rho U_0^2}$$

where

C_p = minimum pressure-drop coefficient

K_t = pressure-drop coefficient due to turbulence

$\frac{p^*}{\frac{1}{2}\rho U_0^2}$ = pressure coefficient containing effect of gas-nuclei size

C_p is a function of Reynolds number and may increase or decrease depending on boundary-flow conditions. For immersed bodies, C_p is known to become nearly constant at sufficiently high Reynolds numbers.

Turbulence measurements show that K_t decreases with Reynolds number, becoming negligible at sufficiently high Reynolds numbers.

$p^*/(\frac{1}{2}\rho U_0^2)$ is a function of the Reynolds and Weber numbers. The influence of this ratio can be reduced by increasing velocity and/or by increasing the size of nuclei in the flow. The latter may be a way of controlling this effect experimentally to reduce variations in the observed K_i between model and prototype.

7 If the main source of nuclei is the boundary crevices, dissolved-gas content should have little or no effect on K_i for small bodies, with steep pressure gradients tested at high velocities. However, for large bodies with flat pressure gradients tested at low velocities, it is believed that variations in the dissolved gas content may noticeably affect K_i.

Acknowledgment

These investigations are being conducted in the M.I.T. Hydrodynamics Laboratory under the sponsorship of the Office of Naval Research, U. S. Department of the Navy, Contract Number N5ori-07873. This paper is based on one of the same title presented as part of the National Physical Laboratory Symposium on Cavitation in Hydrodynamics in Teddington, England, September, 1955.

Bibliography

1 "Cavitation Mechanics and Its Relation to the Design of Hydraulic Equipment," by R. T. Knapp, James Clayton Lecture, Proceedings of The Institution of Mechanical Engineers, London, England, series A, vol. 166, 1952, pp. 150–163.

2 "Mechanism of Cavitation Inception and the Related Scale-Effects Problem," by R. W. Kermeen, J. T. McGraw, and B. R. Parkin, Trans. ASME, vol. 77, 1955, pp. 533–541.

3 "Incipient Cavitation Scaling Experiments for Hemispherical and 1.5 Caliber Ogive Nosed Bodies," by B. R. Parkin and J. W. Holl, a joint study by the Hydrodynamics Laboratory, California Institute of Technology and Ordnance Research Laboratory, The Pennsylvania State College, May 15, 1953.

4 "A Brief Survey of Progress on the Mechanics of Cavitation," by Phillip Eisenberg, David Taylor Model Basin Report No. 842, June, 1953.

5 "On Cavity Formation in Water," by E. N. Harvey, Wm. D. McElroy, and A. H. Whitely, *Journal of Applied Physics*, vol. 18, 1947, pp. 162–172.

6 "The Onset of Cavitation in Liquids," by F. G. Blake, Jr., Acoustics Research Laboratory, Harvard University, Technical Report No. 12, September, 1949.

7 "Properties of Liquids at High Sound Pressures," by H. B. Briggs, J. B. Johnson, and W. P. Mason, *Journal of the Acoustical Society of America*, vol. 19, July, 1947, pp. 664–667.

8 "Air Resorption in Water Tunnels," by F. B. Brown, Hydrodynamics Laboratory, California Institute of Technology, Report No. N-62, March, 1949.

9 "Investigation of Turbulent Flow in a Two-Dimensional Channel," by John Laufer, NACA TN 2123, July, 1950.

10 "The Mean Value of the Fluctuations in Pressure and Pressure Gradient in a Turbulent Fluid," by G. I. Taylor, Proceedings of the Cambridge Philosophical Society, 1936, pp. 380–384.

11 "The Theory of Homogeneous Turbulence," by F. K. Batchelor, The University Press, Cambridge, England, 1953.

12 "Cavitation in the Mixing Zone of a Submerged Jet," by Hunter Rouse, *La Houille Blanche*, January-February, 1953.

13 "Applied Hydro and Aeromechanics," by L. Prandtl and O. G. Tietjens, Engineering Societies Monographs, McGraw-Hill Book Company, Inc., New York, N. Y., 1934, p. 295.

14 "The Structure of the Turbulent Boundary Layer," by A. A. Townsend, Proceedings of the Cambridge Philosophical Society, vol. 47, part 2, 1951, pp. 375–395.

15 "The Mechanism of Energy Loss in Fluid Friction," by B. A. Bakhmeteff and William Allan, Trans. ASCE, 1946, pp. 1043–1102.

16 "Reduction of Turbulence Data With an Electrodynamometer," by J. P. Lawrence, MS thesis, Massachusetts Institute of Technology, Cambridge, Mass., Course I, 1953.

Discussion

B. R. Parkin[4] and R. W. Kermeen.[5] The results which the authors summarize in the present paper represent an important contribution toward the understanding of the mechanics of cavitation inception in situations of technical interest. Since in many practical situations we are concerned with the inception of cavitation in liquids flowing past solid bodies, the emphasis in the present paper upon the relationships between cavitation nuclei and the real fluid effects observed in a flow makes this paper one of broad interest.

In this discussion we would like to compare some of the present findings with those of reference (2) of the paper, where cavitation inception in the boundary layer was studied without appreciable amounts of entrained air being present in the flow. As the authors have already pointed out, the flows in the present study and those past circular cylinders with hemispherical noses (reference 2) differed in the relative dimensions of the solid boundaries and in streamline curvatures produced by these boundaries. Perhaps a more striking way to compare these differences is in terms of the streamwise pressure gradients in the neighborhoods of the boundary points where cavitation inception was observed in the two cases.

For example, from Figs. 3(*a*) and 3(*b*) of the paper we see that a favorable pressure gradient of about $\frac{1}{4}$ ft of water per ft of streamwise travel might characterize the present experiments. From Fig. 5 of reference (2) the adverse pressure gradient which appeared to obtain at the points of microscopic bubble growth on the 2-in-diam hemisphere may be estimated to be about 400 ft of water per ft of streamwise travel. Thus we see that in the two cases the magnitudes of the pressure gradients differ by a factor of about 1600 and the direction of decreasing pressure points downstream in the present case while it points upstream in the experiments of reference (2). Of course, in this latter case, the flow curvature would also imply that even in the boundary layer we might expect the pressure to decrease toward the wall. These significant differences in the pressure fields enable us to understand, at least qualitatively, why during part of the growth phase of the microscopic bubbles reported in reference (2) the bubbles remained fixed with respect to the boundary, while the bubbles observed in the present investigation moved with the flow at all times.

As shown in our Report E-35.2,[6] the growth of these small bubbles at fixed points on the body appeared to be due entirely to air diffusion from the water. These fixed bubbles were observed to grow in regions where the static pressure was from 2 to 4 times the vapor pressure of the water and their observed growth rates from air diffusion could only be accounted for if the effect of the liquid transport velocity past the bubble was considered. These bubbles were lifted up to move with the boundary layer flow when they reached a size about equal to the displacement thickness. During this transport phase the microscopic bubbles

[4] Research Fellow in Engineering, California Institute of Technology, Pasadena, Calif.

[5] Research Engineer, Hydrodynamics Laboratory, California Institute of Technology, Pasadena, Calif. Mem. ASME.

[6] "Incipient Cavitation and Boundary Layer Interaction on a Streamlined Body," by B. R. Parkin and R. W. Kermeen, California Institute of Technology, Hydrodynamics Laboratory Report E-35.2, December, 1953.

grew slowly until they reached the neighborhood of the fuzzy band of macroscopic cavitation (Fig. 4, reference 2) ordinarily associated with inception. At this point over the body they were observed to explode and definitely to merge with the fuzzy band of macroscopic cavitation.

In certain respects the two pictures of the cavitation-inception process appear to be in agreement. Thus, in our experiments and those described by the authors, we find a bubble growth on the body caused by air diffusion, followed by a brief period of translation with the boundary-layer flow. Finally, in both cases a regime of very rapid bubble growth was observed. It is certainly satisfying to be able to draw such close parallels between physical phenomena which were observed under such widely varying experimental environments. On the other hand, it is important also to note the salient features which were different in the two sets of experiments. The great differences in the static-pressure fields caused by the radical differences in flow curvatures have been noted already.

There also appears to be some sort of difference in the origin of the nuclei which grew into observable bubbles in the two cases. For example, we found that as the free-stream static pressure was lowered from the condition of inception described, the fuzzy macroscopic cavitation became a series of small clear cavities with their leading edges attached to the body. The establishment of this flow regime was accompanied by the disappearance of the microscopic bubbles (Fig. 6, reference 2). Evidently these small clear cavities are sustained by evaporation from and by the diffusion of air through the cavity walls, as is the case for full cavity flows such as those studied by Reichardt.[7] Direct measurements indicated that this change in flow regimes was accompanied by an increase in the static pressure at the minimum pressure point from a tensile stress of about 6 cm of mercury to a positive pressure which was about the vapor pressure of water, 2.3 cm of mercury. This pressure change was sufficient to drop the local supersaturation in the region of cavitation inception from about 20 times saturation to about 18 times saturation. This latter value is still extremely high, so that this high degree of supersaturation together with the continuous transport of such air-rich water into the region where the diffusion was observed to take place at inception should still permit very high diffusion rates to exist upstream from the small clear cavities after they are established.

It does not seem possible to explain the suppression of the microscopic cavitation solely on the basis of changes in an air-diffusion process. Instead it seems to us much more likely that the microscopic cavitation originates in regions of the boundary layer where the static pressure is less than the vapor pressure. Thus we could expect the cavitation nuclei to grow initially as vapor bubbles and, after these growing bubbles had been transported to the higher-pressure zone where the observations of reference (2) were made, the process of air diffusion produced additional growth. When the cavitation number is lowered to the point where the fuzzy macroscopic cavitation band becomes a series of clear cavities attached to the body, the microscopic cavitation disappears, not because air diffusion is suppressed, but because the pressure increase accompanying the formation of the clear macroscopic cavitation prevents the initial phase of dynamic bubble growth.

Thus we see that the sequence of events associated with the inception process studied in reference (2) differs from and seems somewhat more complex than that described by the present authors. Therefore it is not surprising that there are still other differences between our experiments and the Daily-Johnson observations.

One of the most striking differences, which is shown by a comparison of the data is that the smallest bubbles which were observed to expand rapidly by the authors, appear from Fig. 7 to be about 0.008 in. diam while the bubbles investigated by us were from 0.001 to 0.003 in. diam at the end of their growth to their maximum size by air diffusion. Moreover the authors have indicated that with their apparatus they could not generate cavitation in their test section from air nuclei smaller than those shown in Fig. 7 because the pressures were never low enough to permit the growth of the smaller nuclei. It would appear that the presence of the larger bubbles in the flow made it impossible for the static pressure to be less than vapor pressure in much the same way that the clear attached cavities on the hemispheres were found to relieve the liquid tensions which were found to exist at inception in our experiments. It seems safe to say that the growth of the very small nuclei can be promoted only in flows which produce very low pressures over a small region and that we cannot expect to maintain tensions over large volumes of nuclei-filled liquid. Investigations into the zone separating these two extremes would be of interest.

It is important to note that the present experiments clearly relate the findings of Knapp and Hollander[8] to more recent cavitation experiments. In their experiments, Knapp and Hollander observed the growth and collapse of cavitation bubbles which originated from large air nuclei in the flow. However, they used 2-in-diam axially symmetric bodies to generate the low pressures required to promote bubble growth. The cavitation bubbles which originated from the large air nuclei were very large compared to the boundary-layer thickness so that we may regard their histories as being typical of bubbles which grow in an essentially irrotational flow.

Aside from bubble asymmetries caused by the proximity of the boundary and the presence of large pressure gradients[9] in the flow, such bubbles grow and collapse without being greatly distorted by the flow. However, when the flow is intensely rotational as is the case when the bubbles are in a turbulent boundary layer, it is evident from Fig. 3(a) of the paper that the bubbles assume highly distorted shapes as their size increases. These facts are in agreement with the results reported in reference (2) where the fuzzy intermittent macroscopic cavitation with characterized inception resulted from extreme bubble distortions. This tearing apart of the exploding microscopic bubbles to form the macroscopic cavitation is due primarily to the turbulence of the boundary layer. The fact that there are large pressure gradients in the region and that the boundary layer is quite thin permits this zone of macroscopic cavitation to become stabilized at a single location on the body while the absence of these factors in the present experiments would seem to preclude the formation of a similar structure. Thus we see that the authors' observations, when compared with previously known results, lead to a better understanding of the relationships between a broad class of phenomena which are common to the inception of cavitation under widely varying circumstances.

We agree with the authors that the presence of a resorber in a water-tunnel circuit does effectively remove the large masses of entrained air from the flow and this does have a decided effect on cavitation inception from relatively large gas nuclei. For example, it is possible to observe the cavitation of the type studied by

[7] Ministry of Aircraft Production Reports and Translations No. 776; in U. S. A. distributed by the Office of Naval Research, Navy Department, Washington, D. C., 1946.

[8] "Laboratory Investigations of the Mechanics of Cavitation," by R. T. Knapp and A. Hollander, Trans. ASME, vol. 70, 1948, p. 419.

[9] "Observations on Cavitation Bubble Collapse," by A. T. Ellis, California Institute of Technology, Hydrodynamics Laboratory Report No. 21-12, December, 1952, figs. 15 and 16.

Knapp and Hollander in the present high-speed water tunnel[10] only if the dissolved air concentration is extremely high. Similarly, experiments of the type reported by the authors could only be performed in the high-speed water tunnel under the same extreme conditions. On the other hand, the presence or the lack of a resorber in no way compromises the validity of the results of cavitation studies once this fundamental difference is recognized.

In particular, the scale-effect studies reported in reference (3) of the paper were made in the Garfield Thomas water tunnel which has no resorber and in the high-speed water tunnel which has a resorber. In both facilities, only the cavitation which occurred in the boundary layer was studied.

At the Ordnance Research Laboratory, the absence of a resorber permitted the recirculation of entrained air so that the type of cavitation observed by Knapp and Hollander also was observed. It was found that the growth and collapse of these large bubbles outside the boundary layer did not interfere with the inception of cavitation inside the boundary layer on models as large as 8 in. diam. The two effects appeared to be superposable and the agreement between the California Institute of Technology and the Ordnance Research Laboratory results was excellent. Of course, there are probably many flows of practical interest in which there will be large amounts of entrained air and there are undoubtedly just as many technically important situations in which there will be no appreciable entrained air present. It is certainly important to recognize the possibility that the cavitation phenomenon will be different in the two cases.

In conclusion, we wish to thank the authors for presenting a paper which all workers in the field of cavitation undoubtedly will find very stimulating.

M. Strasberg.[11] This paper is of particular interest because it indicates the complete turnabout in the opinions on cavitation inception which has occurred among hydraulic engineers in the last decade. Ten years ago it was the general belief that cavitation occurred at vapor pressure, and any available data indicating that pressures below vapor pressure were required were viewed with skepticism and disbelief. The present paper illustrates the opposite point of view; although the measurements seem to indicate that the pressure at cavitation was above vapor pressure, the authors insist, and rightly so, that this cannot be, and that some unmeasured negative pressure increment must have existed which caused the net pressure to be below vapor pressure.

Nowadays it is generally accepted that vaporous cavitation requires a pressure below vapor pressure, in accordance with the theory discussed by the authors and shown in their Fig. 9. For those who remain skeptical, it may be of interest to point out that although the pressure measurements themselves may indicate pressure above vapor pressure, certain of the data presented by the authors do indicate that the pressure is below vapor pressure.

In Fig. 3(b) of the paper, the size of a bubble is plotted as a function of its position. It is possible to estimate the pressure required for this observed rate of growth. The growth of a bubble follows the differential equation

$$\rho\left(r\ddot{r} + \frac{3}{2}\dot{r}^2\right) + (2\sigma/r) = p_v - p \quad \ldots\ldots [11]$$

where the notation is that of the paper under discussion; i.e., r is the instantaneous radius of the bubble, p is the pressure in the water around the bubble, $(2\sigma/r)$ is the surface-tension pressure, and the dots indicate first and second derivatives with respect to time. When the bubble has grown to 5 or 10 times its original size, the $\ddot{r}$ and $(2\sigma/r)$ terms become negligible, and the radius then increases at a constant rate given by

$$\frac{3}{2}\rho\dot{r}^2 = (p_v - p) \quad \ldots\ldots [12]$$

Fig. 3(b) shows that the bubble does indeed grow at a constant rate of $\dot{r} = 25$ ips (assuming the flow velocity $U = 27.5$ fps). Substituting this value of $\dot{r}$ into Equation [12] the calculated value of $(p_v - p)$ is 0.2 ft of water; i.e., the pressure in the water is 0.2 ft below the vapor pressure.

The pressure required for the growth of this bubble also can be estimated in an alternative way, by means of the authors' Fig. 9. The initial size of the bubble indicated in Fig. 3(b) is about 0.012 in.; this is the critical diameter d^* of the bubble just before it becomes unstable and grows. From Fig. 9, this critical diameter corresponds to a pressure of 0.2 ft of water below vapor pressure.

Accordingly, both the rate-of-growth calculation and the instability calculation give a pressure of about 0.2 ft of water below vapor pressure. Since the two calculations involve different theories and different experimental data, the agreement between them indicates that the calculated pressure is correct.

The difference between this calculated value and the pressure measured at the roof for this bubble is about 0.6 ft of water. If this difference is indeed associated with the pressure fluctuations in the turbulent boundary layer, then, as pointed out by the authors, the instantaneous pressure fluctuations must exceed the rms fluctuations by a factor of from 5 to 10. It would be most interesting to determine experimentally whether the pressure fluctuations are so "peaky." This could be done by inserting a pressure-sensitive electrical pickup into the turbulent region and observing the wave form of the output on an oscilloscope.

Authors' Closure

The authors appreciate the thoughtful remarks of the discussers and are gratified at the degree of agreement with this attempt to clarify the cavitation-inception process and the source and role of nuclei.

Messrs. Parkin and Kermeen compare the results of the present experiments with their own experiments described in reference (2). They note certain similarities but state that there appears to be a difference in the origin of nuclei in the two cases. The authors believe that there is essentially no difference. Both experiments involve cavitation from nuclei containing gas and vapor and it is suggested again that it is equally plausible for the microscopic cavitation bubbles described in reference (2) to have originated from trapped gas volumes in hydrophobic boundary crevices.

The reasons are as follows:

(a) It is interesting to note that the bubbles observed and reported in Fig. 6 of reference (2) originated at selected spots, each spot giving birth to a series of bubbles.

(b) These bubbles must have been attached to the boundary during the period of growth prior to being swept downstream into the macroscopic cavitation zone. A calculation of the forces acting on a small free spherical bubble in the boundary layer will show that the drag force is many times the combination of pressure-gradient forces tending to keep the observed bubbles fixed.

(c) Trapped gas nuclei will grow by diffusion provided the partial pressure of the trapped gas is less than the saturation pressure for the surrounding liquid-gas solution. In such a gas volume trapped in a boundary crevice, the actual gas partial pressure will exceed the surrounding fluid pressure by an amount equal to the surface-tension pressure minus the vapor pressure.

[10] "The Hydrodynamics Laboratory at the California Institute of Technology," by R. T. Knapp, Joseph Levy, F. B. Brown, and J. P. O'Neill, Trans. ASME, vol. 70, 1948, p. 437.

[11] David Taylor Model Basin, Washington, D. C.

The magnitude of the surface-tension pressure will depend on the characteristics of the crevice and thus the type of boundary material. It is quite possible that this pressure is sufficiently high to require the observed supersaturation before gas can be released. In this particular case the surface-tension pressure may be represented by a spherical gas volume with a radius of about 5×10^{-6} in. Furthermore, there is some critical condition at which even the small changes in the degree of supersaturation noted by the writers will cause or prevent release of gas.

Argument (*c*) makes another point clear; namely, that the formation and growth of nuclei and the actual occurrence of cavitation can be independent. In particular it is not necessary for the local pressure to fall below the vapor pressure to cause growth and release of nuclei from hydrophobic boundaries. Cavitation, which the authors define as the explosive expansion taking place when the nucleus reaches its limit of stability, will occur when the bubble grows to its critical size for its given environment.

Messrs. Parkin and Kermeen note that the smallest critical diameter appearing in the authors' Fig. 7 is about 0.008 in. and suggest the presence of larger bubbles in the flow made it impossible for the static pressure to be less than the vapor pressure. In the present experiments, the limit was imposed because on reducing the pressure to values less than that required to cause instability of 0.008-in. bubbles, so many of the larger sized cavities exploded that the stream became too cloudy for observations.

On the other hand, the authors agree that the existence of many large nuclei in a low-pressure region may prohibit the growth of smaller nuclei. There must be a point reached in a system such as the M.I.T. water tunnel where severe cavitation will choke the flow and only nuclei larger than a certain critical size will expand.

Referring to the scale-effects studies mentioned by Messrs. Parkin and Kermeen, the agreement between CIT and ORL experiments is not necessarily evidence that the scale effects observed in references (2) and (3) are not peculiar to a system which eliminates all undissolved gas (such as a resorber). Reference (3) points out that in the ORL study, tests were made "raising the pressure to 40 psia for 10 min to drive the entrained air back into solution. Then the pressure was lowered and readings were taken before air came out of solution." Such a test procedure simulates the use of a resorber. The authors suspect that the scale effects observed would not exist or at least would be less pronounced if water containing relatively large entrained gas nuclei were used.

Mr. Strasberg's interesting calculations of the pressure for bubble instability showed an agreement between two different methods of determination which does not hold generally for the bubbles observed in this experiment. (*a*) He assumes in effect that $(p_v - p)$ remains constant during the life of the expanding bubble. This can only be approximately true at best. Actually p which is the local liquid ambient pressure is a function of time and space. It follows then that $(p_v - p)$ calculated for a later phase of the bubble-expansion process should not be expected to agree exactly with the critical value at which the bubble became unstable and began its rapid expansion. (*b*) The procedure neglects the effect of surface-tension pressure and of gas partial pressure within the bubble. The latter appears to be small which justifies its omission from the right-hand side of Equation [11] of the paper. However, surface-tension pressure is not negligible for the range of bubble sizes and expansion rates encountered.

Including a surface-tension effect in Equation [11] will give a decreasing value of $(p_v - p)$ so long as $\dot{r}$ is constant. On the other hand, while most of the expanding bubbles analyzed did increase in size at nearly a constant time rate, it should be noted [as for the example in Fig. 3(*a*)] that bubbles often deformed becoming nonspherical with growth. Thus, since Equation [11] is for a spherical bubble, the range over which it applies limited.

In his calculations, Mr. Strasberg used the flow velocity for the bubble pictured in Fig. 3(*b*) as 27.5 fps. This is the mainstream velocity, however, while the bubble moved at a reduced velocity within the boundary layer of approximately 21 fps. Reducing the rate of bubble growth accordingly but including an effect of surface tension, Equation [11] gives a value of $(p_v - p)$ that agrees closely but not exactly with that predicted by the stability relation, Equation [4]. This was found true also for other bubbles having a linear-growth rate.

The authors agree that knowledge of the instantaneous pressure fluctuations in the turbulent region would be very informative, although this has not yet been accomplished in the relatively thin boundary layer of this liquid stream. Of course, such measurements give only the local pressure, while as noted in the paper, it is believed that the bubble which travels with the liquid is subjected to the less than average pressures for some sustained period.

Critical Considerations on Cavitation Limits of Centrifugal and Axial-Flow Pumps

By G. F. WISLICENUS,[1] UNIVERSITY PARK, PA.

This is the presentation of a problem, not of its solution. A critical examination of the cavitation problem of centrifugal and axial-flow pumps indicates that such pumps are operated at higher speeds than reasonably can be expected to exclude cavitation or local pressures below the vapor pressure of the fluid pumped. This fact is revealed by relating the over-all cavitation characteristics of pumps for which empirically determined values are available to detail characteristics usually described as blade-pressure coefficients which are sufficiently backed by empirical and theoretical information to permit rational interpretation and an estimate of future developments, including pump operation with fully developed cavitation.

Nomenclature

The following nomenclature is used in the paper:

n = speed of rotation, rpm
Q = rate of volume flow, ft³/sec
S = suction specific speed, Equation [1]
H_{sv} = total inlet head, ft
H = total pump head, ft
p = static pressure of stream far away from blade, lb/ft²
p_{min} = minimum local static pressure at blade surface, lb/ft²
V = absolute velocity of flow, fps
W = relative velocity of flow, fps
U = peripheral velocity of runner inlet, fps
C = total pressure coefficient of absolute inlet flow
C_b = blade pressure-reduction coefficient, Equation [2]
g = gravitational acceleration, 32.2 ft/sec²
V_θ = peripheral component of absolute flow, fps
V_m = meridional component of flow, usually axial, fps
r = radius (distance from axis of rotation), ft
$\lambda = \frac{V_{\theta 0}}{V_{m0}}$ = ratio of peripheral to meridional velocity component

Subscripts

0 = outer periphery of inlet passage
avg = average as determined by condition of continuity

Outline of the Problem

The object of this paper is to present a group of problems connected with flow conditions in centrifugal and axial-flow pumps when operating within and beyond conventional limits with respect to cavitation. It is not the intent of this paper to describe details of specific solutions of these problems.

By the cavitation limits of centrifugal-pump operation we understand primarily the limits in speed of rotation for given operating conditions (such as inlet pressure and capacity) determined by the onset of cavitation within the pump. The most convenient expression describing the inlet operating condition has been found to be the "suction specific speed"

$$S = \frac{n\sqrt{Q}}{H_{sv}^{3/4}} \quad \ldots\ldots\ldots\ldots\ldots\ldots [1]$$

The suction specific speed[2] may be defined as that combination of inlet operating conditions which, if held constant, permits similar flow and cavitation conditions in geometrically similar passages of centrifugal and axial-flow pumps. Its value characterizes the hydrodynamic design of the inlet passages with respect to local pressure reductions that can lead to cavitation. An increase in the suction specific speed means an increase in the speed of rotation for a given rate of flow and given inlet head, and constitutes thereby an advancement in the art of designing better inlet-flow passages.

It is well known that an increase in the speed of rotation for a given operating condition is the most effective available method for reducing size and weight of a pump as well as its driver. The before-mentioned advancement toward higher suction specific speeds is therefore a matter of obvious practical importance.

The cavitation limits of centrifugal and axial-flow pumps are today mostly given in form of *empirical* limit values of the suction specific speed (or another convenient cavitation parameter) which have been found by an over-all test of the unit regarding cavitationwise satisfactory performance. It will be c ear, however, that the effect of changes in the inlet pressure on the *over-all performance* of the machine, or the absence of such effects, is at best a very indirect way of judging the existence or extent of cavitation within the machine.

This empirical background of the cavitation behavior of centrifugal and axial-flow pumps is insufficient for two reasons:

1 Since we do not know whether a pump is really operating free from cavitation when operating within conventional cavitation limits, it is not certain whether such limits guarantee satisfactory behavior under as yet untried operating conditions. Such conditions may be higher velocities of flow than previously attempted, or the use of relatively unconventional materials of construction, or finally, the handling of unconventional liquids as, for example, liquid metals.

2 The present empirical background gives no assurance as to the true nature of presently accepted cavitation limits of

[1] Professor of Aeronautical Engineering, Pennsylvania State University. Mem. ASME.

Contributed by the Hydraulic Division and presented at the Diamond Jubilee Annual Meeting, Chicago, Ill., November 13–18, 1955, of The American Society of Mechanical Engineers.

Note: Statements and opinions advanced in papers are to be understood as individual expressions of their authors and not those of the Society. Manuscript received at ASME Headquarters, August 25, 1955. Paper No. 55—A-144.

[2] In this paper the suction specific speed will be used with the capacity Q measured in cubic feet per second, somewhat in contrast to the more conventional but inconvenient gpm unit (gallons per minute). The numerical values of S used in this paper are therefore by a factor of approximately 21.2 lower than those conventionally quoted.

pumps, and therefore no information about the possible advancements of such limits by appropriate design measures.

In this paper an attempt will be made to rationalize on this situation by interpreting the conventional cavitation limits in suction specific speed in terms of the "cavitation coefficients" or "pressure reduction coefficients" of the impeller blades, meaning the local pressure reduction at the blades divided by the velocity pressure of the mean flow past the blade. There exists considerable information on such pressure-reduction coefficients from the theoretical pressure distribution of airfoil profiles as published, for example, in the well-known NACA Report No. 824.[3] Cavitation data on the same hydrofoil shapes when tested in the cavitation tunnel essentially confirm the theoretical expectations, although this statement cannot be made without considerable reservations. Not always is cavitation observed when the local pressure has just reached the vapor pressure. This may be illustrated by the conventional practice of determining incipient cavitation on hydrofoils in the cavitation tunnel by raising rather than lowering the tunnel pressure at constant velocity of flow. The disappearance of cavitation under the influence of a slow pressure increase in the tunnel yields reasonably consistent data on the flow limits of incipient cavitation of the hydrofoil concerned, these data being usually in fair agreement with theoretical expectations. Far less consistent data are obtained when attempting to observe limits of incipient cavitation by lowering the tunnel pressure, either because the first beginnings of cavitation are harder to detect or because of deeper reasons of the nature of cavitation that have not yet been fully explored. Some cases of considerable tension in flowing water have repeatedly and reliably been observed, although mostly under somewhat artificial test conditions. Therefore the concurrence of cavitation with the vapor pressure cannot be assumed categorically in all cases, but the existence of the vapor pressure is the only criterion of cavitation that can be used for its theoretical prediction in a reasonably simple fashion, and hence must form the basis for the analysis of cavitation conditions in turbomachinery.

Analysis of Pump Inlet Without Prerotation

The preceding considerations have led to the following question:

Which values of the blade pressure coefficient

$$C_b = \frac{p - p_{min}}{\frac{\rho W^2}{2}} \quad \ldots\ldots [2]$$

are connected with the empirically known cavitation limits of pumps in terms of their suction specific speed?

To express the necessary relation between S and C_b one relates the flow conditions at the impeller inlet to the total inlet head as follows

$$H_{sv} = C\frac{V^2}{2g} + C_b\frac{W^2}{2g} \quad \ldots\ldots [3]$$

where C is a coefficient larger than unity, indicating that because of unavoidable irregularities of flow the static pressure in the stationary inlet passages of the pump is somewhat lower than indicated by the absolute fluid velocity in these passages as calculated under the assumption of a frictionless fluid.

Throughout this paper C will be assumed to be 1.1 which is a rather low value.

[3] "Summary of Airfoil Data," by I. H. Abbott, A. F. von Doenhoff, and L. S. Stivers, Jr., NACA Report No. 824.

It has been shown[4] that Equation [1] also may be written in the form

$$S = 384.5\left(\frac{U^2}{2gH_{sv}}\right)^{3/4}\sqrt{\frac{V_{m\,avg}}{U}} \quad \ldots\ldots [1a]$$

which applies to zero hub diameter in the inlet passage of the impeller.

Considering first the case of no prerotation which is the presently predominant practice for single-suction centrifugal and axial-flow pumps, one obtains by substitution of Equation [3] into Equation [1a] the following expression

$$S = 384.5\frac{U/V_{m\,avg}}{\left[C + C_b\left(1 + \frac{U^2}{V_{m^2\,avg}}\right)\right]^{3/4}} \quad \ldots\ldots [4]$$

The numerical results of Equation [4] are plotted in Fig. 1 as solid-line curves designated by $\lambda = 0$, for $C_b = 0.3$, $C_b = 0.2$, and $C_b = 0.1$. Of these three values of the blade-pressure coefficient C_b, only the highest, 0.3, can possibly be regarded as a practically obtainable value within present-day centrifugal-pump practice. The other two values are fictitiously small in so far as they would require an agreement between the direction of a very slender impeller blade and the direction of the relative flow within a fraction of a degree. It will be seen, however, that existing centrifugal-pump-design practice does not justify the assumption that such close agreement exists under any circumstances.

Discussion of Standard Centrifugal-Pump Performance Regarding Cavitation

Before considering the more general case of inflow with prerotation it is well to discuss the implications of the foregoing results, particularly since zero prerotation conforms best to present standard practice.

In Fig. 1 the dash and dot line at $S = 385$ represents approximately standard practice of commercial centrifugal pumps as expressed by the standards of the "Hydraulic Institute." It is seen that this line corresponds roughly to the best values obtainable with $C_b = 0.3$ which may well be regarded as the lowest practical limit obtainable if the inlet-vane edges agree with the direction of the flow within not more than ± 2 deg. It will be seen later that such agreement is at least questionable. More significant is the fact that very accurate tests of over-all performance have given S-values as high as 550 so that the range in the neighborhood of the curve $C_b = 0.2$ must be regarded as well covered by special, highly efficient pumps, with a capacity range of apparently cavitation-free operation well in excess of the range in angle of attack that can be expected to be permissible in connection with $C_b = 0.2$. With condensate pumps and some pumps in the chemical and refinery field much higher S-values are regularly used but the operation of such pumps is known to be connected with considerable local cavitation.

Before drawing conclusions from this situation it is well to say a few words about the design flow conditions with which the before-mentioned cavitation performances of centrifugal pumps have been obtained. Referring to Fig. 2, it would seem natural to approximate the meridional flow at the inlet by a potential flow distribution, possibly modified as shown there to account empirically for some frictional effects. Under these assumptions, the meridional velocity at the outer shroud of the inlet V_{mo} would be considerably larger than the average value of the meridional velocity $V_{m\,avg}$. This would lead in Equations [3] and [4] to

[4] "Fluid Mechanics of Turbomachinery," by G. F. Wislicenus, McGraw-Hill Book Company, Inc., New York, N. Y., 1947, particularly Chapters 4, 11, and 13.

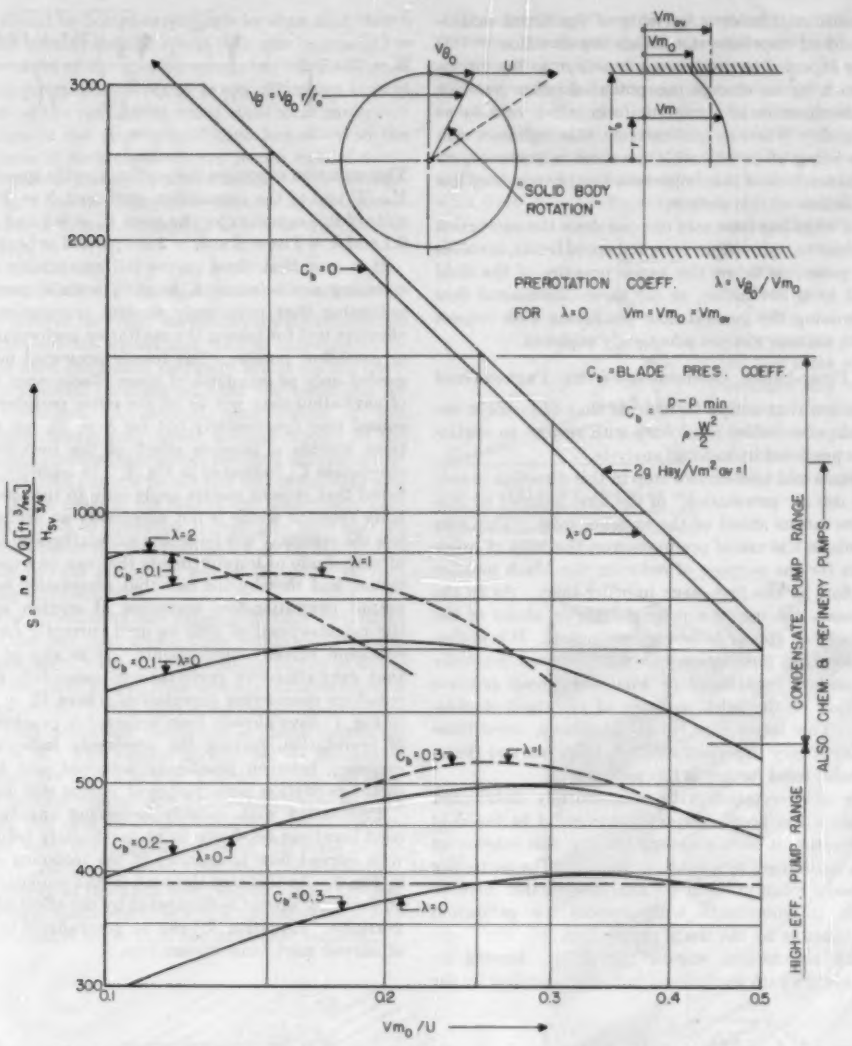

FIG. 1 RELATION BETWEEN SUCTION SPECIFIC SPEED (S) AND BLADE PRESSURE COEFFICIENT (C_b) FOR CENTRIFUGAL AND AXIAL-FLOW PUMPS

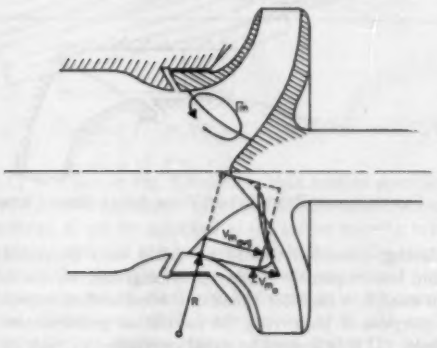

FIG. 2 STANDARD CENTRIFUGAL PUMP-IMPELLER INLET

far higher values of C than assumed and therefore to less favorable S-values than indicated by the solid curves in Fig. 1. This consideration therefore tends to widen the apparent gap between empirical pump-performance data and theoretical expectations. To make it worse, very satisfactory results in cavitation performance as well as in efficiency have been obtained by designing the inlet edges of the impeller vanes for a constant value of $V_m = V_{m\,avg}$ as determined by the condition of continuity. This standard design practice indicates that the present status of the theory of impeller inflow design can hardly justify the assumption of close agreement between the flow and the direction of the vanes as implied by the low values of the vane pressure coefficients C_b that correspond to the empirical data on centrifugal pump performance.

A likely compensating action by the impeller vanes can be shown to result from the fact that the bound vortex lines of the vanes have an inclination against radial planes in such a manner

as to give the meridional inflow a vorticity of significant magnitude. With standard impeller-vane design the direction of this vorticity may be expected to produce a circulation in the meridional flow Γ_m such as to change the potential inflow velocity distribution in the direction of a more uniform inflow velocity as indicated in Fig. 2. Whereas qualitatively this influence can be estimated as being of considerable practical importance, no adequate rational analysis of this important flow phenomenon has come to the attention of this author.

On the basis of what has been said one can draw the conclusion that operation close to, but within accepted speed limits, involves either (*a*) local pressures below the vapor pressure of the fluid (tension), or (*b*) local cavitation, or (*c*) three-dimensional flow phenomena improving the general flow conditions with respect to cavitation in a manner not yet adequately explored.

Analysis of Pump-Inlet Conditions With Prerotation

The first question that comes to mind is that of possible improvements in impeller inflow conditions with respect to cavitation that may be predicted by rational analysis.

The most obvious and best-known step in this direction is connected with the use of "prerotation" of the fluid induced by stationary, directive means ahead of the impeller inlet. This idea is quite analogous to the use of prerotation at the inlet of axial-flow compressors for the purpose of reducing the Mach number of the relative flow at the first-stage impeller inlet. As in the case of compressors, the use of a potential vortex ahead of the impeller inlet does not appear to be very promising. It is probably for this reason that prerotation has not yet been generally employed in standard centrifugal or axial-flow pump practice with the exception of the inlet passages of standard, double-suction pumps. This latter case, in all likelihood, constitutes hydrodynamically a very imperfect solution, however, and therefore will not be considered further in this paper.

Since the use of prerotation with nonuniformly distributed angular momentum has been reasonably successful in the field of axial compressors, it seems natural to try this scheme in connection with centrifugal or axial-flow pumps. The particular case of "solid-body rotation" will be analyzed further here to explore possible improvements with respect to cavitation performance obtainable by the use of prerotation.

The flow with nonuniform angular momentum leaving an axial-flow vane system with irrotational inflow is described by the equation

$$V_\theta\left(\frac{\partial V_\theta}{\partial r}+\frac{V_\theta}{r}\right)+V_m\frac{\partial V_m}{\partial r}=0 \qquad [5]$$

which is derived in several recent publications.[5] Integration of this equation under the special assumption of a solid-body rotation as pictured in the upper right-hand corner of Fig. 1, leads to

$$\frac{V_{m\,avg}}{U}=\frac{V_{m0}}{U}\frac{1}{3}\frac{1}{\lambda^3}\left[(2\lambda^3+1)^{1.5}-1\right] \qquad [6]$$

For the case of prerotation, Equation [3] when applied to the outer periphery of the inflow passage can be written in the following form

$$\frac{2gH_{sv}}{U^2}=(C+C_b)(1+\lambda^2)\frac{V_{m0}^2}{U^2}+C_b\left(1-2\lambda\frac{V_{m0}}{U}\right) \qquad [7]$$

Substitution of Equations [6] and [7] into Equation [1*a*] leads to the following expression

$$S=384.5\,\frac{\sqrt{\frac{V_{m0}}{U}}\frac{1}{\lambda}\sqrt{\frac{1}{3}\left[(2\lambda^3+1)^{1.5}-1\right]}}{\left[(C+C_b)(1+\lambda^2)\frac{V_{m0}^2}{U^2}+C_b\left(1-2\lambda\frac{V_{m0}}{U}\right)\right]^{3/4}} \qquad [8]$$

This equation expresses the suction specific speed as a function of V_{m0}/U and of the prerotation coefficient $\lambda = V_{\theta 0}/V_{m0}$. The results of this equation for the cases $C_b = 0.3$ and $\lambda = 1$, and $C_b = 0.1$ and $\lambda = 1$ as well as $\lambda = 2$ are plotted as broken lines in Fig. 1

It is seen that these curves fall appreciably above the corresponding curves (same values of C_b) without prerotation ($\lambda = 0$), indicating that judiciously applied prerotation is certainly an effective tool for raising the cavitation performance of centrifugal or axial-flow pumps. The results presented here should be regarded only as estimates of these effects since the critical point of cavitation may not lie at the outer periphery passage as assumed here (particularly not for $\lambda = 2$), nor do these calculations include a possible effect of the impeller blade induced circulation Γ_m indicated in Fig. 2. In addition, it will be remembered that present results apply only to the special case of solid-body rotation which is not necessarily an optimum. Nevertheless the results of the foregoing calculations do indicate the order of magnitude of improvements that can be expected from prerotation, and thereby the fact that prerotation is not sufficient to permit cavitation-free operation at suction specific speeds in the neighborhood of 1000 as used currently for pumps with exceptional suction requirements. It is also of interest to note that cavitation-free performance tentatively predicted by calculations considering prerotation (curve $C_b = 0.3$ and $\lambda = 1$, in Fig. 1) have already been achieved in practice without the use of prerotation, leaving the previously indicated apparent discrepancy between practically achieved and theoretically predicted cavitation performance of pumps still unanswered.

Prerotation with radially increasing angular momentum (as used here) can be shown to be particularly helpful in connection with curved flow boundaries of the incoming stream, as shown in Fig. 2. In this case the peak in the potential V_m-distribution at the outer shroud is eliminated by the effect of prerotation with vorticity. Equation [5] can be generalized[6] to include the case of curved meridional streamlines.

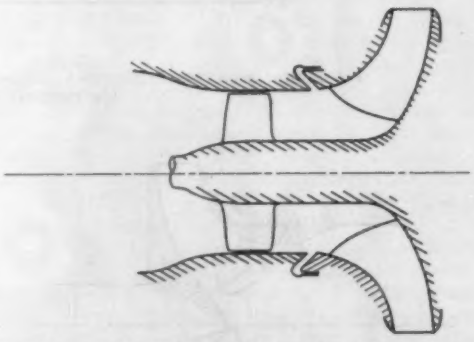

Fig. 3 Centrifugal Pump Inlet With Axial-Flow "Inducer"

In passing, attention should be called to a frequently proposed, but less frequently employed, arrangement shown in Fig. 3, using an axial-flow impeller ahead of the radial-flow impeller inlet for the purpose of improving the cavitation performance of the entire unit. If it is desired to avoid cavitation in both impellers within customary limits there is no reason why the arrangement

[5] "A Practical Solution of a Three-Dimensional Flow Problem of Axial-Flow Turbomachinery," by L. H. Smith, Jr., S. C. Traugott, and G. F. Wislicenus, Trans. ASME, vol. 75, 1953, p. 789.

shown in Fig. 3 should be better cavitationwise than that shown in Fig. 2 since the suction specific speed that can be reached is essentially independent of the specific speed, i.e., of the type of the pump impeller involved. If there is any difference then it would be in favor of the radial-flow wheel since local cavitation near the inlet edges of the vanes would have less effect on the over-all performance of such a wheel than in the case of axial-flow machines of more or less conventional design. The arrangement shown in Fig. 3 has therefore no foreseeable advantage unless a different form of flow is considered as will be discussed in the following section.

Pump Operation With a Fully Developed Cavitation

The previously derived fact that conventional pump operation at advanced suction specific speeds may well be expected to involve considerable local cavitation naturally brings up the question whether pumps could be designed from the beginning for operation with cavitation. A rational consideration of this question is relatively simple only under the assumption of the extreme case of fully developed cavitation, meaning the case where the vapor-filled cavitation pockets do not end within the vane system considered. There exists in the field of turbomachinery only one case where this form of operation is regularly used and intended, namely, the case of the Pelton-type water turbine. The reversal of its principle for pump use will be the principal subject of the following considerations.

The incentive for considering the extreme of fully developed cavitation lies in the fact that under these conditions substantially higher suction specific speeds, and thereby higher absolute speeds of rotation can be employed than under conditions covered by conventional practice. In the light of the foregoing considerations the case of fully developed cavitation is characterized by the condition $C_h = 0$. The suction specific speeds obtainable under this condition are shown in Fig. 1 as an inclined straight line for the most natural case of zero prerotation ($\lambda = 0$). As would be expected, this case involves a rapid increase of the suction specific speed with diminishing values of the ratio of the axial-flow velocity V_m to the peripheral velocity U of the runner, since the kinetic energy of the axial flow (multiplied by the previously used correction coefficient $C = 1.1$) is the only reason why the pressure in the fluid is lower than the total inlet head H_{sv}.

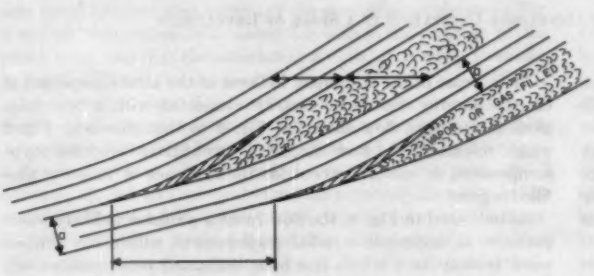

Fig. 4 Cascade Flow With Fully Developed Cavitation

The $C_h = 0$ line in Fig. 1 indicates that suction specific speeds in excess of 3000 (in excess of 60,000 in the more conventional gpm units of S) can be achieved as the inflow velocity is reduced to about one tenth of the peripheral velocity of the runner. It thus follows that by this form of operation one should be able to achieve speeds two to six times higher than under present-day empirical limitations. Still lower values of V_m/U and correspondingly higher suction specific speed appear to be entirely possible.

The previously mentioned analogy to the Pelton turbine indicates the essential difficulty connected with the use of fully developed cavitation for pump operation. It can be seen that in the pump case such operation necessarily involves the conversion of the kinetic energy of vapor or gas-bounded free jets into static pressure, a problem for which we can today no more than guess at possible methods for its practical solution.

Fig. 4 shows the rather obvious form of two-dimensional flow with fully developed cavitation in a cylindrical section through an axial-flow runner.[6] Since the jets are bounded by vapor or gas-filled regions the mean velocity in these jets before entering and after leaving the vane system must necessarily be the same except for minor changes due to fluid friction. Disregarding the latter, a typical velocity diagram for two-dimensional cascade flow with fully developed cavitation is shown in Fig. 5. The practically most essential characteristic of this form of flow appears to be the fact that the entire work input to the flow by the runner manifests itself in an increase in the kinetic energy of the

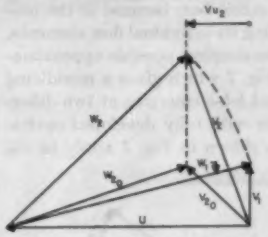

Fig. 5 Velocity Diagram of Two-Dimensional Cascade Flow With Fully Developed Cavitation

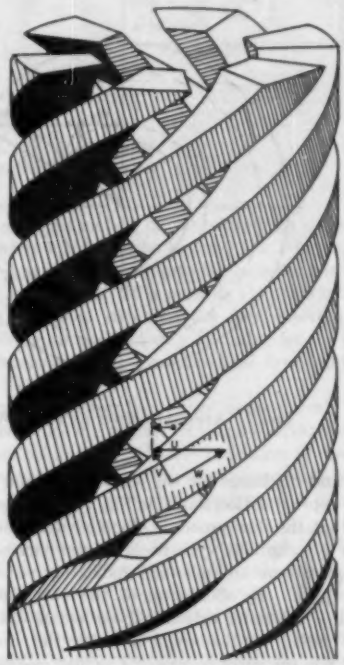

Fig. 6 Helical Free-Jet Discharge From an Axial-Flow Runner
(Disregarding distortion and radial flow.)

[6] For the case of cascades with straight and parallel vanes, this flow has been investigated by Betz and Petersohn by means of the Hodograph method as early as 1931,[7] giving very useful theoretical and some experimental data.

[7] "Anwendung der Theorie der Freien Strahlen" (Application of the Theory of Free Jets), by A. Betz and E. Petersohn, *Ingenieur-Archiv*, vol. 2, 1931, pp. 190–211.

absolute flow. To better visualize the problem of the conversion of this energy into static pressure, Fig. 6 shows a highly simplified picture of the form of the flow leaving such a runner. In this flow, only the relative velocity coincides with the direction of the helical elements of this flow, whereas the absolute motion is more or less normal to the direction of these elements. In other words, the entire flow configuration shown in Fig. 6 rotates with its front part moving from right to left, and at the same time moves axially up as indicated by the velocity diagram.

The rotating motion of this system immediately indicates that this flow configuration cannot be stable but, because of the uniformity of static pressure surrounding its individual flow elements, must move radially outward. The simplest possible approximation for this motion is shown in Fig. 7 which gives a meridional picture of two streamlines *a-a-a* and *b-b-b* emerging at two different radii from an axial-flow runner with fully developed cavitation. The two velocity diagrams shown in Fig. 7 apply to the runner inlet and discharge for the sections *a-a* and *b-b*, respectively. The approximation shown in Fig. 7 is based on the simple assumption that the flow proceeds along straight lines in planes tangential to the originally cylindrical stream surfaces, although closer approximations are possible, indicating some curvature of this flow path. By this motion, the entire flow will be crowded against the outer cylindrical surface of the casing thus progressively filling up the voids between the flow elements shown in Fig. 6 in the outer regions. The flow eventually should form a "solid ring" at the outer wall with the gas or vapor collected in the inner region of the space between the casing and the hub.

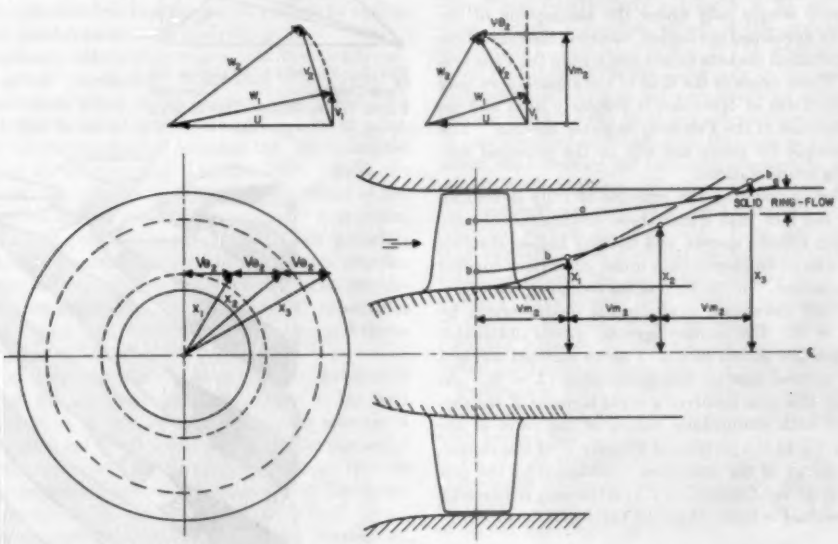

FIG. 7 APPROXIMATION OF FLOW WITH FULLY DEVELOPED CAVITATION IN A SPACE OF REVOLUTION

It is entirely possible that the form of flow with fully developed cavitation just described offers a practical method by which one could derive some distinct advantages from the arrangement shown in Fig. 3, whereby the centrifugal part of this runner arrangement receives a solid flow from the outer "ring" space indicated in Fig. 7, whereas the axial-flow impeller operates with fully developed cavitation. It should be understood that the real problem, however, is not nearly that simple as obviously the dynamics of the flow approaching the solid ring in Fig. 7 offers some very interesting and at best incompletely understood problems.

Referring to the velocity diagrams in Figs. 5 and 7, it is seen that the velocity of the stream discharging from an axial-flow impeller with fully developed cavitation has in this case a greater axial than peripheral component. Fig. 7 indicates how this discontinuous stream may be expected to transform itself into a "solid-ring flow" that may then be fed to a vane system with noncavitating flow. However, the problem of how the high kinetic energy of this stream can be converted into static pressure is as yet unanswered.

One answer to this problem appears possible in the alternate case where the peripheral component of the discharging stream is decidedly greater than its axial component, because the kinetic energy of the peripheral component could be recovered in a radially expanding diffuser away from the free surface (inner boundary) of the ring flow.

An increase of the peripheral in favor of the axial component of the discharging flow is necessarily connected with a transition from the form of flow shown in Fig. 4 to that shown in Fig. 8 which resembles the flow through conventional "impulse"-type compressors or turbines except for the existence of vapor or gas-filled regions.

As indicated in Fig. 8, the flow in such a runner is likely to experience an appreciable radial displacement within the runner-vane system itself which has been estimated here qualitatively by the same means as explained in principle in connection with Fig. 7. Generally, the three-dimensional problem of flow with an open boundary may be tractable on the basis that "a surface of constant pressure must be normal to a surface containing the resultant curvature of the absolute flow" (in other words, normal to the radii of the resultant curvature of the absolute streamlines).

It may be possible to discharge this flow from the vane system rather smoothly into a ring flow which subsequently can be handled in a vaneless diffuser followed in the example given here by a volute-type collector.

The foregoing considerations on the cavitation characteristics

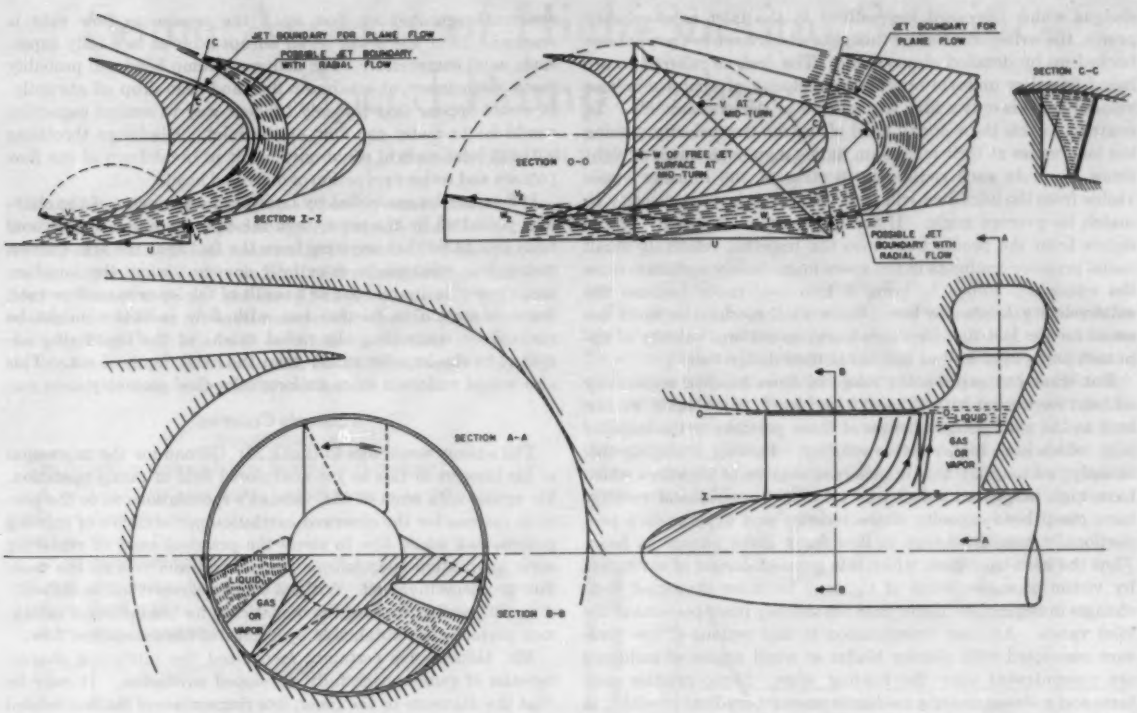

FIG. 8 "IMPULSE" PUMP WITH FULLY DEVELOPED CAVITATION

of pumps with fully developed cavitation have indicated that the greatest benefit of this form of operation results from the use of low values of V_m/U. Using therefore a value of 1/10 for this ratio one arrives at the conclusion that with a resulting suction specific speed of about 3500 one obtains a ratio of the pump head H to the total inlet head H_{tv} of approximately 270, and a specific speed of the unit in the neighborhood of 45 (capacity measured in cu ft per sec). This rather high head ratio and low specific speed indicate that pumps of the arrangement shown in Fig. 8 are by themselves best suited for rather high values of the pump head, and that the addition of a radial-flow wheel as shown in Fig. 3, will rarely be necessary.

In closing, it may be of interest to consider an example of specific operating characteristics for a pump as shown in Fig. 8. Assuming a total inlet head H_{tv} = 20 ft and a rate of flow Q = 3 cfs, one arrives at a pump head of over 5000 ft at a pump speed between 15 and 20 thousand rpm and a runner diameter in the neighborhood of 4.5 in. The casing may have an outside diameter of 10 in. The power consumption of this pump if handling water would be in the neighborhood of 2000 hp at an arbitrarily assumed efficiency of 70 per cent. The practical significance of such a machine with respect to weight, size, and cost in connection with steam or gas-turbine drive appears rather obvious.

SUMMARY AND CONCLUSIONS

The results of the foregoing considerations may be summed up as follows:

1 It is to be expected that standard centrifugal or axial-flow pumps when operating near conventional cavitation limits are not free from local cavitation or local pressures below the vapor pressure of the fluid pumped. This fact may be of practical importance with respect to cavitation erosion when using unusual liquids such as liquid metals, or unusually high velocities of flow.

2 Conclusion 1 is tentative because the interaction between the impeller vanes and the inflow to the impeller has not yet been adequately investigated. It is possible that this interaction has a corrective, beneficial effect on the flow entering a standard centrifugal-pump runner, and may be usable for the achievement of further improvements. Its theoretical investigation appears imperative.

3 The use of prerotation with nonuniformly distributed angular momentum will permit significant advancements in the limits of predictable cavitation-free operation of centrifugal and axial-flow pumps. However, these advancements alone cannot be expected to meet foreseeable requirements for greatly advanced suction specific speeds.

4 Pump operation with fully developed cavitation offers serious possibilities of *major* advancements in the suction specific speed of centrifugal and axial-flow pumps. The principal unsolved flow problems connected with this form of operation lie in the field of open-surface (constant-pressure boundary) flow under various three-dimensional conditions encountered in turbomachinery.

Discussion

F. C. GILMAN.[3] In this thought-provoking paper the author raises some questions for which answers may not be found for some years to come. Nevertheless, the stating of these mysteries will stimulate and guide the increasing number of investigators who are working in this field.

Regarding the strangely good cavitation performance of certain

[3] Research Engineer, Worthington Corporation, Harrison, N. J. Mem. ASME.

designs which disregard inequalities in the inlet axial-velocity profile, the writer offers some thoughts which have not as yet been backed up by detailed observation. The designs referred to are based on a low uniform nonrotating velocity of approach whose velocity head is only a fifth to a quarter of the available H_{sv}. In contrast to this the velocity head of the relative velocity passing the inlet vanes at their maximum radius may be as much as eight times H_{sv}. At each radius the portion of the impeller vanes visible from the inlet duct will tend to control the inlet velocity to match its average angle. If the upstream axial-velocity profile differs from the profile built into the impeller, relatively small radial pressure gradients in the space immediately upstream from the vanes will suffice to bring it into conformity because the axial-velocity heads are low. Some such mechanism must account for the fact that impellers based on uniform velocity of approach perform as well as they do at their design flow.

But what can explain the range of flows handled apparently without cavitation with $C_b = 0.2$ and less? Here again we can look to the stabilizing influence of those portions of the impeller inlet which have high relative velocity. Putting it slightly differently, we may say that impellers or regions of impellers which have high tangential velocity in relation to meridional velocity have steep head-capacity characteristics and experience a proportionally smaller change in flow for a given change in head. Thus the inlet-tip region, which is in greatest danger of cavitation by virtue of a low value of C_b, may be more protected from changes in angle of incidence than the radially inner portions of the inlet vanes. Another consideration is that regions of low pressure associated with slender blades at small angles of incidence are concentrated near the leading edge. Here, cavities may form and collapse under a moderate pressure gradient resulting in little effect whether of noise, damage, or performance change.

The author's intriguing suggestion for a pump which might be said to have descended from the rotary snow plow immediately raises the question in a pump man as to what the head-capacity characteristic might be. If first we consider the case of constant speed and no inlet rotation then the Euler head should remain constant regardless of flow until the maximum flow rate is reached. Here there will be an abrupt limit as in a fully supersonic axial compressor. The delivered pump head will probably reach a maximum at maximum flow and then drop off abruptly. It would appear that the only efficient way to control capacities would be to meter the flow at the inlet. Discharge throttling without inlet control could only result in breakdown of the flow pattern and serious reduction of delivered head.

If flow can be controlled by limiting the thickness of the shavings peeled off by the rotor, then the only reduction in delivered head should be that resulting from the fact that the skin-friction power loss will remain essentially constant while the impeller-input power is diminishing as a result of the lower mass-flow rate. Some reduction in friction loss with flow reduction might be realized by controlling the radial extent of the liquid ring admitted to the impeller rather than the axial depth of cut. This also would maintain more uniform inlet-flow geometry.

Author's Closure

The author would like to thank Mr. Gilman for the expression of his interest in this as yet unexplored field of pump operation. He agrees with most of Mr. Gilman's speculations as to the possible reasons for the observed cavitation performance of existing pumps, but would like to stress the practical need of replacing such qualitative speculations by rational analyses of the basic flow problems involved. Without such analyses it will be difficult, if not impossible, to design systematically for the optimum cavitation performance obtainable by means of cavitation-free flow.

Mr. Gilman has certainly recognized the intriguing characteristics of pumps with fully developed cavitation. It may be that the diameter of the inner, free ring surface of the flow behind the impeller has an additional influence on the head-capacity characteristics of this type of pump, but the existence of a stable, free flow surface under the conditions described is as yet by no means assured. In other words, an as yet quite unexplored field of fluid mechanics is involved, namely, that of open surface flow in a centrifugal field.

Some Aspects of High-Suction Specific-Speed Pump Inducers

By C. C. ROSS[1] and GORDON BANERIAN,[2] AZUSA, CALIF.

Some aspects of the design and performance characteristics of high-suction specific-speed pumps (cavitating inducer) are discussed. Although conventional pump-suction specific speeds are limited by incipient cavitation limits, the properly designed cavitating inducer can operate at values of suction specific speeds many times that limited by incipient cavitation. Owing to the restricted nature of this material, the authors regret leaving out much of the design information.

Nomenclature

The following nomenclature is used in the paper:

A = axial flow area inside impeller entrance, ft²
D = diameter, ft
F = thrust, lb
g = gravitational constant, ft/sec²
h_{sv} = suction head above vapor pressure, ft
H = head rise, ft
k = impeller-vane coefficient
k_a = vane area correction factor = $\frac{4A}{\pi D_t^2(1-r^2)}$
N = shaft speed, rpm
N_s = specific speed, $\frac{\text{rpm} \times \text{gpm}^{1/2}}{\text{ft}^{3/4}}$
P = pressure, psia
Q = volume flow rate, gpm
r = impeller diameter ratio, hub to tip
R = radius, ft
S = suction specific speed, $\frac{\text{rpm} \times \text{gpm}^{1/2}}{\text{ft}^{3/4}}$
t = time, sec
U = velocity, impeller vane, fps
V_a = velocity, absolute, fps
W = velocity, fluid, relative to impeller, fps
β = vane angle, deg
η = efficiency, per cent
ρ = mass density, slugs/ft³
Δh = head drop resulting from axial velocity of fluid to vane, ft
Δh_1 = head drop due to relative velocity of fluid after entering impeller, ft

Subscripts

c = centrifugal impeller
i = inducer
m = meridional
o = optimum
t = tip
1 = initial
2 = final

Introduction

The use of various devices to improve the suction characteristics of centrifugal pumps is important in many applications. To accomplish an improvement in the suction characteristics at a minimum addition of weight, minimum loss in over-all efficiency, and with minimum complexity, is of particular interest to the rocket-engine designer. In the case of rocket engines, it has been demonstrated that the suction specific-speed parameter is a prime variable in determining the total dry weight of a complete power plant. Fig. 1, which is reproduced from another paper,[3]

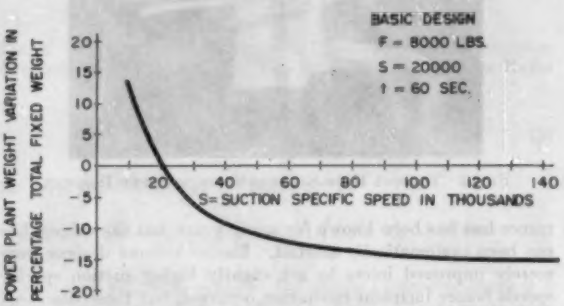

Fig. 1 Curve Showing Total Power-Plant Weight Variation as a Function of S

shows this general relationship. In more conventional applications, improvements in suction characteristics are desirable for such items as boiler feed pumps and similar applications in which liquids with high boiling points are pumped. Improvement of the pump-suction characteristic is reflected in the increased values of suction specific speed

$$S = \frac{NQ^{1/2}}{h_{sv}^{3/4}}$$

at which a pump can be designed to operate.

It is noted that improvement in suction characteristic will permit an initial design to operate at a higher rotative speed or at a lower value of h_{sv} as compared with a pump having conventional suction characteristics. In the rocket application the higher rotative speed is reflected in lower pump weight and in conventional applications the higher speed may result in a lower-cost unit or a unit which is more adaptable for use with high-speed drives such as turbines and universal electrical motors.

Higher suction specific speed may be obtained by a variety of methods, such as the employment of double-suction pumps or jet pumps which circulate part of the high-pressure discharge fluid back to the inlet in order to add momentum to the incoming fluid, viscous-drag inducers that add momentum with a minimum

[1] Manager, Liquid Engine Division, Aerojet-General Corporation. Mem. ASME.

[2] Principal Engineer, Head of Rotating Machinery, Aerojet-General Corporation. Mem. ASME.

Contributed by the Hydraulic Division and presented at the Diamond Jubilee Annual Meeting, Chicago, Ill., November 13–18, 1955, of The American Society of Mechanical Engineers.

Note: Statements and opinions advanced in papers are to be understood as individual expressions of their authors and not those of the Society. Manuscript received at ASME Headquarters, August 25, 1955. Paper No. 55—A-124.

[3] "Principles of Rocket Turbopump Design," by C. C. Ross, *Journal of the American Rocket Society*, no. 84, March, 1951, pp. 21–33.

of disturbance to the fluid, slow-speed boosters geared to the main drive, vapor-separator impellers, "cavitating inducers," and combinations of these devices.

Of all the methods mentioned, the cavitating inducer appears promising for many applications and represents the latest approach for obtaining high-suction specific speeds. The employment of inducers to induce the fluid with the least amount of entrance loss has been known for many years, but the subject has not been systematically studied. Earlier inducer designs were merely improved inlets to get slightly higher suction specific speeds before incipient cavitation occurred, but those discussed in this paper operate with considerable cavitation. The data reported in this paper are introductory and represent only a portion of the work accomplished and of that yet to be done. The simple design considerations of inducers are relatively easy to cover, but the more complex problems of optimization from the standpoint of minimum cavitation damage, and maximum efficiency require further investigation as will be seen from the ensuing discussion.

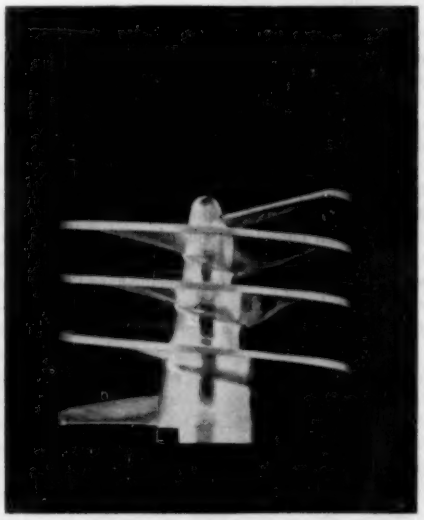

FIG. 2 TYPICAL HIGH-SUCTION SPECIFIC-SPEED INDUCER

In radial impellers it is customary to design the leading edge of the vanes for both the hub section and outside surface section at nearly the same radius, so that when incipient cavitation occurs the entire blade section at the entrance begins to cavitate simultaneously. On the other hand, in axial impellers, the tip usually cavitates first, and since this section then no longer develops as much pressure as sections near the hub, secondary flows within the impeller tend to adjust the flow velocities to correct for the shortcomings of the tip section, and the impeller continues to pump under slightly adjusted conditions. When the suction pressure is dropped further to the point at which most sections of the impeller are cavitating, the pump fails to generate pressure unless the impeller is specifically designed to handle the saturated vapor.

The primary function of an inducer is to act as a specially designed axial stage which will operate with cavitation and gradually add momentum to the fluid as it enters advanced sections until the vapor is recompressed and rapid momentum addition can be made as in a conventional impeller. Fundamentally, these conditions imply long passages, with certain sections of the blade operating under cavitating conditions. In turn, the long passages mean added frictional losses and consequent reduction in over-all efficiency. Also, the presence of cavitation is conducive to possible damage. Experiments and practical use of inducers have shown that these shortcomings can be minimized and that lower efficiency and the possibility of damage are more than compensated for by the improvement in suction conditions for some of the applications mentioned. Fig. 2 shows a typical inducer used in a rocket turbopump installation.

INLET CONDITIONS

The first consideration in the design of the inducer is the inlet condition which will be based on the case of fluid flow with no prerotation as shown in Fig. 3. Theoretically the total inlet pressure is available to accelerate the liquid into the impeller, but in order for the pressure just inside the inlet section to exist below vapor pressure, the liquid would have to be capable of supporting tension. Under the highly agitated conditions of the impeller entrance and because of impurities in the liquid, this is not possible, and the fluid enters the vapor phase at fluid vapor pressure. Thus it follows that for an impeller designed to operate with cavitation the passage areas must be increased to accommodate the lower density saturated vapor. Ordinarily only the net positive suction head (the difference between the total inlet pressure and the vapor pressure of the fluid) is considered available to induce the flow into the impeller.

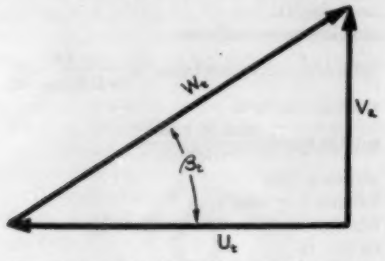

FIG. 3 INDUCER INLET-VELOCITY DIAGRAM

A useful parameter for describing pump suction conditions[4,5] is the suction specific speed

$$S = \frac{NQ^{1/2}}{h_{sv}^{3/4}} \quad \ldots\ldots [1]$$

This parameter can be rewritten in terms of the inlet geometry condition and the volume flow as

$$S\left(\frac{1}{1-r^2}\right)^{1/2} = \frac{1897\left[\frac{Q}{ND_t^3}\left(\frac{1}{1-r^2}\right)\right]^{1/2}}{\left\{0.00293\left(\frac{1+k}{k_a^2}\right)\left[\frac{Q}{ND_t^3}\left(\frac{1}{1-r^2}\right)\right]^2 + k\right\}^{3/4}} \quad \ldots\ldots [2]$$

where k is the impeller vane coefficient and k_a is the area correction factor due to vane interference.

The net h_{sv} for incipient cavitation can be considered to consist of two components, that which is caused by the axial velocity V_a of the fluid ($\Delta h = V_a^2/2g$), and that which is caused by the relative velocity W of the fluid to the impeller vane ($\Delta h_1 = kW^2/2g$).

[4] "Fluid Mechanics of Turbomachinery," by G. F. Wislicenus, McGraw-Hill Book Company, Inc., New York, N. Y., 1947.

[5] "Die Kreiselpumpen," by C. Pfleiderer, Julius Springer-Verlag, Germany, 1949.

A plot of the suction specific speed parameter

$$S\left(\frac{1}{1-r^2}\right)^{1/2}$$

as a function of the design parameter

$$\frac{Q}{ND_t^3}\left(\frac{1}{1-r^2}\right)$$

is shown in Fig. 4 for constant values of k from 0 to 0.1, where k_a is assumed to have a value of unity.

Optimum Inlet Diameter

It can be noted from Fig. 4 that there is a maximum value of suction specific speed for every value of k and a corresponding optimum design parameter

$$\left[\frac{Q}{ND_{to}^3}\left(\frac{1}{1-r^2}\right)\right]_o$$

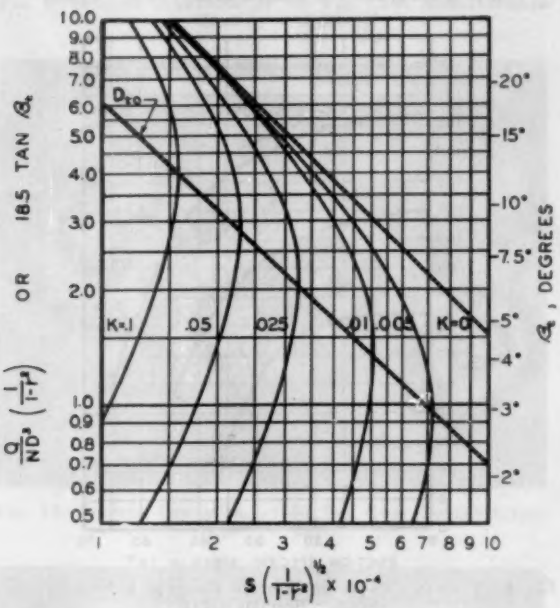

Fig. 4 Calculated Values of Inducer-Design Parameter as a Function of Suction Specific-Speed Parameter

By differentiating Equation [2] with respect to the design parameter and setting the result equal to zero, the following expression for the optimum inlet diameter is obtained

$$D_{to} = \frac{0.423\left[\frac{Q}{N}\left(\frac{1}{1-r^2}\right)\right]^{1/3}(k+1)^{1/6}}{k_a^{1/3}k^{1/6}} \quad \ldots\ldots [3]$$

Substituting Equation [3] into Equation [2], the expression for the maximum value of the suction specific speed is

$$S_{max} = \frac{5060\,k_a^{1/3}(1-r^2)^{1/2}}{k^{1/2}(1+k)^{1/6}} \quad \ldots\ldots [4]$$

The effect of the hub-to-tip diameter ratio on S_{max} and D_{to} is shown in Fig. 5, which applies for constant values of k and k_a.

From the foregoing relationship it can also be shown that

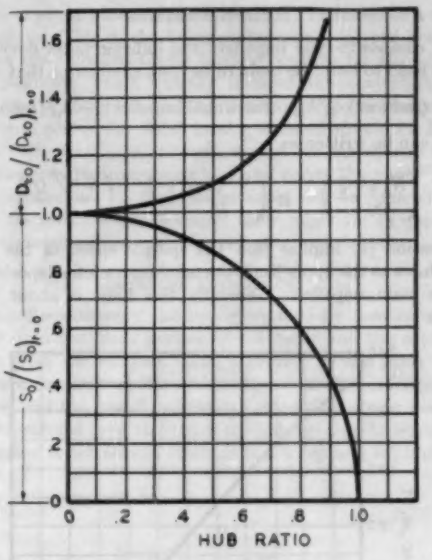

Fig. 5 Ratios of Optimum Inducer-Inlet Diameter and Suction Specific-Speed Values as a Function of Inducer-Hub Ratio

$$\tan\beta_t = \frac{V_a}{U_t} = 0.0541\,\frac{Q}{ND_t^3}\left(\frac{1}{1-r^2}\right) \quad \ldots\ldots [5]$$

for shockless entrance at the blade tip, or

$$18.5\tan\beta_t = \frac{Q}{ND_t^3}\left(\frac{1}{1-r^2}\right) \quad \ldots\ldots [6]$$

Therefore for every value of the design parameter there is a given β_t, values of which are shown in Fig. 4. Test results show that angles up to 2 deg greater than that required for shockless entrance (zero angle of incidence) are necessary at the optimum diameter. This is perhaps due to prerotation.

If incipient cavitation were the only prerequisite to limitations on S, then it follows that, by taking the best value of k from streamlined-body tests, S would be limited to values of around 15,000 for conventional centrifugal pumps. Usually, however, lower values of S are encountered in conventional centrifugal pumps. Fortunately, incipient cavitation does not limit S in well-designed inducers, since the well-designed inducer gradually recompresses the vapor into the liquid state before the fluid leaves the impeller.

Determination of the optimum inlet diameter for cavitating conditions would be rather difficult owing to the complicated nature of the mixed-phase flow, but test data show that the behavior of the flow and the diameter requirement are nearly in accordance with the simplified theory. A point to be noted from Fig. 4 is that the general type of curves applies not only to incipient cavitation but also to fully cavitating flow up to the point of complete breakdown, corresponding to the lower values of k.

In applying the results to the determination of the optimum inlet diameter required, it is necessary to estimate the hub-to-tip diameter ratio, r. The diameter ratio is generally dictated by mechanical design considerations. The suction specific-speed parameter can be evaluated from the desired suction specific speed and the diameter ratio, r. The optimum eye diameter can be determined from Fig. 4 where Q and N are known from the optimum value of design parameter corresponding to the maximum value of suction specific-speed parameter.

Head Generation

For composite-type impellers the inducer must develop sufficient head to keep the main rotor from cavitating, that is

$$H \text{ (inducer)} \geq h_{sv} \text{ (centrifugal impeller)} - h_{sv} \text{ (inducer)}$$

which can be written as

$$\left(\frac{N\sqrt{Q}}{N_{si}}\right)^{4/3} \geq \left(\frac{N\sqrt{Q}}{S_c}\right)^{4/3} - \left(\frac{N\sqrt{Q}}{S_i}\right)^{4/3} \quad \ldots\ldots [7]$$

Equation [7] implies that the specific speed of the inducer must have as the upper limit the maximum suction specific speed of the main impeller. Generally this limit is about 8000 to 13,000.

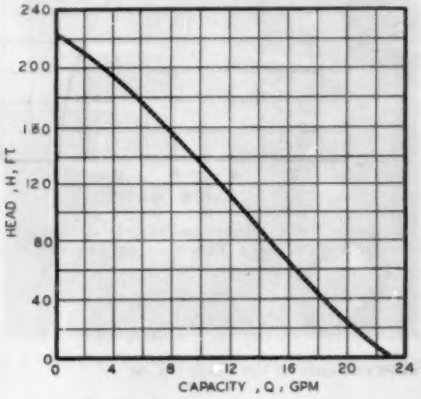

Fig. 6 Typical Inducer Head-Capacity Curve

The nature of the head-capacity curve or head-generated curve versus specific speed at constant suction specific speed depends on the geometry of the inducer, the design suction specific speed, and the specific speed. Fig. 6 shows a head-capacity curve for an inducer operating under noncavitating conditions. The curve is typical for pumps operating at design-point specific speeds of around 10,000.

A term which is useful in describing the performance of an inducer operating with cavitation is the "per cent noncavitating discharge head," which is defined as the ratio of the head generated under cavitating conditions to the head generated under noncavitating conditions for the same speed and capacity. Fig. 7 shows per cent of noncavitating discharge head versus operating specific speed at a constant suction specific-speed value of 30,000 for different types of inducers. The variations in performance that can be expected with different inducer designs are represented by curves A through C; of course, for most applications, design A would be desirable.

In some cases a plot of per cent head versus suction specific speed shows the head to rise as the inducer first begins to operate in the cavitation region, and gradually the head begins to fall off as the degree of cavitation increases. This is attributable to the decrease in friction resulting from a slight amount of cavitation, but as the intensity of cavitation increases, the mechanism of recompression, separation, etc., decreases both the efficiency and head generation. Fig. 8 shows typical curves of discharge head versus suction specific speed where lines of constant per cent of noncavitating head are also shown.

To observe the phenomenon of cavitation, a lucite housing was constructed to permit observation of pump tests. Figs. 9, 10, and 11 show an inducer in operation with decreasing values of

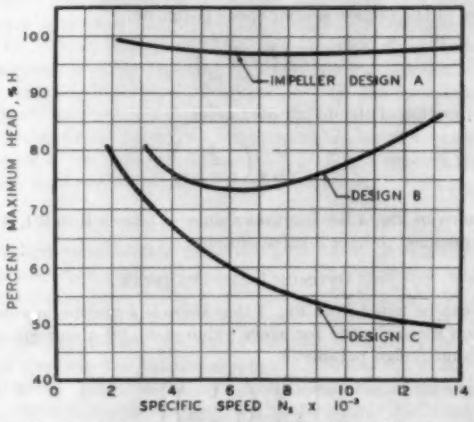

Fig. 7 Typical Values of Inducer Per Cent Noncavitating Head as a Function of Specific Speed for $S = 30{,}000$

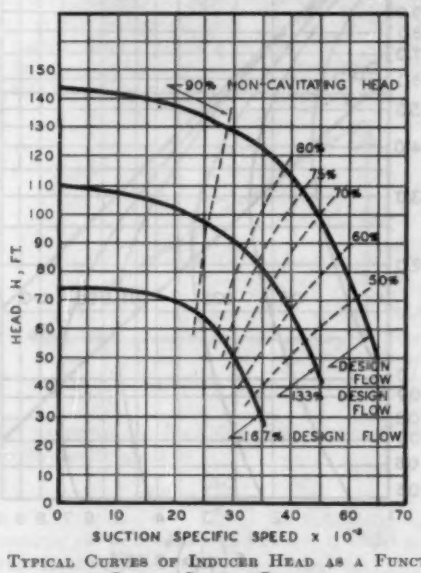

Fig. 8 Typical Curves of Inducer Head as a Function of Suction Specific Speed

suction pressure at the same capacity, and speed of rotation, showing per cent of noncavitating head and suction specific speed ranging from 100 to 36 per cent and 15,500 to 42,000, respectively. Note how the intensity of cavitation increases and also moves toward the exit of the impeller with increasing values of suction specific speed. When the cavitation reaches the exit, the discharge pressure falls off completely.

With fluid entering axially the head generated by backward curved vanes can be written as

$$H = \frac{U_m^2}{g}\left[1 - \frac{V_m}{U_m \tan \beta_m}\right] \quad \ldots\ldots [8]$$

for a given geometry, so that under noncavitating conditions the head drops with increasing flow, the flow being proportional to V_m. Under cavitating conditions, as the degree of cavitation increases with decreasing suction pressure, even though the flow is kept constant, the local V_m increases in order to pass the lower density fluid. Thus partial unloading of the blades occurs for

FIG. 9 INDUCER OPERATING AT 100 PER CENT NONCAVITATING HEAD (S = 15,500)

FIG. 10 INDUCER OPERATING AT 80 PER CENT NONCAVITATING HEAD (S = 25,000)

FIG. 11 INDUCER OPERATING AT 36 PER CENT NONCAVITATING HEAD (S = 42,000)

that portion of the passage length where V_m increases as a result of cavitation. This might be advantageous from one point of view since the unloaded blades tend to readjust for the adverse loading condition which initially induced the cavitation. If, near the end of the rotor, the vapor-mixture fluid is compressed to the liquid phase, the total head generated should be in accordance with the V_m at the exit, except for the change in efficiency that results from going into and out of the vapor phase within the impeller. If the passage areas can be controlled to keep the transition near isentropic, there might be an improvement in expected performance for present-day inducers.

IMPELLER EFFICIENCY

The impeller efficiency can be determined by combining the efficiency from the main portion of the rotor and the expected efficiency from the inducer. The efficiency of the main rotor portion is a function of the specific speed of that portion, the clearances, and the flow distribution leaving the inducer portion. What is considered to be the end of the inducer and the beginning of main rotor is not always obvious in a composite impeller design.

The net efficiency will be

$$\eta_{\text{total}} = \frac{H_{\text{total}}}{\frac{H_i}{\eta_i} + \frac{H_e}{\eta_e}} \quad \ldots\ldots\ldots\ldots\ldots\ldots [9]$$

Because of the long passages of an inducer, the efficiency is generally lower than would be expected of pumps of that same specific speed. Tests show that efficiencies ranging from 40 to 65 per cent can be expected from inducers.

Sometimes higher over-all efficiencies are obtained with inducers than were obtained for the main rotor before an inducer was incorporated. This is particularly true for very low specific-speed pumps that had originally a poor inlet design. As the over-all specific speed increases, the inducer supplies more of the total head, and hence the over-all efficiency is generally lower than for a pump of that same over-all specific speed without an inducer.

CAVITATION DAMAGE

The amount or degree of cavitation damage is determined by the pressure in the immediate vicinity of the cavitation, the dimensions of the cavity before and after collapse, the proximity of the cavity to the inducer surface at collapse, fluid, and material of construction, etc. No attempt will be made here to discuss the mechanics of cavitation, but the following simplified explanation will help to visualize an otherwise complicated phenomenon. Lord Rayleigh's equation for the collapse of the cavity indicates an approximate pressure resulting from the collapse of cavitation cavity to be

$$P_2 = 0.1575 \left(\frac{R_1}{R_2}\right)^3 P_1 \quad \ldots\ldots\ldots\ldots [10]$$

It is evident that very high pressures are obtained when the cavity collapses. However, with small amounts of gas entrained in the liquid, it is not likely that R_2 drops to zero. From Figs. 9 through 11 it can be seen that the foaming resulting from cavitation cannot be rigorously described by single-cavity approach. Test data on water show that when P_1 is less than 10 psi above vapor pressure, very little or no cavitation damage results. By controlling the vane shape, it is possible to produce a gradual pressure increase throughout the impeller. This increased pressure will tend to reduce the radius R_1 of the cavity and hence reduce the cavity collapsing pressure P_2. Also, by careful design

it may be possible to cause the cavity to collapse in the fluid instead of against the structure.

Conclusions

Almost all of the inducers tested have had the inlet area obstructed by 10 or 15 per cent by the impeller blades. The effect on performance resulting from impellers with fixed values of inlet-area obstruction and with one or more blades has not been completely evaluated. Neither has the effect on performance been completely determined resulting from varying the number of blades with the same value of solidity. The range of solidities tested has been from 2.5 to 3.5, with the ratio of length of inducer to diameter varying from 0.4 to 0.6. No optimization with respect to the foregoing parameters has been performed.

There is definite evidence that an outside shroud reduces the maximum suction specific speed obtainable from inducers. Apparently the flow over the impeller tips tends to unload the blades in the region of most severe cavitation. This also suggests the possibility that holes or slots in the blades in cavitation areas may permit blade unloading or even provide a fluid cushion against the blade surface against which the cavitation bubbles may collapse.

Scale factors of 2 or 3 do not materially affect over-all performance in the range tested, but for much larger scale differences, performance may be affected by the actual time required for the formation and collapse of the cavity.

The head developed by the inducer or impeller at each section definitely affects performance, since rapid turns, etc., can cause low local pressures and possible separation.

Discussion

F. C. Gilman.[6] The authors and their company are to be commended for making available to the pump industry as much as they have of this significant piece of pioneer work. Applications for high-suction specific-speed pumps which operate beyond the range of incipient cavitation are rapidly increasing with the variety of liquids being pumped. A few parts of the paper seem to need clarification, however.

In the introduction, it is suggested that improvements in suction characteristics are desirable for applications in which liquids with high boiling points are pumped. Is not the significant feature of the type of application that the suction pressure does not exceed the vapor pressure by a wide margin? Boiling point by itself has little significance.

The jet pump is mentioned as a means of increasing suction specific speed. Jet pumps which use a portion of the pumped liquid to increase impeller-suction pressure have a definite place where suction pressure as such needs to be boosted. This is usually in a low specific-speed range. Where high-suction specific speed is desired to achieve high specific speed, this method soon encounters the law of diminishing returns since the impeller must handle not only the quantity required externally but also a significant additional quantity for recirculation.

Under the subject of inlet conditions, the authors state that in an impeller designed to operate with cavitation the passage areas must be increased to accommodate the lower density saturated vapor. This gives the impression that the vapor demands space as would a noncondensable gas. With some liquids this actually may be so, especially if Stahl and Stepanoff[7] are correct in their claim that heat-transfer limitations control the rate of vapor evolution and collapse. When pumping liquids like cold water the vapor merely fills up the space avoided by the moving liquid. If we provide extra area in the passages it is because either we do not know just how the liquid is going to move or we know that under varying capacity the liquid will fill different paths and we try to provide for variation within the fixed geometry.

Equation [2] needs some correction as it appeared in the preprint. On the right side of the denominator of Equation [2] the factor $(1+k)/k_a^2$ should be replaced by $(k + k_a)$ if k_a is defined as in the preprint by

$$\Delta h_i = \frac{k_a V_a^2}{2g}$$

Equations [3] and [4] are also inconsistent with this definition of k_a.

The writer would urge the avoidance of the term "shockless" to indicate zero angle of incidence in turbomachines. The term shock should be reserved for the phenomenon of velocity and pressure discontinuity associated with supersonic flow.

The authors suggest that prerotation may be the reason why they find a slightly larger entrance-vane angle required than would correspond to zero incidence based on the approach axial velocity. It is the writer's view that unless the angle is increased to compensate for the area occupied by the vane, not only will an axial acceleration be required, but the same precentage increase will be needed in the much higher relative velocity.

The single-vane inducer form described in this paper results in minimum blockage for a given minimum vane thickness. It also provides a long passage in relation to cross section which is helpful for consolidating the liquid within the limits of the inducer. The length-over-width ratio at the root-mean-square radius appears to be about 50 which seems excessive from considerations of best efficiency. If actual cavitation can be tolerated without prohibitive damage, then one of the forms of impeller suggested by Dr. Wislicenus[8] would seem to offer an opportunity for a significant forward step in this field.

Authors' Closure

The authors appreciate the comments of Mr. F. C. Gilman. We are in agreement on the comments made relative to the jet pump.

The increase in inlet size, we feel, is required because the mean specific volume of the fluid increases as the intensity of the cavitation increases. The increase in specific volume may be considered to result from pure separation or vaporization. The vaporization may occur at a constant temperature (heat from external source being required) or expansion isoenthalpically beyond the saturated liquid line with no addition of heat being required. In either case, the velocity of the fluid is limited by the available ΔH to vapor pressure, but since the specific volume increased due to separation or vapor expansion, it follows that the area required to pass the flow must increase.

Tests were performed (with cold water) that confirmed the need for added area. Test data also showed (within experimental error) that the pressure in some areas dropped below vapor pressure. This factor would imply that the inlet area increase requirements be a function also of the properties of the fluid.

The Δh_i term as defined in the preprint of this paper was not used in the derivation of Equation [2]. The analysis was based on Δh_i and k_a as defined in the present text. The factor $(1 + k)/k_a^2$ in Equation [2] is therefore correct. However, Equations [2] and [3] as stated in the preprint were incorrect due to a typographical error. The typographical error consisted of the omis-

[6] Research Engineer, Worthington Corporation, Harrison, N. J. Mem. ASME.

[7] "Thermodynamic Aspects of Cavitation in Centrifugal Pumps," by H. A. Stahl and A. J. Stepanoff, published in this issue, pp. 1691–1693.

[8] "Critical Considerations on Cavitation Limits of Centrifugal and Axial Flow Pumps," by G. F. Wislicenus, published in this issue, pp. 1707–1714.

sion of required brackets which have been incorporated in the present text.

The slightly larger entrance vane angle can be explained in part by the area occupied by the impeller vane, but over and above this, an increase in entrance vane angle was noted to be necessary. Test data have shown that the highest suction specific speed for a given design was obtained for a lower value of flow than that required for zero angle of incidence, vane obstruction being considered.

It is true that the composite impeller with long passage length is lower in efficiency for the design specific speed than one designed with a shorter passage length; however, it was not possible to make the shorter impeller operate at as high a value of suction specific speed. It has also been observed that the short-vaned impeller received severe cavitation damage in a matter of minutes due to the more rapid turning, whereas many hours of operation have been attained with an impeller that has long passage with no visible cavitation damage.

The Design of Axial Flow Pumps[1]

By R. D. BOWERMAN,[2] PASADENA, CALIF.

A design procedure for axial-flow pump impellers is presented that accounts for induced interference effects in the prediction of performance. Induced interference velocities at an impeller blade have been calculated using a three-dimensional model that includes the effects of the other blades and of the total downstream vorticity along the center line of the pump. The design method considers improvement of cavitation conditions by specifying the radial variation of the design parameters such that the pressure distributions on all radial sections are similar. An analysis of optimizing the impeller geometric parameters for cavitation conditions is presented to permit the initial choices of the quantities appearing in the design procedure. Experimental work on a two-bladed impeller has yielded results that give good support to all aspects of the design method.

Nomenclature

The following nomenclature is used in the paper:

- a = annular area of impeller = $\pi(r_2^2 - r_1^2)$
- A, B = constants appearing in streamline equation
- C_θ = dimensionless tangential interference velocity = $\frac{V_\theta r_2}{\Gamma_b}$, given by the linearized equation $C_\theta = K_0 + K_1(\xi/\xi_t)$
- C_p = static head coefficient = $\frac{(h_2 - H_T)g}{u_2^2}$
- ΔC_p = static head differential coefficient
- C_L = lift coefficient
- C_{l_d} = design section lift coefficient
- c = chord
- g = gravitational constant
- H = head of impeller
- H_0 = free-stream total pressure, psi (as in reference 9)
- H_T = total head in impeller eye
- h_s = local static head
- K_0, K_1 = constants in equation for C_θ
- L' = lift force per unit width
- N = rpm
- n = number of blades
- P = local static pressure
- P_t = total pressure in impeller eye
- P_v = vapor pressure
- Q = flow rate, cfs
- q_0 = free stream dynamic pressure
- R = reaction
- r = radial co-ordinate
- S = blade pressure-distribution coefficient
- s = spacing = $2\pi r/n$
- T = torque
- u = impeller speed = ωr
- V = velocity
- V_R = relative velocity (average)
- V_θ = tangential component of interference velocity
- V_a = axial velocity (through-flow)
- x = co-ordinate along chord line
- y = co-ordinate perpendicular to chord line
- z = axial co-ordinate
- β = angle from horizontal
- β_c = blade angle (chord-line angle)
- Γ_b = circulation of a single blade
- Γ = total circulation value
- η = radius ratio = r/r_2
- η_1 = hub ratio = 0.6 for this work
- η^* = efficiency
- θ = angular co-ordinate, also camber angle
- ξ = dimensionless axial co-ordinate
- ξ_t = axial extent ratio = z_t/r_2
- ρ = fluid density
- σ = cavitation coefficient = $\frac{\text{NPSH}}{H} = -\frac{C_p}{\psi}$
- τ = torque coefficient = $\frac{T}{\rho a u_2^2 r_2}$
- ϕ = flow-rate coefficient = $V_a/u_2 = Q/au_2$
- χ_ω = speed coefficient = $\frac{\omega Q^{1/2}}{\pi^{1/2}(1-\eta_1^2)^{1/2}H^{3/4}g^{1/4}}$
- χ_{r_2} = size coefficient = $r_2\frac{H^{1/4}g^{1/4}\pi^{1/2}(1-\eta_1^2)^{1/4}}{Q^{1/2}}$
- ψ = head coefficient = $\frac{Hg}{u_2^2}$
- ψ' = input head coefficient = τ/ϕ
- ω = angular velocity
- c/s = solidity
- NPSH = net positive suction head
- N_s = specific speed = $\frac{NQ^{1/2}}{H^{3/4}}$
- N_{ss} = suction specific speed = $\frac{NQ^{1/2}}{(\text{NPSH})^{3/4}}$
- $\frac{v}{V}$ = velocity ratio due to thickness
- $\frac{\Delta v}{V}$ = velocity ratio due to camber
- $\Delta v_a/V$ = velocity ratio due to angle of attack

Subscripts

- 1 = hub radius; also, angle at leading edge
- 2 = case radius; also, angle at trailing edge
- t = trailing edge
- b = refers to a single blade
- s = streamline quantity
- i = isolated airfoil quantity
- ∞ = far downstream
- d = design-point value

[1] This work was supported by the Office of Naval Research, under Contract N6onr-244, Task Order 2. Reproduction in whole or in part is permitted for any purpose of the U. S. Government.

[2] Research Engineer, Hydrodynamics Laboratory, California Institute of Technology. Assoc. Mem. ASME.

Contributed by the Hydraulic Division and presented at the Diamond Jubilee Annual Meeting, Chicago, Ill., November 13–18, 1955, of The American Society of Mechanical Engineers.

Note: Statements and opinions advanced in papers are to be understood as individual expressions of their authors and not those of the Society. Manuscript received at ASME Headquarters, August 25, 1955. Paper No. 55—A-127.

Introduction

In recent years, axial-flow pump impellers have been designed by applying the data of two-dimensional isolated airfoil theory to each cylindrical section of a blade. In general, the results have been good. However, there has been some disagreement and doubt as to the corrections that should be applied to the two-dimensional airfoil sections when they are subjected to the influence of the cylindrical boundaries of the pump where there are mutual interference effects between the blades. Previous attempts to account for interference have been based on calculations of simple cascades of airfoils in two dimensions. Following the general suggestions of Spannhake (4),[1] the present design procedure uses corrections based on a three-dimensional model, i.e., with the blades treated as spokes of a wheel.

The design method proposed includes the very important consideration of designing for optimum cavitation conditions. The basic presumption in the cavitation consideration is that the blade-pressure distribution can be closely predicted by the correction process of the design procedure. Optimum cavitation design is meant to describe the choosing of the optimum speed and size in connection with the performance desired to give the impeller the least susceptibility to cavitation. It is thought that making all radial sections equally susceptible to cavitation produces a pump with better over-all cavitation performance. The optimizing analysis affords the first step in the design procedure by permitting proper choices of the blade-section coefficients, the number of blades and the approximate geometric quantities and speed of operation. The interference corrections are then applied to determine the finished blade-section shapes.

It is only proper to concede that the present correction for blade mutual interference method of designing is based on assumptions that are not entirely proved. Furthermore, theories that may be employed in the design of turbomachinery are still subject to argumentation. Cascade theories are reasonably accurate in the design of axial-flow compressors; however, it is shown in the present work that cascade theories do not give proper predictions of pump-impeller operation. The present three-dimensional interference calculation and two-dimensional cascade calculations do not agree. Also, there apparently is no logical transition between the two-dimensional flow model and the three-dimensional model which will allow a continuous theory for turbomachine design. The author suggests continuation of investigations of turbomachine theories; however, this presentation is made in the belief that it now offers worthwhile improvements over existing axial-flow-pump design methods.

An extensive experimental study of a two-bladed impeller designed by the three-dimensional method has been conducted and the results are presented. As this impeller represents a nominal specific speed (10,000) of the usual axial-flow designs, it is presumed that the experimental results substantiate the use of the design method for most axial-flow pumps. The limitations on the present method are not known and further experimental verifications are needed—especially in the realm of lower specific speeds where the solidity must become high.

The Interference Calculation

The basis of the design procedure is to fit a camber line to a curving streamline in the annular-blade region in the same manner that a camber line is placed on a straight streamline for an isolated airfoil in an infinite field of uniform flow. The performance of the designated camber line is then assumed to be the same in both cases. The fact that the relative flow is slightly retarded is neglected. The main consideration then is to determine the curved streamline which is composed of the through-flow velocity, the tangential velocity of the impeller, and the induced interference velocities from all sources. Thickness effects have been neglected and only vorticity has been considered. The total vorticity effect cannot easily be handled; therefore the interference has been calculated by approximating the total influence by the influence of the vorticity of the blades from the case to the hub center line and downstream on the center line to infinity. Case and hub boundary conditions were placed in effect. The center-line vorticity of the "removed" blade has been included, but the cyclic effect of the removed blade (if there is such an effect) has been omitted.

The interference of the center-line vorticity of the removed blade was found using the equation derived in a previous work (1) where it was assumed that the vorticity grows linearly through the blade row. The exact solution is

$$C_{\theta b} = \frac{V_{\theta b} r_2}{\Gamma_b} = \frac{1}{4\pi\eta}\left[1 + \frac{1}{\xi_t}\left(\sqrt{\xi^2 + \eta^2} - \sqrt{(\xi_t - \xi)^2 + \eta^2}\right)\right] \quad \ldots\ldots[1]$$

The interference velocity depends on the axial extent of the blade and on the radius ratio. Typical curves of the dimensionless interference velocity of the removed blade are shown in Fig. 1.

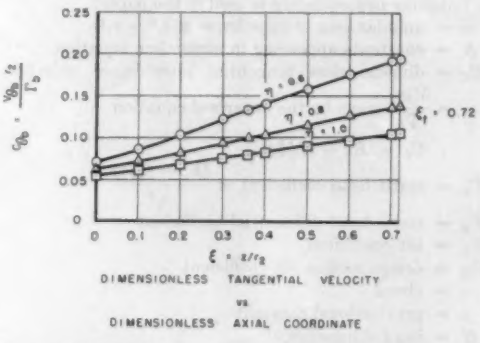

Fig. 1 Induced Tangential Velocity Due to Downstream Vorticity of a Blade for the Example $\xi_t = 0.72$

The interference velocities due to the other blades were found by employing the velocity values due to a single vortex element as presented by H. N. Tyson, Jr. (2). The solution presented by Tyson did not lend itself to rapid calculations and could not be further analytically summed to represent a blade with distributed vorticity. Therefore graphical summations of the limited data Tyson presented were made for several blade representations. It was necessary to add to Tyson's values correction values due to a center-line vorticity of $\Gamma/2$ (per blade) to achieve conditions of zero prewhirl and total circulation downstream as Tyson considered symmetrical splitting of the radial vortex element, half upstream and half downstream. Also, only the tangential component was retained in the final interference analysis, as the radial and axial components are comparatively small. Interference-velocity values were summed for four values of the axial extent ratio $\xi_t = z_t/r_2 = 0.2, 0.4, 0.6$, and 0.72. A single vortex element was used to approximate the blade vorticity for $\xi_t = 0.2$, three vortices of equal strength dispersed along the chord line for $\xi_t = 0.4$, and five vortices for $\xi_t = 0.6$ and 0.72. These very approximate blade representations are believed to be satisfactory for the solidities involved in these summations. In instances where greater values of ξ_t and greater numbers of blades combine to give high solidity, then more precise distribution of the blade

[1] Numbers in parentheses refer to the Bibliography at the end of the paper.

vorticity would be necessary. Dispersion of the singularities could be made only along a single helical surface (corresponding to a blade angle of 32.4 deg at the hub and 20.9 deg at the case). Actual blade angles can be a few degrees different from this helical representation without suffering serious error. Summations were made at the hub, mid-radius, and tip sections. Blade representation and summation regions are illustrated in Fig. 2 for the case $\xi_t = 0.4$.

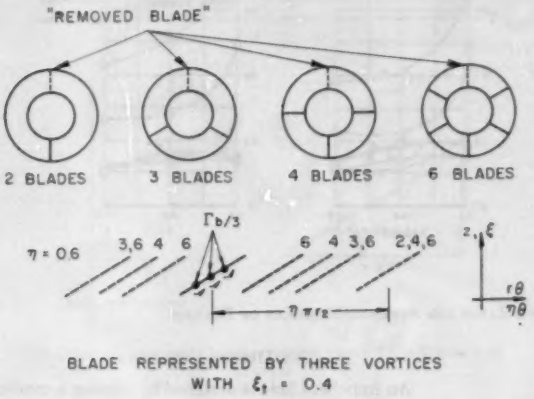

BLADE REPRESENTED BY THREE VORTICES WITH $\xi_t = 0.4$

THE DOTTED LINES SHOW THE SUMMATION REGIONS AND THE NUMBERS ABOVE CORRESPOND TO THE NUMBER OF BLADES ON THE IMPELLER

FIG. 2 TYPICAL BLADE REPRESENTATIONS FOR SUMMATION OF MUTUAL INTERFERENCE VELOCITIES

The final total interference is the sum of the effects of the other blades and the downstream vorticity of the removed blade. In Fig. 3 values of the total tangential interference velocity are plotted against the axial-blade extent ($\xi = z/r_2$) for the case of a two-vaned impeller with $\xi_t = 0.72$. The shape of these curves is typical of all cases summed.

As the curves deviate only slightly from straight lines, each curve for the dimensionless induced tangential velocity (C_θ) was approximated by a line with the equation

$$C_\theta = K_0 + K_1(z/z_t) \quad \ldots\ldots [2]$$

where K_0 is the interference-velocity value at the removed blade leading edge and K_1 is the difference in values between the trailing edge and leading edge. The value of z/z_t varies from 0 to 1 from the leading edge to trailing edge. In this manner, all of the cases have been reported by presenting values of the constants K_0 and K_1. In Table 1 these values are tabulated and, in Fig. 4(a), K_0 and K_1 are plotted as functions of the radius ratio. It should be noted that C_θ is the dimensionless total interference velocity equal to $V_\theta r_2/\Gamma_b$ where V_θ is the total interference velocity and Γ_b is the value of circulation of a single blade. Γ_b is used because the number of blades is taken into account in the summation and so included in the values of K_0 and K_1.

TABLE 1 VALUES OF K_0 AND K_1, DEFINING TOTAL INDUCED TANGENTIAL VELOCITY

Axial extent	No. of blades	K_0			K_1		
		$\eta = 0.6$	$\eta = 0.8$	$\eta = 1.0$	$\eta = 0.6$	$\eta = 0.8$	$\eta = 1.0$
$\xi_t = 0.2$	2	0.212	0.180	0.134	0.106	0.038	0.051
	3	0.299	0.269	0.186	0.198	0.059	0.105
	4	0.371	0.352	0.231	0.319	0.092	0.174
	6	0.463	0.501	0.306	0.665	0.192	0.348
$\xi_t = 0.4$	2	0.180	0.161	0.118	0.170	0.076	0.083
	3	0.241	0.235	0.156	0.315	0.128	0.159
	4	0.274	0.288	0.180	0.514	0.220	0.277
	6	0.289	0.310	0.191	1.015	0.574	0.574
$\xi_t = 0.6$	2	0.152	0.142	0.103	0.227	0.114	0.112
	3	0.183	0.167	0.125	0.430	0.224	0.228
	4	0.187	0.191	0.128	0.687	0.415	0.581
	6	0.191	0.184	0.127	1.210	0.826	0.701
$\xi_t = 0.72$	2	0.135	0.130	0.093	0.258	0.137	0.129
	3	0.149	0.159	0.103	0.493	0.280	0.268
	4	0.138	0.144	0.100	0.781	0.505	0.433

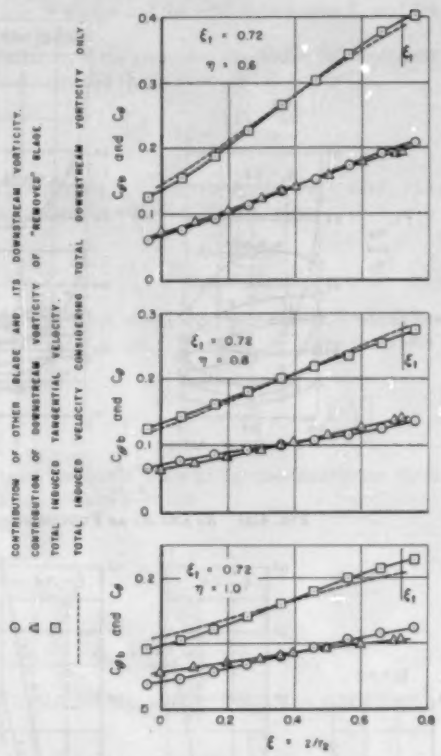

FIG. 3 TANGENTIAL INTERFERENCE VELOCITIES AS A FUNCTION OF THE AXIAL CO-ORDINATE FOR THE EXAMPLE OF A TWO-BLADED IMPELLER WITH $\xi_t = 0.72$

It is of interest to note that the present interference calculation supports certain known limits concerning fluid flows. In the three-dimensional calculation there cannot be a limit that corresponds to the isolated airfoil; however, the case of zero blades has a similar significance. In Fig. 4(b) a plot of the K_0 and K_1 values are shown as functions of the number of blades on an impeller. It can be seen that K_0 and K_1 approach zero for zero blades corresponding to no interference effects. The limit as the number of blades is increased is the Euler result for an infinite number of blades. This limit requires exact guidance of the flow, so the total circulation must be achieved at the impeller exit. In other words, the "interference" is the total effect of the impeller. Therefore K_0 must become zero and K_1 become equal to the total circulation velocity. It can be seen (Fig. 4b) that the K_0-curves do seem to reach a maximum and begin to approach zero as the number of blades is increased. Similarly K_1 appears to approach the total tangential circulation velocity. Fig. 4(b) also shows that neither isolated airfoil data alone nor Euler theory can give correct results for designing pump impellers.

The effect of the axial extent of the blades is demonstrated in Figs. 4(a) and 4(b). If the axial extent is small, K_0 is near to half the total circulation far downstream. K_0 becomes smaller as the

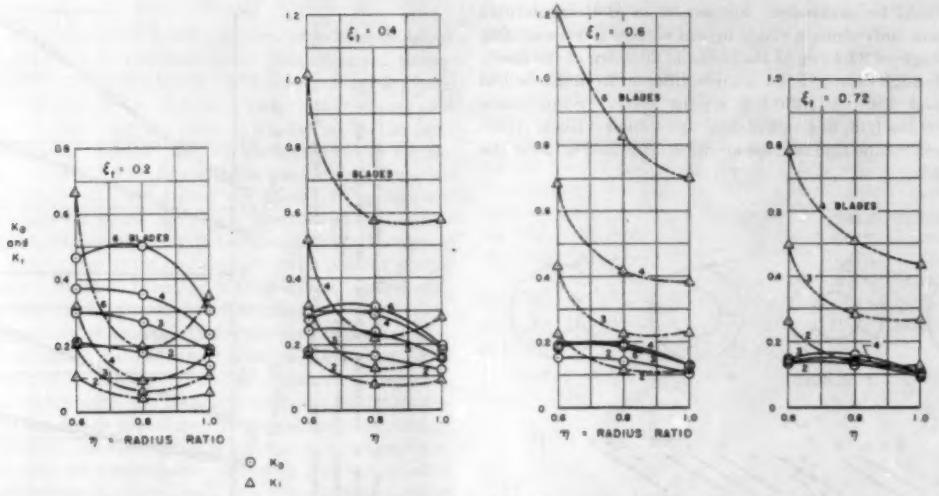

FIG. 4(a) K_0 AND K_1 AS FUNCTIONS OF THE RADIUS RATIO FOR SEVERAL NUMBERS OF BLADES

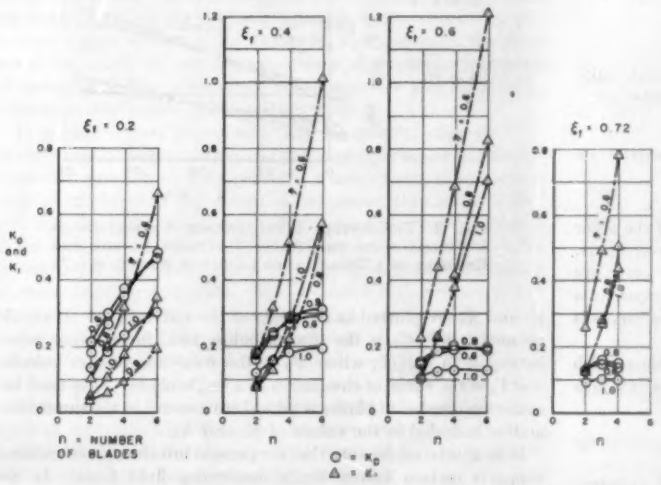

FIG. 4(b) K_0 AND K_1 AS A FUNCTION OF THE NUMBER OF BLADES

axial extent increases. On the other hand, as the axial extent gets small K_1 approaches zero and for large axial extent K_1 becomes large. These results show that as the axial extent of the blade becomes large with respect to the case radius of the pump, more of the circulation growth occurs within the blade region.

In Fig. 3 the individual contributions to the total induced velocity have been plotted as well as the total value. It can be seen that the effect of another blade and its downstream vorticity is little different than the downstream effect of the removed blade. The effects of the mutual blade interference are compared to the effects of the total downstream vorticity by the dotted curves which represent simply the downstream vorticity results multiplied by the number of blades on the impeller. For the two-vaned case given in Fig. 3, the separate effect of the other blade is seen to be small. It appears, then, that two-vaned impellers with small axial extent might be designed with reasonable success by considering only the downstream vorticity. However, when the axial extent is large, or there are several blades, then mutual blade interference should be included.

THE DESIGN EQUATIONS

An impeller blade is designed by placing a camber line on the pre-existing streamline in the blade region. The camber line could be put on the streamline at an angle of attack; however, for consideration of improved cavitation conditions it is thought that the best way to achieve the design head is by using camber only rather than by operation at angle of attack. Normally for a cambered blade shape, shockless entry occurs approximately at zero angle of attack to the chord line and a smoother pressure distribution is obtained. If the pressure distribution has a large negative area at the leading edge, which is the case with angle of attack, then cavitation is more likely to occur.

The streamline equation is derived from the geometric relation illustrated in Fig. 5(a). It is seen that

$$\tan \beta = \frac{dz}{rd\theta} = \frac{Va}{u - V_\theta} = \frac{Va}{u - \dfrac{\Gamma_b}{r_1} C_\theta}$$

C_θ is given by Equation [2].

Integrating, solving for θ, and introducing the dimensionless parameters ϕ_e, ξ, and η gives

$$\theta = \frac{\xi}{\phi_e} - \frac{\Gamma_b}{\phi_e r_2^2 \omega \eta}\left[K_0 \xi + \frac{K_1 \xi^2}{2\xi_t}\right] \quad \ldots\ldots\ldots\ldots [3]$$

The hub blade angle β_{c1} is determined as follows

$$\tan \beta_{c1} = \frac{z_t}{r_1 \theta_{1t}} = \frac{\xi_t}{\eta_1 \theta_{1t}}$$

where θ_{1t} is the value of θ at the trailing edge of the root section. Substituting Equation [3] for θ_{1t} (properly evaluated), then

$$\cot \beta_{c1} = \frac{\eta_1}{\phi_e} - \frac{\Gamma_b}{\phi_e \omega r_2^2}\left[K_{01} + \frac{K_{11}}{2}\right] \quad \ldots\ldots\ldots\ldots [4]$$

where K_{01} and K_{11} are the interference velocity constants at the root section.

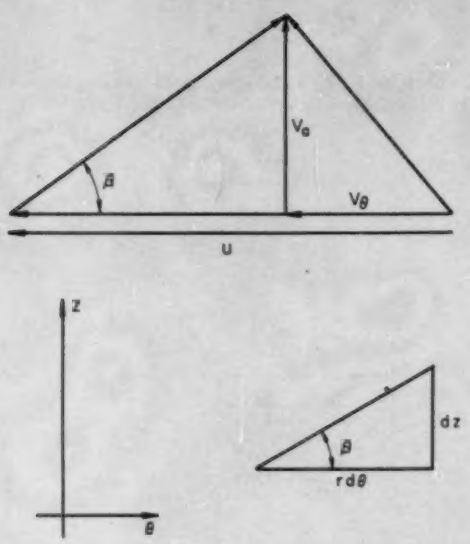

FIG. 5(a) VELOCITY COMPONENTS AND THE CO-ORDINATE SYSTEM

Lift coefficient is introduced from the equations of airfoil theory

$$L' = \rho V \Gamma_b = \frac{1}{2}\rho V^2 c C_L$$

where V is approximated by V_R average—the average relative velocity

$$V \cong V_R \cong \frac{V_a}{\sin \beta_c}$$

Solving for Γ_b, dividing through by ωr_2^2, and evaluating at the root section produces

$$\frac{\Gamma_b}{\omega r_2^2} = \frac{1}{2}\phi_c \xi_t \frac{C_{L1}}{\sin^2 \beta_{c1}} \quad \ldots\ldots [5]$$

Equations [4] and [5] may be resolved for ϕ_c and $\Gamma_b/\omega r_2^2$ with the results

$$\phi_c = \frac{2\eta_1 \sin \beta_{c1}}{2 \sin \beta_{c1} \cos \beta_{c1} + \xi_t C_{L1}\left(K_{11} + \frac{K_{11}}{2}\right)} \quad \ldots\ldots [6]$$

$$\frac{\Gamma_b}{\omega r_2^2} = \frac{\xi_1 \eta_1 C_{L1}}{2 \sin \beta_{c1} \cos \beta_{c1} + \xi_t C_{L1}\left(K_{11} + \frac{K_{11}}{2}\right)} \quad \ldots\ldots [7]$$

and also

$$\frac{\Gamma_b}{\phi_c \omega r_2^2} = \frac{C_{L1}\xi_t}{2 \sin^2 \beta_{c1}} \quad \ldots\ldots [8]$$

Equation [3] can be rewritten as

$$\theta = A\xi - \frac{B}{\eta}\left(K_0 \xi + \frac{K_1 \xi^2}{2\xi_t}\right) \quad \ldots\ldots [9]$$

where $A = 1/\phi_c$ and ϕ_c is given by Equation [6] and B is given by Equation [8]. A and B are constants determined by the performance desired and depend on the choices of the parameters C_{L1}, ξ_t, ω, and the number of blades n. K_0 and K_1 depend upon the number of blades and the axial extent ratio ξ_t, and are functions of the radius.

The variation of the amount of the camber (lift coefficient) with radius is determined thus: From airfoil theory

$$C_L = \frac{2\Gamma_b}{V_R c}$$

where $V_R = Va/\sin \beta_c$, $c = z_t/\sin \beta_c$, and $Va = \omega r_2 \phi_c$. Combining these expressions with Equation [8] gives

$$C_L = \frac{C_{L1} \sin^2 \beta_c}{\sin^2 \beta_{c1}} \quad \ldots\ldots [10]$$

The blade angle β_c varies with radius as determined from the relation $\tan \beta_c = \xi_t/\eta\theta_t$. Equation [9] gives the value of θ_t. Thus

$$\beta_c = \cot^{-1}\left[A\eta - B\left(K_0 + \frac{K_1}{2}\right)\right] \quad \ldots\ldots [11]$$

The head coefficient is found by considering the theoretical head relation for zero prewhirl

$$H = \frac{u V_{\theta\infty}}{g}$$

Then

$$\psi_c = \frac{Hg}{u_2^2} = \frac{u V_{\theta\infty}}{u_2^2} = \frac{r V_{\theta\infty}}{\omega r_2^2}$$

where all values are taken at the design flow rate. Since

$$V_{\theta\infty} = \frac{n\Gamma_b}{2\pi r}$$

is the circulation velocity far downstream, then

$$\psi_c = \frac{n\Gamma_b}{2\pi\omega r_2^2} \quad \ldots\ldots [12]$$

$\Gamma_b/\omega r_2^2$ is given in Equation [8].

When all of the performance quantities and parameters have been chosen properly by the cavitation-optimizing analysis, the streamline constants A and B can be calculated from Equations [6] and [8] and the streamline co-ordinates can be computed from Equation [9]. The values of the blade angle at various radii are calculated from Equation [11], and the variations of C_L are determined from Equation [10]. These are the necessary quantities to determine the final blade shape.

DESIGNING FOR OPTIMUM CAVITATION CONDITIONS

Investigations of the best relations between size and speed to reduce cavitation susceptibility in pumps have been made in the past. The analyses have usually been made at the tip section of the impeller which was considered to be the critical section for cavitation. If the cavitation due to tip clearance flow is neglected, then it seems reasonable that the over-all cavitation susceptibility might be reduced if the impeller blades were designed with all radial sections equally critical. If the effect of the thickness function on minimum static pressure can be assumed to vary only slightly with change in radius, then the pressure distribution at each radius can be made equal by considering the head produced at each radial section. For a free-vortex design, the head is constant for all radial sections. It can be shown that to achieve the same head at each section, the tangential force must be the same; so to have similar pressure distributions (same minimum pres-

sures) the axial extent of a blade must be the same at all radii. In this manner the chord increases from hub to case as the cosecant of the chord angle in contrast to past designs where the chord was kept nearly constant. By the foregoing qualitative reasoning, constant axial extent is specified in the design procedure.

With each radial section equally susceptible to cavitation, the hub section will be given preference in the optimizing procedure since it will have the highest loading. Combining the method of calculating approximate pressure distributions on isolated airfoils as given in reference (9) with the geometric relations concerning the flow through a pump, permits calculating the incipient cavitation coefficient $\sigma = \text{NPSH}/H$ as a function of specific speed and of the impeller size. (Note σ here stands for incipient cavitation and not cavitation breakdown.) The equation for the pressure distribution is

$$S = \frac{H_0 - P}{q_0} = \left[\frac{v}{V} + \frac{C_L}{C_{L_i}}\frac{\Delta v}{V} + \frac{\Delta v_a}{V}\right]^2 \quad \ldots\ldots [13]$$

where

$$H_0 = \frac{1}{2}\rho V_R^2 + P_T - \frac{1}{2}\rho V_a^2$$

$$q_0 = \frac{1}{2}\rho V_R^2$$

and

$$V_a = V_R \sin \beta_c \text{ (as seen in Fig. 5}b\text{)}$$

The term $\Delta v_a/V$ is the pressure drop due to angle of attack which is neglected by virtue of specifying that the optimum operation is at zero angle of attack. When $P = P_v$, the vapor pressure of the liquid, then cavitation is imminent. Equation [13] can be rearranged giving

$$\text{NPSH} = \frac{P_t - P_v}{\rho g} = \frac{V_R^2}{2g}(S - 1 + \sin^2\beta_c)$$

$$= \frac{V_a^2}{2g}\left(\frac{S-1}{\sin^2\beta_c} + 1\right) \quad \ldots\ldots [14]$$

From the head relations

$$\psi_s = \frac{H_s g}{u_2^2} \text{ and } H_s = \frac{uV_{\theta\infty}}{g}$$

then

$$V_{\theta\infty} = \frac{\psi_s u_2}{\eta}$$

Also, with $\phi_s = V_a/u_2$, and employing the velocity triangle (Fig. 5b) the chord angle is determined

$$\beta_c = \cot^{-1}\left(\frac{\eta - \dfrac{\psi_s}{2\eta}}{\phi_s}\right) \quad \ldots\ldots [15]$$

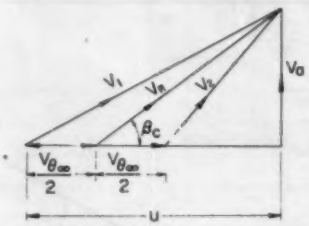

FIG. 5(b) INLET, OUTLET, AND MEAN VELOCITY TRIANGLE

Dividing through Equation [14] by the head gives

$$\sigma = \frac{\text{NPSH}}{H} = \frac{\phi_s^2}{2\psi_s}\left(\frac{S-1}{\sin^2\beta_c} + 1\right) \quad \ldots\ldots [16]$$

Two dimensionless quantities may be defined from ϕ_s and ψ_s, one dependent only on speed and the other on size

$$\chi_\omega = \frac{\phi_s^{1/2}}{\psi_s^{3/4}} = \omega\frac{Q^{1/2}}{\pi^{1/2}(1-\eta_1^2)^{1/2}H^{3/4}g^{3/4}} \quad \ldots\ldots [17]$$

$$\chi_{r_2} = \frac{\psi_s^{1/4}}{\phi_s^{1/2}} = r_2\frac{H^{3/4}g^{1/4}\pi^{1/2}(1-\eta_1^2)^{1/2}}{Q^{1/2}} \quad \ldots\ldots [18]$$

Then Equation [16] can be rewritten as

$$\sigma = \chi_\omega\chi_{r_2}\frac{\phi_s^2}{2\psi_s^{1/2}}\left(\frac{S-1}{\sin^2\beta_c} + 1\right) \quad \ldots\ldots [19]$$

The specific speed for a hub ratio η_1 of 0.6 is

$$N_s\left(\frac{\text{rpm (gpm)}^{1/2}}{\text{ft}^{3/4}}\right) = 3880\chi_\omega \quad \ldots\ldots [20]$$

In Fig. 6, σ is plotted as a function of N_s for various values of

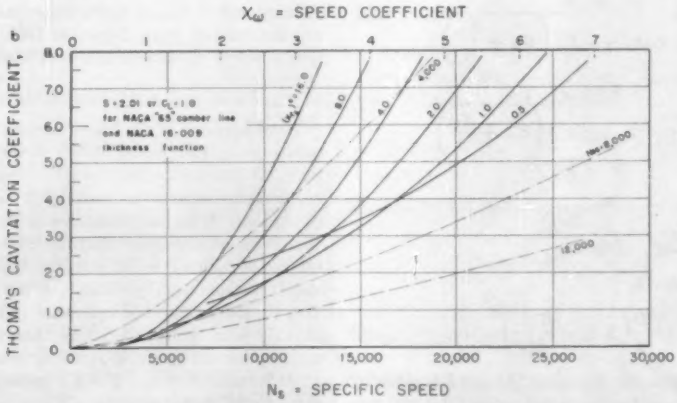

FIG. 6 EXAMPLE OF CAVITATION COEFFICIENT AS A FUNCTION OF SPEED AND SIZE FOR A PARTICULAR BLADE SECTION
(NACA 65 refers to the camber type found in reference 9.)

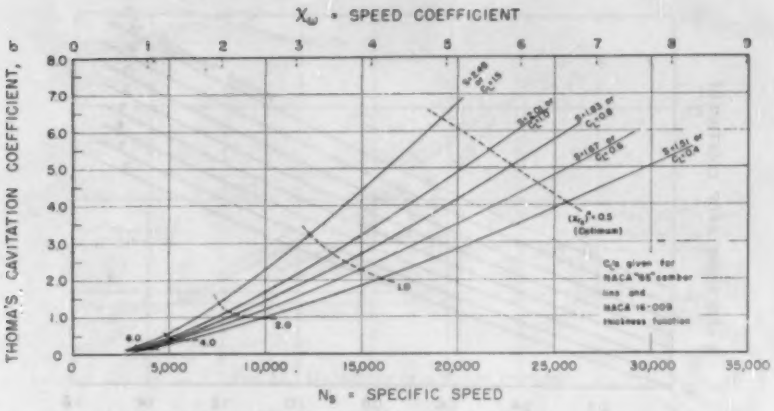

FIG. 7 OPTIMUM σ FOR SEVERAL VALUES OF S OR C_L

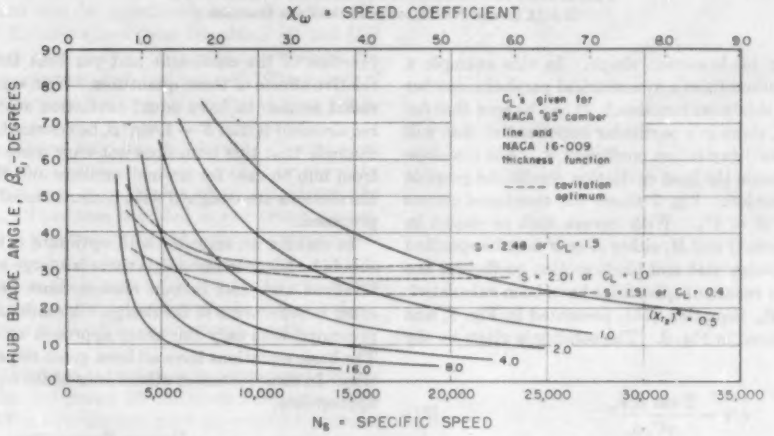

FIG. 8 HUB BLADE ANGLE AS A FUNCTION OF SPEED AND SIZE

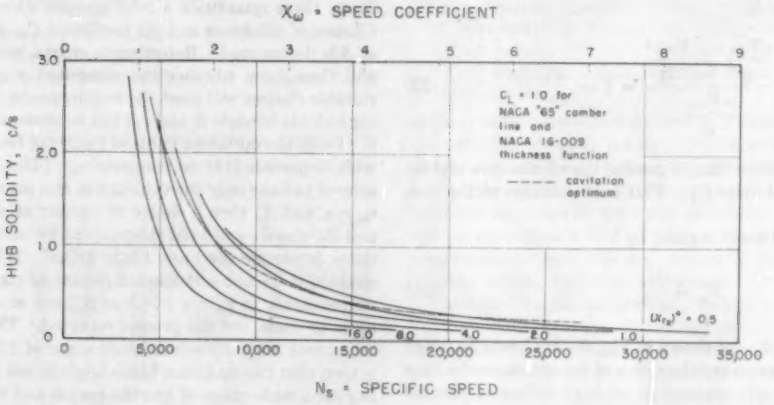

FIG. 9 SOLIDITY (c/a) AS A FUNCTION OF SPEED AND SIZE FOR ONE PARTICULAR BLADE SHAPE

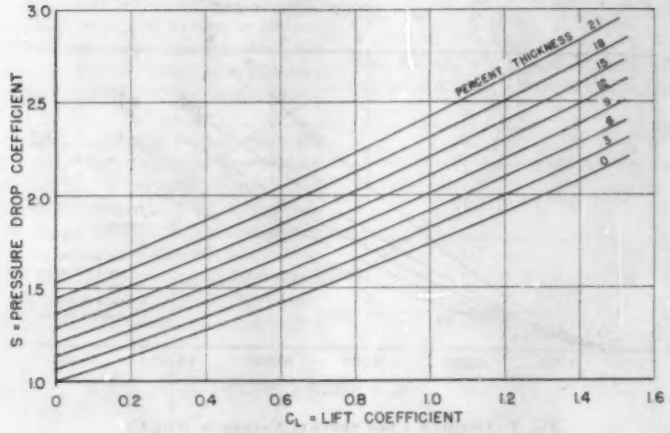

FIG. 10 PRESSURE-DROP COEFFICIENT S AS A FUNCTION OF C_L AND PER CENT THICKNESS FOR SYMMETRICAL PARABOLIC CAMBER LINES (NACA 65 and NACA series 16 thickness functions.)

$(\chi_{r_3})^4$ for a particular blade-section shape. In this example a value of $S = 2.01$ resulted from a symmetrical parabolic camber and an NACA 16-009 thickness function.[4] It can be seen that for a given specific speed, there is a particular impeller size that will provide the best (lowest) cavitation coefficient σ. The envelope of these curves represents the best cavitation conditions possible for the given blade section. Fig. 7 shows the enveloped curves for several values of S or C_L. With curves such as shown in Figs. 6 and 7, for a given Q and H, either N or σ may be specified and the resultant optimum size and blade section coefficient can be determined. Other resultant quantities have been calculated; the hub blade angle β_e, Equation [15], presented in Fig. 8, and the solidity c/s, presented in Fig. 9. The solidity is given by the equation

$$c/s = \frac{2 \sin \beta_e \psi_e}{\eta C_L \phi_e} \quad \ldots\ldots [21]$$

where at the hub section, $\eta = \eta_1 = 0.6$. The reaction is sometimes of interest, and lines of constant reaction could be drawn in Fig. 6. The reaction is defined by

$$R = \frac{\dfrac{uV_{\theta\infty}}{g} - \dfrac{V_{\theta\infty}^2}{2g}}{\dfrac{uV_{\theta\infty}}{g}} = 1 - \frac{\psi_e}{2\eta^2} \quad \ldots\ldots [22]$$

It is important to consider that in general the efficiency is highest for high reactions and large C_L. This is in contrast to the conditions for least σ.

The suction specific speed is given by

$$N_{ss} = \frac{N_s}{\sigma^{3/4}} \quad \ldots\ldots [23]$$

and lines of constant N_{ss} are shown in Fig. 6. It should be noted that $N_{ss} = \text{const}$ is not an envelope line of the optimum-size lines although they are nearly equivalent at high values of specific speed.

In Fig. 10 the pressure-drop coefficient S has been plotted as a function of lift coefficient and per cent thickness to show the relative effects of these quantities. With regard to designing each radial section to have equal cavitation susceptibility, the exact requirement is that $S - 1/\sin^2 \beta_e$ be constant. It can be shown by example that this term does not vary more than 2 or 3 per cent from hub to case for normal cambers and thickness functions if the sections are designed with constant axial extent as previously proposed.

In making an impeller with optimum cavitation operation, it should be borne in mind that there is a large number of parameters involved and that certain choices must be made according to other requirements of the design. A minimum of curves has been presented with only the usual approach to a design considered. The basic equations have all been given to permit further calculation. In some instances other forms of the equations may be more appropriate.

DESIGN PROCEDURE

Generally for a new design, the head, flow rate, and desired submergence are given and certain motor speeds are available. From these quantities a trial specific speed can be computed. Choices of thickness and lift coefficient C_{L1} are made and a value of S is determined. Referring to charts, such as given in Fig. 6, will then show whether the computed σ can be achieved. If suitable choices will meet the requirements, then the corresponding hub blade angle β_e and c/s can be determined from Figs. 8 and 9. From the optimum value of $(\chi_{r_3})^4$ the fourth root can be used with Equation [18] to compute r_3. (The hub ratio η_1 is considered to have only the value 0.6 in this presentation.) Knowing r_3, c/s, and β_e, then a choice of number of blades n can be made and the chord c and axial extent z_1 can be calculated. These quantities determine the basic blade design. If any of the foregoing quantities do not suit special requirements or turn out to be unreasonable (e.g., $c/s >> 1$ or β_e very small) then new choices must be made and the process repeated. The interference calculation was made for a hub blade angle of 32.4 deg. In Fig. 8, it is seen that the optimum blade angle is not too different from 30 deg for a wide range of specific speeds and values of C_L. Therefore the interference-calculation results should be reasonably appropriate for a large number of pump designs. In the event that the solidity is small, then the blade-to-blade interference may be neglected and the streamline can be calculated using a linear representation for the C_θ given in Equation [1] where the

[4] The camber shape is listed in reference (9) for 6 per cent camber as NACA 65. For other than 6 per cent camber the ordinates and lift coefficient are scaled linearly.

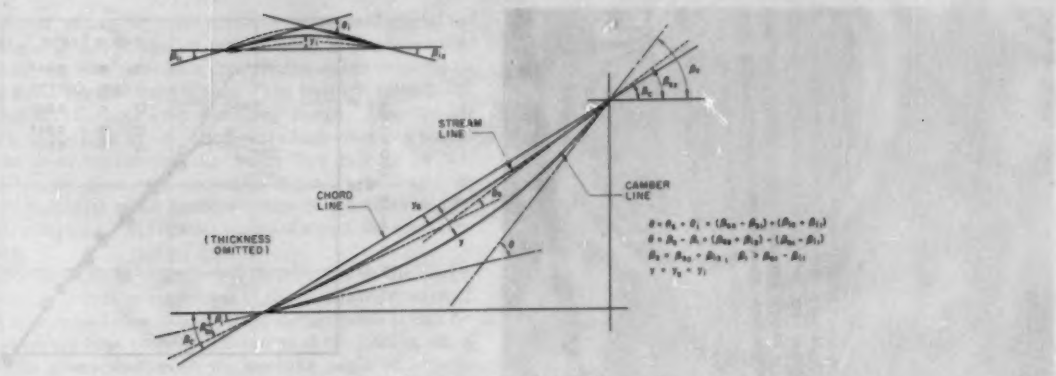

FIG. 11 GEOMETRY OF A BLADE SECTION

blade angle is not restricted. With the basic blade quantities chosen, the values of n and ξ_t are used to find values of K_0 and K_1 in Fig. 4, ψ_e and ϕ_e can be computed, and the streamline for several radial sections can be calculated from Equation [9]. (Note, the values of β_{s1} determined from Equations [4] and [15] should agree, although there may be an unimportant slight difference resulting from the use of plotted values.) The values of β_s and C_L at the other radial sections are computed from Equations [11] and [10].

The blade-section shapes may now be drawn. The simplest method is to plot the streamlines and then graphically place the camber on the streamline using NACA data scaled for the proper values of C_L. Thickness is added in the usual manner. A typical blade section is shown in Fig. 11. Some designers prefer using the camber angles instead of displacements, in which case the isolated camber angle may be added to the streamline "camber" angle and the resultant drawn from the straight chord line at the correct blade angle. The camber-angle method is also demonstrated in Fig. 11.

Mention has been made of the symmetrical parabolic camber lines (NACA 65) and the Series 16 thickness functions. The author believes that this combination gives an excellent pressure distribution for a pump impeller; however, other camber lines and thicknesses may be used with the design procedure.

EXPERIMENTAL STUDY

An experimental impeller was designed by the method presented and all of its descriptive quantities are given in Table 2. The angular and axial co-ordinates of the upper and lower blade surfaces were determined by spotting points and then trimming the material to these points. Plaster-mold halves were made and several identical blades were cast. The blades were bolted into a hub with the receiving slots machined at the correct angle. Sectional drawings of the vanes are shown in Fig. 12(*a*) and the test pump is shown in Fig. 12(*b*). No inlet or discharge vanes were employed as it was the purpose of this test to evaluate the impeller without any other influences.

TABLE 2 VALUES DESCRIBING EXPERIMENTAL IMPELLER

Design performance coefficients $\psi_e = 0.126$, $\phi_e = 0.315$; expected $\phi_e = 0.295$

$r_1/r_2 = \eta_1 = 0.6$			$r_1 = 2.25$ in.			$r_2 = 3.75$ in.			
η	K_0	K_1	β_c, deg.	C_L	c. in.	c/s	β_1	β_2	θ
0.60	0.117	0.295	32.4	1.000	5.04	0.713	11.90	53.5	41.6
0.65	0.121	0.229	29.5	0.845	5.49	0.716	12.5	46.7	34.2
0.70	0.125	0.191	27.2	0.728	5.91	0.716	12.7	41.8	29.1
0.75	0.126	0.167	25.3	0.636	6.32	0.715	12.7	37.9	25.2
0.80	0.123	0.151	23.6	0.558	6.74	0.716	12.6	34.6	22.0
0.85	0.121	0.142	22.1	0.493	7.18	0.717	12.5	31.8	19.4
0.90	0.115	0.139	20.9	0.441	7.59	0.716	12.2	29.5	17.3
0.95	0.104	0.137	19.7	0.393	8.04	0.718	11.9	27.4	15.5
1.00	0.090	0.137	18.6	0.355	8.46	0.718	11.6	25.5	13.9

$\xi_t = 0.72$ $\quad r_t = 2.7$ in. $\quad$ Test rpm = 210

For N = 210: $\quad Q$ (cfs) = 1.35 ϕ_e, $\quad H$ (ft) = 1.47 ψ (or C_p)

Calculated coefficients: $\quad N_s = 10,300$, $\quad e' = 1.7$ $\quad N_{ss} = 6,900$

C_L of isolated airfoil that is placed on curved streamline.

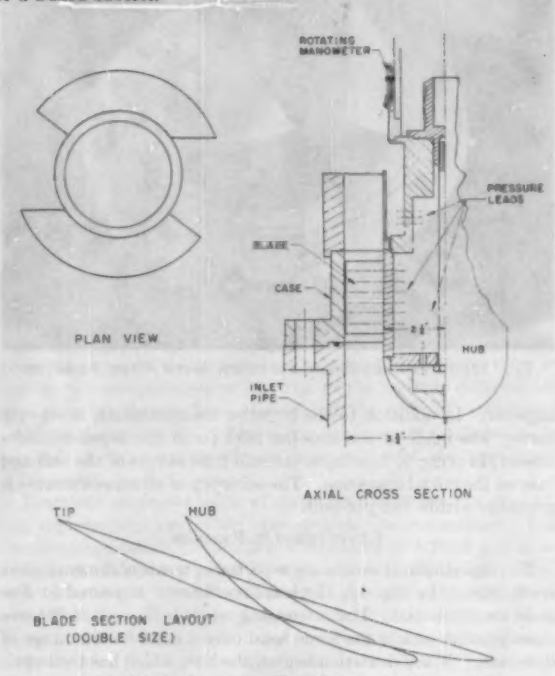

FIG. 12(*a*) VIEWS OF TEST PUMP AND BLADES

The experimental facilities and testing techniques of the rotating channels laboratory of the California Institute of Technology have been described many times in Hydrodynamics Laboratory reports. Briefly, the test impeller is driven by a dynamometer which permits torque measurement and is speed-controlled. The flow rate is measured with venturi meters. Impeller-head measurement is made with total-head probes at the impeller inlet and immediately behind the impeller blades. Static-pressure distributions on the blades were measured by casting static tap leads into the blades which connect with a manometer rotating with the

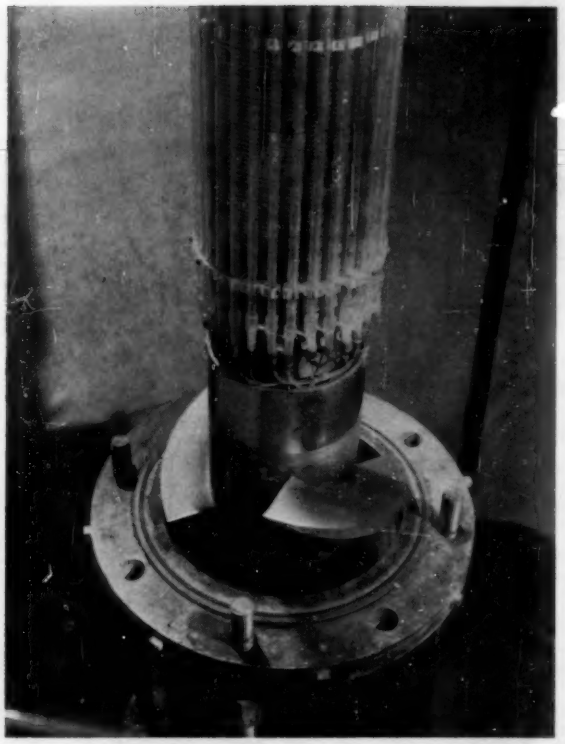

FIG. 12(*b*) INSTRUMENTED IMPELLER WITH CASE REMOVED

impeller. In addition to the impeller measurements, a velocity survey was made at the impeller inlet (with the impeller blades absent) in order to determine the real fluid effects of the hub and case on the model operation. The accuracy of all measurements is probably within two per cent.

EXPERIMENTAL RESULTS

The experimental results are reported in terms of dimensionless coefficients. In Fig. 13, the head coefficients measured at five radii are presented. The interesting result is that all radial sections produce nearly the same head over a considerable range of flow rate. When deviation begins, the hub, which has the heaviest loading, stalls off first. Then successive radial sections stall, the tip section being the last to stall. A weighted average of the five head curves was taken as the head of the impeller, and the resultant characteristic curves are shown in Fig. 14. The performance is compared with the predicted values by first considering the inlet-velocity profile shown in Fig. 15. There it is seen that the axial-velocity component is about 5 to 7 per cent above the average value over the greater portion of the passageway. Thus, in Fig. 14, the calculated value of design performance as indicated by the dotted cross is corrected by 6 per cent to give an expected design point indicated by the solid cross. It is seen that the head produced is about 4 per cent lower than the expected design point, whereas the "input" head ψ' is about 1 to 2 per cent greater. The input head is the head that would be produced if the efficiency were 100 per cent and is found by dividing the torque by the flow rate τ/ϕ. The input head is the one that should correspond to the theory. Thus it is seen that the expected design performance was closely achieved in the experimental test.

The best efficiency point occurs close to the expected design

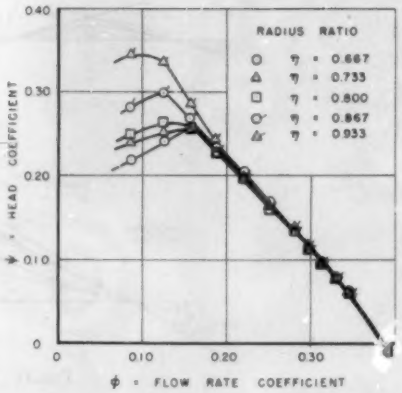

FIG. 13 DEVELOPED HEAD COEFFICIENT MEASURED AT FIVE RADIAL POSITIONS

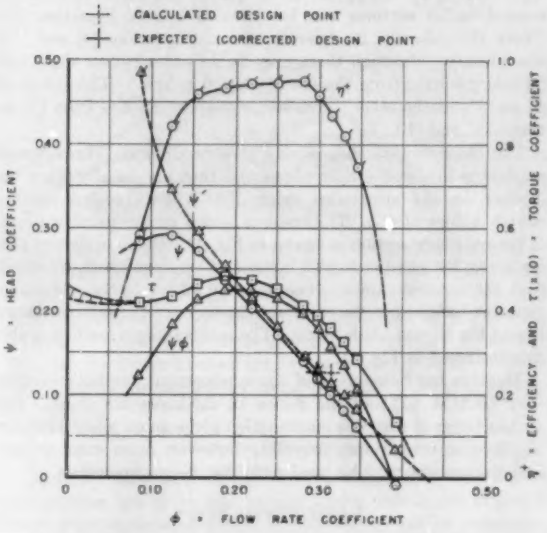

FIG. 14 PERFORMANCE CHARACTERISTICS OF TEST IMPELLER

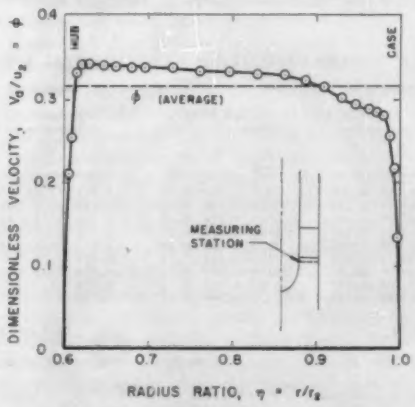

FIG. 15 MEASURED INLET-VELOCITY PROFILE

point; however, the shape of the efficiency curve is of special interest. The efficiency drops off rapidly beyond the maximum point, although at flow rates from one half the design value up to the design point the efficiency is high. The best efficiency point occurs at a flow rate about 4 per cent below design. Thus the design point is at the high flow-rate end of the high-efficiency range. This results from considering the design flow rate to be the "shockless" entry flow rate corresponding to zero angle of attack. Operating at small positive angles of attack evidently gives better efficiency. At negative angles of attack the operation is not good.

In Fig. 16 the static head (pressure) distribution on the blades of the pump is shown as a function of the flow rate for several radii. At flow rates below the expected design point it can be seen that there are large pressure differences at the leading edges of the blades corresponding to the positive angle of attack. Above the expected design flow rate the angle of attack is negative and the resultant pressure distributions are "crossed over." Near expected design flow rate the flow streams smoothly onto the blade giving an oval-shaped pressure profile. The actual shockless point seems to occur at a flow rate slightly greater than $\phi = 0.284$ which is about 4 per cent less than the expected design point. The correspondence of the correct pressure distribution and the best efficiency is excellent. The 4 per cent deviation

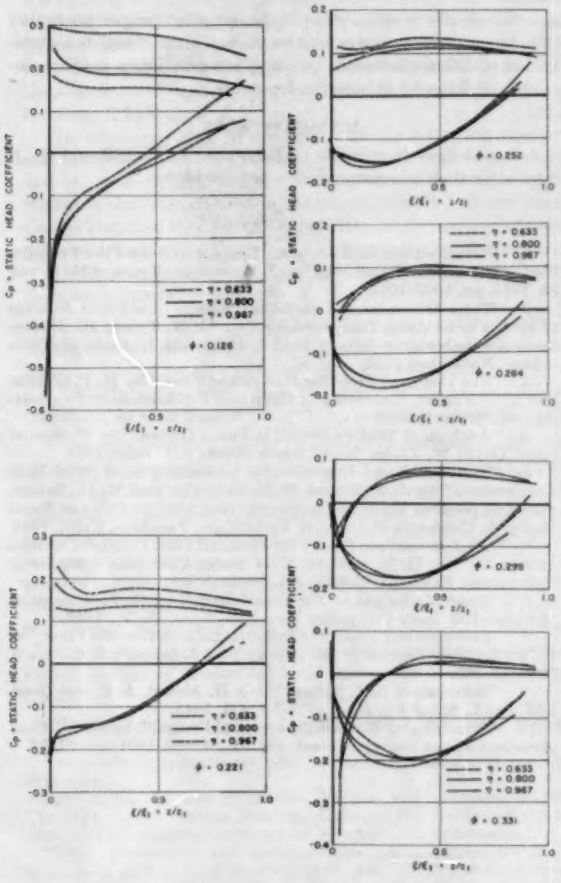

Fig. 16 Static Head Distribution as a Function of Axial Extent

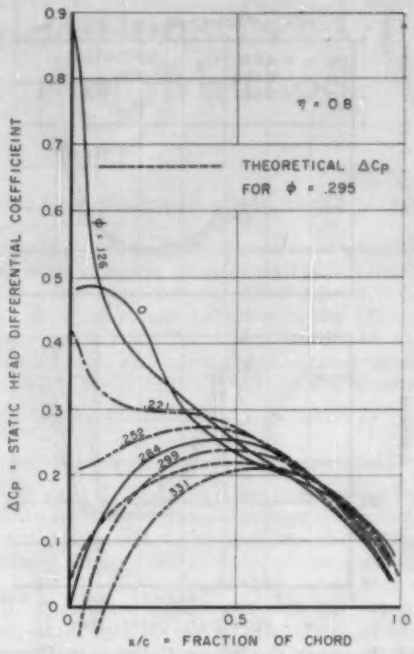

Fig. 17 Static Head Differentials as a Function of Chord at Mid-Radius Position

from the expected design point represents the maximum error in the performance prediction. In Fig. 17 the pressure differentials along the blade have been plotted and the smooth entry point is again demonstrated. The theoretical pressure differential is plotted at the expected design flow rate and the agreement is favorable.

From the minimum value of static-head coefficient in Fig. 16, the experimental cavitation operation can be determined. For incipient cavitation, $(-)C_P$ is a dimensionless NPSH and $\sigma = (-)C_P/\psi$. Both $(-)C_P$ and σ are plotted in Fig. 18 and the value of σ determined by the optimizing analysis is indicated. It is seen that operation at small angle of attack is not detrimental to cavitation susceptibility, but the true best cavitation coefficient does occur at the shockless entry flow rate. It is of interest to note that σ is less at a lower flow rate than $(-)C_P$ due to the greater increase of ψ. However, σ plotted as a function of flow rate is misleading; NPSH is the absolute quantity to consider.

Discussion

The agreement between the theoretical performance predicted by the design procedure and the performance achieved is believed to be good. The best efficiency point, the shockless entry point, and best conditions for cavitation all occur at the same flow rate, which is about 4 per cent less than the expected design point. The design method predictions and the experimental results agree then to within 5 per cent. This discrepancy is not large and may be due to any number of causes. In Fig. 19 a comparison of the experimental performance (based on C_L), the performance predicted by the design procedure, and the performance of the blade shape as an isolated airfoil is made as percentage of the isolated performance. Also shown are the results of two modern cascade theories. The usefulness of the present design method is clearly demonstrated.

One result of the experimental work that was not expected

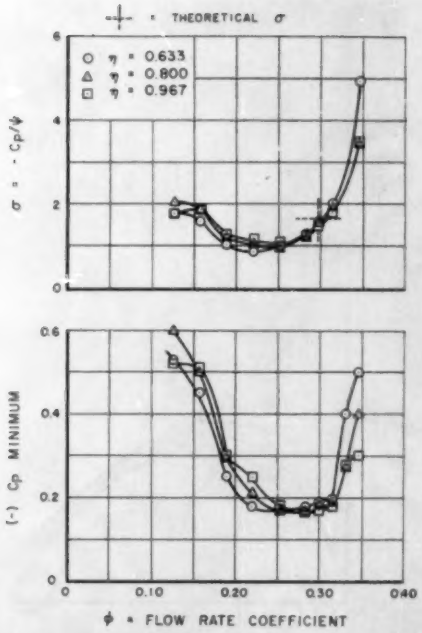

FIG. 18 INCIPIENT CAVITATION COEFFICIENT DETERMINED FROM STATIC HEAD DISTRIBUTION

concerns the nearly similar head developed at all radial sections over a large range of flow rate. This means that free-vortex operation is approximate over a range of flow rather than at a single flow rate, as is the usual case. This result is not completely understood at the present time. The design method was only intended to deal with the desired design performance quantities, so investigation of the prediction of off-design performance would provide valuable additional material for the present procedure.

With regard to the allowance for the inlet-velocity profile in evaluating the experimental results, it is important to realize that the inlet of the test setup consisted of a long section of pipe which permitted growth of a thick boundary layer. The inlet of a normal commercial pump should not include this boundary-layer difficulty and no allowances in the design procedure would be necessary.

For the complete pump a diffusing section also must be considered. The experimental impeller herein described has a reaction of from 90 to 95 per cent at the design point. This means that only about 5 to 10 per cent of the total energy produced by the impeller is recoverable from the tangential-velocity component. It seems reasonable then that diffusing blades need not be very large or heavily loaded. In fact considering that diffusion blades in themselves will add losses, perhaps the most efficient diffuser in this case would be no diffuser blades at all. In cases where the reaction is lower and diffuser blades are necessary, then from interference consideration the diffuser blades should be some distance removed downstream of the impeller. If the diffuser-blade row is quite close to the impeller, proper prediction of impeller performance cannot be made. More complete investigation of diffuser influence on impeller operation is another desirable addition for this design procedure.

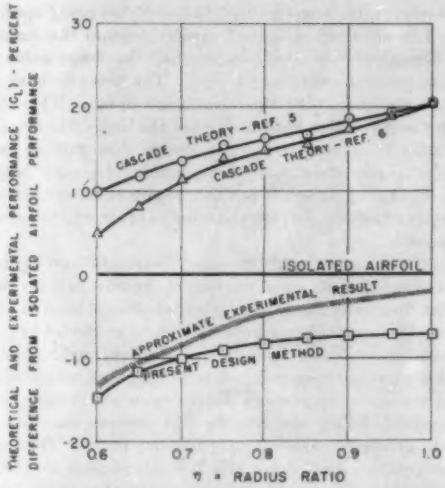

FIG. 19 COMPARISON OF THEORETICAL EXPECTATION AND EXPERIMENTAL RESULT AS PERCENTAGE FROM ISOLATED AIRFOIL PERFORMANCE

ACKNOWLEDGMENT

Acknowledgment is made to Profs. D. A. Morelli and A. J. Acosta for their interest and very helpful advice.

BIBLIOGRAPHY

1 "Pressure Distributions on the Blade of an Axial-Flow Propeller Pump," by D. A. Morelli and R. D. Bowerman, Trans. ASME, vol. 75, 1953, pp. 1007–1013.

2 "Three-Dimensional Interference Effects of a Finite Number of Blades in an Axial Turbomachine," by H. N. Tyson, Jr., Hydrodynamics Laboratory Report E-19.1, California Institute of Technology, November, 1952.

3 "The Design of Propeller Pumps and Fans," by M. P. O'Brien and R. G. Folsom, University of California Publications in Engineering, vol. 4, no. 1, 1939.

4 "Analysis of Modern Propeller-Pump Design," by W. Spannhake, David W. Taylor Model Basin Report 621, June, 1948.

5 "Theoretical and Experimental Investigations of Axial Flow Compressors," by J. T. Bowen, R. H. Sabersky, and W. D. Rannie, report on research conducted under contract with the Office of Naval Research, California Institute of Technology, Pasadena, Calif., 1949.

6 "An Approximate Theory for Potential Flow Through Cascades of Airfoils," by G. E. Hlavka, PhD thesis, California Institute of Technology, Pasadena, Calif., 1954.

7 "Fluid Mechanics of Turbomachinery," by G. F. Wislicenus, McGraw-Hill Book Company, Inc., New York, N. Y., 1947.

8 "Problems and Results of Investigations on Cascade Flow," by H. Schlichting, *Journal of the Aeronautical Sciences*, vol. 21, no. 3, 1954, p. 163.

9 "Summary of Airfoil Data," by I. H. Abbott, A. E. von Doenhoff, and L. S. Stivers, Jr., NACA TR 824, 1945.

10 "Principles of Rocket-Turbopump Design," by C. C. Ross, *American Rocket Society Journal*, vol. 21, March, 1951, pp. 21–33.

Suppression of Pump Vibrations Set Up at Starting Up—Preopening Method

By F. NUMACHI,[1] SENDAI, JAPAN

Cases occur in large water pumps, wherein, after installation, vibrations exceeding allowable limits are found to set in when starting up, and as a measure to meet such situations without resorting to reconstruction of the pump itself, a method of "preopening" is presented in this paper, which consists of opening up the delivery valves to a certain extent while the pump is gradually being worked up to full speed. The method of estimating the quantity of reverse flow, the torque required, and the time necessary for attainment of normal speed is explained. An example of application in actual practice is further given.

Introduction

In large pump installations, cases are encountered in which vibrations exceeding allowable limits are found to be set up in the water pipes and other parts, causing instability and disorders in operation. This phenomenon stems from transient pressure occurring inside the pump. In constructing large pumps, model experiments are conducted to confirm the fulfilment of the given specifications, but phenomena such as the vibrations mentioned tend to be overlooked, and in many cases not foreseen (1, 2).[2]

The vibrations may be classified into the following two general categories: (*a*) Vibrations at the normal speed of operation; and (*b*) those setting in when starting up. An example of the former is that encountered in the pumps installed at the Grand Coulee Dam and studied on that occasion, while the present paper deals with a situation featuring the latter category of vibrations.

Measures that naturally suggest themselves for coping with these forms of vibration are:

1 To prevent resonance by stiffening, and at the same time, raising the natural frequency of the parts of machinery connected with the pump and involved in the vibration.

2 To replace or reconstruct the source of the vibration, i.e., the pump, so as to limit the vibrations to within allowable limits.

These two measures, applied to case (*a*) have been discussed in detail in papers dealing with the Grand Coulee pump (1, 2, 3). Similar methods might be applied quite successfully to case (*b*) also, but considerable cost and, in particular with the latter measure cited, also much time, would be involved in execution, since it would not be a technically simple problem to find out a point of compromise between the demand for small vibration and the other stringent conditions to be satisfied. For this reason the present paper sets forth a method whereby, in the case where application of the first of the foregoing measures does not suffice, instead of proceeding with the second one of rebuilding the pump, other measures are applied which avoid alteration to the pump itself.

The method was devised by the author as a measure to cope with the situation met in the centrifugal pumps installed at the Numazawanuma Pumped-Storage Electric Power Station on the Tadami River Basin, and belonging to the Tōhoku Electric Power Company, Ltd. Preliminary experiments had yielded satisfactory results, and subsequent application to actual practice by the company further confirmed the soundness of the method, which has been given the designation "preopening method."

Vibrations Set Up in the Numazawanuma Pumps

The first stage is constituted of two single-suction pumps with a delivery head of 100 m, the second stage of one double-suction pump with 111 m head. Two such sets of centrifugal pumps are installed. The pumps were designed after due study (4, 5) at the Kameari Works of Hitachi, Ltd., where they were constructed. The author collaborated with the company to the following extent, upon the request of the Tōhoku Electric Power Company, Ltd.: (*a*) Appraisal of the pump and needle-valve design; (*b*) guidance in model experiments, and in particular, in cavitation tests; (*c*) appraisal of plans for conducting the test runs; (*d*) responsibility for flow measurements (6) in the efficiency tests; and (*e*) plans for suppressing starting-up vibrations.

Technical conferences were held more than thirty times with engineers in charge in the two companies mentioned, and the author further collaborated in the field tests.

The original specifications of the pumps are as follows:

Delivery head: Normal, 211 m; maximum, 226.2 m; minimum, 194.8 m
Capacity: Normal, 7.9 m³/s; maximum, 8.8 m³/s; minimum, 6.95 m³/s
Speed: 500 rpm
Power input: 20,100 kw (maximum)

The pump is installed with its horizontal axis common to the generator and the Francis turbine, which latter is utilized for starting up. Upon the revolutions reaching synchronous speed, the generator is connected in parallel to the electric mains, and operated as a motor, supplying power to the pumps. Thereupon the water turbine is cut out and delivery of water is started. The level of the water turbine being below the discharge water level, the cutting out of the water turbine is performed by pushing down the water level inside the water turbine by compressed air after closing the main valves, until the water turbine is running freely in air. The vibrations in question set in during this period between starting up, water turbine cutout, and opening of the delivery valves.

Theory of the Preopening Method

Preopening. The usual procedure in starting up pumps is to let the driving motor reach normal speed with the delivery valves closed, and then to proceed with opening them. With the method which we call preopening, the delivery valve is opened at a speed N_0, and a suitable flow established prior to attainment of the normal revolutions. To illustrate the process from starting up to normal operation on the complete character-

---

[1] Professor, Director, Institute of High Speed Mechanics, Tōhoku University.

[2] Numbers in parentheses refer to the Bibliography at the end of the paper.

Contributed by the Hydraulic Division and presented at the Diamond Jubilee Annual Meeting, Chicago, Ill., November 13–18, 1955, of The American Society of Mechanical Engineers.

Note: Statements and opinions advanced in papers are to be understood as individual expressions of their authors and not those of the Society. Manuscript received at ASME Headquarters, August 25, 1955. Paper No. 55—A-145.

istics diagram shown in Fig. 1, the orthodox method of starting up with the delivery valves fully closed may be represented by the curve AA_2A_1BCD, during which stage violent vibrations might be experienced in the range A_1BC. One way of eliminating the vibrations would be to provide a by-pass pipe connecting the suction and delivery sides of the pump and thus to

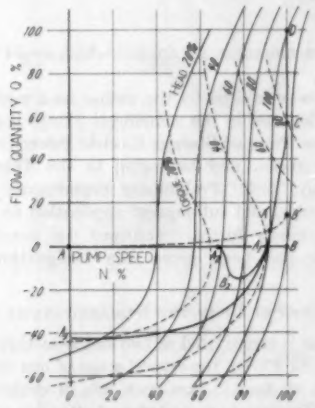

FIG. 1 PREOPENING METHOD ILLUSTRATED ON COMPLETE CHARACTERISTICS DIAGRAM

let some of the water circulate before normal speed is attained. This would be represented by the line $AB'CD$ on the same figure. This method, however, would not help in the cases where the vibrations occur in the section $B'C$.

With our present method, the delivery valve is opened prior to reaching normal speed in starting up, in such manner as to avoid the ranges of dangerous vibrations appearing in the complete characteristics diagram, and the vibrations which set in at start-up are lowered to within tolerable limits.

To explain this diagrammatically—if we take a pump that creates a delivery head of 100 per cent specified head at 90 per cent normal speed, and with which the range A_1BC involves excessive vibrations, while the range AA_1 is safe in this respect, the delivery valve is opened at the point A_1 of 90 per cent normal speed, upon which the path AA_1CD is followed, and the starting up accomplished without having to traverse the dangerous section $A_1BB'C$. In the case where the danger zone extends only to the stretch A_2A_1, the valve is opened at A_2, whereupon the path $AA_2B_2A_1CD$ is followed and the zone in question avoided. The location of the point A_2 is determined by the conditions to be fulfilled of avoiding the danger zone and of limiting to a minimum the amount of reverse flow incurred in the passage of the stage $A_2B_2A_1$. Finally, if the whole range AA_1 lies in the danger zone and if a large amount of reverse flow may be tolerated, cases might occur when the valve would be opened before the pump is set in motion, and then the path AA_2A_1CD would be followed.

To classify the cases just cited according to the timing of the moment when the delivery valve begins to open:

A, valve begins to open before starting up
B-I, valve opening commenced simultaneously with starting up
B-II, valve opening commenced after starting up, at speed N_0

Of these three cases, *B*-II should be the most commonly used, and the others only would constitute exceptional cases.

In adopting the preopening method, the conditions to be set for the procedure must be determined upon the basis of a series of experiments varying the timing, extent, and rate of the valve opening, to find out the optimum conditions for bringing the vibrations down to a tolerable amount. When conducting these experiments on full-size machinery, prior consideration should be given to the following points: (*a*) That the reverse flow through the pump and the required torque should not exceed allowable limits; (*b*) that the time required between starting up and the attainment of normal speed should be reasonably short. This entails the necessity of estimating previously the limits to be set for varying the degree and timing of preopening in the experiments so as to reduce the accompanying danger and cost to a minimum.

Flow Rate and Torque of Pump. We will first treat the method of estimating the rate of flow (either direction) and pump torque at any given intermediate speed N prior to attaining normal speed N_n. We will assume that the complete characteristics diagram (7) of the pump has already been drawn and that the characteristics of the delivery valve also are known.

These assumptions should hold in the case of pumps of large capacity, since in constructing pumps of such size, it is necessary to estimate the complete characteristics of the prototype by means of model experiments as a measure against the occurrence of water-hammer phenomena (4, 7) and cavitation (3, 5).

When

H = total head between upper and lower water levels
H_p = pump head
Q = pump flow rate
T_p = torque required by pump
h_v = loss of head at delivery valve
v = mean velocity at delivery valve
s = degree of delivery-valve opening, per cent
A = cross-sectional area of passage at opening s

it is already known (4, 7) that

$$h_v = \zeta_v v^2/2g = \zeta_v (Q/A)^2/2g \quad [1]$$

$$\zeta_v = f_v(s) \quad [2]$$

$$H_p = f_p(NQ) \quad [3]$$

Neglecting the head loss and velocity head in the suction and delivery channels (being very small in pumps of this variety; 0.2-0.3 per cent of H_p in the case of the Numazawanuma pumps) the following relationship holds

$$H = H_p \pm h_v \quad [4]$$

where the negative sign pertains to flow in the normal direction and the positive sign to that in the reverse.

In describing our method of estimation, we will distinguish the two general cases of preopening timing mentioned in the preceding section under preopening.

Case A. Considering first the case where the valve has been opened to the degree s prior to starting up, we utilize Equations [1] and [2], from which we may express the head loss h_v for various values of s by curves representing it as a function of Q with s as parameter

$$h_v = f_v(sQ) \quad [5]$$

This relationship is presented in Fig. 2. Next, the H_p-Q relationship for a given speed N may be obtained from the complete characteristics diagram represented by Equation [3], and so we divide N into a suitable number of steps between 0 and the normal speed, and find the H_p-Q relation, and from that the (h_v-$+ H_p$)-Q relation for each step, and plot the curve in Fig. 2. The delivery rate Q_{sN} corresponding to the given s and N may then be found as the point of intersection of the curve with the straight line $H = H$. Q_{sN} may thus be obtained as a function of N with s as parameter

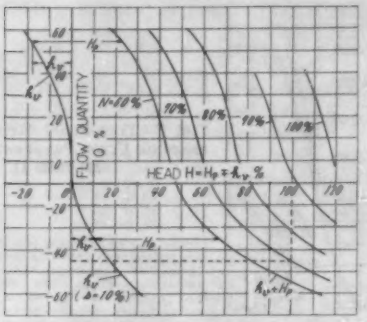

FIG. 2 ESTIMATE OF PUMP FLOW (NORMAL AND REVERSE) AT INTERMEDIATE SPEED N AND WITH A CONSTANT VALVE OPENING s

$$Q_{sN} = f_Q(sN) \quad [6]$$

Next, T_p the torque required by the pump also may be read from the complete characteristics diagram as a function of N and Q, thus

$$T_p = f_T(NQ) \quad [7]$$

Therefore T_{ps} the torque corresponding to s and N in Equation [6] may be obtained as a function of s and N by utilizing the values of Q_{sN}

$$T_{ps} = f_{Ts}(sN) \quad [8]$$

Neglecting in these relationships the effects stemming from transient phenomena of flow occurring during the period of mounting speed, the Relations [6] and [8] represent the changes in the flow rate and required torque occurring in conformance with mounting speed at starting up with the delivery valve open from the outset (case A). This is represented graphically in Figs. 3 and 4 by the full lines denoted A. Both the abscissa and co-ordinates in these figures are represented in percentage of normal ratings.

Case B. In a manner similar to the foregoing case, we neglect the effect of transient-flow phenomena, and further give the relationship holding between the degree of opening and the speed N expressed by

$$s = f_s(N) \quad [9]$$

Plotting several points satisfying this equation on the Q-N and T_p-N curves for constant s in Figs. 3 and 4, we may directly obtain curves for Q_N-N and T_p-N

$$Q_N = f_Q(N) \quad [10]$$

$$T_{pN} = f_T(N) \quad [11]$$

The factors determining the relationship expressed by Equation [9] are the following: (*a*) Characteristics of the driving prime mover; (*b*) the pump characteristics represented by Equations [3] and [7]; (*c*) the delivery-valve characteristics, Equations [1] and [2]; (*d*) characteristics of the mechanism for manipulating the delivery valves. With regard to (*d*), let us assume, for instance, that the time rate of valve opening be as represented in Fig. 5, and the s-t relationship be as expressed by

$$s = f_s(t) \quad [12]$$

In actual practice, Relations [10] and [11] may be made to

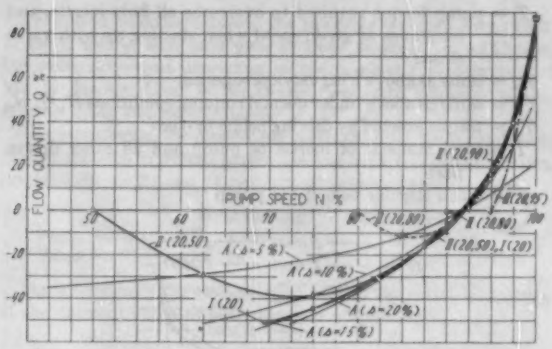

FIG. 3 PUMP FLOW (NORMAL AND REVERSE)—SPEED RELATION DEPENDING UPON VALVE PREOPENING s

(*A*, Preopening begins before starting up; I, at moment of start; and II, at speed N = 50, 80, 90, 95 per cent of normal N_n.)

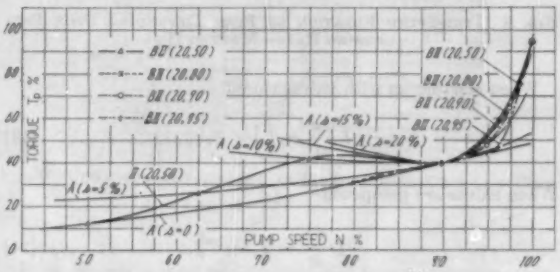

FIG. 4 PUMP TORQUE-SPEED RELATION DEPENDING UPON VALVE PREOPENING s

(*A*, I, and II: as with Fig. 3)

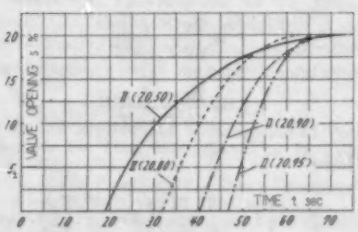

FIG. 5 TIME-OPENING RELATION OF DELIVERY VALVE

assume a suitable form by adjusting Relationship [9] through appropriate determination of [12] by proper manipulation of the delivery-valve operating mechanism. As an example of calculation, the curves in Figs. 3 and 4 represent cases where s and N are linearly related. The notation I pertains to the case where valve opening is started at the instant when $N = 0$, while the curves denoted II represent cases where the valve begins to open when speed has reached 50, 80, 90, and 95 per cent, respectively, of normal revolutions, and becomes 20 per cent open in all four cases simultaneously with the pump reaching full speed.

Time Required. The N-t curve for the period prior to attainment of normal speed actually may be measured for the case where full speed is caused to be attained with the valves closed (orthodox procedure, cf. bottom line in Fig. 6). Based on this curve, we will now describe the method of estimating the time required for starting up with the preopening method.

The following notations will be used:

T = pump torque required to overcome all fluid inertia, and resistance at given speed when starting up with valve closed
T_p = same as above with valve preopened
T_n = same as above under normal running conditions H_n Q_n N_n
T_t = torque exerted by driving prime mover
I = total moment of inertia of pump and all other driven part
ω = mean angular velocity of pump

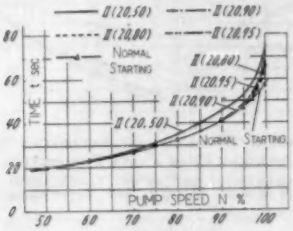

FIG. 6 TIME-SPEED RELATION OF PUMP DEPENDING UPON PREOPENING RATE—METHOD II

When starting up with valves closed

$$I \frac{d\omega}{dt} = T_t - T \quad \ldots\ldots [13]$$

When valves are preopened

$$I \frac{d\omega}{dt} = T_t - T_p \quad \ldots\ldots [14]$$

Therefore, if we let i represent the gradient of the curve for closed starting (bottom curve) in Fig. 6, and i_p the same for preopened starting (all except bottom curve)

$$i = \frac{2\pi}{60} \frac{I}{T_t - T}$$

$$i_p = \frac{2\pi}{60} \frac{I}{T_t - T_p}$$

Then, we have

$$\frac{i_p}{i} = \left(1 - \frac{T}{T_n}\frac{T_n}{T_t}\right)\left(1 - \frac{T_p}{T_n}\frac{T_n}{T_t}\right) \quad \ldots\ldots [15]$$

The values of T/T_n and T_p/T_n in Equation [15] may be obtained from Fig. 4, while the working characteristics of the driving prime mover being known, T_n/T_t may be found, from which i_p/i may be calculated. Consequently, we may obtain from Equation [15] the gradients of the various curves at different speeds. The t-N curves all pass through the point $t = 0$, $N = 0$, so that the curves may be drawn with this origin as starting point, the result being a group of curves such as shown in Fig. 6. We have thus been enabled to grasp the whole process from $N = 0$ to $N = 100$ per cent from which the time required for the process may be obtained. Fig. 6 has been drawn from the cases where the valves have started to open when N reached 50, 80, 90, and 95 per cent, respectively, of the normal N_n and have attained the opening $s = 20$ per cent when N reached full speed.

Estimation of the Total Reverse Flow. To estimate the total volume of reverse flow, the speed at each instant is read from Fig. 6, while the rate of flow at these speeds is obtained from Fig. 3, and the relation between Q and t thus found plotted as in Fig. 7 for each instant. The total flow will then be obtained as the area surrounded by the negative portion of the curve and the abscissa.

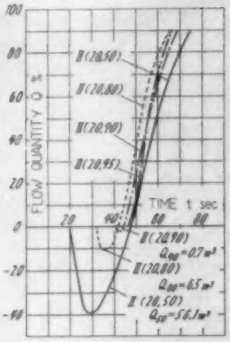

FIG. 7 TIME-FLOW RELATION DEPENDING UPON PREOPENING RATE—METHOD II

EXAMPLE OF ACTUAL APPLICATION OF PREOPENING

Vibrations Set Up in Numazawanuma Pumps. After the primary tests conducted in November, 1952, the Tōhoku Electric Power Company kept taking measurements at intervals, making a special point of observing the vibrations set up, by means principally of wire strain gages set on the bearings and combined with a cathode-ray oscillograph, use also being made of a vibrometer. The result of measurements undertaken in January and April, 1953, was that with the delivery valves fully open and at normal speed, the amplitude was of the order of (15–18)/1000 mm, but that when starting up, pumps Nos. 1 and 2 set up vibrations reaching as high as 60/1000 mm, raising a noise of the level of 120 phons and causing resonance in the connecting machine parts and the windows and doors of the housing, filling it with reverberations and vibration to an alarming extent. Fatigue was feared in the material constituting the machine parts, and countermeasures were called for. However, it may be noted that no marked vibration was detected in the delivery pipes; which contrasted with the situation met in the Grand Coulee pump installation. A general layout of the piping already has been reported (6).

On April 10, 1953, the author made the suggestion at the 23rd study conference held between the Tōhoku Electric Power Company, the Hitachi, Ltd., and the author's Institute, that the preopening method be adopted.

Preliminary Tests. Tests were performed under the direction of Section Chief M. Abe of the Tōhoku Power, with the assistance of staff members from the two companies, on pump No. 2 during the period July 6–12, 1953, to investigate the possibilities of the preopening method in suppressing the vibrations. The author participated in the experiments as adviser. Prior to this, calculations were made for various cases according to the present method, at the Kameari Works of the Hitachi and at the author's Institute, to obtain from the volume of reverse flow and the required torque a general estimate of the optimum values for the degree of preopening s and the speed N_0 for starting the preopening. The result indicated that the values $N_0/N = 80$–100 per cent and $s = 10$–20 per cent should be aimed at.

In performing the tests, the opening operation—by hand—of the valve was started when the speed reached N_0 and manipulated so as to reach the opening s after t_s seconds.

The data of the actual tests turned out to be as in Table 1, from which it will be seen that neither N_0 nor s became round figures.

The values obtained with the vibrometer were considered to

TABLE 1 RESULT OF PRELIMINARY TESTS

Test no.		2-1	2-2	2-3	3-1	3-2	3-3	4-1	5-1	5-2
N_0 rpm		510	469	416	511	469	411	463	480	465
N_0/N_n%	aimed	100	90	80	100	90	80	90	94	90
	experi.	102	93.8	83.2	102.2	93.8	82.2	92.6	96.0	93.0
s %	aimed	10	10	10	20	20	20	13.3	16.7	16.9
	experi.	8.13	10.8	11	19.8	19.7	19.3	13.3	17.3	17.5
t_0 sec		11.3	9.9	13.0	13.1	13.4	11.0	11.5	11.8	12.2
N_s rpm		505	492	465	500	487	450	485	485	485
t_N sec			21.5	34.7		33.8	38.0	27.3	25.0	30.2
v_0		1.25	0.94	0.52	0.82	0.52	0.42	0.63	0.73	0.83
v_s		0.73	0.63	0.78	0.32	0.31	0.73	0.42	0.32	0.42
v_N			0.63	0.68		0.31	0.42	0.42	0.32	0.42

N = Normal revolutions per minute
N_0 = Speed at which preopening was started
s = Preopening of valve at final stage (%)
N_s = Speed when opening s was reached
t_0 = Time required for opening to reach s from 0
t_N = Time required for speed to reach N
v_0, v_0 = Amplitude of vibrations at opening 0 and s, respectively
v_N = Amplitude when speed N was reached

be somewhat less reliable than those of the wire strain gage-oscillograph combination, so the values of v_0, v_s, v_N are indicated in ratios to the value corresponding to the normal speed 500 rpm with delivery valve fully closed, the amplitude under these conditions being measured with the oscillograph. The reading of the televibrometer in this instance was 60/1000 mm.

Fig. 8 shows the change with time of the values of valve opening a_t, pump speed N, and amplitude ratio v_t. The results indicate that when N_0 is too small, the time required for attainment of full speed becomes unduly long, over and above which the

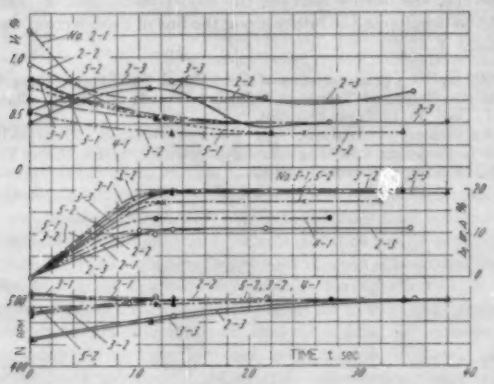

FIG. 8 RATIO v_t OF VIBRATION AMPLITUDE AT INTERMEDIATE TIME t ON PRELIMINARY TEST
(a_t: valve opening at time t.)

vibrations are magnified by the reverse flow. The optimum values were found to be in the range N_0 = 90–94 per cent and s = 16.7–20 per cent, under which conditions it was ascertained that the vibrations at starting up could be reduced to less than half.

Test Runs on Preopening. The Tōhoku Power followed the preliminary tests with the installation of electrical and mechanical apparatus constructed by Hitachi for manipulating the valves in preparation for the adoption of the preopening method. Test runs were performed from June 25–30, 1954, at which the author again participated, the methods of measurement being the same as before. The maximum vibration amplitude was found to have dropped from the (15–18)/1000 mm recorded during the preliminary tests to 2.5/1000 mm at full speed and with valve fully open, while at starting up, the same had been reduced from the original (55–60)/1000 mm down to (17.5–18)/1000 mm. The cause of this improvement is believed to have been the reinforcement of the by-passage part at the main valve of the water turbine and other pump accessories found to have caused resonance during the previous tests of July, 1953. These measures were analogous to those taken at Grand Coulee, but were carried out according to the original considerations of Mr. K. Honda, Chief of the Design Section of Kameari Works, Hitachi, Ltd., and his colleagues.

The adoption of the preopening method under these conditions proved that the vibration amplitude had been reduced as follows, respectively, to 29 and 44 per cent of previous values:

	Closed starting	Preopened starting
Pump No. 1.....	17.5	5/1000 mm
Pump No. 2.....	18	8/1000 mm

Fig. 9 illustrates the changes with time of the speed N, opening of the delivery valve a_t, and vibration amplitude V.

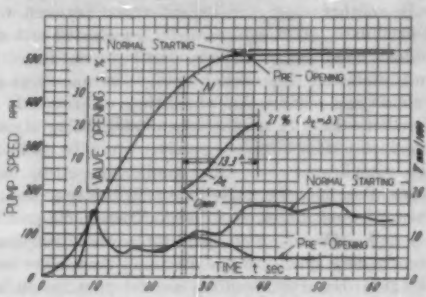

FIG. 9 VIBRATION AMPLITUDE V AT INTERMEDIATE TIME t ON TEST RUN

ACKNOWLEDGMENT

In conclusion, it must be acknowledged with appreciation that valuable assistance was given by Assistant Professors S. Saitō and H. Murai in performing the calculations involved in the work reported in the paper, while the author is greatly indebted to Mr. M. Shirakawa, Vice-President of the Tōhoku Electric Power Company, Ltd., and to Mr. M. Abe, Chief of the Electrical Construction Section of the same company, for their courtesy in permitting the publication of the experimental results.

BIBLIOGRAPHY

1 "Grand Coulee Model-Pump Investigation of Transient Pressures and Methods for Their Reduction," by E. Lindros, Trans. ASME, vol. 76, 1954, p. 775.

2 "Vibration of the Grand Coulee Pump-Discharge Lines," by J. Parmakian, Trans. ASME, vol. 76, 1954, p. 783.

3 "Development of the Hydraulic Design for the Grand Coulee Pumps," by Carl Blom, Trans. ASME, vol. 72, 1950, p. 53.

4 "Experimental Research on Water Hammering of a Pump of the Numazawanuma Storage Power Station," by T. Kobori, *Journal of the Japan Society of Mechanical Engineers*, vol. 56, 1953, p. 479.

5 "Model Test on Cavitation Characteristic of Pumps for the Numazawanuma Storage Power Station," by S. Yokoyama, *Journal of the Japan Society of Mechanical Engineers*, vol. 56, 1953, p. 332.

6 "Streamlined Pitot-Tube Bar for Measuring Water Flow in Large Pipe," by F. Numachi, H. Murai, and S. Abe, Trans. ASME, vol. 78, 1956, pp. 1079–1089.

7 "Typical Analysis of Water Hammer in a Pumping Plant of the Colorado River Aqueduct," by R. M. Peabody, Trans. ASME, vol. 61, 1939, p. 117.

Discussion

R. T. KNAPP.[3] This paper is very timely because it focuses attention on a type of problem that is relatively new in the centrifugal-pump field and also offers a new method of attack for its solution.

[3] Professor of Hydraulic Engineering, California Institute of Technology, Pasadena, Calif.

Hydraulic turbines and pumps are close relations and have many things in common, particularly in their hydrodynamic characteristics. In fact, a good turbine can be operated as a pump with high efficiency and a good pump is also an excellent turbine. However, there is one striking difference in their fields of application. Hydraulic turbines are usually installed in large units. Thus a turbine whose output is measured in hundreds of horsepower is considered small and is rarely seen. On the other hand, the vast majority of centrifugal pumps are driven by motors of under 100 hp, and pumps requiring thousands of horsepower to operate them are very uncommon and have only been developed in relatively recent times. Thus pump manufacturers and users have had relatively little experience with troubles peculiar to large installations.

There is another characteristic difference between the two types of machines. Turbines normally are started and stopped under no-load conditions. Usually, the basic nature of the installation is such that they cannot be made to operate as a pump nor can conditions occur under which they will rotate in the reverse direction. Pumps, on the other hand, either start under load or against a closed discharge valve, which in itself imposes extremely complicated hydraulic conditions. Also, in many installations, they may be made to run in the reverse direction as turbines, at least for brief periods. These facts create comparatively little difficulty with small units where starting times are inherently very short and the machines themselves are compact and rigid. However, troubles like the ones the author discusses are beginning to arise in the transient operation of large units.

The author's use of the complete characteristic diagram to explore and calculate the characteristics of special methods of starting is most interesting. In the past the use of the characteristic diagram has been restricted largely to the calculation of water hammer produced during normal or abnormal shutdown of large pumps.[4] This new use should serve to emphasize the wide possibilities inherent in this type of diagram.

There is still one weak point in the present situation. This weak point is not with the author's method, but rather with deficiencies in laboratory methods of testing model pumps. Thus in Figs. 3 and 4 of the paper various possible starting procedures are plotted, the evaluation of the relative desirability of which requires field testing. The only reason that field tests are necessary is that the normal laboratory tests do not yield the necessary information about the amount of vibration-producing pressure fluctuations along the different paths. It seems quite certain that the pressure fluctuations occur in the model pump as well as in the prototype but the relative vibration is usually very much smaller because in the past the model pump has never been a structural model but only a hydrodynamic one. Thus it seems quite clear that there is a need to improve model-testing techniques so that troubles of this kind can be anticipated and avoided in the field installation.

Author's Closure

The author wishes to express his appreciation of the understanding discussion given by Prof. Robert T. Knapp.

His suggestion that model testing techniques should be improved from the viewpoint of a structural model is a valuable one.

Though there are some difficulties in seeking the principles of similarity in elastic vibration concerning the model and its prototype, the author believes the model techniques of pumps ought to develop in the future along the line of Prof. Knapp's suggestion.

---

[4] "Complete Characteristics of Centrifugal Pumps and Their Use in the Prediction of Transient Behavior," by R. T. Knapp, Trans. ASME, vol. 59, 1937, pp. 683–689.

"Waterhammer Analysis," by John Parmakian, Prentice-Hall Civil Engineering and Engineering Mechanics Series, New York, N. Y., 1955; see chapters 11 and 12.

Evaluation of Factors Affecting Heat Transfer in Furnaces

By MURRAY GREYSON,[1] G. P. MAZIE,[2] J. W. MYERS,[3] R. C. COREY,[4] AND E. G. GRAF[5]

The problem of correlating the heat-absorption efficiencies of coal-burning equipment has been studied for many years with little more than a modicum of success. It has been consistently pointed out that one of the major problems of correlating data such as these has been the lack of precise furnace data. This paper describes the attempt at using statistics to correlate more reliable furnace data by means of the Broido, Hudson-Orrok, a modified Hudson-Orrok, Wohlenberg, and Hurvich correlations. Results suggest that information about flame temperatures, flame volumes, and emissivities and temperatures of flames and slag-ash-covered boiler-tube walls are necessary before precise correlations can be made.

Introduction

THE combustion of fuels in furnaces has been, and for a great many years will continue to be, the major source of thermal energy for the production of electric power and for the processing of materials. Indeed, there are few commercial or industrial operations that do not employ some sort of furnace in either a primary or auxiliary capacity. Despite the long history of the use and development of furnaces, and their technological importance, furnace design still is highly empirical, owing to a lack of knowledge of the complex heat and mass-transfer processes that occur within a combustion chamber. As with any technology that depends heavily upon empiricism, innovations are usually rare, and developments follow conventional lines until a high degree of perfection is achieved. Central-station boiler furnaces, for example, in which some 25 per cent of the nation's coal production is burned to generate steam for turbogenerators, have slowly evolved to a high degree of perfection by empirical means. It is highly improbable, however, that substantial improvements in dependability and performance, or reduction in capital and operating costs will come until there is better understanding of the nature of combustion and heat-transfer processes in flames and burning fuel beds, and the effects of these processes on the net heat transfer within the furnace cavity.

In the past 25 years, a great deal of both theoretical and experimental work has been done to elucidate the fundamental problems related to furnace design. This work, however, has been hampered by the great difficulty in isolating the individual processes that are related to combustion and heat transfer, and by poor co-ordination between combustion research and combustion engineering, especially from the standpoint of applying the results of the type of research that is presently being done. Moreover, the experimental procedures for measuring physical and chemical properties of flames and hot gases are difficult and subject to errors of unknown origin. For example, where nonluminous flames are concerned, it is possible to calculate the radiant-heat transfer to various parts of the furnace quite accurately, if the temperature, composition, and dimensions of the flame are known. Radiation from a luminous flame, however, is influenced by the presence of radiating particles in the flame, the effects of which are very difficult to evaluate experimentally.

Because of these difficulties, the amount of luminous-flame radiation is generally approximated by computing the theoretical nonluminous component of the flame, and then multiplying it by a relatively large factor, the magnitude of which depends upon experience with the types of fuel and furnace being used. This technique is necessary because, although it is known that carbon and ash particles in a flame markedly increase radiation from the flame and that size and concentration of the particles determine the contributions of the particles to the emissivity of the flame, information is meager, except for very simple systems, on mechanisms of particle formation, methods of characterizing the size and concentrations of particulate matter, and the quantitative effects of these factors on the radiation characteristics of clouds of particles.

Although it is generally believed that small-scale experiments in connection with luminous-flame radiation cannot provide the dynamic similitude that is necessary for the generalized correlation of flame variables, especially with regard to the aerodynamic factors that affect the size and shape of flames and the amount of recirculation of spent gases, the optimum scale for experimental work is not known, and probably will not be known until sufficient data have been obtained from furnaces of various sizes.

Data from full-scale furnaces are of immediate practical value if they are sufficiently precise and comprehensive, and may be used to develop empirical relationships between the operating variables and the furnace heat-absorption efficiency. Such relationships, however, are necessarily limited in scope, and do not achieve the ultimate objective in this field of research, that of relating flame radiation to heat absorption by a general equation. Moreover, experiments on full-scale equipment are limited in the range of operating variables that can be studied, the number and location of points where observations and measurements can be made, and the constancy of operating conditions within a given time interval. Notwithstanding these difficulties and limitations, full-scale experimentation is an essential phase of research in this field.

A large number of experimental data have been obtained from a wide variety of furnaces over a period of some 35 years, and numerous empirical equations have been proposed to relate the heat-absorption efficiency of a furnace to the operating variables of that furnace, such as percentage of excess air and heat-release rate. Attempts also have been made to correlate these data by means of such theoretical equations as the Stefan-Boltzmann law. However, owing to a lack of precision in the collection of data, or to the inadequacies of the equations, none of these re-

[1] Physical Chemist, Combustion Section, Bureau of Mines, Pittsburgh, Pa.
[2] Chemical Engineer, Armstrong Cork Company, Lancaster, Pa.
[3] Chemical Engineer, Combustion Section, Bureau of Mines, Pittsburgh, Pa.
[4] Chief, Division of Solid Fuels Technology, Region V, Bureau of Mines, Pittsburgh, Pa. Mem. ASME.
[5] Chemical Engineer, Fluchtgasse, Vienna, Austria, U. S. Zone.

Contributed by the Research Committee on Furnace Performance Factors and presented at a joint session of the Research Committees on Furnace Performance Factors and Corrosion and Deposits From Combustion Gases and the Power Division at the Diamond Jubilee Annual Meeting, Chicago, Ill., November 13–18, 1955, of THE AMERICAN SOCIETY OF MECHANICAL ENGINEERS.

NOTE: Statements and opinions advanced in papers are to be understood as individual expressions of their authors and not those of the Society. Manuscript received at ASME Headquarters, Sept. 26, 1955. This paper was not preprinted.

lationships has been found to be satisfactory for describing the data. Between 1948 and 1953, however, the United States Bureau of Mines, in co-operation with the Special Research Committee on Furnace Performance Factors of THE AMERICAN SOCIETY OF MECHANICAL ENGINEERS, published a series of papers covering details of experimental studies made on five industrial boiler furnaces (1–5),[6] the data from which were believed to be more reliable than many of the previous furnace data. These studies included work on three pulverized-coal-fired (Paddy's Run, Tidd Station, and Willow Island), one spreader-stoker-fired (Whiting), and one gas-fired furnace (Sterlington), and were made for the purpose of evaluating the factors affecting the heat-absorption efficiencies of these furnaces.

In 1953 the Committee decided that before any further experimental work was done the data from these installations should be analyzed to determine whether or not a generalized correlation of furnace heat-absorption efficiency could be obtained in terms of the operating parameters of the furnace. Accordingly, the Bureau of Mines initiated a detailed study of the data to determine whether any of a number of correlations that have been proposed could be used to describe these data. Although the analysis is not yet complete, some significant limitations of the data that, it is believed, can act as guides for future experimental work have become evident.

This paper is, therefore, a progress report and will cover the work that has been completed to the present time.

EXAMPLES OF PREVIOUS WORK

Hudson (6) in 1890 attempted to relate the heat transmission in a furnace to the radiant-surface area, the rate at which the fuel was consumed, and the air-fuel ratio, and proposed the following empirical equation for the heat-absorption efficiency of the furnace

$$\mu = \frac{XF}{Q} = 1 - \frac{A}{A + 45F} \quad [1]$$

where μ is the heat-absorption efficiency, X is the rate of heat transmission per hour per square foot of radiant wall surface, Q is the available heat per pound of coal fired, F is the number of square feet of radiant wall surface per pound of coal fired per hour, and A is the air-fuel weight ratio.

This equation was not universally applicable, and in 1925 was modified by Orrok (7) as follows

$$\mu = \frac{X}{C_r Q} = \frac{1}{1 + \dfrac{A\sqrt{C_r}}{27}} \quad [2]$$

where μ, X, and Q are defined as before, and C_r is the reciprocal of F.

At the same time that Orrok suggested his empirical modification of Hudson's equation, Broido (8) presented an empirical curve that was obtained from the average data of six boiler stations, and which related available heat per unit area of radiant surface to the heat-absorption efficiency of the furnace. Broido claimed that most existing data could be fitted to the curve with a precision of ±10 per cent.

Empirical correlations such as the Hudson, Hudson-Orrok, and Broido techniques supplied information about the over-all performance of a furnace, but gave no information about operating variables such as flame emissivities, flame temperatures, cold-wall temperatures, flame volumes, and specific burning rates of fuel. Moreover, the effects of ash and slag on the emissivity and temperatures of the cold wall of the furnace were not considered.

[6] Numbers in parentheses refer to the Bibliography at the end of the paper.

One of the first attempts to place furnace data on a fundamental basis was made by Wohlenberg and his associates (9–12), who, since 1925, have published a series of papers that relate various effects within a furnace to the operating parameters of the furnace. The approach used by these investigators was to apply certain heat-transfer equations to furnaces having specific assumed characteristics, and to calculate the theoretical heat-absorption efficiencies for these assumed furnaces. Experimentally determined furnace heat-absorption efficiencies were then compared with the calculated efficiencies when individual operating parameters were varied. The corrections to the theoretical efficiencies were then plotted as functions of the level of the operating parameters, and a series of factor curves were developed. By applying the proper set of factors to the calculated efficiency, it was then possible to calculate the heat-absorption efficiency of a real furnace. The equation used by Wohlenberg for the application of correction factors was

$$\mu = \mu_0 \prod_{i=1}^{i=8} K_i + C \quad [3]$$

where μ is the actual furnace heat-absorption efficiency, μ_0 is the efficiency of the assumed furnace, K_i are corrective factors related to furnace volume, fraction of total furnace wall that is cold, heat-liberation rate, per cent excess air, heating value of fuel, size of fuel particle, effective radiant-heating surface, and combinations thereof, and C is a factor related to preheated air temperature.

Other fundamental approaches have also been tried.

By a dimensional analysis of the furnace system, Hurvich (13) developed the following equation

$$B_0 = \frac{BQ\mu}{HC_e T_t^4 (1 - \theta_0)} \quad [4]$$

where μ is the furnace heat-absorption efficiency, B_0 is a modified Boltzmann number, B is the fuel-consumption rate, Q is the heating value of the fuel, H is the radiant wall area, C_e is the over-all emissivity of the combustion chamber, T_t is the adiabatic flame temperature, and θ_0 is the dimensionless ratio of the flue-gas temperature at the furnace outlet to the adiabatic flame temperature (the term B/R in this equation is equal to C_r in the Hudson-Orrok equation, Equation [2]). Hurvich showed by experiment that θ_0 and B_0 were related by an equation of the form

$$\theta_0 = \frac{B_0^{\alpha}}{1 + B_0^{\alpha}} \quad [5]$$

where α is a constant equal to 0.6 for coal-fired furnaces.

Konokov (14) improved upon Hurvich's equation by suggesting the heat-balance equation

$$Z_0^4 P_t \left[\frac{T_2}{T_t}\right]^4 + \frac{T_2}{T_t} - 1 = 0 \quad [6]$$

where

$$P_t = \frac{C_0 \left(\dfrac{T_t}{100}\right)^3 H}{100\, BVC_p} \quad [7]$$

$$Z_0 = \frac{T_2}{T_1}\sqrt[4]{\epsilon} \quad [8]$$

T_t is the adiabatic flame temperature, T_1 is the temperature of the flame surface, T_2 is the flue-gas temperature at the furnace outlet, B is the fuel-consumption rate, V is the volume of flue gas per unit weight of fuel, C_p is the average specific heat of the flue gas,

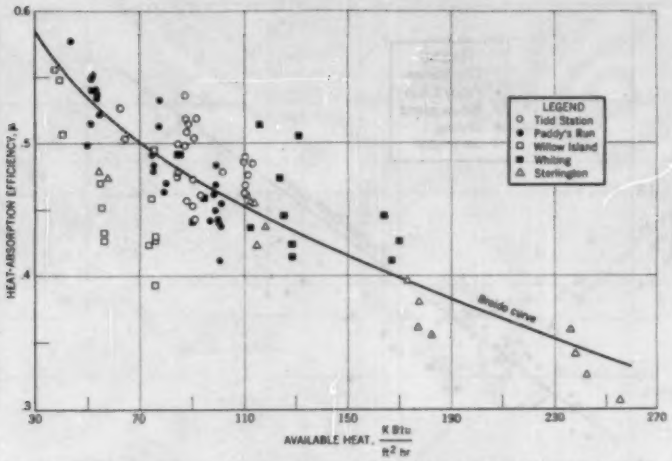

FIG. 1 CORRELATION OF EXPERIMENTAL HEAT-ABSORPTION EFFICIENCIES BY A BROIDO CURVE

C_0 is the Stefan-Boltzmann constant, H is the radiant surface area of the furnace, and ϵ is its emissivity.

The equations cited are just a few examples of the many attempts that have been made to correlate furnace-performance data and operating parameters, and have been selected to illustrate the variety of approaches that have been used in this work. It is sufficient to state here that the lack of precision of data collected in the past has prevented a comprehensive evaluation of the applicability of most of these correlations.

PROCEDURES

The analyses made by the Bureau of Mines of the data from the five boiler stations were divided into three separate steps. The first analysis was concerned with the general correlation of all of the data as a group with any one or all of five correlations: namely, the Broido, the Hudson-Orrok, a modified Hudson-Orrok, the Wohlenberg, and the Hurvich equations. In this phase, limited statistical techniques were used to compare heat-absorption efficiencies that were determined experimentally and those that were calculated or predicted from the proposed correlations. Accordingly, it was possible to determine whether or not the differences that were observed were statistically significant. The statistical method that was used in this and the other analyses is illustrated in the Appendix.

The second analysis was concerned with individual correlations and consisted of fitting the experimental data from individual stations to these proposed equations, and determining the significance of any differences that were observed between experimental efficiencies and those calculated from the equations. This phase was found to be necessary because in some instances the over-all data were adequately described by an equation, whereas data from individual stations differed appreciably from those calculated by the equation.

The third analysis was an attempt to find a generalized correlation that would describe the furnace data both as a group and individually by station. This phase of the work, of course, depended upon the results of the previous phases.

To date, most of the data correlation has been completed. The data from all five stations have been compared with the Broido, Hudson-Orrok, modified Hudson-Orrok, and Wohlenberg relationships. In addition, the data from the gas-fired furnace have been plotted, by means of estimated adiabatic flame temperatures, in the manner suggested by Hurvich and Konokov. It

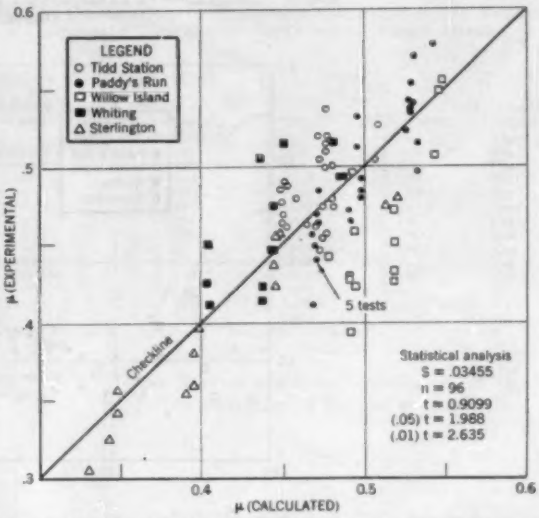

FIG. 2 CORRELATION OF PREDICTED EFFICIENCIES AND EXPERIMENTALLY DETERMINED EFFICIENCIES (BROIDO)

was not possible to plot data from the coal-fired units by means of the latter two equations because no comparable data on coal-flame temperatures are yet available. However, calculations of these flame temperatures are presently being done, and as soon as these data are available, the comparisons will be made.

RESULTS

Fig. 1 shows the 96 furnace tests from the five stations plotted according to Broido's curve, which is shown in the figure. To show better the relationship between the predicted and experimental efficiencies, the same data have been replotted around a "check line" in Fig. 2.

The spread of points around the line is characterized by an average difference of —0.00288 and a standard deviation of 0.03455. If the average difference between the predicted and experimental heat-absorption efficiencies is assumed to be due to a random distribution of experimental errors, and this average is compared with zero by means of the Student t-test, no significant

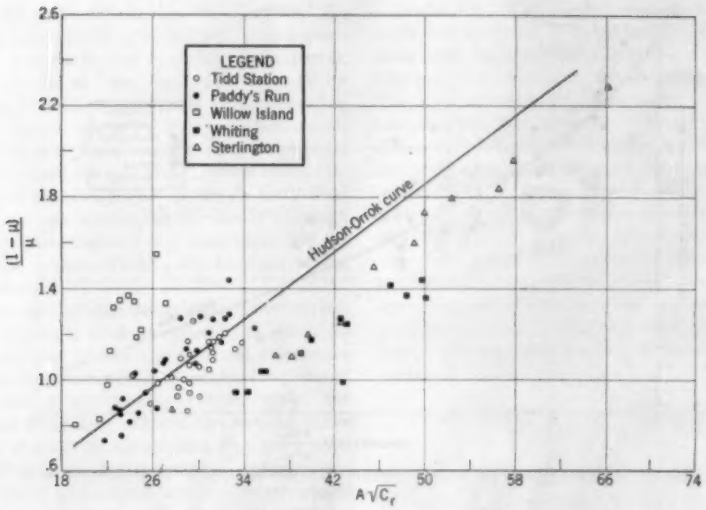

FIG. 3 CORRELATION OF EXPERIMENTAL HEAT-ABSORPTION EFFICIENCY BY A HUDSON-ORROK EQUATION

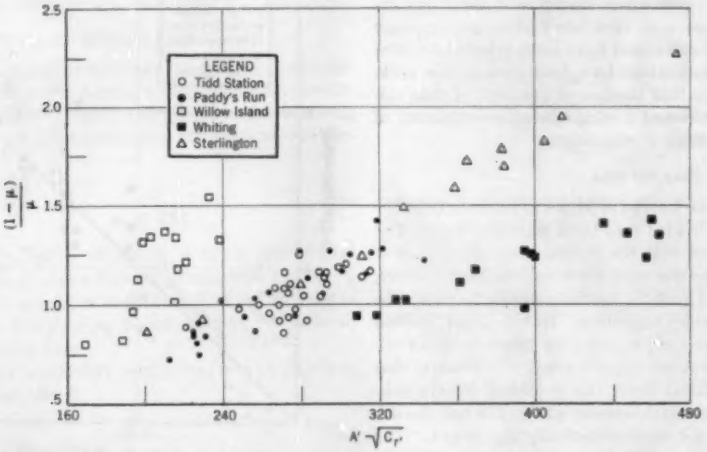

FIG. 4 CORRELATION OF EXPERIMENTAL HEAT-ABSORPTION EFFIENCY BY A MODIFIED HUDSON-ORROK EQUATION

difference is found between the predicted and experimentally determined efficiencies. The calculated t-value is equal to 0.9099, and compares favorably with values from a double-sided t-table of 2.635 and 1.988 per the 1 and 5 per cent probability levels, respectively.

The experimentally determined heat-absorption efficiencies are plotted in Fig. 3 according to the Hudson-Orrok equation, together with the curve obtained from the equation. In Fig. 4 the same data are plotted according to a modified Hudson-Orrok equation in which fuel consumption is expressed as thousands of Btu of available heat per square foot of radiant heating surface, and the air-fuel ratio as pounds of air per thousand Btu of available heat.

The differences between the predicted efficiencies calculated from the Hudson-Orrok equation and experimental results are shown in Fig. 5, in which the check-line technique was used. The plot is characterized by a mean difference of +0.00494 and a standard deviation of 0.0441. The calculated value of t of 1.097, when compared with table values of 2.635 and 1.988 for the 1 and 5 per cent probability levels, respectively, indicates that there is no significant difference between the calculated and the experimentally determined efficiencies.

Fig. 6 shows the experimental data plotted against the efficiencies calculated by the Wohlenberg equation. In this plot, the mean difference of —0.02984 and the standard deviation of 0.04150, and the t-value for 69 test points (gas-fired-furnace data could not be used) of 5.964 indicates that the Wohlenberg equation cannot be used to describe these furnace data. The table values of t for the 1 and 5 per cent probability levels are 2.657 and 1.998, respectively.

Similar analyses of data from individual stations were also made. Experimental data were compared with predicted data from each of the three equations. The results are shown in Table 1. No significant differences were observed between Paddy's Run data, and the data calculated from the Broido and Hudson-Orrok equations. These two techniques also could be used to describe the data from the gas-fired unit at Sterlington. The Wohl-

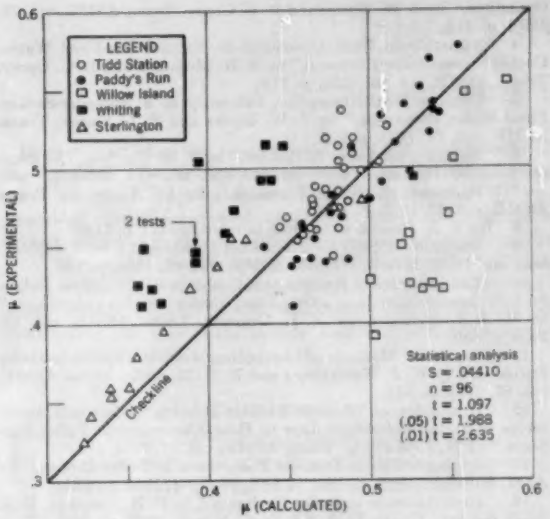

FIG. 5 CORRELATION OF PREDICTED EFFICIENCIES AND EXPERIMENTALLY DETERMINED EFFICIENCIES (HUDSON-ORROK)

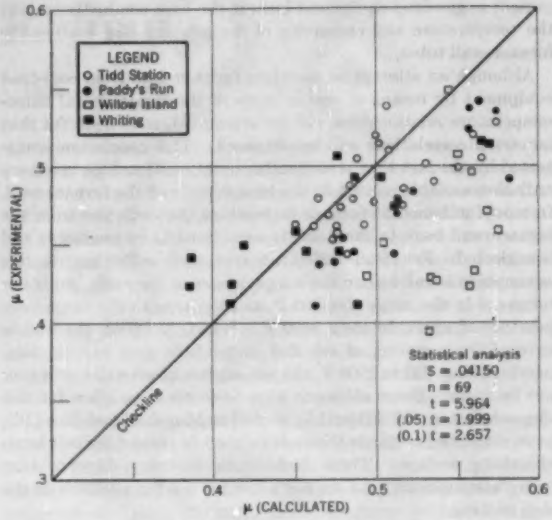

FIG. 6 CORRELATION OF PREDICTED EFFICIENCIES AND EXPERIMENTALLY DETERMINED EFFICIENCIES (WOHLENBERG)

TABLE 1 STATISTICAL TESTS OF FURNACE DATA

Station	Type of firing	Type of correlation	No. of (n)	Average difference between efficiencies	Standard deviation	t	t at 95 per cent	Significant variation
Tidd.....	Pulverized fuel	Broido	26	+0.016115	0.023090	3.621	2.060	Yes
		Hudson-Orrok	26	+0.010884	0.019443	2.918	2.060	Yes
		Wohlenberg	26	−0.015000	0.025456	2.999	2.060	Yes
Paddy's Run..	Pulverized fuel	Broido	28	−0.006714	0.024244	1.4654	2.052	No
		Hudson-Orrok	28	−0.005110	0.020780	1.3010	2.052	No
		Wohlenberg	15	−0.031800	0.019139	6.4350	2.145	Yes
Willow Island.	Pulverized fuel	Broido	13	−0.049770	0.036255	4.9400	2.180	Yes
		Hudson-Orrok	13	−0.071600	0.035160	7.3430	2.180	Yes
		Wohlenberg	13	−0.084020	0.042450	7.2140	2.180	Yes
Whiting.....	Spreader-stoker	Broido	15	0.022067	0.031721	2.6942	2.145	Yes
		Hudson-Orrok	15	0.067466	0.017869	16.1822	2.145	Yes
		Wohlenberg	15	−0.005867	0.038118	0.5961	2.145	No
Sterlington....	Gas	Broido	14	−0.015857	0.017974	1.0439	2.160	No
		Hudson-Orrok	14	0.018071	0.015340	1.3940	2.160	No
		Wohlenberg	This type of correlation not applied to gas-fired furnaces.					

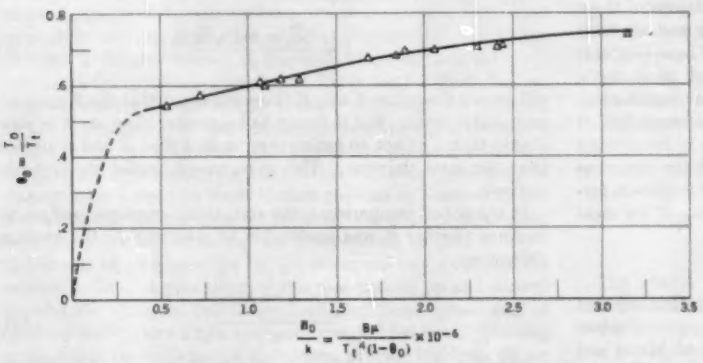

FIG. 7 CORRELATION OF STERLINGTON HEAT-ABSORPTION EFFICIENCY BY A HURVICH EQUATION

enberg equation, however, was only satisfactory for describing the spreader-stoker data from Whiting. On the whole, no one correlation described the data from all of the stations taken individually, and in two instances, Tidd Station and Willow Island, none of the correlations was adequate.

The Hurvich and the Konokov equations, both involving adiabatic flame temperatures, were used to correlate the data from the gas-fired unit at Sterlington. These data are plotted by a Hurvich equation (Equation [5]) in Fig. 7. The parameters of the plot are θ_0 and

$$\frac{B\mu}{T_i^4(1-\theta_0)} \times 10^{-6}$$

which have been defined in a previous section of the paper. The parameter k in Fig. 7 is equal to Q/HC_v, which is a constant for the furnace. In both instances very satisfactory correlations of the data were obtained, despite the estimated flame temperatures that were used.

DISCUSSION AND CONCLUSIONS

As demonstrated by the Sterlington data, the correlation of furnace data from clean-walled combustion chambers may be obtained in many ways. The small variations that are observed can be attributed to a number of factors such as changes in flame shapes and volumes with load, excess air, and burner arrangement. As soon as the furnace walls become covered by ash and slag, however, the differences between predicted and experimental values for heat transfer become larger, and the whole problem becomes extremely complex. Factors that are present and influence the operation of coal-fired equipment, and which are not

present in gas-fired equipment include the heat conductivity, and the temperature and emissivity of the ash and slag coating the furnace-wall tubes.

Although an attempt to correlate furnace data from coal-fired equipment by means of one or more of the fundamental flame-temperature relationships will be attempted, it is doubtful that improved correlations will be obtained. This conclusion is suggested by the fact that most fundamental relationships involve a radiation variable related to the temperature of the furnace wall. In most fundamental furnace expressions the radiation from the furnace wall back to the flame is considered to be negligible and is neglected. For clean-walled furnaces, such as Sterlington, this assumption is valid since the temperatures of the walls and boiler tubes are in the range 700–800 F, as compared to the flame temperature of approximately 3000 F. When, however, the wall is covered by a coating of ash and slag, which may vary in temperature from 700 to 2000 F, the assumption is not valid, and may not be made. Some attempts have been made to allow for this slag-ash factor. Mullikin (15), as well as Mumford and Bice (16), have suggested methods that can be used to correct radiant heat-absorbing surface. These techniques, however, involve very many assumptions, and do not allow for the temperature of the slag coating.

Recommendations

To evaluate properly the heat transfer in a furnace, it is necessary to know flame temperature and flame emissivities, and the effects on these factors of such variables as flame shape, flame length, type of fuel, degree of mixing of fuel and air, and per cent excess air. It is possible that such information can be obtained by designing experimental furnaces as sectionalized calorimeters, such as is being done at the International Flame-Radiation Trials at Ijmuiden, Holland. However, the experimental problems are numerous and complex and will only be solved by the application of experimental experience.

In addition to information on flames, future experimental work should be directed at obtaining the radiation and conductivity characteristics of the slag and ash coatings of furnace walls, as well as the fraction of wall area covered by ash and slag. In large-scale industrial experimentation, some indications of these characteristics may be obtained by measuring slag and ash temperatures as well as tube-metal temperatures. These temperatures are necessary if the reradiation from the wall back to the flame and the heat transfer to the boiler tubes is to be evaluated.

The third, and perhaps most important recommendation, is that all future work be planned so that all data can be interpreted statistically, and an estimate of the precision of the measurements be made. This approach probably would require a factorially designed program to facilitate the gathering of the most meaningful data with least amount of effort.

Acknowledgment

The authors gratefully acknowledge the co-operation received from the Research Committee on Furnace Performance Factors which was supported in its work by the Bureau of Mines and financially assisted by industry and the Engineering Foundation.

BIBLIOGRAPHY

1 "An Investigation of the Variation in Heat Absorption in a Pulverized-Coal-Fired Water-Cooled Steam-Boiler Furnace," by W. T. Reid, Paul Cohen, and R. C. Corey, Trans. ASME, vol. 70, 1948, pp. 569–586.

2 "Furnace Heat Absorption in Paddy's Run Pulverized-Coal-Fired Steam Generators Using Turbulent Burners," by R. C. Corey and Paul Cohen, Trans. ASME, vol. 71, 1949, p. 925.

3 "Furnace Heat Absorption in Pulverized-Coal-Fired Steam Generator," by J. W. Myers and R. C. Corey, Trans. ASME, vol. 73, 1951, p. 419.

4 "Variation in Heat Absorption in Natural-Gas-Fired Water-Cooled Steam-Boiler Furnaces," by A. R. Mumford and R. C. Corey, Trans. ASME, vol. 74, 1952, p. 1191.

5 "Furnace Heat-Absorption Efficiency in a Spreader-Stoker-Fired Steam Generator," by J. W. Myers and R. C. Corey, Trans. ASME, vol. 75, 1953, p. 909.

6 "Heat Transmission in Boilers," by J. G. Hudson, *The Engineer*, vol. 70, December, 1890, pp. 449, 450, 483, 484, 523–525.

7 "Radiation in Boiler Furnaces," by G. A. Orrok, Trans. ASME, vol. 47, 1925, p. 1148.

8 By B. N. Broido, work cited in reference (7), p. 1123.

9 "Radiation in the Pulverized-Fuel Furnace," by W. J. Wohlenberg and D. G. Morrow, Trans. ASME, vol. 47, 1925, p. 127.

10 "The Influence of Radiation in Coal-Fired Furnaces on Boiler-Surface Requirements and a Simplified Method for Its Calculation," by W. J. Wohlenberg and E. L. Lindseth, Trans. ASME, vol. 48, 1926, p. 849.

11 "Review of Methods of Computing Heat Absorption in Boiler Furnaces," by W. J. Wohlenberg and H. F. Mullikin, Trans. ASME, vol. 57, 1935, p. 531.

12 "Evaluation of Effective Radiant Heating Surface and Application of Stefan-Boltzmann Law to Heat Absorption in Boiler Furnaces," by H. F. Mullikin, Trans. ASME, vol. 57, 1935, p. 517.

13 "Analogy of Heat-Transfer Phenomena in Boiler Houses," by A. M. Hurvich, Acad. des Sci., USSR, No. 1–2, 1943, p. 23.

14 "Heat Emission in Boiler Fireboxes," by P. K. Konokov, Bull. Acad. des Sci., USSR, Tech. Sci. Sect., March, 1952, pp. 367–373.

15 By H. F. Mullikin, work cited in reference (12).

16 "An Investigation Into the Variation in Heat Absorption in a Pulverized-Coal-Fired Water-Cooled Steam Boiler Furnace," by A. R. Mumford and G. W. Bice, Trans. ASME, vol. 70, 1948, p. 604.

Appendix

Predicted heat-absorption efficiencies were compared statistically with values that were determined experimentally to ascertain whether or not the differences between values were due to a random distribution of experimental errors. The method is based on the theorem of statistics that states that if $\bar{X}$ and s are estimates of the mean and standard deviation of a random set of n samples taken from a normally distributed universe with a true mean equal to m and a standard deviation equal to ρ, the t-ratio, which is defined by the equation

$$t = \frac{(\bar{X} - m)\sqrt{n}}{s} \qquad [9]$$

will exceed the value A only B times out of a 100 at the B per cent probability level. If t is found to be greater than A, it is concluded that $\bar{X}$ is not an estimate of m, and that $\bar{X}$ and m are not from the same universe. This is commonly called the null hypothesis.

In the actual comparisons, the statistical tests were used to determine whether it was reasonable to assume that the average difference

$$\frac{\Sigma(\mu_{exp} - \mu_{calc})}{n} \qquad [10]$$

was due to experimental error and that no real difference between calculated and experimentally determined efficiencies existed. For the particular case in question, Equation [8] becomes

$$t = \frac{\left[\left(\frac{\Sigma(\mu_{exp} - \mu_{calc})}{n}\right)\right]\sqrt{n}}{S} \qquad [11]$$

The 1 and 5 per cent probability levels were chosen to determine the significance of t.

Fly-Ash Refiring

By F. G. FEELEY, JR.,[1] NEW YORK, N. Y.

Over a period of 30 years a vast expansion of plants of the Carbide and Carbon Chemicals Company has taken place on the Kanawha River, South Charleston, W. Va. The accompanying growth of power plants has created a fly ash-disposal problem. Three years ago when the addition of a new 250,000-lb-per-hr boiler installation was contemplated, it was decided to incorporate refiring features which largely would eliminate the difficulty. A description of the installation and its performance is given in the paper.

Introduction

FORTUNATE indeed is the industry or individual who is able to select the site of a plant with the idea of providing facilities for the disposal of fly ash resulting from the combustion of coal. Considerations of this type can sometimes, although not always—particularly in urban areas—influence the selection of public-utility plant sites; but it is rare indeed for major industrial plants to be able to consider fly-ash disposal among the desirable features of a plant site. Cooling water and raw materials usually predominate in site selections. Even though fly-ash disposal might be a factor in the selection of a modern plant site, it certainly could not have been envisioned thirty years ago when some of the now vast plants of Carbide and Carbon Chemicals Company had their beginnings.

Fly-Ash Disposal Becomes a Problem

The latter situation is certainly true of the company's plant on the Kanawha River at South Charleston, West Virginia. The first boiler plant consisted of six 20,000-lb-per-hr Sterling boilers—stoker-fired. Three boiler plants presently serve the plant, with a capacity many times the original 120,000 lb per hr. During years of expansion, fly ash has been pumped to first one low-lying area after another until the adjacent topography no longer provides a natural source of disposal. Fly-ash disposal costs have mounted to figures exceeding $1.75 per ton. Future disposal costs will rise even more sharply because of the need for pumping fly ash over adjacent ranges of hills into new low-lying ground.

New Boiler Plant Needed. Three years ago the need arose for a new 250,000-lb-per-hr boiler installation. Management insisted that at least a start be made toward the end of eliminating the ever-increasing fly-ash disposal problem. A number of avenues were investigated, including an independent device to burn carbon out of, and melt the fly ash from, the new as well as the existing boilers. A pilot plant of this type was set up and showed considerable promise (although requiring large quantities of auxiliary fuel) before a new approach was decided upon. Bearing in mind that the fuels native to the area average less than 10 per cent ash, and that coals are being burned elsewhere in the country with ash contents approaching 40 per cent, it was reasoned that a properly designed boiler should be able to refire ash up to a point where the total inert dust loading in the furnace approached that which would prevail with a coal of 40 per cent initial ash content.

Drawing in every way possible upon the experience of other plants, the boiler design shown in Fig. 1 was finally evolved. As can be seen, it is a slagging bottom boiler but is unconventional in that the hearth is of purely refractory construction and is completely separate from the structural and pressure parts of the boiler. This design was utilized because of a reluctance to involve the pressure parts of the boiler in the corrosive and erosive effects of molten slag. It is also intended to promote the highest possible temperatures to deal with the relatively high ash-fusion temperatures of native coals. The boiler is fired by downwardly inclined adjustable burners—three in the front wall, three in the rear wall, and staggered—to promote maximum turbulence with the higher temperature zone in the center of the hearth in a line parallel to the boiler drums. The slag-tap opening is in the near side of the hearth. Dust is collected from a gravity hopper below the last boiler pass, from a mechanical separator after the air heater, and from a vertically oriented electrostatic precipitator following the induced-draft fan. A total of 11 reinjection feeds, utilizing hot air from a separate single-stage blower for motive source, pick up the dust from the hoppers and refire to nozzles located between and below the rear-wall coal burners. Pocket-type, motor-driven dust feeders are located on all connections of the two dust collectors.

Characteristics. The boiler shown is rated at 289,000 lb of steam per hr, at 615 psig pressure, 670 F total temperature when supplied with boiler feedwater at 388 F. It should be noted that the capacity of the originally planned unit was increased to the 289,000-lb-per-hr figure when it was decided to add to the steam cycle a 200-psi steam feedwater-heating system. Design furnace-heat release is 15,800 Btu/cu ft/hr and the entire furnace envelope is composed of 3 1/4-in. tubes on 3 3/8-in. centers. Design efficiency of the unit was set at 87.0 per cent but its performance has consistently been at 88.6 per cent when operating at design steam flow. Attention is called to the fact that this boiler was built initially without soot blowers and without any future provision therefor. A single long retractable deslagger was installed ahead of the slag screen but this blower has never been used and has now been removed to storage.

Operating Results

The results achieved with this method of firing and refiring have exceeded all expectations. Total stack discharge at 300,000-lb-per-hr steam flow is less than 0.5 lb per 1000 lb of flue gas. All ash is recovered as a slag which is a readily disposable, and sometimes salable, product. The boiler is tapped once a day, requiring approximately seven man-hours of labor. The slag has been used for roads, driveways, and parking lots and is under investigation as a raw material for the fabrication of building blocks, bricks, etc.

A similar, but smaller, boiler at the Chemicals Company's Institute plant, West Virginia, also is performing satisfactorily and this unit is consuming, without detrimental effect, the fly ash from an adjacent dry-bottom boiler. At South Charleston plans are under way to refire to the new unit dust from adjacent units.

---

[1] Purchasing Agent, Carbide and Carbon Chemicals Company. Mem. ASME.

Contributed by the Research Committee on Furnace Performance Factors, Research Committee on Corrosion and Deposits From Combustion Gases, and Power Division and presented at the Diamond Jubilee Annual Meeting, Chicago, Ill., November 13–18, 1955, of The American Society of Mechanical Engineers.

Note: Statements and opinions advanced in papers are to be understood as individual expressions of their authors and not those of the Society. Manuscript received at ASME Headquarters, September 27, 1955. Paper No. 55—A-182.

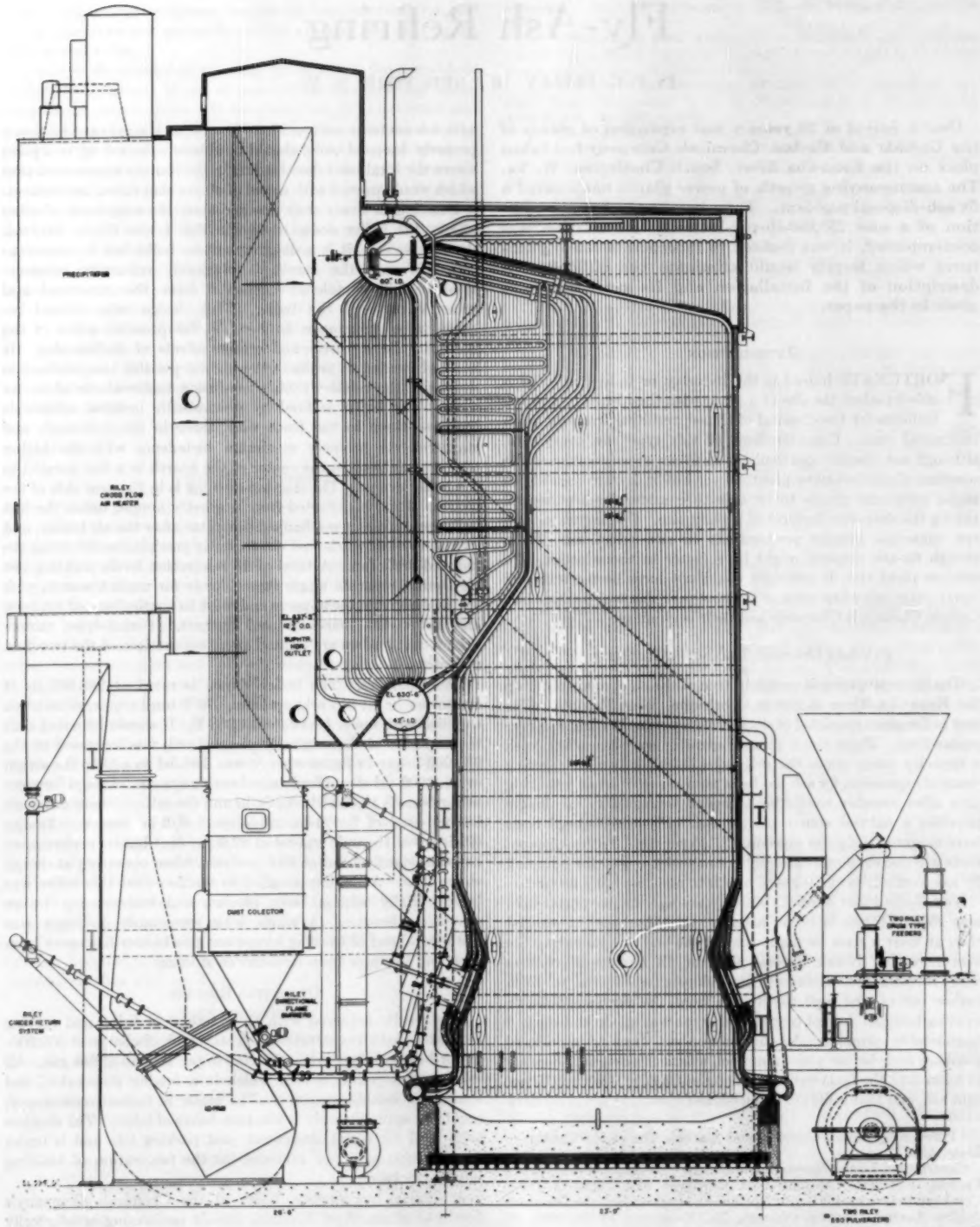

FIG. 1 VIEW OF CARBIDE AND CARBON BLAINE ISLAND PLANT, SO. CHARLESTON, W. VA.

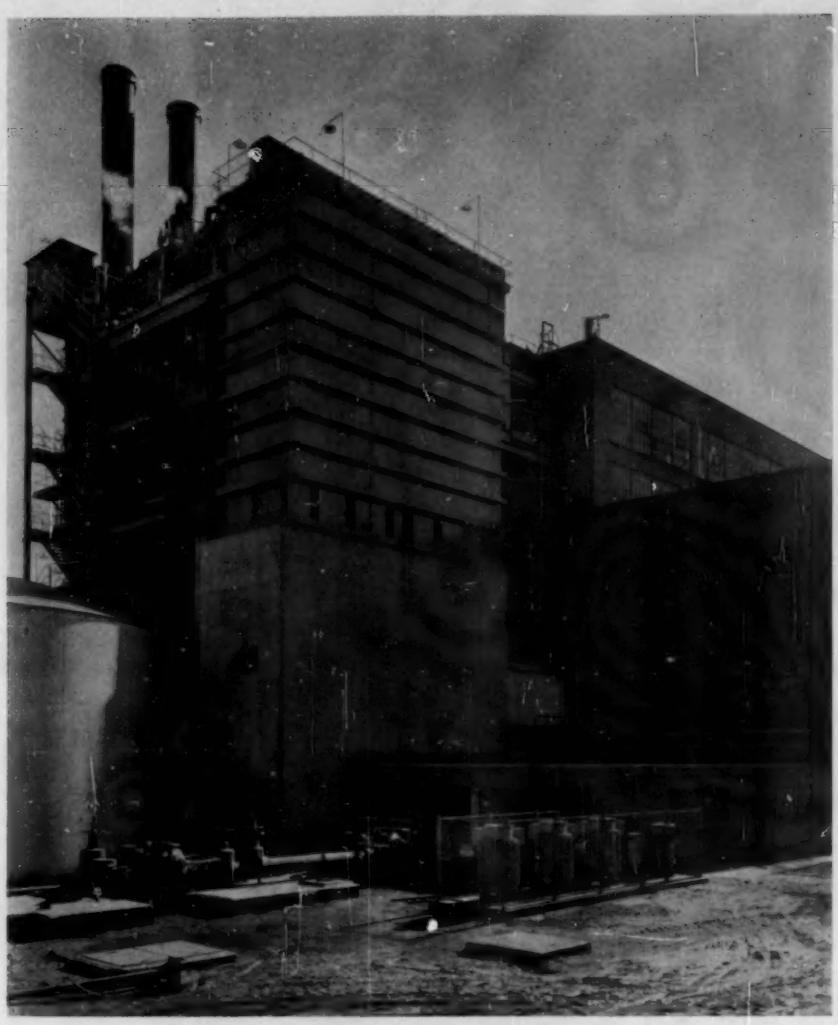

FIG. 2 VIEW LOOKING TOWARD ENCLOSURE AT BOILER FRONT

Installed cost of the entire unit was about $6.76 per lb of design steaming capacity.

Heating-Surface Slagging Eliminated. Quite apart from achieving our basic objective, the South Charleston boiler and its smaller partner at Institute, have produced an unexpected benefit. Absolutely no slagging or heating surface fouling of any sort has so far occurred above the burners or at any point thereafter. It was mentioned earlier that the deslagging blower originally installed has been removed. No manual cleaning of the boiler, in service or out of service, has ever been required. The fact that this cleanliness is complete is indicated by the fact that the gas temperature entering the slag screen averages 200 F below the manufacturer's expectation. In considering the implications of the foregoing statements, bear in mind that this boiler serves a process which never permits a drop in load except on scheduled semiannual outages. In addition, because of its demonstrated capabilities, this boiler is consistently operated at loads in the vicinity of 310,000 lb per hr, and we contemplate changing the range of the flowmeters to permit its operation in the future at loads approximating 325,000 lb per hr.

POTENTIALITIES OF SYSTEM

It is the primary purpose of this paper to point out the cleanliness of, and to introduce to the steam-generating industry the potentialities of the system described. It is equally the intent of this paper to bring about consideration of, and interest in, the cause of the ability of this boiler to eliminate the usual slagging and fouling characteristics—which incidentally are handsomely demonstrated by normal slagging difficulties in the conventional boilers elsewhere in the plant.

The author would like to offer for consideration the possibility that the high inert dust loading in the combustion zone and adjacent furnace atmosphere of this boiler may possibly be serving as an absorbing medium for the deposition of the vapor-phase products of combustion, such as alkali sulphides, which normally are associated with adherence of fly ash—and subsequently slag—to metallic surfaces. It would seem essential to the progress of the fuel-burning art to learn more about this phenomenon in the hope that the good features of this design can be extended to other boilers.

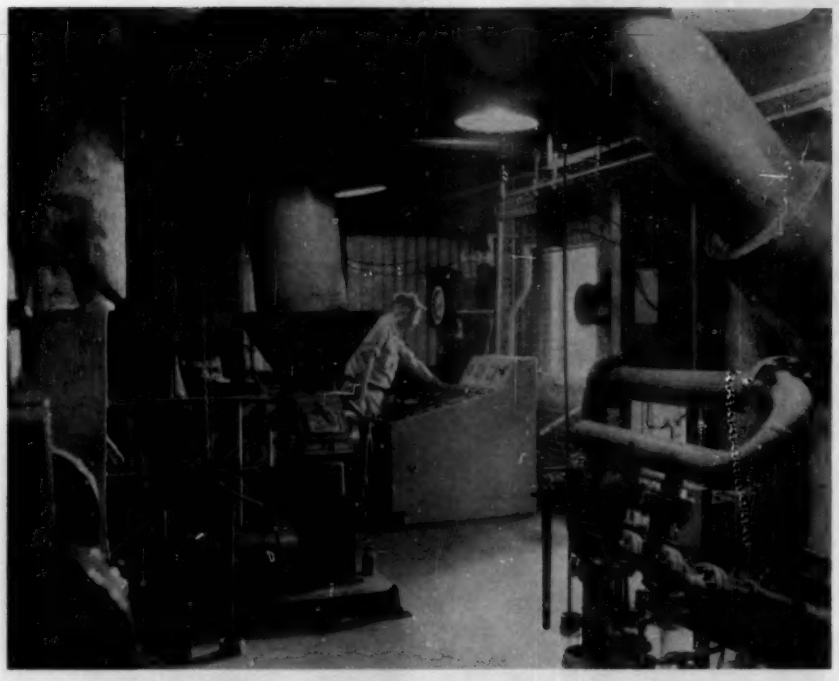

FIG. 3 VIEW INSIDE BOILER-FRONT ENCLOSURE

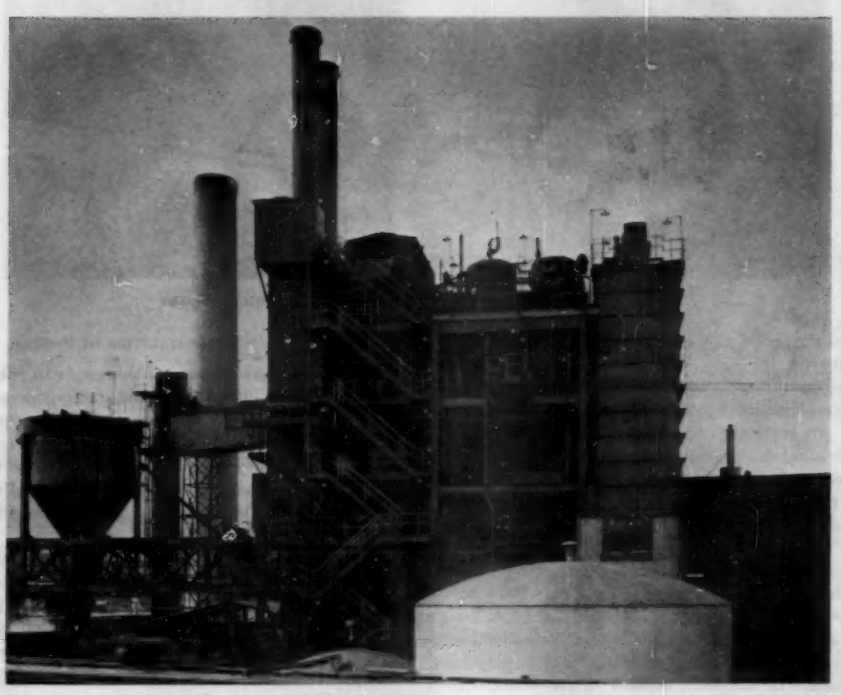

FIG. 4 VIEW OF COMPLETE BOILER-UNIT INSTALLATION

To anticipate one question which may arise, let it be said that the original hearth lining of the Institute boiler, which was No. 1 firebrick, failed in approximately six weeks of service. It was subsequently replaced with Carborundum brick which failed in sixteen days of service and caused us to call in refractory experts who pointed out that the brick-maintenance problem in a structure such as this is similar to an open-hearth steel furnace wherein the major attack is chemical and not thermal. A synthetic mullite brick lining was recommended and installed on both boilers and at present seems to have a satisfactory life. The indicated cost of annual maintenance of the hearth is approximately $5000.

General Details of Plant

To round out the story of this job, a brief description and a few pictures of the over-all installation may be of interest. The unit and its auxiliaries are installed completely out-of-doors, the only enclosure being that space under the coal bunker in which are located the front burners, the coal feeders and pulverizers, and the control console (Figs. 2 and 3). Fig. 4 shows the complete plant. It is intended to erect a duplicate unit in the future.

The relative simplicity of auxiliary equipment should be noted. Two deaerating feedwater heaters are installed, one operating at 10 psig and one at 200 psig. Within the pressure shell of each deaerator is located a continuous blowdown compartment, one cascaded into the other; a heat exchanger (counterflow to incoming feedwater) serves to cool the effluent of the 10-lb blowdown compartment. Two 100 per cent capacity turbine-driven, high-speed chrome-alloy feed pumps are installed. These are of the re-entry type each having a first section taking suction from the 10-lb heater and delivering to the 200-lb heater through a level control device, and a second section receiving from the 200-lb heater and delivering to the boiler with water-level regulation in the boiler achieved by regulation of turbine speed.

The ash-handling system is visible in this view and consists of a "Jetpulsion" pump serving a decanting tank which will hold approximately 4 days' run of slag and can be discharged equally well to either railroad cars or trucks. Antifreeze protection on important lines is electrical.

Drafting of the boiler is a little unusual. Forced draft is provided by four motor-driven 40-hp single-stage blowers—two in each side of a plenum chamber at the rear base of the air heater. Each blower is fitted with a balanced multileaf check damper which prevents back-flow when the blower is stopped; each blower also has a vane inlet control, all four of which are operated simultaneously by the combustion control through a jack shaft. Three blowers will handle the boiler well beyond rated capacity, leaving one in reserve. This system avoids heavy foundations and extensive duct work, and it provides very good fan efficiencies at all loads since blowers can be started or stopped from the panel board as load varies. The induced-draft fan is conventional but has no dampers. Draft control is achieved by varying fan speed with a hydraulic coupling. The two circular stacks are free-standing and equipped with discharge orifices to give a full-load exit velocity of 4500 fpm.

Operation of Auxiliaries. Operation of the auxiliary system serving this boiler has proved simple and reliable except that we underestimated the problem of placing the spare boiler feed pump in service on a job where deaerating heater pressures are not related to unit loading. A superb operating crew finally figured out a way of placing the 200-lb heater in service with the unit running, but it can be imagined that the procedure was a precarious one. A low-capacity by-pass was finally installed around the 200-lb heater to permit this operation to be handled more safely and expeditiously. To those who plan the installation of a re-entry pump and open feed-heater system such as this (and we certainly recommend it from a maintenance and first-cost standpoint) it should be pointed out that the stand-by feed pump will vapor-bind its low-pressure suction (due to normal pump leakage) if it is permitted to stand with communications open to both deaerators. We learned the hard way that the result of trying to start the feed pump in this condition can produce the most terrifying water hammer it has ever been the author's experience to hear. The practice now is to leave the stand-by pump and its pipe lined up to by-pass the 200-lb heater, then to cut that heater into service after water flow is established through the pump.

Fluidizer Petroleum Coke Tested. It may be known to some that this boiler has been used successfully in burning test lots of the fluidized petroleum coke which is produced by the new Standard Oil process. The features which permit the successful combustion of this fuel perhaps are not related to the furnace performance which is the subject of this paper, but it is likely that complete reinjection of dust is required with this fuel in order to completely burn out its carbon content.

Conclusion

We hope most sincerely that the excellent performance of this boiler, which has been the product of so many people in both the manufacturing and operating branches of the steam-generating industry, can be proved not to be an isolated example and that we individually, and the Society collectively, will prove that our management's insistence on placing a stop to the fly-ash disposal problem will be able to benefit the entire industry.

Discussion

G. W. Bice.[2] This is an unusually interesting paper on what certainly appears to be an unusual steam-generating unit.

Fly-ash refiring has been tried a number of times in furnaces of various design, but has seldom been found satisfactory, and has nearly always been abandoned because of the practical difficulties encountered. No mention was made of fly-ash refiring difficulties experienced during initial operation of this unit. Surely there were some. It might be enlightening if the author would discuss this subject briefly in his closure.

Also, no mention was made of the ability of this unit to handle low-quality coals, in addition to the relatively good coals normally available in the Charleston, W. Va., area. If such coals have been burned, even on an experimental basis, it would be of interest, and helpful in evaluating the possible versatility of this design of furnace and its fly-ash refiring equipment.

During the past summer, several members of the ASME Special Research Committee on Furnace Performance Factors visited the subject plant, where they were afforded the opportunity of seeing this boiler in operation, and of talking with members of the operating staff. While they were impressed with the ease with which fly ash was being refired, they were even more impressed with the freedom from fouling of the unit, and especially the furnace above the burners. Their interest and their curiosity were apparently contagious, as they have succeeded in convincing the committee as a whole that it would be worth while to invest a portion of the funds remaining in the committee's treasury in a series of formal tests on this unit. Tentative agreements have been reached with the owner, the boiler manufacturer, and the Bureau of Mines for furnishing the necessary materials, installation labor, test facilities, and test personnel, either on a no-charge basis or at cost. Thus it is hoped that additional detailed performance data on this very interesting installation will be

[2] Assistant Mechanical Engineer, American Gas & Electric Service Corporation, New York, N. Y. Mem. ASME.

obtained soon, and can be presented to the Society within the next year.

OLLISON CRAIG.[3] The author points out that by this method of firing there is an unexpected result in that no slag accumulation is experienced on the walls of the furnace above the burners or in any of the gas passages. It might be said that this is due to the high ash-fusion temperature of this particular coal. However, there is also a boiler of the same design, with the same method of firing, in a paper mill in Maine which uses Minto coal from New Brunswick. This coal contains an average of over 20 per cent ash and an average of over 8 per cent sulphur. The sulphur is mostly in the form of pyrites. Ash-fusion temperatures vary from 1800 to 2000 F. There are no wall blowers, slag blowers, or soot blowers in this boiler and there has never been any requirement for any such blowers. Also, no hand lancing is used. The furnace walls and the gas passes are just as clean as those mentioned in the paper.

The author develops the point that the temperature of the gases leaving the furnace is considerably less than would be the case with dry-bottom firing but with the same heat release per square foot of furnace envelope. This at first seems somewhat puzzling but, upon giving the matter some thought, it becomes quite evident why this was so.

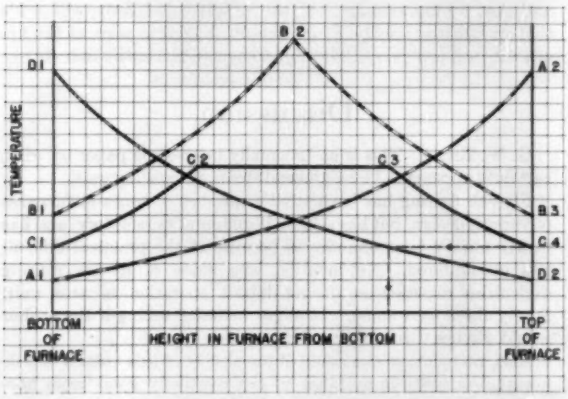

FIG. 5 FURNACE-TEMPERATURE CURVES

In Fig. 5 herewith, several curves are shown which are used merely as illustrations to follow a line of reasoning. Vertical distances represent temperatures in the furnace, while horizontal distances represent distances from furnace bottom. The left ends of the curves are at the bottom of the furnace and the right ends of the curves at the top of the furnace. Assume that all the heat generated is released in a very narrow vertical zone immediately at the top of the furnace. The maximum possible temperature of the gases at the top of the furnace would then be experienced and this temperature could be represented by the point A2. At any point lower down in the furnace measured temperatures would be less, so that at the bottom of the furnace the temperature could be represented by A1 and the curve between A1 and A2 could be taken as representing the change of temperature of the gases throughout the furnace height.

Again, assume all the heat release in a very narrow vertical band within half the height of the furnace. The temperature at this point could be represented by B2 while at the bottom and top of the furnace the temperatures could be represented by B1 and B3. The curves B1, B2, and B3 would then represent the change in temperatures throughout the furnace height. Obviously, B1 would be greater than A1. Assume that the heat release occurred not in a narrow band but over a considerable distance of the height from C2 to C3. These temperatures, of course, would be much less than A2 or B2. The temperatures C1 and C4 at the bottom and the top of the furnace obviously would be less than the temperatures B1 and B3.

Assume, finally, that all the heat is released in a narrow vertical band at the extreme bottom of the furnace. This would be represented by the point D1. Since no further heat is released, the temperature of the gases rising in the furnace can only decrease from the furnace bottom to the furnace top. At the furnace top the temperature leaving the furnace would be represented by some point such as D2. It is obvious that temperature D2 will be less than that of B3 or C4. The curves C1, C2, C3, and C4 would come the nearest to representing the conditions that would be experienced when firing a dry-bottom furnace. Consequently the difference between C4 and D2 would represent the drop in temperature at the top of the furnace because of the method of firing by which all the heat is released at the bottom of the furnace. If the point C4 is projected horizontally to the curve D1-D2 the point of intersection would indicate the point in the height of the furnace where the temperature would be the same as in the case of dry-bottom-furnace firing. In other words, this would indicate that by releasing the heat entirely in the bottom of the furnace a smaller furnace can be used and a higher heat release per square foot of furnace envelope can be used to obtain the same temperature leaving the top of the furnace as would be the case with dry-bottom firing.

This line of reasoning also would seem to indicate that the temperature of the gases leaving the furnace is affected, not only by the heat release per square foot of furnace envelope, but is also affected by the way in which heat is released in the furnace. It would seem, then, that making use of the factor of heat release per square foot of envelope only could be very much of a fallacy and very misleading.

When natural gas is fired into the bottom of one of these furnaces, through the same burners as are used for coal firing, a very luminous flame fills the furnace bottom. This flame has very much the same appearance as the flame with coal burning. It appears to have about the same degree of luminosity and the same ability to radiate heat. This fact led to the thought that possibly the temperature of products of combustion leaving the furnace when burning natural gas would be about the same as when burning coal. Temperatures of gases at the top of the furnace were measured when burning gas and it was found that at the same load being developed by the boiler these temperatures were almost identical with those obtained when firing coal. It is to be presumed that the same thing will be true when firing oil. For these reasons it has been found that this type of design with this method of firing is particularly desirable in those installations which will burn natural gas but expect that at some time in the future to find it desirable to change to coal firing. When the time comes to fire coal it will be unnecessary to make any changes to the furnace or to the burners and, of course, there will be no outage of the boiler in order to make the change-over.

There is a new form of fuel appearing which is called fluid coke. This is a by-product from a new process of petroleum refining. Fluid coke, however, is quite different from the petroleum cokes which have been obtained in the past. Fluid coke is very dense, exposes a minimum of surface for oxidation, is extremely hard to ignite, extremely difficult to maintain in stable combustion, and contains only from 4 to 5 per cent volatile matter. It has been expected, of course, that it is necessary to burn some auxiliary fuel in the form of oil or gas in order to obtain stable ignition.

[3] Vice-President, Riley Stoker Corporation, Worcester, Mass. Fellow ASME.

Fluid coke has been burned quite successfully at the Blaine Island Plant and with as little as 6 per cent auxiliary fuel in the form of natural gas. This method of firing lends itself particularly to the burning of a very difficult fuel, such as fluid coke, because of the high turbulence and the high temperature that are obtained in the bottom of the furnace. There is now being installed in Delaware, for the Delaware Power and Light Company, three boilers, each having a capacity of 500,000 lb of steam per hr, the basic fuel being fluid coke. Fluid coke will be fired in the same manner as described in the paper.

C. F. Hawley.[4] The author makes the following statement: "It would seem essential to the progress of the fuel-burning art to learn more about this phenomenon in the hope that the good features of this design can be extended to other boilers."

One of the phenomena mentioned is the fact that the furnace-exit temperatures were much lower than predicted. Further investigation on the basis of measurements with high-velocity thermocouples while burning pulverized coal, and also while burning gas, resulted in the furnace-temperature-performance curves shown as Fig. 6 of this discussion. These curves show the furnace-exit temperature plotted against the net heat release per square foot of effective furnace surface. The upper two curves

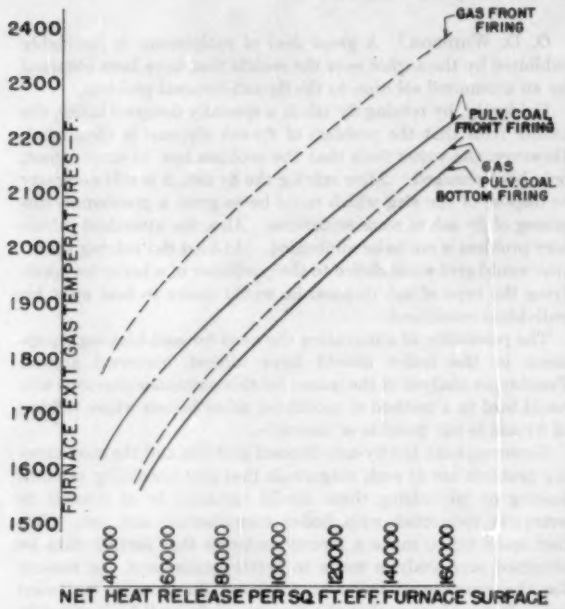

Fig. 6 Furnace Temperature

are those for conventional front-wall firing, while the lower two curves are the measurements taken at the author's installation. It will be noted that when burning pulverized coal the temperatures with this arrangement are about 100 to 125 deg F below the conventional design and that when burning gas the spread becomes even greater. The two bottom curves also show that the temperatures at the exit of the furnace when burning either pulverized coal or gas are approximately the same.

The beneficial result of the lower temperatures is immediately apparent by comparing the net heat release which produces the same furnace-exit temperature. If we assume a desired exit temperature of 1950 F the conventional front firing requires a heat release per square foot of furnace envelope of 85,000 Btu. The unit with the bottom firing produces the same exit temperature with 110,000 release and permits a 20 per cent reduction in required furnace surfaces.

The absence of furnace slag above the burner throat and the elimination of furnace blowers remove the most serious operating problems connected with pressure-furnace operation and allow full use of the operating economics of pressure firing.

The design of unit shown as Fig. 7, herewith, is based on this experience and is in line with the hope expressed by the author that the good features of this design can be extended to other boilers. The arrangement is such that natural gas, oil, coal, lignite, fluid coke, delayed coke, or a combination of these fuels can be utilized. The furnace is of the same general design as the

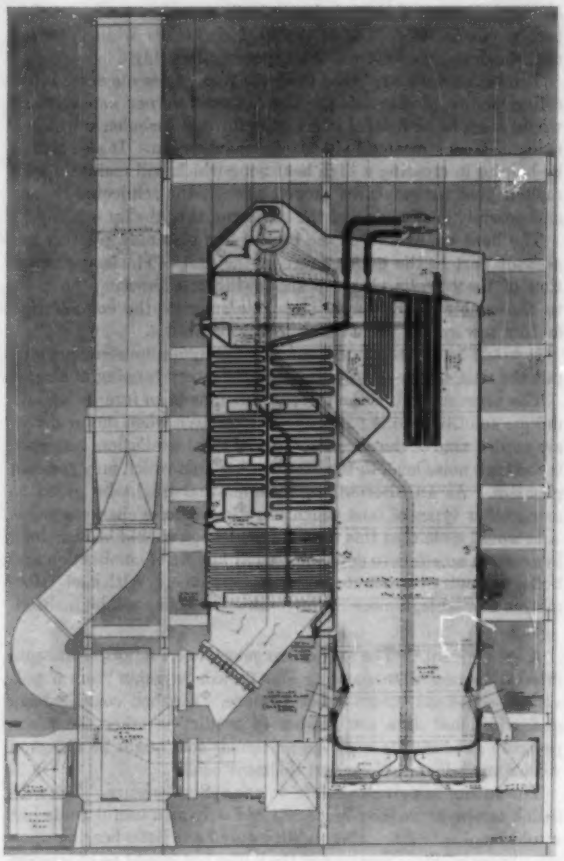

Fig. 7 New-Type Boiler Incorporating Pressure Furnace

arrangement described in the paper with the same type of burners placed at the bottom, but in this case a completely water-cooled furnace floor. The fact that all the fuels burn with a radiant flame allows superheater-tube platens spaced across the upper part of the furnace to obtain the required steam temperatures while still making full use of the low furnace-exit temperatures resulting from the bottom firing. Two units of this type are now on order, one for 850,000 lb of steam per hr at 1550 psig with steam and reheat temperatures of 1005 F, and one designed for 1,550,000 lb of steam per hr at 1925 psig, with steam and reheat

[4] Chief Mechanical Engineer, Riley Stoker Corporation, Worcester, Mass. Mem. ASME.

temperatures of 1005 F. These units are designed for pressure-furnace operation.

M. L. Jones.[5] The author's paper on the problem of disposal of fly ash and the method and equipment being used is timely. It would appear that both the manufacturers and the users of coal-fired boilers must take stock of our situation and ask if we are going in the right direction. The installations as discussed in the paper may give some leads which should be investigated.

The slag-tap or wet-bottom furnace had a period of popularity some 25 years ago and many units were installed. However, this type of unit became less popular until the early 1950's when the cyclone furnace was developed.

In the intervening period, air pollution became a problem in all coal-burning installations along with the resulting disposal nuisance of fly ash resulting from the installation of dust collectors. During this period we, both operators and manufacturers, continued to install dry-bottom boilers while knowing that the dust emission from this type of boiler is high.

The boiler design referred to in the paper presents some interesting points of discussion. The opposed-burner arrangement would seem to be helpful in creating furnace turbulence which is recognized as a material aid to good combustion. It also should be helpful in creating a high heat zone which will maintain high molten pool temperatures as well as melt the reinjected fly ash and possibly gasify some of the components of the fly ash.

The bent wall tubes of the burner line also may play an important part in the performance of the unit. The heat absorption of these walls plus the shadowing and directing the gases to the center of the furnace may be some of the contributing factors toward the performance being realized.

It would be of interest to know at what minimum steaming output the unit can be operated with satisfactory tapping of slag.

The arrangement of the forced-draft fans is an interesting and unique solution and is particularly attractive when motor drives are used. One of the disadvantages of this installation, however, is the high noise level in the surrounding area which may create a problem. As an alternative, consideration might be given to using other types of fans which have lower noise characteristics.

It would seem that this type of installation should be examined in detail in an effort to determine what factors of combustion and boiler geometry contribute to the performance. With such information available, a more rational design of boiler will be realized.

A. A. Orning.[6] The author has presented a report of unusual interest in regard to slagging and fly-ash emission from a pulverized-coal-fired steam-boiler furnace. Further consideration and additional data are needed to predict whether the unexpectedly good results with the particular coal might be expected with similar installations and different coals.

The author has given no data on ash characteristics. The ash-fusion temperature may be considered only as a useful guide but would be of interest. Slag fluidity may have little bearing upon cleanliness of upper sections of the boiler but would be of interest with regard to feasibility of using the design for other coals. Alkali metal content of the coal ash is possibly of greatest importance.

The unique shape factors are certainly important in reducing slagging on wall areas immediately above the burners. Low angles of incidence of radiation, from the hearth and the flame volume below the burners, account for much of the absence of slagging in these areas. Flame impingement is probably absent or at low angles in these areas. Information regarding contours of slag deposits on the side walls would aid interpretation of these effects.

Data are given on heat-release rates per unit volume but not per unit projected area of wall surface in the primary furnace. Indicated low exit-gas temperatures depend upon these rates. Exit-gas temperatures are not given.

The absence of bonded deposits at the furnace exit and in the first passes of the superheater results from a combination of effects. An increase in dust loading due to recycling is indicated but no data are given. The long path from the flame zone to the furnace outlet favors selective absorption of offensive components by the fly ash. High dust loading would favor this effect. The long path and the outlet geometry also indicate a low solid angle for flame radiation into the outlet. With other coals, of high sulphur and high alkali-metal content, these effects together with even lower exit-gas temperatures might not be adequate to pervent bonded deposits in the slag screen and the first passes of the superheater.

The furnace design presented offers interesting possibilities for control of ash deposits and fly-ash emission. Careful consideration of ash loading and composition must be given any application to coals with ash characteristics differing widely from those in the present application.

O. D. Whiddon.[7] A great deal of enthusiasm is justifiably exhibited by the author over the results that have been obtained by an attempted solution to the fly-ash-disposal problem.

Evidently, by refiring fly ash in a specially designed boiler, the author feels that the problem of fly-ash disposal is eliminated. However, the writer feels that the problem has, to some extent, only been changed. After refiring the fly ash, it is still necessary to dispose of the slag which could be as great a problem as disposing of fly ash in some situations. Also, the attendant refractory problem is not to be minimized. At least the refiring operation would give some choice to the purchaser of a boiler for specifying the type of ash disposal he would desire to best meet his individual conditions.

The possibility of eliminating the need for soot-blowing equipment in the boiler should have almost universal appeal. Possibly an analysis of the reason for this particular characteristic could lead to a method of modifying other boilers where refiring of fly ash is not possible or desirable.

However, both the fly-ash-disposal problem and the soot-blowing problem are of such magnitude that any possibility of eliminating or minimizing them should certainly be of interest to everyone connected with boiler manufacture and use. This fact leads me to make a recommendation that further data be obtained and analysis made to better understand the reasons for the exceptional boiler performance for possible universal use. It would seem that the Society might well be justified in such an undertaking through appropriate committees.

The author is to be commended for publicizing his experiences which could be a major step in improving boiler design and operation.

Author's Closure

Mr. Bice asks for information on the difficulties with refiring. Briefly, they have been limited to excessive wear of the original pipe-fitting material. Fittings have been replaced with some designed for use in pneumatic fly-ash handling systems. The refiring of dust from the boiler hopper has been discontinued in view of the fact that the amount of dust so handled was so small

[5] Principal Power Engineer, E. I. du Pont de Nemours & Company, Inc., Wilmington, Del. Mem. ASME.

[6] Member Staff, Coal Research Laboratory, Carnegie Institute of Technology, Pittsburgh, Pa. Mem. ASME.

[7] Technical Engineer of Power Plants, The Detroit Edison Company, Detroit, Mich. Assoc. Mem. ASME.

as to not justify the presence and maintenance of the pipe involved.

Except for avoiding fuels with nominal ash fluid temperatures in excess of 2700 F, no effort has been made to specify any special coal for this unit. It has handled everything the local mines make available as well as some more distant coals whose purchase was dictated by price and availability only.

The minimum load at which subject boiler can be tapped has never been determined. It would, of course, vary with the fluid temperature of the coal ash and with the excess air required for good combustion of the coal. With ash fluid temperatures around 2350 F, it is likely that good tapping would prevail down to about three-quarters of maximum rating, but it is my contention that no slag-tapping installation should be made where continuous service at less than nominal full load is contemplated.

Mr. Jones will be interested to know that steps are currently being taken in conjunction with the fan manufacturer to apply low draft-loss sound-absorption devices to the forced-draft fans.

Mr. Orning asks about the contours of slag deposits on the side walls of the furnaces. The answer is that above the throat of the furnace there are none whatever and it therefore appears that the freedom from slagging of this furnace design is associated with factors other than its shape and dimensional relationships.

The Supercharged-and-Intercooled Free-Piston-and-Turbine Compound Engine—A Cycle Analysis

By A. L. LONDON,[1] STANFORD, CALIF.

This paper supplements a previous study.[2] Its purpose is to clarify the position occupied by the supercharged-and-intercooled cycle variant of the free-piston-and-turbine compound engine relative to the simple cycle. Two points of view are employed in these considerations—one relating to question of whether or not to supercharge an existing simple-cycle prototype; and the second relating to the basic decision of whether to develop a supercharged-and-intercooled cycle, or alternatively to develop the simple cycle for the same degree of pressure charging of the engine cylinder. From the first viewpoint, as an example, it appears to be attractive to supercharge a 6:1 pressure-ratio simple cycle up to 8:1 by a blower of 1.33 pressure ratio. The gain is roughly 50 per cent in power output and this must be weighed against the additional complexity, bulk, weight, and cost associated with the supercharger and its turbine drive, together with the intercooler and its ducting. Moreover, the cylinder combustion rate is increased in proportion to the power gain so that cylinder and piston heat problems are more severe. From the second viewpoint, the supercharged-and-intercooled cycle possesses no significant advantages and many disadvantages.

Nomenclature

The following nomenclature is used in the paper:

- c_p = air constant pressure specific heat for compressor process, Btu/(lb deg F)
- $\bar{c}_p$ = air constant pressure specific heat for turbine process, Btu/(lb deg F)
- k = air specific heat ratio for compressor process, dimensionless
- $\bar{k}$ = air specific heat ratio for turbine process, dimensionless
- LHV = fuel lower heating value at fuel supply temperature, Btu/lb
- m = molal mass of air = 28.97 lb/lb mol
- P = pressure, psi, or psf abs
- P^* = pressure ratio, dimensionless
- PD = piston displacement, cu in., or cu ft per cycle
- q = coolant heat-transfer rate, Btu/hr
- q^* = coolant heat-transfer fraction relative to fuel-energy input, dimensionless
- R = universal gas constant = 1545 ft #/(lb mol deg R)
- SAR = specific air flow rate for cycle, lbs/net shphr
- sfc = specific fuel consumption for cycle, lb/net shphr
- T = air temperature, deg R
- Wk = work as qualified by subscript, Btu
- Δ on P^* means flow-friction pressure drop fraction
- η = efficiency as qualified by subscript
- ρ = gas density as qualified by subscript, pcf
- ω = flow rate as qualified by subscript, lb/hr
- # = pounds force in distinction to lb for lb mass

Introduction

This paper is presented as a supplement to a previous study.[2] In this reference three variations of the free-piston-and-turbine compound engine were considered—the simple cycle, the supercharged-and-intercooled cycle, and the reheat cycle. Thermodynamic considerations resulting in a convenient cycle-analysis procedure were formulated and the method was illustrated by specific calculations.

One of the conclusions reached from these limited calculations was as follows:

"The supercharged-and-intercooled cycle, contrary to intuitive expectations, offers no advantage in terms of compressor size and possesses many disadvantages in terms of specific fuel consumption and system complexity. The increased density of the charge to the reciprocating compressor is more than nullified by the great increase in specific air-flow rate."

The foregoing conclusion resulted in some substantial differences of opinion,[3] so it became evident, therefore, that points of view needed to be clearly formulated, and further studies of the supercharged-and-intercooled cycle were required. It is the purpose of this paper to fulfill these needs.

The supercharged-and-intercooled cycle is described in the flow diagram, Fig. 1. This illustration also defines the meaning of the cycle pressure ratio P^*, the supercharge pressure ratio P_s^*, and the pressure ratio of what might be termed the simple-cycle portion of the over-all cycle

$$P^*_{\text{simple cycle}} = P^*/P_s^*$$

The over-all turbine expansion is pictured schematically as occurring in three stages: (1) The main expansion down to a pressure equal to the inlet pressure to the F-P compressor; (2) a supercharger-drive-turbine expansion down to a pressure level just sufficient to provide the necessary supercharger work; and (3) a final expansion down to atmospheric pressure. If P_{23} is greater than P_0 work is derived, but if P_{23} is less than P_0 work is required, and then this last flow machine functions as a compressor. In any practical system this last turbine, of course, would not be used, but probably at least two turbines would be employed—one for the load and the other to drive the supercharger. The presentation shown in Fig. 1 is given in this more complex manner

[1] Professor of Mechanical Engineering, Stanford University. Mem. ASME.

[2] "The Free-Piston-and-Turbine Compound Engine—A Cycle Analysis," by A. L. London, Trans. ASME, vol. 77, 1955, pp. 197–210.

Contributed by the Gas Turbine Power Division and presented at a joint session of the Gas Turbine Power and Oil and Gas Power Divisions at the Diamond Jubilee Annual Meeting, Chicago, Ill., November 13–18, 1955, of The American Society of Mechanical Engineers.

Note: Statements and opinions advanced in papers are to be understood as individual expressions of their authors and not those of the Society. Manuscript received at ASME Headquarters, August 29, 1955. Paper No. 55—A-147.

[3] Discussions to reference (2) presented by A. J. Ehrat, H. A. Steiger, and P. de Haller.

for the purpose of allowing a later comparison of the simple cycle with the supercharged-and-intercooled cycle performance.

The meaning of the term "supercharged" will now be considered. The reciprocating-engine cylinder is obviously supercharged, even in the simple cycle, by the reciprocating compressor. As used in this paper supercharged refers to pressure increase provided by the centrifugal blower pictured in Fig. 1 and

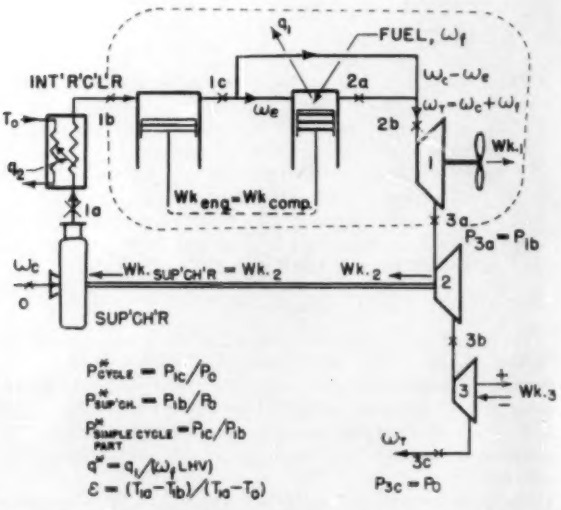

FIG. 1 FLOW DIAGRAM FOR SUPERCHARGED-AND-INTERCOOLED CYCLE

is expressed in terms of $P_s^* = P_{1b}/P_0$. The "pressure-charging" of the F-P reciprocating-engine cylinder is expressed in terms of the cycle pressure ratio P^*. It is evident that the contribution of the F-P reciprocating compressor is P^*/P_s^* and this ratio, equal to P_{1c}/P_{1b}, has been referred to previously as the pressure ratio of the "simple part" of the complex supercharged-and-intercooled cycle, hereafter abbreviated to the S-and-I cycle.

This consideration sets the stage for formulating two useful points of view for comparison of the S-and-I and the simple cycles:

1 The S-and-I cycle versus the simple cycle with a pressure ratio $P^*_{\text{simple cycle}} = (P^*/P_s^*)_{\text{S-and-I cycle}}$

2 The S-and-I cycle versus the simple cycle with a pressure ratio $P^*_{\text{simple cycle}} = P^*_{\text{S-and-I cycle}}$

The first point of view is one that might be assumed by an engineer who has an existing model of a simple-cycle F-P unit and is faced with the requirement of increasing the output. The second point of view is one that a design engineer may elect if he has to make a decision as to whether to develop the simple cycle or the S-and-I cycle, assuming that the pressure charging of the engine cylinder is the criterion to use with respect to the severity of combustion conditions. It is well appreciated that severity of combustion in an IC engine cylinder is related to top combustion temperature and rate of change of pressure during the combustion process, as well as top combustion pressure. Nevertheless, as this complex question is debatable, the simple, though admittedly superficial, criterion of pressure charging of the engine cylinder is the one which will be adopted here.

It is just the difference in these two points of view that results in the contrary opinions as to whether or not the S-and-I cycle is a "good" one. In the following section on Results, both points of view will be employed. They will be abbreviated to the following:

1 Supercharging an existing model.

2 Comparable combustion loading conditions.

THERMODYNAMIC ANALYSIS

Since the thermodynamic analysis used is essentially the same as presented in detail in the parent paper,[2] it will not be repeated here. The parameters specified as fixed for the cycle calculations are summarized in Table 1. Note that the centrifugal supercharger efficiency (η_s = 78 per cent in this case) is considered to include an allowance for pressure drop through the intercooler. The intercooler is specified to have a heat-transfer effectiveness of 80 per cent.

TABLE 1 SPECIFIED PARAMETERS FOR CYCLE CALCULATIONS

1	Fuel LHV 18,300 Btu/lb
2	Inlet-air state P_0 = 14.7 psia, T_0 = 530 deg R (70 deg F)
3	Free-piston efficiencies:
	Compressor, η_c = 80 per cent
	Mechanical, η_m = 90 per cent
	Engine indicated thermal, $\eta_{ith\ eng}$ = 41.1 per cent (corresponding to an engine compression ratio of about 10:1)
4	Engine air-fuel ratio ω_e/ω_f = 30:1
5	Coolant heat-transfer fraction, q^* = 0.20
6	Fraction pressure drop total for both engine valve events, ΔP^* = 10 per cent
7	Supercharger efficiency, η_s = 78 per cent[a]
8	Intercooler effectiveness, ϵ = 80 per cent
9	Turbine isentropic efficiency, η_t = 80 per cent
10	Working-substance properties:
	Air with R/m = 53.34 ft#/(lb deg R)
	For compressor and supercharger processes: c_p = 0.243 Btu/(lb deg R), $\bar{k}$ = 1.392
	For turbine processes: $\bar{c}_p$ = 0.255 Btu/(lb deg R), $\bar{k}$ = 1.366

[a] This somewhat low efficiency allows for flow-pressure losses in the intercooler.

RESULTS

Figs. 2(*a*) and 2(*b*) together with Table 2 summarize the calculated performance for the S-and-I cycle described in Fig. 1. These results are for various supercharger pressure ratios $P_s^* = P_{1c}/P_0$ from 1 (no supercharge) to 2.6, all for a fixed-cycle pressure ratio of $P^* = P_{1c}/P_0 = 6$. Cycle parameters held constant for the analysis are summarized in Table 1.

Figs. 3(*a*) and 3(*b*) are similar to the previous ones except here the cycle pressure ratio is maintained at $P^* = 8$ instead of 6. Points for these curves are summarized in Table 3.

Figs. 4(*a*) and 4(*b*) summarize the same kind of information, except the supercharge pressure ratio is kept constant at $P_s^* = 1.7$, while the cycle pressure ratio P^* is varied from 3 to 12. Additionally, the performance of the simple cycle is shown for comparison. Table 4 contains the calculated results leading to these curves.

Fig. 5 presents the conditions for zero work from the third turbine pictured in the flow diagram, Fig. 1. This corresponds to $P_{3b} = P_0$, and then the fuel-economy performance of the S-and-I cycle with $P^* = P_{1c}/P_0$ is identical to that of a simple cycle with $P^* = P_{1c}/P_{1b}$. For instance, from Fig. 5, an S-and-I cycle with a P^* of 12.5 and a P_s^* of 2.1 will have the same fuel economy as a simple cycle of $P^* = 6$. If $P_s^* < 2.1$, still maintaining a P^* of 12.5, the S-and-I cycle will have a better sfc. If $P_s^* > 2.1$, the reverse will obtain. These calculations were made for a supercharger efficiency of η_s = 80 per cent and an intercooler effectiveness ϵ = 100 per cent. For η_s = 78 per cent and ϵ = 80 per cent, as for the other calculations, the performance would be modified only slightly in favor of the simple cycle.

The foregoing results, particularly those shown in Figs. 2 and 3, may now be examined employing the two viewpoints formulated in the introduction.

Supercharging an Existing Model. Suppose an existing model

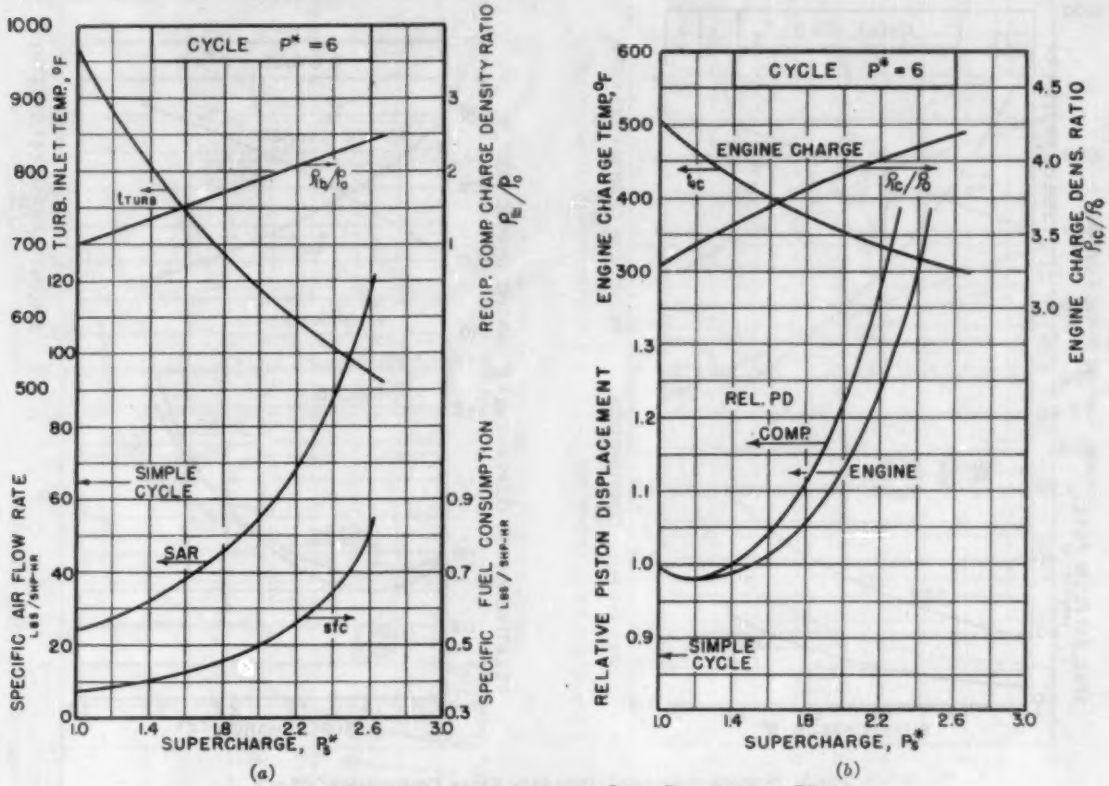

FIG. 2 SUPERCHARGED-AND-INTERCOOLED CYCLE PERFORMANCE; $P^* = 6$
(See Table 1 for specified parameters used in cycle analysis and Table 2 for calculated points.)

of a simple-cycle system has a pressure ratio $P^* = 6$. It is now proposed to supercharge it with a centrifugal compressor with a $P_s^* = 1.333$. The resulting S-and-I cycle will then have a $P^* = 8$. The performance of the original simple cycle can be read from Figs. 2(*a*) and 2(*b*) (at $P_s^* = 1$, the condition of no supercharge); and the S-and-I cycle performance for $P^* = 8$, $P_s^* = 1.333$ can be determined from Figs. 3(*a*) and 3(*b*) (or interpolated from Table 3). This comparison is given in Table 5.

The evident conclusions are (1) the thermodynamic performance of the two cycles is nearly the same with respect to sfc, SAR, and turbine-inlet temperature; (2) more severe combustion conditions will exist in the S-and-I cycle because of the moderately higher engine-charge density coupled with a slightly higher engine-charge temperature; (3) if the operating frequencies are the same, the S-and-I model will have a power increase of about (1/0.75 — 1) or 33 per cent. A less evident conclusion is that the S-and-I model will operate at a higher speed than the simple-cycle model, roughly in proportion to the $\sqrt{P^*}$, because of the greater "stiffness" of the "gas springs" (Ehrat's discussion).[3] Under these circumstances one could anticipate a power boost of the order of $1.33 \times \sqrt{8/6} - 1 = 53$ per cent with no loss in sfc performance.

Against this substantial gain must be weighed the disadvantages of increased severity of engine combustion conditions and additional complexity resulting from two more flow machines, a heat exchanger, and the associated ducting.

From the comparison in Table 5, it is evident that the engine-charge density is 30 per cent greater and the charge temperature is slightly higher, 528 versus 506 F. As the simple cycle with $P^* = 6$ has an imep of about 334 psi,[4] it is self-evident that for the S-and-I cycle, with 30 per cent greater loading, cylinder heat problems of greater magnitude can be anticipated. Higher speed of operation, of the order of $\sqrt{8/6} - 1 = 15$ per cent, can only accentuate the difficulties because of higher rates of pressure change and higher heat-transfer coefficients.

Because the specific air-flow rate, SAR, is 23.0 lbs of air/shphr, about three times that of a conventional diesel, one anticipates that the supercharger and its turbine drive will be a more bulky

TABLE 2 $P^* = 6$—PERFORMANCE OF SUPERCHARGED-AND-INTERCOOLED CYCLE

Supercharger Pressure Ratio, P_s	1	1.2	1.4	1.7	2.0	2.3	2.6
Specific Fuel Consumption SFC, lbs/(shp hr)	0.370	0.388	0.408	0.439	0.501	0.598	0.800
Specific Air Flow Rate SAR, lbs/(shp hr)	23.0	27.6	32.4	41.5	55.0	75.8	117
Turbine Inlet Temperature, °F	972	883	809	715	636	577	530
Comp. to Engine Air Ratio ω_c/ω_e	2.13	2.41	2.69	3.15	3.66	4.22	4.86
Engine Charge Density Ratio ρ_e/ρ_0	3.29	3.45	3.58	3.76	3.93	4.05	4.16
Engine Charge Temperature, °F	506	462	429	386	352	326	308
Recip. Comp. Charge Density Ratio ρ_2/ρ_0	1.00	1.162	1.365	1.62	1.90	2.165	2.41
Recip. Comp. Displ. Relative to Simple Cycle	1.00	0.98	1.00	1.07	1.22	1.48	2.04
Engine Displ. Relative to Simple Cycle	1.00	0.98	0.99	1.03	1.13	1.305	1.66

[4] Reference (2), Table 2.

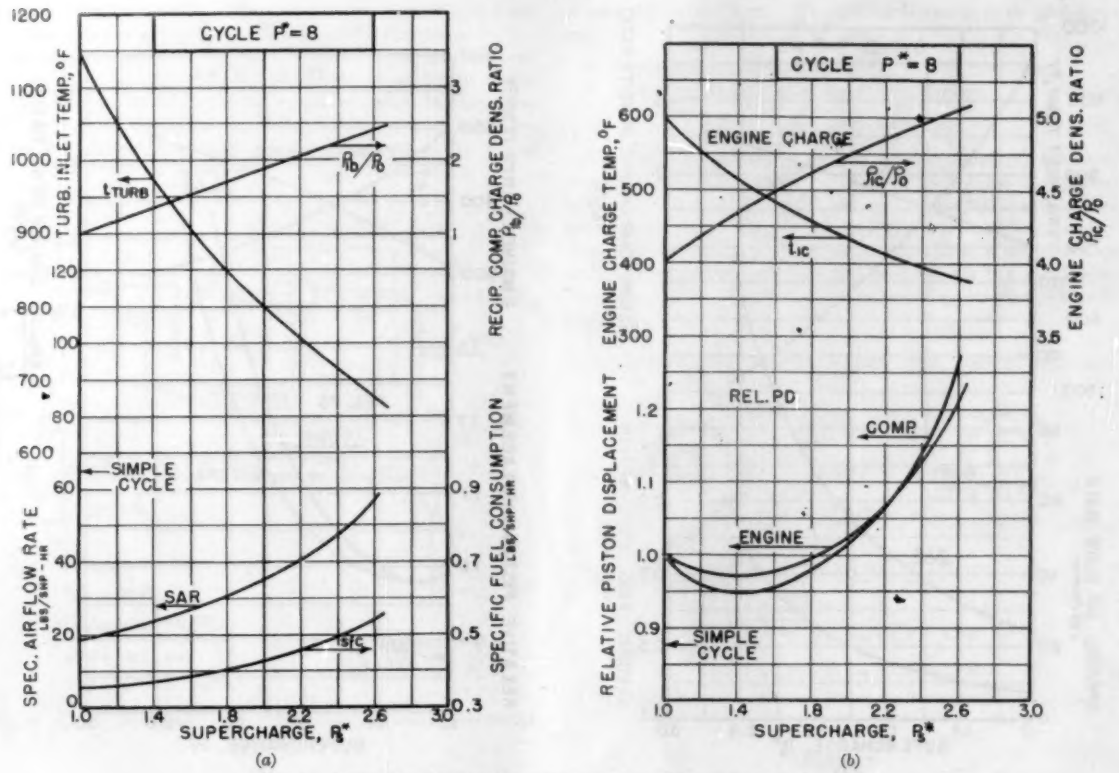

FIG. 3 SUPERCHARGED-AND-INTERCOOLED CYCLE PERFORMANCE; $P^* = 8$
(See Table 1 for specified parameters used in cycle analysis and Table 3 for calculated points.)

TABLE 3 $P^* = 8$—PERFORMANCE OF SUPERCHARGED-AND-INTERCOOLED CYCLE

Supercharge Pressure Ratio, P_s^*	1.0	1.2	1.4	1.7	2.0	2.3	2.6
Specific Fuel Consumption sfc, lbs/(shp hr)	0.352	0.359	0.370	0.394	0.430	0.470	0.536
Specific Air Flow Rate SAR, lbs/(shp hr)	16.5	21.1	23.9	29.1	35.6	43.9	56.3
Turbine Inlet Temperature, °F	1149	1055	976	878	797	736	675
Comp. to Engine Air Ratio w_c/w_e	1.76	1.95	2.15	2.45	2.76	3.11	3.49
Engine Charge Density Ratio ρ_c/ρ_o	4.01	4.19	4.34	4.56	4.75	4.91	5.05
Engine Charge Temperature, °F	599	551	516	470	433	404	378
Recip. Comp. Charge Density Ratio, ρ_b/ρ_o	1.00	1.165	1.365	1.63	1.90	2.155	2.41
Recip. Comp. Displ. Relative to Simple Cycle	1.00	0.96	0.945	0.965	1.015	1.095	1.26
Engine Displ. Relative to Simple Cycle	1.00	0.977	0.973	0.985	1.03	1.09	1.21

TABLE 4 $P_s^* = 1.7$—PERFORMANCE OF SUPERCHARGED-AND INTERCOOLED CYCLE

Cycle Pressure Ratio, p^*	2.89	4	6	8	10	12
Specific Fuel Consumption SFC, lbs/(shp hr)	0.990	0.566	0.439	0.396	0.373	0.368
Specific Air Flow Rate SAR, lbs/(shp hr)	248	84.8	41.5	29.2	23.3	20.2
Turbine Inlet Temperature, °F	333	497	715	868	1020	1104
Comp. to Engine Air Ratio w_c/w_e	8.34	4.95	3.15	2.46	2.08	1.85
Engine Charge Density Ratio ρ_{ic}/ρ_o	2.31	2.87	3.76	4.56	5.31	6.01
Engine Charge Temperature, °F	203	280	386	470	539	599
Recip. Comp. Charge Density Ratio ρ_b/ρ_o	1.632	1.632	1.632	1.632	1.632	1.632
Recip. Comp. Displ. Relative to Simple Cycle	1.50	1.45	1.07	0.985	0.915	0.900
Engine Displ. Relative to Simple Cycle	1.31	1.32	1.05	0.969	0.969	0.970

(and expensive) unit than required for a crank-type diesel. As the supercharger turbine operates at such moderate temperatures, about 500–600 F, there is some compensation afforded by the use of less expensive blade materials.

The intercooler requirements are fairly substantial, again due to the high SAR relative to a crank-type diesel. Assuming the availability of water as a coolant and a desired effectiveness, ϵ = 80 per cent, elementary heat-transfer considerations indicate a transfer-area requirement of the order of 0.5 to 0.7 sq ft/shp. This is the same as the specific heat-transfer area required in a condenser of a steam power plant and about 20–25 per cent of the area needed in a 75 per cent effective regenerator for a marine-type gas-turbine plant.

TABLE 5 SUPERCHARGING AN EXISTING MODEL

	Simple-cycle model $P^* = 6$	S-and-I cycle model $P^* = 8$, $P_s^* = 1.33$
Specific fuel consumption	0.370	0.366
Specific air rate	23.8	23.0
Turbine-inlet temperature, deg F	972	1,003
Relative piston displacement:		
Compressor	1	0.74
Engine	1	0.75
Engine-charge temperature, deg F	506	528
Engine-charge density relative to atmospheric ρ_{ic}/ρ_o	3.29	4.29

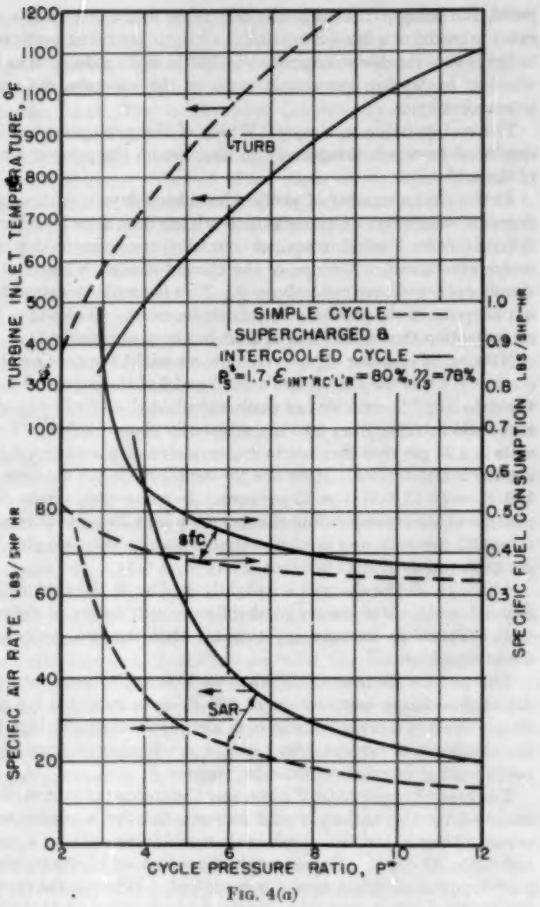

FIG. 4(a)

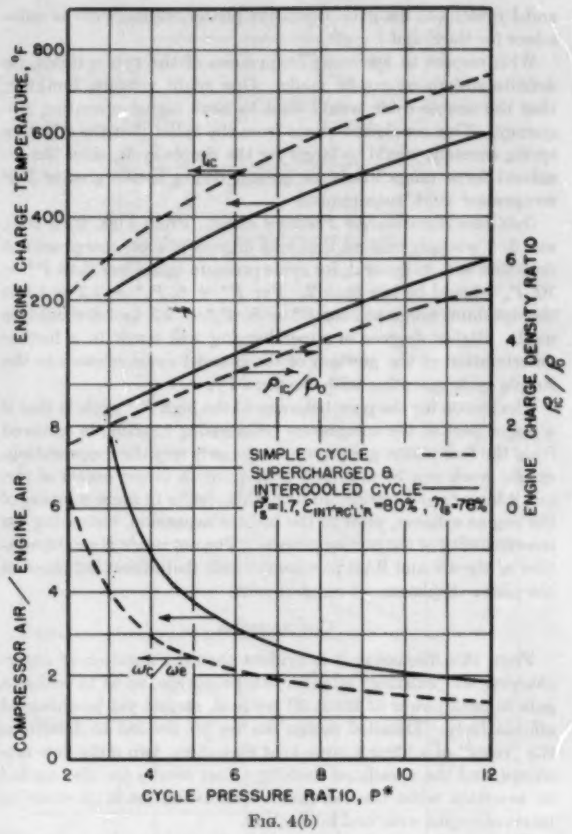

FIG. 4(b)

FIG. 4 SUPERCHARGED-AND-INTERCOOLED CYCLE PERFORMANCE; $P_s^* = 1.7$

(See Table 1 for specified parameters used in cycle calculation and Table 4 for calculated points.)

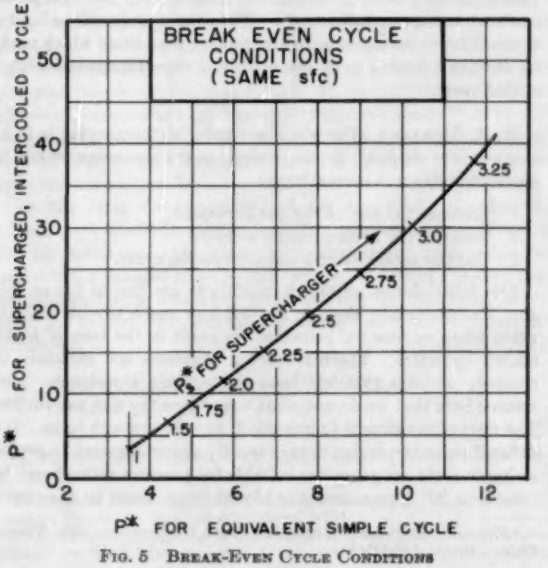

FIG. 5 BREAK-EVEN CYCLE CONDITIONS

Comparable Combustion Loading Conditions. As indicated in the introduction, this comparison will specify a common pressure-charging magnitude for the engine cylinder, say, $P^* = 8$, for example. The contrast, Table 6, will now be between a simple-cycle operating with $P^* = 8$ and an S-and-I cycle operating with $P_s^* = 1.33$ and $P^* = 8$.

TABLE 6 COMPARISON FOR EQUAL COMBUSTION LOADING

	Simple cycle $P^* = 8$	S-and-I cycle $P^* = 8$, $P_s^* = 1.33$
Specific fuel consumption	0.352	0.366
Specific air rate	18.5	23.0
Turbine-inlet temperature, deg F	1149	1003
Relative piston displacements:		
Compressor	1	0.95
Engine	1	0.97
Engine-charge temperature, deg F	599	528
Engine-charge density relative to atmospheric ρ_{1c}/ρ_0	4.01	4.29

The evident conclusions from Table 6 are: (1) The specific fuel consumptions are nearly the same, with the simple cycle possessing a 4 per cent advantage; (2) the S-and-I cycle has the advantage of a moderately lower turbine-inlet temperature; (3) the engine-charge conditions indicate a moderate advantage for the S-and-I cycle with respect to temperature and a slight disadvantage with respect to density; thus the engine combustion conditions may be considered to be somewhat less severe for the S-

and-I cycle; (4) the gain in relative piston displacement is quite minor for the S-and-I cycle.

With respect to operating frequencies of the two systems, no definite statement can be made. One might venture, however, that the simple cycle would tend to have higher operating frequency. This conclusion stems from the belief that the effective spring constant would be larger for the simple cycle, since the resultant force range would be greater owing to the greater F-P compressor work requirement.

Optimum Supercharger Pressure Ratio. From Figs. 2(*b*), 3(*b*), and 5, it is amply evident that high degrees of supercharge are not desirable and, in general, for cycle pressure ratios less than $P^* = 10$, P_s^* should be less than 2. For $P^* = 6$, $P_s^* = 1.2$ to 1.4 is the optimum range and for $P^* = 8$, $P_s^* = 1.3$ to 1.8 should be used. Higher degrees of supercharging will result in a further deterioration of the position of the *S*-and-I cycle relative to the simple cycle operating with the same P^*.

The reason for the poor behavior of the high P_s^* cycle is that if a major part of the compressor pressurizing function is removed from the free-piston gas generator the only way the reciprocating-engine work can be absorbed is to pump a larger excess of air, i.e., a larger ω_c/ω_s ratio. In turn, this results in more dilution of the engine exhaust, prior to the turbine expansion, increasing the irreversibility of the mixing process. The net result is a deterioration of the sfc and SAR parameters with their direct influence on the piston-displacement requirements.

Conclusions

From this discussion it is evident that the question of supercharging an "existing" simple-cycle prototype, so as to realize a gain in peak power of about 50 per cent, cannot yet be answered affirmatively. Detailed design studies are needed to determine the "costs" of adding a large heat exchanger, two more flow machines, and the associated ducting. Test results are also needed to ascertain what the increased combustion loadings mean in terms of engine wear and lubrication.

The second point of view enunciated is the one which might be used to make a basic decision as to whether or not to develop the S-and-I cycle, or alternatively a simple cycle for a specified P^*. On this question the cycle studies give a clear answer. The S-and-I cycle possesses no advantage in terms of compactness; in fact, it may be less compact because of its added complexity. Moreover, its specific fuel consumption is not as good. Interestingly enough, the advantages of the S-and-I cycle in this comparison lie in an unexpected quarter to one familiar with conventional crank-engine practice. Supercharging in this instance reduces the severity of the combustion conditions. The engine-charge temperature is reduced substantially (about 70 deg F for $P^* = 8$ and $P_s^* = 1.33$). An additional cycle advantage is the lower gas-turbine temperature by about 150 deg F.

Acknowledgments

This work was accomplished as one phase of a research program sponsored by the USN Office of Naval Research, the Atomic Energy Commission, and the Bureau of Ships. Stanford engineering students, H. Satterlee, B. Bruch, and C. E. Newman, assisted in the calculations and drafting.

Discussion

A. J. Ehrat.[5] It is regrettable that, in spite of his resolve that points of view be clearly formulated, the author seems to have clouded the basic issue. The question cannot be split into two parts, one being pertinent in the case of an engineer who has an existing model of a free-piston unit, and the other being pertinent in the case of the design engineer who has to make a decision as to whether to develop the simple cycle or the supercharged-and-intercooled cycle.

The real question is, simply: Which of the two cycles can be employed more advantageously to improve on the present state of the art?

At this time a number of gasifiers have been developed to a fair degree of reliability. Although this work has been done by several different firms located in several countries, one common denominator stands out. Not one of the current models is rated at a simple-cycle pressure ratio above 6. This is ample evidence, for our purpose, of the present state of development. It also may be an indication that some form of limit has been approached.

Now let us consider objectively how we might improve on this state. We find the answer in Tables 5 and 6 of the paper. From the data listed therein we can easily calculate that the cycle pressure-ratio increase from 6 to the arbitrarily chosen value of 8 results in a 25 per cent decrease in engine-piston displacement, if we use the S-and-I cycle. If we use the simple cycle the decrease is 100 [1 — (0.75/0.97)] = 23 per cent. In compressor-piston displacement the corresponding changes are minus 26 per cent versus minus 22 per cent, and in engine-charge density they are plus 30 per cent versus plus 22 per cent.

Although all the changes are slightly greater in the case of the S-and-I cycle, there are no great differences in orders of magnitude. Therefore we may say thus far that the two cycles are about equal.

This picture alters abruptly when we look at the temperatures. An engine-charge temperature of 506 F, as is indicated for the simple cycle at a pressure ratio of 6, already is extremely high by the standards of anyone who has had practical experience with reciprocating internal-combustion engines.

The supercharged cycle, if given only the amount of intercooling assumed by the author, would increase this by a moderately severe 22 deg F, but the simple cycle would increase it by a very unhealthy 93 deg F. The same trend is evidenced by the turbine-inlet temperatures, but here it is magnified. Whereas the supercharged-and-intercooled cycle results in an increase of 31 deg F, the simple cycle results in one 5¾ times as great, or 177 deg F. This great inequality in the rates of temperature rise with power can lead to one conclusion only. The simple cycle will be limited to much lower pressure ratios and powers than those which might be obtained from a properly exploited supercharged-and-intercooled cycle.

W. A. Morain.[6] The main reason for supercharging is to increase power output. In the free-piston gas generator we can increase the output in several ways:

1 Increase the size of the gas generator.
2 Increase the cycle pressure ratio.
3 Use the supercharged-and-intercooled cycle.

The principles of geometric similitude are fine as far as they go. Unfortunately, they do not tell how much trouble may develop when substantial increases are made in the bore of highly loaded cylinders. Thermal-loading problems are certainly increased; at least that has been the writer's experience. Let's assume here that we do not want to increase the size any further. The next alternative is to increase the cycle pressure ratio. It is difficult, with the design data presently at our disposal, to project a simple-cycle gas generator suitable for pressure ratios much beyond 8 or 9. The scavenging blowthrough tends to decrease as

[5] American Machine & Foundry Company, Greenwich, Conn.

[6] Research Engineer, Cooper-Bessemer Corporation, Mt. Vernon, Ohio. Mem. ASME.

the pressure ratio increases, and in the region noted, the blow-through approaches zero. The writer would not go so far as to say we cannot operate without completely purging the power cylinder of combustion gases, but he would rather not take the gamble. Also, the turbine-inlet temperature would soon get quite out of hand.

This, it is felt, makes a definite case for the supercharged-and-intercooled cycle. Table 5 of the paper shows rather promising results and if P_s is increased still further the results continue to improve. We note that if we leave the gas-generator pressure ratio at 6 and go to $P_s = 1.7$, giving an over-all ratio of 10, the SFC and SAR are improved over the simple cycle, and the power increases substantially. In our studies on the C-B Model R unit, we concluded that we would install heavier pistons in a unit designed for supercharged operation and that we would open out the inner end clearance to hold the peak pressure to a 2000 psi limit. These changes, we felt, would reduce the severity of loading in the power cylinder to acceptable conditions. Substantial power gains were indicated with slight improvement in the specific fuel and air rates.

The equipment we have provided for turbocharged operation has not turned out to be particularly bulky. The turbocharger selected was taken from a conventional 1700 engine, and will give us a 1.5-atm boost. If we develop the anticipated horsepower increase, the added bulk and complexity will certainly be justified.

The writer wishes to compliment the author on his outstanding work in promoting the free-piston gas turbine, both through his valuable technical contributions, and his enthusiasm and encouragement to the other workers in the field. While most of us engaged in this work are more convinced than he that supercharging is a "good" thing, his work should be most carefully considered in arriving at any final evaluation, for his criticisms are both constructive and sincere.

S. L. Soo.[7] The writer, who has been a student of the author's many brilliant papers, has the highest regard for him as a pioneer in the field of free-piston machines.

It is highly illuminating that in the present paper he considers a comparison of the supercharged and unsupercharged free-piston turbine plant. The supercharged-and-intercooled cycle amounts to operating a simple cycle in an atmosphere at the equivalent state of that at the outlet of the intercooler with the added advantage of reduced power-turbine back pressure. The latter fact is that, owing to current figures of machine efficiencies (80 per cent blower efficiency and 82 to 85 per cent blower-turbine efficiency) equilibrium running of the turbocharger set [Fig. 5(*a*) of the paper by Morain and Soo][8] at ordinary generated gas temperature of 1000 F, the blower-turbine pressure ratio will be lower than the blower pressure ratio.

In this view, the net output of the supercharged-and-intercooled cycle would be greater than the proportionate increase in the air density at the reciprocating compressor inlet. The reduced firing pressure ratio (permissible firing pressure/scavenging air pressure) is the source of reduced ideal cycle efficiency. However, the factors contributing to increased thermal efficiency are as follows:

1 Reduced percentage power-cylinder cooling loss.
2 Increased power-turbine pressure ratio.

The problems in regard to optimum charging pressure ratio, intercooler requirement, and combustion loading were clarified in the reference cited.[8]

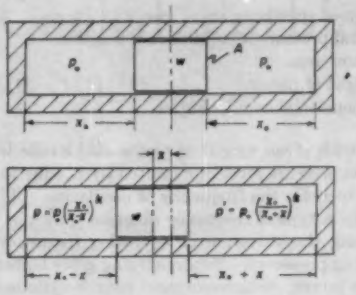

FIG. 6 A SIMPLE OSCILLATING WEIGHT IN A GAS-CHARGED CYLINDER

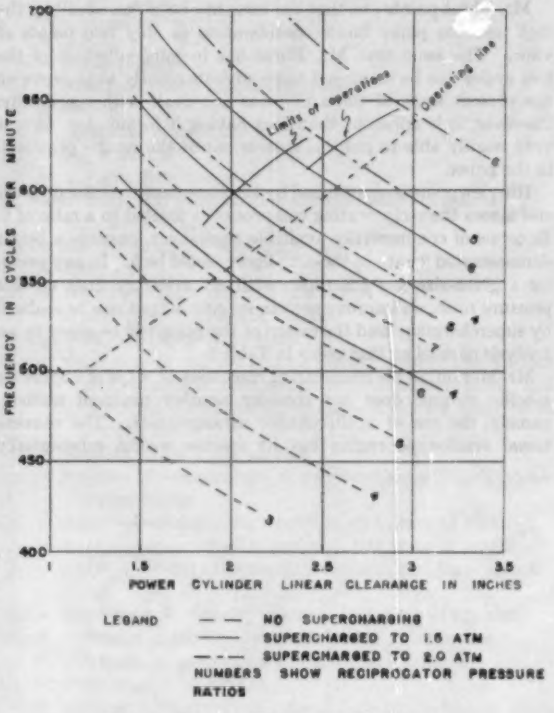

FIG. 7 TYPICAL FREQUENCY DIAGRAM

There is probably a typographical error in the statement regarding the change in operating frequency of a given machine due to supercharging: The simple cycle would have lower operating frequency. By considering the simplified system depicted in Fig. 6 of this discussion a frictionless and leakproof piston in a cylinder closed at both ends with identical amounts of perfect gas at identical states to start with but insulated from each other and the surroundings, it can be shown that a small disturbance would result in an oscillating frequency of (linearized solution)

$$\text{Frequency} = \frac{1}{\pi}\sqrt{\frac{gkp_sA}{2w\,x_0}} \text{ cycles per unit time}$$

where

g = gravitational acceleration

[7] Assistant Professor of Mechanical Engineering, Princeton University, Princeton, N. J. Assoc. Mem. ASME.

[8] "Some Design Aspects of the Free-Piston Gas Generator Turbine Plant," by W. A. Morain and S. L. Soo, ASME Paper No. 55—A-155.

k = ratio of specific heats of gas
p_0 = initial pressure at equilibrium position
A = piston area
w = weight of piston
x_0 = dimension shown in Fig. 6

Therefore, with given weight of piston and stroke length, an increase of the pressure level represented by p_0 (due to supercharging) would increase the frequency of oscillation. This is further confirmed by a typical frequency diagram shown in Fig. 7, herewith, showing the variation in operating frequency at various supercharging pressures. Supercharging gives higher mean pressures in the power, compressor, and bounce cylinders.

Author's Closure

Mr. Ehrat points out that the issue has been "clouded" by the fact that the paper limits consideration to only two points of view. The issue that Mr. Ehrat has in mind—"which of the two cycles can be employed more advantageously to improve on the present state of the art"—was not dealt with specifically. However, it is apparent that once having it formulated, he was very readily able to pull his answer out of the results presented in the paper.

His viewpoint is quantitized by the statement that the pressure rise across the reciprocating compressor is limited to a ratio of 6. In terms of commercially available equipment, possibly a better demonstrated "state-of-the-art" figure would be 5. In any event, for a given-size gas generator, with an arbitrary limit on this pressure ratio, an improvement in specific output can be realized by supercharging; and the extent of the gains will be given by an analysis paralleling that given in Table 5.

Mr. Morain, in his illuminating discussion of ways of improving specific output, does not consider another practical method, namely, the use of multicylinder arrangements. The conventional crank-type engine has its specific weight substantially improved thereby; and there are reasons to believe that this procedure is even more advantageous for the free-piston engine concept.

It is encouraging that the Cooper-Bessemer studies indicate the gains from supercharging an existing model are well worth the complexity of the turbocharger and intercooler auxiliaries.

Professor Soo's initial comments are to the effect that the hot gas pressure expansion ratio across the turbine of the turbocharger may well be less than the pressure rise across the compressor of the turbocharger. The fact that $P_{3a} = P_{1b}$ is specified in the flow diagram of Fig. 1 does not obviate this possibility, because of the existence of the No. 3 turbine, which was introduced for convenience in analysis. The arbitrariness of the specification of $P_{3a} = P_{1b}$ is, in effect, compensated for by the degree of freedom the third turbine provides for P_{3b}. This pressure may be greater or less than atmospheric pressure. If the Nos. 2 and 3 turbines are combined into a single unit to drive the supercharger, which would be the case for any practical system, then one cannot arbitrarily make $P_{3a} = P_{1b}$ because the exhaust pressure is fixed at atmospheric. In this case P_{3a} would be established by the requirement of providing the necessary supercharger input work.

In agreement with Professor Soo's analysis, the author indicated that supercharging a given machine will increase its operating frequency. Evidently, this more or less obvious conclusion was confused with a later statement made in respect to the comparison afforded by Table 6, where two different machines, one operating on the simple cycle and the other on the S-and-I cycle, both with a $P^* = 8$, are considered. Here, the "on-the-fence" position assumed by the author was—"With respect to operating frequencies of the two systems, no definite statement can be made. One might venture, however, that the simple cycle would tend to have the higher operating frequency." The studies reported in Fig. 7 do not apply to this situation involving two different machines, each designed for its own cycle.

The Thermodynamics of Cooled Turbines[1]

Part 1—The Turbine Stage

By W. R. HAWTHORNE,[2] CAMBRIDGE, MASS.

A procedure has been obtained for calculating the effect of cooling on turbine-stage efficiency by visualizing the flow in the blade passages as one-dimensional compressible flow in a conical tube with heat transfer and friction. The use of Reynolds' analogy between friction and heat transfer permits the results to be correlated in terms of the blade-profile loss coefficient in low-speed flow, the change of passage area in the blade section and the ratio of average blade-surface temperature to the stagnation temperature of the gas relative to the blades. Simple expressions are obtained for the amount of heat abstracted in a cooled row of blades and the drop in turbine-stage efficiency resulting from cooling. Calculations for some typical stages show that, with blades cooled appreciably below the gas temperature, the amount of heat removed may be as much as 5 per cent of the calorific value of the fuel per row of cooled blades and the decrease in turbine-stage efficiency as much as 3 per cent when both nozzles and blades are cooled appreciably. The use of impulse and low reaction stages reduces to a small fraction of a per cent the effect on the stage efficiency of cooling the rotor blades only.

Nomenclature

The following nomenclature is used in the paper:

a = $\dfrac{1 - T_w/T_{01}}{1 + T_w/T_{02}}$, assumed to be constant in turbine-blade passage

A = cross-sectional area of turbine blade or nozzle passage

B = loss coefficient for three-dimensional flow through blades equal to $\dfrac{h_2 - h_{2s}}{w_2^2/2}$

c_1 = absolute velocity entering blades or leaving nozzles

c_2 = absolute velocity leaving blades

c_p = specific heat at constant pressure

c_v = specific heat at constant volume

c_x = axial velocity (subscript 1 identifies axial velocity entering rotor blades; subscript 2 identifies axial velocity leaving)

f = wall-friction coefficient

g = gravitational constant

h = enthalpy

k = ratio of specific heats, c_p/c_v

l = blade height

J = conversion factor from ft-lb to Btu

M = Mach number

n = $\dfrac{1}{\tan \theta/2}$

N = loss coefficient for three-dimensional flow through nozzles equal to $\dfrac{h_1 - h_{1s}}{c_1^2/2}$

p = static pressure

Q = heat transferred to cooled surfaces

s = entropy

S = perimeter of duct

R = gas constant

T = absolute temperature

T_w = average wall temperature of cooled blade or nozzle

u = velocity of blades

U = film coefficient of heat transfer

V = stream velocity

w_1 = relative velocity entering blades

w_2 = relative velocity leaving blades

W = work done by turbine stage

W_s = work done in an ideal process at constant entropy without cooling in which inlet and outlet velocities (c_1 and c_2) and inlet and outlet pressures (p_1 and p_2) are same as in actual process

x = distance along blade passage

y = fraction of temperature drop across stage which occurs across blades

α_1 = angle between velocity vector w_1 and plane of rotation

α_2 = angle between velocity vector w_2 and plane of rotation

β_1 = nozzle angle between velocity vector c_1 and plane of rotation

β_2 = angle between velocity vector c_2 and plane of rotation

ϵ_B = deflection of gas stream going through rotor blades

ϵ_N = deflection of gas stream going through nozzles

ρ = mass density of stream

θ = angle of convergence of conical duct equivalent to blade passage

η_{st} = stage efficiency

ξ = profile loss factor (two-dimensional)

ξ_0 = $\displaystyle\int_0^x f \frac{S\,dx}{A}$

ξ_p = loss factor normally measured in low-speed cascades; used here to define loss characteristics of blade

Subscripts

$( )_0$ applied to h, p, or T refers to stagnation conditions

$( )_{0i}$ refers to stagnation conditions at nozzle inlet

$( )_{0e}$ refers to stagnation conditions at nozzle outlet

$( )_{01}$ refers to relative stagnation conditions corresponding to state 1 in rotor blades

$( )_{02}$ refers to relative stagnation conditions corresponding to state 2 in rotor blades

$( )_{0f}$ refers to stagnation conditions at rotor-blade outlet

$( )_1$ refers to conditions at inlet to blades or outlet of nozzles

---

[1] This paper contains work done under the sponsorship of the Office of Naval Research Contract N5ori—78 to 21, March, 1949. The work was carried out when the author was George Westinghouse Professor of Mechanical Engineering at the Massachusetts Institute of Technology.

[2] Hunsaker Professor of Aeronautics, Massachusetts Institute of Technology, on leave from the Professorship of Applied Thermodynamics, University of Cambridge, England.

Contributed by the Gas Turbine Power Division and presented at the Diamond Jubilee Annual Meeting, Chicago, Ill., November 13–18, 1955, of The American Society of Mechanical Engineers.

Note: Statements and opinions advanced in papers are to be understood as individual expressions of their authors and not those of the Society. Manuscript received at ASME Headquarters, August 29, 1955. Paper No. 55—A-186.

( )$_2$ refers to conditions at outlet of blades
( )$_{1s}$ refers to conditions at state 1s which is the state at p_1 reached from state 0i by an isentropic process (see Figs. 2 to 6)
( )$_{2s}$ similarly defined for isentropic expansion through blades
( )$_{2ss}$ state reached in isentropic expansion through stage from 0i to p_2
( )$_B$ refers to blades
( )$_N$ refers to nozzles
( )$'$ refers to cooled turbine stage

Introduction

The use of cooled blades in gas turbines should make possible an increase in turbine-inlet temperature and hence output and thermal efficiency. However, the removal of heat from the gas passing through the turbine blading may reduce the work output from the turbine and thereby appreciably offset the gain in thermal efficiency arising from an increase in turbine-inlet temperature.

Some estimates of the effect of removing heat on the turbine performance have already been made (3, 4).[3] It is possible, if the heat removed and work done per stage and the stage efficiency are known, to calculate stage by stage the effect of cooling. The calculation of the effect of cooling on the stage efficiency is more difficult and forms the subject of this paper. By regarding the blades as conical tubes and using the techniques of handling one-dimensional flow problems (1), a method of calculation is derived, assuming a knowledge of profile loss coefficients and the amount of heat transferred in the blading. Results are presented in such a way that calculations may be made for any stage. Making estimates for the loss coefficients, a number of typical stages are studied primarily to determine which types of stage show the smallest effect of cooling.

A turbine stage consists of a row of fixed nozzles followed by a row of moving blades shown developed in Fig. 1. Fig. 1 also contains a diagram showing the nomenclature used in the velocity triangles. The velocities and physical geometry of the blading usually vary with radius, but these variations will be neglected in the following analysis.

The method of determining the effect of cooling on the stage efficiency will be illustrated by analyzing and discussing, in turn, (a) the uncooled stage with losses, (b) the reversible and cooled stage, and (c) the cooled stage with losses. Solutions for these expressions will then be obtained by treating the flow through the blades as one-dimensional flow in a conical tube.

A value of k, the ratio of the specific heats, of 1.4 has been assumed throughout the calculations because accurate tables for compressible flow functions with $k = 1.4$ are available.

1 The Uncooled Turbine Stage

The enthalpy-entropy diagram is shown in Fig. 2. Point 0i represents stagnation conditions before the nozzles; point 1 represents the condition of the fluid after expansion through the nozzles; point 2 represents the condition of the fluid after expansion through the blades.

Applying the steady flow-energy equation to flow through nozzles and blades

$$h_{0i} = h_1 + \frac{c_1^2}{2} \quad [1a]$$

and

$$h_1 + \frac{w_1^2}{2} = h_2 + \frac{w_2^2}{2} \quad [1b]$$

[3] Numbers in parentheses refer to the Bibliography at the end of the paper.

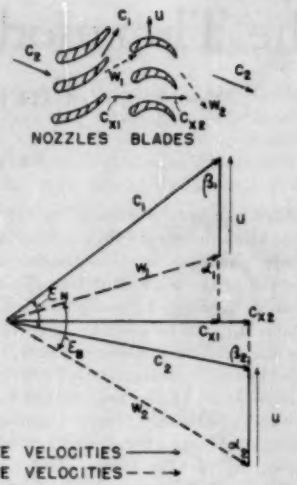

Fig. 1 Diagram of Nozzles and Blades and Corresponding Velocity Triangles

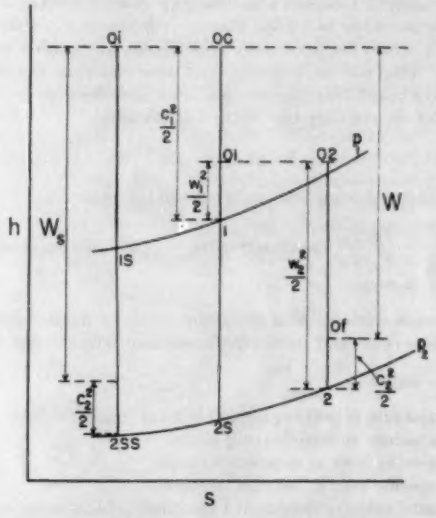

Fig. 2 Enthalpy-Entropy Diagram for Uncooled Stage

and across the stage

$$h_{0i} - h_{0f} = h_{0i} - h_2 - \frac{c_2^2}{2} = W \quad [2]$$

Note that the constants g and J have been omitted from the foregoing equations to simplify the presentation.

There are numerous ways of expressing the turbine efficiency, involving comparison of the actual work with that obtainable in some ideal process. It is customary to choose a reversible process as the ideal, i.e., the one at constant entropy when there is no heat transfer between the fluid and its surroundings. We shall select such an isentropic process with the same pressures and velocities at inlet to, and outlet from, the stage as the actual process. Then the ideal work W_s is given by

$$W_s = h_{0i} - h_{2ss} - \frac{c_2^2}{2} \quad [3]$$

and the stage efficiency

$$\eta_{os} = \frac{W}{W_s} \quad \ldots\ldots [4]$$

Equation [3] may be rewritten

$$W_s = h_{0i} - h_2 - \frac{c_2^2}{2} + h_2 - h_{2s} + h_{2s} - h_{2ss}$$

$$= W + (h_2 - h_{2s}) + h_{2s} - h_{2ss} \quad \ldots\ldots [5]$$

Now

$$\frac{h_{2s} - h_{2ss}}{h_1 - h_{1s}} \backsimeq \frac{(\partial h/\partial s)p_2}{(\partial h/\partial s)p_1} \quad \ldots\ldots [6]$$

and since

$$\left(\frac{\partial h}{\partial s}\right)_p = T \quad \ldots\ldots [7]$$

Equation [5] becomes approximately

$$W_s = W + (h_2 - h_{2s}) + (h_1 - h_{1s})\frac{T_2}{T_1} \quad \ldots\ldots [8]$$

Defining thermodynamic-loss coefficients N and B for flow through nozzles and blades, respectively, by

$$(h_1 - h_{1s}) = N\frac{c_1^2}{2} \quad \ldots\ldots [9a]$$

and

$$(h_2 - h_{2s}) = B\frac{w_2^2}{2} \quad \ldots\ldots [9b]$$

and combining Equations [4], [8], and [9]

$$\frac{1}{\eta_{os}} - 1 = \frac{B\left(\frac{w_2}{u}\right)^2 + \frac{T_2}{T_1}N\left(\frac{c_1}{u}\right)^2}{W/(u^2/2)} \quad \ldots\ldots [10a]$$

or

$$1 - \eta_{os} = \frac{B\left(\frac{w_2}{u}\right)^2 + \frac{T_2}{T_1}N\left(\frac{c_1}{u}\right)^2}{W_s/(u^2/2)} \quad \ldots\ldots [10b]$$

2 The Reversible and Cooled Turbine Stage

The performance of this idealized stage will depend on the conditions under which the heat is removed from the fluid. These conditions will be examined in detail later, but for purposes of illustration it will be assumed for the moment that the heat is removed reversibly at constant pressure. A further assumption is necessary for the value of the pressure at which heat is removed. Two cases have been examined, one in which the pressure at which heat is removed is the stagnation pressure (corresponding roughly to nozzle and blade-inlet conditions) and the other in which the pressure is the pressure at outlet from the nozzles or blades.

Reversible Cooling at Constant Stagnation Pressure. The enthalpy-entropy diagram is shown in Fig. 3. An amount of heat Q_N per lb of fluid is removed[4] between points 0*i* and 0*c*, and an amount Q_B is removed at the stagnation pressure relative to the rotor.

[4] In this analysis heat removed from and work done by the fluid will be accounted positive.

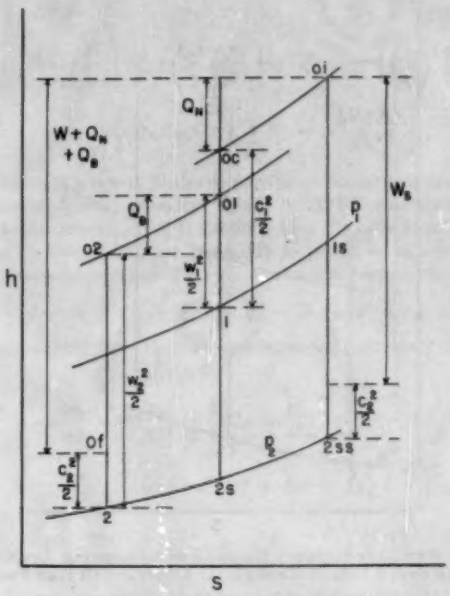

Fig. 3 Enthalpy-Entropy Diagram of Reversible and Cooled Turbine Stage. Heat Removal at Constant Stagnation Pressure

Applying the steady flow-energy equation across the stage

$$W + Q_B + Q_N = h_{0i} - h_2 - \frac{c_2^2}{2} \quad \ldots\ldots [11]$$

The ideal process with which the foregoing will be compared is still a reversible but uncooled process, i.e., an isentropic one. The work done in this latter process is then given by

$$W_s + \frac{c_2^2}{2} = h_{0i} - h_{2ss}$$

$$= h_{0c} - h_2 + h_2 - h_{2s} + h_{2s} - h_{2ss}$$

or

$$W_s = W + Q_B + Q_N - (h_{2s} - h_2) - (h_{2ss} - h_{2s}) \ldots [12]$$

Now, from Equations [6] and [7]

$$\frac{h_{2ss} - h_{2s}}{h_{0i} - h_{0c}} = \frac{h_{2ss} - h_{2s}}{Q_N} \backsimeq \frac{T_2}{T_{0c}} \quad \ldots\ldots [13a]$$

and

$$\frac{h_{2s} - h_2}{Q_B} \backsimeq \frac{T_2}{T_{0s}} \quad \ldots\ldots [13b]$$

whence

$$W_s = W + Q_B\left(1 - \frac{T_2}{T_{0s}}\right) + Q_N\left(1 - \frac{T_2}{T_{0c}}\right) \quad \ldots\ldots [14]$$

and

$$1 - \frac{W}{W_s} = \frac{Q_B\left(1 - \frac{T_2}{T_{0s}}\right) + Q_N\left(1 - \frac{T_2}{T_{0c}}\right)}{W_s} \quad \ldots\ldots [15]$$

Reversible Cooling at Constant Outlet Pressure. The enthalpy-entropy diagram is shown in Fig. 4. An amount of heat Q_N per

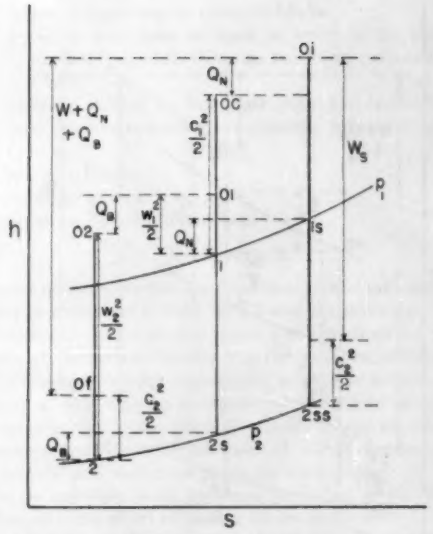

FIG. 4 ENTHALPY-ENTROPY DIAGRAM OF REVERSIBLE AND COOLED TURBINE STAGE. HEAT REMOVAL AT CONSTANT OUTLET PRESSURE

lb is removed between points 1s and 1, and Q_B is removed between points 2s and 2. We have, by the same method as before

$$W + Q_B + Q_N = h_{0i} - h_2 - \frac{c_2^2}{2} \quad \ldots\ldots [16]$$

and

$$W_s + \frac{c_2^2}{2} = h_{0i} - h_{2ss}$$

$$= h_{0i} - h_2 + h_2 - h_{2s} + h_{2s} - h_{2ss}$$

or

$$W_s = W + Q_B + Q_N - Q_B - Q_N \frac{T_2}{T_1}$$

$$= W + Q_N \left(1 - \frac{T_2}{T_1}\right) \quad \ldots\ldots [17]$$

or

$$1 - \frac{W}{W_s} = \frac{Q_N\left(1 - \frac{T_2}{T_1}\right)}{W_s} \quad \ldots\ldots [18]$$

Discussion of Reversible and Cooled Turbine Stage. Some tentative conclusions may be drawn from the foregoing analysis. Assuming that a turbine stage is to be designed for given inlet conditions and outlet pressure and velocity, it is apparent from Equations [15] and [18] that the work output from a cooled turbine will be less than that from an uncooled one. The amount of decrease in work due to cooling will be less than that given by Equation [15] and greater than that of Equation [18]. The effect of lowering the pressure or temperature at which heat is removed is to increase the amount of work obtainable. This may be seen by noting that[5]

$$ds = \frac{-dQ}{T}$$

[5] dQ is assumed positive when heat is removed in this expression.

for a reversible process and that for a given amount of heat removed, the larger the decrease in entropy, the larger the work obtainable.

In an impulse stage the temperature entering the blades is nearly the same as that leaving; consequently, the heat will be removed at a low temperature in the blades. This is equivalent to cooling at constant outlet pressure so that the effect of cooling the blades will be negligible. The maximum effect of cooling the nozzles will be, from Equation [15]

$$1 - \frac{W}{W_s} = \frac{Q_N\left(1 - \frac{T_2}{T_{0c}}\right)}{W_s} \quad \ldots\ldots [19]$$

A real effect will be intermediate between that shown in Equations [18] and [19], depending on the exact process of heat removal in flow through the nozzles. With no cooling of the nozzles, the value of $(1 - W/W_s)$ for an impulse stage is reduced almost to zero. As the reaction is increased, the value of $(1 - W/W_s)$ also will increase. From this it may be deduced that the smallest effect due to cooling on the work output will occur with the impulse stage. As velocities and, therefore, temperature drops are decreased $(W_s - W)$ also will decrease.

The foregoing discussion is based on an analysis of the reversible stage. However, it may be used as a guide to interpret qualitatively the more exact analysis given in the following.

3 THE COOLED TURBINE STAGE

The procedure is similar to that used in the previous paragraphs. Fig. 5 shows the enthalpy-entropy diagram. Applying the steady flow-energy equation, in turn, across the nozzles, rotor blades, and complete stage

$$h_{0i} - h_1 - \frac{c_1^2}{2} = Q_N \quad \ldots\ldots [20]$$

$$h_1 + \frac{w_1^2}{2} - h^2 - \frac{w_2^2}{2} = Q_B \quad \ldots\ldots [21]$$

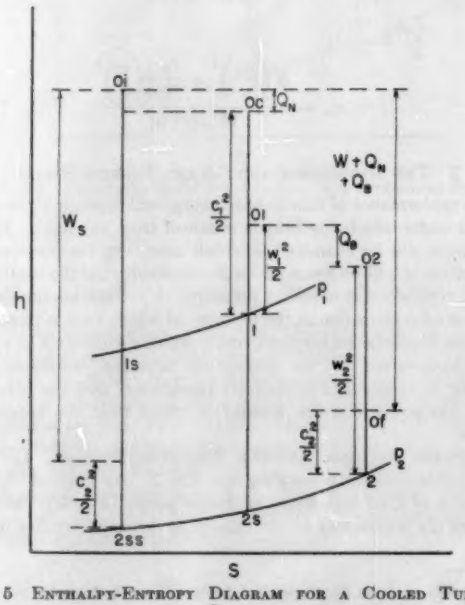

FIG. 5 ENTHALPY-ENTROPY DIAGRAM FOR A COOLED TURBINE STAGE

$$W + Q_N + Q_B = h_{2s} - h_2 - \frac{c_2^2}{2} \quad \ldots\ldots [22]$$

As before

$$W_s = h_{0i} - h_{2ss} - \frac{c_2^2}{2}$$

$$= h_{0i} - h_2 - \frac{c_2^2}{2} + h_2 - h_{2s} + h_{2s} - h_{2ss}$$

$$= W + Q_N + Q_B + h_2 - h_{2s} + \frac{T_2}{T_1}(h_1 - h_{1s}) \quad \ldots\ldots [23]$$

New thermodynamic-loss coefficients for the cooled stage may be defined

$$N' = \frac{h_1 - h_{1s}}{c_1^2/2} \quad \ldots\ldots [24a]$$

and

$$B' = \frac{h_2 - h_{2s}}{w_2^2/2} \quad \ldots\ldots [24b]$$

whence

$$W_s = W + \left\{[Q_N/(c_1^2/2)] + \frac{T_2}{T_1}N'\right\}\frac{c_1^2}{2} + \left\{[Q_B/(w_2^2/2)] + B'\right\}\frac{w_2^2}{2} \quad \ldots\ldots [25]$$

and defining $\eta_{ss}' = W/W_s$

$$\frac{1}{\eta_{ss}'} - 1 = \frac{\left\{[Q_N/(c_1^2/2)] + N'\frac{T_2}{T_1}\right\}\frac{c_1^2}{2} + \left\{[Q_B/(w_2^2/2)] + B'\right\}\frac{w_2^2}{2}}{W} \quad \ldots\ldots [26a]$$

or

$$1 - \eta_{ss}' = \frac{\left\{[Q_N/(c_1^2/2)] + N'\frac{T_2}{T_1}\right\}\frac{c_1^2}{2} + \left\{[Q_B/(w_2^2/2)] + B'\right\}\frac{w_2^2}{2}}{W_s} \quad \ldots\ldots [26b]$$

Combining Equations [20], [21], and [22] to eliminate terms in h, we obtain

$$W = \frac{c_1^2 - w_1^2}{2} + \frac{w_2^2 - c_2^2}{2} \quad \ldots\ldots [27]$$

from which it is concluded that, provided the velocities are the same, cooled and uncooled stages give the same work. Comparing the efficiencies of cooled and uncooled stages on this basis, Equations [26a] and [10a], and using a prime (′) to designate the cooled stage

$$\frac{1}{\eta_{ss}'} - \frac{1}{\eta_{ss}} = \frac{\left\{[Q_N/(c_1^2/2)] + N'\frac{T_2'}{T_1'} - N\frac{T_2}{T_1}\right\}\frac{c_1^2}{2} + \left\{[Q_B/(w_2^2/2)] + B' - B\right\}\frac{w_2^2}{2}}{W} \quad \ldots\ldots [28]$$

which to a first approximation gives

$$\eta_{ss} - \eta_{ss}' = \frac{\eta_{ss}^2}{W/(u^2/2)}\left[\left\{\left[Q_N\Big/\left(\frac{c_1^2}{2}\frac{T_2'}{T_1'}\right)\right]\right\} + N' - N\left\{\left(\frac{c_1}{u}\right)^2\frac{T_2}{T_1} + \left\{[Q_B/(w_2^2/2)] + B' - B\right\}\left(\frac{w_2}{u}\right)^2\right] \quad \ldots\ldots [29]$$

The losses in a row of blades or nozzles are made up of profile or skin-friction losses, secondary losses, and tip clearance and annulus-wall effects. If it is assumed that the only loss factors affected by the cooling are those due to profile or skin-friction effects (sometimes called the two-dimensional losses), then

$$N' - N = \xi_N' - \xi_N \text{ and } B' - B = \xi_B' - \xi_B \quad \ldots\ldots [30]$$

Equation [29] may then be rewritten approximately in the form

$$\frac{\eta_{ss} - \eta_{ss}'}{\eta_{ss}} = \frac{\Delta\eta_{ss}}{\eta_{ss}} = \frac{\eta_{ss}}{W/(u^2/2)}\left\{[Q_N/(c_1^2/2)] + \xi_N' - \xi_N\right\}\left(\frac{c_1}{u}\right)^2 + \frac{\eta_{ss}}{W/(u^2/2)}\left\{[Q_B/(w_2^2/2)] + \xi_B' - \xi_B\right\}\left(\frac{w_2}{u}\right)^2 + \frac{\eta_{ss}}{W/(u^2/2)}\left[(\xi_N - \xi_N')\left(\frac{T_1 - T_2}{T_1}\right)\right]\left(\frac{c_1}{u}\right)^2 \quad \ldots\ldots [31]$$

The second term on the right-hand side of Equation [31] is the contribution arising from cooling of the blades. The first and third terms arise from cooling of the nozzles, the third term being due to the reduction of the reheating effect in the nozzles. It is to be noted that the term

$$\sqrt{\frac{\eta_{ss}}{W/(u^2/2)}}$$

is similar to the conventional velocity ratio, being equal to the wheel speed divided by the velocity equivalent to the isentropic enthalpy drop from a stagnation state at inlet to a state at outlet from the stage where the enthalpy is $(h_{2ss} + c_2^2/2)$ and the entropy is the same as the value at inlet.

The remaining problem in this analysis is to determine the values of the terms in brackets for any conditions. This will be done by treating the nozzles and blades as passages in which the flow is one-dimensional.

4 One-Dimensional Flow in Blade Passages

A method of solving the equations of continuity, energy, and momentum for a compressible gas flowing in one dimension along a duct with friction, area change, and heat transfer has been presented in reference (1). The solutions may be obtained by considering a differential length of the duct. Expressions have been derived for changes in Mach number, velocity, pressure, etc., in terms of the changes in area, frictional drag, and changes in stagnation temperature. A table of these expressions for a gas with constant specific heats and molecular weight is given in reference (1), Table 2, part of which is shown here as Table 1. Solutions of interest here can be obtained by integrating expressions obtained from this table along the length of the blade passage.

Analogy Between Heat Transfer and Friction. In order to relate the heat transfer to distance along the duct, use is made of Reynolds' analogy between skin friction and heat transfer, namely

$$\frac{U}{c_p\rho V} = \frac{f}{2} \quad \ldots\ldots [32]$$

For an element of the duct of length dx, perimeter S, and wall temperature T_w, the heat-balance equation is

TABLE 1 INFLUENCE COEFFICIENTS FOR FLOW WITH CONTINUOUS CHANGES, CONSTANT SPECIFIC HEAT, AND MOLECULAR WEIGHT[a]

	$\frac{dA}{A}$	$\frac{dT_0}{T_0}$	$f\frac{Sdx}{A}$
$\frac{dM^2}{M^2}$	$-\frac{2\left(1+\frac{k-1}{2}M^2\right)}{1-M^2}$	$\frac{(1+kM^2)\left(1+\frac{k-1}{2}M^2\right)}{1-M^2}$	$\frac{kM^2\left(1+\frac{k-1}{2}M^2\right)}{1-M^2}$
$\frac{dV}{V}$	$-\frac{1}{1-M^2}$	$\frac{1+\frac{k-1}{2}M^2}{1-M^2}$	$\frac{kM^2}{2(1-M^2)}$
$\frac{dT}{T}$	$\frac{(k-1)M^2}{1-M^2}$	$\frac{(1-kM^2)\left(1+\frac{k-1}{2}M^2\right)}{1-M^2}$	$-\frac{k(k-1)M^4}{2(1-M^2)}$
$\frac{dp}{p}$	$\frac{kM^2}{1-M^2}$	$-\frac{kM^2\left(1+\frac{k-1}{2}M^2\right)}{1-M^2}$	$-\frac{kM^2[1+(k-1)M^2]}{2(1-M^2)}$
$\frac{dp_0}{p_0}$	0	$\frac{-kM^2}{2}$	$\frac{-kM^2}{2}$
$\frac{ds}{c_p}$	0	$1+\frac{k-1}{2}M^2$	$\frac{(k-1)M^2}{2}$
$\frac{d\rho}{\rho}$	$\frac{M^2}{1-M^2}$	$-\frac{1+\frac{k-1}{2}M^2}{1-M^2}$	$-\frac{kM^2}{2(1-M^2)}$

[a] Reference (1).

$$US(T_w - T_0)dx = A\rho V c_p dT_0 \quad \ldots\ldots [33][b]$$

whence, from Equation [32]

$$\frac{dT_0}{T_0} = \left(\frac{T_w}{T_0} - 1\right)\frac{f}{2}\frac{S\,dx}{A} \quad \ldots\ldots [34]$$

This equation may be integrated to give

$$\frac{T_{01} - T_{02}}{T_{02}} = \left(1 - \frac{T_w}{T_{02}}\right)\left[\left(\exp\frac{1}{2}\int_0^x f\frac{S\,dx}{A}\right) - 1\right] \quad \ldots [35]$$

assuming T_w remains constant along the blade passage. This latter is a reasonable assumption for liquid-cooled blades.

The enthalpy-entropy diagram for the flow through a cooled blade passage is shown in Fig. 6. If the blades are uncooled $h_{01} = h_{02}$, and from Table 1

$$\int_{2s}^{2}\frac{ds}{c_p} = \int_0^x \frac{k-1}{2}M^2 f\frac{S\,dx}{A} \quad \ldots\ldots [36]$$

Noting that

$$\left(\frac{\partial h}{\partial s}\right)_p = T, \text{ and } \frac{k-1}{2}M^2 = \frac{V^2}{2c_pT}$$

when the Mach number M is small, then

$$h_2 - h_{2s} \simeq \frac{V_2^2}{2}\int_0^x \frac{V^2}{V_2^2} f\frac{S\,dx}{A}$$

an approximation which gets better as M gets smaller.

Comparing the foregoing equation with the definition of two-dimensional loss factor, viz.

[b] A wall-recovery factor of unity has been assumed. In practice the recovery factor is somewhat less than unity, but a value of unity is taken because of the great simplification made possible in the analysis. The use of a factor of unity gives an overestimate of the heat transferred, and is, therefore, on the conservative side.

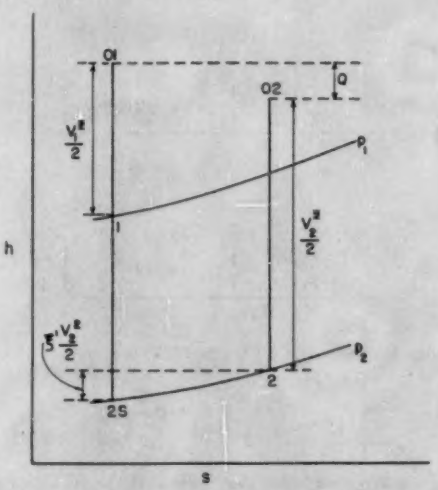

FIG. 6 ENTHALPY-ENTROPY DIAGRAM FOR FLOW THROUGH A TWO-DIMENSIONAL COOLED PASSAGE

$$\xi = \frac{h_2 - h_{2s}}{V_2^2/2}$$

we find that

$$\xi_{M\to 0} = \int_0^x \frac{V^2}{V_2^2} f\frac{S\,dx}{A} \quad \ldots\ldots [37]$$

This latter loss factor is the one normally measured in low-speed cascade tunnels and conveniently defines the loss characteristic of the blade. It varies in value between 0.02 and 0.08. Abbrevi-

ating it to ξ_p it will be used as a basic parameter in the later analysis of turbine stages.

In addition we shall define another important parameter

$$\xi_0 = \int_0^x f \frac{S\,dx}{A} \quad \ldots\ldots [38]$$

When the area change is zero, $\xi_0 = \xi_p$. When a finite area change occurs through the blades, V becomes inversely proportional to the area A. Then, assuming that the blade passages may be treated as conical tubes and using Equations [54] and [55a], it may be shown that

$$\xi_p = \xi_0 \left(\frac{1 - A_2^2/A_1^2}{2 \log_e A_1/A_2} \right) \quad \ldots\ldots [38a]$$

A curve of ξ_p/ξ_0 versus A_1/A_2 is shown in Fig. 21.

Equation [35] may now be written

$$\frac{T_{01} - T_{02}}{T_{02}} = \left(1 - \frac{T_w}{T_{02}}\right)\left(e^{\frac{\xi_0}{2}} - 1\right) \quad \ldots\ldots [39]$$

and since $Q = c_p(T_{01} - T_{02})$, one of the terms in Equation [31] is obtained in the form

$$Q/(V_2^2/2) = \frac{1 + \frac{k-1}{2} M_2^2}{\frac{k-1}{2} M_2^2} \left(1 - \frac{T_w}{T_{02}}\right)\left(e^{\frac{\xi_0}{2}} - 1\right) \quad [40]$$

or approximately

$$\frac{Q}{V_2^2/2} \frac{M_2^2}{\xi_0\left(1 - \frac{T_w}{T_{02}}\right)} = \frac{1 + \frac{k-1}{2} M_2^2}{k-1} \quad \ldots\ldots [41]$$

The right-hand side of this expression varies between 2.5 and 3.0 as M_2 increases from zero to unity.

Effect of Cooling on Loss Factor. A comparison will be made between two cascades of identical shape and values of M_2, T_2, T_{02}, V_2, p_2, p_{02}, and approach angle. One cascade will be uncooled and the other cooled, the superscript (′) being used to indicate the cooled cascade.

From the definition of loss factor

$$\xi \frac{V_2^2}{2} = c_p\,(T_2 - T_{2s})$$

or

$$\xi = \frac{1 - T_{2s}/T_2}{\frac{k-1}{2} M_2^2} \quad \ldots\ldots [42]$$

From Fig. 6

$$\xi' \frac{V_2^2}{2} = c_p\,(T_2 - T_{2s}')$$

or

$$\xi' = \frac{1 - T_{2s}'/T_2}{\frac{k-1}{2} M_2^2} \quad \ldots\ldots [43]$$

Now for the uncooled cascade $T_{02} = T_{01}$, hence

$$\frac{T_{2s}}{T_{02}} = \left(\frac{p_2}{p_{01}}\right)^{\frac{k-1}{k}} \quad \text{and} \quad \frac{T_2}{T_{02}} = \left(\frac{p_2}{p_{02}}\right)^{\frac{k-1}{k}}$$

Similarly, from Fig. 6

$$\frac{T_{2s}'}{T_{01}} = \left(\frac{p_2}{p_{01}'}\right)^{\frac{k-1}{k}} \quad \text{and} \quad \frac{T_2}{T_{02}} = \left(\frac{p_2}{p_{02}}\right)^{\frac{k-1}{k}}$$

Hence

$$\frac{k-1}{2} M_2^2 (\xi - \xi') = \frac{T_{2s}'}{T_2} - \frac{T_{2s}}{T_2} = \frac{T_{01}}{T_{02}}\left(\frac{p_{02}}{p_{01}'}\right)^{\frac{k-1}{k}} - \left(\frac{p_{02}}{p_{02}}\right)^{\frac{k-1}{k}} \quad \ldots\ldots [44]$$

In this equation T_{01}/T_{02} may be obtained from Equation [39] and is very closely given by

$$\frac{T_{01}}{T_0} = 1 + \frac{1}{2}\xi_0\left(1 - \frac{T_w}{T_{02}}\right) \quad \ldots\ldots [45]$$

$\left(\frac{p_{02}}{p_{01}'}\right)^{\frac{k-1}{k}}$ and $\left(\frac{p_{02}}{p_{02}}\right)^{\frac{k-1}{k}}$

may be obtained by integration of the one-dimensional equations of flow along the blade passage.

Before the accurate method of performing this integration is outlined, an approximate solution will be given.

From Table 1 the stagnation-pressure change with heat transfer and friction is given for a differential length of duct by

$$\frac{dp_0}{p_0} = -\frac{kM^2}{2}\left(\frac{dT_0}{T_0} + f\frac{S\,dx}{A}\right) \quad \ldots\ldots [46]$$

From Equations [34] and [46]

$$\frac{dp_0}{p_0} = -\frac{kM^2}{4}\left(1 + \frac{T_w}{T_0}\right) f\frac{S\,dx}{A} \quad \ldots\ldots [47]$$

Now

$$\left(\frac{p_{02}}{p_{01}'}\right)^{\frac{k-1}{k}} = 1 + \frac{k-1}{k}\frac{\Delta p_0'}{p_{02}}$$

very approximately where $\Delta p_0' = p_{02} - p_{01}'$. Whence using Equation [45], Equation [44] becomes approximately

$$\frac{k-1}{2} M_2^2(\xi - \xi') = \frac{1}{2}\xi_0\left(1 - \frac{T_w}{T_{02}}\right) + \frac{k-1}{k}\frac{\Delta p_0'\left[1 + \frac{1}{2}\xi_0\left(1 - \frac{T_w}{T_{02}}\right)\right] - \Delta p_0}{p_{02}} \quad \ldots\ldots [48]$$

From Equation [47]

$$\frac{\Delta p_0'}{p_{02}} = -\frac{k\overline{M}'^2}{4}\left(1 + \frac{T_w}{T_{02}}\right)\xi_0$$

The same blade passage when uncooled gives $T_w = T_{02}$ and

$$\frac{\Delta p_0}{p_{02}} = -\frac{k\overline{M}^2}{2}\xi_0$$

where the $\overline{M}'$ and $\overline{M}$ denote the appropriate average Mach numbers in the two cases, i.e.

$$\xi_0\overline{M}^2 = \int_0^x M^2 f\frac{S\,dx}{A}$$

With these substitutions Equation [48] becomes, neglecting terms in ξ_0^2

$$\frac{k-1}{2}M_2^2(\xi-\xi') = \frac{1}{2}\xi_0\left(1-\frac{T_w}{T_{02}}\right)\left\{1+\frac{k-1}{2}\overline{M}^2 + \frac{k-1}{2}\left(\frac{1+T_w/T_{02}}{1-T_w/T_{02}}\right)(\overline{M}^2-\overline{M}'^2)\right\} \quad [49]$$

In many instances, particularly when the change in passage area is large, it may be possible to ignore the difference between $\overline{M}$ and $\overline{M}'$, i.e., to assume that the cooling has small effect on the variation in Mach number. Then Equation [49] yields the approximate result

$$(\xi-\xi')\frac{M_2^2}{\xi_0\left(1-\frac{T_w}{T_{02}}\right)} = \frac{1+\frac{k-1}{2}\overline{M}^2}{k-1} \quad [50]$$

The right-hand side of Equation [50] varies from 2.5 to 3.0 as M_2 increases from zero to unity. This approximate solution may be compared with the accurate solutions shown in Fig. 7.

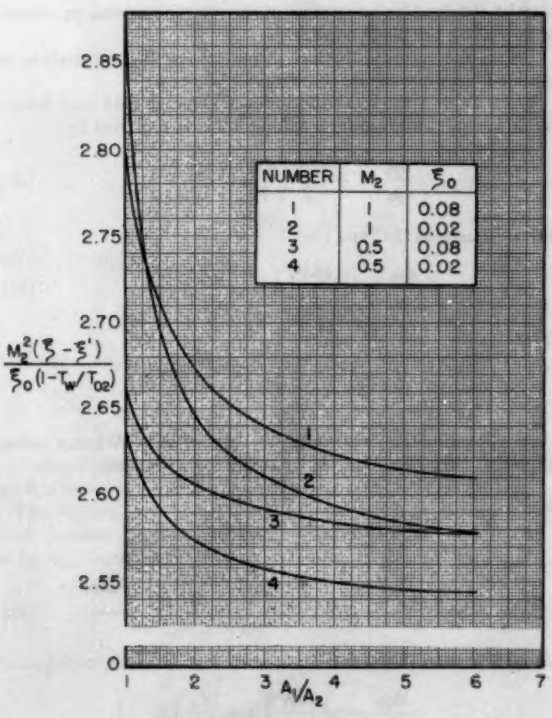

FIG. 7 VARIATION OF $\frac{M_2^2(\xi-\xi')}{\xi_0(1-T_w/T_{02})}$ WITH AREA RATIO, M_2, AND ξ_0

Two of the terms in the square brackets in Equation [31] may now be obtained by combining Equations [41] and [50]

$$\left(\frac{Q}{V_2^2/2}+\xi'-\xi\right)\frac{1}{\xi_0\left(1-\frac{T_w}{T_{02}'}\right)} = \frac{1}{2}\left(1-\frac{\overline{M}^2}{M_2^2}\right) \quad [51]$$

The right-hand side of this equation varies numerically from zero at small values of M_2 and small changes of area to nearly 0.5 when M_2 is unity and the Mach-number change is large. The change in Mach number is likely to be large when there is considerable convergence of the blade passage in the direction of flow as, for instance, in a reaction blade.

When the velocities are small so that density changes are negligible, M varies inversely as A and it may be shown that the right-hand side of Equation [51] becomes

$$\frac{1}{2}\left(1-\frac{1}{2}\frac{1-(A_2/A_1)^2}{\log_e A_1/A_2}\right)$$

i.e., $\overline{M}$ becomes the log mean of M_1 and M_2. This relationship is shown by the curve marked $M_2 \to 0$ in Fig. 8.

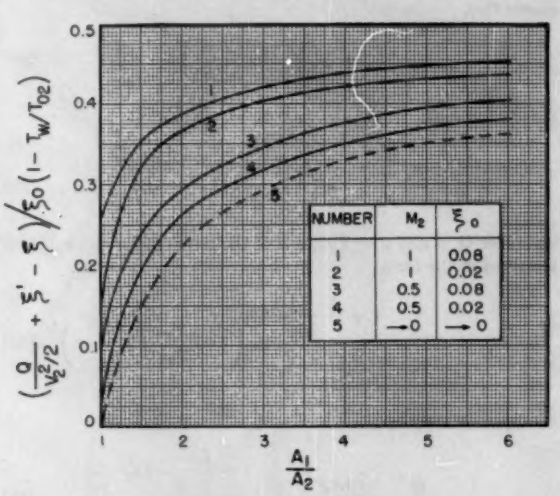

FIG. 8 VARIATION OF $\left(\frac{Q}{V_2^2/2}+\xi'-\xi\right)\Big/\xi_0(1-T_w/T_{02})$ WITH AREA RATIO, ξ_0, AND M_2

One of the difficulties in the accurate calculation becomes apparent from Equation [51]. The expression on the left-hand side is the difference between two quantities—Equation [41] and Equation [50]—which vary between 2.5 and 3. The accurate calculation of $\overline{M}$ is, hence, essential to an accurate determination of the effect of cooling on stage efficiency.

Accurate values are shown in Fig. 8, which it will be noted cover the range from zero to $^1/_2$ as predicted by the approximate relation of Equation [51].

Accurate Calculation of Loss Factors. This section describes in outline the main features in the calculation of the curves shown in Figs. 7 and 8 for which approximate expressions were derived in the preceding section. Equations [44] and [47] are used, viz.

$$\frac{k-1}{2}M_2^2(\xi-\xi') = \frac{T_{01}}{T_{02}}\left(\frac{p_{02}}{p_{01}'}\right)^{\frac{k-1}{k}} - \left(\frac{p_{02}}{p_{01}}\right)^{\frac{k-1}{k}} \quad [44]$$

$$\frac{dp_0}{p_0} = -\frac{kM^2}{4}\left(1+\frac{T_w}{T_0}\right)f\frac{S\,dx}{A} \quad [47]$$

From Table 1

$$\frac{(1-M^2)dM^2}{\left(1+\frac{k-1}{2}M^2\right)M^2} = -2\frac{dA}{A} + (1+kM^2)\frac{dT_0}{T_0} + kM^2 f\frac{S\,dx}{A} \quad [52]$$

Substituting for dT_0/T_0 from Equation [34]

$$\frac{(1-\mathbf{M}^2)d\mathbf{M}^2}{\left(1+\frac{k-1}{2}\mathbf{M}^2\right)\mathbf{M}^2} = -2\frac{dA}{A} + \frac{1}{2}\left(1+\frac{T_w}{T_0}\right)(k\mathbf{M}^2-a)f\frac{S\,dx}{A} \quad \ldots\ldots [53]$$

where $$a = \frac{1-T_w/T_0}{1+T_w/T_0}$$

As $\int f(S\,dx/A)$ is < 0.15, T_w/T_0 and a may be taken as constant. If a suitable geometric relation between $S\,dx$ and dA is obtained, and $\mathbf{M}_2$ is chosen, Equation [53] may be solved to give $\mathbf{M}_1$, the inlet Mach number. Elimination of $S\,dx/A$ from Equation [47] then gives an equation between p_0 and $\mathbf{M}$ which also may be integrated to obtain (p_{02}/p_{01}'). The value of p_{02}/p_{01} is obtained by putting $T_w = T_{02}$, whence Equation [44] may be solved.

For reaction blading and nozzles a relation, which is suggested by analogy with tapered circular pipes, is

$$S\,dx = n\,dA \quad \ldots\ldots [54]$$

For the conical pipe $1/n = \tan\theta/2$, where θ is the total included angle of the cone. Hence assuming n is constant

$$\int_0^x f\frac{S\,dx}{A} = \xi_0 = -nf\int_1^2\frac{dA}{A} = nf\log_e\frac{A_1}{A_2} \quad \ldots [55a]$$

Now

$$A_1/A_2 = \frac{\sin\alpha_1}{\sin\alpha_2}$$

(see Fig. 1) and hence

$$nf = \frac{\xi_0}{\log_e\frac{\sin\alpha_1}{\sin\alpha_2}} = \frac{\xi_0}{\log_e A_1/A_2} \quad \ldots\ldots [55b]$$

Values of $\xi - \xi'$ have been calculated for $\mathbf{M}_2 = 1$, $\mathbf{M}_2 = 0.5$, $T_w/T_0 = 0.25$, 0.5, and 0.75, for values of $\xi_0 = 0.02$ and 0.08 and for various values of A_1/A_2. These are shown in Fig. 7. The calculations showed that good correlation of the results for the various values of T_w/T_{02} is possible by using the parameter

$$(\xi-\xi')\frac{\mathbf{M}_2^2}{\xi_0(1-T_w/T_{02})}$$

which was found to be practically independent of T_w/T_{02}. The use of this parameter was suggested by the approximate solutions given in the section, *Effect of Cooling on Loss Factor*.[7]

In Fig. 8 values of

$$\left(\frac{Q}{V_2^2/2}+\xi'-\xi\right)\frac{1}{\xi_0(1-T_w/T_{02})}$$

have been plotted. The use of this parameter also permits good correlation of the results for various values of T_w/T_{02}. The curve for $\mathbf{M}_2 = 0$ obtained as described is also shown in Fig. 8. To enable interpolation of the results of the calculations for an impulse blade row to be readily achieved, Fig. 20 has been included.

Finally Equation [42] has also been solved to give the loss factor for uncooled blades with varying A_1/A_2 for $\mathbf{M}_2 = 0.5$ and $\xi_0 = 0.02$ and 0.08. The results for these uncooled blade-loss factors are shown in Fig. 21.

[7] Both Figs. 7 and 8 were constructed for $T_w/T_{02} = 0.5$.

5 Discussion and Application of Results to Typical Turbine Stages

In the foregoing sections enough results have been obtained to permit fairly approximate estimation of two problems of importance in the design of cooled turbines. The first is the amount of heat required for cooling which is abstracted from the gas passing through the blades and nozzles. The second is the effect of the cooling on the turbine-stage efficiency.

The amount of heat removed per lb of gas passing through turbine blade row is

$$c_p(T_{02}-T_{w2})$$

which from Equations [39] and [45] is given by

$$c_pT_{02}\frac{1}{2}\xi_0(1-T_w/T_{02})$$

The value of the average wall temperature requires estimation. Guidance for this estimate may be obtained from reference (4). The value of T_{02} is easily obtained for the nozzles.

As an example, the gas-temperature drop

$$(T_{01}-T_{w1}) = T_{02}\frac{1}{2}\xi_0\left(1-\frac{T_w}{T_{02}}\right)$$

may be calculated for blades at a wall temperature of 300 F (760 R) and a gas-stagnation temperature of 2000 F (2460 R) at the outlet. A value of $\xi_0 = 0.06$ is assumed. The gas-temperature drop is 51 deg F. For a fuel-air ratio of 60 to 1 and a typical hydrocarbon fuel this represents an amount of heat to be removed equal to about 4.5 per cent of the calorific value of the fuel per row of cooled blades. If the cooling medium is water with a permissible temperature rise of 100 deg F, the water flow required is approximately 15 per cent of the gas flow.

It is to be noted that the amount of heat removed is dependent only on the profile-loss factor ξ_p, the area change, and the wall and gas-stagnation temperature. Apart from their effect on the profile loss and wall temperature, shape, size, and number of blades are not significant.

The decrease of turbine-stage efficiency due to cooling may be obtained from Equation [31], viz.

$$\frac{\Delta\eta_{st}}{\eta_{st}} = \frac{\eta_{st}}{W/(u^2/2)}[Q_N/(c_1^2/2)+\xi_N'-\xi_N]\left(\frac{c_1}{u}\right)^2 + \frac{\eta_{st}}{W/(u^2/2)}[Q_R/(w_2^2/2)+\xi_R'-\xi_R]\left(\frac{w_2}{u}\right)^2 + \frac{\eta_{st}}{W/(u^2/2)}(\xi_N-\xi_N')\left(\frac{T_1-T_2}{T_1}\right)\left(\frac{c_1}{u}\right)^2 \quad \ldots\ldots [31]$$

The first two terms in the square brackets of Equation [31] may be obtained by interpolation in Fig. 8, which covers the useful range of variables. The last term on the right-hand side requires some rearrangement. Approximately

$$\frac{\eta_{st}}{W/(u^2/2)}(\xi_N-\xi_N')\frac{T_1-T_2}{T_1}\left(\frac{c_1}{u}\right)^2 = \frac{\eta_{st}}{W/(u^2/2)}(\xi_N-\xi_N')\frac{w_2^2-w_1^2}{2c_pT_1}\left(\frac{c_1}{u}\right)^2$$

$$= \frac{\eta_{st}}{W/(u^2/2)}[(\xi_N-\xi_N')\mathbf{M}_{c1}^2]\frac{k-1}{2}\left\{\left(\frac{w_2}{u}\right)^2-\left(\frac{w_1}{u}\right)^2\right\} \quad \ldots [56]$$

The term on the right-hand side in the square brackets may be

obtained from Fig. 7 noting that $\mathbf{M}_{c1}$ is the Mach number leaving the nozzles.

Another approximation is possible if it is noted that $(w_2^2 - w_3^2)/W$ is approximately equal to the fraction of the reaction y ($100y$ is the percentage reaction) and that

$$\frac{(\xi_N - \xi_N')(k-1)\mathbf{M}_{c1}^2}{\xi_0(1 - T_w/T_0)}$$

from Equation [50] lies between unity and 1.2. Then the last term in Equation [31] becomes approximately

$$\frac{y}{4}\eta_{si}\xi_0\left(1 - \frac{T_w}{T_{c2}}\right) \quad \ldots\ldots\ldots\ldots\ldots\ldots [56a]$$

The foregoing relations and Fig. 8 permit calculation of $\Delta\eta_{si}/\eta_{si}$ for any turbine stage. Some generalizations may be made from Fig. 8 which add further to the remarks in the section, *Discussion of Reversible and Cooled Turbine Stage.*

When the rotor blades only are cooled and the velocities are low the value of $\Delta\eta_{si}/\eta_{si}$ is negligible for an impulse stage ($A_1 = A_2$ in the rotor blades).

At higher outlet velocities the difference between reaction and impulse stages depends on the variation in ξ_0 between the stages. In impulse blades $\xi_0 = \xi_p$, but in reaction blades Fig. 21 shows that ξ_0 is greater than ξ_p. It is probable that the loss factor for reaction blades is smaller than that for impulse blades, whence ξ_0 may not be much different for the two types of blading.

In the absence of more precise information, it may be assumed, for instance, that ξ_0 is the same for both types of blading, in which case it is clear from Fig. 8 and Equation [31] that cooled impulse blading gives appreciably lower values for $\Delta\eta_{si}/\eta_{si}$ than cooled reaction blading. The assumption of the same values of profile-loss coefficient ξ_p for impulse blades and reaction blades gives even larger differences in $\Delta\eta_{si}/\eta_{si}$ for impulse and reaction blades, in favor of the impulse blade. With either assumption it appears that cooling the rotor blades in an impulse stage gives a lower decrease in efficiency than that to be expected from a cooled reaction stage.

Some Examples of Turbine Stages. For purposes of illustration and orientation the results of the analysis have been applied to three typical turbine stages. These are shown in Fig. 9 and are designated as symmetrical, axial, and impulse-type stages. The axial velocity is assumed to be unchanged in flow through the rotor. The work done may be expressed in terms of the nozzle angle β_1 and the value of c_x/u for these three stages as follows:

Symmetrical

$$\frac{W}{u^2/2} = 4\frac{c_x}{u}\cot\beta_1 - 2 \quad \ldots\ldots\ldots\ldots [57a]$$

Impulse

$$\frac{W}{u^2/2} = 4\frac{c_x}{u}\cot\beta_1 - 4 \quad \ldots\ldots\ldots\ldots [57b]$$

Axial

$$\frac{W}{u^2/2} = 2\frac{c_x}{u}\cot\beta_1 \quad \ldots\ldots\ldots\ldots [57c]$$

Curves for these expressions are given in Figs. 10, 11, and 12. The values of the deflection angles ϵ_N in the rotor blading are shown on the curves.

A generalized expression for the profile-loss coefficient ξ_p has been assumed giving the coefficient in terms of the deflection angle only

$$\xi_{pB} = 0.025\left[1 + \left(\frac{\epsilon_B}{90}\right)^2\right] \quad \ldots\ldots\ldots\ldots [58a]$$

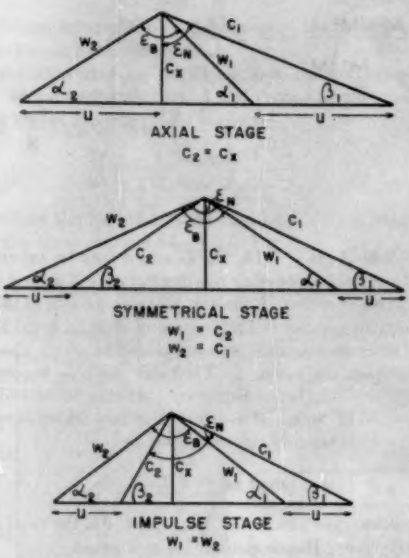

FIG. 9 TYPICAL VELOCITY TRIANGLES SHOWING THE RELATION BETWEEN ABSOLUTE AND RELATIVE VELOCITIES

$$\xi_{pN} = 0.025\left[1 + \left(\frac{\epsilon_N}{90}\right)^2\right] \quad \ldots\ldots\ldots\ldots [58b]$$

In view of the remarks in the preceding section, this assumption leads to the result that ξ_0 is larger for reaction blades than for impulse blades. The effect of this assumption which favors the impulse blade will be discussed later.

The stage efficiencies have been calculated from Equation [10a], assuming $T_2 \cong T_1$ and loss factors N and B given by the relation

$$B = \xi_{pB}\left(1 + 3.2\frac{b}{l}\right) \quad \ldots\ldots\ldots\ldots [59a]$$

$$N = \xi_{pN}\left(1 + 3.2\frac{b}{l}\right) \quad \ldots\ldots\ldots\ldots [59b]$$

where b equals the blade width and l the blade height. In addition to the foregoing allowance for boundary-layer effects, the stage efficiency has been reduced to 0.96 times the value obtained from Equation [10a] to allow for tip leakage.

For purposes of calculation b/l has been put equal to $0.4\,c_x/u$. The resulting curves for the efficiency of the three stages are shown in Figs. 13, 14, and 15. Maximum values are given in Table 2.

Effect of Rotor Blade Cooling Only. The curves obtained in the previous section have been used to calculate the effect of cooling the rotor blades only on the stage efficiency. The decrease in stage efficiency given in Equation [31] may be written as

$$\frac{\Delta\eta_{si}}{\eta_{si}} = \frac{\eta_{si}}{W/u^2/2}\left(\frac{w_2}{u}\right)^2\xi_{0B}\left(1 - \frac{T_w}{T_{c2}}\right)\left[\frac{Q_B/V_2^2/2 + \xi_B' - \xi_B}{\xi_{0B}(1 - T_w/T_{c2})}\right]$$

the term in the bracket being obtained from Fig. 8. The value of this term depends only slightly on ξ_{0B} which has been estimated for each point from Equations [58a] and [38a]. The results are shown in Fig. 16 for Mach numbers of 0.5 and unity relative to the rotor blades at outlet. The impulse stage is affected least, the effect on the symmetrical stage being several times that of the impulse stage.

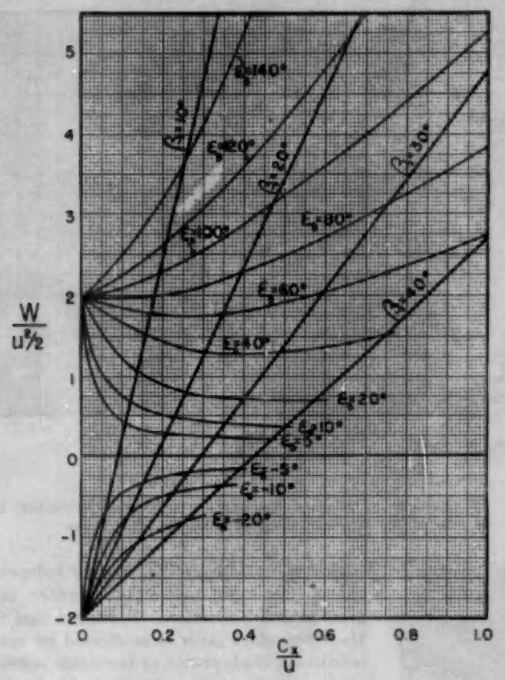

FIG. 10 STAGE WORK IN SYMMETRICAL STAGE

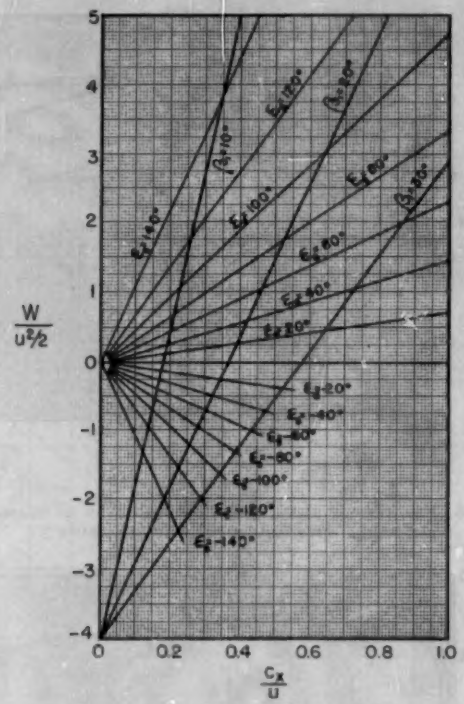

FIG. 11 STAGE WORK IN IMPULSE STAGE

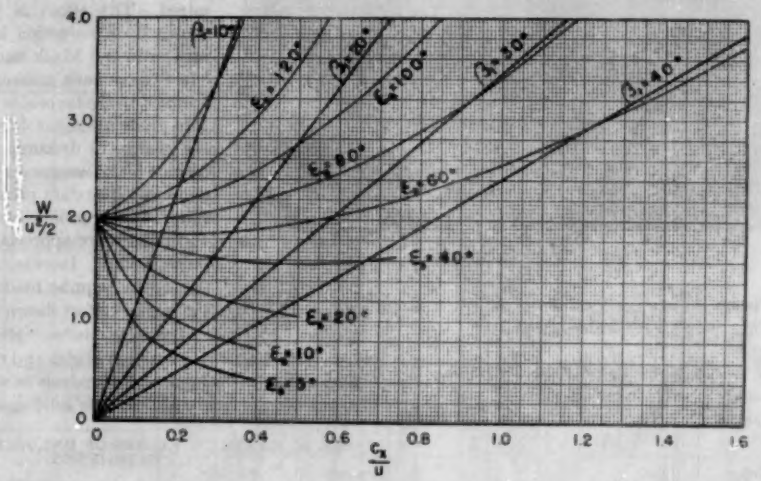

FIG. 12 STAGE WORK IN AXIAL STAGE

If the values of ξ_{sB} are the same in both impulse and reaction stages, it will be seen that the symmetrical stage has values of $\Delta\eta_{st}/\eta_{st}$ three to six times as large as the impulse stage. In Fig. 17 the results are shown plotted for values of ξ_{sB} obtained from Equations [58a] and [38a], i.e., on the assumption that the profile losses, ξ_p, depend only on deflection and not on area change. This tends to make the difference between $\Delta\eta_{st}/\eta_{st}$ for the two types of stage larger and gives a 1 per cent or more decrease in efficiency of the symmetrical stage when the outlet Mach number relative to the rotor is unity.

It will be seen that the minimum effect of cooling occurs above values of the "velocity ratio" giving maximum stage efficiency (cf. Table 2). As the outlet Mach number decreases, the effect of cooling on the stage efficiency is lessened.

A few points for the axial stage are shown on the curves.

Effect of Cooling Nozzles and Blades. Calculations of the effect of cooling both nozzles and blades have been made for the three typical stages for Mach number of unity at outlet from the nozzles. The results are shown in Figs. 18 and 19. In Fig. 18 the values of ξ_0 have been obtained from Equations [38a] and [58a],

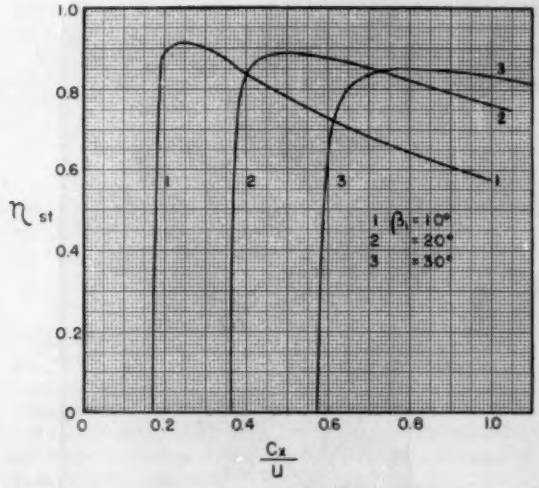

FIG. 13 EFFECT OF NOZZLE ANGLE ON VARIATION OF STAGE EFFICIENCY WITH c_x/u FOR AN IMPULSE STAGE

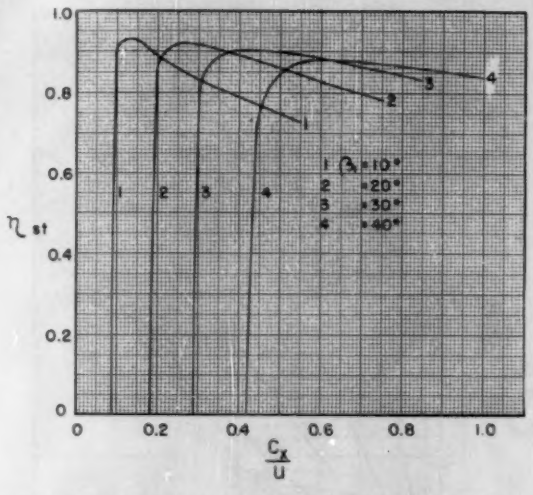

FIG. 15 EFFECT OF NOZZLE ANGLE ON VARIATION OF STAGE EFFICIENCY WITH c_x/u FOR A SYMMETRICAL STAGE

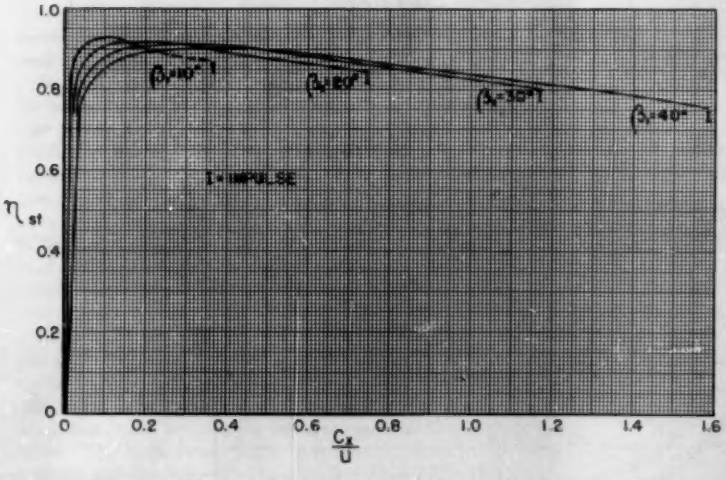

FIG. 14 EFFECT OF NOZZLE ANGLE ON VARIATION OF STAGE EFFICIENCY WITH c_x/u FOR AN AXIAL STAGE

i.e., on the assumption that ξ_p depends only on deflection. A few points for the axial stage are shown on the curves.

The results for the symmetrical stage are shown in Fig. 19 in terms of

$$\frac{\Delta\eta_{st}}{\eta_{st}} \frac{1}{\xi_0(1 - T_w/T_0)}$$

permitting introduction of other assumptions for ξ_0. For $T_w/T_{02} = 0.25$ the values of $\Delta\eta_{st}/\eta_{st}$ range from about $1^1/_2$ to over 3 per cent. The difference between symmetrical and impulse stages is less marked than for blade cooling only.

6 Discussion and Conclusions

In a general analysis of this type it is necessary to make a number of assumptions for the sake of simplification. Several of the assumptions made here when taken separately are clearly in error.

The assumption that the blade passages can be treated as conical tubes with friction factor f independent of area ratio and Mach number is a gross oversimplification. It implies that the blade boundary layer is unaffected by entry conditions, blade profile, or favorable pressure gradient. By assuming that blades are normally designed to minimize form-drag effects, the effect of blade profile is minimized. The effect of pressure gradient is shown by a reduction in ξ_p with increasing area ratio and Mach number, Fig. 21. Such effects have been noticed but are better attributed to the favorable influence of the pressure gradient on the boundary layer than to the change in dynamic head with constant friction factor assumed in the one-dimensional analysis. The data presented in reference (5) show that the profile losses for reaction blades and nozzles are appreciably less than for impulse blades. Increasing Mach number reduces ξ for impulse blades but does not have the marked effect shown in Fig. 21 on reaction and nozzle blades. Hence values of ξ/ξ_p taken from Fig. 21 for reaction blades and nozzles are too low.

The ratio ξ_p/ξ_0 is used in this analysis as a means of estimating heat transfer by means of Reynolds' analogy. Reynolds' analogy

TABLE 2 MAXIMUM VALUES OF UNCOOLED TURBINE-STAGE EFFICIENCY[a]

Nozzle angle	c_x/u	$W/(u^2/2)$	$v_{2_{max}}$	Velocity ratio $\sqrt{v_{st}/[W/(u^2/2)]}$
		Impulse		
10	0.29	2.6	0.886	0.58
20	0.55	2.0	0.867	0.66
30	0.87	2.0	0.835	0.65
		Symmetrical (50 Per Cent Reaction)		
10	0.14	1.1	0.93	0.92
20	0.275	1.02	0.92	0.95
30	0.43	0.97	0.905	0.97
40	0.62	0.95	0.88	0.96
		Axial		
10	0.11	1.22	0.93	0.88
20	0.21	1.18	0.92	0.883
30	0.31	1.04	0.912	0.936
40	0.41	1.0	0.903	0.951

[a] From results of Figs. 13, 14, 15.

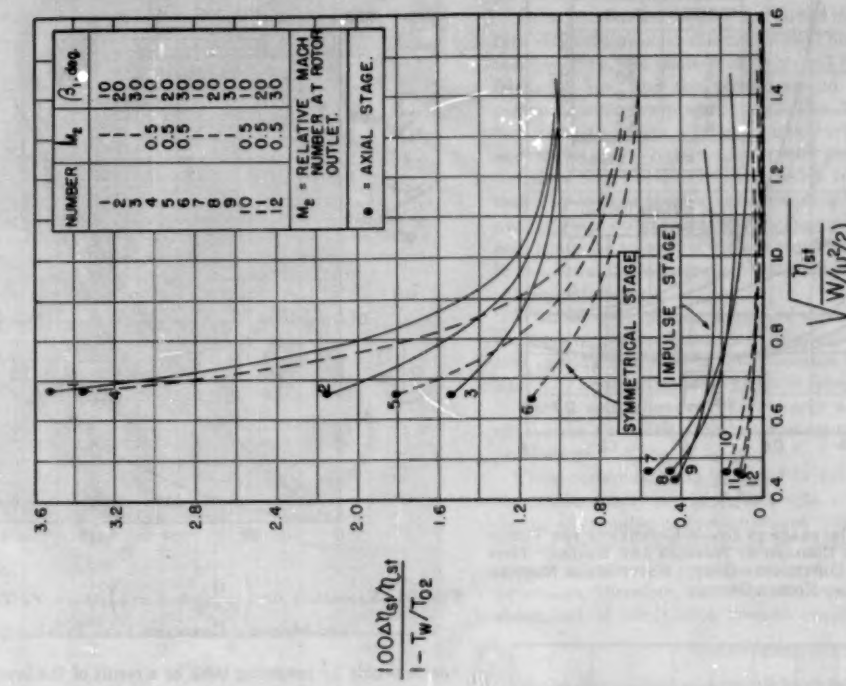

FIG. 17 PERCENTAGE DECREASE IN STAGE EFFICIENCY FOR THREE TYPICAL STAGES WITH ROTOR BLADES ONLY COOLED USING LOSS FACTORS DEPENDENT ON DEFLECTION ONLY

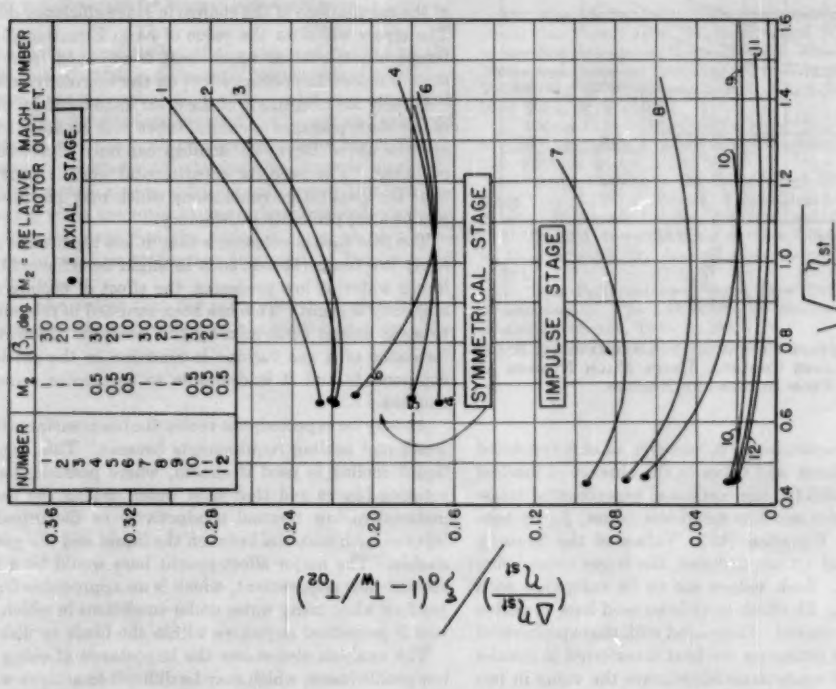

FIG. 16 DECREASE IN STAGE EFFICIENCY FOR THREE TYPICAL STAGES WITH ROTOR BLADES ONLY COOLED

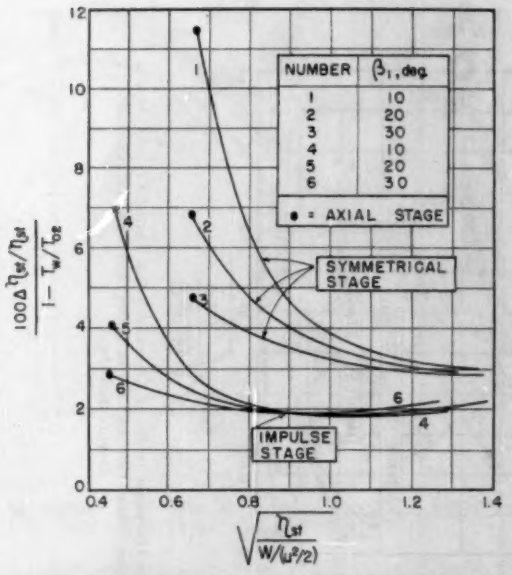

FIG. 18 PERCENTAGE DECREASE IN STAGE EFFICIENCY FOR THREE TYPICAL STAGES DUE TO COOLING OF NOZZLES AND BLADES. LOSS FACTOR DEPENDENT ON DEFLECTION ONLY. UNITY MACH NUMBER AT NOZZLE OUTLET

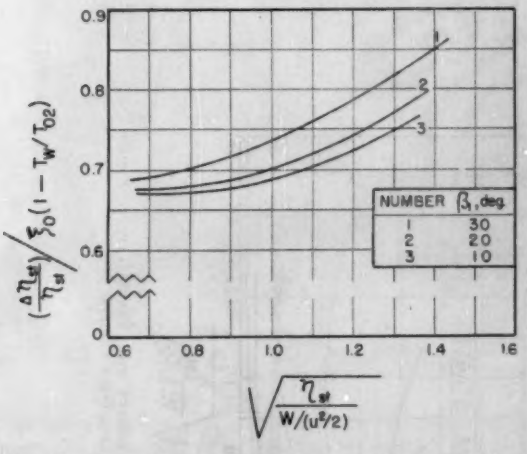

FIG. 19 DECREASE IN STAGE EFFICIENCY FOR SYMMETRICAL STAGE WITH NOZZLES AND BLADES COOLED. UNITY MACH NUMBER AT OUTLET FROM BLADES AND NOZZLES

in its simple or more complex forms is, however, of only restricted validity, e.g., to flat plates and tubes in the absence of marked pressure gradients. Smith (2) has correlated experimental measurements of heat transfer and low speed-loss factor, ξ_p, by substituting $\chi\xi_p$ for ξ_0 in Equation [45]. Values of the factor χ ranging between 1.0 and 1.7 are deduced, the larger value being obtained with nozzles. Such values are to be compared with values of ξ_0/ξ_p from Fig. 21 which have been used here to derive the amount of heat transferred. Compared with the experimental results this analysis overestimates the heat transferred in nozzles and reaction blades and tends to underestimate the value in impulse blades. Smith (2) has calculated a value of $\chi = 1.35$ for a

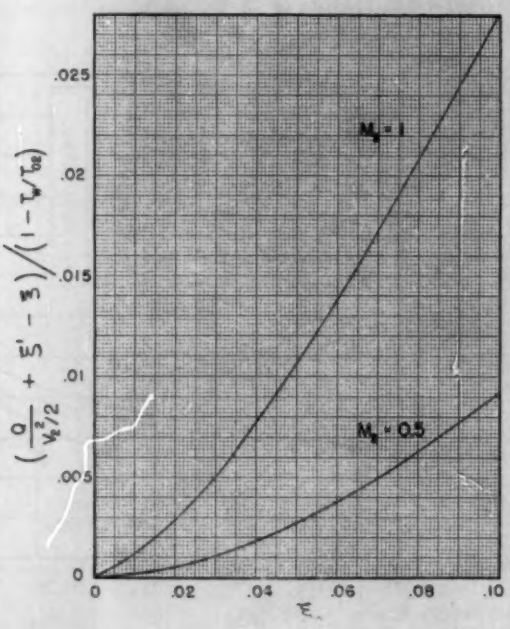

FIG. 20 VARIATION OF $\left(\frac{Q}{V_2^2/2} + \xi' - \xi\right)/(1 - T_w/T_{02})$ WITH ξ_2 AND M_2 FOR A CONSTANT-AREA PASSAGE

nozzle profile by assuming that, as a result of the favorable pressure gradient, the boundary layer is laminar.

Errors in the assumptions for the detailed mechanism of the heat-transfer and frictional-loss processes will affect the results of the calculations of the change in stage efficiency due to cooling. The errors will alter the value of $\overline{M}$ in Equation [51], since the temperature level at which heat is removed from the moving stream has an important effect on the thermodynamic results.

Clearly the magnitude of the error introduced by the treatment of the blade passages as conical tubes with constant friction factor and the use of Reynolds' analogy can only be determined by experiment. The need for experimental work is apparent. However the qualitative conclusions which may be drawn from this analysis are probably satisfactory.

The first such conclusion is that unless the nozzles are cooled to fairly low temperatures, such as might be achieved by the use of liquid water at low pressures, the effect of cooling on the stage efficiency is slight. This has been assumed in reference (3) and is to some extent confirmed by this analysis. However, the performance of a gas turbine is sensitive to the efficiencies of its components and it is desirable to emphasize some other conclusions.

As may be expected, the cooler the blade surfaces the larger the losses and cooling requirements become. This suggests that if liquid cooling is used it should, where possible, be confined to rotating blades and that with water cooling the use of a blade material of low thermal conductivity or the introduction of a layer of such material between the liquid and the gas may be desirable. The major effect sought here would be a reduction in coolant-flow requirement, which is an appreciable fraction of the gas flow when using water under conditions in which no evaporation is permitted anywhere within the blade or disk passages.

The analysis also shows the importance of using blades with low profile losses, which may be difficult to achieve with hollowed shapes.

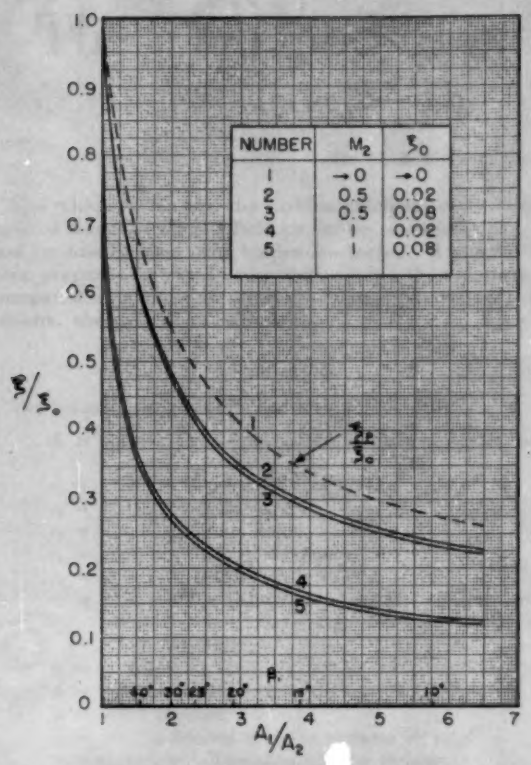

FIG. 21 VARIATION OF ξ/ξ_0 WITH AREA RATIO FOR BLADE PASSAGES IDEALIZED AS CONICAL TUBES—NO COOLING

(β_1 = outlet angles for nozzles; inlet angle, zero.)

The results of the examination of the effect of cooling on the typical stages indicate that a decrease of turbine-stage efficiency of 1 per cent or more is possible when rotor blades only are cooled considerably. This decrease can amount to as much as 3 per cent for certain stages in which both nozzles and blades are cooled to low temperatures. Fortunately the impulse stage is markedly better than the reaction stages, suffering only a very small reduction in efficiency when the rotor blades only are cooled considerably. The impulse stage has the added advantage of a considerable drop in relative stagnation temperature between the nozzles and the blades.

The analysis also shows that the use of lower Mach numbers tends to reduce the effect of cooling on the stage efficiency. Unfortunately this leads to a reduction in work output per stage, which, as emphasized in the following, is not desirable in cooled turbines.

These conclusions suggest that in the most effective cooled turbine stage the velocity diagram should be of the impulse or small reaction type, the blade profiles should be shaped for minimum frictional loss, and the nozzles should be cooled slightly, for example, with low-pressure air. The blade speed should be high both to insure a large temperature drop between nozzles and blades and to obtain a large work output. This will involve the use of high gas speeds in the blades, together with some diffusion after the last stage to reduce leaving losses. Large work output per stage is important both to minimize the number of stages and, hence the amount of coolant required and because the cooling in any one stage reduces the work available in expansion through subsequent stages.

With the type of stage suggested the most important effect on the work output in the turbine will occur as a result of the reduction in work available in the expansion in the following stages. This may be regarded as a "negative reheat" effect and, as shown in Part 2 and reference (3), is clearly a much more important effect than the small drop in the stage efficiency in a cooled impulse stage.

These considerations also point to the desirability of keeping the pressure ratio low in a plant with a cooled turbine. By reducing the number of turbine stages, this reduces the amount of coolant required and the effect of cooling on the turbine work output. Cycles with pressure ratios of the order of 5:1 using regenerators, therefore, seem to be the most desirable from the standpoint of minimizing coolant requirement.

ACKNOWLEDGMENT

All the calculations and curves were made by Mrs. Antonia B. Walker, whose assistance is gratefully acknowledged.

BIBLIOGRAPHY

1 "The Mechanics and Thermodynamics of Steady One-Dimensional Gas Flow," by A. H. Shapiro and W. R. Hawthorne, *Journal of Applied Mechanics*, Trans. ASME, vol. 69, 1947, pp. A-317–336. Numerical tables of functions derived in this paper given in "Gas Tables," by J. H. Keenan and J. Kaye, John Wiley & Sons, Inc., New York, N. Y., 1948.

2 "Heat Flow in the Gas Turbine," by A. G. Smith, Proceedings of The Institution of Mechanical Engineers, London, England, vol. 159, 1948, p. 245.

3 "Some Factors in the Use of High Temperatures in Gas Turbines," by T. W. F. Brown, Proceedings of The Institution of Mechanical Engineers, London, England, vol. 162, 1950, p. 167.

4 "NACA Investigations of Gas Turbine Blade Cooling," by H. H. Ellerbrock, Jr., *Journal of Aeronautical Sciences*, vol. 15, 1948, p. 721.

5 "The Performance of Axial Flow Turbines," by D. G. Ainley, Proceedings of The Institution of Mechanical Engineers, London, England, vol. 159, 1948, p. 230.

The Thermodynamics of Cooled Turbines[1]

Part 2—The Multistage Turbine

By W. R. HAWTHORNE,[2] CAMBRIDGE, MASS.

The reheat factor and the turbine efficiency can be calculated from the stage efficiency for an uncooled turbine and for one in which the blades are cooled. A chart has been prepared for rapid computations and the results are compared with those obtained from stage-by-stage calculations, showing good agreement.

Nomenclature

The following nomenclature is used in the paper:

- A = cross-sectional area of turbine blade or nozzle passage
- c_0 = absolute velocity entering nozzles
- c_1 = absolute velocity entering blades or leaving nozzles
- c_2 = absolute velocity leaving blades
- c_p = specific heat at constant pressure
- c_v = specific heat at constant volume
- c_x = axial velocity (subscript 1 identifies axial velocity entering rotor blades, subscript 2 identifies axial velocity leaving)
- h = enthalpy
- k = c_p/c_v, ratio of specific heats
- p = static pressure
- q = heat transferred to cooled surfaces per stage
- r = p_e/p_b, over-all pressure ratio for turbine
- s = entropy
- T = absolute temperature
- T_w = average wall temperature of cooled surface
- u = velocity of blades
- w_1 = relative velocity entering blades
- w_2 = relative velocity leaving blades
- W = work done per stage per pound
- W_t = ΣW, work done per pound for the whole turbine
- W_{sr} = work done per pound in an ideal process at constant entropy with same inlet and outlet pressures
- β_1 = nozzle angle between velocity vector c_1 and plane of rotation
- $(1+\rho)_N$ = $\dfrac{\Sigma \Delta h_{ss}}{\Delta h_{st}}$, reheat factor for turbine consisting of N-stages
- η_{st} = η_p, stage efficiency
- η_s = $\eta_p(1 + q/W)$ for a cooled turbine
- η_t = turbine efficiency
- ξ_p = loss factor normally measured in low-speed cascades, used here to define loss characteristics of blade
- ξ_b = $\xi_p \dfrac{2 \log_e A_1/A_2}{1 - A_2^2/A_1^2}$, see reference (1)[3]
- Δh_s = $h_{0s} - h_{es}$, isentropic enthalpy drop for the turbine from inlet stagnation pressure p_0^0, to final pressure p_e, and zero velocity
- Δh_{st} = $h_b - h_{es}$, isentropic enthalpy drop for turbine from inlet static pressure p_b, to final pressure p_e, and zero velocity
- Δh_{ss} = $h_0 - h_{2s}$, isentropic enthalpy drop per stage from inlet pressure p_0 to outlet pressure p_2
- ϵ_R = deflection of gas stream going through blades
- ϵ_N = deflection of gas stream going through nozzles

Subscripts and Superscripts

- $(\ )_0$ = refers to inlet conditions to a stage
- $(\ )_b$ = refers to inlet conditions to turbine
- $(\ )_2$ = refers to conditions at outlet of a stage
- $(\ )_e$ = refers to conditions at outlet of turbine
- $(\ )^0$ = refers to stagnation conditions
- $(\ )_{es}$ = refers to state reached in isentropic expansion through turbine from p_b to p_e

Introduction

In Part 1 (1),[3] the effect of cooling the nozzles and blades of a turbine stage on its efficiency has been examined. In a multistage turbine, the cooling in each stage reduces the gas temperature at entry to the next stage, thereby reducing the amount of work available in this and subsequent stages.

A method of calculating the effect has been published by T. W. F. Brown (3) and methods of calculating reheat factors in uncooled turbines have been published by Kaye and Wadleigh

[3] Numbers in parentheses refer to the Bibliography at the end of the paper.

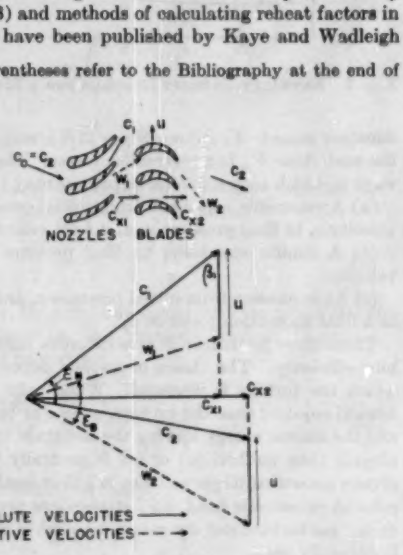

Fig. 1 Diagram of Nozzles and Blades and Corresponding Velocity Triangles

[1] This paper contains work done under the sponsorship of the Office of Naval Research Contract N5ori—78 to 21, March, 1949. The work was carried out when the author was George Westinghouse Professor of Mechanical Engineering, Massachusetts Institute of Technology.

[2] Hunsaker Professor of Aeronautics, Massachusetts Institute of Technology, on leave from the Professorship of Applied Thermodynamics, University of Cambridge, England.

Contributed by the Gas Turbine Power Division and presented at the Diamond Jubilee Annual Meeting, Chicago, Ill., November 13–18, 1955, of The American Society of Mechanical Engineers.

Note: Statements and opinions advanced in papers are to be understood as individual expressions of their authors and not those of the Society. Manuscript received at ASME Headquarters, August 29, 1955. Paper No. 55—A-191.

(4). The treatment follows closely that used in references (3) and (4), but includes an allowance for the effect of cooling on the stage efficiency and a chart for computational purposes. The assumption for k, the ratio of the specific heats, is $k = 1.4$ since in reference (4) it is shown that this only slightly overestimates the reheat factor. Equal pressure ratio per stage and equal ratio of heat removed to work done per stage are assumed.

The notation of Part 1 will be used. Fig. 1 shows the velocity diagram for the stage. The amount of heat removed per stage may be estimated by the methods of Part 1.

Thermodynamics of Flow in a Multistage Turbine

Fig. 2 shows the enthalpy-entropy diagram for a multistage turbine. By the definition of stage efficiency η_{st} used in Part 1 the work per stage W is

$$W = \eta_{st}\left(\Delta h_{ss} + \frac{c_0^2}{2} - \frac{c_2^2}{2}\right) \quad \ldots\ldots [1]$$

To define an efficiency η_t for the whole turbine the total work

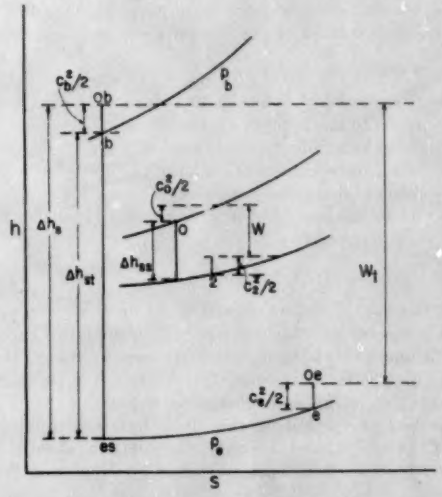

Fig. 2 Enthalpy-Entropy Diagram for a Multistage Turbine

done per pound, W_t (where $W_t = \Sigma W$), may be compared with the work done W_{tr} in a reversible process. There are a number of ways in which such a reversible process may be done.

(a) A reversible expansion from initial pressure p_b and initial velocity c_b to final pressure p_e and final velocity c_e.

(b) A similar expansion to final pressure p_e and zero final velocity.

(c) An expansion from initial pressure p_b and initial velocity c_b to a final stagnation pressure p_e^0.

These three methods will give different values for W_{tr} and turbine efficiency. The choice of method depends on the duty for which the turbine is intended. When only a fixed amount of work is required from the turbine, as in a turbojet aircraft engine, and the kinetic energy leaving the last stage may be usefully employed, then method (a) or (c) is generally used. Method (c) gives a somewhat larger value to W_{tr} than method (a). When the exhaust pressure is fixed, e.g., atmosphere pressure in an "open-cycle" gas turbine and the maximum work is required, method (b) is generally used.

Referring to Fig. 2, method (a) gives

$$\eta_t = \frac{W_t}{W_{tr}} = \frac{\Sigma W}{\Delta h_{st} + \dfrac{c_b^2 - c_e^2}{2}} = \frac{\Sigma W}{\Delta h_s - \dfrac{c_e^2}{2}} \quad \ldots\ldots [2]$$

and method (b)

$$\eta_t = \frac{\Sigma W}{\Delta h_{st} + \dfrac{c_b^2}{2}} = \frac{\Sigma W}{\Delta h_s} \quad \ldots\ldots [3]$$

In the following the efficiency expression for method (b), Equation [3], will be developed.

In order to develop the expression it is necessary to assume that η_{st} is the same for all stages; then Equations [3] and [1] give

$$\eta_t = \eta_{st}\left(\frac{\Sigma \Delta h_{ss}}{\Delta h_s} + \frac{c_b^2 - c_e^2}{2\Delta h_s}\right)$$

$$= \eta_{st}\frac{\Delta h_{st}}{\Delta h_s}\left(\frac{\Sigma \Delta h_{ss}}{\Delta h_{st}} + \frac{c_b^2 - c_e^2}{2\Delta h_{st}}\right) \quad \ldots\ldots [4]$$

From the h-s diagram, Fig. 2, it will be seen that $\Sigma \Delta h_{ss}/\Delta h_{st}$ is greater than unity. This factor is known as the "reheat factor."

Suppose the turbine consists of a large number of stages of efficiency $\eta_{st} = \eta_p$, so that the pressure drop Δp_{ss} and work W across each stage is small. Then since $Tds = dh - vdp$, for any stage

$$\Delta h_{ss} = v(p_0 - p_4) \quad \ldots\ldots [5]$$

But by the definition of stage efficiency given in reference (1)

$$W = \eta_p\left(\Delta h_{ss} + \frac{c_0^2 - c_2^2}{2}\right)$$

$$= h_0 - h_2 + \frac{c_0^2 - c_2^2}{2} \quad \ldots\ldots [6]$$

whence $$h_0 - h_2 + (1 - \eta_p)\frac{c_0^2 - c_2^2}{2} = \eta_p v(p_0 - p_2) \quad \ldots\ldots [7]$$

If the fluid is a perfect gas, $h_0 - h_2 = c_p(T_0 - T_2)$, and $pv = RT$. Then in the limit as $p_0 \to p_2$, $W \to 0$, $c_0 \to c_2$, we have

$$c_p dT = \eta_p \frac{RT}{p} dp$$

or $$\frac{dT}{T} = \eta_p\left(\frac{k-1}{k}\right)\frac{dp}{p} \quad \ldots\ldots [8]$$

Hence the equation of the line of state is

$$\frac{T}{T_b} = \left(\frac{p}{p_b}\right)^{\eta_p \frac{k-1}{k}} \quad \ldots\ldots [9]$$

Now the reheat factor for an infinite number of stages is

$$(1 + \rho)_\infty = \frac{\Sigma \Delta h_{ss}}{\Delta h_{st}} = \int_{p_e}^{p_b} vdp / c_p(T_b - T_{ss})$$

$$= \frac{1}{\eta_p}\frac{1 - (T_e/T_b)}{1 - (T_{ss}/T_b)}$$

$$(1 + \rho)_\infty = \frac{1}{\eta_p}\frac{1 - r^{\eta_p \frac{k-1}{k}}}{1 - r^{\frac{k-1}{k}}} \quad \ldots\ldots [10]$$

where $r = p_e/p_b$.

If the turbine consists of a finite number of stages N with the same equation for the line of state as Equation [9] and with equal pressure ratio per stage

$$\Delta h_{ss} = c_p(T_0 - T_{bs}) = c_p T_0 \left[1 - \left(\frac{p_2}{p_0}\right)^{\frac{k-1}{k}}\right] = c_p T_0 \left[1 - \left(\frac{p_e}{p_b}\right)^{\frac{1}{N}\frac{k-1}{k}}\right] \quad [11]$$

Since

$$\left(\frac{p_2}{p_0}\right)^N = \frac{p_e}{p_b}$$

and

$$h_0 - h_2 = c_p(T_0 - T_2) = c_p T_0 \left(1 - \left(\frac{p_2}{p_0}\right)^{\eta_p \frac{k-1}{k}}\right) = c_p T_0 \left(1 - \left(\frac{p_e}{p_b}\right)^{\frac{\eta_p}{N}\frac{k-1}{k}}\right) \quad [12]$$

Then by the definition of η_{ss}, reference (1), if $(c_0^2 - c_2^2)/2$ is negligible

$$\eta_{ss} = \frac{h_0 - h_2}{\Delta h_{ss}} = \frac{1 - r^{N\frac{\eta_p}{k}\frac{k-1}{k}}}{1 - r^{N\frac{1}{k}\frac{k-1}{k}}} \quad [13]$$

Now the reheat factor for N-stages of equal stage efficiency[4]

$$(1+\rho)_N = \frac{\Sigma \Delta h_{ss}}{\Delta h_{ss}} = \frac{1}{\eta_{ss}} \frac{h_0 - h_e}{h_0 - h_{es}} = \frac{1}{\eta_{ss}} \frac{1 - \frac{T_e}{T_0}}{1 - \frac{T_{es}}{T_0}} = \frac{1}{\eta_{ss}} \frac{1 - r^{\eta_p \frac{k-1}{k}}}{1 - r^{\frac{k-1}{k}}}$$

and substituting for η_{ss} from Equation [13]

$$(1+\rho)_N = \frac{1 - r^{\frac{1}{N}\frac{k-1}{k}}}{1 - r^{\eta_p \frac{1}{N}\frac{k-1}{k}}} \frac{1 - r^{\eta_p \frac{k-1}{k}}}{1 - r^{\frac{k-1}{k}}} \quad [14]$$

Plots of $(1+\rho)_\infty$ as defined in Equation [10] are given in Fig. 3 against r for different values of η_p and for $k = 1.4$.

These plots may be used to determine $(1+\rho)_N$ by noting that Equation [14] is equivalent to

$$(1+\rho)_N = \frac{(1+\rho)_\infty \text{ for } \eta_p \text{ and } r}{(1+\rho)_\infty \text{ for } \eta_p \text{ and } r^{1/N}} \quad [15]$$

If η_{ss} is known η_p may be obtained from Equation [13] which gives the approximate relation (4)

$$\eta_{ss} = \eta_p \left[1 - \left(\frac{1 - \eta_p}{2} \log_e r^{\frac{1}{N}\frac{k-1}{k}}\right)\right] \quad [16]$$

Reheat Factor for a Turbine With Cooled Blades

The treatment for the normal uncooled turbine may be extended to the turbine with cooled blades.

[4] The analysis is due to Prof. C. R. Soderberg (see reference 4).

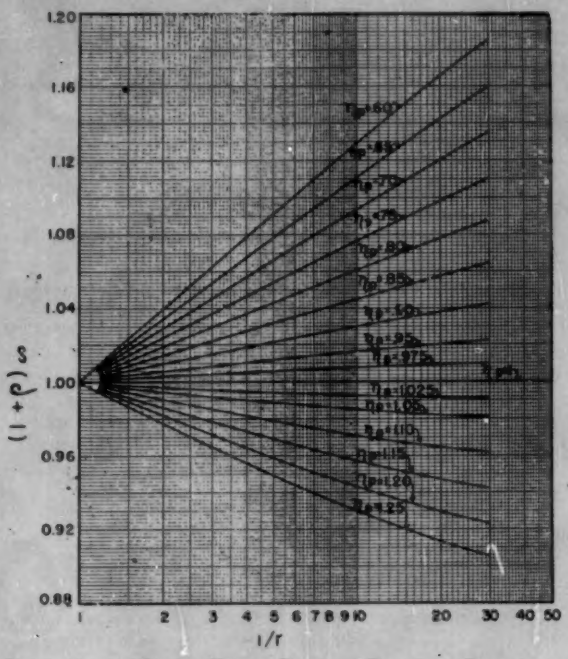

Fig. 3 Reheat Factor Versus Pressure Ratio and Polytropic Efficiency—$k = 1.4$

The procedure is the same until Equation [7] is reached which, to allow for heat removal equal to q Btu/lb per stage,[5] is modified to

$$W = \eta_p \left(\Delta h_{ss} + \frac{c_0^2 - c_2^2}{2}\right) = h_0 - h_2 + \frac{c_0^2 - c_2^2}{2} - q \quad [17]$$

Defining

$$W + q = \eta_e \left(\Delta h_{ss} + \frac{c_0^2 - c_2^2}{2}\right) \quad [18]$$

$$h_{0i} - h_{0f} + (1 - \eta_e)\frac{c_0^2 - c_2^2}{2} = \eta_e r(p_0 - p_2) \quad [19]$$

It is now assumed that q/W and the stage-pressure ratio are the same for all stages. Hence Equation [8] becomes

$$\frac{dT}{T} = \eta_e \frac{k-1}{k}\frac{dp}{p} \quad [20]$$

The substitution of η_e for η_p follows throughout the remainder of the expressions derived in the previous section. However, Equation [13] should be written

$$\frac{W + q}{\Delta h_{ss}} = \frac{1 - r^{N\frac{\eta_e}{k}\frac{k-1}{k}}}{1 - r^{N\frac{1}{k}\frac{k-1}{k}}} \quad [21]$$

giving for an infinite number of stages

$$\eta_e = \eta_p \left(1 + \frac{q}{W}\right) \quad [22]$$

[5] q is positive when heat is removed.

where $\eta_p = \dfrac{W}{\Delta h_{os}}$

for the cooled stage and for a finite number of stages approximately

$$\eta_{st}\left(1 + \frac{q}{W}\right) = \eta_q\left[1 - \left(\frac{1 - \eta_q}{2}\log_e r^{\frac{1}{N}\frac{k-1}{k}}\right)\right] \quad [23]$$

where

$$\eta_{st} = \frac{W}{\Delta h_{ss}}$$

for the cooled stage.

The curves in Fig. 3 may be used to find the new reheat factor for the cooled turbine, substituting η_q for η_p. It will be seen that η_q can be greater than unity, since it is possible that $(1 + q/W)$ is greater than $1/\eta_p$.

The turbine efficiency defined as the ratio of actual work output to that obtained in a reversible and adiabatic expansion from initial pressure p_b and initial velocity c_b to final pressure p_e and zero final velocity is

$$\eta_t = \eta_{st}\frac{\Delta h_{st}}{\Delta h_s}\left\{\frac{\Sigma\Delta h_{ss}}{\Delta h_{st}} + \frac{c_b^2 - c_e^2}{2\Delta h_{st}}\right\} \quad [24]$$

where η_{st} is the efficiency of the cooled stage.

The difference between the efficiencies of the cooled and uncooled stages may be found from Part 1, reference (1).

Example

Taking as an example a turbine consisting of five impulse stages with stage inlet and outlet velocities axial and the relative inlet velocity to the rotor equal to the relative outlet velocity, the reheat factor and turbine efficiency were calculated for an uncooled turbine and for one in which the blades were cooled at a ratio of blade wall temperature to stagnation gas temperature relative to the blades, $T_w/T_0 = 0.25$. The nomenclature and methods of Part 1, reference (1) were used and the following conditions were assumed:

ξ_p, profile loss factor = 0.06 (= ξ_0 in an impulse stage)
u, wheel speed = 800 fps
T_b^0, inlet stagnation temperature = 2960 F abs
β_1, nozzle angle = 20 deg

From Part 1, reference (1), Figs. 14 and 17, it was found that for an axial impulse stage, with $\beta_1 = 20$, η_{ss}, the stage efficiency = 0.845 for an uncooled stage and 0.842 for a cooled stage (assuming the relative Mach number at the rotor outlet is equal to unity). Equation [16] gives $\eta_p \doteq \eta_{st}$ with an error of less than 1 per cent so that for the purposes of the computation the error will be neglected.

Also from reference (1), $W/(u^2/2)$ for an axial impulse stage is equal to 4 where W is the work per stage, so that $W = 51.20$ Btu/lb.

The reheat factor and the turbine efficiency were calculated for the cooled and uncooled turbines with the help of reference (2) in a stage-by-stage computation as outlined in reference (4), and the results were compared with those obtained by using Fig. 3. In both methods of calculation the working fluid was assumed to be air.

Uncooled Turbine. Since the work per stage is equal to 51.20 and the stage efficiency is 0.845, the isentropic enthalpy drop per stage is 60.59. By use of the gas tables (2) these values and an inlet stagnation temperature of 2500 F showed that the over-all pressure ratio for the turbine was equal to 5.98 in a stage-by-stage calculation.

Then the isentropic enthalpy drop for the turbine was 295.45 and the turbine efficiency was found to be equal to

$$\eta_t = \frac{(5)(51.20)}{295.45} = 0.866$$

The reheat factor was $\dfrac{0.866}{0.845} = 1.025$

For a pressure ratio of 5.98 in a 5-stage turbine, Fig. 3 yields

$$(1 + \rho)_N = \frac{1.0375}{1.008} = 1.029$$

and

$$\eta_t = (1.029)(0.845) = 0.870$$

Turbine With Cooled Rotor Blades, $T_w/T_{0s} = 0.25$. Again the work per stage is equal to 51.20, but the stage efficiency this time equals 0.842, so that the isentropic enthalpy drop per stage is 60.81. By using the gas tables and the fact that (Part 1, reference 1)

$$\frac{\Delta T_0}{T_{0s}} = \left(1 - \frac{T_w}{T_{0s}}\right)\left(e^{\frac{1}{2}\xi_0} - 1\right) = 0.228 \quad [25]$$

where ΔT_0 refers to the drop per stage in stagnation temperature of the gas caused by cooling, it was found that in this case the over-all pressure ratio was equal to 6.68, so that the isentropic enthalpy drop for the turbine was 309.84. Then the turbine efficiency was equal to

$$\eta_t = \frac{5(51.20)}{309.84} = 0.826$$

and the reheat factor was

$$(1 + \rho)_N = \frac{0.826}{0.842} = 0.981$$

In order to use Fig. 3 for a cooled turbine q, the heat per stage removed by cooling, has to be computed. Assuming the same amount of heat was removed in each stage and using an average value of the stagnation temperature in Equation [25], it was found that the total drop in stagnation temperature due to cooling was 270 deg F. Then

$$q/\text{stage} = \tfrac{1}{5}(270) = 15.37 \text{ Btu/lb}$$

and

$$q/W = \frac{15.37}{51.20} = 0.3002$$

Consequently

$$\eta_q = \eta_p(1 + q/W) = (0.842)(1.3002) = 1.095$$

Using this value and a pressure ratio of 6.68 in Fig. 3

$$(1 + \rho)_N = \frac{0.976}{0.996} = 0.980$$

and

$$\eta_t = (0.980)(0.842) = 0.825$$

The results are summarized in Table 1. The different methods of calculation show substantial agreement.

TABLE 1 RESULTS OF CALCULATIONS

	Stage by stage calculation		From Fig. 3	
	Uncooled	Cooled	Uncooled	Cooled
η_t	0.866	0.826	0.870	0.825
$(1 + \rho)_N$	1.025	0.981	1.029	0.980

Conclusions

A method of calculating the effect of cooling on the efficiency of a multistage turbine has been presented and found to give results in substantial agreement with accurate calculations. The results show the importance of the effect in turbines with blades cooled substantially below the gas temperature, a 4–5 per cent reduction in turbine efficiency being obtained in the example quoted.

Acknowledgment

The help of Mrs. Antonia B. Walker in making the calculations and preparing the diagrams is gratefully acknowledged.

BIBLIOGRAPHY

1 "The Thermodynamics of Cooled Turbines: Part 1—The Turbine Stage," by W. R. Hawthorne, published in this issue, pp. 1765–1779.
2 "Gas Tables," by J. H. Keenan and Joseph Kaye, John Wiley & Sons, Inc., New York, N. Y., 1948.
3 "Some Factors in the Use of High Temperatures in Gas Turbines," by T. W. F. Brown, Proceedings of The Institution of Mechanical Engineers, vol. 162, 1950, p. 167.
4 "A New Method of Calculation of Reheat Factors for Turbines and Compressors," by J. Kaye and K. R. Wadleigh, *Journal of Applied Mechanics*, Trans. ASME, vol. 73, 1951, p. 387.

Discussion

L. S. Dzung.[6] Professor Hawthorne's papers are certainly a much welcomed contribution to a timely subject. The treatment is accurate and the assumptions and limitations are well recognized and defined.

The assumption of constant friction coefficient is justified on account of its simplification. The mathematics could be further simplified by making another assumption, which is perhaps just as good, namely, by assuming constant polytropic efficiency.

Using the author's symbolism (except the obvious difference in sign of heat and work) one may write in differential form the First Law ($K = c^2/2$ is the kinetic energy)

$$dh + dK = dw + dq$$

the Second Law ($d_i s$ is the internal irreversible entropy production)

$$Tds = dq + Td_i s$$

the Gibbsian fundamental equation

$$dh = Tds + vdp$$

and define for a steady-flow process the three inexact differentials, i.e., the hydraulic work (per unit mass)

$$dy = v\,dp \quad [26]$$

the internal energy transformation

$$dz = dw - dK \quad [27]$$

the dissipation

$$dj = Td_i s \quad [28]$$

which is essentially positive. In case of turbine, it is more convenient to define y and z with the opposite sign, so that

$$dz = dy \pm dj$$

where the minus sign is used for turbine.

The polytropic efficiency for turbine may be defined as

$$\eta = dz/dy \quad [29]$$

Now assume

$$dq = \vartheta dj \quad [30]$$

ϑ is negative in case of cooling. The polytropic coefficient φ, defined by[7]

$$\varphi = dh/dy \quad [31]$$

can be expressed as

$$\varphi = \eta + (1 - \eta)\vartheta \quad [32]$$

which is identical with Equation [22] of author's second paper.

The "reheat factor," being the ratio of hydraulic work (integration of Equation [26] along actual state path) to isentropic work (integration along isentropic path) can be written as

$$F = \frac{\nu(1 - r^{1/\nu})}{\lambda(1 - r^{1/\lambda})}$$

$\lambda = k/(k-1)$, k is isentropic exponent, ν depends on λ and φ.[7] For ideal gas, this formula reduces to Equation [10] in author's second paper. The present formula is applicable to a stage or to the whole turbine. Correction to finite number of stages is not necessary. This formula would be useful if φ and ϑ were constant along the whole turbine, which is seldom the case. Actually, it is necessary to take the variation of ϑ and φ into account as follows.

The change of state in a cooled turbine with constant blade wall temperature T_w may be obtained by writing

$$\vartheta = \frac{bc_p(T - T_w)}{2K'} + \frac{br'}{2}, \quad b = \frac{\mathrm{St}}{(f/2)} \quad [33]$$

b takes care of cases where Reynolds' analogy does not strictly apply. St is Stanton's number defined by the left-hand side of author's Equation [32], first paper. K' is the kinetic energy of the relative flow, r' is the recovery factor.

Substitution of Equation [33] into [30], [31], [32] and using ideal-gas equations $pv = RT$, $dh = c_p dT$ result in

$$\frac{d\tau}{\tau[\gamma + \beta(\tau - 1)]} = \frac{\eta}{\lambda}\frac{dp}{p} \quad [34]$$

where

$$\tau = T/T_w$$

$$\beta = bc_p T_w \left(\frac{1}{\eta} - 1\right) \Big/ 2K'$$

$$\gamma = 1 + \left(\frac{1}{\eta} - 1\right)\frac{br'}{2}$$

This integrates readily between inlet 1 and exhaust 2, assuming constant β, into

$$\log \frac{\beta\tau_1 - (\beta - \gamma)}{\beta\tau_2 - (\beta - \gamma)} - \log \frac{\tau_1}{\tau_2} = (\beta - \gamma)\frac{\eta}{\lambda}\log\frac{p_1}{p_2} \quad (\beta \neq \gamma) \quad [35]$$

This gives a relation between temperature and pressure along the state path.

The hydraulic work can be obtained by integrating Equation [26] using [34]; the energy transformation is then obtained by multiplication by η. The result is

[6] Brown, Boveri & Company, Ltd., Baden, Switzerland.

[7] "Thermostatische Zustandsänderungen des trockenen und des nassen Dampfes," by L. S. Dzung, *Zeitschrift für angewandte Mathematik und Physik*, vol. 6, 1955, p. 207.

$$\frac{z}{c_p T_\infty} = \frac{\eta y}{c_p T_\infty} = \frac{1}{\beta} \log_e \frac{\beta\tau_1 - (\beta - \gamma)}{\beta\tau_2 - (\beta - \gamma)} \quad (\beta \neq 0) \ldots [36]$$

The turbine work w is just z corrected to change of kinetic energy between inlet and exhaust.

Equations [35] and [36] together give the turbine work as function of pressure ratio with one of the τ's as parameter. The special case of $\beta = \gamma$ in Equation [35] and $\beta = 0$ (adiabatic) in Equation [36] can be easily deduced.

By nondimensionalizing the turbine work as in Equation [36] it is emphasized that the work is increased by cooling at constant blade wall temperature and hence constant thermal stress. Author's (adiabatic) efficiency makes this point obscure.

Effect of Turbine-Blade Cooling on Efficiency of a Simple Gas-Turbine Power Plant

By W. M. ROHSENOW,[1] CAMBRIDGE, MASS.

The efficiency of a simple gas-turbine cycle can be increased by designing it to operate at higher turbine-inlet temperatures. In order to operate these turbines at higher temperatures it is necessary to cool the blades and possibly the casing and rotors in the earlier stages until the gases are reduced to a value between 1000 and 1500 F depending on the kind of metal employed. Various methods of cooling turbine blades have been investigated by the NACA and published in various unclassified technical reports since 1947. A survey of some of this work is presented by Ellerbrock (1).[2] The present work is an investigation of the effects of blade cooling on the thermodynamic performance of a simple gas-turbine plant. A companion paper (9) extends the present analysis to include the effect of cooling-system losses.

Nomenclature

The following nomenclature is used in the paper:

- A = heat-transfer surface, sq ft
- c_p = specific heat at constant pressure, Btu/lb deg F
- G = rate of flow per unit cross-sectional area, lb/hr cu ft
- g_0 = 32.2 lb_m ft/lb_f sec^2, conversion factor
- h = enthalpy, Btu/lb
- h_{ss} = isentropic enthalpy difference across a stage
- J = 778 ft lb/Btu
- K_1 = defined in Equation [4]
- N = number of stages in a turbine
- P = wetted perimeter for flow through the blade passage
- P_r = relative pressure as used in reference (5)
- Q/W_A = heat transfer to cooled blades per unit turbine work
- Q = heat transferred to cooled blade per pound of fluid
- r = pressure ratio, less than unity
- r_A = pressure ratio across cooled part of turbine, p_4/p_3
- r_B = pressure ratio across uncooled part of turbine, p_5/p_4
- S = cross-sectional area for flow through blade passage, sq ft
- T_i = exit temperature of turbine part A
- T_0 = stagnation temperature
- T_w = wall temperature taken equal to T_i
- u = blade speed, fps
- V_{axial} = axial velocity leaving last stage
- V_n = velocity of jet leaving turbine-stage nozzle blades
- W_A = work per lb of fluid done by cooled part of turbine
- W_B = work per lb of fluid done by uncooled part of turbine
- W_C = compressor work per lb of fluid
- W_T = turbine work per pound of fluid
- $(W_T - W_C)$ = cycle net work per pound of fluid
- α = surface coefficient of heat transfer, Btu/hr sq ft deg F
- β = nozzle angle
- Δh_{ts} = isentropic enthalpy difference across a turbine
- Δh_{stg} = enthalpy drop across a stage
- η = cycle efficiency
- η_c = compressor efficiency
- η_p = polytropic turbine efficiency (efficiency of an infinitesimal stage)
- η_s = $\eta_p(1 + Q/W_A)$ for a cooled part of turbine (reference 4)
- η_{stg} = stage efficiency of a finite turbine stage
- η_t = turbine efficiency
- ξ_n = loss factor defined by Equation [23] of Appendix 2
- ξ_p = profile-loss factor
- R_m = reheat factor

Introduction

With currently available metal alloys, gas turbines can be expected to be operated uncooled at temperatures around 1500 F. In the region where the gases exceed these temperatures, the turbine must be cooled. Hence, in this analysis, the turbine is considered to have two parts—A, a cooled part, and B, an uncooled part, Fig. 1. The turbine is cooled until the temperature T_i is reached along its condition curve. The magnitude of T_i depends upon the kind of metal used in the turbine construction.

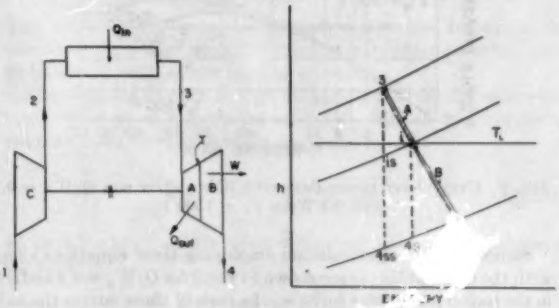

Fig. 1 Diagram and Enthalpy-Entropy Chart of Simple Gas-Turbine Process With Part A of the Turbine Cooled

[1] Associate Professor of Mechanical Engineering, Massachusetts Institute of Technology. Mem. ASME.

[2] Numbers in parentheses refer to the Bibliography at the end of the paper.

Contributed by the Gas Turbine Power Division and presented at the Diamond Jubilee Annual Meeting, Chicago, Ill., November 13–18, 1955, of The American Society of Mechanical Engineers.

 Manuscript received at ASME Headquarters, August 29, 1955. Paper No. 55—A-120.

The following three conditions were investigated for the effect on thermal efficiency and specific air consumption for turbines with an infinite number of stages:

(*a*) T_i = 1500 F, T_3 varying
(*b*) T_i = 1000 F, T_3 varying
(*c*) T_i = varying, T_3 = 1500 F

Also the effect of finite number of stages was investigated for conditions (*a*) and (*b*).

Method of Analysis

For this analysis the compressor efficiency was assumed to be 85 per cent, and the turbine polytropic efficiency (efficiency of an infinitesimal stage) was assumed to be 88 per cent for both the cooled and uncooled portions of the turbine and for a turbine with a finite number of stages the stage efficiency was assumed to be 85 per cent. Hawthorne (3) showed that the difference in η_p for a cooled and an uncooled stage was probably of the order of 1 to 2 per cent, changing slightly with Mach number and type of stage. The actual turbine efficiency for the uncooled part of the turbine was calculated from

$$\eta_t = R_\infty \eta_p \quad [1]$$

where the reheat factor is given by

$$R_\infty = \frac{1}{\eta_p}\left(\frac{1 - r_B^{\eta_p \frac{k-1}{k}}}{1 - r_B^{\frac{k-1}{k}}}\right) \quad [2]$$

For the cooled portion of the turbine Appendix 1 shows that Equation [2] would apply if η_p and r_B in this equation is replaced by η_e and r_A where

$$\eta_e = \eta_p\left(1 + \frac{Q}{W_A}\right) \quad [3]$$

assuming Q/W_A is uniform along the length of the cooled portion.

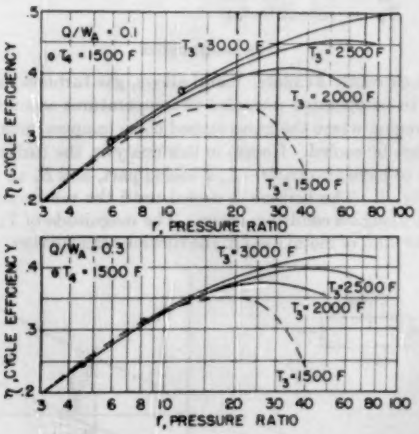

Fig. 2 Cycle Efficiency-Pressure Ratio Plot for Q/W_A = 0.1 and 0.3 With T_i = 1500 F

Sample results of calculation employing these equations along with the Gas Tables (5) are shown in Fig. 2 for Q/W_A = 0.1 and 0.3 in the cooled part of the turbine. In each of these curves the turbine was cooled to T_1 = 1500 F. Of course, when T_3 = 1500 F there is no cooling in the turbine.

In order to interpret the results of these calculations it is necessary to investigate how Q/W_A changes as the design value of T_3 changes. The required amount of cooling, hence Q/W_A, increases as T_3 is assumed higher because the rate of heat transfer increases with the difference between gas and metal temperature. The following approximate analysis is made to aid in this interpretation.

The maximum work per stage of infinite-staged turbine or best efficiency of a single-stage turbine is obtained when the magnitude of the term

$$\frac{W}{u^2/2g_0 J} = K_1 \quad [4]$$

is approximately $K_1 = 4$ for impulse blading and $K_1 = 2$ for reaction blading (6). Actual values will be slightly less than these.

An approximate relation for the heat transfer per pound of fluid flowing in a cascade of blades is shown in Appendix 2 to be

$$Q = c_p(T_0 - T_w)(e^{k\theta/2} - 1) \quad [5]$$

or approximately twice this value for a turbine stage. This relation assumes the Reynolds' analogy between friction and heat transfer to exist.

Then dividing Equation [5] by Equation [4] an expression for Q/W for a stage can be written as

$$\frac{Q}{W} = \frac{2c_p(T_0 - T_w)(e^{k\theta/2} - 1)}{K_1(u^2/2g_0 J)} \quad [6]$$

If all stages of a multistage turbine have the same velocity diagram the enthalpy drop (and hence temperature drop) per stage of an uncooled turbine is uniform throughout the turbine. Then the temperature varies nearly linearly with axial distance for a uniform blade width for all stages. This is also approximately true for a cooled turbine. If the blade temperature in the first part of the turbine is to be maintained at T_w = 1500 F to a point where the gas temperature is T_i = 1500 F, then the heat-transfer rate will vary linearly with axial position for this part of the turbine. To obtain an average value of Q/W_A, the temperature T_0 may be interpreted as the mean value between T_3 and T_w (or T_i). Then

$$T_0 = \frac{1}{2}(T_3 + T_i) \quad [7]$$

By using Equations [1] through [7] in conjunction with the condition curve (Fig. 1) a series of calculations were made for various values of u and ξ_0. Figs. 3 through 12 show the results of these computations for both impulse and reaction stage.

The foregoing results were for a turbine having an infinite number of stages. In actuality these results have neglected the effect of the leaving loss normally associated with turbines having a finite number of stages. To investigate the effect of the leaving loss associated with turbines having finite-size stages the calculation proceeds in the same manner as before except that the reheat factor for the uncooled turbine is calculated from Equation [2]

$$R_N = \frac{\left[1 - r_B^{\frac{1}{N}\frac{k-1}{k}}\right]\left[1 - r_B^{\eta_p \frac{k-1}{k}}\right]}{\left[1 - r_B^{\frac{\eta_p}{N}\frac{k-1}{k}}\right]\left[1 - r_B^{\frac{k-1}{k}}\right]} \quad [8]$$

For a cooled turbine an analysis similar to that in Appendix 1 will show that Equation [8] is valid if η_p is replaced by η_e and r_B by r_A.

In the finite-staged-turbine calculations the stage efficiency η_s was selected as 85 per cent. Then to calculate R_N above, η_p and η_e are found from the following relations (Appendix 3)

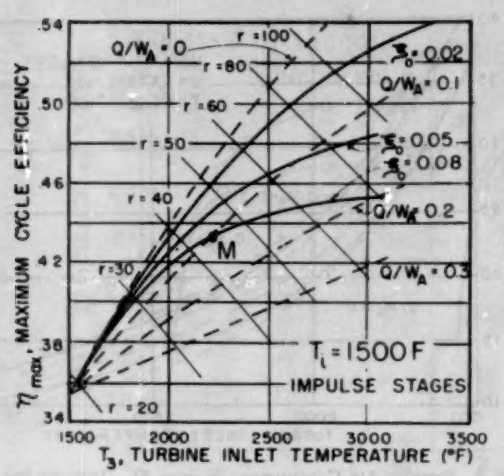

FIG. 3 MAXIMUM CYCLE EFFICIENCY VERSUS TURBINE-INLET TEMPERATURE AT VARIOUS VALUES OF ξ_b. IMPULSE STAGES WITH u = 1000 FPS AND T_i = 1500 F

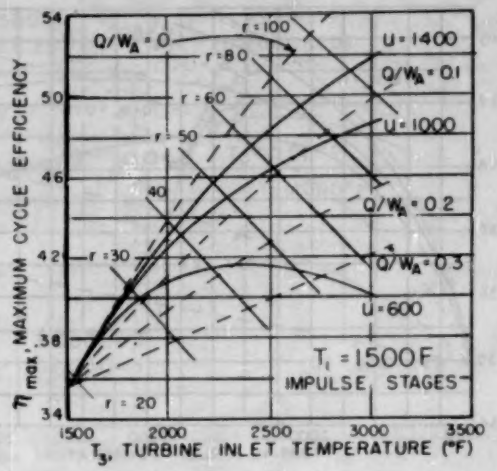

FIG. 4 MAXIMUM CYCLE EFFICIENCY VERSUS TURBINE-INLET TEMPERATURE AT VARIOUS VALUES OF u. IMPULSE STAGES WITH ξ_b = 0.05 AND T_i = 1500 F

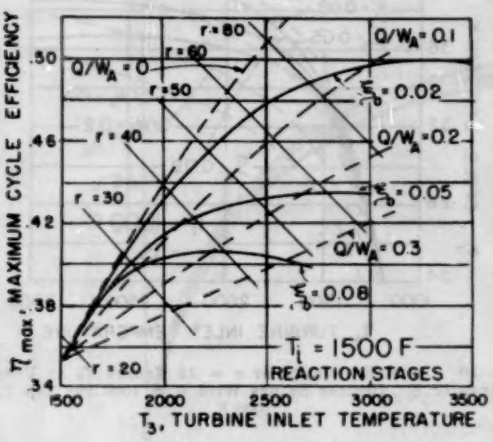

FIG. 5 MAXIMUM CYCLE EFFICIENCY VERSUS TURBINE-INLET TEMPERATURE AT VARIOUS VALUES OF ξ_b. REACTION STAGES WITH u = 1000 FPS AND T_i = 1500 F

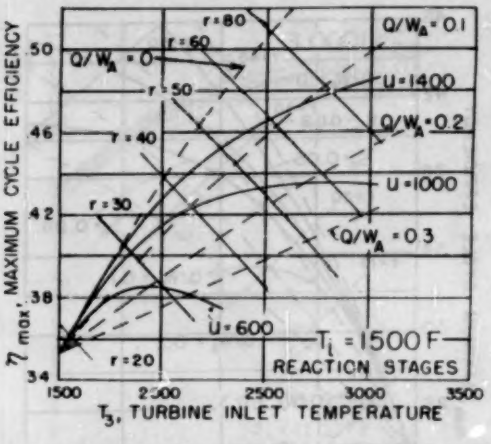

FIG. 6 MAXIMUM CYCLE EFFICIENCY VERSUS TURBINE INLET TEMPERATURE AT VARIOUS VALUES OF u. REACTION STAGES WITH ξ_b = 0.05 AND T_i = 1500 F

$$\text{(Uncooled)}\quad \eta_{st} = \frac{1 - r^{N\frac{\eta_p}{}\frac{k-1}{k}}}{1 - r^{N\frac{1}{}\frac{k-1}{k}}} \qquad [9]$$

$$\text{(Cooled)}\quad \eta_{st} = \frac{1}{1 + Q/W}\,\frac{1 - r^{N\frac{\eta_c}{}\frac{k-1}{k}}}{1 - r^{N\frac{1}{}\frac{k-1}{k}}} \qquad [10]$$

Also, for a turbine with a finite number of stages there will be a "leaving loss" associated with the velocity of the gas leaving the last stage. If the blade speed is selected to cause this leaving velocity to be in the axial direction and if the axial velocity is assumed to be uniform throughout the turbine the kinetic energy of the leaving gas for impulse stages will be approximately

$$\frac{V^2_{axial}}{2g_c J} = \frac{\Delta h_{st}}{N}\sin^2\beta \qquad [11]$$

since the nozzle velocity neglecting frictional effects is given by

$$\sqrt{2g_c J\Delta h_{ss}},\quad \Delta h_{ss} = \Delta h_{st}/N,\quad \text{and}\quad V_{axial} = V_n \sin\beta$$

This kinetic energy must be subtracted from the turbine work calculated by neglecting the leaving loss in order to obtain the turbine work with a finite number of stages.

The results are shown in Figs. 13 and 14 showing the effects on cycle efficiency of magnitudes of T_3, T_i, N, and ξ_b. For each point on these curves the blade speed was taken as

$$u = \frac{1}{2}\cos\beta\sqrt{2g_c J\Delta h_{st}/N} \qquad [12]$$

which is the approximate relation required to have an axial leaving velocity.

DISCUSSION OF RESULTS

The values of efficiency plotted in Figs. 3 through 6 are the maximum efficiency points of curves similar to those of Fig. 2.

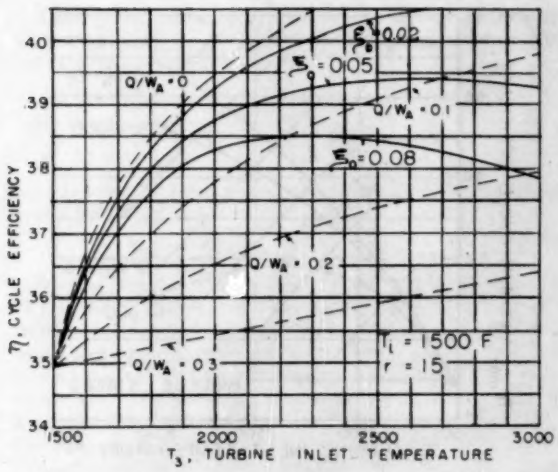

FIG. 7 CYCLE EFFICIENCY VERSUS T_3 AT VARIOUS VALUES OF ξ_0 WHEN r = 15. IMPULSE STAGES WITH u = 1000 FPS AND T_i = 1500 F

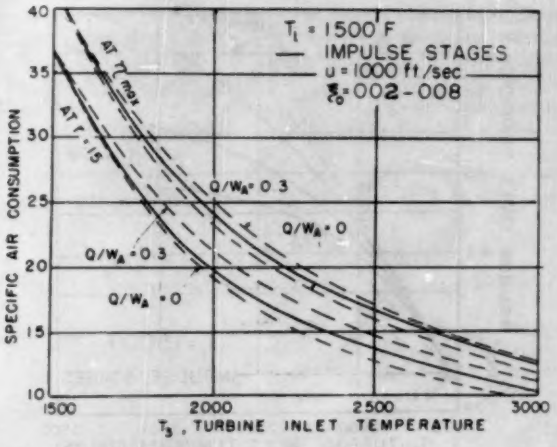

FIG. 8 SPECIFIC AIR CONSUMPTION VERSUS T_3. IMPULSE STAGES WITH u = 1000 FPS, ξ_0 = 0.02–0.08 AND T_i = 1500 F

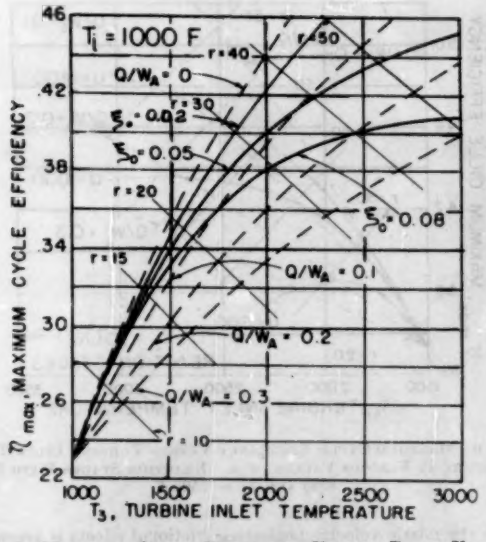

FIG. 9 MAXIMUM CYCLE EFFICIENCY VERSUS T_3 AT VARIOUS VALUES OF ξ_0. IMPULSE STAGES WITH u = 1000 FPS AND T_i = 1000 F

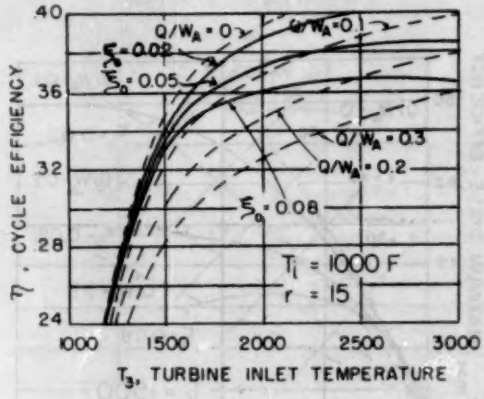

FIG. 10 CYCLE EFFICIENCY AT r = 15 VERSUS T_3 AT VARIOUS VALUES OF ξ_0. IMPULSE STAGES WITH u = 1000 FPS AND T_i = 1000 F

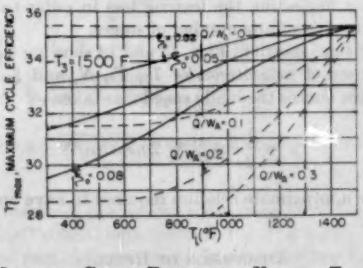

FIG. 11 MAXIMUM CYCLE EFFICIENCY VERSUS T_i AT VARIOUS VALUES OF ξ_0. IMPULSE STAGES WITH u = 1000 FPS AND T_3 = 1500 F

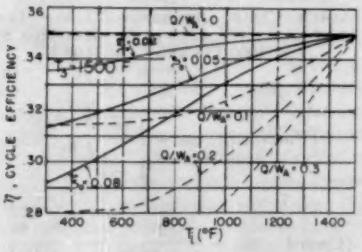

FIG. 12 CYCLE EFFICIENCY AT r = 15 VERSUS T_i AT VARIOUS VALUES OF ξ_0. IMPULSE STAGES WITH u = 1000 FPS AND T_3 = 1500 F

The dashed lines represent constant Q/W_A and T_3 values. From Equations [6] and [7] values of Q/W_A associated with a value of T_3 may be obtained. Then, the heavier solid curves of Figs. 3 through 6 may be drawn showing the effects of ξ_0 and u.

A reasonable design value for u is around 1000 fps and a reasonable value for ξ_0 to obtain η_p = 0.88 is probably in the range 0.02–0.08 (Appendix 3). The effect of changes in the magnitude

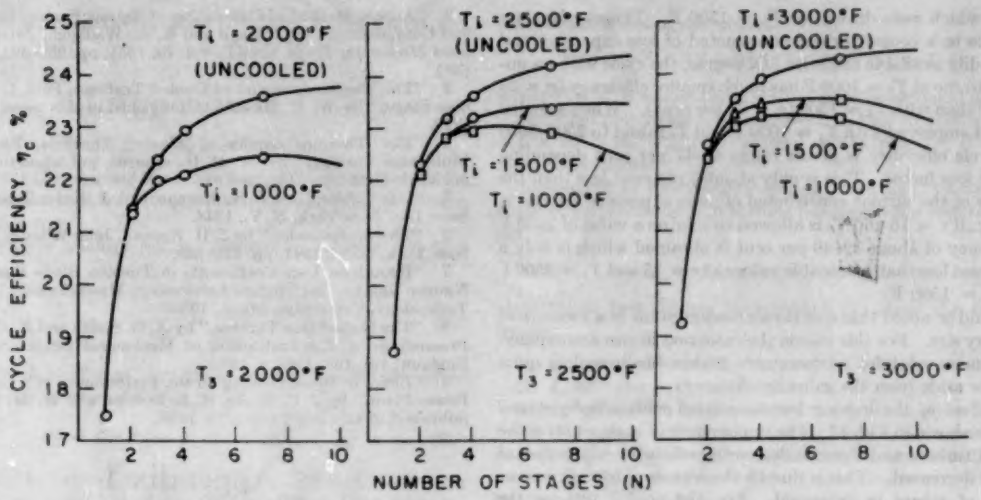

FIG. 13 EFFECT OF FINITE NUMBER OF STAGES ON CYCLE EFFICIENCY FOR IMPULSE STAGES WITH $\xi_0 = 0.08$ AND PRESSURE RATIO OF 4.4

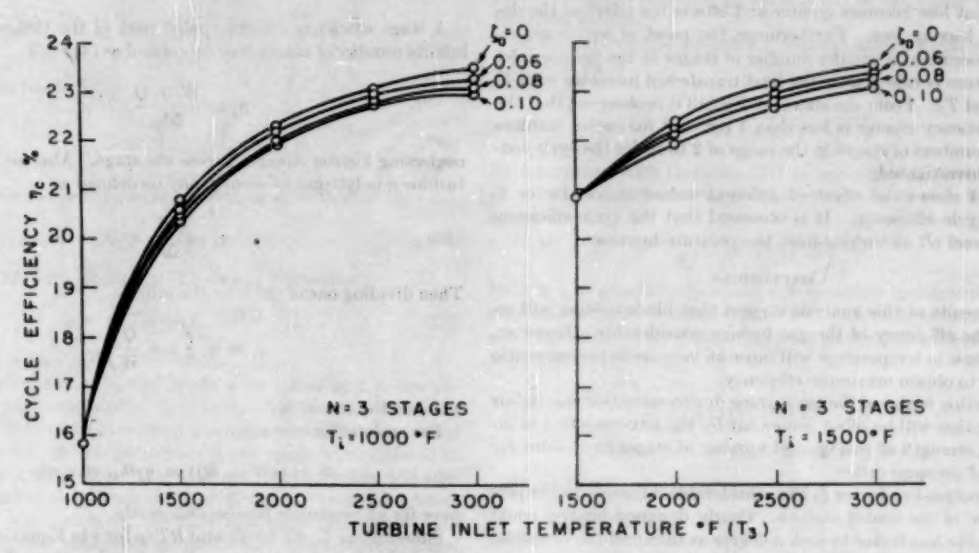

FIG. 14 EFFECT OF T_3 AND ξ_0 ON EFFICIENCY OF A CYCLE WITH A TURBINE OF THREE IMPULSE STAGES AND PRESSURE RATIO OF 4.4

of the loss factor ξ_0 on the value of η_s is not great since the profile loss is only 1/3 to 1/2 of the stage-loss factor. From Figs. 3 and 5, it appears that with T_i = 1500 F the maximum cycle efficiency occurs in the temperature range of 3500 to 4000 F for the cooled impulse turbine and in the temperature range of 3000 to 3500 F for the cooled reaction turbine. Here it was assumed that only the blades (rotor and stator) were cooled and that the blades could be designed for the minimum loss factor. If any part of the casing is also cooled or if the value of ξ_0 is higher than 0.02–0.05 the peak of these efficiency curves would be at lower values of T_3.

The efficiency of the cycle employing the uncooled turbine with T_3 = 1500 F is about 35 per cent. Depending upon the blade design and consequently the loss factor, it appears feasible, with cooling, to attain efficiencies in the range 45–50 per cent. This can be done by raising the turbine-inlet temperature T_3 to values in the range 2500-3000 F. Simultaneously, the specific air consumption decreases as shown in Fig. 8 and the pressure ratio at maximum cycle efficiency rises from around 15 to between 50–80. This reduction in specific air consumption results in smaller turbine and compressor diameters but the large increase in pressure ratios requires more stages and thicker casings and piping. Because of this it might be desirable to avoid the use of high-pressure ratios. Curves for cycle efficiency and air consumption were prepared for a pressure ratio of 15 in Figs. 7 and 8. Under these conditions the maximum cycle efficiency occurs at T_3 between 2500–3000 F and shows an increase of efficiency from 35 to about 41 per cent.

Figs. 11 and 12 show the effect on efficiency of lowering the magnitude of T_i for a constant value of T_3 = 1500 F.

Figs. 9 and 10 are drawn for T_i = 1000 F and are similar to Figs.

3 and 7 which were drawn for $T_4 = 1500$ F. These curves are applicable to a cooled turbine constructed of less expensive and more readily available material. Of course, the cycle with an uncooled turbine at $T_3 = 1000$ F has much smaller efficiency ($\eta = 23$ per cent) than with $T_3 = 1500$ ($\eta = 35$ per cent). When a cooled turbine is employed with $T_4 = 1000$ F and T_3 raised to 2500–3000 F the cycle efficiency is in the range 40–47 per cent depending upon the loss factor. This is only about 5 per cent less than the efficiency of the turbine constructed of more expensive materials. Similarly, if $r = 15$ and T_3 is allowed to take on a value of 2500 F an efficiency of about 39–40 per cent is obtained which is only a few per cent less than attainable values at $r = 15$ and $T_3 = 2500$ F with $T_4 = 1500$ F.

It should be noted that specific air consumption is a measure of machinery size. For this reason the reduction in size accompanying the increased inlet temperatures makes blade cooling quite attractive aside from the gains in efficiency.

The effect of the leaving loss associated with a finite-staged turbine is shown in Fig. 13. The upper curve of each set is for the uncooled turbine and shows a decreasing efficiency as number of stages is decreased. This is due to the increased leaving loss as number of stages is decreased. For the cooled turbine the efficiency passes through a maximum value for some finite number of stages because as the number of stages increases, the effect of the heat loss becomes greater and offsets the effect of the decreasing leaving loss. Furthermore, the point of maximum efficiency occurs at a smaller number of stages as the turbine-inlet temperature is raised since the heat transferred increases with T_3 for a fixed T_4. From the curves of Fig. 13 it is observed that the cycle-efficiency change is less than 1 per cent for cooled turbines having numbers of stages in the range of 2 to 10 for the cycle conditions investigated.

Fig. 14 shows the effect of different values of loss factor ξ_0 on the cycle efficiency. It is observed that the cycle-efficiency curves level off as turbine-inlet temperature increases.

Conclusions

The results of this analysis suggest that blade cooling will increase the efficiency of the gas turbine considerably. However, the increase in temperature will cause an increase in pressure ratio in order to obtain maximum efficiency.

Reduction in size of the gas turbine due to decreased specific air consumption will be offset somewhat by the adverse effect of increasing strength of casings and number of stages to account for increased pressure ratios.

The cooling-loss factor ξ_0 has considerable influence on the performance of the cooled turbine. Poorly designed blading could increase the loss factor to such a degree as to cancel the beneficial results of increased turbine-inlet temperature.

The turbine requiring cooling to 1000 F obtains efficiencies which are within 2 or 3 per cent of those obtained by the turbine using more expensive materials when the two performances are compared at similar inlet temperatures or pressure ratios.

Acknowledgment

This program of investigation was originally undertaken by Dr. W. R. Hawthorne, now at Cambridge University, Cambridge, England. The present paper represents an application of the methods developed by him. Calculations were performed by Mrs. Antonia B. Walker and Mr. T. B. Luzzi. The financial support of the Office of Naval Research is gratefully acknowledged.

BIBLIOGRAPHY

1 "Some NACA Investigations of Heat Transfer of Cooled Gas Turbine Blades," by H. H. Ellerbrock, Jr., general discussion on Heat Transfer, London, England, September 11–13, 1951, Part 5, Special Problems.

2 "A New Method of Calculation of Reheat Factors for Turbines and Compressors," by J. Kaye and K. R. Wadleigh, *Journal of Applied Mechanics*, Trans. ASME, vol. 73, 1951, pp. 387–392, Equation [30].

3 "The Thermodynamics of Cooled Turbines, Part, 1—The Turbine Stage," by W. R. Hawthorne, published in this issue, pp. 1765–1779.

4 "The Thermodynamics of Cooled Turbines, Part 2—The Multistage Turbine," by W. R. Hawthorne, published in this issue, pp. 1781–1786.

5 "Gas Tables," by J. H. Keenan and J. Kaye, John Wiley & Sons, Inc., New York, N. Y., 1948.

6 "Thermodynamics," by J. H. Keenan, John Wiley & Sons, Inc., New York, N. Y., 1941, pp. 129–130.

7 "Report on Loss Coefficients in Turbine Blade Passages," by Nguyen Van Le, Gas Turbine Laboratory, Massachusetts Institute of Technology, Cambridge, Mass., 1950.

8 "The Cooled Gas Turbine," by A. G. Smith and R. D. Pearson, Proceedings of The Institution of Mechanical Engineers, London, England, vol. 163, 1950, p. 221.

9 "Effect of Blade Cooling on the Performance of a Gas-Turbine Power Plant," by J. C. Burke, B. L. Buteau, and W. M. Rohsenow, published in this issue, pp. 1795–1806.

Appendix 1

Derivation of Equations [2] and [3] for a Cooled Turbine of Infinite Stages

A stage efficiency for the cooled part of the turbine with an infinite number of stages may be defined as (4)

$$\eta_q \equiv \frac{W + Q}{\Delta h_{ss}} \quad \ldots\ldots [13]$$

neglecting kinetic changes across the stage. Also for the cooled turbine a polytropic efficiency may be defined as

$$\eta_p \equiv \frac{W}{\Delta h_{ss}} \quad \ldots\ldots [14]$$

Then dividing one of these by the other

$$\eta_q = \eta_p \left(1 + \frac{Q}{W}\right) \quad \ldots\ldots [15]$$

which is Equation [3].

For an infinitesimal stage

$$dh = (\delta W + \delta Q) = \eta_q dh_{ss} = \eta_q v dp \quad \ldots\ldots [16]$$

since for an isentropic process $dh_{ss} = vdp$.

Substituting $C_p\,dT$ for dh and RT/p for v in Equation [16] and integrating between any two points, m and n, along the condition curve of the turbine

$$\frac{T_m}{T_n} = \left(\frac{p_m}{p_n}\right)^{\eta_q\left(\frac{k-1}{k}\right)} \quad \ldots\ldots [17]$$

The reheat factor for a cooled turbine with an infinite number of stages is defined as

$$R_\infty \equiv \frac{\Sigma \Delta h_{ss}}{\Delta h_{st}} = \frac{(1/\eta_q)c_p(T_3 - T_4)}{c_p T_3 \left[1 - r^{\frac{k-1}{k}}\right]} \quad \ldots\ldots [18]$$

Then substituting Equation [17] into [18]

$$R_\infty = \frac{1}{\eta_q} \frac{1 - (r_A)^{\eta_q \frac{k-1}{k}}}{1 - (r_A)^{\frac{k-1}{k}}} \quad \ldots\ldots [19]$$

which is the same form as Equation [2] with η_p replaced by η_s and r_B by r_A.

Appendix 2

Derivation of Equation [5]

Hawthorne (3) suggests the following approximate analysis for determining the heat transfer per pound of fluid flowing across a turbine-blade row.

The Reynolds' analogy relating momentum transfer and heat transfer is

$$\frac{\alpha}{c_p G} = \frac{f}{2} \quad \ldots\ldots [20]$$

An energy balance for an element of length dx along the blade surface in the direction of flow is

$$dq = \alpha P(T_0 - T_w)dx = SGc_p dT_0 \quad \ldots\ldots [21]$$

Substituting Equation [20] into Equation [21] and integrating between points 1 and 2 at inlet and outlet of the blade passage results in

$$\frac{T_{01} - T_{02}}{T_{02}} = \frac{T_{02} - T_w}{T_{02}}\left(e^{\int_0^L \frac{fP}{2S}dx} - 1\right) \quad \ldots\ldots [22]$$

Define a loss factor ξ_0 by

$$\xi_0 \equiv \int_{x=0}^{L} f\frac{P}{S}\,dx \quad \ldots\ldots [23]$$

Then since the heat transferred per pound of fluid is

$$Q = c_p(T_{01} - T_{02}) \quad \ldots\ldots [24]$$

Equation [22] with Equations [23] and [24] becomes

$$Q = c_p(T_{02} - T_w)(e^{\xi_0/2} - 1) \quad \ldots\ldots [25]$$

which is Equation [5].

Initial calculations for this study were made with a loss coefficient in the range $0.05 < \xi_0 < 0.08$. Because of the varying opinions as to the correct value of ξ_0 and because of its pronounced effect on cooled turbine performance, the range was extended to include $0.02 < \xi_0 < 0.08$. It is believed that this range will adequately bracket the actual value of ξ_0 for any particular blade design. It will also bring the data into closer agreement with more recent work completed on profile-loss factors as mentioned subsequently.

A discussion on the determination of ξ_0 is presented here to show some of the reasoning behind the variance of opinion and to verify, if possible, the use of a loss coefficient in the range $0.02 < \xi_0 < 0.08$.

For low Mach number and for the case in which (P/S) does not vary along the flow path, Hawthorne (3) shows that $\xi_0 = \xi_p$, the profile-loss factor. This would correspond to the case of impulse blading. For reaction blading and nozzles having decreasing area in the direction of gas flow, and for values of Mach number greater than zero, ξ_p becomes less than ξ_0.

Hawthorne (3) combined the following equation for the heat-transfer coefficient from gas to blade

$$\mathrm{Nu} = 0.14(\mathrm{Re})^{0.68}(\mathrm{Pr})^{1/3} \quad \ldots\ldots [26]$$

with the heat-balance equation for a blade passage

$$\alpha A(T_0 - T_w) = S\rho V c_p(T_{01} - T_{02}) \quad \ldots\ldots [27]$$

and Reynolds analogy to obtain

$$(e^{\xi_0/2} - 1) = 0.14\,(\mathrm{Re})^{-0.32}\,(\mathrm{Pr})^{-0.67}\Gamma \quad \ldots\ldots [28]$$

where $\Gamma = A/S$ = heat-transfer surface/cross-sectional flow area.

Equation [28] yields $\xi_0 = 0.026 - 0.084$ for Reynolds number of $5 \times 10^6 > \mathrm{Re} > 2 \times 10^4$ where Γ varies from $5 < \Gamma < 10$ for most blade shapes.

Subsequent to Hawthorne's analysis, Van Le (7) completed a study of loss coefficients in turbine passages. His results showed that

$$\xi_p = f(i, \alpha_1/\alpha_2, \theta, \mathrm{Re}, S/C)$$

Data taken from charts in reference (7) show the following trends:

(*a*) ξ_p decreases as α_1/α_2, Re, and S/C increase.
(*b*) ξ_p increases as θ and i increase.
(*c*) ξ_p for reaction blades is less than ξ_p for impulse blades.
(*d*) For normal variations in turning angle θ, degree of reaction α_1/α_2, pitch chord ratio S/C, incidence angle i, and blade Reynolds number Re, the profile-loss coefficient was found to vary within the limits, $0.02 < \xi_p < 0.14$.

These values of ξ_p would seem to agree fairly well with Hawthorne's analysis that $\xi_0 = \xi_p$, particularly at the higher values of Reynolds number.

Smith and Pearson (8) define a heat-extraction coefficient ϵ for a turbine stage

$$\epsilon = \frac{\Delta H}{W}\,\frac{u^2}{Jgc_p(T_0 - T_w)} \quad \ldots\ldots [29]$$

By comparison with Equation [27] for a cascade of blades, where $K_1 = 4$ for impulse blades the followiag relation can be established

$$\epsilon = (e^{\xi_0/2 - 1}) = \xi_0/2 \quad \ldots\ldots [30]$$

Reference (7) includes plots of ϵ versus flow coefficient which show that ϵ varies between $0.01 < \epsilon < 0.03$. These values show good agreement with Hawthorne's values for $\xi_0/2$ between $0.012 < \xi_0/2 < 0.042$.

Appendix 3

Derivation of Equations [9] and [10]

The definition of stage efficiency is

$$\eta_{stg} = \frac{W_{stg}}{\Delta h_{ss}} = \frac{\Delta h_{stg} - Q}{\Delta h_{ss}} \quad \ldots\ldots [31]$$

if the difference between the kinetic energy of the gases entering and leaving the stage is negligible. Then

$$\eta_{stg} = \left(1 + \frac{Q}{W}\right) = \frac{\Delta h_{stg}}{\Delta h_{ss}} = \frac{c_p(\Delta T_{stg})}{c_p(\Delta T_{ss})} \quad \ldots\ldots [32]$$

Assuming equal pressure ratio per stage and the condition curve Equation [17] defining η_s, Equations [32] become Equation [10]. Then if Q/W is zero (uncooled stage) $\eta_s = \eta_p$ from Equation [15] and Equation [10] reduces to Equation [9].

Discussion

J. B. Esgar.[3] One of the main questions in determining the

[3] Aeronautical Research Scientist, Lewis Flight Propulsion Laboratory, National Advisory Committee for Aeronautics, Cleveland, Ohio.

desirability of using turbine-blade cooling to permit increasing gas temperatures in gas-turbine engines is whether the quantity of heat removed from the cycle by cooling will cause losses that would cancel performance gains due to increased gas temperature. Most cycle analyses of cooled engines have required a knowledge of the engine configuration and rather tedious heat-transfer analyses to determine the quantity of heat removed from the cycle. The author presents a unique type of solution to determine the quantity of heat rejected by cooling without use of extensive heat-transfer analyses. To make intelligent use of his results, however, a knowledge of the magnitude of his loss factor ξ_0 is required. The range considered ($0.02 < \xi_0 < 0.08$) is probably greater than will be encountered on most cooled turbines.

Using methods of calculating heat-transfer rates for turbine blades that have been published in unclassified NACA reports, corresponding values of ξ_0 have been calculated at NACA using the relation between ξ_0 and heat-transfer rate presented by the author. These calculations were made for a wide variety of engines and it was found that ξ_0 was in the range 0.023 to 0.045. In most cases it was found that ξ_0 was less than 0.03. These results used in conjunction with the curves presented in the paper should give a reasonable indication of the effects of heat rejection on cooled turbine-engine performance.

It also should be stated that the analysis presented in the paper cannot be generalized to cover the effects of all types of turbine-cooling methods. The method applies only to the case where heat is removed from the turbine blades and is rejected to a sink that is external to the engine. A simple liquid-cooled system where the coolant circulates through the turbine blades and then carries the heat to a radiator or cooling tower would be one example of a type of cooled-turbine engine where this analysis is applicable. The analysis does not apply to air-cooling systems where air is bled from the compressor and used for cooling turbine blades. In general, air-cooling systems will result in somewhat poorer performance than presented in the paper.

In conjunction with the efficiency results presented for finite-staged turbines where "leaving losses" must be considered, it appears that some confusion might result owing to the fact that the efficiency levels are so very low compared with results previously presented. If the number of stages is greater than 2 or 3 the efficiency is probably approaching the efficiency that would be obtained with an infinite number of stages. The primary cause of the low efficiency shown for the finite-staged turbine is due to the fact that the curves are presented for very much lower pressure ratios than the results presented for turbines with an infinite number of stages.

In conclusion it can be said that the concept of the loss factor ξ_0 is not easy to understand completely, but by using the recommended values of this factor the paper presents a rather comprehensive picture of the effect of heat removal by turbine cooling on liquid-cooled gas-turbine power plants.

DAVID G. WILSON.[4] In the past I have been alternately encouraged and disillusioned, during some elementary work on blade cooling, by people who could prove conclusively that turbine cooling could either endow prize-winning efficiencies or crippling losses on gas-turbine power plants. In this paper most disadvantages of cooling are taken into account; in fact, some assumptions, such as the compressor efficiency of 85 per cent, would seem pessimistic for design point values. However, the heat losses connected with duct cooling and the power losses due to coolant pumping had been ignored, which could be significant factors. On the other hand, it is conceivable that the heat losses could be turned partly to heat gains by transferring the heat removed from blades and ducts to the air stream before combustion; or power could be recovered by using a steam turbine with liquid cooling. I should much appreciate the author's views on the general magnitude of the favorable and unfavorable effects of both extremes on their conclusions.

AUTHOR'S CLOSURE

It is indeed gratifying to receive the discussions of Messrs. Esgar and Wilson, both of whom have devoted a considerable amount of energy to the practical solution of the turbine-cooling problem. When our analysis was begun some years ago the magnitude of ξ_0 was not well established; so we used a rather wide range of values, 0.02 to 0.08. It is quite pertinent to the interpretation of the present results to know the proper reasonable range, 0.023 to 0.045, as suggested by Mr. Esgar.

Mr. Esgar and I seem to have some disagreement regarding the efficiencies of the finite-staged turbine but I suspect they can be resolved when we see each other. The results in Figs. 13 and 14 are presented to show the effect of number of stages on turbine performance. To keep the calculations from being too lengthy a lower pressure ratio was chosen; so the level of cycle efficiency is lower than in the previous curves. Nevertheless, the effect of number of stages is clearly shown. As number of stages increases the leaving loss decreases but the heat-transfer loss in the cooled part increases. These two opposing effects result in a maximum efficiency at a particular value of N for given design conditions.

Some of the questions regarding auxiliary losses are discussed in a companion paper, reference (9). We have not investigated the suggestions of Dr. Wilson regarding the recovery of some of the heat removed in cooling. They obviously would increase the efficiency and should be investigated to determine their economic feasibility.

---

[4] Visiting Fellow, Commonwealth Fund, Gas Turbine Department, Massachusetts Institute of Technology, Cambridge, Mass.

Analysis of the Effect of Blade Cooling on Gas-Turbine Performance

By J. C. BURKE,[1] B. L. BUTEAU,[2] and W. M. ROHSENOW[3]

This paper is an analytical study of the effects on specific air consumption and thermal efficiency of three types of blade-cooling systems. The methods considered are: (a) Air forced-convection cooling; (b) air transpiration cooling; (c) liquid forced-convection cooling.

The analysis was applied to a simple gas-turbine power plant containing a cooled turbine and an uncooled turbine both of which were composed of an infinite number of infinitesimal stages. Certain general design parameters were chosen for each coolant system and the effect of variation of these parameters on power-plant performance was studied. The three cooling methods also were compared against one another for otherwise identical conditions in the basic power plant.

The results of this work make it possible to predict, in a semiquantitative manner, the effect of cooling-system design on power-plant performance. In particular, the results of this paper show that for well-designed cooling systems operating at design conditions, appreciable net gains in performance can be realized by increasing turbine-inlet temperature beyond the temperature which the uncooled blades can withstand.

Nomenclature

The following nomenclature is used in the paper:

A_t = $(A_t)_N = (A_t)_B$, total transpiration area for blades, ft²

C_p = specific heat at constant pressure, Btu/lb$_m$–deg R
- C_{p1}, average for cooled turbine, 0.283, Btu/lb$_m$–deg R
- C_{p2}, average for mixing process, 0.277, Btu/lb$_m$–deg R
- C_{p3}, average for coolant in blades, 0.264, Btu/lb$_m$–deg R

$De \equiv \frac{4S}{P'}$, equivalent diameter of blade-coolant passages, ft

$f \equiv 2g_0\tau_0/\rho V^2$, friction factor

$G_c \equiv \frac{m_N}{S}$ or $\frac{m_B}{S}$, coolant flow per unit area, lb$_m$/sq ft–sec

$G_t \equiv \frac{m_N}{A_t}$ or $\frac{m_B}{A_t}$, coolant flow per unit area, lb$_m$/ft²–sec

ΔH = mixing loss per unit mass of main working fluid, Btu/lb$_m$

h = enthalpy, Btu/lb$_m$

K_1 = impulse-blade factor (defined in reference 8)[4]

$k_1 \equiv M/S$, turbine constant, lb$_m$/sq ft–sec

K = thermal conductivity, Btu/sec–ft–deg R

k = ratio of specific heats

l = blade length, ft

M = main working fluid mass flow, lb$_m$/sec

m = $m_N + m_B$, total coolant mass flow, lb$_m$/sec

P' = $(P')_N = (P')_B$, total perimeter of coolant passages, ft

P = power, ft–lb$_f$/sec

P_B = power output of turbine B, ft–lb$_f$/sec

Q = heat flow, Btu/sec

Q = heat flow per unit mass to infinitesimal blade row, Btu/lb$_m$

Q_1 = heat loss to blades per unit mass of M, Btu/lb$_m$

Q_{in} = power-plant heat input per unit mass of M, Btu/lb$_m$

R_A = reheat factor for turbine A

R_B = reheat factor for turbine B

$r \equiv \frac{P_{03a}}{P_{0a}}$, total power-plant pressure ratio

$r_A = \frac{P_{03a}}{P_{04a}}$, expansion ratio turbine A

$r_B = \frac{P_{04a}}{P_{0a}}$, expansion ration turbine B

r_h = turbine wheel-blade root radius, ft

r_T = turbine wheel-blade tip radius, ft

S = $(S)_N = (S)_B$ — total cross-sectional flow area for blades, sq ft

T_w = blade wall temperature, deg R

$\bar{T}$ = average temperature, deg R

u = turbine-wheel tip velocity, fps

$\bar{u} \equiv \frac{u(r_h + r_T)}{2r_T}$ — mean blade velocity, fps

V_t = tangential velocity, fps

V_{rel} = velocity relative to rotor coolant passages, fps

W = maximum work for infinitesimal stage, Btu/lb$_m$

$W_A \equiv \frac{\mathsf{P}_A}{JM}$, work output turbine A, Btu/lb$_m$

$W_B \equiv \frac{\mathsf{P}_B}{(M+m)J}$, work output turbine B, Btu/lb$_m$

$W_{C1} \equiv \mathsf{P}_{C1}/M + mJ$, work input main compressor, Btu/lb$_m$

$W_{C2} \equiv$ work required to circulate liquid coolant

$W_{net} \equiv \frac{\mathsf{P}_{net}}{MJ}$ — net power-plant work output, Btu/lb$_m$

η = power-plant cycle efficiency

η_{C1} = main-compressor efficiency

$\xi_0 \equiv \int_{x=0}^{l} f\frac{P'}{S}\,dx$, loss factor (defined in reference 8)

τ = torque, lb$_f$–ft

ω = angular velocity, rad/sec

α = heat-transfer coefficient, Btu/sq ft–sec–deg R

η_P = turbine polytropic efficiency

η_T = turbine efficiency

η_x = blade-coolant passage effectiveness

η_x' = apparent effectiveness (defined in Appendix 2)

Subscripts

0 = total stagnation conditions

---

[1] Mechanical Engineer, Boeing Airplane Company, Seattle, Wash. Assoc. Mem. ASME.

[2] Lieutenant, USN, Long Beach Naval Shipyard, Long Beach, Calif.

[3] Associate Professor of Mechanical Engineering, Massachusetts Institute of Technology, Cambridge, Mass. Mem. ASME.

[4] Numbers in parentheses refer to the Bibliography at the end of the paper.

Contributed by the Gas Turbine Power Division and presented at the Diamond Jubilee Annual Meeting, Chicago, Ill., November 13–18, 1955, of The American Society of Mechanical Engineers.

Note: Statement and opinions advanced in papers are to be understood as individual expressions of their authors and not those of the Society. Manuscript received at ASME Headquarters, August 30, 1955. This paper was not preprinted.

0_r = relative stagnation conditions
s = constant entropy process
N = nozzles
B = blades
$*$ = zero transpiration mass flow
$1a$–$4a$ = states of main working fluid
$1b$–$3b$ = states of total coolant
$4d$–$6d$ = states of bucket coolant
$4e$–$6e$ = states of nozzle coolant
7, 8 = states of total mixture
M = main working fluid
m = coolant

Introduction

In reference (8) the performance of a simple gas-turbine power plant utilizing cooled blades was analyzed for a wide range of operating conditions. This analysis considered only the effect of heat loss from the working fluid to the cooled blades and did not investigate the losses which might be incurred in circulating the coolant. In this paper the analysis is extended to include the over-all effects on power-plant efficiency and specific air consumption of three types of cooling systems:

1 Forced-convection air cooling—air is pumped through radial passages in the blades and discharges into the working fluid.

2 Transpiration air cooling—air is forced through hollow porous blades and discharges into the working fluid.

3 Liquid cooling—liquid is circulated through passages in the blades in a closed circuit and cooled externally.

Forced Convection—Air-Cooled Power Plant

Description of System. The basic power plant studied in this investigation is composed of a compressor C_1, a burner D, a cooled turbine A, and an uncooled turbine B, Fig. 1. Each turbine is composed of an infinite number of infinitesimal impulse stages of polytropic efficiency η_p. The coolant air is supplied by a bleed connection from the discharge of C_1. The expansion ratio of turbine A varies so that the inlet temperature to turbine B remains constant at the maximum allowable blade temperature.

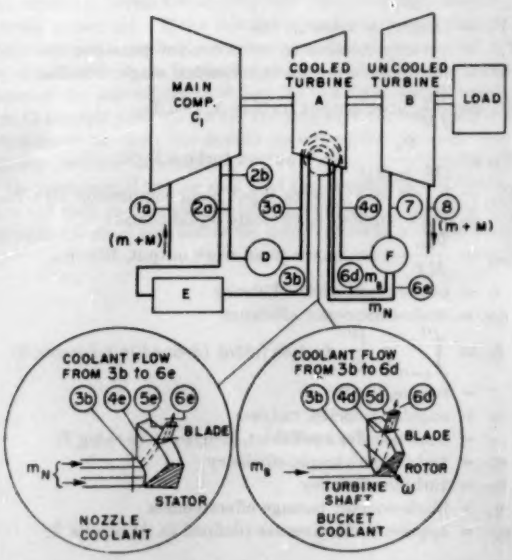

Fig. 1 Schematic of Gas-Turbine Power Plant With Forced-Convection Air-Cooled Blades

The coolant m is compressed in C_1, passes through a heat exchanger E, and is ducted to coolant passages leading to the buckets and nozzles. Appropriate portions of the coolant, m_N and m_B, emerge from the nozzles and buckets, and, at states 6e and 6d, respectively, mix with the main working fluid in the mixing chamber F. The resultant mixture, now at state 7, expands through the uncooled turbine B.

This viewpoint assumes that any work done by the coolant within turbine A would be counterbalanced by the aerodynamic losses which it causes. According to this hypothesis, the coolant would discharge against local turbine pressure—which for the limiting case would be the inlet pressure of turbine A.

In this power plant it is seen that, in addition to the heat loss to the blades, other losses are present; such as, (*a*) the work input to the coolant in the compressor, (*b*) the pumping work done on the coolant as it passes through the rotor and blades, and (*c*) the enthalpy loss of the main working fluid due to mixing with the coolant at F. However, to some extent, energy will be recovered when the coolant expands through the uncooled turbine B.

The two design parameters listed in the following were chosen as being important to the cooling system and its effect on the over-all power plant. The base value represents the value at which each was fixed when either of the other two parameters was varied.

Design parameter	Base value	Range studied
η_x-coolant-passage effectiveness	0.6	0.4–0.8
T_{0a} coolant inlet temperature	1200 R	500–1500 R

η_x is defined as (see nomenclature)

$$\eta_x \equiv \frac{T_{0_{6e}} - T_{0_{4e}}}{T_w - T_{0_{4e}}} \quad [1]$$

As just shown, η_x may be written immediately in terms of nozzle-coolant temperatures but the effect of centrifugal temperature rises must be considered (see Appendix 2) in order to relate η_x to bucket-coolant temperatures.

The coolant temperature T_{0a} in this analysis is maintained independent of the outlet conditions of the auxiliary compressor by the heat exchanger E. The power plant is not, however, charged with the heat added or subtracted from the coolant in E. The base value of T_{0a}, 1200 R, corresponds to what would be the available coolant temperature if the coolant air were bled from the top of the main compressor without passing through the heat exchanger.

Method of Analysis—Forced-Convection Air-Cooled Power Plant. The general expression for the efficiency of a heat engine is

$$\eta \equiv \frac{W_{net}}{Q_{in}} \quad [2]$$

Referring to Fig. 1, the efficiency of the forced-convection air-cooled power plant may be written as follows

$$\eta = \eta_M + (m/M)\eta_m \quad [3]$$

where

$$\eta_M \equiv \frac{W_A + W_B - W_{C1}}{Q_{in}} \quad [4]$$

and

$$\eta_m \equiv \frac{W_B - W_p - W_{C1}}{Q_{in}} \quad [5]$$

The term W_p in Equation [5] is the pumping work done by the rotor on the coolant flowing within the rotor.

As shown in Appendix 1, η_M, the efficiency of the main working-fluid cycle, may be determined by the method outlined in reference (8) if the values of Q_1/W_A and $\Delta H/W_A$ are known. Q_1 represents the heat loss from the working fluid to the cooled blades. ΔH represents the enthalpy loss to the main working fluid caused by mixing with the coolant. The analysis used to evaluate Q_1/W_A and $\Delta H/W_A$ is described in the following.

Reference (8) presents a relation for the ratio Q_1/W_A for a cascade of blades. To obtain average values of this ratio for the nozzle or bucket rows, T_0 should be interpreted as the average stagnation temperature relative to either nozzles or buckets. Making use of the average stagnation temperatures (Equations [7] and [8]) and noting from Fig. 2(a) that $T_{03a} = T_w + \Delta H/C_{p2}$ where $T_w = T_{2r}$, expressions for $(Q_1/W_A)_N$, $(Q_1/W_A)_B$, and Q_1/W_A are determined

$$\frac{Q}{W} = \frac{C_p(T_0 - T_w)(e^{\xi_0/2} - 1)}{K_1 \dfrac{u^2}{2g_0J}} \quad \ldots\ldots [6]$$

$$(T_{0r})_N = \frac{T_{03a} + T_{04a}}{2} \quad \ldots\ldots [7]$$

$$(T_{0r})_B = \frac{T_{03a} + T_{04a} - \dfrac{u^2}{C_pJg_0}}{2} \quad \ldots\ldots [8]$$

$$\left(\frac{Q_1}{W_A}\right)_N = \frac{C_{p1}\left(T_{03a} - T_w + \dfrac{\Delta H}{C_{p2}}\right)(e^{\xi_0/2} - 1)}{2K_1 \dfrac{u^2}{2g_0J}} \quad \ldots\ldots [9]$$

$$\left(\frac{Q_1}{W_A}\right)_B = \frac{C_{p1}\left(T_{03a} - T_w + \dfrac{\Delta H}{C_{p2}} - \dfrac{u^2}{C_pJg_0}\right)(e^{\xi_0/2} - 1)}{2K_1 \dfrac{u^2}{2g_0J}} \quad \ldots\ldots [10]$$

$$\frac{Q_1}{W_A} = \left(\frac{Q_1}{W_A}\right)_N + \left(\frac{Q_1}{W_A}\right)_B \quad \ldots\ldots [11]$$

$\Delta H/W_A$, the enthalpy-loss term, is found by applying an energy balance to the adiabatic mixing at F. This derivation is carried out in Appendix 3 and results in Equation [12]. The terms ϵ and σ, which are defined and tabulated in Appendix 3, account for temperature rises due to rotational work. The term η_s' (see Appendix 2) is an apparent effectiveness which includes rotational effects as well as heat transfer

$$\frac{\Delta H}{W_A} = \frac{C_{p2}}{C_{p3}}\left[\left(\frac{Q_1}{W_A}\right)_N\left(\frac{1-\eta_s}{\eta_s}\right) + \left(\frac{Q_1}{W_A}\right)_B\left(\frac{1-\eta_s'-\epsilon}{\eta_s'-\sigma}\right)\right] \quad \ldots\ldots [12]$$

Equations [9] to [12] have been solved by iteration for Q_1/W_A and $\Delta H/W_A$, employing the additional relation that

$$\frac{\Delta H}{C_{p2}} = \frac{\Delta H}{W_A}\frac{W_A}{C_{p2}} = \frac{\Delta H}{W_A}\left(\frac{1}{C_{p2}}\right)\left(\frac{h_{03a} - h_{07}}{1 + \dfrac{Q_1}{W_A} + \dfrac{\Delta H}{W_A}}\right)$$

Having obtained values for Q_1/W_A and $\Delta H/W_A$, η_M was calculated as indicated in Appendix 1. The values of η_M obtained are plotted in Fig. 3.

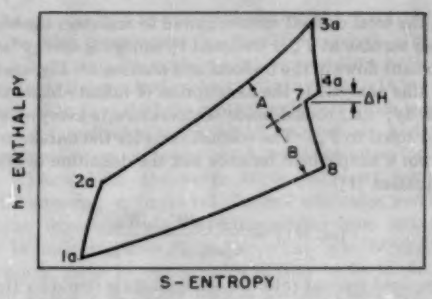

(a) FORCED CONVECTION AIR COOLED BLADES

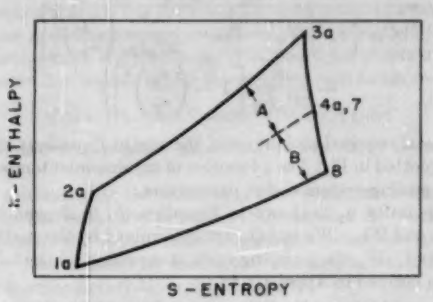

(b) TRANSPIRATION AIR COOLED BLADES

FIG. 2 TYPICAL CYCLE DIAGRAMS FOR MAIN WORKING FLUID, M

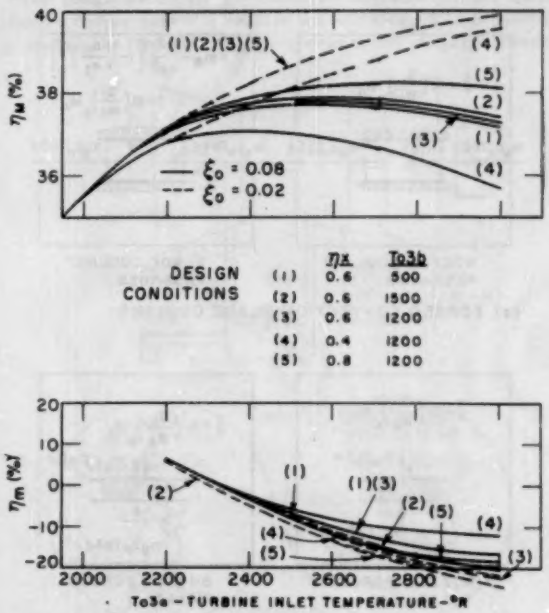

FIG. 3 VARIATION IN η_M AND η_m WITH TURBINE-INLET TEMPERATURE AND SYSTEM DESIGN PARAMETERS FOR FORCED-CONVECTION AIR-COOLED POWER PLANT

m/M, the total coolant ratio required to maintain the blades in the cooled turbine at T_w is obtained by applying energy balances to the coolant flows in the buckets and nozzles, see Fig. 4(*a*). Implicit in this analysis is the assumption of infinite-blade thermal conductivity; i.e., cooled-blade temperature is everywhere constant and equal to T_w. The coolant ratio for the nozzles is determined from a simple heat balance and the definition of effectiveness (Equation [1])

$$(m/M)_N = \frac{(Q_1/W_A)_N W_A}{C_{pg}\eta_s(T_w - T_{02b})} \quad \ldots\ldots [13]$$

The required coolant ratio for the buckets is found by the same general technique but the details are complicated by centrifugal effects. The derivation is carried out in Appendix 2

$$(m/M)_B = \frac{(Q_1/W_A)_B W_A}{C_{pg}\left\{\eta_s'\left[T_w - T_{02b} - \frac{u^2}{2C_pJg_0}\left(\frac{r_h}{r_T}\right)^2\right] - \frac{u^2}{2C_pJg_0}\left[1-\left(\frac{r_h}{r_T}\right)^2\right]\right\}} \quad \ldots\ldots [14]$$

The total required coolant ratio, the sum of Equations [13] and [14], is plotted in Fig. 5 as a function of turbine-inlet temperature and the cooling-system design parameters.

The quantity η_m is shown in Equation [5] to depend on W_B, Q_{1a}, W_p, and W_{C1}. W_B and Q_{1a} are determined by the methods of Appendix 1. W_p, the pumping work, is expressed by the following equation derived in Appendix 4

$$W_p = \frac{(m/M)_B}{m/M}\frac{u^2}{g_0 J} \quad \ldots\ldots [15]$$

The work done by compressor C_1 on the coolant is a function of both the net stagnation pressure drop in the coolant-flow path and the stagnation pressure at the blade tips, p_{02b}. For simplicity, the pressure drops in both nozzles and buckets are considered to be similar. It is further assumed that the stagnation pressure at the turbine-inlet nozzle tips is low enough to permit positive flow from the compressor-bleed point. This reasoning permits the use of a single compressor-bleed connection. This study assumes that all of the coolant will be bled at compressor discharge pressure and the correct distribution of coolant will be maintained by throttling the paths of lower resistance. This assumption furnishes a conservative estimate of the compressor work accomplished in the coolant cycle.

η_m, as calculated in accordance with the preceding discussion, is plotted in Fig. 3. Now, in conjunction with the values of η_M and m/M previously obtained it is possible to determine η per Equation [3]. The power-plant efficiency η and specific air consumption are plotted in Figs. 6 and 7. In this investigation specific air consumption is based on total air flow as follows

$$\text{Specific air consumption}\left(\frac{\text{lb}_m}{\text{hp-hr}}\right) = \frac{(2545)(1 + m/M)}{(\eta)(Q_{1a})} \quad \ldots [16]$$

Results of Analysis—Forced Convection. In Fig. 3, η_M and η_m are plotted against turbine-inlet temperature for a range of cooling-system design parameters. It is seen that η_M, the efficiency of the main working-fluid cycle, is primarily a function of η_s and turbine-inlet temperature. This is because, at constant T_{02a}, changes in η_M result from variations in the mixing loss $\Delta H/W_A$. $\Delta H/W_A$ is relatively unaffected by coolant-inlet temperature since, say, increasing T_{02b} tends both to increase coolant flow and increase coolant-discharge temperature. Both of these effects work in opposite directions and tend to be mutually canceling.

η_m, which may be thought of as a measure of the efficiency of the coolant cycle is, to a first approximation, a function of η_s and T_{02a}. This is because, at constant T_{02a}, changes in η_m result primarily from changes in W_B. These changes in W_B are the result of variations in the mixing loss $\Delta H/W_A$, which is relatively unaffected by changes in T_{02b}.

The coolant ratios required at various turbine-inlet temperatures are plotted in Fig. 5. As might be expected, increasing η_s

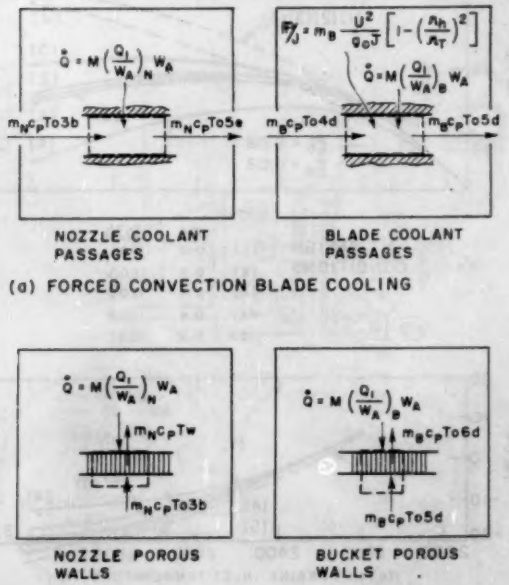

FIG. 4 ENERGY BALANCES APPLIED TO COOLING PROCESSES

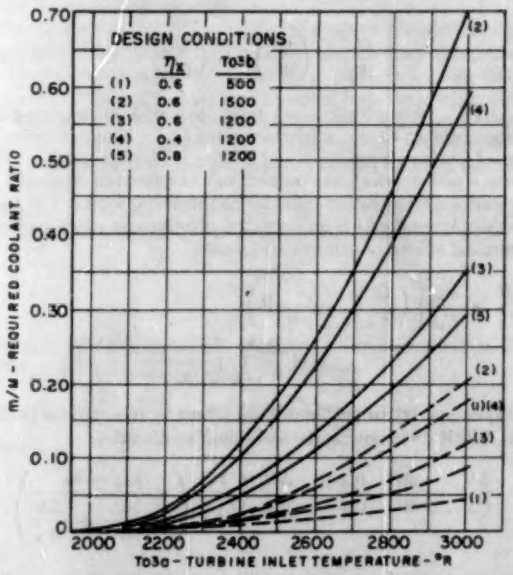

FIG. 5 EFFECT OF TURBINE-INLET TEMPERATURE AND DESIGN PARAMETERS ON REQUIRED COOLANT RATIO FOR FORCED CONVECTION ON AIR-COOLED POWER PLANT

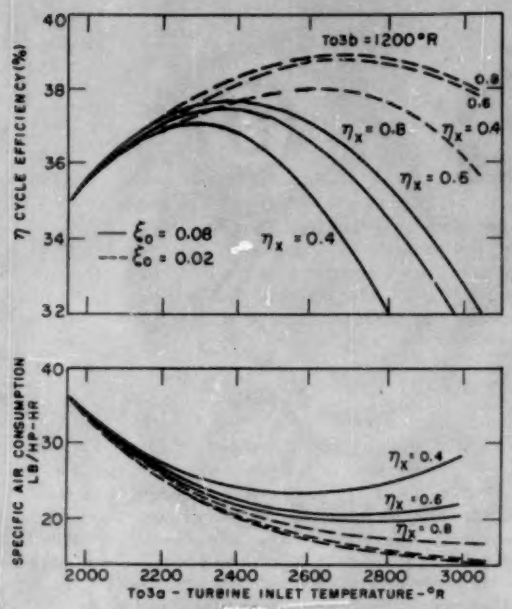

FIG. 6 EFFECT OF BLADE-COOLANT PASSAGE EFFECTIVENESS ON PERFORMANCE OF FORCED-CONVECTION AIR-COOLED POWER PLANT

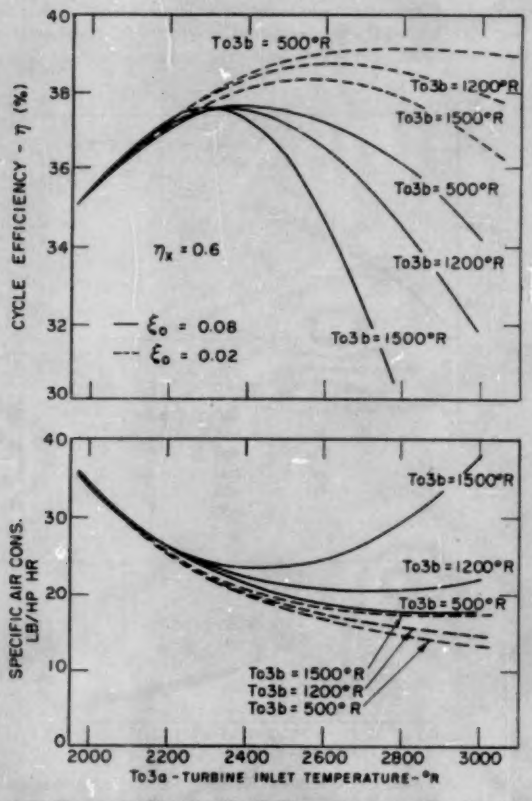

FIG. 7 EFFECT OF COOLANT-INLET TEMPERATURE ON PERFORMANCE OF FORCED-CONVECTION-COOLED POWER PLANT

and reducing T_{3b} help to minimize the coolant ratio. The effect of coolant-inlet temperature is especially marked. At T_{3a} = 3000 R, decreasing the coolant-inlet temperature from 1500 to 500 R reduces the required coolant ratio from 71 to 18 per cent for $\xi_0 = 0.08$. For $\xi_0 = 0.02$ the coolant ratios are much less.

In Fig. 6 the effect of turbine-inlet temperature and coolant-passage effectiveness on power-plant design-point performance is shown. Throughout the range of turbine-inlet temperature studied, increasing η_x improved thermal efficiency, and lowered specific air consumption. The gains arising from increasing η_x are due to the increases in η_M and decreases in m/M which result. The greatest gains in performance appear to lie in eliminating very low values of η_x rather than in attaining near 100 per cent effectiveness.

The effect of coolant-inlet temperature on power-plant performance is shown in Fig. 7. T_{3a} is found to have little effect on maximum efficiency, but reducing T_{3b} does result in much lower minimum specific air consumption and much better efficiency at high turbine-inlet temperatures. The beneficial effects of reducing T_{3b} are due mainly to the decreased coolant ratios required.

TRANSPIRATION-COOLED POWER PLANT

The basic transpiration air-cooled power plant is shown in Fig. 8.

It is assumed that the addition of the coolant mass has no net effect on the expansion process within turbine A; that is, the work done by the coolant mass is exactly counterbalanced by the enthalpy losses caused by mixing and the aerodynamic losses resulting from boundary-layer thickening.

In general, the losses for the transpiration-cooled power plant are similar in nature to those in the forced-convection-cooled power plant. Two major differences exist, however: (*a*) As mentioned previously, it is assumed there is no net enthalpy loss due to mixing of the coolant and working fluid (i.e., $\Delta H/W_A = 0$); (*b*) The heat flow to the blades Q_1 will be reduced materially because of the insulating film produced by the transpiring coolant.

The design parameter governing the operation of the transpiration cooling system is listed in the following. The parameter η_x used in the forced-convection system is now dropped because

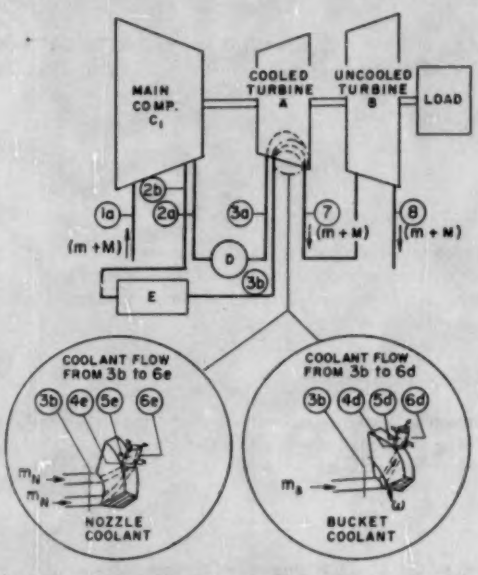

FIG. 8 SCHEMATIC OF GAS-TURBINE POWER PLANT WITH TRANSPIRATION AIR-COOLED BLADES

the contact between coolant and wall is so great that no significant temperature difference exists between the emerging coolant and the blade wall.

Design parameter	Base value	Range
T_{03b} coolant-inlet temperature	1200 R	500–1500

T_{03b} has approximately the same effect on the transpiration system as on the forced-convection system. The discussion at the beginning of the preceding section for T_{03b} also applies here.

Method of Analysis—Transpiration. The efficiency of the transpiration-cooled power plant may be expressed by Equations [3], [4], [5]. However, because of the differences in the physical processes the determination of the component terms of these equations is different from the methods developed in the second part of the preceding section.

The calculation of η_M for given values of Q_1/W_A is similar to the method for forced convection. The details are outlined in Appendix 1. As will be shown later, however, the term Q_1/W_A can no longer be evaluated solely by the equations developed in the preceding section.

In a transpiration-cooled power plant, the coolant forms an insulating layer which reduces the gas-to-blade heat-transfer coefficient. Allowing starred terms to denote heat-transfer conditions for zero transpiration mass flow, the following equations are written

$$(Q_1/W_A)_N = (Q_1/W_A)_N^*(\alpha/\alpha^*)_N \quad [17]$$

$$(Q_1/W_A)_B = (Q_1/W_A)_B^*(\alpha/\alpha^*)_B \quad [18]$$

Now $(Q_1/W_A)_N^*$ and $(Q_1/W_A)_B^*$ can be evaluated from Equations [9] and [10]. (Noting that, for transpiration, $\Delta H/C_{p3} = 0$.)

Several methods are given in the literature for determining the ratio α/α^* (references 1, 2). A simple relation is the "film-theory" expression proposed by Mickley (7)

$$\alpha/\alpha^* = \frac{\frac{G_t C_p}{\alpha^*}}{e^{\left[\frac{G_t C_p}{\alpha^*}\right]} - 1} \quad [19]$$

In Appendix 5, Equation [19] is rewritten in terms of the nozzle-coolant ratio and the loss factor ξ_b. This equation applies well for the buckets if $(\alpha/\alpha^*)_N$ and $(m/M)_N$ are replaced by $(\alpha/\alpha^*)_B$ and $(m/M)_B$

$$(\alpha/\alpha^*)_N = \frac{(m/M)_N/(e^{\xi_b^*/2} - 1)}{e^{\left[\frac{(m/M)_N}{e^{\xi_b^*/2}-1}\right]} - 1} \quad [20]$$

The coolant ratio for the nozzles is determined from a simple energy balance applied to the cooling process, see Fig. 4(*b*). It is assumed in this energy balance that the coolant leaves the blade wall at wall temperature

$$(m/M)_N = \frac{(Q_1/W_A)_N W_A}{C_{p3}(T_w - T_{03b})} \quad [21]$$

The coolant ratio for the buckets is obtained in a similar manner. The energy balance is applied at a mean blade radius such that the blade tangential velocity is

$$\bar{u} = u\left(\frac{r_T + r_h}{2r_T}\right)$$

Therefore the absolute stagnation temperatures of the coolant before and after the porous wall are

$$T_{03d} = T_{03b} + \frac{\bar{u}^2}{C_p J g_0}, \quad \text{and} \quad T_{04d} = T_w + \frac{\bar{u}^2}{2C_p J g_0}$$

$$(m/M)_B = \frac{(Q_1/W_A)_B W_A}{C_{p3}\left(T_w - T_{03b} - \frac{\bar{u}^2}{2C_p J g_0}\right)} \quad [22]$$

From Equations [17] through [22] the coolant ratios and heat-loss terms (Q_1/W_A) are calculated. The resulting curves of η_M and m/M are plotted in Figs. 9 and 10.

η_m is determined by evaluating W_B, Q_{in}, W_p, and W_{C1}. W_{C1}, W_B, and Q_{in} are calculated as shown in Appendix 1. An expression for W_p, the rotor pumping work is derived in Appendix 4, assuming that the rate of transpiration per unit radial length is constant in the buckets

$$W_p = 0.730\,\frac{(m/M)_B}{m/M}\,\frac{u^2}{g_0 J} \quad [23]$$

Results of Analysis—Transpiration Cooling. In Fig. 9, η_M and η_m are plotted against turbine-inlet temperature for various constant values of the cooling-system design parameter. It is seen that increasing coolant-inlet temperature causes a small increase in the quantity η_M. This is because higher values of T_{03b} result in larger coolant flows which in turn increase the coolant insulating effect and reduce heat loss to the blades.

The required coolant ratios are plotted in Fig. 10. As in the case of the forced-convection cooling system, increasing T_{03b} increases the coolant ratio. The most important feature of these curves is the low coolant ratios required for transpiration as compared to those required for forced convection. When $T_{03b} = 1200$ R and $T_{03a} = 3000$ R, the coolant ratio required for transpiration is less than one third of that required for forced convection.

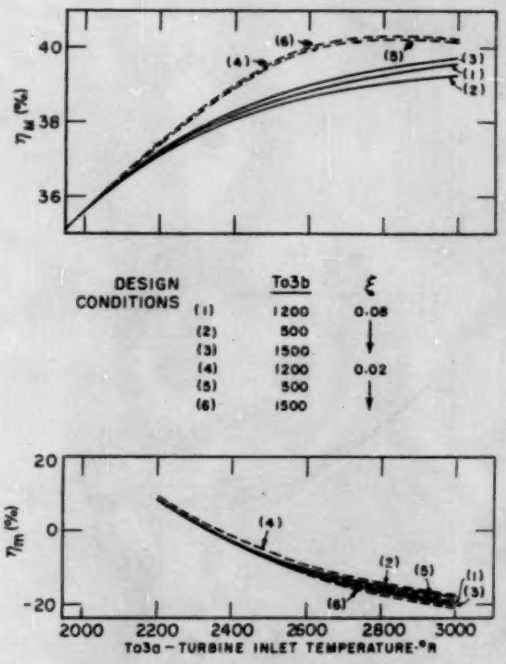

FIG. 9 VARIATION IN η_M AND η_m WITH TURBINE-INLET TEMPERATURE AND SYSTEM-DESIGN PARAMETERS FOR TRANSPIRATION AIR-COOLED POWER PLANT

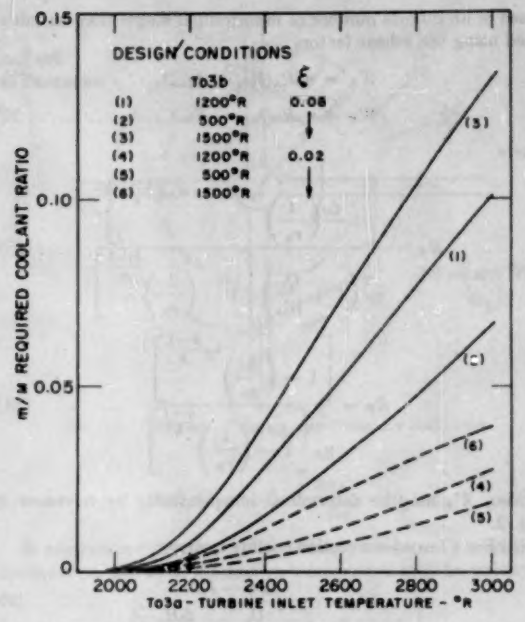

FIG. 10 EFFECT OF TURBINE-INLET TEMPERATURE AND DESIGN PARAMETERS ON REQUIRED COOLANT

In Fig. 11 the effects of the design parameter T_{o3} on power-plant performance is shown. As in the case of forced convection, reducing coolant-inlet temperature tends to increase efficiency and lower specific air consumption. However, the transpiration-cooled power plant is much less sensitive to variation in T_{o3} than was the forced-convection power plant.

It should be noted here that the results as predicted for the transpiration-cooled power plant are probably considerably better than could be obtained in practice. The assumptions (see beginning of this section) are considered to be adequate for this semiquantitative analysis. In practice, however, the large wakes caused by transpiring coolant would increase the aerodynamic losses and the low energy level of the coolant would create higher enthalpy mixing losses in the initial stages of turbine A. These losses probably would overbalance the work done by the coolant mass in expanding through the cooled turbine. Furthermore, transpiration cooling requires that the coolant be at a higher pressure than the main working-fluid pressure. This would create the need for a small auxiliary compressor to supply coolant to the first-stage stator at pressures somewhat higher than main-compressor discharge pressure. The use of such a compressor would tend to reduce the optimistic results obtained in this analysis.

LIQUID-COOLED POWER PLANT

The liquid-cooled power plant considered in this study is cooled by a closed liquid circuit. The liquid flows through loop-type passages in the blades and is cooled externally in a heat exchanger. If the coolant flows through both nozzles and buckets in series, the analysis of Appendix 6 shows that, for a wide range of operating variables, the net coolant pressure rise in the buckets and rotors is sufficient to overcome all the system frictional pressure drops and no circulating pump is necessary. Also, since the

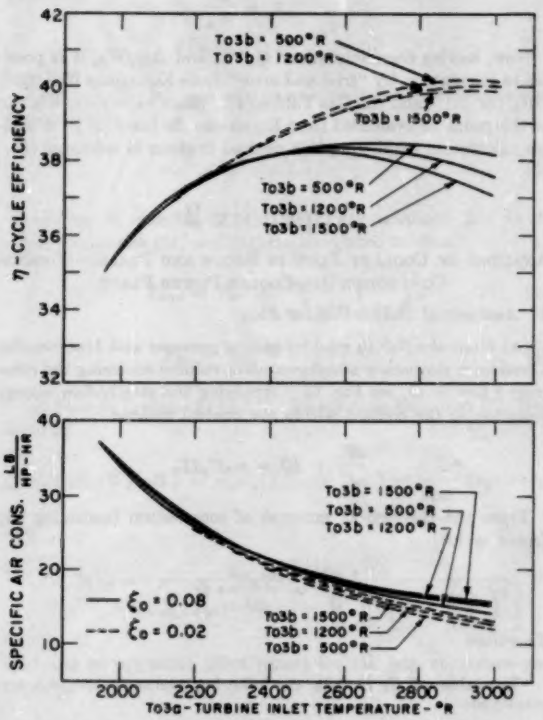

FIG. 11 EFFECT OF BLADE-COOLANT INLET TEMPERATURE ON PERFORMANCE OF TRANSPIRATION-COOLED POWER PLANT

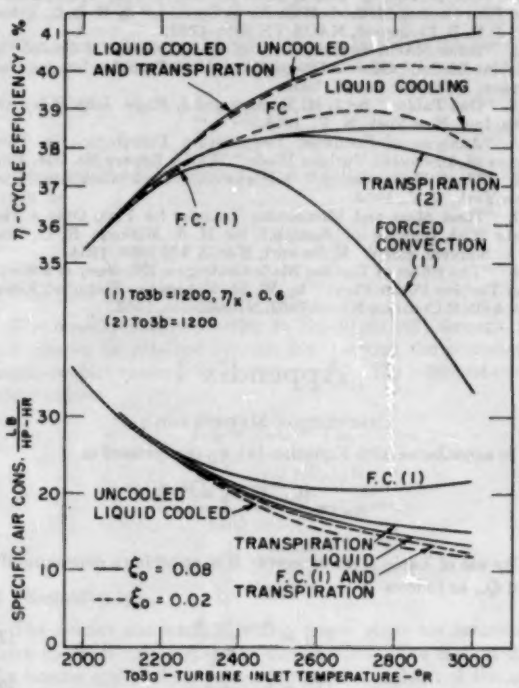

FIG. 12 COMPARISON OF PERFORMANCE OF POWER PLANTS EMPLOYING DIFFERENT SYSTEMS OF COOLING

coolant flows both outward and inward in the rotor and buckets no net pumping work is done by the rotor.

From the foregoing discussion it is seen that the quantity η_m (Appendix 6) is zero and η is just equal to η_M. The cycle efficiency for the water-cooled power plant is then calculated according to the methods of Appendix 1. The results of these calculations are plotted in Fig. 12.

Conclusions

1 The results of this investigation show that appreciable net improvements in gas-turbine performance can be attained by the companion processes of increasing turbine-inlet temperature and blade cooling.

2 Liquid-cooled turbines are capable of lower specific air consumption than air-cooled turbines.

3 Transpiration air cooling results in lower specific air consumption and less sensitivity to cooling-system design parameters than forced-convection air cooling.

4 For both types of air-cooled power plants, decreasing coolant-inlet temperature and reducing coolant-discharge pressure improved power-plant performance. For the forced-convection system, blade internal geometry (i.e., coolant-passage effectiveness) has significant effects on performance.

Acknowledgment

This work was sponsored by the Office of Naval Research. We gratefully acknowledge the financial support of that organization.

Bibliography

1 "The Effect of Mass Transfer on the Compressible Turbulent Boundary-Layer Skin Friction and Heat Transfer," by W. H. Dorrance and F. J. Dore, *Journal of the Aeronautical Sciences*, vol. 21, 1954, pp. 404–410.

2 "Comparison of Effectiveness of Convection, Transpiration, and Film Cooling Methods With Air as Coolant," by E. R. G. Eckert and J. N. B. Livingood, NACA TN 3010. 1953.

3 "Some NACA Investigations of Heat Transfer of Cooled Gas Turbine Blades," General Discussion on Heat Transfer, London Conference, IME and ASME, 1951.

4 "Gas Tables," by J. H. Keenan and J. Kaye, John Wiley and Sons, Inc., New York, N. Y., 1948.

5 "Analysis of Spanwise Temperature Distribution in Three Types of Air-Cooled Turbine Blade," NACA Report No. 994, 1950.

6 "Heat Transmission," McGraw-Hill Book Company, Inc., New York, N. Y., 1954.

7 "Heat Mass and Momentum Transfer for Flow Over a Flat, Plate With Blowing or Suction," by H. S. Mickley, R. C. Ross A. L. Squyers, and W. E. Stewart, NACA TN 3208, 1954.

8 "The Effect of Turbine Blade Cooling on Efficiency of a Simple Gas Turbine Power Plant," by W. M. Rohsenow, Technical Report No. 4 ONR Contract N5-ori-7862, NR-091-158, 1953.

Appendix 1

Calculation Method for η_M

In accordance with Equation [4], η_M is expressed as

$$\eta_M \equiv \frac{W_A + W_B - W_{C1}}{Q_{in}}$$

By use of Table 1, reference (4), it is possible to determine W_{C1} and Q_{in} as follows

$$W_{C1} = \frac{h_{02a'} - h_{01a}}{\eta_{C1}} \quad [24]$$

$$Q_{in} = h_{03a} - h_{02a} \quad [25]$$

Reference (8) shows that the work output of turbines composed of an infinite number of infinitesimal stages may be calculated using the reheat factors

$$W_A = \eta_P R_A (h_{03a} - h_{04a'}) \quad [26]$$

$$W_B = \eta_P R_B (h_{07} - h_{08'}) \quad [27]$$

where

$$R_A = \frac{\left[1 - \left(\frac{1}{r_A}\right)^{\eta_P(1 - Q_1/W_A)\frac{k-1}{k}}\right]}{\eta_P\left(1 + \frac{Q_1}{W_A}\right)\left[1 - \left(\frac{1}{r_A}\right)^{\frac{k-1}{k}}\right]} \quad [28][b]$$

$$R_B = \frac{\left[1 - \left(\frac{1}{r_B}\right)^{\eta_P\frac{k-1}{k}}\right]}{\eta_P\left[1 - \left(\frac{1}{r_B}\right)^{\frac{k-1}{k}}\right]} \quad [29][b]$$

Also, W_A may be determined independently by reference to Fig. 2:

(*a*) For a forced-convection cooling system

$$W_A = \frac{h_{03a} - h_{07}}{1 + \frac{Q_1}{W_A} + \frac{\Delta H}{W_A}} \quad [30]$$

(*b*) For a transpiration air-cooling system or liquid cooling

$$W_A = \frac{h_{03a} - h_{07}}{1 + \frac{Q_1}{W_A}} \quad [31]$$

Now, having once determined Q_1/W_A and $\Delta H/W_A$, it is possible to calculate r_A by "trial and error" from Equations [26], [28], [30], (or [31]) and the Gas Tables (4). Since $r_B = r/r_A$, W_B can at this point be evaluated from Equations [29] and [27]. A sample calculation employing this method is given in reference (8).

Appendix 2

Analysis of Coolant Flow in Rotor and Blades—Forced-Convection Air-Cooled Power Plant

1 *Analysis of Bucket-Coolant Flow*

(*a*) *General—flow in rotating coolant passages with heat transfer.* Consider a stationary annular control volume enclosing the rotor from r to $r + dr$, see Fig. 13. Applying the steady-flow energy equation to the coolant within the control volume

$$\frac{dP}{J} + d\dot{Q} = \dot{m}_B C_p dT_s$$

From the theorem of moment of momentum (assuming slip factor = 1.0)

$$\frac{dP}{J} = \frac{2\dot{m}_B\omega^2}{g_o J} r\,dr$$

Therefore

[b] In evaluating R_A and R_B, the following average values of k were employed:

k(cooled turbine) = 1.32

k(uncooled turbine) = 1.35

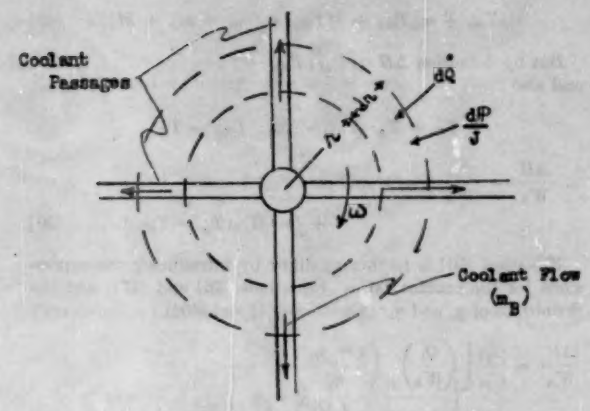

FIG. 13 CONTROL VOLUME FOR COOLANT ANALYSIS

$$m_B C_p dT_0 = d\dot{Q} + \frac{2m_B\omega^2}{g_0 J} r\,dr \quad [32]$$

At any radius r the relative (to coolant passage wall) stagnation temperature and total stagnation temperature may be written

$$T_0 = T + \frac{1}{2}\left[\frac{(V_{rel})^2}{C_p J g_0} + \frac{r^2\omega^2}{C_p J g_0}\right]$$

$$T_{0r} = T + \frac{1}{2}\frac{(V_{rel})^2}{C_p J g_0}$$

Therefore

$$dT_{0r} = dT_0 - \frac{\omega^2}{C_p J g_0} r\,dr$$

Equation [32] can now also be written in terms of relative temperatures

$$m_B C_p dT_{0r} = d\dot{Q} + \frac{m_B\omega^2}{g_0 J} r\,dr \quad [33]$$

(*b*) *Flow in rotor* (*3b* to *4d*). Assuming adiabatic flow in the rotor, Equations [32] and [33] are integrated to show

$$T_{0r4d} = T_{0r3b} + \frac{1}{2}\frac{u^2}{C_p J g_0}\left(\frac{r_A}{r_T}\right)^2 \quad [34]$$

$$T_{04d} = T_{03b} + \frac{u^2}{C_p J g_0}\left(\frac{r_A}{r_T}\right)^2 \quad [35]$$

(*c*) *Flow in buckets* (*4d* to *5d*). Integrating Equation [33] from *4d* to *5d*

$$\dot{Q} = M(Q_1/W_A)_B W_A = m_B C_p(T_{0r4d} - T_{0r4d}) - \frac{m_B\omega^2}{2g_0 J}(r_T^2 - r_A^2)$$

and

$$(m/M)_B = \frac{(Q_1/W_A)_B W_A}{C_{pB}(T_{0r4d} - T_{0r4d}) - \frac{1}{2}\frac{u^2}{g_0 J}\left[1 - \left(\frac{r_A}{r_T}\right)^2\right]}$$

Defining an apparent effectiveness for the bucket-coolant passages as

$$\eta_s' \equiv \frac{T_{0r4d} - T_{0r4d}}{T_w - T_{0r4d}} \quad [36]$$

$$(m/M)_B = \frac{(Q_1/W_A)_B W_A}{C_{pB}\left\{\eta_s'\left[T_w - T_{0B} - \frac{1}{2}\frac{u^2}{C_p J g}\left(\frac{r_A}{r_T}\right)^2\right] - \frac{1}{2}\frac{u^2}{C_p J g}\left[1 - \left(\frac{r_A}{r_T}\right)^2\right]\right\}} \quad [37]$$

(*d*) *Relation of* η_s' *to coolant flow conditions.* Combining Newton's law of cooling with Equation [33]

$$d\dot{Q} = \alpha P'(T_w - T_{0r})dr = m_B C_p dT_{0r} - m_B\frac{\omega^2}{g_0 J} r\,dr \quad [38]$$

Assuming $\alpha P'/m_B C_p$ and T_w do not vary with r the Equation [38] is integrated to yield

$$\frac{T_w - T_{0r4d}}{T_w - T_{0r4d}} = e^{-\left(\frac{4\alpha}{G_e C_p}\frac{l}{De} + \beta\right)} \quad [39]$$

where

$$\beta \equiv \frac{\omega^2}{C_p J g_0}\int_{r_A}^{r_T}\frac{r\,dr}{T_w - T_{0r}}$$

β is later integrated assuming a linear variation of T_{0r} with radius; however, for the moment, comparing Equation [39] with [36] it is seen that

$$\eta_s' = 1 - e^{-\left(\frac{4\alpha}{G_e C_p}\frac{l}{De} + \beta\right)} \quad [40]$$

Neglecting the effect of free convection on the heat-transfer process within the blade-coolant passage, the Stanton number is expressed by the empirical pipe-flow reference (6)

$$\frac{\alpha}{G_e C_p} = 0.023\left(\frac{G_e De}{\mu}\right)^{-0.2}\left(\frac{C_p\mu}{K}\right)^{-0.67} \quad [41]$$

The same reference relates the friction factor to the Reynolds number (for $5000 < G_e De/\mu < 200{,}000$) as follows

$$f = 0.046\left(\frac{G_e De}{\mu}\right)^{-0.2} \quad [42]$$

Assuming that $C_p\mu/K \approx 0.69$, Equations [40], [41], and [42] result in

$$\eta_s' = 1 - e^{-\left(2.56f\frac{l}{De} + \beta\right)} \quad [43]$$

2 Analysis of Nozzle-Coolant Flow

The equations corresponding to Equations [32] through [43] can readily be attained for the flow through the nonrotating nozzle-coolant passages by equating $\omega = 0$. The pertinent results are as follows

$$T_{04c} = T_{0r4c} = T_{03B} \quad [44]$$

$$(m/M)_N = \frac{(Q_1/W_A)_N W_A}{C_{pB}\eta_s(T_w - T_{03B})} \quad [45]$$

$$\eta_s = 1 - e^{-2.56f\frac{l}{De}} \quad [46]$$

3 Evaluation of η_s'

The nozzles and buckets in this power plant are assumed to have identical coolant-passage construction. The coolant flows for nozzles and buckets will certainly be of at least the same order of magnitude. Therefore it is assumed that the term, $f\,l/De$ is nearly the same for both. Comparing Equations [43] and [46]

$$\eta_z' = 1 - (1 - \eta_z)e^{-\beta} \quad [47]$$

Now, returning to the definition of β (Section 1), and performing the integration, assuming that T_{0r} is linear with r

$$\beta = E(F \log_e A - 1) \quad [48]$$

where

$$E \equiv \frac{\frac{u^2}{C_p J g_0}\left[1 - \frac{r_h}{r_T}\right]^2}{\eta_z'\left[T_w - T_{03b} - \frac{u^2}{2C_p J g_0}\left(\frac{r_h}{r_T}\right)^2\right]}$$

$$F \equiv \frac{1}{\eta_z'} + \frac{r_h/r_T}{1 - r_h/r_T}$$

$$A \equiv \frac{1}{1 - \eta_z'}$$

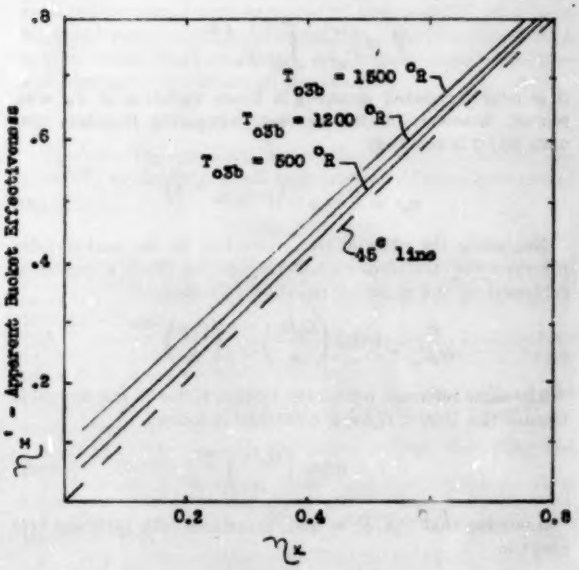

FIG. 14 PLOT η_z' VERSUS η_z

The combination of Equations [47] and [48] determines η_z' in terms of η_z, T_{03b}, and certain power-plant operating constants. In Fig. 14, η_z' is plotted against η_z for the three values of T_{03b} used in this investigation. The values of η_z' used in the calculations are as follows:

η_z'	η_z	T_{03b}, deg R
0.438	0.4	1200
0.630	0.6	1200
0.820	0.8	1200
0.617	0.6	500
0.650	0.6	1500

Appendix 3

DERIVATION OF EXPRESSION FOR ENTHALPY LOSS DUE TO MIXING ($\Delta H/W_A$) IN FORCED-CONVECTION AIR-COOLED POWER PLANT

Assuming adiabatic mixing of coolant and working fluid, and neglecting variation in specific heat, the steady-flow energy equation applied to the mixing chamber F is written as follows

$$m_N T_{03c} + m_B T_{03d} + M T_{04a} = (m_N + m_B + M) T_{07} \quad [49]$$

But by definition $\Delta H \equiv C_{p2}(T_{04a} - T_{07})$
and also

$$T_{07} = T_w; \quad T_{03c} = T_{03c}; \quad T_{03d} = T_{03d}$$

$$\therefore \frac{\Delta H}{W_A} = \frac{C_{p2}}{W_A}[(m/M)_N(T_w - T_{03c}) + (m/M)_B(T_w - T_{03d})] \quad [50]$$

Equation [50] is further modified by introducing the expressions for the coolant ratios (Equations [36] and [37]) and the definitions of η_z and η_z' (Equations [1] and [40])

$$\frac{\Delta H}{W_A} = \frac{C_{p2}}{C_{p3}}\left[\left(\frac{Q_1}{W_A}\right)_N\left(\frac{1 - \eta_z}{\eta_z}\right) + \left(\frac{Q_1}{W_A}\right)_B\left(\frac{1 - \eta_z' - \epsilon}{\eta_z' - \sigma}\right)\right] \quad [51]$$

where

$$\epsilon \equiv \frac{\frac{u^2}{2C_p J g_0}}{T_w - T_{03b} - \frac{u^2}{2C_p J g_0}\left(\frac{r_h}{r_T}\right)^2}$$

$$\sigma \equiv \frac{\frac{u^2}{2C_p J g_0}[1 - (r_h/r_T)^2]}{T_w - T_{03b} - \frac{u^2}{2C_p J g_0}(r_h/r_T)^2}$$

Values of ϵ and σ used in this investigation are as follows:

T_{03b}	ϵ	σ
500	0.0488	0.0253
1200	0.096	0.0497
1500	0.164	0.0847

Appendix 4

DERIVATION OF EQUATIONS FOR ROTOR PUMPING WORK

General Analysis—Varying Coolant Flow in Rotating Passages. Consider stationary annular-control volume which encloses rotor between r and $r + dr$ (see Fig. 13). For this derivation only, the following definitions exist:

$n \equiv$ mass flow within coolant passages at radius r
$\delta_n \equiv$ mass leaving coolant passages between r and $r + dr$ (i.e., due to transpiration)

From the theorem of moment of momentum:
Net external torque = net efflux of angular momentum from control surface

$$d\tau = \delta_n\left(r + \frac{dr}{2}\right)^2\frac{\omega}{g_0} + \left[n + \left(\frac{dn}{dr}\right)dr\right](r + dr)^2\frac{\omega}{g_0} - \frac{r^2\omega n}{g_0} \quad [52]$$

From the continuity equation

$$\delta_n = -\left(\frac{dn}{dr}\right)dr \quad [53]$$

Combining these two equations, and neglecting terms containing $(dr)^2$ results in

$$d\tau = \frac{2n\omega\tau\, dr}{g_0} \quad \ldots\ldots [54]$$

Forced-Convection Cooling: $n = m_B = const$

$$\tau = \frac{m_B r_T^2 \omega}{g_0}$$

$$W_{F'} = \frac{P_F}{m_B J} = \frac{\tau\omega}{m_B J} = \frac{u^2}{g_0 J}$$

$$W_F = \frac{P_F}{mJ} = \frac{(m/M)_B}{m/M}\,\frac{u^2}{g_0 J} \quad \ldots\ldots [55]$$

Transpiration Cooling

$$0 < r < r_h \qquad n = m_B$$

$$r_h < r < r_T \qquad n = m_B\left(1 - \frac{r - r_h}{r_T - r_h}\right)$$

(assuming that n varies linearly with r within the blades).

Integrating Equation [54], using this variation in n results in

$$\tau = \frac{m_B\omega r_T^2}{g_0}\left[1 - \frac{2}{3}\left\{\frac{1 - (r_h/r_T)^3}{1 - r_h/r_T}\right\} + \frac{r_h}{r_T} + \left(\frac{r_h}{r_T}\right)^2\right]$$

$$\tau = 0.730\,\frac{m_B\omega r_T^2}{g_0}$$

$$W_F = 0.730\,\frac{(m/M)_B}{(m/M)}\,\frac{u^2}{g_0 J} \quad \ldots\ldots [56]$$

Appendix 5

Derivation of Equation [17]

Equation [19] (film theory) expresses the effect of mass transfer on the heat-transfer coefficient as

$$\alpha/\alpha^* = \left(\frac{G_t C_p}{\alpha^*}\right)\Big/\left(e^{\left(\frac{G_t C_p}{\alpha^*}\right)} - 1\right)$$

In reference (8) the heat transfer to a cascade of blades (no mass transfer present) is expressed

$$MQ_1^* = MC_p(T_0 - T_w)(e^{b^*/2} - 1) \quad \ldots\ldots [57]$$

Newton's law of cooling relates the heat transfer to the temperature difference

$$MQ_1^* = \alpha^* A_t(T_0 - T_w) \quad \ldots\ldots [58]$$

From Equations [57] and [58]

$$\frac{MC_p}{\alpha^* A_t} = \frac{1}{e^{b^*/2} - 1} \quad \ldots\ldots [59]$$

Noting that for the nozzles, say

$$\left(\frac{MC_p}{\alpha^* A_t}\right)_N = \frac{G_t C_p}{(m/M)_N \alpha^*}$$

therefore

$$\left(\frac{G_t C_p}{\alpha^*}\right)_N = (m/M)_N/(e^{b^*/2} - 1)$$

and

$$\left(\frac{\alpha}{\alpha^*}\right)_N = \frac{(m/M)_N/(e^{b^*/2} - 1)}{\left[\frac{(m/M)_N}{e^{b^*/2} - 1}\right]} \quad \ldots\ldots [60]$$

$$e - 1$$

Appendix 6

Analysis of Water-Cooled Power Plant

The efficiency of a cooled power plant is, as seen from Equation [3], exactly equal to η_M if the quantity η_m is zero. For the water-cooled power plant studied, since the coolant does not mix with the working fluid

$$\eta_m(\text{water-cooled}) = -\frac{W_F + W_{C_2}}{Q_{in}} \quad \ldots\ldots [61]$$

The term W_{F_1} rotor pumping work, is zero since the coolant flows both inward and outward in the rotor. Therefore, in order that η_m be zero, W_{C_2} the work required to circulate the liquid coolant also must be zero. This condition is fulfilled if the net centrifugal pressure rise of the coolant as it passes through the rotor and blades is equal to, or greater than, the net pressure loss in the remainder of the circuit. It is assumed that any excess pressure rise will be dissipated in throttling rather than converted into useful work.

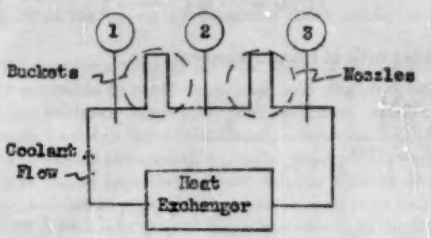

Fig. 15 Coolant-Flow Schematic

The net pressure rise caused by the centrifugal field and density change is obtained by assuming the outward flowing coolant is all at density ρ_1 and the inward flow coolant at density ρ_2, see Fig. 15. Successive application of Bernoulli's equation yields

$$\Delta p \text{ rise } 1 \to 2 = \frac{u^2}{2g_0}(\rho_1 - \rho_2) \approx \frac{\bar{\rho}u^2}{2g_0}\left[1 - \frac{\rho_2}{\rho_1}\right] \quad \ldots\ldots [62]$$

The total frictional pressure loss in the coolant circuit is approximated by multiplying the nozzle pressure drop by 6 since the nozzles, buckets, rotor, stator, heat exchanger, and coolant lines may be thought to cause approximately equal pressure losses)

$$\Delta p \text{ friction} = 6(\Delta p)_N = 24f\,\frac{l}{De}\,\frac{k_1^2(m/M)_N^2}{2\bar{\rho}g_0} \quad \ldots\ldots [63]$$

From combination of Equations [62] and [63] it is seen that W_{C_2} is zero if

$$B \equiv \frac{24f(l/De)k_1^2(m/M)_N^2}{\bar{\rho}^2 u^2[1 - \rho_2/\rho_1)]} < 1 \quad \ldots\ldots [64]$$

The coolant ratio required for the nozzles is obtained by applying a heat balance to the nozzle-coolant passages

$$(m/M)_N = \frac{(Q_1/W_A)_N W_A}{C_p(T_w - T_2)\eta_{s1}} \quad \ldots\ldots [65]$$

where

$$\eta_{s1} \equiv \frac{T_3 - T_2}{T_w - T_2} \quad \ldots\ldots [66]$$

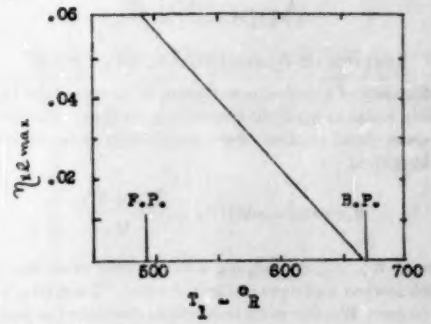

FIG. 16 η_{z1max} VERSUS COOLANT-INLET TEMPERATURE

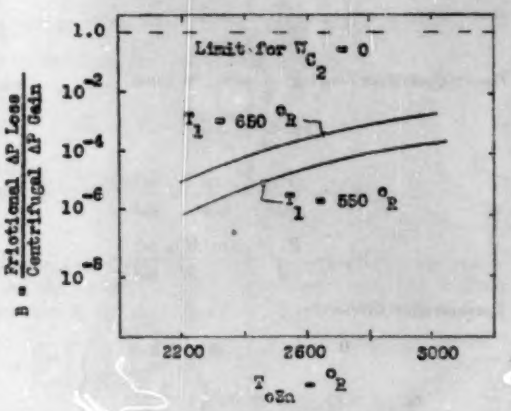

FIG. 17 B VERSUS TURBINE-INLET TEMPERATURE

The term $f\,l/De$ is obtained by an analysis similar to that carried out in Appendix 2

$$f\,l/De = \frac{1}{\phi} \ln \left(\frac{1}{1 - \eta_z} \right) \quad \ldots\ldots\ldots\ldots [67]$$

where ϕ is a ratio of Prandtl numbers

$$\phi \equiv \frac{\left(\frac{C_p u}{K}\right)^{-0.67} \text{ at } T = \frac{T_3 + T_2}{2}}{\left(\frac{C_p u}{K}\right)^{-0.67} \text{ at } T = 510 \text{ deg R}}$$

$$= \frac{\left(\frac{C_p u}{K}\right)^{-0.67} \text{ at } T = \frac{T_3 + T_2}{2}}{(0.75)}$$

In order to prevent boiling in the coolant system, it is necessary to limit the temperature rise in the blades and hence the effectiveness. Assuming equal temperature rises in nozzles and buckets the maximum effectiveness as limited by T_3 is

$$\eta_{z1max} = \frac{1}{2} \frac{T_3 - T_1}{T_w - T_1} \quad \ldots\ldots\ldots\ldots [68]$$

In Fig. 16 the foregoing relation is plotted for the case where T_3 is limited to the boiling point of water at atmospheric pressure (T_3 = 670 R). Larger values of T_3 could, of course, be obtained if the system were pressurized.

B, the ratio of frictional pressure drop to centrifugal pressure rise, is plotted in Fig. 17 for two values of coolant-inlet temperature, T_1. In this plot η_{z1} is assumed equal to η_{z1max} as per Fig. 16. It is seen that throughout the range of turbine-inlet temperatures investigated, B is considerably less than unity. Hence the required pumping work, W_{C_2}, is zero and η is just equal to η_M.

Test of an Experimental Coal-Burning Turbine

By D. L. MORDELL[1] and R. W. FOSTER-PEGG,[2] MONTREAL, QUEBEC, CANADA

In 1949 one of the authors suggested[3] that, by the use of the exhaust-heated cycle for a gas-turbine power plant, the new problems and difficulties then besetting those who were trying to produce a coal-burning gas turbine, including (*a*) feeding of pulverized coal under pressure, (*b*) burning pulverized coal under pressure, (*c*) gasifying coal under pressure, (*d*) separating ash from high-temperature gases, (*e*) establishing the tolerance of turbine blades to ash erosion, might be replaced by two problems different in degree but not in nature from those encountered in the design of boilers, namely, (1) combustion of coal in a furnace at essentially atmospheric pressure; (2) heating of a compressed gas by transfer of heat from hot combustion products. It appeared that adaptation of the existing technology to the gas-turbine conditions should prove easier than the evolution of a completely new technology. It was recognized, however, that the differences in degree made it impossible to design, with confidence, a power plant which might be expected to be immediately successful. It was, therefore, suggested that a purely experimental plant should be designed, constructed, and tested to lay the foundations for a future successful design. Representatives of the two major Canadian railroads considered that this proposal might lead to the evolution of a coal-burning gas-turbine locomotive that would play a useful part in their operations. The Dominion Coal Board felt that such a program might lead to the development of improved ways of utilizing coal and thereby effectively help the Canadian coal industry. The Department of Mines and Technical Surveys then placed a contract with McGill University for such a program to be carried out under the senior author's direction. Since that time, a vast amount of work has been done. The experimental plant has been built and has now completed its first series of tests. A great deal of theoretical design and economic consideration has been given to possible applications. The present paper reviews what has been done, and discusses the lessons that have been learned and their application in the future.

The Main Problem

THE major problem of the exhaust-heated gas turbine is that of designing a suitable furnace and heater to transfer the heat liberated from coal, burned in preheated air, to compressed air, at pressures of about 60–90 psia and temperatures of 1250–1350 F (650–730 C). By comparison, in a modern steam-generating unit, heat is transferred to steam at pressures of about 1000–2500 psia and temperatures of 1000–1100 F.

Experimental Design

The Heat Exchanger. In considering the design of the heat exchanger it was clear that, apart from the obvious mechanical problems arising from thermal expansion and pressure loading, and the problems of pressure loss and heat transfer, there were three basic problems that would be encountered in the design:

1 Strength of materials at elevated temperatures.

2 Deterioration of heat transfer and increase of pressure loss resulting from ash depositions.

3 Attack on the tubing by substances contained in the coal or ash.

Of all the problems, (2) and (3) were the only ones which were not really amenable to exact calculation and precise design.

Available evidence suggested that chemical attacks from vanadium and sulphur were to be feared. However, vanadium is not found in significant quantities in the coals which were to be used. In so far as high-temperature sulphur attacks in boilers are not too serious, in spite of low excess air, and tests had shown that sulphur attack is in general much less serious as the free oxygen in the gas is increased, we did not anticipate too much trouble, as in the exhaust-heated cycle there is much excess air.

The question of deterioration of performance by fouling was considered the most serious. As a result of this the decision was made to use a simple gas-tube-type heater, in which the combustion products passed straight through the inside of circular tubes, which it was considered would be least likely to suffer from fouling, and would be the easiest type to clean. Rig tests carried out in the Fuels Research Laboratories of the Department of Mines and Technical Surveys confirmed these opinions. It might be mentioned at this time that the use of a gas-tube heater involves certain mechanical and thermodynamic penalties which will be referred to later.

The Furnace. From the beginning it was recognized that practically any conventional furnace might be used and the use of a traveling-grade furnace was independently recommended by the late Mr. W. A. Newman of the Canadian Pacific Railway and by the Locomotive Development Committee. However, at that time the Fuels Research Laboratory of the Mines Department was experimenting with the cyclone furnace, originally developed by The Babcock & Wilcox Company, and in use in many utility applications. The cyclone appeared to offer advantages, including compactness, flexibility in choice of fuel, absence of moving parts, and its need for and ability to use the highly preheated air which is available in the exhaust-heated cycle. It appeared, therefore, to be a natural choice, and in view of the work already done, the decision was taken to use the cyclone furnace. Owing to unforeseen circumstances, the Mines Department program was slowed up, and some preliminary tests of a furnace were made on a rig in our own laboratory which showed a combustion performance that appeared satisfactory, although it was not good mechanically. These tests already have been reported.[4]

[1] Chairman, Department of Mechanical Engineering and Director, Gas Dynamics Laboratory, McGill University. Mem. ASME.

[2] Engineer, Department of Mines and Technical Surveys—Canada, Gas Dynamics Laboratory, McGill University.

[3] "The Exhaust-Heated Gas-Turbine-Cycle," by D. L. Mordell, Trans. ASME, vol. 72, 1950, pp. 323–329.

Contributed by the Gas Turbine Power Division and presented at the Diamond Jubilee Annual Meeting, Chicago, Ill., November 13–18, 1955, of The American Society of Mechanical Engineers.

Note: Statements and opinions advanced in papers are to be understood as individual expressions of their authors and not those of the Society. Manuscript received at ASME Headquarters, August 30, 1955. Paper No. 55—A-158.

[4] "Tests of a Furnace for a Coal Burning Turbine," by D. L. Mordell, R. E. Chant, and R. W. Foster-Pegg, *The Engineering Journal*, vol. 36, September, 1953, pp. 1122–1130.

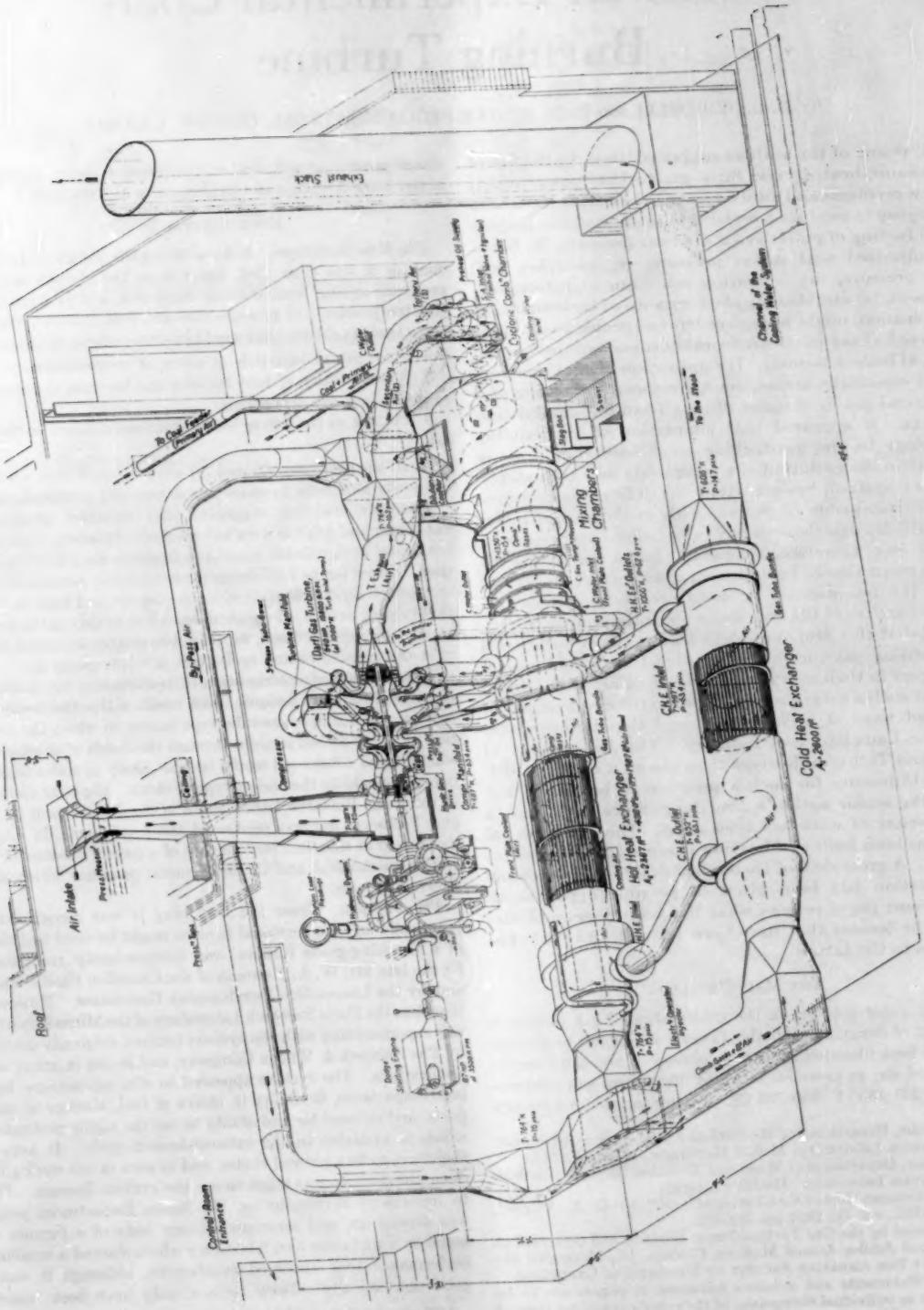

FIG. 1 GENERAL LAYOUT OF PLANT

FIG. 2 THE COMPLETED PLANT, MACHINERY LINE

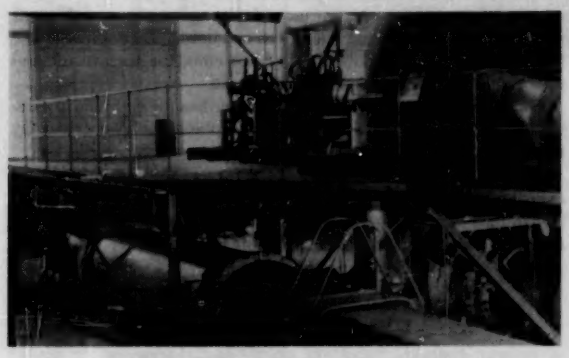

FIG. 3 THE COMPLETED PLANT, MACHINERY AND HEATERS

FIG. 4 THE COMPLETED PLANT, FURNACE

The mechanical faults appeared susceptible of solution by redesign, and a rebuilt furnace was used for engine tests. It should be pointed out that the combustion section was essentially as specified by B & W, except that we had deleted a re-entrant throat to determine if the pressure loss could be reduced, without undue penalty.

ENGINE TESTS

The plant was ready for test in November, 1953. A complete description together with an account of many of the design problems has already been given,[5] and Figs. 1 to 4, reproduced from that paper, show the general layout of the plant in its original state. The first five months of operation showed up various mechanical problems incident to the use of an aircraft engine as a test engine, but these were satisfactorily overcome, and since May, 1954, the plant, excluding the furnace and heater, has given no trouble whatever and has required very little maintenance. During this preliminary period certain faults in the heat-exchanger aerodynamic and thermodynamic performance became evident, but these were and are not regarded as being important as they are all accounted for to make sure that they will not be repeated. However, the cyclone furnace and coal system were definitely unsatisfactory in many respects. As soon as the mechanical troubles had been overcome, attention was concentrated on improvement to the furnace and a great many tests have been run.

Before describing the results of engine tests in more detail, it should be pointed out, as described previously,[5] that the main object of the plant was to serve as a detailed test of the performance of the furnace and heat-exchanger system, and their interaction on the gas-turbine unit. The plant was not designed as a prototype power plant, but as a research engine, on which it would be possible to determine fairly precisely the individual performances of all its elements. This requirement, together with the equally important one of having great facility in inspection, modifications, or rearrangement of components, led to a layout being adopted which incurred considerable penalties in terms of heat losses from ducting and hot casings, and pressure losses in interconnecting ductings.

RESULTS

Operation. The exhaust-heated gas turbine has demonstrated that it possesses many advantages. Perhaps the most striking is the fact that the machine is not critically affected by deterioration of combustion by any reason. Circumstances that would necessitate or cause the immediate shutdown of a conventional gas turbine may result in a gradual deterioration of over-all performance and can frequently be corrected without, in fact, any significant performance loss although such deterioration is likely to lead to increased maintenance. We would sum it up in the words that the exhaust-heated machine possesses a great capacity to withstand abuse or maloperation, which we regard as a most important characteristic in an industrial engine and especially in a locomotive power plant, where gradual deterioration is much to be preferred to abrupt stoppages.

TABLE 1 SUMMARY OF TROUBLES EXPERIENCED

Nature of trouble	Number of occasions (a) Emergency stop necessary	(b) Test interrupted to rectify trouble	(c) Test continued in spite of trouble
Slag drain	..	12	9
Slag flushing system	..	5	3
Coal entry	1	3	6
Coal processing	..	2	1
Gas leak from furnace	..	1	1
Refractory failure	..	1	0
Combustion	..	1	5
Turbine manifold expansion	..	1	6
Coal feed	..	..	15
Tube-plate deposit	..	..	6
Leaking heater tubes	..	..	4
Heater shell cooling	..	..	3
Cold exchanger expansion	..	..	2
	1	26	61

Between November, 1954, and April, 1955, the plant was run under power for a total of 314 hr, and 56 starts and stops have been made. The longest nonstop run was of 56-hr duration. It is perhaps noteworthy, for an experimental plant, that only on one occasion has an immediate stop been enforced by considerations of plant safety. Table 1 summarizes the more serious troubles which occurred during running.

Starting Procedure. The gas-turbine unit is rotated by a gasoline starting and barring engine to produce a flow of air through the plant and furnace. A propane-gas burner is then ignited by an electrical spark and used to light off an oil burner. The

[5] "An Experimental Coal Burning Gas Turbine," by D. L. Mordell, Proceedings of The Institution of Mechanical Engineers, vol. 169, no. 7, 1955, pp. 163–180.

plant is then brought up to self-sustained running on oil fuel by increments of 0.01 lb/sec of oil at 5-min intervals up to a maximum quantity during starting of 0.1 lb/sec. A start from cold usually takes about 1 hr. When the plant is hot it has been restarted from stationary in 15 min. The time required before applying load naturally depends on the temperature from which the start is made. Typical start records are shown in Fig. 5. The plant usually became self-sustaining at a turbine-inlet tempera-

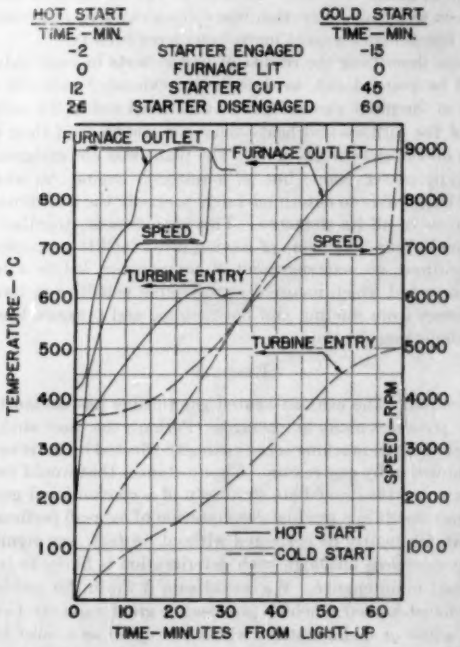

FIG. 5 TRANSIENT CONDITIONS IN HOT AND COLD STARTS

ture of about 600 C and, after declutching of the gasoline engine, would accelerate up to about 9000 rpm. The oil-fuel supply was increased to maintain this turbine-inlet temperature and the plant was adjusted to run at 9000–10,000 rpm (69–77 per cent of full speed). The change from oil to coal is effected very simply by opening the coal shutoff valve and progessively reducing the oil supply while the coal is increased until no oil is being used and the plant is operating entirely on coal.

Stopping and Shutdown. No difficulty or danger is experienced in a stop from full temperature in a few minutes and this has been done on many occasions to allow a change to be made for test purposes or for adjustments. The plant is normally run for a few minutes at no power before shutting off the fuel completely. Following most tests an inspection of the inside of the furnace or heater has been required as soon as possible when the plant was motored by the gasoline engine for several hours for quick cooling. To prevent recycling of heat by the heaters during motoring for cooling the access door of the furnace is opened so that air is discharged at its hottest temperature. Fig. 6 illustrates a quick stop and motoring for cooling.

Control. Overspeed protection is afforded by a valve arranged to spill compressor delivery air directly into the furnace inlet and operated automatically by high-pressure oil from a modified aircraft-propeller governor. This is necessary to protect the plant in case of overfueling or failure of the dynamometer or water supply. The speed at which the governor operates may be selected manually so that power may be cut instantaneously by reducing the governed speed to below the previous operating speed. The governor then opens the blowoff valve so that the useful power is dissipated in compressing additional air and the plant continues to run at the selected governed speed. An override also is provided which will fully open the blowoff valve at any speed. This control stops the plant in a few seconds in an emergency. The air discharged by the blowoff valve was ducted into the furnace inlet so that the air flow through the furnace would be increased rather than decreased by blowoff operation and heater-entry temperature consequently reduced.

Changes in the power output of the plant were exceedingly rapid following a change in the fuel-supply rate and were more rapid than the response of the pyrometry equipment which was by no means slow. As described previously, power could be dropped instantaneously by use of the governor and blowoff valve but this method normally was not used. By control of the fuel supply only, full power (250 bhp) could be thrown off and restored in about equal intervals of 15 sec.

During the present tests no attempt has been made to develop a coupled control system, and the plant has been driven by the fuel flow and the dynamometer torque controls.

Gas Turbine and Compressor. In so far as the gas turbine is not exposed to violent temperature changes or combustion products no trouble was anticipated, nor has it been experienced. Apart from replenishment of lubricating oil and checking filters, the

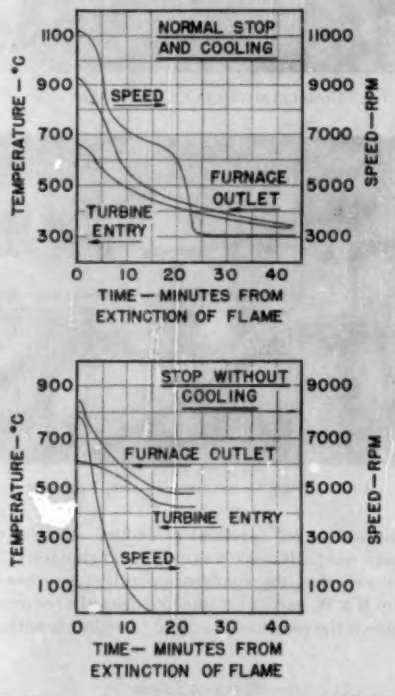

FIG. 6 TRANSIENT CONDITIONS FOR QUICK AND NORMAL STOPS

turbine, compressor, and reduction gearbox have received no attention at all.

Hot Heat Exchanger, Fig. 7. The original design used a combined counter and parallel-flow heater. This was adopted partly to keep tube temperatures down at the hot end and partly to insure a uniform distribution of the air at the hot end. The thermal design was based on standard results for longitudinal flow within and outside tubes. No allowance was made for the effect of the

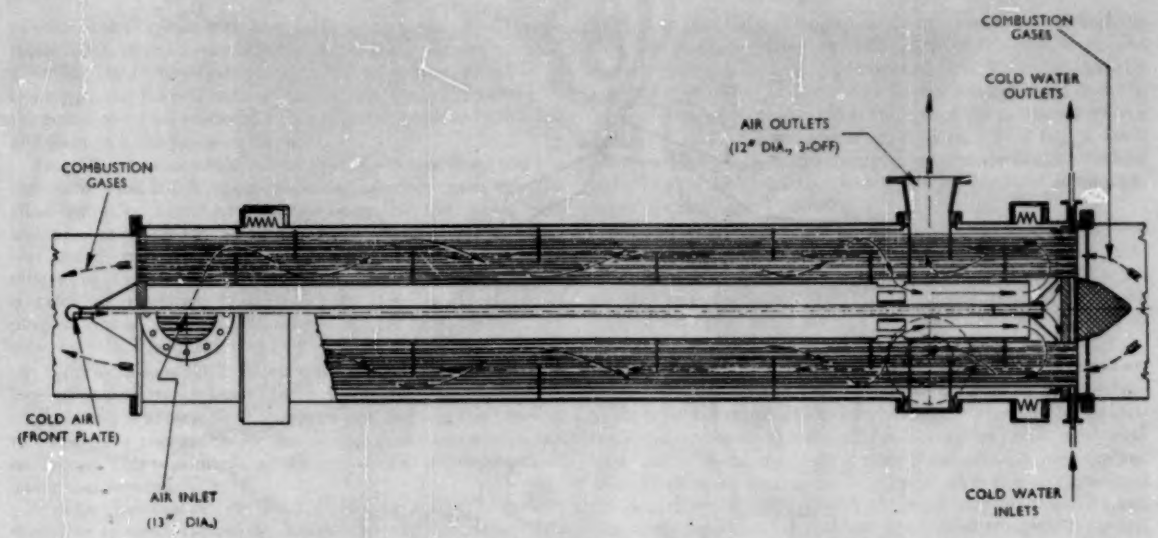

FIG. 7 DIAGRAM SHOWING LAYOUT OF HOT HEAT EXCHANGER

tube-supporting baffles which were regarded as a safety factor on the right side. Owing to the difficulty of a precise determination of a representative tube temperature it is not easy to sort out the individual heat-transfer coefficients. Fig. 8 plots the observed values of the over-all gas-to-air coefficient plotted against a parameter representing the flow conditions.

For the parallel and counterflow sections, the dotted lines on the curves show the design value based on the McAdams' correlation. The discrepancies are due to the effects of the baffles which increase the counterflow transfer and to the effect of an excessive amount of tube-plate cooling air. This is used to cool the rear surface of the tube plate and by-passes the heat exchanger, reducing the outlet temperature and the useful parallel-flow transfer. The pressure losses in the tubes are closely in accord with the values estimated by the usual methods. The air-side losses are a lot higher than was first estimated, but a detailed calculation of the exact flow path, making full allowance for the changes in direction and velocity induced by the baffles and the reversal necessary to combine the counter and parallel flow showed good agreement with the measured values, which are about three times higher than the original design values. It is now clear that the parasitic losses introduced by this arrangement are such as to require considerable justification by its other advantages, a point which will be referred to later.

The front tube plate is exposed to the hottest gas, and to maintain a reasonable temperature, a cooling system using water inside a "hollow" plate, and cooling air on the rear side was adopted. This has worked very well but is costly. The cooling water extracts some 9 per cent of the heat supply, while the effect of the cooling air has already been mentioned.

The deterioration of performance by fouling that was feared has not occurred. The gas velocity is high enough to keep the tubes clean under normal circumstances. Severe corrosion of the Nimonic tubes has occurred. Investigations are still proceeding so that conclusions must necessarily be tentative. It appears that sulphur in an oxidized state does not cause trouble, but there have been occasions in which reduced sulphur has been in contact with the tubes, causing severe local penetration. The influence of temperature is not precisely known and on occasion our tubes have been hotter than was anticipated when designed. In view of the relatively large excess air the presence of unoxidized sulphur

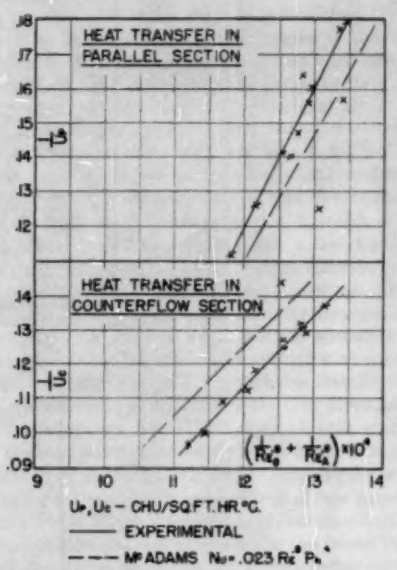

FIG. 8 COMPARISON OF MEASURED AND CALCULATED HEAT-TRANSFER COEFFICIENTS

is at first sight surprising. It must presumably arrive in the tubes in unburned or incompletely burned coal carried over. Provided there is a strong flow of gas through the tubes, there should be an oxidizing atmosphere, but circumstances can arise in which the gas flow through the tube is arrested by a blockage at the front end, and then clearly the circumstances are favorable for attack. The first indication of the corrosion was a deposit on the inside of the tubes first noticed after 170-hr running. Up to this time, the tubes had been clean, free from any trace of corrosion, and any particles of slag or ash had been easily removed. The deposit was an even coating around the tubes and when first noticed extended for about 12 in. inside the hot end. During each run the deposit extended further down the tubes. Attempts were made

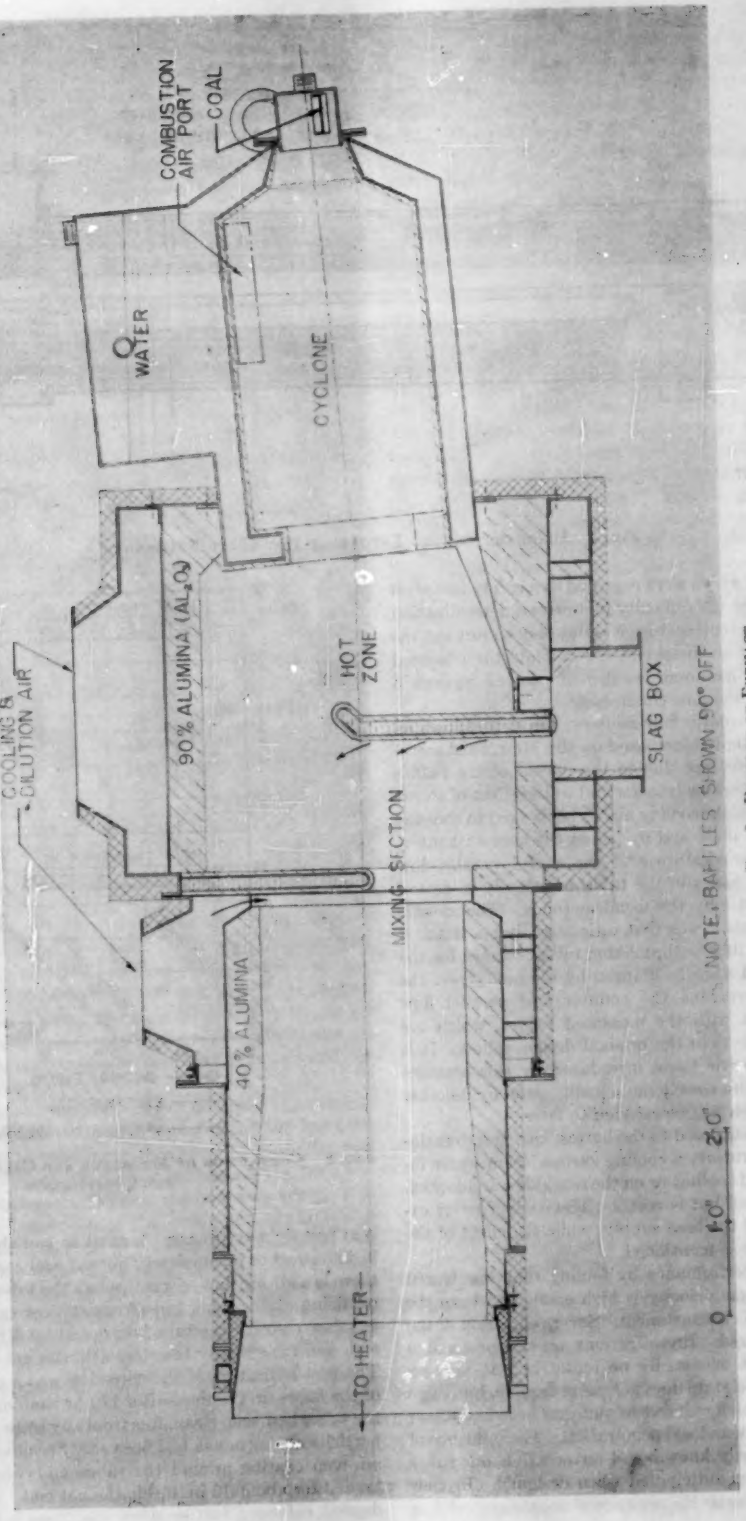

FIG. 9 DIAGRAM OF FURNACE

to remove the deposit with very little success because of the extreme hardness and strong adhesion to the tube. It was not until a further 100 hr had been run that the tubes were found to be leaking and it was realized that the deposit was really caused by the corrosion which produced sticky nickel sulphide on which ash and slag stuck like flies on a fly paper.

The serious nature of the corrosion of the heater tubes was not discovered until 250 hr of operation had been accomplished. To allow testing to continue for the last 60 hr the tubes which were leaking were plugged in the tube plates. Pressure tests were carried out at intervals thereafter and additional leaking tubes plugged as discovered. On the final test before the plant was dismantled for rebuilding, it was run with 71 tubes (14 per cent) plugged and an additional 73 tubes (14.6 per cent) leaking. In this condition the plant was still capable of delivering power. On many occasions the front tube plate of the heater has been blocked to a greater or lesser extent by slag deposits. The effect on the heater is to increase the pressure loss, and it is also believed to be partially responsible for the corrosion, as suggested in the foregoing. This is primarily a furnace fault and will be discussed under that heading.

Furnace: Combustion. So that the pressure drop in the cyclone should be as small as possible, it was originally designed with a vestigial throat of 46 per cent of the through area of the main cyclone. In all other respects it was a copy of the furnace tested at the Department of Mines, which was based on The Babcock & Wilcox design. Fig. 9 shows the arrangement. With this arrangement under almost all running conditions carry-over was excessive at up to 10 per cent of the weight of the coal fired, and with about 70 per cent carbon content. After about 200-hr operation a reentrant throat of 23 per cent of the cyclone area was installed so that its effect on combustion and carry-over could be observed. So that the installation of the throat would interrupt the test program for the shortest time, a method of construction with a life of only a few hours between repairs was used. While the throat was complete at the beginning of test runs a big improvement in all aspects of combustion could be noticed, even though a considerable discharge of ash particles through the slag passage in the throat must have occurred. After a few hours a deterioration in combustion usually took place and at the end of the run the refractory material of the throat was generally found perforated. It is thought that the collapse of the throat was responsible for the deterioration of combustion.

Cinder Formation. The word "cinder" is used to describe any accumulation of partly burned coal in the form of a lump or lumps. Formation of cinders within the cyclone was a frequent source of trouble in several ways. Cinders could form in the coal entry to the furnace and completely close off the passage, thus shutting off the fuel, or worse still, causing the coal to back up into other parts of the plant where combustion could occur with damaging results. On other occasions cinders would form in the cyclone and when they had grown to 2 to 3 in. across, would break away and be blown into the mixing section where they would sometimes cover the slag drain to a depth of several inches. It is thought that these cinder formations are caused when an excess quantity of coal is deposited onto a hot surface. The air distribution is by no means uniform and the problem is to distribute the coal in the correct proportions on the surface of the cyclone.

Many different designs of entry, all injecting through a bolted flange on the closed end of the cyclone, were tried. The first and last entries tried were similar to the entry arrangements developed by B & W, in which the coal is mixed into a quantity of air approximately equal to its weight, the energy of which is used to impart a swirl to the coal-air mixture as it enters the cyclone. Tests of the first B & W type entry nearly ended in disaster as coal coked in the entry completely blocking the pipe. The coal then backed up into the turbine-exhaust duct where it ignited and, before the plant could be stopped, much of the duct work was seriously overheated and had to be replaced. To insure that this could not recur, the coal-injection system was separated from the turbine-exhaust air until almost the end of the test series when a somewhat similar system was again tried. This had a small throat to give a high axial velocity to prevent combustion flashing back into the swirl chamber which was water-cooled as an additional precaution.

As described in the section on coal feeding, the coal was metered and pumped by a compressed-air injector using air either from compressor delivery or from the laboratory system. For all running except with the B & W type entries, the coal was blown directly into the furnace by this air which was equal to 20 to 40 per cent of the weight of the coal.

The best conditions for combustion in the cyclone were not exactly determined because of limitations dictated by the combustion system being part of a gas-turbine unit with restricted operating characteristics. It was established that the lowest carry-over and most efficient combustion were obtained with hot combustion close around the coal entry. Operation in this way increased the tendency for obstruction of the coal-entry pipe by coke and slag formations and for freedom from these troubles flame was best kept away from the coal entry. The smaller the quantity of air injected with or around the coal the more intense was the combustion at the entry. It is evident that sufficient air for combustion of the fines in the coal reaches the region of the coal entry from the main combustion-air port, and that additional quantities of air only chill and dilute the combustion of these fines and distilled volatiles. Hence control of additional air at the coal entry provides a ready means of controlling the flame front.

Many hours running were with a simple 2-in-diam pipe inclined at an angle of 35 deg to the axis of the cyclone. Best operation was with the discharge of the coal directed at a point just below the main combustion air port. Rotation of the pipe around the center line of the cyclone only a few degrees would cause formation of cinders, and with further rotation cinder formation became so severe as to prevent operation. Following success with the single inclined pipe, a similar arrangement using four pipes discharging at equal angles equally spaced around the axis was tried but completely filled the cyclone with coke in quite a short time. Attempts to obtain a workable distribution by alteration of the direction of injection of the four pipes failed completely and this system was abandoned. A coal entry in the shape of a crescent had similar results to the single 2-in. pipe.

The satisfactory results of the single inclined-pipe entry may be explained by the completely unsymmetrical flow pattern of the air in the cyclone to which a symmetrical coal distribution is not suited. The air-flow pattern often seen in the frozen slag of the cyclone and also traced by carbon deposits following operation on oil, indicates that the main path of the air within the cyclone is of only $^3/_4$ of a revolution before passing through the throat. Also a back flow under the secondary port is indicated. The best direction for coal discharge is into this back flow by which it is distributed over the rest of the surface of the cyclone. With a symmetrical discharge of coal as given by the B & W type entries and the other arrangement, it does not seem possible to obtain as hot combustion on the end of the cyclone as with the unsymmetrical discharge. It was observed that carry-over was at a minimum when combustion was against the end with fluid slag on all surfaces. However, it is expected that a proper throat will make the cyclone less critical in this respect. Fig. 10 shows the cyclone and inclined 2-in-pipe coal injector following a test.

Mixing. It was intended to operate the furnace with all combustion taking place within the cyclone. The following zone called "hot zone" was to be a quiescent region in which residual

FIG. 10 CYCLONE AND COAL NOZZLE AFTER TEST

slag would be deposited in the corner formed by the first baffle and in which the slag drain would be located. Dilution air was introduced in the wakes formed by the baffles which were to produce turbulence for mixing and also to shield the heater and tube plate from radiation from the hot parts of the furnace.

As described later, the coal-feed rate frequently was unsteady resulting in operation with alternately more and less air than was desirable. As well as the effect of the unsteady coal-feed rate it was impossible to maintain the air and coal quantities in adequate adjustment during speed and load changes of the plant. Satisfactory operation of the furnace depended on precise control of the air-fuel ratio in the cyclone between chemically correct and 20 per cent excess air. A greater excess of air reduced operating temperature in the cyclone, caused greatly increased carry-over and difficulties with slag drainage. With less air than the chemically correct quantity the cyclone operated as a gas producer, discharging combustible gases into the mixing section. These gases burned in the dilution air, but as this was not introduced until after the baffles combustion was still proceeding up to the heat-exchanger tube plate with bad effects on fusion and deposition of slag.

Provided that all ash particles are below fusion temperature when they strike the tube plate no deposition should occur, but it was found during plant test that ash would still adhere to the tube plate at a gas temperature into the heater of 1650 F (900 C), using coal with an ash-softening temperature in excess of 1900 F. Fig. 11 shows a bad degree of slagging and a record of the local gas-temperature distribution, which indicates clearly the effects of gas temperature. The longer the residence time of the gases, and hence the ash particles, at the heater-inlet temperature before actual entry to the heater, the closer the gas temperature may be allowed to approach ash-softening temperature without

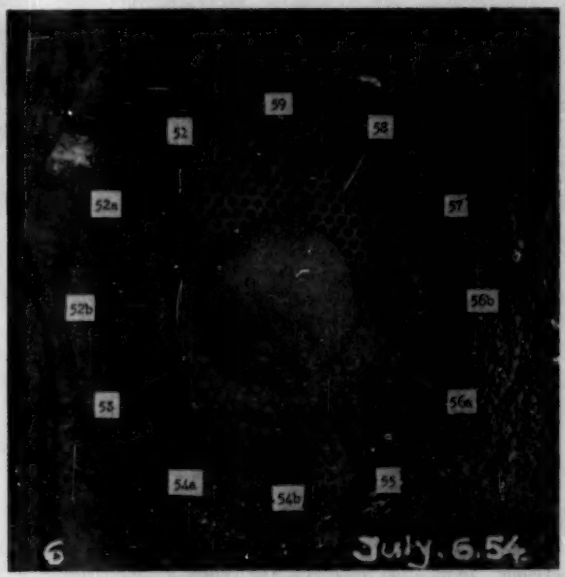

TABLE OF NUMBERS OF READINGS RECORDED AT 30 MIN INTERVALS AT OR ABOVE THE INDICATED TEMPERATURES

POSITION	1025°C	1050°C	1070°C	1100°C
58	2	-	-	-
59	3	-	-	-
57	4	3	-	-
51	4	3	1	1
52_A	5	3	1	-
56_B	6	3	2	2
52_B	7	7	2	2
56_A	12	9	6	4
55	13	9	8	6
53	14	11	4	4
54_B	14	11	8	8
54_A	14	12	9	7

FIG. 11 SLAGGING ON TUBE PLATE, AND CORRELATION WITH INLET TEMPERATURE

ash deposition on the heater. Where a uniform velocity prevails through a space, the residence time of any molecule of gas is given by the volume of the space divided by the rate of flow in units of volume per unit time. After the plant had been operated for some time it became very obvious that any calculations of residence time on this basis were completely incorrect because of the very high local velocities which were caused by the unsymmetrical flow around the baffles. Where the velocity is not uniform the residence time of some of the gas may be of as short a duration as the length of the flow path divided by the average of the maximum velocities. Undoubtedly a large proportion of the gases and carry-over closely approached this minimum residence time in the cooler regions of the furnace and thus struck the tube plate in a sticky condition. Furthermore, the local gas velocities were high enough to sweep large lumps of plastic slag off the surfaces of the furnace including the floor, carry them onto the tube plate where they would stick, the larger lumps closing off several tubes. Fig. 12 shows a case when plastic slag has been piled up by the gas velocity.

Slag Removal. Failure of the slag-removal system stopped testing more than any other cause, 17 interruptions being experienced in spite of over 30 different designs of the slag drain. Some of these failures were due to faulty combustion which buried the

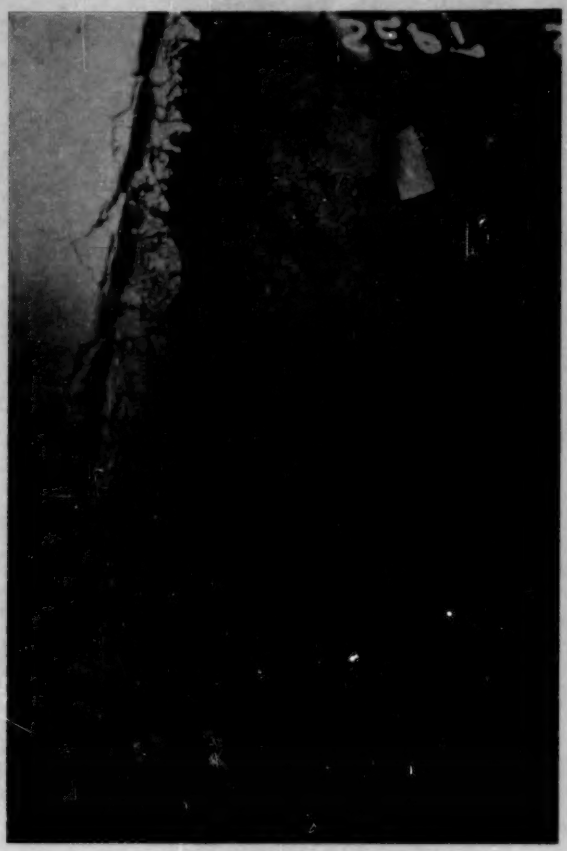

FIG. 12 PILED-UP SLAG

drain hole in several inches of cinders when no drain could be expected to operate satisfactorily, but most of the failures were caused by slag freezing in the drain hole.

The drain was located in the hot zone of the mixing section in front of the first baffle. It was thought that in this position slag deposited on all surfaces would flow into the drain. The unsatisfactory performance of the drain hole in this position can be attributed to the following reasons: The region of the drain was cool compared to other parts of the furnace so that slag could be fluid in other hotter regions and flow to the drain which was not yet up to slag-fluid temperature. It would then freeze in and over the drain, thus partially insulating it from further heating. On no occasion did the drain melt out after once being blocked with frozen slag without some assistance such as heating by supplementary external combustion.

The refractory materials of the furnace were slowly fluxed by the slag, the resulting mixture of refractory and slag having a melting temperature intermediate between the two constituents. On many occasions fusion-temperature checks on the substance which had frozen in the slag drain gave fusion temperatures several hundred degrees higher than the fusion temperature of the coal slag, 2200 F, demonstrating that lumps of the mixture had entered the drain.

It was found necessary to drop the slag direct from a lip at or near the level of the internal surface of the refractories straight into the water. If the slag was allowed to trickle down the walls of the drain it cooled slowly and formed icicles or failed to granulate on quenching in the water. Many designs of drain initially operated well, but after only a few hours running icicles accumulated until the drain was completely blocked. This was due to fluxing or melting of the material of the drain until the shape was changed. Of all the refractory materials tried, silicon carbide withstood the washing action of the slag longest, but even this material slowly vanished under operating conditions. A water-cooled carbon-steel design gave the best results but operation was always delicate because if once a layer of slag froze on top of the drain hole it could not be melted out and could necessitate stoppage of the plant.

The slag flowed into a water tank below the slag drain hole and, provided it dropped into the water in a fluid state, it granulated into pieces the largest of which was 0.250 in. This granulated slag was removed by hydraulic flushing with a system of jets through a water leg to seal against the internal pressure of the slag box. When troubles were experienced with this system, it was because of unsatisfactory performance of the drain and formation of icicles, which either blocked the outlet pipe or a screen intended to hold a few small pieces, or because of an excessive quantity of cinders entering the box and floating on the water surface, a result of poor combustion. The solution to these problems is sought in better drain design and combustion control.

Operating Experience of Refractories. Loss of heat to the cooling water from the cyclone reduces the thermal efficiency of the plant. It is therefore desirable that the heat lost in this way shall be as small as possible. It is regarded as normal for the refractory lining of cyclones to be very thin, 0.1 to 0.250 in., and after 100 hr of operation to consist almost entirely of pure slag it having fluxed away the original lining, which is only applied to provide a surface "wettable" by the slag during the starting period. There seems to be no problem in obtaining this type of lining, both plastic chrome ore and plastic alumina giving good results. If a material could be found which would operate at a greater thickness then the heat lost to cooling water could be reduced, but no such material has yet been forthcoming.

The products of combustion were discharged from the cyclone at temperatures frequently in excess of 3000 F and the inside surfaces of the hot zone reached this figure as measured by optical pyrometer. No material was found which would completely withstand the conditions of the high temperatures and slag attack though silicon carbide was better than the other materials. Some spalling occurred usually at the maximum penetration of the slag into the brick. No difficulty was experienced with refractories wherever the slag was frozen. The method of cooling the refractories by the air entering the furnace was very successful, and a temperature gradient from 3000 to 1200 F was maintained across $4^1/_2$ in. of brick without penalty of a high heat loss.

Coal-Feed System. A system of pneumatic injection was used for most of the operation of the plant in which the energy of a stream of air at approximately compressor delivery pressure was used to inject the coal against the pressure in the furnace. At first a vibrating feeder was used to meter the coal and the injector was only called upon to overcome the furnace back pressure. However, the particular feeder was not found satisfactory and rig tests showed that the pneumatic injector could combine both operations at least as well as the dual system by control of the forcing air pressure. The feeder was discarded and both operations performed by the pneumatic injector for all running, from 30 to 290 hr. This system was chosen because of its simplicity and its expected suitability for the plant.

Preliminary small-scale rig tests gave promising results and some good engine runs were made. However, results were never completely satisfactory and operation of the plant was usually adversely affected by unsteadiness of the feed rate and the power at which the plant could be operated was often limited by the

maximum rate which could be squeezed out of the system. After about 150-hr operation the coal-storage hopper was arranged for pressurizing to reduce the pressure difference across the injector. However, steadiness was not improved and it became important that hopper pressure be not allowed to exceed furnace pressure, or excess quantities of coal would flow into the furnace, as could happen if the plant slowed down. Rig tests and a few test runs of the plant showed that the system was capable of operating well under ideal conditions of dry loose coal. Experience obtained during the rest of the time showed that the system was also susceptible to variations in moisture content, degree of aeration of the coal, and was too sensitive to back pressure. Several attempts were made in between engine tests to carry out full-scale rig tests of the system but no really satisfactory method of simulating engine operating conditions was found or of assessing the steadiness of the feed rate from the rig test.

Toward the end of the series of tests various factors contributed to an increase of furnace pressure. These were plugging of heater tubes, reduction in by-pass flow to reduce gas temperature into the heater, addition of a throat in the furnace, and fouling of the heater resulting from slag carry-over. As a result of these factors the furnace pressure against which the coal had to be injected was considerably increased and the system became more and more unreliable. The decision was therefore taken to abandon the pneumatic system and to develop a screw feeder and the last 20-hr operation of the plant was with this system. During this short period it was not possible to evolve a completely satisfactory system or furnace entry to go with it but some very steady operation was achieved which holds promise for the future.

Thermodynamic Performance. The exhaust-heated machine differs essentially from the conventional simple cycle in that the heat is supplied indirectly. In analyzing it, therefore, it is convenient to make a division of efficiency by defining two terms as follows.

Actual Cycle Efficiency. This is the thermal efficiency of the gas-turbine set, reckoned as the work output divided by the heat actually supplied in the heat exchanger. It includes all losses in the turbine set, and the effects of the heat-exchanger pressure loss and, in fact, corresponds to the over-all thermal efficiency of a conventional set divided by its combustion efficiency. Fig. 13 shows typical results for the actual cycle efficiency.

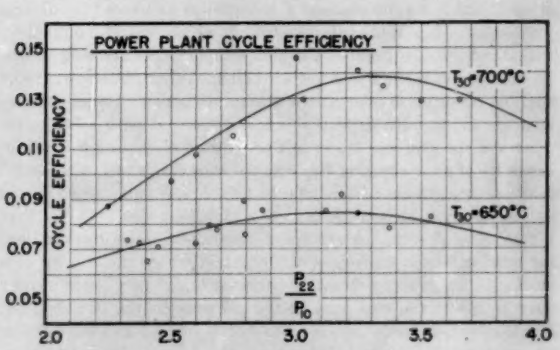

FIG. 13 MEASURED CYCLE EFFICIENCIES

Heating Ratio. This is defined as the heat actually supplied to the compressed air in the heat exchanger divided by the heat input to the furnace. It should be noted that this can be more than one depending upon the amount of surface of the heat exchanger. To have a maximum value of unity it should be defined as heat input to compressed air divided by the heat supplied in the coal plus the excess in sensible heat of the air entering the furnace over that finally leaving the heat exchanger. In the split cycle used, this excess is designed to be zero. Clearly in the present tests it is the heating ratio which interests us. The factors which reduce it are as follows:

(*a*) Unburned combustible in gas or ash.
(*b*) Furnace cooling-water losses.
(*c*) Tube-plate cooling-water losses.
(*d*) Heat losses by radiation and convection from the heat surfaces.

Table 2 shows a typical heat balance.

TABLE 2 TYPICAL HEAT BALANCE FOR HEATING SYSTEM

	Per cent
Heat supply in fuel	100
Furnace losses:	
(*a*) Unburned combustible and heat in slag	4
(*b*) Furnace cooling water	15
(*c*) Heat loss from casings	7
Total furnace losses	26
Hot heat exchanger:	
(*a*) Tube-plate cooling loss	9
(*b*) Heat loss from casings	3
Cold heat exchanger:	
(*a*) Heat loss from casings	1
Manifold and ductings	1
Total plant losses	40
Effective heating efficiency	60

DISCUSSION AND APPLICATION

In this section the lessons so far learned from operation are discussed in terms of their application to the design of useful power plants, and more specifically in the modifications now being incorporated in the experimental plant before starting the next test series.

Thermodynamic Cycle. The simplest exhaust-heated cycle uses a single heat exchanger to transfer the heat to the compressed air. Assuming a given gas-turbine performance and turbine-inlet temperature, the variable factors are three in number.

(*a*) The pressure losses imposed by the furnace and heat exchanger. A high value diminishes both power and thermal efficiency, but reduces the cost of the heat exchanger.

(*b*) The surface area of the exchanger. Increase of area does not affect power, but improves the thermal efficiency at the expense of first cost. Decrease, on the other hand, not only cuts the efficiency and cost, but forces an increase of exchanger gas-inlet temperature. There is thus a limit on the reduction possible caused by (1) the increasing tube temperature, and (2) the necessity of insuring that the gas-inlet temperature is safely below the ash-freezing temperature, if heat-exchanger slagging is to be avoided.

(*c*) Heat losses from the system, which simply reduce the thermal efficiency and can always be reduced at the expense of insulation.

The first and last of these three factors are easily settled. It is found that as the pressure loss is increased, although the heat-exchanger cost comes down, so does the power output and efficiency, so that for any required utilization and fuel cost, the optimum pressure loss to be used can be determined quickly. Even

more simple is the determination of the amount of insulation to use. However, in the choice of the surface area, there are some factors which cannot easily be embraced in a formula.

These are the effects of high-exchanger inlet temperature in terms of slagging, tube strength, ducting heat losses, and furnace cooling. With the simple cycle as soon as the inlet temperature is chosen, the thermal efficiency is fixed. At the time of the original design it was desired to use a temperature as high as could be contemplated in terms of the factors listed, and at the same time obtain a higher value of the thermal efficiency than the simple cycle would have given. To achieve this it is necessary to split the heat-exchanger surface. Some of the excess air normally used to cool the furnace gases is not mixed in until after a first pass of the heating surface. The effect can be shown by quoting results of a particular analysis.

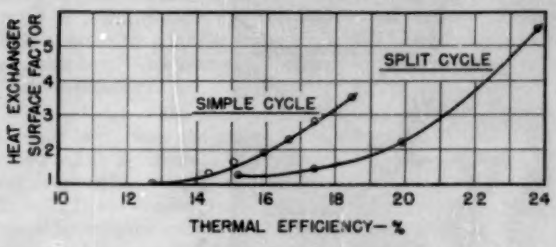

FIG. 14 RELATION BETWEEN EXCHANGER SURFACE AREA AND THERMAL EFFICIENCY, COMPARISON OF SIMPLE AND SPLIT CYCLES

Fig. 14 shows a plot of heat-exchanger surface area ratio against over-all thermal efficiency from a study of a particular gas turbine, allowing a constant total pressure loss, and varying only the heat-exchanger surface.

For the simple cycle, the value of 1.0 for heater area corresponds to a temperature at heater entry of 1800 F. As the efficiency and area are increased, this temperature comes down. For the split cycle, the heater-entry temperature is kept constant at 1800 F, but the proportion of air by-passed around the first heater unit is gradually increased.

Hence the split cycle will always require appreciably less heat-transfer surface for the same thermal efficiency; and it was for this reason that the experimental engine was designed to work with two heat exchangers. Also for obvious reasons it was first desirable to try and operate at the highest temperature which could be contemplated. Experience suggests however that the less tangible factors mentioned earlier, together with the fact that it is always cheaper to put extra surface into one heat exchanger than to put the same surface into an additional unit (especially if the use of an air tube heater can be considered), lessen the advantages of the split cycle. The present plant is being modified to run a series of tests with the simple cycle, so that a direct comparison can be made, to facilitate future judgment.

Heater. The present tests have shown quite clearly that the dry fouling of heat-exchanger surface is not nearly as critical as was feared, and it is in fact possible to use an air-tube heater with considerable savings in size and cost, and the elimination of the cooled hot-end tube sheet, with its far from negligible heat loss. At the same time the use of an air-tube heater, rather than a gas-tube type, permits much better control of tube temperature and eliminates the possibility of developing reducing conditions over any appreciable fraction of the tube area. It appears that, in the absence of gross reducing conditions, high-temperature sulphur attack is likely only if unburned or partially burned coal is burned out while actually in contact with the metal. Clearly the furnace must be designed to prevent carry-over of unburned material as far as possible, but it cannot be expected that none will ever come. Experience shows that, provided care is taken to avoid dead pockets, the gas velocity will sweep any such unburned matter along with it, and not permit it to remain in contact with the tube wall for any length of time. Finally, rig tests also show that the straight chromium steels of the 440 series possess much better resistance to this form of attack than the Nimonic which was chosen in the first place by reasons of ready availability. The experimental heat exchanger is having six tubes of each of twelve different alloys fitted to gain first-hand experience on this problem.

It is concluded that for a future design an air-tube heater will be smaller and cheaper than the gas-tube type, have a better thermal performance, as there will be no need of tube-plate cooling, and should give much greater freedom from corrosion troubles.

It is not practical to rebuild our present heater as an air-tube type, but it is being rebuilt as a straight counterflow gas-tube type to confirm the opinion expressed about the effect of the parasitic losses of the combined parallel-counterflow type. Rig tests of a small-scale tube matrix have been employed to develop a baffle system which, as far as possible, will give a uniform air distribution at the hot end. At the same time the shell-cooling arrangements have been altered to save a little on shell-cooling losses, and the front tube-plate cooling-air circuit rearranged to insure that the necessary cooling air does not dilute the hot air, but that it is mixed into the main stream at the cold end of the heater.

Furnace. The furnace, and especially the mixing section, are being modified extensively. An arrangement of the new design is shown in Fig. 15.

The cyclone itself is being rebuilt to provide a continuous reentrant throat, and a slag drain direct from the combustion section. The coal entries which have given the best results will be used and with the improvement from the full throat and the steadier coal feed are expected to be satisfactory.

The mixing section is as large as can be reasonably accommodated in the present plant. The dilution air is introduced through jets into the hot gases discharging from the cyclone throat. Oxygen will be available to complete combustion of any combustible gases being discharged from the cyclone at the earliest moment and the residence time of gases and carried-over particles after injection of the dilution air and before reaching the heater will be the longest possible. The large volume and cross-sectional area of the mixing zone and the symmetrical gas flow should insure a uniform low velocity of the gases and the lowest quantity of air-borne slag particles.

The early injection of the dilution air eliminates all other than water-cooled surface from contact of the hottest gases and permits use of cheaper refractory materials with prospects of long life. Passages for cooling air are provided in the refractory materials which permit the use of a carbon-steel pressure casing. Hot products of combustion are separated from all joints, glands, and other potential sources of leaks by cooling-furnace-inlet air. Thus any small leak will be of this cooler air and not of the hot gases which would cause overheating and rapid extension of the leak. There is a pressure gradient from outside to inside of all refractory materials so that any leakage through cracks or fissures will be of cool air inward rather than hot gases outward.

The design relies upon adequate separation and removal of the slag in the cyclone but the large cross-sectional area of the mixing section should permit deposition of some slag without deterioration of performance. Experience suggests that any slag deposited on the refractories in this cooler region will be easy to remove at intervals which it is hoped will be of at least 200 hr. The general

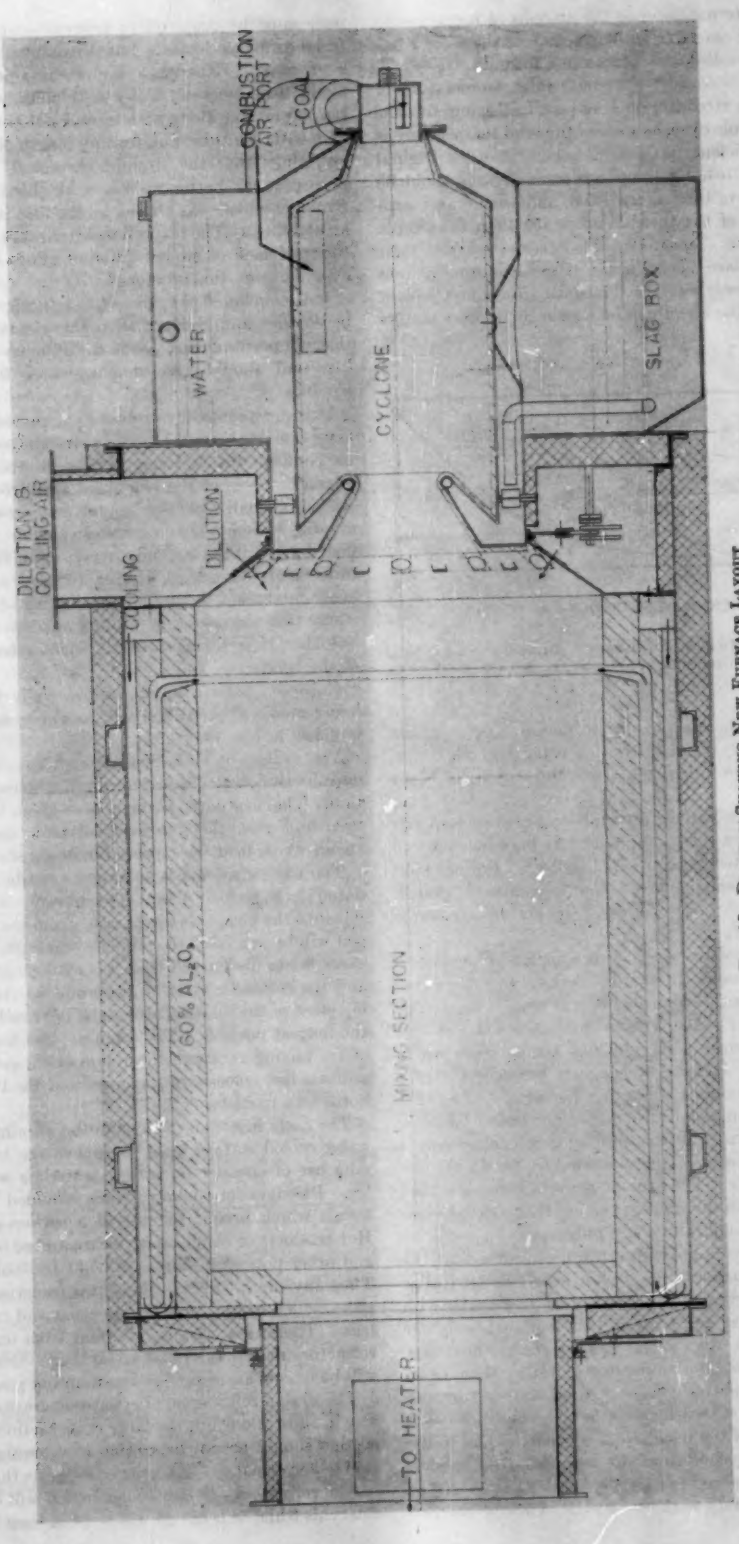

FIG. 15 DIAGRAM SHOWING NEW FURNACE LAYOUT

simplicity of the furnace and connecting duct work should reduce maintenance, leakage, and heat losses.

The slag drain in the new furnace is in the cylinder of the cyclone section. It is expected that the temperature level in the mixing section will not fuse the slag, which will be of a sintered nature and easy to remove. The provision of the drain in the cyclone eliminates the usual channel for slag through the outlet throat of the cyclone and through which considerable carry-over must pass.

The section of the cyclone wall around the slag-drain hole will not be water-cooled. The region of the drain hole will thus be the least-cooled section of the cyclone and, as such, the slag on or in it should melt first and freeze last during transient conditions. The low heat inertia of the system and the large motivating temperature differences should minimize icicle formation. Accessibility is good and there is great freedom for design changes that may be found necessary. The slag is continuously flushed onto a screen by a flow of water circulating between the screen and slag box. This part of the system has been rig-tested and found satisfactory.

The redesign of the plant so that the whole mass flow passes through the furnace and gas side of the heater has increased the pressure in the furnace. The estimated maximum rate of coal consumption has also gone up from 0.3 to 0.5 lb/sec (1080 to 1800 lb/hr). It was decided that a new coal feed using a screw feeder would be designed and extensively rig-tested while the rest of the plant was being rebuilt. At the time of writing these tests are proceeding and results are encouraging. It is believed that the rebuilt cyclone furnace and mixing section will give a vastly improved performance and lead to a design which would be quite practical for some applications.

Conclusions

It is perhaps a little early to make definite conclusions but this first test series has firmly established that the exhaust-heated cycle is a perfectly feasible mode of operation for a coal-burning gas turbine. It has furthermore been demonstrated that it is a particularly rugged machine, capable of operating under conditions of considerable maladjustment and deterioration of components.

Before it could be claimed to be practical, in a commercial sense, as distinct from technically practicable, it remains to be shown that the problems encountered can be resolved, and that the heater is not too expensive. As a result of the work already done, no fear is held that the difficulties cannot be solved, and it is hoped that the next test series, commenced January 8, 1956, will show a large step forward and at the end of which manufacture of an industrial plant giving every hope of successful commercial performance could be considered. It must be remembered that, as pointed out in the Introduction, our problems are essentially those which the boilermakers have already solved. As to the cost factor, our studies show that the heater cost is far from prohibitive in applications requiring relatively small powers, i.e., less than, say, 5000–7500 kw.

Acknowledgments

This entire program has been supported by the Canadian Department of Mines and Technical Surveys and has been helped by the Dominion Coal and Steel Corporation Ltd., Montreal.

Continual help has been freely given by J. I. Yellott, Director of Research, Locomotive Development Committee. The authors' thanks are due to all their colleagues who have worked so hard to make the project successful.

Discussion

A. J. Bachmeier.[4] The role of the gas turbine in the field of industrial power development has frequently been described in rather optimistic terms. The alleged characteristics of the machine which have contributed most to this optimism are its basic simplicity, low capital cost per unit power, and its ability to make use of residual and even solid fuels, and the extent to which these characteristics do not manifest themselves in existing turbine installations may be taken as a measure of the degree of development yet required.

The work the authors have described here is valuable as a piece of research intended to establish whether in principle an exhaust-heated cycle is practical and, as such, complements work carried out in the United States and in Britain. Furthermore, the scale of the work is large enough to allow component design studies to be made without too much danger of being invalidated by scaling factors.

The authors state that their attack on the general problem was to substitute a problem different in degree only from the ones solved in standard boiler practice for the ones plaguing researchers working on a similar program in the United States. When one considers that all the energy entering into the cycle must pass through the heat exchanger, and that in relation to steam boilers which have the same function the over-all conditions for heat transfer are not nearly so favorable, the problem still looks fearsome enough. Now that they have gone through the first set of tests do the authors believe the heat-exchanger costs for a plant of this type will be lower than for a steam plant of comparable rating?

The writer is most emphatically in agreement with the opinion expressed by the authors concerning the desirability of a unit which shows gradual deterioration in performance such as they have on occasion experienced, rather than sudden forced shutdowns. It is not clear, however, how one explains the lack of sensitivity of the cycle to poor combustion and, in particular, to a reduction in heat-transfer surface unless the remaining components are forced to work at a higher temperature stress as well as at a higher pressure loss. If this is so, the apparent reliability of plant operation should not really be taken advantage of except for very short periods.

The response time of 15 sec from zero to full load is somewhat surprising for a plant with such a large total heat capacity and should be adequate for most applications, provided the means for power shutoff in emergencies are maintained as at present for fast shutdown. However, the time for start-up from the cold condition seems long, especially for locomotive application. Do the authors visualize reducing this period and if so, how?

In the discussion on the thermodynamic cycle, the authors mention the two-exchanger design in relation to the cycle efficiency. It should be pointed out that this increase in exchanger capacity is the result of increased temperature differential and therefore increased thermal stresses. There is probably some effect on the rate of chemical attack as well, though this does not necessarily increase. In the same discussion it is concluded that in a future design of the air heater, air-tube construction would be used. While the reasons for going to this construction are set forth, the main reasons for going originally to the gas-tube type, especially the need for cleaning the gas side, does not seem to have been provided for. Do the authors feel present experience warrants this?

With the present experience do the authors deem it possible to install sufficient heat-exchanger area within the space of present locomotive design to give, say, between 2000 and 3000 hp?

---

[4] Gas Dynamics, Division of Mechanical Engineering, National Research Council, Ottawa, Can.

R. M. HARDGROVE.[7] The authors have very kindly admitted that the cyclone furnace was not given the best possible chance for success and should not be judged by the difficulties they experienced with it.

Some years ago Mr. Hudson of the Fuels Research Laboratory of the Mines Department, discussed with us the use of cyclones as a gas-turbine combustor and we did give him a sketch of suggested proportions. Since that time we have had little or no contact with this work, so it is not surprising that difficulties were encountered as the experience and knowledge gained during the development of the cyclone furnace were not utilized. We will be interested in the future success of the rebuilt cyclone.

This cyclone being only 2 ft diam is quite small and the handling of molten slag on these very small units is difficult. As the size of units is increased, the difficulties decrease and on cyclones used on power boilers the handling of the slag is no problem. On locomotives, the space is limited, load fluctuates widely, and the operation must be entirely automatic, as the firemen and engineer can give no time whatever to the equipment, and ash and slag removal must be absolutely trouble-free. The cyclone is also very close to the heat exchanger and the possibility of sticky slag carry-over is greater than with combustors that operate on dry-ash removal. In the larger sizes, the cyclone furnace does possess advantages such as compact size and a shape that is suitable for pressure operation. It also has small ash carry-over and it would seem that the cyclone furnace is well adapted to pressurized combustors for stationary installations.

Heat exchangers can be made in such a variety of designs that studies to optimize the design for lowest cost, weight, pressure drop, etc., can be very rewarding. With clean gases which permit the use of small tubes on close spaces, exchangers can be built that are of such a size that they can be installed on a locomotive. The authors' suggestions for future heat exchangers are in the right direction.

J. I. YELLOTT.[8] The authors are to be commended for their ingenious and persistent attack upon the problem of using coal as gas-turbine fuel. Their work has been followed with particular interest by those of us who have been engaged in the parallel problem of developing the direct-fired coal-burning turbine. The Locomotive Development Committee has consistently followed the policy of aiding all efforts to use coal as gas-turbine fuel, and it is gratifying to learn of the progress which is being made at McGill.

In their introduction, the authors define The Main Problem as the designing of a suitable furnace and heater in which the heat liberated by burning coal at atmospheric pressure can be transferred to compressed air at 60 to 90 psia and thereby heat that air to temperatures as high as 1350 F.

Actually, the main problem turns out to be that of preventing the undesirable constituents of the coal from impairing the operation of the air heater, either temporarily, as by plugging the tubes by ash, or permanently, as by sulphur attack upon the tube materials.

The authors' selection of the cyclone furnace was logical in view of the success enjoyed by this method of coal burning in many large utility and industrial applications. The major difference between the McGill installation and conventional cyclone furnaces for steam generators lies in the distance which the combustion products must travel before they reach small openings where the ash can cause trouble.

[7] Research Consultant, Research Center, The Babcock & Wilcox Company, Alliance, Ohio. Fellow ASME.

[8] Director of Research, Locomotive Development Committee, Bituminous Coal Research, Inc., American Locomotive Company, Dunkirk, N. Y. Mem. ASME.

The writer and his colleagues have found that time must be given for suspended ash particles to freeze before they have an opportunity to hit a surface. In the direct-fired system, the surface first encountered by the ash is the screen which protects the fly-ash separator. Ash coating of this screen, or of the walls of the separator inlet, is annoying but not too serious. Ash coating of the air-heater inlet and tubes, on the other hand, causes reduction in the heat-transfer rate and gives rise to the possibility of the corrosion of the heater tubes.

The use of a simple stoker might greatly simplify both of the major problems of the exhaust-heated cycle. The probability of carrying sticky ash over into the air-heater tubes would also be greatly reduced by air-cooling the furnace walls, thus giving the ash particles a relatively cool surface to which heat could be radiated. Some type of ash separator should be considered, however, in order to keep the ash emission below the levels prescribed by air-pollution ordinances.

The authors mention that severe corrosion of their Nimonic air-heater tubes has taken place. This is probably due to the fact that sulphur-bearing ash has been deposited in hot zones where localized reducing conditions exist. Despite the large amount of total excess air, the solid layer adhering to the tube surfaces may well exist with a deficiency of oxygen, and sulphur attack on the nickel-bearing tube alloy is then inevitable.

The authors have given a good account of their operating experiences; their frank discussion of their troubles as well as their successes is particularly commendable, because progress can only be made by recognizing and then overcoming the difficulties which attend every significant development.

As a final comment on the paper itself, the analysis of the coals used in the test program should be given with their ash characteristics.

AUTHORS' CLOSURE

In answer to Mr. Bachmeier, the question of heat-exchanger costs have been gone into quite thoroughly and possible power plants investigated. For stationary applications a maximum turbine inlet temperature of 1250 F is used and air inlet temperature of 75 F. Component efficiencies and leakage allowances corresponding to the guaranteed performance of continental turbine builders and heat losses based on our test results have been used. For a typical case, 5000 kw, the following results are representative:

Over-all thermal efficiency to generator shaft	27.5	24	21	19	17
Heat-exchanger surface area/kw	16.8	10.2	5.9	3.8	3.0

Clearly, the highest thermal efficiencies will be economically justified only in special cases. At about 20 per cent, however, which is unlikely to be exceeded by a steam plant of 5000 kw capacity, the total installed cost will be in the region $160–180/kw, or less if we can show that ferritic tubing can withstand the sulphur attack. This figure is comparable with the steam-plant cost in that size, and the gas-turbine unit will require less attention and maintenance and virtually no water, so that we believe it can be justified. In larger sizes the steam costs are much more favorable and the efficiency is higher, so that it becomes necessary to use the exhaust of the gas turbine as the combustion air for a steam plant. The combined plant then shows a significant reduction in fuel costs. It is agreed that maintaining power in spite of poor combustion or heater fouling demands increased temperature stress, but it was pointed out that we regarded it as better to keep running, even at reduced power, rather than stopping altogether. Clearly, the power must be reduced to keep the same maximum temperature at the heater inlet. Provided this is done, there is no

question of operation under these conditions being time-limited.

At present it is not believed that really rapid starts from cold can be achieved. The necessity of avoiding severe transient thermal stresses in the heater and furnace is paramount.

The reasons for the air tube heater have been well established in design analysis, and the problems of dry fouling do not appear to be serious. We have ourselves experienced no trouble from this source, and other workers with coal-burning turbines with recuperative heat exchangers report little deterioration due to deposition, and, of course, this problem is overcome in most boilers by soot blowing. With the air tube heater we have projected the design of a locomotive of over-all length 67 feet, 2500 bhp at input to the generator, thermal efficiency 18 per cent, and containing fuel for ten hours' operation.

Mr. Hardgrove's comments are welcomed. As this closure is written some time after the paper was written and we have now had the opportunity of having several hundreds of hours of operation on the modified cyclone shown in Fig. 15, we can now state that exceptionally good performance with much improved slag removal and reduced carry-over has now been obtained. We are grateful to Mr. Hardgrove for his confirmation of our thinking in heat-exchanger design.

Throughout our work we have enjoyed the continual help and support of Mr. Yellott. His present suggestions, as usual, are pertinent and welcome. In the latest series of tests a simple wire-mesh screen placed some four feet ahead of the inlet to the heater has been able to intercept a large part of carried-over slag. From the screen it can easily be shed by an occasional spraying with water, which cracks it off. In the rebuilt furnace, as shown in Fig. 15, the furnace walls are cooled by the coldest air we can use, and this is one of the factors which have reduced the slag deposition rate to much less serious proportions.

We do not consider any ash separator necessary, however, because the slag drain accounts for about 90 per cent of the ash in the coal fired and the exhaust is clean and usually invisible.

The detailed coal analysis was not presented as it was given in footnote 5. A typical approximate analysis is 38 per cent volatile, 7 per cent ash, 55 per cent volatile. The calorific value is 14,000 Btu/lb. The initial softening temperature of the ash is 1900 F, and the ash is about 36 per cent SiO_2, 17 per cent Al_2O_3, and 36 per cent Fe_2O_3. Sodium and potassium account for about 3 per cent, and in the coal as fired, the sulphur can be as high as 3.25 per cent.

Laminar-Free-Convection Heat Transfer From the Outer Surface of a Vertical Circular Cylinder

By E. M. SPARROW[1] and J. L. GREGG,[1] CLEVELAND, OHIO

A solution of the laminar boundary-layer equations has been obtained for free convection from the outer surface of a vertical cylinder. The temperature of the cylinder surface was taken to be uniform. Heat-transfer results have been found for Prandtl numbers of 0.72 and 1 (i.e., for gases) and are presented on graphs. The Nusselt numbers for the cylinder were higher than those for the flat plate. Also, the deviation of the cylinder Nusselt numbers from those for the flat plate was greater for Prandtl number of 0.72 than for Prandtl number of 1. A quantitative criterion was established for determining the conditions under which the heat transfer from a cylinder could be calculated with sufficient accuracy using the flat-plate results. An analysis based on replacing the free-convection problem by a problem in pure conduction through a fictitious layer of stagnant fluid gave good agreement with the boundary-layer solution.

Nomenclature

The following nomenclature is used in the paper:

A = area of surface through which heat transfer is taking place, sq ft

b = thickness of a fictitious layer of stagnant fluid, ft

C_1 = constant appearing in definition of η $\left[\frac{g\beta(t_w - t_\infty)r_0^3}{\nu^2}\right]^{1/4} \frac{r_0^{-1/4}}{2^{3/4}}$, $(\text{ft})^{-3/4}$

C_2 = constant appearing in definition of ξ $\left[\frac{g\beta(t_w - t_\infty)r_0^3}{\nu^2}\right]^{-1/4} r_0^{-1/4}\, 2^{3/4}$, $(\text{ft})^{-1/4}$

C_3 = constant appearing in the definition of f $\left[\frac{g\beta(t_w - t_\infty)r_0^3}{\nu^2}\right]^{-1/4} \frac{2^{3/4}}{\nu r_0^{1/4}}$, $\text{sec}/(\text{ft})^{11/4}$

c_p = specific heat at constant pressure, Btu/lb deg F

f = dimensionless dependent variable, $C_3\psi/x^{1/4}$

$f_0, f_1, f_2, \ldots$ = coefficients in expansion of f in terms of ξ, dimensionless

Gr_x = Grashof number based on x, $\frac{g\beta(t_w - t_\infty)x^3}{\nu^2}$, dimensionless

g = acceleration of gravity, ft/sec^2

h = local coefficient of heat transfer, Btu/hr sq ft deg F

$\bar{h}$ = average coefficient of heat transfer, Btu/hr sq ft deg F

k = thermal conductivity, Btu/hr ft deg F

Nu_x = local Nusselt number based on x, $\frac{hx}{k}$, dimensionless

$\overline{\text{Nu}}_x$ = average Nusselt number based on x, $\frac{\bar{h}x}{k}$, dimensionless

Pr = Prandtl number, $\frac{c_p\mu}{k} = \frac{\nu}{\alpha}$, dimensionless

Q = total rate of heat transfer from surface from $x = 0$ to x, Btu/hr

q = heat-transfer rate per unit area, Btu/hr sq ft

r = co-ordinate measuring radial distance from cylinder axis, ft

r_0 = radius of cylinder, ft

t = static temperature, deg F

t_w = wall temperature, deg F

t_∞ = ambient temperature, deg F

u = velocity component in x-direction, fps

v = velocity component in r-direction, fps

x = co-ordinate measuring longitudinal distance along cylinder or plate from leading edge, ft

α = thermal diffusivity, $\frac{k}{\rho c_p}$, sq ft/sec

β = coefficient of thermal expansion (deg F)$^{-1}$

Δ = thermal boundary-layer thickness for a flat plate, ft

η = dimensionless independent variable, $\frac{C_1(r^2 - r_0^2)}{x^{1/4}}$

θ = dimensionless dependent variable, $\frac{t - t_\infty}{t_w - t_\infty}$

$\theta_0, \theta_1, \theta_2, \ldots$ = coefficients in series expansion of θ in terms of ξ, dimensionless

λ = proportionality constant (in Equation [25]) which increases with decreasing Pr, dimensionless

μ = absolute viscosity, lb/sec-ft

ν = kinematic viscosity, sq ft/sec

ξ = dimensionless independent variable, $C_2x^{1/4}$

ρ = density, pcf

φ = abbreviation for dimensionless factor $-\frac{4}{3}\frac{1}{\sqrt{2}}\theta_0'(0)$

ψ = stream function, cu ft/sec

Subscripts

fp = flat plate

cyl = cylinder

---

[1] National Advisory Committee for Aeronautics.

Contributed by the Heat Transfer Division and presented at the Diamond Jubilee Annual Meeting, Chicago, Ill., November 13–18, 1955, of The American Society of Mechanical Engineers.

Note: Statements and opinions advanced in papers are to be understood as individual expressions of their authors and not those of the Society. Manuscript received at ASME Headquarters, June 20, 1955. Paper No. 55—A-25.

Introduction

There has been relatively little study of laminar free-convection heat transfer from the outer surface of a vertical cylinder. Elenbaas (1)[2] deduced an expression for the average Nusselt number using Langmuir's idea (2) that the free-convection heat-transfer problem might be replaced by a heat-conduction problem in an annulus of stagnant fluid surrounding the cylinder. Free-convection heat-transfer experiments have been carried out by Carne (3) on vertical cylinders of various diameters and lengths.

In the present investigation, a solution for the free-convection heat transfer from the outer surface of a vertical cylinder will be obtained from the differential equations of the laminar boundary layer. Numerical results are given for Prandtl numbers of 0.72 and 1, that is, for gases. In addition, an analysis based on pure conduction through an equivalent stagnant layer of fluid will be made which differs somewhat from that of Elenbaas. The surface temperature of the cylinder will be taken to be uniform.

A priori, it may be expected that when the thermal boundary layer is sufficiently thin, so that the radial co-ordinate of any point in the boundary layer is not appreciably different from the radius of the cylinder, the heat-transfer results for the cylinder should be close to those for the flat plate. As the boundary-layer thickness increases relative to the cylinder radius, it is expected that the cylinder results would depart more and more from those of the flat plate. (An analogous situation occurs in pure conduction, where the heat-transfer results for a thin annulus are very close to those of a plane slab. As the thickness of the annulus increases relative to the inner radius, the results for the annulus depart more and more from those of the slab.)

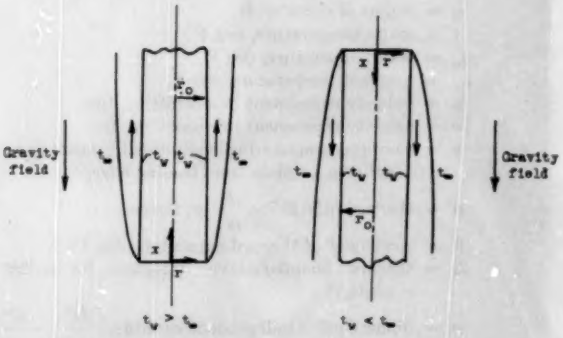

Fig. 1 Physical Model and Co-Ordinate System

Analysis

General Considerations. The physical model and the co-ordinate system are shown in an elevation view in Fig. 1. Two physical situations which come within the scope of the analysis are pictured.

The left-hand sketch depicts the case where the wall temperature t_w exceeds the ambient temperature t_∞. The fluid in the neighborhood of the wall has a higher temperature and lower density[3] than the fluid far from the wall. There will thus be established, due to buoyancy, an upward flow of fluid in the neighborhood of the wall. The region where the upward flow primarily occurs is called the velocity boundary layer. The thermal boundary layer is defined as that region of space where the temperature t deviates markedly from the ambient temperature t_∞. In general, the velocity and thermal boundary layers have different thickness, the relative magnitude depending upon the fluid properties. Both boundary layers will be assumed to have zero thickness at the leading edge ($x = 0$). The velocity boundary layer is shown schematically in Fig. 1.

The right-hand sketch shows the situation where the wall temperature is lower than the ambient temperature. The flow of fluid in the boundary layer is downward as shown.

If the co-ordinates are taken as shown, the distinction between the two problems vanishes when the differential equations expressing conservation of mass, momentum, and energy are made dimensionless; and there will be no need to treat them separately. So the analysis will be carried forward for the case of $t_w > t_\infty$; but it is to be remembered that the results apply to both situations depicted in Fig. 1.

Mathematical Formulation. The equations expressing conservation of mass, momentum, and energy for laminar free convection in a boundary layer on a vertical cylinder are

$$\frac{\partial(ru)}{\partial x} + \frac{\partial(rv)}{\partial r} = 0 \quad [1]$$

$$u\frac{\partial u}{\partial x} + v\frac{\partial u}{\partial r} = g\beta(t - t_\infty) + \frac{\nu}{r}\frac{\partial}{\partial r}\left(r\frac{\partial u}{\partial r}\right) \quad [2]$$

$$u\frac{\partial t}{\partial x} + v\frac{\partial t}{\partial r} = \frac{\alpha}{r}\frac{\partial}{\partial r}\left(r\frac{\partial t}{\partial r}\right) \quad [3]$$

In accord with the usual practice in free convection, the density has been considered a variable only in formulating the buoyancy term $g\beta(t - t_\infty)$. All other fluid properties are taken to be constant. Viscous dissipation and work against the gravity field have been neglected.

The solution of Equation [1] can be written as usual in terms of a stream function ψ

$$\left.\begin{aligned} u &= \frac{1}{r}\frac{\partial\psi}{\partial r} \\ v &= -\frac{1}{r}\frac{\partial\psi}{\partial x} \end{aligned}\right\} \quad [4]$$

Next, the partial differential Equations [2] and [3] are transformed from the (x, r) co-ordinate system to the (ξ, η) system using the following substitutions

$$\eta = C_1\frac{(r^2 - r_0^2)}{x^{1/4}} \quad [5]$$

$$\xi = C_2 x^{1/4} \quad [6]$$

$$f(\xi, \eta) = C_3 x^{-1/4}\psi \quad [7]$$

$$\theta(\xi, \eta) = \frac{t - t_\infty}{t_w - t_\infty} \quad [8]$$

where the variables η, ξ, f, and θ are all dimensionless and the constants C_1, C_2, and C_3, which are made up of fluid properties and dimensions, are defined in the nomenclature. The equations resulting from the transformation are

$$\xi\left(\frac{\partial f}{\partial\eta}\frac{\partial^2 f}{\partial\xi\partial\eta} - \frac{\partial f}{\partial\xi}\frac{\partial^2 f}{\partial\eta^2}\right) - f\frac{\partial^2 f}{\partial\eta^2} = \xi^3\frac{\partial}{\partial\eta}\left((1 + \xi\eta)\frac{\partial^2 f}{\partial\eta^2}\right) + \xi^4\theta \quad [2a]$$

$$\xi\left(\frac{\partial\theta}{\partial\xi}\frac{\partial f}{\partial\eta} - \frac{\partial\theta}{\partial\eta}\frac{\partial f}{\partial\xi}\right) - f\frac{\partial\theta}{\partial\eta} = \frac{\xi^3}{\mathrm{Pr}}\frac{\partial}{\partial\eta}\left((1 + \xi\eta)\frac{\partial\theta}{\partial\eta}\right) \quad [3a]$$

[2] Numbers in parentheses refer to Bibliography at end of paper.

[3] These remarks apply to ordinary fluids which have decreasing density with increasing temperature.

Equations [2a] and [3a] constitute simultaneous equations for the functions f and θ. The coupling of the equations arises because the free-convection flow is initiated by density differences caused by temperature differences.

The method[4] used for solving Equations [2a] and [3a] for f and θ is to expand these functions in power series in terms of ξ, with coefficients which are functions of η. The solution will be found when the coefficients are determined. The series expansions are

$$f(\xi, \eta) = \xi^3[f_0(\eta) + \xi f_1(\eta) + \xi^2 f_2(\eta) + \ldots] \ldots\ldots [9]$$

$$\theta(\xi, \eta) = \theta_0(\eta) + \xi\theta_1(\eta) + \xi^2\theta_2(\eta) + \ldots \quad \ldots\ldots [10]$$

These series are introduced into Equations [2a] and [3a] and the terms are grouped according to the power of ξ which multiplies them. So

$$\xi^2[\theta_0'' + 3\mathrm{Pr} f_0\theta_0'] + \xi^3[\quad] + \ldots = 0 \ldots\ldots [11]$$

$$\xi^4[f_0''' + 3f_0f_0'' - 2f_0'^2 + \theta_0] + \xi^5[\quad] + \ldots = 0 \ldots [12]$$

where the primes represent differentiation with respect to η.

In order that Equations [11] and [12] be satisfied for all values of ξ, it is necessary that each of the brackets be identically zero. In this way there is obtained a set of differential equations for calculating the various coefficients in the series expansions in Equations [9] and [10]. For example, when the first bracket in both Equations [11] and [12] is equated to zero, there is obtained a pair of simultaneous ordinary differential equations for calculating θ_0 and f_0. The differential equations derived in this fashion from Equations [11] and [12] are given in Appendix A.

The boundary conditions still remain to be specified. In terms of the variable f, the velocity components are

$$u = 2\frac{C_1}{C_3}\frac{\partial f}{\partial \eta} \ldots\ldots\ldots\ldots\ldots\ldots [13]$$

$$v = -\frac{1}{C_3C_4rx}\left[\xi\left(f + \xi\frac{\partial f}{\partial \xi}\right) - \eta\xi\frac{\partial f}{\partial \eta}\right] \ldots\ldots [14]$$

The boundary conditions $u = 0$, $v = 0$ at $r = r_0$ and $u = 0$ at $r = \infty$ give rise to the following conditions on f and its derivatives

$$\text{at } \eta = 0 \quad \left\{ \begin{array}{l} f = 0 \\ \dfrac{\partial f}{\partial \eta} = 0 \\ \dfrac{\partial f}{\partial \xi} = 0 \end{array} \right\} \ldots\ldots\ldots\ldots [15a]$$

$$\text{at } \eta = \infty \quad \left\{ \frac{\partial f}{\partial \eta} = 0 \right\}$$

From the definition of θ, Equation [8], it follows that

$$\text{at } \eta = 0, \quad \theta = 1 \qquad \text{at } \eta = \infty, \theta = 0 \ldots\ldots [15b]$$

When the series expansions for f and θ are introduced into Equations [15a] and [15b], the boundary conditions for the f_0, f_1, f_2, . . ., θ_0, θ_1, θ_2, . . ., and their derivatives are found to be

$$\text{at } \eta = 0 \quad \left\{ \begin{array}{l} f_0 = f_1 = f_2 \ldots = 0 \\ f_0' = f_1' = f_2' \ldots = 0 \\ \theta_0 = 1, \quad \theta_1 = \theta_2 = \ldots = 0 \end{array} \right\} \ldots\ldots [16]$$

$$\text{at } \eta = \infty \quad \left\{ \begin{array}{l} f_0' = f_1' = f_2' \ldots = 0 \\ \theta_0 = \theta_1 = \theta_2 \ldots = 0 \end{array} \right\}$$

The primes indicate differentiation with respect to η.

[4] A similar approach has been used by Seban and Bond (4) to solve the forced-convection problem for the circular cylinder.

It is to be noted that $\eta = \infty$ corresponds to $x = 0$ as well as to $r = \infty$. So, the conditions $t = t_\infty$ and $u = 0$ are automatically imposed at $x = 0 (r > r_0)$.

The differential equations for f_0 and θ_0, Equations [29], and their boundary conditions are identical to those for a flat plate. Evidently, then, the succeeding θ_n and f_n give the departures from the flat-plate solution which are due to the cylindrical geometry.

A solution for (f_0, θ_0), (f_1, θ_1), and (f_2, θ_2) has been obtained by numerical integration of the differential Equations [29], [30], and [31] subject to the boundary conditions, Equations [16], using the IBM Card Programmed Calculator. Results have been obtained for Prandtl numbers of 0.72 and 1. Details of the calculation are given in Appendix A.

Derivation of Heat-Transfer Parameters

Local Heat-Transfer Coefficient. The definition of the local heat-transfer coefficient is

$$h \equiv \frac{q}{t_w - t_\infty} = -\frac{k}{t_w - t_\infty}\left(\frac{\partial t}{\partial r}\right)_{r=r_0} \ldots\ldots [17]$$

In terms of the dimensionless variables defined by Equations [5] and [8], the expression for h becomes

$$h = -\frac{2r_0C_1k}{x^{1/4}}\left(\frac{\partial \theta}{\partial \eta}\right)_{\eta=0} \ldots\ldots\ldots [17a]$$

The local Nusselt number is obtained from the definition

$$\mathrm{Nu}_x \equiv \frac{hx}{k} = -2r_0C_1x^{1/4}\left(\frac{\partial \theta}{\partial \eta}\right)_{\eta=0} \ldots\ldots [18]$$

The derivative

$$\left(\frac{\partial \theta}{\partial \eta}\right)_{\eta=0}$$

is written in terms of the series expansion for θ given in Equation [10], and C_1 is evaluated from the symbol list, giving the result

$$\mathrm{Nu}_x = -\frac{1}{\sqrt{2}}\mathrm{Gr}_x^{1/4}[\theta_0'(0) + \xi\theta_1'(0) + \xi^2\theta_2'(0) + \ldots] \ldots [18a]$$

where Gr_x is the Grashof number based on x defined as

$$\mathrm{Gr}_x \equiv \frac{g\beta(t_w - t_\infty)x^3}{\nu^2}$$

Equation [18a] may be rewritten in the form

$$\mathrm{Nu}_x = -\frac{1}{\sqrt{2}}\mathrm{Gr}_x^{1/4}\theta_0'(0)\left[1 + \xi\frac{\theta_1'(0)}{\theta_0'(0)} + \xi^2\frac{\theta_2'(0)}{\theta_0'(0)} + \ldots\right] \ldots\ldots [18b]$$

The factor

$$\left[-\frac{1}{\sqrt{2}}\mathrm{Gr}_x^{1/4}\theta_0'(0)\right]$$

is the local Nusselt number for a flat plate. Introducing additional subscripts to distinguish between the local Nusselt numbers for the cylinder (cyl) and the flat plate (fp), there is finally obtained

$$\frac{\mathrm{Nu}_{x,\,cyl}}{\mathrm{Nu}_{x,\,fp}} = 1 + \xi\frac{\theta_1'(0)}{\theta_0'(0)} + \xi^2\frac{\theta_2'(0)}{\theta_0'(0)} + \ldots \quad \ldots\ldots [19]$$

Equation [19] compares the local Nusselt number for the cylinder at a location x with that for a flat plate at the same x, under the condition that $(t_w - t_\infty)$ is the same for the flat plate and the cylinder.

The quantities $\theta_0'(0)$, $\theta_1'(0)$, $\theta_2'(0)$, . . ., depend only on the Prandtl number. So, for a fixed Prandtl number, the ratio given by Equation [19] is a function only of the variable ξ. When the C_3 appearing in Equation [6] defining ξ is evaluated from the nomenclature, it is found that

$$\xi = \frac{2^{3/4}}{\mathrm{Gr}_x^{1/4}} \left(\frac{x}{r_0}\right) \quad \ldots\ldots [20]$$

Average Heat-Transfer Coefficient. The average heat-transfer coefficient for a length of cylinder between $x = 0$ and x is

$$\bar{h} = \frac{Q}{A(t_w - t_\infty)} = \frac{\int_0^x 2\pi r_0 q\, dx}{2\pi r_0 x (t_w - t_\infty)} = \frac{\int_0^x q\, dx}{x(t_w - t_\infty)} \quad \ldots [21]$$

The heat flux q can be replaced by $h(t_w - t_\infty)$, and since $(t_w - t_\infty)$ is uniform along the cylinder, Equation [21] becomes

$$\bar{h} = \frac{1}{x} \int_0^x h\, dx \quad \ldots\ldots [21a]$$

The result of the integration is

$$\overline{\mathrm{Nu}}_x \equiv \frac{\bar{h}x}{k} = -\frac{4}{3} \frac{1}{\sqrt{2}} \mathrm{Gr}_x^{1/4}\, \theta_0'(0) \left[1 + \frac{3}{4}\xi \frac{\theta_1'(0)}{\theta_0'(0)} + \frac{3}{5}\xi^2 \frac{\theta_2'(0)}{\theta_0'(0)} + \ldots\right] \quad \ldots\ldots [22]$$

The factor

$$\left[-\frac{4}{3} \frac{1}{\sqrt{2}} \mathrm{Gr}_x^{1/4}\, \theta_0'(0)\right]$$

is the average Nusselt number for a flat plate. Introducing additional subscripts to distinguish between the average Nusselt number for the cylinder and for the flat plate, there is finally obtained

$$\frac{\overline{\mathrm{Nu}}_{x,\,cyl}}{\overline{\mathrm{Nu}}_{x,\,fp}} = 1 + \frac{3}{4}\xi \frac{\theta_1'(0)}{\theta_0'(0)} + \frac{3}{5}\xi^2 \frac{\theta_2'(0)}{\theta_0'(0)} + \ldots \quad [23]$$

Equation [23] compares the average Nusselt number for a cylinder for the length between $x = 0$ and x to that for a flat plate for the same length, under the condition that $(t_w - t_\infty)$ is the same for both the cylinder and flat plate.

Results and Discussion

Local Nusselt Number. The ratio of the local Nusselt number for the cylinder to that for the flat plate is determined as a function of

$$\xi = \frac{2^{3/4}}{\mathrm{Gr}_x^{1/4}} \left(\frac{x}{r_0}\right)$$

when the calculated values of $\theta_0'(0)$, $\theta_1'(0)$, and $\theta_2'(0)$ are introduced into Equation [19]. The results are plotted in Fig. 2 for Prandtl numbers of 0.72 and 1.

Once the ratio of Nusselt numbers is obtained from the figure, $\mathrm{Nu}_{x,\,cyl}$ can be calculated as soon as $\mathrm{Nu}_{x,\,fp}$ is given. The results for $\mathrm{Nu}_{x,\,fp}$ have been calculated by Ostrach (5) from an exact solution of the boundary-layer differential equations for Prandtl numbers from 0.01 to 1000. From reference (5), it is found that

$$\left.\begin{array}{ll} \text{for Pr} = 0.72 & \mathrm{Nu}_{x,\,fp} = 0.3568\, \mathrm{Gr}_x^{1/4} \\ \text{for Pr} = 1 & \mathrm{Nu}_{x,\,fp} = 0.4010\, \mathrm{Gr}_x^{1/4} \end{array}\right\} \quad \ldots. [24]$$

The two trends immediately evident from Fig. 2 are: (*a*) That the cylinder Nusselt number deviates more and more from the flat-plate Nusselt number as ξ increases (at a fixed Pr); and (*b*) that

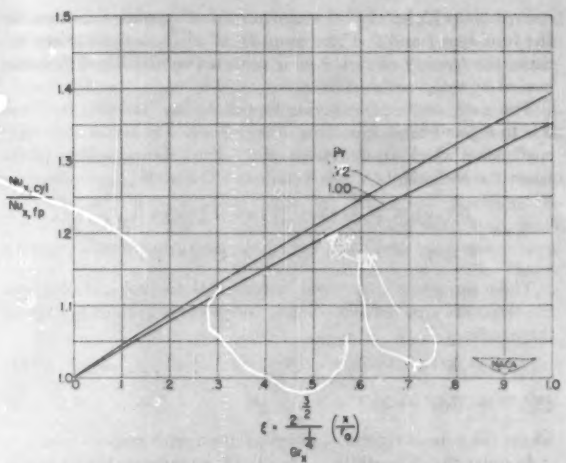

Fig. 2 Comparison of Local Nusselt Number for Cylinder With That for Flat Plate. Curves Are Given for Prandtl Numbers of 0.72 and 1

at a fixed ξ, there are greater deviations of $\mathrm{Nu}_{x,\,cyl}$ from $\mathrm{Nu}_{x,\,fp}$ as Prandtl number decreases. The trends become plausible as soon as the physical interpretation of the variable ξ is considered. For the flat plate, the thickness Δ of the thermal boundary layer is given by

$$\frac{\Delta}{x} = \frac{\lambda(\mathrm{Pr})}{\mathrm{Gr}_x^{1/4}} \quad \ldots\ldots [25]$$

$\lambda(\mathrm{Pr})$ is a number which increases with decreasing Prandtl number. It then follows that

$$\frac{\Delta}{r_0} = \frac{\Delta}{x}\frac{x}{r_0} = \frac{\lambda(\mathrm{Pr})}{\mathrm{Gr}_x^{1/4}} \frac{x}{r_0} = \xi \frac{\lambda(\mathrm{Pr})}{2^{3/4}} \quad \ldots\ldots [26]$$

So ξ is proportional to Δ/r_0. For a fixed Prandtl number, when Δ is small compared with r_0 (small ξ), the cylinder results are close to those for the flat plate; and as Δ increases relative to r_0 (increasing ξ), the cylinder results deviate more and more from those of the flat plate. At a fixed ξ, Δ/r_0 increases with decreasing Prandtl number, so the cylinder results depart more and more from those of the flat plate at a fixed ξ and decreasing Prandtl number.

Average Nusselt Number. Ratios of the average Nusselt number for the cylinder to that for the flat plate are calculated from Equation [23] and are plotted in Fig. 3 with

$$\xi = \frac{2^{3/4}}{\mathrm{Gr}_x^{1/4}} \left(\frac{x}{r_0}\right)$$

as abscissa for Prandtl numbers of 0.72 and 1. Once the ratio of the Nusselt numbers is obtained from the figure, $\overline{\mathrm{Nu}}_{x,\,cyl}$ can be calculated as soon as $\overline{\mathrm{Nu}}_{x,\,fp}$ is given. From the solution of reference (5), it is found that

$$\left.\begin{array}{ll} \text{for Pr} = 0.72 & \overline{\mathrm{Nu}}_{x,\,fp} = 0.4757\, \mathrm{Gr}_x^{1/4} \\ \text{for Pr} = 1 & \overline{\mathrm{Nu}}_{x,\,fp} = 0.5347\, \mathrm{Gr}_x^{1/4} \end{array}\right\} \quad \ldots. [27]$$

The trends of the curves in Fig. 3 are the same as those noted for Fig. 2. It may be noted that at a given ξ and Pr, $\overline{\mathrm{Nu}}_{x,\,cyl}/\overline{\mathrm{Nu}}_{x,\,fp}$ is less than $\mathrm{Nu}_{x,\,cyl}/\mathrm{Nu}_{x,\,fp}$; or in other words, the cylindrical geometry has a lesser effect upon the average Nusselt number than on the local Nusselt number. This result is completely plausible, since the average Nusselt number integrates effects upstream of the location x, where the boundary layer is thinner than at x.

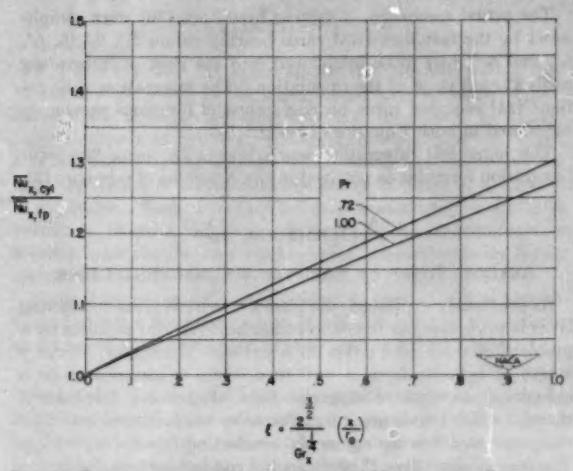

FIG. 3 COMPARISON OF AVERAGE NUSSELT NUMBER FOR CYLINDER WITH THAT FOR FLAT PLATE. CURVES ARE GIVEN FOR PRANDTL NUMBERS OF 0.72 AND 1

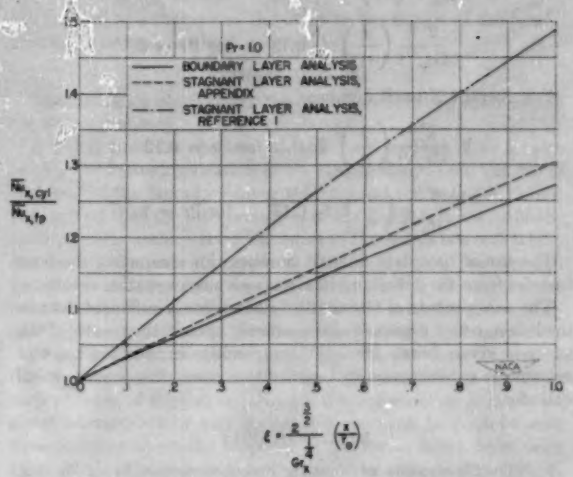

FIG. 4 COMPARISON OF AVERAGE NUSSELT NUMBER RESULTS FROM BOUNDARY-LAYER ANALYSIS WITH THOSE OF STAGNANT-LAYER ANALYSIS. PRANDTL NUMBER EQUALS 1

Comparison of $\overline{Nu}_x$ Results With Those From an Analysis Based on Pure Conduction Through an Equivalent Stagnant Layer. Average Nusselt numbers have been deduced in reference (1) by replacing the free-convection heat-transfer problem by a heat-conduction problem in an equivalent annulus of stagnant fluid. An analysis based on this idea is also made in Appendix B. The basic difference between the analysis in the Appendix B and that of reference (1) is in the manner in which the thickness of the stagnant layer is determined. Although the method of the Appendix is more straightforward than that of reference (1), it cannot be said a priori which method is better.

In Fig. 4, average Nusselt numbers from the stagnant-film analysis are compared to those from the boundary-layer solution for a Prandtl number of 1. The same comparison is made in Fig. 5 for Prandtl number of 0.72. The relatively good agreement of the results of the stagnant-film theory of Appendix B and those from the boundary-layer theory gives a measure of confidence for extending the solution of the Appendix B to other Prandtl numbers for which the boundary-layer solution is not available.

The analysis of the Appendix uses Equations [27] for $\overline{Nu}_{x,\,fp}$ while reference (1) uses the expression

$$\overline{Nu}_{x,\,fp} = 0.6(\mathrm{Pr}\ \mathrm{Gr}_x)^{1/4} \qquad [28]$$

which is an average of experimental results. If Equations [27] had been used for $\overline{Nu}_{x,\,fp}$ in the analysis of reference (1), the results of that analysis would have differed from the boundary-layer solution even more than is shown in Figs. 4 and 5.

Limitations on Results. Equations [19] and [23], which give the heat-transfer results, are truncations of infinite series. Of course, no positive statements about convergence can be made because the behavior of the neglected terms is unknown. For those terms which have been calculated, the coefficients of powers of ξ decrease as the power of ξ increases; also there is a sign change in the coefficient of ξ and ξ^3. Presuming these encouraging trends continue, convergence will be assured if $\xi < 1$.

Assuming that convergence is achieved by taking $\xi < 1$, there is still an error due to neglecting terms of the series. These truncation errors will be largest for ξ near 1 and will decrease as ξ decreases. Assuming the series to be alternating with decreasing terms, it is found that for ξ near 1, the maximum possible error due to truncation for $\mathrm{Pr} = 1$ will be about 3 per cent in Equation [19] and about 2 per cent in Equation [23].

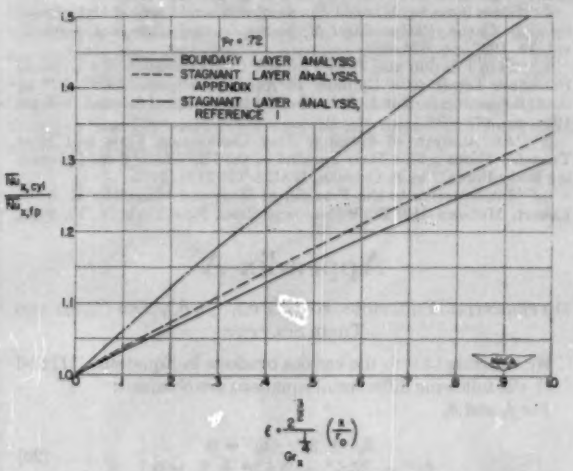

FIG. 5 COMPARISON OF AVERAGE NUSSELT NUMBER RESULTS FROM BOUNDARY-LAYER ANALYSIS WITH THOSE OF STAGNANT-LAYER ANALYSIS. PRANDTL NUMBER EQUALS 0.72

The analysis has been made for laminar boundary-layer flow. Experiments on flat plates have shown that this model is good in the range $10^4 < \mathrm{Gr}_x < 10^9$. For the cylinder, in the absence of experimental data to define the range of validity of the laminar boundary-layer model, the limits $10^4 < \mathrm{Gr}_x < 10^9$ will be imposed.

CONCLUDING REMARKS

For practical purposes, it is desirable to establish a criterion for distinguishing between those conditions under which the flat-plate results are sufficiently accurate for calculating the heat transfer from a cylinder, and those conditions under which the Nusselt number results derived for the cylinder must be used. At present, no quantitative criterion exists. If it is decided that flat-plate results are sufficiently accurate if they give rise to errors of 5 per cent or less in calculating heat-transfer parameters for the cylinder, then the flat-plate results may be used under the following conditions:

For local Nusselt numbers

$$\frac{2^{5/3}}{\mathrm{Gr}_x^{1/4}}\left(\frac{x}{r_0}\right) \leqslant 0.11 \qquad \text{for Pr} = 0.72$$

$$\frac{2^{5/3}}{\mathrm{Gr}_x^{1/4}}\left(\frac{x}{r_0}\right) \leqslant 0.13 \qquad \text{for Pr} = 1$$

For average Nusselt numbers

$$\frac{2^{5/3}}{\mathrm{Gr}_x^{1/4}}\left(\frac{x}{r_0}\right) \leqslant 0.15 \text{ for Pr} = 0.72$$

$$\frac{2^{5/3}}{\mathrm{Gr}_x^{1/4}}\left(\frac{x}{r_0}\right) \leqslant 0.17 \qquad \text{for Pr} = 1$$

The use of flat-plate Nusselt numbers for computing the heat transfer from the cylinder will always give conservative results.

The experiments of Carne (3) do not contain sufficient data in the laminar-flow region to allow a check against the results of the analysis given here. Hence there remains a need for a set of systematic experiments on laminar free convection on a vertical cylinder.

BIBLIOGRAPHY

1 "The Dissipation of Heat by Free Convection From Vertical and Horizontal Cylinders," by W. Elenbaas, *Journal of Applied Physics*, vol. 19, 1948, pp. 1148–1154.

2 "Convection and Conduction of Heat in Gases," by I. Langmuir, *Physical Review*, vol. 34, June, 1912, pp. 401–422.

3 "Heat Loss by Natural Convection From Vertical Cylinders," by J. B. Carne, *Philosophical Magazine Journal of Science*, series 7, vol. 24, 1937, pp. 634–653.

4 "Skin Friction and Heat Transfer Characteristics of a Laminar Boundary Layer on a Cylinder in Axial Incompressible Flow," by R. A. Seban and R. Bond, *Journal of the Aeronautical Sciences*, vol. 19, 1951, pp. 671–675.

5 "An Analysis of Laminar Free Convection Flow and Heat Transfer About a Flat Plate Parallel to the Direction of the Generating Body Force," by S. Ostrach, NACA TR 1111, 1953.

6 "Introduction to the Transfer of Heat and Mass," by E. R. G. Eckert, McGraw-Hill Book Company, Inc., New York, N. Y., 1950.

Appendix A

Differential Equations for (f_0, θ_0), (f_1, θ_1), and (f_2, θ_2) and Their Solution

By equating to zero the various brackets in Equations [11] and [12], the following differential equations are obtained:

For f_0 and θ_0

$$\left.\begin{aligned} \theta_0'' + 3\mathrm{Pr}\, f_0\theta_0' &= 0 \\ f_0''' + 3f_0f_0'' - 2(f_0')^2 + \theta_0 &= 0 \end{aligned}\right\} \quad \ldots\ldots [29]$$

For f_1 and θ_1

$$\left.\begin{aligned} \theta_1'' + \theta_0' + \eta\theta_0'' - \mathrm{Pr}(f_0'\theta_1 - 4f_1\theta_0' - 3f_0\theta_1') &= 0 \\ f_1''' + f_0'' + \eta f_0''' - 5f_0'f_1' + 4f_0''f_1 + 3f_1''f_0 + \theta_1 &= 0 \end{aligned}\right\} \quad [30]$$

For f_2 and θ_2

$$\left.\begin{aligned} \theta_2'' + \theta_1' + \eta\theta_1'' - \mathrm{Pr}(f_1'\theta_1 + 2f_0'\theta_2 \\ \qquad - 5f_2\theta_0' - 4f_1\theta_1' - 3f_0\theta_2') &= 0 \\ f_2''' + f_1'' + \eta f_1''' - 6f_0'f_2' - 3(f_1')^2 + 5f_0''f_2 \\ \qquad + 4f_1''f_1 + 3f_2''f_0 + \theta_2 &= 0 \end{aligned}\right\} \quad [31]$$

The general approach toward solution will be discussed for Equations [29] but it applies also to Equations [30] and [31]. A detailed account of the solution of Equations [29] is given in the Appendix of reference (5).

In order to carry out the numerical integration of Equations [29], the values of f_0, f_0', f_0'', θ_0, and θ_0' are required at $\eta = 0$. From the listing of boundary conditions given in Equations [16], it is seen that only f_0, f_0', and θ_0 are given at $\eta = 0$, while f_0' and θ_0 are given at $\eta = \infty$. So the problem is actually the finding of a pair of values of f_0'' and θ_0' at $\eta = 0$ which will lead to a solution of equations having $f_0' = 0$ and $\theta_0 = 0$ at $\eta = \infty$.

The actual mechanics of solving Equations [30] were complicated by the fact that IBM cards bearing values θ_0', θ_0'', f_0, f_0', f_0'', and f_0''' had to be introduced into the deck of integrating cards at each point of the calculation. The integration of Equations [31] required cards bearing values of functions previously calculated in both Equations [29] and [30].

The numerical integration was achieved by using five-point integration formulas as outlined in the Appendix of reference (5).

Appendix B

Analysis Based on Equivalent Conducting Layer

As previously explained, the idea of the equivalent conducting layer is to replace the free-convection heat-transfer problem by a problem of pure conduction in a cylindrical annulus. Over a length of cylinder from $x = 0$ to x, there is assumed to be a cylindrical annulus of stagnant fluid of uniform thickness b through which heat is being transferred by conduction alone. The temperature difference across the conducting layer is $(t_w - t_\infty)$. The over-all heat flow through such a conducting annulus is

$$Q = \frac{2\pi xk}{\ln\left(\dfrac{r_0 + b}{r_0}\right)}(t_w - t_\infty) \quad \ldots\ldots [32]$$

An average Nusselt number may be obtained from this

$$\overline{\mathrm{Nu}}_{x,\,\mathrm{cyl}} = \frac{\bar{h}x}{k} = \frac{Q}{2\pi r_0 x(t_w - t_\infty)}\frac{x}{k} = \frac{x}{r_0}\frac{1}{\ln\left(1 + \dfrac{b}{r_0}\right)} \quad \ldots\ldots [33]$$

The thickness of the conducting film b is chosen so that when $b/r_0 \ll 1$, Equation [33] will yield the Nusselt number for the flat plate.[5] For $b/r \ll 1$

$$\frac{x}{r_0}\frac{1}{\ln\left(1 + \dfrac{b}{r_0}\right)} \cong \frac{x}{r_0}\frac{1}{b/r_0} = \frac{x}{b} = \overline{\mathrm{Nu}}_{x,\,\mathrm{fp}} \quad \ldots\ldots [34]$$

So

$$\overline{\mathrm{Nu}}_{x,\,\mathrm{cyl}} = \frac{x/r_0}{\ln\left(1 + \dfrac{x/r_0}{\overline{\mathrm{Nu}}_{x,\,\mathrm{fp}}}\right)} \quad \ldots\ldots [35]$$

It has already been noted that

$$\overline{\mathrm{Nu}}_{x,\,\mathrm{fp}} = -\frac{4}{3}\frac{1}{\sqrt{2}}\mathrm{Gr}_x^{1/4}\theta_0'(0) \quad \ldots\ldots [36]$$

$\theta_0'(0)$ is a function of Prandtl number which has been calculated in reference (5) for Prandtl numbers in the range 0.01 to 1000. For convenience let

$$\varphi(\mathrm{Pr}) = -\frac{4}{3}\frac{1}{\sqrt{2}}\theta_0'(0) \quad \ldots\ldots [37]$$

Introducing Equations [36], [37], and the definition of ξ from Equation [20] into Equation [35], there is finally obtained

$$\frac{\overline{\mathrm{Nu}}_{x,\,\mathrm{cyl}}}{\overline{\mathrm{Nu}}_{x,\,\mathrm{fp}}} = \frac{\xi}{2^{3/2}\varphi(\mathrm{Pr})}\frac{1}{\ln\left(1 + \dfrac{\xi}{2^{3/2}\varphi(\mathrm{Pr})}\right)} \quad \ldots\ldots [38]$$

[5] This is analogous to the approach used by Eckert [reference (6), pp. 164–165] for the horizontal cylinder.

Discussion

T. F. Irvine, Jr.[6] It would appear that the information contained in Figs. 2 to 5 of the paper would have an added significance if the abscissas had been chosen as the ratio of boundary-layer thickness to cylinder radius. This representation, which was mentioned by the authors, would enable the reader to visualize the results of the calculations better in terms of a physical flow picture. Such a method of data presentation would also permit a boundary-layer comparison of this free-convection solution with the similar forced-convection calculation by Seban and Bond cited in the paper.[7]

Since there is a great deal of interest at present in free convection at very low Prandtl numbers, it will be helpful for the authors to comment on the extension of their work into this region.

S. I. Pai.[8] In the authors' analysis, the solution is expressed in power series of x, the axial distance along the cylinder. Since one does not know the radius of convergence of such a series, it is usually assumed that the solution holds only for small value of x. On the other hand, the fundamental equations used in this analysis are the boundary-layer equations which hold true only for large value of x. This directly contradicts the method of solution. Have the authors any idea in what range of x their solution holds so that the two limitations mentioned, one due to the method of solution and the other to the nature of the fundamental equations, are both satisfied?

[6] Instructor, Department of Mechanical Engineering, University of Minnesota, Minneapolis, Minn.

[7] See reference (4) of the paper.

[8] Associate Research Professor, University of Maryland, College Park, Md.

Authors' Closure

The authors wish to thank the discussers for their interest and for their comments.

It is felt that the abscissa variable used in Figs. 2 to 5 more readily facilitates application of the results than would the use of the ratio of the boundary-layer thickness to the cylinder radius. It is agreed that the interpretation of the findings in terms of the ratio of the boundary-layer thickness to the radius is worth while, and such a discussion is given in the paper. For low Prandtl number fluids (i.e., liquid metals), the numerical calculations are considerably more time-consuming than are those for gases. Calculations for low Prandtl numbers are now being contemplated.

Professor Pai's remarks cogently describe the usual uncertainties encountered whenever one uses series-expansion methods such as those of this paper. No positive information is available about convergence of such series, and one must be content with some remarks about the behavior of the terms which have been calculated. With reference to the limitations imposed by boundary-layer theory, one can make more definite statements. In the region near the leading edge (small x), the vertical cylinder behaves very much like the vertical flat plate. So, it is quite reasonable to suppose that the value of the Grashof number at which the boundary-layer analysis first begins to give correct heat-transfer results for the flat plate also applies to the vertical cylinder. For air, it is found that this value of the Grashof number is 104. (For Grashof numbers less than 10^4, the heat-transfer results predicted by the boundary-layer analysis are lower than those determined experimentally.)

Combined Forced and Free-Laminar Heat Transfer in Vertical Tubes With Uniform Internal Heat Generation[1]

By T. M. HALLMAN,[2] CLEVELAND, OHIO

Fully developed velocity profiles, temperature profiles, mixed-mean-to-wall temperature differences, Nusselt numbers, and pressure drops are predicted for combined forced and free-laminar convective heat transfer in vertical round pipes. Uniform internal heat generation within the fluid may or may not be present, and a uniform heating or cooling at the tube wall is considered (including the case of the insulated wall). A comparison is made between the analysis and the small amount of experimental data available in the literature.

Nomenclature

The following nomenclature is used in the paper:

A = axial temperature gradient in fluid, $\partial t/\partial x$, deg F/ft

$\mathrm{ber}_0\xi$, $\mathrm{bei}_0\xi$ $J_0(i^{3/2}\xi) = I_0(i^{1/2}\xi) = \mathrm{ber}_0\xi + i\,\mathrm{bei}_0\xi$

$\mathrm{ber}_0'\xi = \dfrac{d}{d\xi}(\mathrm{ber}_0\,\xi)$

$\mathrm{bei}_0'\,\xi = \dfrac{d}{d\xi}(\mathrm{bei}_0\,\xi)$

$\mathrm{ber}_0^2\xi$, $\mathrm{bei}_0^2\xi$ $(\mathrm{ber}_0\xi)^2$, $(\mathrm{bei}_0\xi)^2$

C = pressure-drop parameter, $-\left(\dfrac{dp}{dx} + \rho_w g\right) D^2/32\mu u_m$, dimensionless

c_p = specific heat of fluid at constant pressure, Btu/(lb)(deg F)

D = tube inside diameter, ft

F = heat-source parameter, $\rho g u_m c_p A/Q$, dimensionless

f_x = negative of body force per unit mass, ft/sec^2

g = acceleration due to gravity, ft/sec^2

h = fully developed heat-transfer coefficient, q/θ_m, Btu/(sec)(sq ft)(deg F)

I_0 = modified Bessel function of first kind of order 0

i = $\sqrt{-1}$

J_0 = Bessel function of first kind of order 0

K_0 = modified Bessel function of second kind of order 0

k = thermal conductivity of fluid, Btu/(sec)(sq ft)(deg F/ft)

$\mathrm{ker}_0\xi$, $\mathrm{kei}_0\xi$ $Y_0(i^{3/2}\xi) = K_0(i^{1/2}\xi) = \mathrm{ker}_0\xi + i\,\mathrm{kei}_0\xi$

L = length of tube, ft

N_{Gr} = Grashof number, $\beta g D^4 A/16\nu^2$, dimensionless

N_{Nu} = Nusselt number, hD/k, dimensionless

N_{Pr} = Prandtl number, $\mu g c_p/k$, dimensionless

N_{Ra} = Rayleigh number, $\rho^2\beta g^2 c_p D^4 A/16\mu k$, dimensionless

N_{Re} = Reynolds number, $u_m D/\nu$, dimensionless

p = static fluid pressure, psfa

Q = heat-source term, Btu/(sec)(cu ft)

q = wall heat-flux density from fluid, Btu/(sec)-(sq ft)

r = tube radius, $D/2$, ft

t = absolute static fluid temperature, deg R

t_w = tube wall temperature, deg R

U = dimensionless velocity, u/u_m

u = fluid velocity parallel with tube axis at radius r, fps

u_m = mean velocity of fluid in tube, fps

x = distance measured along axis of tube upward, ft

Y_0 = Bessel function of second kind of order 0

β = thermal coefficient of volume expansivity, $-\dfrac{1}{\rho}\left(\dfrac{\partial\rho}{\partial t}\right)_p$, (cu ft/deg F)/cu ft

η = dimensionless radius, $2r/D$

θ = radial temperature difference, $t - t_w$, deg F

θ_m = mixed-mean-to-wall temperature difference, deg F

λ = $(N_{Re})^{1/4}$, dimensionless

μ = dynamic viscosity of fluid, (lb)(sec)/sq ft

ν = kinematic viscosity of fluid, sq ft/sec

ξ = a variable

ρ = mass density of fluid, (lb)(sec^2)/ft^4

ρ_w = mass density of fluid at wall, (lb)(sec^2)/ft^4

ρ_{wo} = mass density of fluid at wall at an axial position where flow and heat transfer is fully developed, (lb)(sec^2)/ft^4

Φ = dimensionless temperature difference, $16k\theta/QD^2$

Φ_m = dimensionless mixed-mean-to-wall temperature difference, $16k\theta_m/QD^2$

φ = dimensionless temperature difference, $2k\theta/\rho g u_m c_p D^2 A$

φ_m = dimensionless mixed-mean-to-wall temperature difference, $2k\theta_m/\rho g u_m c_p D^2 A$

ψ = angular co-ordinate in cylindrical co-ordinate system, radians

$$\left[\frac{1}{\eta}\frac{d}{d\eta}\left(\eta\frac{d}{d\eta}\right)\right]^2 = \frac{1}{\eta}\frac{d}{d\eta}\left\{\eta\frac{d}{d\eta}\left[\frac{1}{\eta}\frac{d}{d\eta}\left(\eta\frac{d}{d\eta}\right)\right]\right\}$$

Introduction

Combined forced and free-laminar convection in vertical channels is commonly encountered in nuclear-reactor applications,

[1] The material contained herein is a portion of the analytical work to be submitted in partial fulfillment of the requirements for the PhD degree at Purdue University.

[2] Aeronautical Research Scientist, Heat Transfer Section, Lewis Flight Propulsion Laboratory, National Advisory Committee for Aeronautics. Assoc. Mem. ASME.

Contributed by the Heat Transfer Division and presented at the Diamond Jubilee Annual Meeting, Chicago, Ill., November 13–18, 1955, of The American Society of Mechanical Engineers.

Note: Statements and opinions advanced in papers are to be understood as individual expressions of their authors and not those of the Society. Manuscript received at ASME Headquarters, August 16, 1955. Paper No. 55—A-73.

particularly when dealing with after-shutdown cooling problems. These applications approximate a constant heat flux to the fluid at the walls rather than a constant wall temperature. Other applications, in which combined forced and free convection with uniform wall heat flux may be important, occur when fluids are heated in electrically heated vertical tubes and in vertical concentric-tube heat exchangers.

In certain types of nuclear reactors it has been proposed to remove the heat generated by passing a liquid fuel through channels in the reactor and cooling this fuel in an external heat exchanger. One such proposal is that of the externally cooled LMFR (liquid metal fuel reactor) of reference (1).[3] A good approximation in many cases is to assume that the heat is generated uniformly in the fuel during the time it is in the reactor. Shortly after shutdown it is possible for the heat produced in the moderator to be as great as that produced in the liquid fuel. For this reason a useful solution to the heat-transfer problem must allow for any ratio of heat transferred through the tube wall to heat generated within the fluid.

Although considerable attention has been devoted to combined forced and free convection in vertical tubes with constant wall temperature, only recently has much attention been focused upon the uniform wall heat-flux boundary condition. One earlier work dealing with combined forced and free convection without internal heat sources has been given by Ostroumov (2, 3). In references (2) and (3) Ostroumov gives the solution for the fully developed velocity and temperature profiles with constant heat-flux boundary condition. The mixed-mean-to-wall temperature difference was calculated in reference (3) but appears to be in error. No attempt was made to calculate Nusselt numbers. The problem of free convection with no net through-flow in vertical tubes having uniform internal heat generation and constant axial-temperature gradient is treated by Hamilton, et al. (4) and Woodrow (5). Free convection with no net through-flow in vertical tubes and channels having uniform internal heat generation and constant wall temperature (zero axial temperature gradient) is considered by Murgatroyd (6) for both laminar and turbulent flow. Combined forced and free convection between vertical parallel plates with and without uniform heat sources has been treated by Ostrach (7 to 10). Ostroumov (2) and Wordsworth (11) consider combined forced and free convection between vertical parallel plates with uniform wall heat flux and no volume heat sources.

Statement of the Problem and Assumptions

The purpose of the present analysis is to predict the flow and heat-transfer characteristics of a fluid flowing in a vertical tube under the conditions of combined forced and free convection. The fluid may or may not have heat being generated in it as it flows through the tube. Heat may be transferred to or from the fluid at any specified rate (including no heat transfer—the insulated wall case). The solution is expected to be valid only if the temperature and velocity profiles are fully developed and if no turbulence is present.

The assumptions are made that the flow is axially symmetric and flowing in laminar motion, the axis of the pipe lying parallel with the body force. The fluid properties are considered as constant except for the variation of density which is allowed for by considering the thermal coefficient of volume expansivity. The thermal boundary condition is determined by assuming a uniform heat flux at the wall of the tube. When internal heat generation is present it is assumed that the rate of heat generation per unit volume is uniform everywhere in the fluid. Frictional heating effects are assumed to be negligible.

[3] Numbers in parentheses refer to the Bibliography at the end of the paper.

Basic Equations

The equations expressing the conservation of momentum and energy for steady laminar fully developed flow and heat transfer in a vertical round pipe are as follows[4]

$$\frac{\partial p}{\partial x} + \rho g = \frac{\mu}{r}\frac{\partial}{\partial r}\left(r\frac{\partial u}{\partial r}\right) \quad [1]$$

$$\frac{\partial p}{\partial r} = \frac{\partial p}{\partial y} = 0 \quad [2]$$

$$u\rho g c_p \frac{\partial t}{\partial x} = k\left(\frac{1}{r}\frac{\partial t}{\partial r} + \frac{\partial^2 t}{\partial r^2} + \frac{\partial^2 t}{\partial x^2}\right) + Q \quad [3]$$

All symbols are defined in the nomenclature.

Assuming small temperature differences and constant pressure, the equation of state reduces to

$$\rho = \rho_w[1 - \beta(t - t_w)] \quad [4]$$

where the subscript designates a reference condition, here taken as a point on the tube wall.

The thermal boundary condition of constant heat flux at the wall can be expressed by

$$\frac{\partial t}{\partial x} = A \text{ (a constant)} \quad [5]$$

for fully developed flow and heat transfer with uniform heat sources and constant specific heat.

Equations [2], [4], and [5] can be used to simplify Equations [1] and [3] to

$$\frac{1}{r}\frac{d}{dr}\left(r\frac{du}{dr}\right) + \frac{\rho g\beta\theta}{\mu} = \frac{1}{\mu}\left(\frac{dp}{dx} + \rho_w g\right) \quad [6]$$

$$\frac{1}{r}\frac{d}{dr}\left(r\frac{d\theta}{dr}\right) - \frac{\rho g c_p A u}{k} = -\frac{Q}{k} \quad [7]$$

respectively. The temperature difference θ is the difference between the temperature at some radial position and the wall temperature at the same axial position. This variable θ is independent of axial position x. The density ρ appearing on the left-hand side of Equations [6] and [7] is considered to be a constant in further derivations because it was previously assumed that the only density variation was that due to the effect of β.

Analysis

Nondimensional Form of Equations. Equations [6] and [7] can be placed in a more general form by introducing dimensionless variables and parameters which are defined in the nomenclature. The two equations then become

$$\frac{1}{\eta}\frac{d}{d\eta}\left(\eta\frac{dU}{d\eta}\right) + \frac{N_{Ra}}{4F}\Phi = -8C \quad [8]$$

$$\frac{1}{\eta}\frac{d}{d\eta}\left(\eta\frac{d\Phi}{d\eta}\right) - 4F\left(U - \frac{1}{F}\right) = 0 \quad [9]$$

The dimensionless temperature difference Φ is used when dealing with uniform heat generation, and is the same variable as was used by Hamilton, et al. (4), and except for a constant is the same as that used by Woodrow (5) and Murgatroyd (6).

The heat-source parameter F was first introduced by Poppendiek and Palmer (12) and represents the ratio of thermal energy convected downstream per unit volume to heat generated in the fluid per unit volume. A value of F of unity would then corre-

[4] If the force field is not the field of gravity g is replaced by f_x, the negative of the body force, in Equation [1].

spond to an insulated wall because all of the heat generated in the fluid is convected downstream with no heat passing through the walls. Values of F from $-\infty$ to $+\infty$ are possible but positive values are generally of more practical interest than negative values. Fig. 1 shows qualitatively the shape of the velocity u and temperature θ profiles for various F-values. The direction of heat flow q at the wall and the direction of the mean velocity u_m is also indicated. An F of zero corresponds to (i) constant wall temperature, (ii) $u_m = 0$, or (iii) $u \equiv 0$. An F-value of plus or minus infinity corresponds to no volume heat sources.

In the limit of pure forced convection (obtained by letting β approach zero) the pressure-drop parameter C approaches unity. Values of C different from unity then indicate the effect of free convection on the pressure drop.

The Rayleigh number is a grouping which naturally occurs in free-convective flows of this type and is a measure of the amount of free-convection effect. The Rayleigh number is equivalent to the product of the Grashof number and the Prandtl number

$$N_{Ra} = \frac{\beta g D^4 A}{16\nu^2}\frac{\mu g c_p}{k} = N_{Gr}\,N_{Pr} \quad \ldots\ldots\ldots [10]$$

The temperature difference used in the Grashof number is the product $AD/2$ and the tube radius $D/2$ is the characteristic length. Attention will be confined in this paper to positive values of Rayleigh number. The solutions obtained for negative Rayleigh numbers have discontinuities similar to those found by Ostrach (10) for the parallel plate system. A complete physical explanation of this behavior has not been obtained as yet.

Four boundary conditions are necessary to determine the solution to the system [8] and [9]. The four conditions are (a) no-slip at the wall, (b) finite velocity at the tube center line, (c) θ zero at the wall, and (d) finite θ at the tube center line.

Velocity and Temperature Profiles. The dimensionless temperature difference can be eliminated between Equations [8] and [9] and the general solution for the dimensionless velocity is obtained as

$$U = C_1\,\mathrm{ber}_0\lambda\eta + C_2\,\mathrm{bei}_0\lambda\eta + C_3\,\mathrm{ker}_0\lambda\eta + C_4\,\mathrm{kei}_0\lambda\eta \ldots [11]$$

where

$$\lambda = (N_{Ra})^{1/4} \quad \ldots\ldots\ldots [12]$$

When the four boundary conditions are applied the constants C_1, C_2, C_3, and C_4 can be evaluated and the resulting velocity distribution is

$$U = \frac{u}{u_m} = \frac{\lambda}{2}\left[\frac{\mathrm{ber}_0\lambda\eta\ \mathrm{bei}_0\lambda - \mathrm{bei}_0\lambda\eta\ \mathrm{ber}_0\lambda}{\mathrm{ber}_0\lambda\ \mathrm{ber}_0'\lambda + \mathrm{bei}_0\lambda\ \mathrm{bei}_0'\lambda}\right]$$

$$+ \frac{1}{F}\left[1 - \frac{\left(\mathrm{ber}_0'\lambda + \frac{\lambda}{2}\,\mathrm{bei}_0\lambda\right)\mathrm{ber}_0\lambda\eta + \left(\mathrm{bei}_0'\lambda - \frac{\lambda}{2}\,\mathrm{ber}_0\lambda\right)\mathrm{bei}_0\lambda\eta}{(\mathrm{ber}_0\lambda\ \mathrm{ber}_0'\lambda + \mathrm{bei}_0\lambda\ \mathrm{bei}_0'\lambda)}\right] \ldots [13]$$

When no heat sources are present $1/F$ can be set equal to zero. The resulting equation can then be shown to be equivalent to a solution given by Ostroumov (2, 3).

Knowing the velocity distribution, Equation [9] can be solved for the temperature distribution. The result is

$$\Phi = \frac{16k\theta}{QD^2} = \frac{2F}{\lambda}\left[\frac{(\mathrm{ber}_0\lambda\eta\ \mathrm{ber}_0\lambda + \mathrm{bei}_0\lambda\eta\ \mathrm{bei}_0\lambda) - (\mathrm{ber}_0^2\lambda + \mathrm{bei}_0^2\lambda)}{(\mathrm{ber}_0\lambda\ \mathrm{ber}_0'\lambda + \mathrm{bei}_0\lambda\ \mathrm{bei}_0'\lambda)}\right]$$

$$+ \frac{2}{\lambda^2}\left\{\frac{2\left[\left(\mathrm{bei}_0'\lambda - \frac{\lambda}{2}\,\mathrm{ber}_0\lambda\right)\mathrm{ber}_0\lambda\eta - \left(\mathrm{ber}_0'\lambda + \frac{\lambda}{2}\,\mathrm{bei}_0\lambda\right)\mathrm{bei}_0\lambda\eta + \lambda(\mathrm{ber}_0^2\lambda + \mathrm{bei}_0^2\lambda) - 2\,(\mathrm{ber}_0\lambda\ \mathrm{bei}_0'\lambda - \mathrm{bei}_0\lambda\ \mathrm{ber}_0'\lambda)\right\}}{(\mathrm{ber}_0\lambda\ \mathrm{ber}_0'\lambda + \mathrm{bei}_0\lambda\ \mathrm{bei}_0'\lambda)}\right\}$$

$\ldots\ldots [14]$

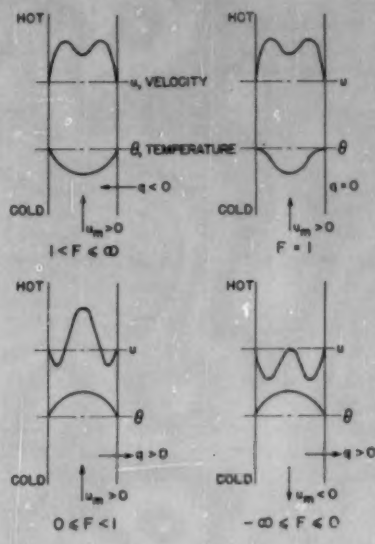

FIG. 1 TYPICAL VELOCITY AND TEMPERATURE PROFILES FOR VARIOUS VALUES OF HEAT-SOURCE PARAMETER F. $N_{Ra} > 0$, $\beta > 0$, $Q \geq 0$

When no heat sources are present the dimensionless temperature difference Φ becomes meaningless because Q is zero. For very small Q (approaching zero) the second term on the right in Equation [14] can be neglected when compared to the first term. In the limit of $Q = 0$ this equation reduces to

$$\varphi = \frac{2k\theta}{\rho g u_m c_p A D^2} = \frac{1}{4\lambda}\left[\frac{(\mathrm{ber}_0\lambda\eta\ \mathrm{ber}_0\lambda + \mathrm{bei}_0\lambda\eta\ \mathrm{bei}_0\lambda) - (\mathrm{ber}_0^2\lambda + \mathrm{bei}_0^2\lambda)}{(\mathrm{ber}_0\lambda\ \mathrm{ber}_0'\lambda + \mathrm{bei}_0\lambda\ \mathrm{bei}_0'\lambda)}\right] \quad \ldots\ldots [15]$$

Equation [15] can be converted to the form given by Ostroumov (2, 3). When the Rayleigh number is allowed to approach zero by letting β approach zero (keeping A fixed) Equation [15] reduces to the pure forced-convection laminar solution which is given by Howarth (13).

If the wall temperature is held constant (perhaps by boiling a liquid on the outside of the tube) and if the tube is very long, then the axial temperature gradient may be assumed to be identically zero throughout the fluid. In such a case Equation [9] has the particularly simple solution

$$\Phi = \frac{16k\theta}{QD^2} = 1 - \eta^2 \text{ (constant wall temperature)} \ldots [16]$$

which is the same solution that would be obtained if the fluid were stationary. If this expression for Φ is used in Equation [8] the dimensionless velocity distribution is found to be

$$U = \frac{u}{u_m} = 2(1-\eta^2) - \frac{N_{Ra}}{4F}\left(\frac{1}{12}\eta^2 - \frac{1}{16}\eta^4 - \frac{1}{48}\right) \text{ (constant wall temperature)} \quad \ldots\ldots [17]$$

Although A is assumed to be zero the ratio N_{Ra}/F remains finite, being

$$\frac{N_{Ra}}{F} = \frac{\rho\beta g D^4 Q}{16\mu k u_m} \quad \ldots\ldots [18]$$

If N_{Ra}/F is negligible then the velocity profile approaches the Poiseuille profile.

Mixed-Mean Temperature Differences and Nusselt Numbers. Either the mixed-mean temperature differences or the Nusselt numbers are necessary in order to apply the results of this analysis. The two temperatures mainly of interest are the mixed-mean temperature and the wall temperature. Given one, it is desirable to know the other.

The mixed-mean-to-wall temperature difference is defined as

$$\theta_m = \frac{\int_0^1 \theta U \eta d\eta}{\int_0^1 U \eta d\eta} \quad \ldots\ldots [19]$$

In terms of dimensionless temperature differences there is defined

$$\Phi_m = \frac{16k\theta_m}{QD^2} \quad \ldots\ldots [20]$$

for cases involving uniform heat sources and

$$\varphi_m = \frac{2k\theta_m}{\rho g u_m c_p A D^2} \quad \ldots\ldots [21]$$

when no heat source is present. The Nusselt number, which is defined as

$$N_{Nu} = \frac{hD}{k} = \frac{qD}{k\theta_m} \quad \ldots\ldots [22]$$

becomes, in terms of Φ_m and F

$$N_{Nu} = \frac{4(1-F)}{\Phi_m} \quad \ldots\ldots [23]$$

with heat sources, and

$$N_{Nu} = -\frac{1}{2\varphi_m} \quad \ldots\ldots [24]$$

without heat sources. When volume heat sources are present it turns out that the Nusselt number is not a very useful quantity because Φ_m becomes zero for certain values of N_{Ra} and F, causing infinite discontinuities in the Nusselt number. A more useful quantity in this instance is Φ_m. Without heat sources no such discontinuities occur because φ_m never changes sign.

For positive Rayleigh numbers with heat sources

$$\Phi_m = -\frac{64C}{\lambda^4} + \left(\frac{1}{F\lambda^4} - \frac{64FC^2}{\lambda^8}\right) \left\{ \frac{2\lambda^2[(\mathrm{ber}_0\lambda\ \mathrm{ber}_0'\lambda + \mathrm{bei}_0\lambda\ \mathrm{bei}_0'\lambda)^2 - (\mathrm{ber}_0\lambda\ \mathrm{bei}_0'\lambda - \mathrm{bei}_0\lambda\ \mathrm{ber}_0'\lambda)^2]}{(\mathrm{ber}_0^2\lambda + \mathrm{bei}_0^2\lambda)^2} + 8\lambda \frac{(\mathrm{ber}_0\lambda\ \mathrm{ber}_0'\lambda + \mathrm{bei}_0\lambda\ \mathrm{bei}_0'\lambda)}{(\mathrm{ber}_0^2\lambda + \mathrm{bei}_0^2\lambda)} \right\} + \frac{64C}{\lambda^4} \left\{ \frac{(\mathrm{ber}_0\lambda\ \mathrm{ber}_0'\lambda + \mathrm{bei}_0\lambda\ \mathrm{bei}_0'\lambda)(\mathrm{ber}_0\lambda\ \mathrm{bei}_0'\lambda - \mathrm{bei}_0\lambda\ \mathrm{ber}_0'\lambda)}{(\mathrm{ber}_0^2\lambda + \mathrm{bei}_0^2\lambda)^2} + \frac{2}{\lambda} \frac{(\mathrm{ber}_0\lambda\ \mathrm{bei}_0'\lambda - \mathrm{bei}_0\lambda\ \mathrm{ber}_0'\lambda)}{(\mathrm{ber}_0^2\lambda + \mathrm{bei}_0^2\lambda)} \right\} \quad \ldots\ldots [25]$$

where the pressure-drop parameter

$$C = \frac{\lambda^2}{16} \left\{ \frac{\lambda(\mathrm{ber}_0^2\lambda + \mathrm{bei}_0^2\lambda) + \frac{1}{F}[2(\mathrm{ber}_0\lambda\ \mathrm{bei}_0'\lambda - \mathrm{bei}_0\lambda\ \mathrm{ber}_0'\lambda) - \lambda(\mathrm{ber}_0^2\lambda + \mathrm{bei}_0^2\lambda)]}{(\mathrm{ber}_0\lambda\ \mathrm{ber}_0'\lambda + \mathrm{bei}_0\lambda\ \mathrm{bei}_0'\lambda)} \right\} \quad \ldots\ldots [26]$$

When no internal heat sources are present the dimensionless mixed-mean-to-wall temperature difference φ_m is given by

$$\varphi_m = \frac{2k\theta_m}{\rho g u_m c_p A D^2} = -\frac{16C^2}{\lambda^6} \left[\frac{(\mathrm{ber}_0\lambda\ \mathrm{ber}_0'\lambda + \mathrm{bei}_0\lambda\ \mathrm{bei}_0'\lambda)^2 - (\mathrm{ber}_0\lambda\ \mathrm{bei}_0'\lambda - \mathrm{bei}_0\lambda\ \mathrm{ber}_0'\lambda)^2}{(\mathrm{ber}_0^2\lambda + \mathrm{bei}_0^2\lambda)^2} + \frac{4}{\lambda} \frac{(\mathrm{ber}_0\lambda\ \mathrm{ber}_0'\lambda + \mathrm{bei}_0\lambda\ \mathrm{bei}_0'\lambda)}{(\mathrm{ber}_0^2\lambda + \mathrm{bei}_0^2\lambda)} \right] \quad \ldots\ldots [27]$$

The pressure-drop parameter is taken from Equation [26] after setting $1/F = 0$. The Nusselt numbers can then be calculated from Equation [24].

When the wall temperature is held constant and the tube is very long so that $A \equiv 0$ then the fluid does not increase in temperature as it passes along the tube. In this instance the center line-to-wall temperature difference is probably of more interest than the mixed-mean-to-wall temperature difference. The former is obtained from Equation [16] by setting $\eta = 0$.

Pressure Drop. The pressure-drop parameter C can be calculated from Equation [26] for positive Rayleigh numbers with heat sources. If no heat sources are present then $1/F$ is set equal to zero. The value of C for zero axial temperature gradient (constant-wall-temperature case) is

$$C = -\frac{\left(\frac{dp}{dx} + \rho_w g\right) D^2}{32\mu u_m} = 1 - \frac{N_{Ra}}{48F} \quad \ldots\ldots [28]$$

The pressure gradient dp/dx will not be strictly constant because ρ_w will vary with distance along the tube. An approximation can be made by assuming

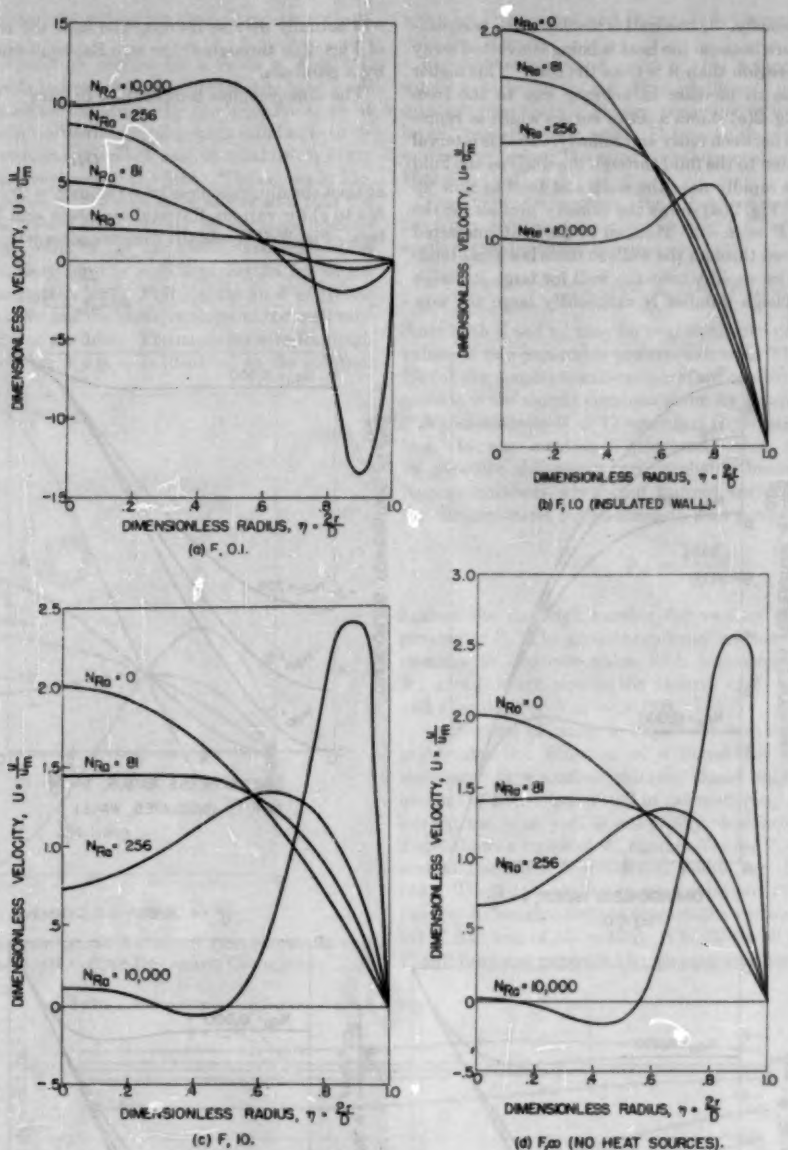

FIG. 2 PREDICTED DIMENSIONLESS VELOCITY DISTRIBUTIONS AGAINST DIMENSIONLESS TUBE RADIUS FOR VARIOUS RAYLEIGH NUMBERS AND HEAT-SOURCE PARAMETERS

$$\rho_w = \rho_{w0}[1 - \beta(t_w - t_{w0})] \quad [29]$$

where the subscript 0 refers to any axial position where the flow and heat transfer are fully developed. The pressure gradient is then approximately

$$\frac{dp}{dx} = -\frac{32\mu u_m C}{D^2} - g\rho_{w0}[1 - \beta A(x - x_0)] \quad [30]$$

since $t_w - t_{w0} = A(x - x_0)$. This expression can then be integrated to obtain the axial pressure drop.

DISCUSSION

Velocity and Temperature Profiles. The dimensionless velocity profiles $U = u/u_m$ against the dimensionless tube radius $\eta = 2r/D$ are shown in Figs. 2(*a–d*). The parameter on each curve is the Rayleigh number. Fig. 4 shows the velocity profiles for the uniform wall-temperature solution, the parameter in this case being N_{Ra}/F.

Fig. 2(*a*) shows velocity profiles for a value of F of 0.1. Since this F-value lies between zero and unity it corresponds to heat removal through the walls of the tube, see Fig. 1. For a positive[1] β this means that the fluid, being cooler near the walls, will tend to fall there. This effect becomes more pronounced as the Rayleigh number is increased. For sufficiently high Rayleigh numbers a reverse flow occurs near the wall. Fig. 2(*b*) shows a similar set of curves for $F = 1$. This corresponds to an insulated wall

[1] β will be considered to be positive during this discussion although the solutions are valid for negative β as well.

as was discussed previously. If the wall is insulated the temperature will be higher there because the heat is being convected away less rapidly from this region than it is from the core. This higher temperature will cause an increase in velocity due to the free-convection effect. Fig. 2(*c*) shows a set of curves which is representative for F-values between unity and infinity. In this interval of F, heat is being added to the fluid through the walls so the fluid will tend to rise more rapidly near the walls and tend to slow up near the center line. Fig. 2(*d*) shows the velocity profiles for the no-heat source case ($F = \pm\infty$). Here all of the heat convected downstream has entered through the walls so there is a great tendency for the fluid to rise rapidly near the wall for large Rayleigh numbers. If the Rayleigh number is sufficiently large the flow will actually reverse its direction near the center line. On each of Figs. 2 (*a* through *d*) the zero Rayleigh-number profile is given by a parabola.

The dimensionless temperature profiles

$$\Phi = \frac{16k\theta}{QD^2}$$

against the dimensionless tube radius $\eta = 2r/D$ are shown in Figs. 3(*a* to *c*) for various Rayleigh numbers and heat-source parameters. Fig. 3(*d*) shows the dimensionless temperature profiles

$$\varphi = \frac{2k\theta}{\rho g u_m c_p A D^2}$$

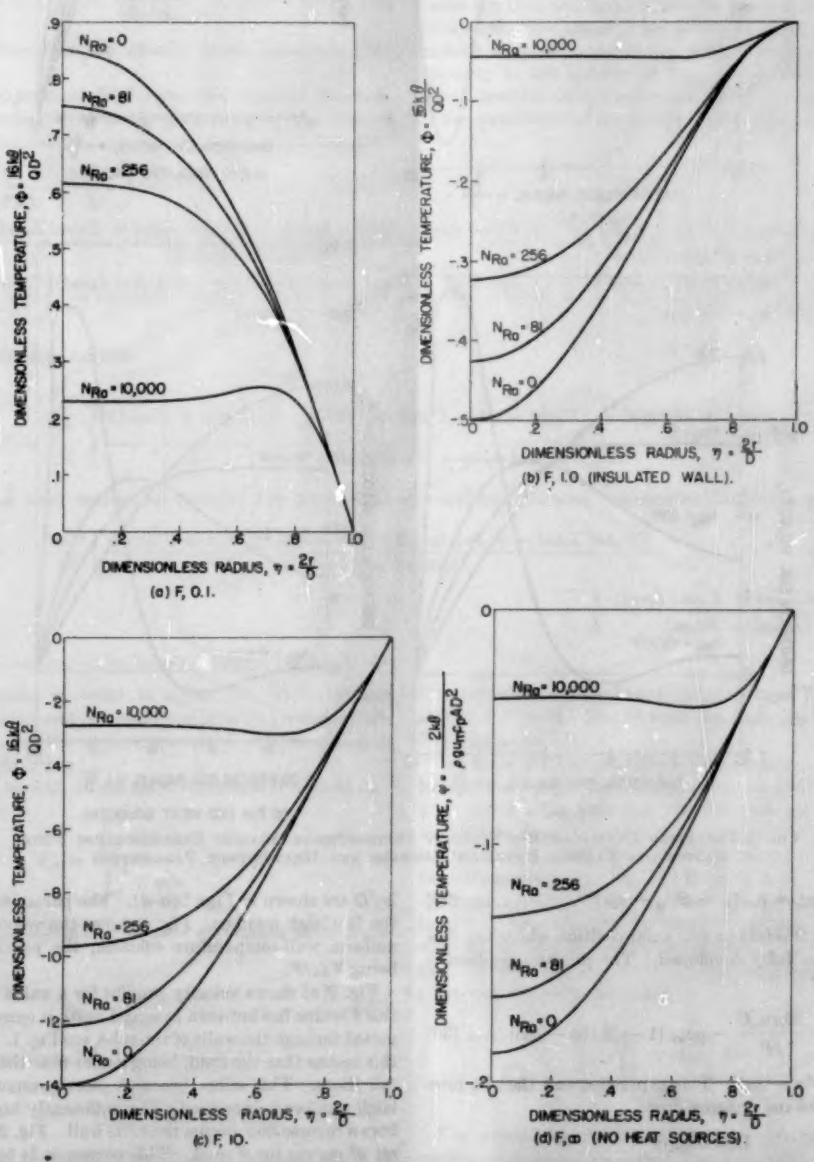

FIG. 3 PREDICTED DIMENSIONLESS TEMPERATURE DISTRIBUTIONS AGAINST DIMENSIONLESS TUBE RADIUS FOR VARIOUS RAYLEIGH NUMBERS AND HEAT-SOURCE PARAMETERS

against the dimensionless tube radius for the no-heat-source case ($F = \pm\infty$).

Fig. 3(a) shows temperature profiles for a value of F of 0.1. This F-value corresponds to heat removal through the tube walls and this is also indicated on the curves by the negative slope at the tube wall. The effect of increasing Rayleigh number is to reduce the radial temperature difference and to establish a fairly flat temperature profile over most of the tube. The curves in Fig. 3(b) for an F of 1 indicates by the zero slope at the wall that the wall is insulated. The values of Φ are now all negative because the wall is hotter as a result of the decreased axial convection there. The same tendency for the profile to flatten for larger Rayleigh numbers is indicated here. Fig. 3(c) for an F of 10 has the same general character but the positive slope at the wall now indicates a heat addition to the fluid. The curve for zero Rayleigh number on each of the Figs. 3(a to c) is identical to the solution given by Poppendiek and Palmer (12) for pure forced convection with heat sources.

Fig. 3(d) shows for $F = \pm\infty$ that a large Rayleigh number causes a fairly flat temperature profile over most of the tube, the greatest temperature change occurring in a "thermal boundary layer" near the tube wall. The curve shown for zero Rayleigh number represents the pure forced-convection profile taken from Howarth (13).

The velocity profiles for the constant-wall-temperature boundary condition are given in Fig. 4. The parameter on each curve is the dimensionless group

$$N_{Ra}/F = \rho\beta g D^4 Q/16\mu k u_m$$

Since both β and u_m may be negative, both positive and negative values of this parameter are represented. The temperature profile for the constant-wall-temperature condition is not shown because it is the simple parabola given by Equation [16].

Mixed-Mean-to-Wall Temperature Differences and Nusselt Numbers. It was mentioned previously that mixed-mean-to-wall temperature differences are probably more convenient than Nusselt numbers when heat sources are present. Fig. 5 gives the dimensionless mixed-mean-to-wall temperature difference

$$\Phi_m = \frac{16k\theta_m}{QD^2}$$

against the Rayleigh number for various values of heat-source parameter F. The general tendency on these curves is for Φ_m to decrease in absolute value with increasing Rayleigh number. Φ_m goes through zero in the vicinity of $F = 0.73$ for $N_{Ra} = 0$, and $F = 0.93$ for $N_{Ra} = 10{,}000$.

An F-value of unity is important technically because it approximates the situation of a liquid-fuel channel piercing a moderator in a nuclear reactor. Since only a relatively small amount of heat is generated in the moderator when the reactor is critical the tube wall is essentially "insulated" at steady state. Fig. 6 shows a replot of Φ_m against N_{Ra} for $F = 1$, to an enlarged scale. The three experimental points are data of Poppendiek (14). These data are for aqueous solutions of sulphuric acid (25 per cent by weight) flowing upward in a vertical Saran tube $^9/_{32}$ in. ID × 3 ft long ($L/D = 128$). The tube wall was insulated ($F = 1$) and heat was generated by passing an alternating electric cur-

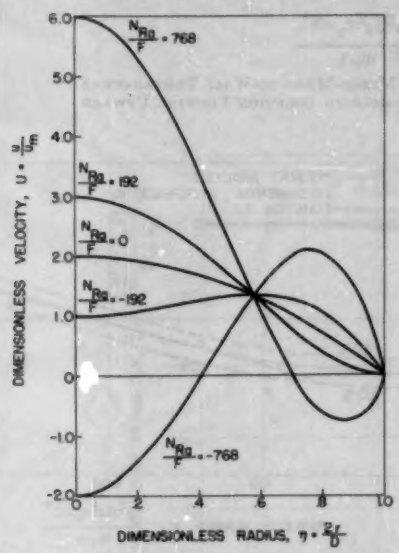

FIG. 4 PREDICTED DIMENSIONLESS VELOCITY DISTRIBUTIONS FOR CONSTANT-WALL-TEMPERATURE BOUNDARY CONDITION

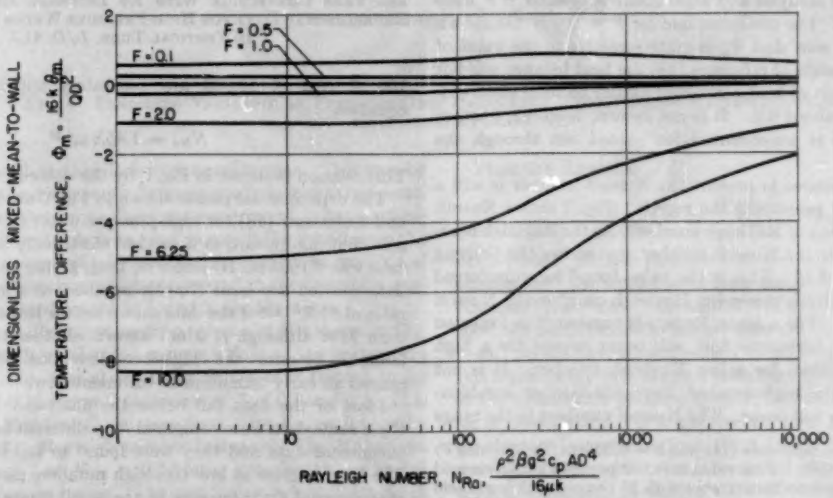

FIG. 5 PREDICTED DIMENSIONLESS MIXED-MEAN-TO-WALL TEMPERATURE DIFFERENCE AGAINST RAYLEIGH NUMBER FOR VARIOUS HEAT-SOURCE PARAMETERS

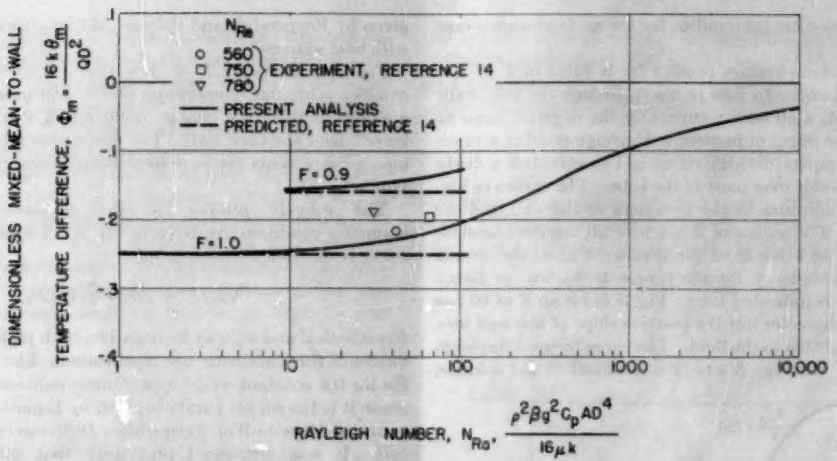

FIG. 6 COMPARISON BETWEEN ANALYSIS AND EXPERIMENT OF MIXED-MEAN-TO-WALL TEMPERATURE DIFFERENCE FOR A HEAT-SOURCE PARAMETER F OF 1. SULPHURIC-ACID SOLUTION FLOWING UPWARD IN VERTICAL TUBE

rent axially through the fluid. Details are given in reference (14). The plotted points are corrected for thermal conductivity of the acid solution according to the more complete data of reference (15).[8] The value of β used was computed by fitting a curve through the density data of reference (17) by the method of least squares and differentiating the density equation to obtain β from the relation

$$\beta = -\frac{1}{\rho}\left(\frac{\partial \rho}{\partial t}\right)_p \quad \text{..... [31]}$$

The Reynolds number of each point is indicated in Fig. 6 and it is observed that the deviation from the analysis increases with increasing Reynolds number. It is also noted that all three points lie closer to zero than does the analysis. This behavior is consistent with an argument that some turbulence may be present, although considerably more data are needed to confirm this. The dashed line for $F = 1$ shown in Fig. 6 is the pure forced-convection analysis of reference (14) with which the data were originally compared by Poppendiek. Another explanation of the discrepancy of analysis and experiment is possible if F were not exactly unity. The predicted line for $F = 0.9$ is also shown in Fig. 6 and it is seen that Φ_m is quite sensitive to the value of F. In the experiments of reference (14) the heat balance was not perfect and the ratio of heat convected axially to total electrical-energy input was about 0.9. It is not known, however, whether this energy which is unaccounted for passed out through the tube walls.

When no heat source is present the Nusselt number is still a convenient way of presenting the results. Fig. 7 shows Nusselt number as a function of Rayleigh number. As the Rayleigh number approaches zero the Nusselt number approaches the limiting value of $48/11 \approx 4.36$. This is the value found for pure forced convection (13). With increasing Rayleigh number the Nusselt number increases. For a given Reynolds number it is expected that transition to turbulent flow will occur sooner for a high Rayleigh number than for a low Rayleigh number. It is not known at what Rayleigh-number Reynolds-number combination this transition will occur. The Nusselt numbers in the range

[8] The value used in reference (14) was $k = 0.30$ Btu/(hr)(ft)(deg F) given by reference (16). This value is for 30 per cent sulphuric acid at 86 F whereas the experiments were with 25 per cent sulphuric acid at ≈75 F. The value of k given in reference (15) was $k = 0.32$ Btu/(hr)(ft)(deg F).

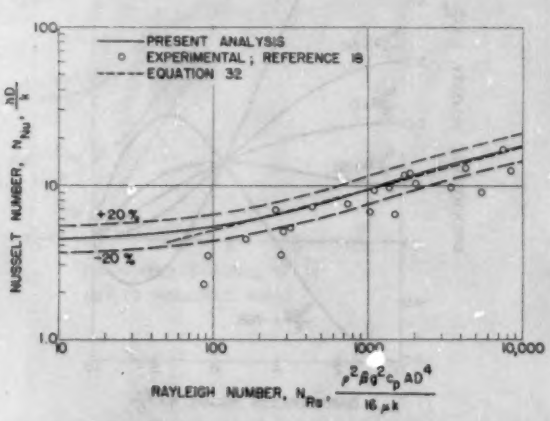

FIG. 7 COMPARISON BETWEEN ANALYSIS AND EXPERIMENT OF NUSSELT NUMBER AGAINST RAYLEIGH NUMBER FOR COMBINED FORCED AND FREE CONVECTION WITH NO INTERNAL HEAT GENERATION. EXPERIMENTAL DATA FOR HIGH-PRESSURE WATER FLOWING UPWARD IN VERTICAL TUBE, L/D, 41.5

$100 \leq N_{Ra} \leq 10{,}000$ are accurately approximated by the equation

$$N_{Nu} = 1.45 N_{Ra}^{0.37} \quad \text{..... [32]}$$

This relation is shown in Fig. 7 by the dotted line.

The experimental points shown in Fig. 7 are the data of Clark and Rohsenow (18) for high-pressure water (2000 psia and 1500 psia) flowing upward in a vertical electrically heated tube. The tube was 0.1805 in. ID and 9 in. long, giving an L/D of 50. The data plotted are local Nusselt numbers at a length-to-diameter ratio of 41.5. All of the data shown are for Reynolds numbers less than 2130 although it is not known whether the flow is always laminar because the high-free-convection effects may have caused an early transition to turbulent flow.

Most of the data fall below the analysis. In reference (19) these same data were compared on a different basis with other experimental data and they were found to fall low there as well. The large scatter at low Rayleigh numbers can be attributed to experimental error because of the small temperature differences involved. It was noted in reference (18) that large heat losses

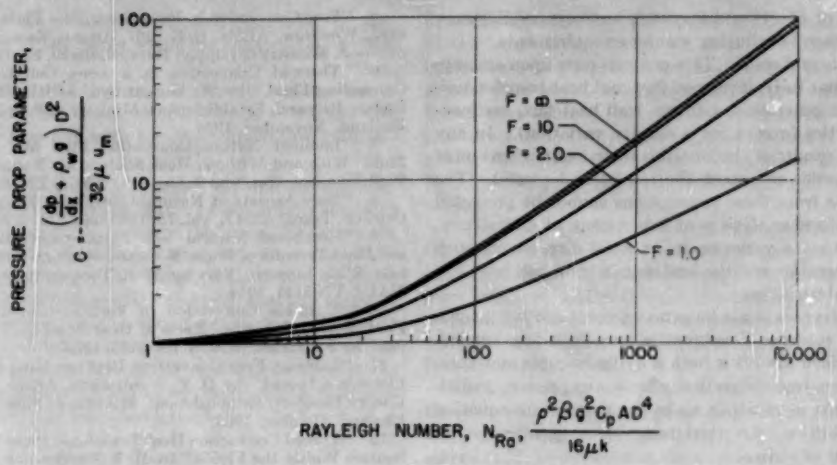

(a) F, 1, 2, 10, ∞.

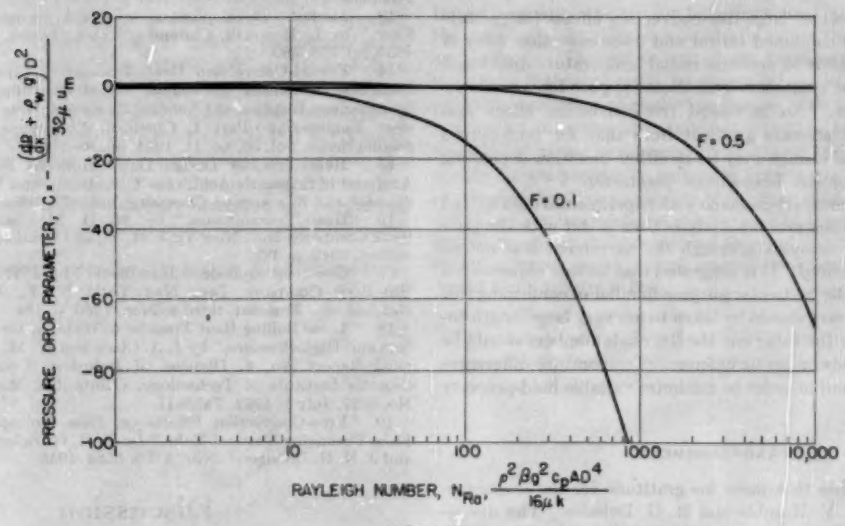

(b) F, 0.1, 0.5

FIG. 8 PREDICTED VARIATION OF PRESSURE-DROP PARAMETER C FOR VARIOUS RAYLEIGH NUMBERS AND HEAT-SOURCE PARAMETERS

were involved with the low-Reynolds-number runs. This may be the reason for the discrepancy between analysis and experiment. The agreement between analysis and experiment is not particularly good but it probably is as good as may be expected since the apparatus was not specifically designed to confirm an analysis of this type. No other data which correspond to the boundary conditions of this analysis could be found in the literature.

Pressure Drop. The pressure-drop parameter C is shown in Fig. 8 against Rayleigh number for various values of the heat-source parameter F. Fig. 8(a) shows C for values of F from 1 to infinity, and Fig. 8(b) shows C for values of F of 0.5 and 0.1. It is seen from Fig. 8(a) that C increases from 1 for $N_{Ra} = 0$ to quite high values as the Rayleigh number increases. Fig. 8(b) shows that C goes from 1 at $N_{Ra} = 0$ to large negative values as the Rayleigh number increases. The particular value of Rayleigh number at which C is zero depends upon F but F always lies between zero and 1.

From the definition of C

$$\frac{dp}{dx} = -\frac{32\mu u_m C}{D^2} - \rho_w g \quad \text{[33]}$$

For liquids in laminar flow the first term on the right is generally smaller than the second term even though C is quite large. For example, in one run of reference (18) in which $N_{Ra} = 1560$, $N_{Ra} = 5000$, the contribution to the pressure gradient was —4.7 pcf and —45.7 pcf for the first and second terms, respectively. However, this is not to say that the first term may be ignored because most of the hydrostatic pressure drop will be recovered on the return leg in closed loop. For a gas the first term in Equation [33] will be of more importance than for a liquid because $\rho_w g$ is much smaller. It must be stressed that this relationship for pressure drop is valid only in that portion of the tube where fully developed flow and heat transfer exist.

The fact that C decreases below 1 and even becomes negative

for certain values of $F(<1)$ and Rayleigh numbers possibly may be used to advantage in reducing pumping requirements.

Range of Validity of Results. This analysis rests upon assumptions such as laminar fully developed flow and heat transfer, uniform internal heat generation, uniform wall heat flux, and constant fluid properties (except for a density variation). In any application of the results of this analysis these assumptions must be good ones in order to expect the results to be valid. The effect of deviations from these assumptions cannot be predicted without a more refined analysis or an experiment. Qualitatively, it can be stated that a variation in an axial direction of such things as fluid properties and the heat-source term will have less effect than a radial variation.

The effect of entrances is not known at present nor is it known how far from an entrance these results may be safely applied. In an entrance, which always is both a hydrodynamic and thermal entrance when free-convection effects are present, radial-velocity components exist which make the momentum equation nonlinear. In addition, the axial temperature gradient is no longer independent of radius.

Conclusions

The general effect of large free-convection effects (large Rayleigh numbers) in combined forced and free-convection flows of the type considered is to decrease radial temperature differences and increase Nusselt numbers over those for pure forced-convection heat transfer. An increased free-convection effect also changes the axial pressure gradient from that for pure forced convection but the change may be in either direction depending upon the value of the heat-source parameter.

In all cases the comparison made with experimental data agreed more closely with the present analysis than it did with the pure forced-convection analyses although the agreement was not as good as may be desired. It is suggested that further experiments be designed with the particular purpose in mind of confirming this analysis. Special care should be taken to use very large length-to-diameter ratios for the tubes and the Reynolds numbers should be kept very low to insure no turbulence. Temperature differences should be kept small in order to minimize variable fluid-property effects.

Acknowledgments

The author wishes to express his gratitude for the encouragement given by L. V. Humble and R. G. Deissler. The discussions with E. M. Sparrow were particularly helpful. Thanks are also extended to Mrs. Shirley Snider, who performed the computations, A. F. Lietzke and C. E. de Bogdan, who read the manuscript, and A. L. Loeffler, who checked the equations.

BIBLIOGRAPHY

1 "Heat Exchange in a Liquid-Metal-Fuel Reactor for Power," by O. E. Dwyer, published by American Institute of Chemical Engineers, New York, N. Y., Nuclear Engineering—Part I, Chemical Engineering Progress Symposium Series, vol. 50, no. 11, 1954, pp. 75–91.

2 "Free Convection Under the Conditions of the Internal Problem," by G. A. Ostroumov, translation by S. Reiss, NACA, Cleveland, Ohio, of the book "Svobodnaia Konvektsiia v Usloviiakh Vnutrennei Zadachi," by G. A. Ostroumov, State Publishing House, Technico-Theoretical Literature, Moscow, Leningrad, Russia, 1952.

3 "Matematicheskaya teoria ustanovivsheisya teploperedachi v krugloi vertikalnoi skvazhine pri superpozitsii vynuzhdennoi i svobodnoi laminarnoi konvektsii," by G. A. Ostroumov, *Zhurnal Tekhnicheskoi Fiziki*, vol. 20, no. 6, 1950, pp. 750–757.

4 "Free Convection in Fluids Having a Volume Heat Source," by D. C. Hamilton, H. F. Poppendiek, R. F. Redmond, and L. D. Palmer, ORNL 1769 Engineering, Reactor Exp. Eng. Division, Oak Ridge National Laboratory, Oak Ridge, Tenn., Nov. 15, 1954, Contract No. W-7405, eng. 26.

5 "Free Convection in Heat Generating Fluid (Laminar Flow)," by J. Woodrow, AERE E/R 1267, Atomic Energy Research Establishment, Ministry of Supply, Harwell, Berks, England, October, 1953.

6 "Thermal Convection in a Long Cell Containing a Heat Generating Fluid," by W. Murgatroyd, AERE ED/R 1559, Atomic Energy Research Establishment, Ministry of Supply, Harwell, Berks, England, November, 1954.

7 "Laminar Natural-Convection Flow and Heat Transfer of Fluids With and Without Heat Sources in Channels With Constant Wall Temperatures," by S. Ostrach, NACA TN 2863, 1952.

8 "New Aspects of Natural-Convection Heat Transfer," by S. Ostrach, Trans. ASME, vol. 75, 1953, pp. 1287–1290.

9 "Combined Natural- and Forced-Convection Laminar Flow and Heat Transfer of Fluids With and Without Heat Sources in Channels With Linearly Varying Wall Temperatures," by S. Ostrach, NACA TN 3141, 1954.

10 "Unstable Convection in Vertical Channels With Heating From Below Including Effects of Heat Sources and Frictional Heating," by S. Ostrach, NACA TN 3458, 1955.

11 "Laminar Free Convection Between Heat Producing Vertical Plates in a Liquid," by D. V. Wordsworth, AERE E/R 1270, Atomic Energy Research Establishment, Ministry of Supply, Harwell, Berks, England, October, 1953.

12 "Forced Convection Heat Transfer in Pipes With Volume Heat Sources Within the Fluids," by H. F. Poppendiek and L. D. Palmer, ORNL 1395 Physics, Reactor Exp. Eng. Division, Oak Ridge National Laboratory, Oak Ridge, Tenn., December 17, 1952, Contract No. W-7405, eng. 26.

13 "Modern Developments in Fluid Dynamics—High-Speed Flow," by L. Howarth, Clarendon Press, Oxford, England, vol. II, 1953, pp. 778–780.

14 "Forced-Convection Heat Transfer in Pipes With Volume-Heat Sources Within the Fluids," by H. F. Poppendiek, published by American Institute of Chemical Engineers, New York, N. Y., Nuclear Engineering—Part I, Chemical Engineering Progress Symposium Series, vol. 50, no. 11, 1954, pp. 93–104.

15 "Heat Transfer Design Data—Aqueous Solutions of Nitric Acid and of Sulphuric Acid," by T. R. Bump and W. L. Sibbitt, *Industrial and Engineering Chemistry*, vol. 47, 1955, pp. 1665–1670.

16 "Heat Transmission," by W. H. McAdams, McGraw-Hill Book Company, Inc., New York, N. Y., and London, England, second edition, 1942, p. 389.

17 "Chemical Engineer's Handbook," by J. H. Perry, McGraw-Hill Book Company, Inc., New York, N. Y., Toronto, Canada, and London, England, third edition, 1950, p. 184.

18 "Local Boiling Heat Transfer to Water at Low Reynolds Numbers and High Pressure," by J. A. Clark and W. M. Rohsenow, Technical Report No. 4, Division of Industrial Cooperation, Massachusetts Institute of Technology, Cambridge, Mass., DIC Project No. 6627, July 1, 1952, Table II.

19 "Free-Convection Effects on Heat Transfer for Turbulent Flow Through a Vertical Tube," by E. R. G. Eckert, A. J. Diaguila, and J. N. B. Livingood, NACA TN 3584, 1955.

Discussion

Simon Ostrach.[7] From the introduction of the paper, it appears that the only part of the considered problem, which was not previously solved for tube flows, is that with a net through-flow including heat sources. However, the analysis is made for the entire problem and although it is pointed out that some of the presented solutions coincide with those previously obtained, the results in no way indicate distinctly the new contribution and the relationship of the duplicated work with that done earlier. The duplication is perhaps justified because some of the earlier work appears in Russian literature which is not readily available. However, the author's personal contribution should be clearly set apart from that which has already been done. Further, it is indicated (and not clearly so) that all aspects of the problem have been treated for the same types of flows between two parallel plates and it would be interesting to see what the relationship is between the flow in tubes and in the

[7] Aeronautical Research Scientist, National Advisory Committee for Aeronautics, Lewis Flight Propulsion Laboratory, Cleveland, Ohio.

channel formed by the plates, but no such comparison is presented. The value of the paper would be enhanced by such a discussion.

The case where $N_{Ra} = 0$ is always referred to in the paper as the pure-forced-convection case. However, $N_{Ra} = 0$ could also be a natural-convection flow with no axial temperature gradient.

MYRON TRIBUS.[8] It should be pointed out that the solutions quoted in this paper are all in the nature of asymptotic solutions and apply only far from the entrance to the tubes. Whether the boundary conditions associated with these solutions are physically realizable is not at present clear. This writer surmises, based on a study of the differential equations, that the entrance length in the absence of free-convection effects should be about the same for flow with internal heat sources as without. In the presence of free convection, no similar calculations were made. Can the author comment on the entry length for a fluid-flow system in the presence of free convection?

AUTHOR'S CLOSURE

Dr. Ostrach's comments concerning the part of the considered problem which was previously solved are incorrect. The statements made in the introduction are correct and are repeated here for emphasis. In references (2) and (3) Ostroumov gives the solution for the fully developed velocity and temperature *profiles* with constant-heat-flux boundary condition without internal heat sources. The mixed-mean-to-wall temperature differences are incorrectly given in reference (3) and the Nusselt numbers were never calculated. These results are given in the present paper. The fact that the velocity and temperature profiles, with constant-heat-flux boundary condition and no internal heat sources, were first obtained by Ostroumov is clearly indicated immediately after the derivations of Equations [13] and [15] of the text. Other results which are not new, but are pointed out because they represent limiting cases of the present analysis, are the pure-forced-convection temperature solution without internal heat sources (13) and the pure-forced-convection temperature solution with internal heat sources (12). This is also clearly indicated in the text. With these exceptions, to the best knowledge of the author, the remainder of the analysis is original.

A comparison with the corresponding solutions given by Dr. Ostrach for the same type of flows between parallel plates would be interesting. Mixed-mean-to-wall temperature differences were not given by Dr. Ostrach in reference (9), nor were the corresponding Nusselt-number relationships indicated, so a direct comparison of results of practical interest is not possible without further computations.

It is true that the case $N_{Ra} = 0$ could also be a natural-convection flow with no axial temperature gradient and this is discussed when presenting Equations [16], [17], and [18]. It should be emphasized, however, that the curves marked $N_{Ra} = 0$ in Figs. 2 and 3 are for $\beta = 0$ and A finite.

It is well that Professor Tribus has pointed out that the solutions given here are only for fully developed flows which satisfy the assumed boundary conditions because this should be reemphasized. Whether or not these boundary conditions are physically realizable could be shown by experiment but to the author's knowledge no such experiments have been run. There is no reason to expect that the situation will be any different from the case of pure forced-convection, where the same boundary conditions are physically realizable (within the accuracy of the experiments and the variability of the fluid properties).

The author has made no calculations of the entry lengths required to obtain fully developed flows of the types considered in the present paper. Such calculations, or an experiment, would be of definite value.

[8] Associate Professor, University of California, Los Angeles, Calif. Mem. ASME.

Free-Convection Heat Transfer From a Horizontal Right Circular Cylinder to Freon 12 Near the Critical State[1]

By D. L. DOUGHTY[2] and R. M. DRAKE, JR.[3]

Free-convection heat-transfer coefficients have been measured on a horizontal circular cylinder to Freon 12 near the critical-state conditions as a function of the temperature difference between the test cylinder and the Freon environment. Experimental heat-transfer coefficients have been determined for constant Freon temperatures of 233, 244, and 259 F, and for a constant pressure of 580 psia, the critical pressure of Freon 12. In all cases the heat-transfer coefficients have been determined as functions of the temperature difference between the test cylinder and the Freon for densities varying from supercritical to subcritical. In the region near the critical state the experimental heat-transfer coefficients are shown to increase tenfold over the typical values in the superheated-vapor region. Satisfactory correlation of the present results with the work of other investigators in the field of free-convection heat transfer has been made for state conditions removed from the critical.

Introduction

FREE-CONVECTION heat transfer is that mode of convective heat transfer in which the fluid motion is produced and sustained by virtue of the temperature gradients which exist during the transfer of heat from a solid boundary to a fluid. The cause of fluid motion is a net buoyant force existing between two adjacent regions of fluid, which force is a result of the differential thermal expansion caused by the temperature difference associated with the flow of heat and which can be shown to be equal to the product of the thermal-expansion coefficient, density, and temperature difference between the regions. The amount of heat convected away from a solid boundary in this manner by a fluid depends upon the specific heat, density, viscosity, thermal-expansion coefficient, the temperature difference existing between the bulk of the fluid and the solid boundary, and the thermal conductivity of the stagnant-fluid layer adjacent to the solid boundary. These variables are conveniently arranged in the form of a Grashof-Prandtl-number product

$$\frac{g\beta\Delta TL^3}{\nu\alpha}$$

Thus if one were able to maximize the expansion coefficient β, the density ρ, the specific heat C_p, and the thermal conductivity k, and minimize the viscosity μ, the free-convection heat transfer would be enhanced.

The behavior of most substances in the gaseous phase is such that as the critical point is approached, the quantities mentioned, with the exception of viscosity, increase greatly from their typical values in the superheat region. Viscosity is at least that of the gaseous state and is certainly much less than that of the liquid state, and since viscosity increases with temperature in the gaseous state, and decreases with temperature in the liquid state the viscosity at the critical state may well take on its minimum value. This combination of conditions near the critical state provides for maximum buoyant forces and for minimum viscous restoring forces and therefore for a condition of maximum free-convection heat transfer.

Interest in obtaining high free-convection heat-transfer coefficients, or high thermal-flux densities, stems from the recently recognized requirements of gas-turbine-blade cooling and heat removal from nuclear reactors. If the expected high heat-transfer coefficients, or high heat fluxes, are obtainable for a practical system it might then be possible to fashion a hollow gas-turbine blade and remove large amounts of heat from the blade surface and exhaust it to a reservoir in the hub of the turbine rotor. In the turbine application the free-convection heat transfer would be further enhanced by the high-acceleration field experienced by the blading itself. The problem of heat-removal from a nuclear reactor is one of obtaining high heat fluxes in confined spaces. The possibility of using a free-convection system has real merit since it would then be possible to use sealed systems, eliminate pumps and associated problems, and thus simplify the over-all installation.

Very little work has been done in the field of critical-state free-convection heat transfer, and none has been published in the unclassified literature with the exception of the work of E. Schmidt, E. Eckert, and U. Grigull (1)[4] in 1939. These investigators measured the apparent heat-transfer coefficient per unit temperature difference between a source and sink connected by an ammonia-filled loop charged to near-critical density. The system involved a two-phase flow of liquid and gas under certain conditions, giving rise to high heat-transfer coefficients due to simultaneous free convection and boiling in the test loop. E. Schmidt in recent years had made measurements of the apparent thermal conductivity of small hollow blocks charged to the critical volume, but the results of this work are not available in the technical literature at the present time.

The objective of the present work was to measure the effect of approaching critical-state conditions in a fluid on the free-convection heat transfer from a horizontal cylinder.

General Considerations

Since the objective of the experimental program was the verification of the existence of high free-convection heat-transfer co-

[1] The opinions of the authors are not necessarily those of the Shell Development Company or of the General Electric Company.

[2] Engineer, Shell Development Company, Emeryville, Calif. Assoc. Mem. ASME.

[3] Development Department, Aircraft Gas Turbine Division, General Electric Company, Cincinnati, Ohio. Mem. ASME.

Contributed by the Heat Transfer Division and presented at the Diamond Jubilee Annual Meeting, Chicago, Ill., November 13–18, 1955, of The American Society of Mechanical Engineers.

Note: Statements and opinions advanced in papers are to be understood as individual expressions of their authors and not those of the Society. Manuscript received at ASME Headquarters, August 16, 1955. Paper No. 55—A-100.

[4] Numbers in parentheses refer to the Bibliography at the end of the paper.

efficients as critical-state conditions are neared in the fluid it was felt that a simple system, in which only free convection would take place, was desirable. While a system of the type used by Schmidt, Eckert, and Grigull did have certain advantages of commercial importance it did not verify the existence of high heat-transfer coefficients due solely to free convection, since it was possible to have simultaneous free convection and boiling. The present system comprises a horizontal circular cylinder, actually a wire, mounted in a test chamber. This test chamber was so constructed as to allow charging with a test fluid and having the possibility of charge, pressure, and temperature variation.

The value of the heat-transfer coefficient is determined from an energy balance on the cylinder and a measurement of the temperature difference which exists between the cylinder surface and the test fluid. The determination of the surface temperature of the cylinder and its departure from the bulk fluid temperature is the source of greatest difficulty in this type of experiment. The cylinder, or wire, is used as a resistance thermometer to determine both the fluid temperature and the cylinder surface temperature. Since there exists the possibility of considerable error in such an application from heat conduction to the supports and thermal radiation, the choice of cylinder dimension must be such that these errors are minimized to an acceptable degree.

Freon 12, Table 1, a commercial refrigerant, was chosen as the test fluid because of its favorable critical point, low cost, ready availability, and low toxicity.

TABLE 1 CRITICAL CONSTANTS OF FREON 12[a]

Critical pressure, psia	580
Critical temperature, deg F	232.7
Critical volume, cu ft/lb	0.029

[a] Kinetic Chemicals, Inc., Wilmington, Del.

Because adequate thermodynamic data regarding the behavior of Freon 12 near the critical state were not available it was necessary to determine pressure, temperature, and Freon charge independently during the experimental program.

Description of Equipment

Test Element. The test element consisted of a horizontal platinum cylinder, chosen for its low emissivity and high physical stability, supported at the mid-point of a vertical steel vessel, nominally 8 in. diam and 15 in. tall. The test cylinder was supported from above by two 14-gage copper wires, installed in such a manner as to maintain a slight tension on the test cylinder at all times. A chromel-alumel thermocouple, silver-soldered one to each end of the test cylinder, served to indicate the test cylinder end temperature. The copper supporting wires were covered with porcelain insulators around which were wound nichrome resistance wire for guard-heating purposes. These guard heaters were so connected electrically as to allow individual control and yet require a minimum number of packing glands for wire egress. The guard heaters were thermally insulated from the test gas by mica tubing inside of which Sauereisen cement had been forced as an insulating medium between adjacent turns of the heating wire.

Test Vessel. The test vessel consisted of an 8-in-diam steel-pipe center section and two 13-in-diam × 2-in-thick steelheads attached to the center section and each other by means of draw bolts. The ends were sealed to the center section by use of an annealed-copper gasket installed in a suitable recess. This test vessel was heated by passing an electric current through Teflon-insulated nichrome heating wire wound over the surface of the test vessel in such a way as to obtain a uniform surface temperature. The test vessel was insulated with 4 in. of 85 per cent magnesia on top of which was applied 6 in. of fiberglas. The test vessel was supported on the lower face of the bottom head by three leveling screws. Each leveling screw was fitted with a small ball bearing, which ball provided almost point contact between the test vessel and its supporting structure, thus minimizing the possibility of large heat leakage to the supporting structure. The entire test vessel and commensuration equipment with the exception of the type K potentiometer was supported on a platform-type scale. In this way the system fluid charge could be measured. The scale was used as a null balance by equipping the scale beam with an electrical null-point indicator. The actual system weight was not important except in so far as scale sensitivity was concerned.

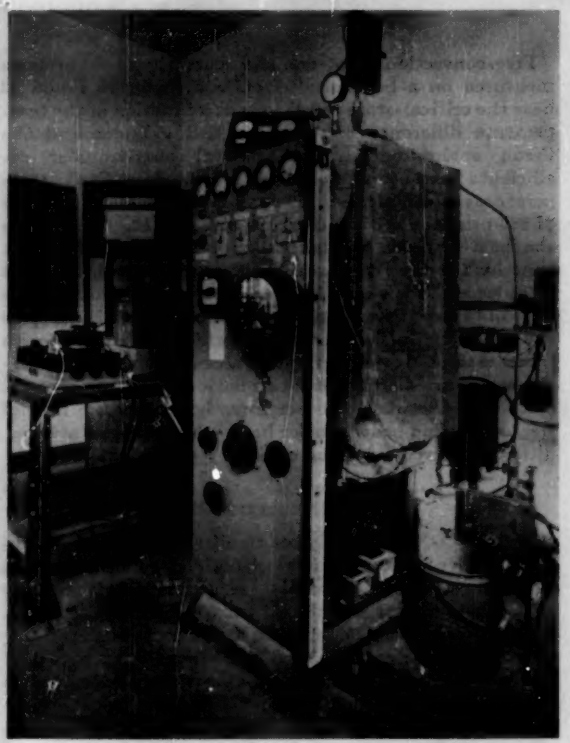

Fig. 1 Test System

Instrumentation. The control panel was made an integral part of the equipment as shown in Fig. 1. A type K Leeds and Northrup potentiometer was used as the primary electrical measuring instrument. The voltage drop across a precision resistor gave an indication of the amount of heating current being supplied to the test cylinder. The voltage drop across the test cylinder was noted by using the attached thermocouples at each end as potential leads. The system pressure was indicated on a 0 to 1000 psia bourdon-tube gage which had been carefully calibrated using a dead-weight tester. When the system was evacuated, the absolute pressure was determined by aid of a Pirani gage. During the air-calibration tests a mercury manometer was used to obtain the desired precision in the pressure measurement. Four chromel-alumel thermocouples inserted from the bottom of the test vessel to varying lengths gave an indication of the fluid temperature. Several thermocouples attached to the outside of the test vessel indicated its surface temperature. The over-all system temperature was maintained constant by controlling only 10 per cent of the heat input to the system heaters. The heat input to the test cylinder itself was negligible in comparison to the system-heater input. The control of 10 per cent of the system-heater input was accomplished by shorting a suitable series resistance in the heating

circuit with a microswitch mounted on a Brown recorder and actuated by a suitable cam. To cool the test vessel after a series of elevated-temperature runs had been taken, compressed air was circulated through copper tubing which had been wound around the test vessel for this purpose.

Procedure

Experimental Technique. A direct current, obtained from a lead storage battery, was used to heat the test cylinder. It was possible to pass the current through the test cylinder in either direction, to determine if any error was being induced in the end-temperature measurement. This error was found to be negligible. A thermocouple-type ammeter was used to indicate nominally the amount of heating current being supplied, a precise determination being made by noting the voltage drop across a 0.0100-ohm standard resistor.

The guard heaters, as well as the over-all system heaters, were supplied with alternating current to minimize the effect of stray direct currents on the various voltage measurements. The various heating circuits were individually controlled by use of autotransformers. The alternating-current input to the system was maintained constant with a regulating ballast transformer and metered constantly with a suitable panel instrument.

The energy input to the test cylinder was determined from the product of the voltage drop across and the current through the test cylinder, and its average resistance from the quotient.

All temperature measurements, with the exception of the test-cylinder temperature, were made with chromel-alumel thermocouples. Each thermocouple was carefully gas-welded and had its own cold junction. A sample thermocouple was calibrated against a standard thermometer in a free-convection oven and found to agree satisfactorily with the National Bureau of Standards, 1938, calibration. Separate ice baths were used for the two thermocouples attached to the ends of the test cylinder in order to avoid any deleterious effect from possible electrolytic action in a common bath. Another thermocouple was installed in each ice bath to insure that each was at the same temperature.

Test Program. Initial operation of the equipment involved determination of the free-convection heat-transfer coefficient for air as a check on the proper performance of the equipment. These data were compared with the results of the work of other investigators (2, 3, 4) for similar experimental conditions. Air data were taken for several different values of the temperature difference between the cylinder and the test gas and for a range of pressures from a few inches of mercury absolute to 107 psia.

Heat-transfer coefficients were determined for Freon 12 at nominally constant temperatures of 233, 244, and 259 F and at a constant pressure of 580 psia. Starting with supercritical charge densities, the deliberate release of small amounts of test gas then produced a series of state conditions, at each of which heat-transfer data were taken, ranging from supercritical to subcritical. It was impractical to drop below the critical pressure when charged to supercritical densities because of the incipience of boiling; however, some data far into the superheat region at pressures below the critical were taken.

Data Reduction. The heat-transfer coefficient was calculated using the relationship derived in Appendix 2. The power input was the product of the voltage drop and current through the test cylinder. The temperature difference between the test-cylinder surface and the test gas was calculated by taking the difference between the heated and unheated resistance of the test cylinder and dividing by the temperature coefficient of resistance.

TABLE 2 SYSTEM CONSTANTS

Wire (cylinder) length, ft	0.533
Wire diameter, in.	0.0100
System volume, cu ft	0.402
Standard resistor, ohm	0.0100
Wire temperature coefficient of resistance, ohm/deg F	5.66×10^{-3}
Condensate allowance, lb[a]	0.300

[a] To allow for that part of system at room temperature which contains liquid Freon and is not included in "system volume." Calculated from piping and gage values for room temperature and 580 psia.

Results

The test results consist of free-convection heat-transfer coefficients for a horizontal cylinder in Freon 12 at a variety of state conditions, near the critical state, and also for the same horizontal cylinder in air at near room conditions. The air data serve to verify the proper operation of the experimental equipment and the Freon 12 data comprise the primary results of the investigation.

Table 3 demonstrates the range of values encountered in the experimental variables of the test program.

TABLE 3 RANGE OF VARIABLES

Freon 12 Tests	
Temperature difference, deg F	7.25–100
Heat-transfer coefficient, Btu/hr sq ft deg F	48–375
Density (charge of Freon), lb	9.17–22.2
Power input, watts	0.169–4.17
Voltage drop, volts	0.02378–1.587
Current, amp	0.0547–3.141
Resistance, ohm	0.3453–0.5037
Pressure, psia	160–980
Freon 12 temperature, deg F	72–262
Air Tests	
Temperature difference, deg F	19.4–49.8
Heat-transfer coefficient, Btu/hr sq ft deg F	6.62–15.2
Density (from perfect-gas law), pcf	0.016–0.104
Power input, watts	0.072–0.272
Voltage drop, volts	0.1929–0.3167
Current, amp	0.05629–0.863
Resistance, ohms	0.3433–0.3714
Pressure, psia	3.18–107
Air temperature, deg F	76

The results of the Freon 12 tests are summarized in Table 4. This table summarizes the test conditions for the data presented

TABLE 4 SUMMARY OF TEST CONDITIONS

Freon temp, deg F	Pressure, psia	P/P_c	Charge[a] (reduced)	Symbol
Freon 12—Nominal Constant Temperature 233 F				
232.9	637	1.095	1.36	○
237.0	683	1.18	1.40	□
233.0	589	1.015	1.19	△
234.5	617	1.06	1.07	▽
233.5	590	1.02	1.04	×
232.8	581	1.00	1.01	+
233.2	596	1.025	0.90	◇
233.0	575	0.990	0.86	⌀
233.5	577	0.993	0.78	⌀
232.8	554	0.958	0.61	◈
235.5	540	0.930	0.46	◈
Freon 12—Nominal Constant Temperature 244 F				
244.0	597	1.025	0.53	
244.0	615	1.060	0.75	
243.0	607	1.040	0.80	
244.0	633	1.092	0.88	
246.0	644	1.11	0.99	
242.0	642	1.105	1.07	
243.0	667	1.145	1.17	
244.0	604	1.04	1.31	
Freon 12—Nominal Constant Temperature 259 F				
258	714	1.230	1.01	
259	696	1.200	0.91	
259	693	1.195	0.82	
261	673	1.160	0.74	
258	653	1.125	0.61	
256	953	1.608	1.28	

Freon temp, deg F	T/T_c	Pressure, psia	Charge[a] (reduced)	Symbol
Freon 12—Constant Pressure Data 580 psia (critical)				
236.6	1.018	580	0.74	○
240	1.030	580	0.81	□
233.8	1.002	580	0.85	△
231.2	0.993	580	0.90	▽
232.0	0.995	580	0.91	+
232.1	0.997	580	0.93	×
231.9	0.994	580	0.99	◇
230.5	0.989	580	1.03	⌀
230.5	0.989	580	1.05	⌀

[a] Reduced charge—system charge minus condensate allowance divided by critical charge (13.7 lb).

in this section and gives the symbol used on the graphical presentation. Inspection of this table shows that heat-transfer data were taken at three nominally constant temperature levels for a series of pressures, or charge densitites, varying from supercritical to subcritical. One series of tests at a constant pressure of 580 psia, the critical pressure of Freon 12, was made for temperatures, or charge densities, varying from supercritical to subcritical.

The primary results of the investigation are presented as plots of the heat-transfer coefficient and the heat rate per unit area Q versus the temperature difference between the cylinder surface and the test fluid. These data are shown in Figs. 2 and 3.

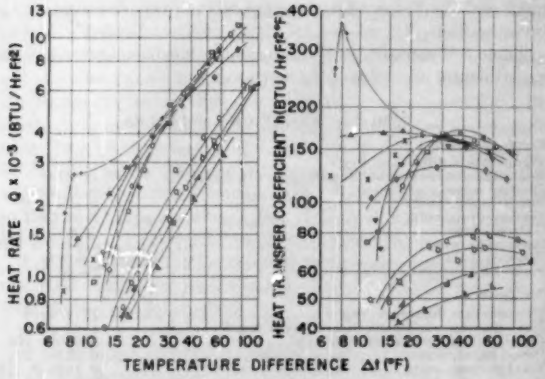

FIG. 2 HEAT-RATE AND HEAT-TRANSFER COEFFICIENTS FOR CONSTANT FREON TEMPERATURE 233 F

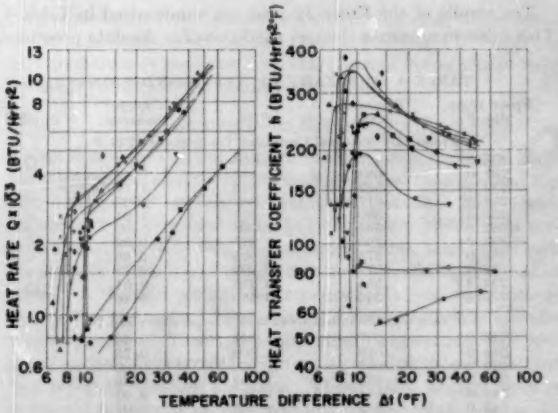

FIG. 3 HEAT-RATE AND HEAT-TRANSFER COEFFICIENTS FOR CONSTANT FREON PRESSURE 580 PSIA

It may be noted that for each of the given state conditions the heat-transfer coefficient is a function of the temperature difference between the cylinder and gas, usually having a maximum value. Figs. 4 and 5 are plots of this maximum value as a function of the state variables "reduced pressure" and "reduced charge."

To determine if free-convection heat transfer involving Freon 12 could be correlated in the superheat region using available property data, several measurements of the free-convection heat-transfer coefficient were made at a pressure of 283 psia and a temperature of 172 F. Fig. 6 plots the Nusselt modulus versus the Grashof-Prandtl modulus for this set of data. Also included in this figure is the recommended correlation curve of McAdams (2).

The air-control curve, Fig. 7, plots the dimensionless heat-transfer coefficient, the Nusselt modulus, versus the product of the Grashof modulus and the Prandtl modulus. These dimensionless groupings have been shown previously by McAdams to be suitable for correlation of free-convection heat-transfer data.

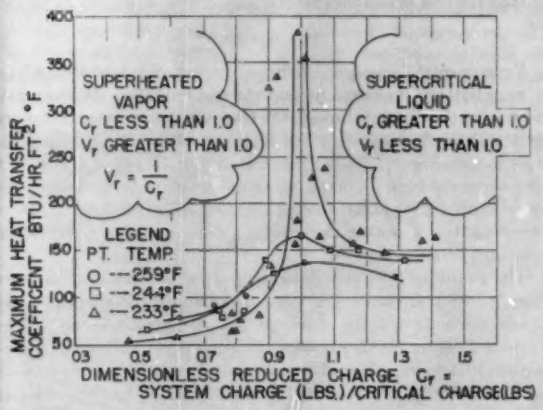

FIG. 4 MAXIMUM HEAT-TRANSFER COEFFICIENT AS A FUNCTION OF SYSTEM CHARGE WITH TEMPERATURES AS A PARAMETER, PRESSURE 580 PSI

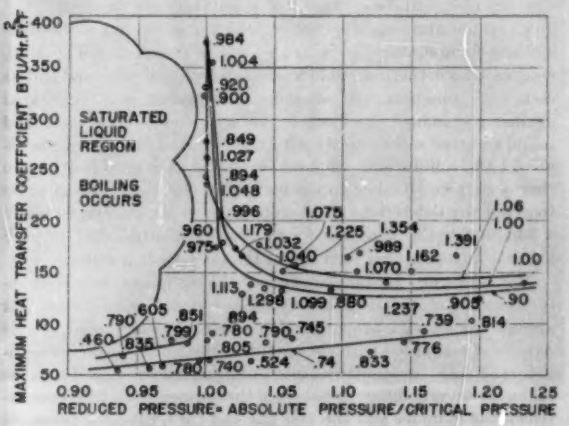

FIG. 5 MAXIMUM HEAT-TRANSFER COEFFICIENT AS A FUNCTION OF REDUCED PRESSURE WITH REDUCED CHARGE AS PARAMETER, TEMPERATURE 233 F

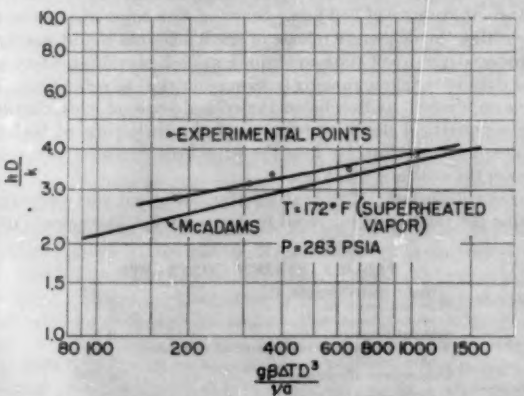

FIG. 6 HEAT TRANSFER FROM HORIZONTAL CIRCULAR CYLINDER TO SUPERHEATED FREON VAPOR

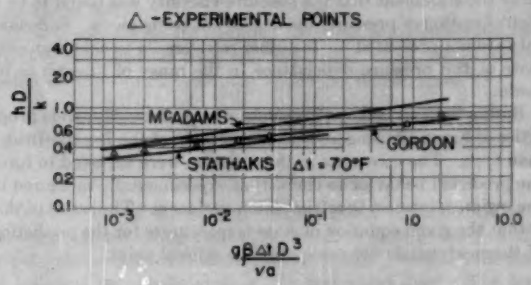

FIG. 7 HEAT TRANSFER FROM HORIZONTAL CIRCULAR CYLINDER TO Δt2

Comparison of the present experimental results with the work of Gordon and Stathakis and the recommended correlation curve of McAdams indicates that the equipment was operating satisfactorily. When taking heat-transfer data for air, the heat-transfer coefficients were of such small magnitudes that it was necessary to guard-heat the ends of the test cylinder to insure that the conduction loss was a negligible percentage of the total heat input to the test cylinder. The correction for radiation was calculated to be less than 0.4 per cent of the convective heat-transfer coefficient and was therefore neglected.

DISCUSSION

Experimental data showing the magnitude of free-convection heat transfer from a horizontal circular cylinder to Freon 12 at, or near, the critical state are shown in Figs. 2 to 5. Since the heat-transfer coefficient h in free convection becomes a function of the temperature difference, the real merit of defining such a coefficient is not as justifiable as for the case of forced convection where the coefficient may be defined to be independent of the temperature difference. For the present case, especially as the critical state is approached, the heat-transfer coefficient, as usually defined, becomes strongly a function of the temperature difference. This is due to the fact that the fluid properties vary greatly with the average film temperature and the additional fact that the critical state is not very well known. The result is that for certain temperature differences between the cylinder and the fluid, when the fluid is at the apparent critical state, the true critical-state condition occurs locally in the region near the cylinder. This condition and effect may be seen in Figs. 2 and 3. Since the designer is interested in the total heat transferred, the experimental results are presented in terms of energy transferred per unit area. This quantity exhibits no maximum values as are seen in the heat-transfer coefficients.

Consistent presentation of the heat-transfer coefficient is possible on the basis of the maximum values of the coefficient. Such presentations are made in Figs. 4 and 5 which show h_{max} against the reduced charge and the reduced pressure, respectively. It is clear from these plots that the heat-transfer coefficient increases greatly in the region of the critical state, by a tenfold factor. The scatter in the data is due in great part to the lack of adequate property data for Freon 12 in the test state. This lack of knowledge regarding the thermodynamic behavior of Freon 12 would result in a miscalculation of the critical charge.

An interesting observation regarding Fig. 5 is that supercritical charges are to be preferred in the interest of large heat-transfer coefficients.

That the heat-transfer coefficients as obtained by means of the experimental system for a fluid state removed from the critical state can be correlated by the dimensionless parameters usually associated with free convection is indicated in Fig. 6. The experimental data as shown are 5 to 15 per cent higher than McAdams' recommended curve. This variance most probably is the result of poor property data on Freon.

In general, the behavior of the free-convection heat-transfer coefficient in the region near the critical point agrees with that observed by Schmidt, Eckert, and Grigull, even though the two test systems were of different configurations. The absolute magnitudes of the heat-transfer coefficients do not compare.

The random error in the heat-transfer coefficient is calculated to be less than 3 per cent, with 5 per cent systematic error in the same quantity. The error attributable to radiation is always less than 0.5 per cent because of the relatively high value of the free-convection heat-transfer coefficient. Conduction to the supporting structure is such that the temperature difference should be systematically less than 4 per cent below that value which would result with no conduction. The error in determination of the heat input should be less than 1 per cent. The leak rate of the equipment was so slight it is felt that no error could be attributed to nonsteady-state operation as regards density. The test-vessel temperature was maintained steady within a fraction of a degree during the constant temperature-data runs, and its surface was uniform in temperature to within 1 deg F. It is felt that no error accrued from nonsteady-state operation of the test cylinder because of its small time constant and the fact that the data were readily reproduced. Determination of the system pressure and temperature was considered precise, as was the over-all system charge. There is, however, the possibility of some error being made in the amount of Freon within the test space itself, owing to the possible variation of the position of the liquid-gas interface with changes in temperature of the over-all equipment. It is felt that this error may have been appreciable, perhaps of the order of 10 to 15 per cent in net charge density.

In conclusion, it may be noted that while the increase in the heat-transfer coefficient for the present system is appreciable, the effect is limited to a rather narrow region of state conditions. Use of a system of the type employed by Schmidt, Eckert, and Grigull would tend to broaden the range of state conditions in which the large increase in the free-convection heat transfer is observed because of the possibility of simultaneous heat transfer and change of phase.

It was possible during certain of the experimental runs to obtain a twofold value of the heat-transfer coefficient for a given heat rate, depending upon whether the data were taken with increasing steps in the heat rate or decreasing. Unfortunately, this effect was an elusive phenomenon and it was not always possible to obtain it under similar operating conditions. It is to be noted though, that the larger value of the heat-transfer coefficient always occurred when the heat rate was being increased so that the present data represent the maximum since all reported data were taken within increasing increments in the heat rate.

The possibility of dissociation of the Freon 12 test gas exists although it is presumed that such was not the case during the present investigation.

CONCLUSIONS

1 Heat-transfer coefficients from a heated, horizontal, right circular cylinder to Freon 12 near critical-state conditions have been obtained. These experimentally determined coefficients show clearly that a tenfold increase at the critical state may be realized.

2 Heat-transfer coefficients in the superheated vapor region away from the critical state are shown to be within 15 per cent of the curve recommended by McAdams for free convection.

BIBLIOGRAPHY

1 "Heat Transfer by Liquids Near the Critical State," by E.

Schmidt, E. Eckert, and U. Grigull, AAF Translation No. 527, Air Materiel Command, Wright Field, Dayton, Ohio.

2 "Heat Transmission," by W. H. McAdams, McGraw-Hill Book Company, Inc., New York, N. Y., second edition, 1942.

3 "Heat Transfer by Free Convection From Small Diameter Wires," by H. S. Gordon, PhD dissertation, University of California, 1950.

4 "Heat Transfer by Free Convection to Gases at Low Pressures From a Small Diameter Hot Wire," by G. J. Stathakis, MS thesis, University of California, 1953.

5 "Thermal Conductivity of Gases at Atmospheric Pressure," by J. M. Lenoir, University of Arkansas, Engineering Experiment Station Bulletin No. 18, August, 1953.

6 "The Viscosities of Freon Refrigerants," by A. F. Benning and W. H. Markwood, *Journal of American Society of Refrigeration Engineers*, April, 1939.

7 "Thermodynamic Properties of Freon 12 and Other Related Gases," by R. M. Buffington and W. K. Gilkey, American Society of Refrigeration Engineers Circular No. 12, 1931.

8 "Gas Tables," by J. H. Keenan and J. Kaye, John Wiley & Sons, Inc., New York, N. Y., 1945.

Appendix 1

Nomenclature

The following nomenclature is used in the Appendixes:

A = cross-sectional area of test cylinder, sq ft
b = constant in differential equation
β = expansion coefficient
D = cylinder diameter, ft
e = voltage drop over length of test cylinder, volts
g = acceleration of gravity, ft/sec^2
h = heat-transfer coefficient, Btu/hr sq ft deg F
i = current flowing in test cylinder, amp
k = thermal conductivity, Btu/hr ft deg F
l = length of test cylinder, ft
m = constant in differential equation, 1/ft
p = perimeter of test cylinder, ft
P = pressure in test vessel, psia-lb/in.^{2} abs.
Q = heat rate per unit area, Btu/hr sq ft
R = measured wire resistance, ohms
R_0 = measured wire resistance at gas temperature, ohms
T_c = temperature of cylinder, deg F
T_g = temperature of gas, deg F
x = distance along test cylinder, ft
v = $T_c - T_g$
t = average temperature difference, deg F
w = charge of Freon 12 in test system, lb
ρ = gas density, pcf
μ = viscosity, lb/ft sec
α = temperature coefficient of resistance, ohms/deg F

Subscript c to either P or T denotes the critical state when so used.

Property Values of Freon 12

The transport properties of Freon 12, dichlorodifluoromethane, C Cl_2F_2, are generally not well known throughout the thermodynamic realm, although for practical use such data exist as to enable engineering estimates to be made in the region of interest in the field of refrigeration engineering.

Lenoir (5) gives the thermal conductivity of Freon 12 at a pressure of approximately 1 atm. These data were obtained by use of a calibrated thermal-conductivity cell.

Benning and Markwood (6) present the absolute viscosity for several of the Freon refrigerants. These data were obtained by use of a falling-ball viscosimeter, pressurized and calibrated against air. Unfortunately, the authors do not present data for pressures other than 1 atm for the case of Freon 12, but they do make the statement that the absolute viscosity was found to be a slight function of pressure, the degree not being given. Sufficient data are not presented for the other refrigerants to enable an estimate of the pressure dependence in the range of interest to be made.

Buffington and Gilkey (7) calculated the thermodynamic properties of Freon 12 using an equation of state of the Beattie-Bridgman type. The constants in the equation were adjusted to force the predicted behavior to check that experimentally measured in the region of interest to refrigeration engineers. The result of this is that the given equation of state is inaccurate for the prediction of thermodynamic behavior near the critical point.

Appendix 2

Reduction of Data

The calculation of the average heat-transfer coefficient over the length of the test cylinder was accomplished by use of an energy balance on the cylinder. The necessary constants for such a calculation were determined experimentally, with the exception of the calculation of the heat loss from the end of the cylinder caused by heat conduction through the support structure.

An energy balance on the wire yields the following:

Heat input: $3.413ei$ Btu/hr
Heat convected: $\pi Dlh(T_c - T_g)$

The design of the test cylinder, or wire, was such that the average temperature of the wire, determined from the measured average resistance, differed from the mid-point temperature by less than 4 per cent of the total temperature difference between the test wire and test gas. Equating the energy input to that convected yields for h the average heat-transfer coefficient over the length of the cylinder

$$h = \frac{3.413ei}{\pi Dl(T_c - T_g)}$$

where

D = 0.0100 in.
l = 0.533 ft.
π = 3.14

then

$$h = \frac{2.445 \times 10^3\, ei}{(T_c - T_g)}$$

The gas temperature was determined by using the test cylinder as a resistance thermometer and noting its "cold" resistance. For heating currents less than 100 milliamp the resistance heating is negligible and this technique is justified. The temperature difference between the test cylinder and gas was calculated using the relationship

$$(T_c - T_g) = \frac{Rc - Rg}{dR/dT}$$

The temperature derivative of resistance, or temperature coefficient, was determined from the resistance calibration of the wire to be 5.66×10^{-4} ohm/deg F. This technique eliminates any errors arising from direct use of a temperature-resistance calibration where the random error, made reading the curve and then taking the difference of two large numbers, may mask the result.

The Nusselt modulus was calculated using the thermal conductivity as noted in Appendix 1, evaluated at the gas temperature.

The heat transferred per unit area was calculated from the

product of the voltage drop and cylinder current and a suitable conversion factor.

The Grashof-Prandtl modulus used for correlating free-convection heat-transfer data was calculated using the properties noted in Appendix 1 evaluated at the gas temperature.

Appendix 3

Test-Cylinder Design

The selection of the diameter and length of the test cylinder is dictated by the temperature distribution within the cylinder which results under the boundary conditions present at the time of test, and by the diameter of the test vessel itself. The test-vessel diameter sets the length of the test cylinder at about 6 in. The diameter of the test cylinder was determined such that the difference between the mid-point temperature of the cylinder and the average temperature, based upon the measured average resistance, will be less than 4 per cent of the total temperature rise of the test cylinder mid-point above the gas temperature. The end temperature will be assumed to be equal to the gas temperature, for the purposes of design; anything greater tends to minimize the departure between the mid-point temperature and the mean temperature. The uniformity of the cylinder temperature is important because the mean cylinder resistance and hence cylinder temperature is that quantity which is measured when the current through and the voltage drop across the test cylinder are noted.

The differential equation governing the longitudinal temperature distribution is

$$\frac{\partial^2 v}{\partial x^2} - m^2 v + b = 0$$

$$x = 0, l \qquad v = 0$$

The solution of this differential equation subject to the given boundary conditions is

$$v = \frac{b}{m^2}\left(1 - \frac{\sinh mx + \sinh m(l-x)}{\sinh ml}\right)$$

The mean temperature of the cylinder may be calculated from the integral

$$v_{avg} = \frac{1}{l}\int_0^l v\,dx$$

Performing the indicated integration yields

$$v_{avg} = \frac{b}{m^2}\left(1 - \frac{2(\cosh ml - 1)}{ml \sinh ml}\right)$$

The temperature at the mid-point of the cylinder is

$$v_{l/2} = \frac{b}{m^2}\left(1 - \frac{2\sinh\frac{ml}{2}}{\sinh ml}\right)$$

The departure of the mid-point temperature from the mean temperature may be determined by forming the ratio of the mid-point temperature to the average temperature

$$\frac{v_{l/2}}{v_{avg}} = \frac{\sinh ml - 2\sinh\frac{ml}{2}}{\sinh ml - \frac{2}{ml}(\cosh ml - 1)}$$

The departure of the mid-point temperature from that of an ideal cylinder, that is, one in which no heat is lost through the ends, is given by

$$\psi = \frac{v_{ideal} - v_{l/2}}{v_{ideal}} = \frac{2\sinh\frac{ml}{2}}{\sinh ml}$$

A plot of ψ and $v_{l/2}/v_{avg}$ as a function of the cylinder parameter ml shows that the departure of the mid-point temperature from that of the ideal cylinder is negligible for ml greater than 10 and that the average temperature is within 4 per cent of the mid-point temperature for ml greater than 60.

For a 10-mil platinum wire operating in air, a nominal value of the heat-transfer coefficient is 10 Btu/hr sq ft deg F, and the other constants necessary to calculate m are

$p = 2.62 \times 10^{-3}$ ft $k = 40.2$ Btu/hr ft deg F

$A = 54.5 \times 10^{-6}$ sq ft $i = 0.532$ amp

$\alpha = 2.2 \times 10^{-3}$/deg F $\rho_G = 0.4 \times 10^{-6}$ ohm ft

$$m = \sqrt{\frac{hp}{kA} - \frac{3.413 i^2 \rho_G \alpha}{kA^2}} = 36 \qquad ml = 19.1$$

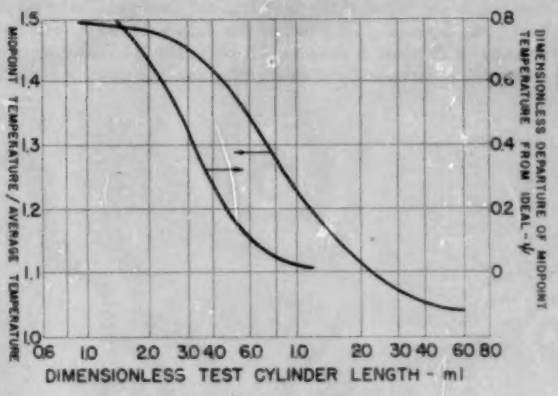

Fig. 8 Relationship of Cylinder Mid-Point Temperature to Average Temperatures

Since ml is below that value said to be the lowest acceptable, guard-heating of the cylinder ends is indicated and this was done for all runs. A similar calculation for the case of free convection to Freon 12 shows that ml is well above the required minimum value so that guard-heating of the cylinder ends was not required. Fig. 8 is a plot of the design parameters mentioned in the foregoing.

A calculation which assumes that all of the heat generated in the test cylinder is liberated at the center line indicates that the radial temperature gradient is negligible.

Discussion

T. W. Jackson.[8] For some time the writer has wondered whether or not free-convection Nusselt numbers can be correlated precisely by a Grashof-Prandtl number product. However, because of past experience this appears to be the convenient method of approach, and the authors are justified in its use.

Obtaining high free-convection heat-transfer coefficients, as stated by the authors, would offer possibilities of sealed heat-transfer systems and, consequently, eliminate pumps and

[8] Chief, Mechanical Sciences Division, Georgia Institute of Technology, Atlanta, Ga. Mem. ASME.

associated problems. The paucity of data on free convection at or near the critical state, however, indicates the difficulty of doing this and of obtaining experimental results in this region. The writer regrets that the data were not for water which would be a more interesting fluid from an engineering standpoint. Perhaps the present paper will inspire someone to consider a water system with its high pressure (P_{cr} = 3206 psi) and comparatively high temperatures (T_{cr} = 705 F).

The writer concurs with the authors that, since the heat-transfer coefficient h in free convection becomes a function of the temperature difference, the real merit of defining a coefficient may not be as justifiable as for the case of forced convection. In addition, at or near the critical point the dependency of the physical properties of the heat-transfer medium on temperature makes a correlation difficult. Therefore the authors' procedure of plotting heat rate and heat-transfer coefficient versus temperature differences and reduced pressure seems practical. The practical use of, say, a tenfold increase in heat-transfer coefficient may not be possible because of the temperature and pressure dependencies. However, the final decisions on this must await further experimental data.

The authors' comment that it was possible to obtain a twofold increase in the value of the heat-transfer coefficient for a given heat rate, depending on whether the data were taken with increasing or decreasing steps in the heat rate, is interesting. In determining the viscosity of steam using the transpiration method the writer experienced this type of elusive phenomenon. Perhaps it is the result of distortions in the normal steady-state distribution of molecular energies of the fluid. The distributions may be affected by a temperature gradient—one way for a positive gradient and another for a negative gradient.

The writer wishes to congratulate the authors for tackling a difficult problem. It is hoped that they can continue or encourage the continuance of this work so that data on water will become available.

Authors' Closure

The authors thank Mr. Jackson for his discussion of the paper and agree with him that it would be of greater engineering interest to have used water vapor as the test gas. Experimental difficulties with pressures and temperatures near the critical for water are most formidable however.

Since the preparation of this paper Mr. R. B. Ramsey, Jr., of the E. I. du Pont de Nemours Co., has called to our attention new data on the thermodynamic properties of Freon 12. Time has not permitted a re-evaluation of the experimental data in the light of this new thermodynamic information, but it is hoped that this will be done in the near future.

Since this work was intended only as a preliminary effort, it is the authors' hope, of course, that it will encourage others to investigate, both analytically and experimentally, this interesting field of heat transfer.

A Selected List of ASME Reference Texts to Meet Specific Problems

APPLIED MECHANICS

APPLIED MECHANICS REVIEWS Published monthly
$65.50 Annually ($10.00 to ASME members)

Covering the advances made throughout the world in the fields of applied mechanics and related engineering science, this magazine provides its readers with reliable appraisals of contributions on important investigations, new discoveries in the fields, advanced techniques, and applications of experimental methods—culled from over a thousand sources including 750 engineering periodicals in thirty countries, reports of industrial research laboratories everywhere, and new technical books in all languages. Additionally, each issue contains a feature article by an international authority which reviews and evaluates progress in a specialized area.

PROCEEDINGS OF THE SECOND U. S. NATIONAL CONGRESS OF APPLIED MECHANICS 1954
(No discount allowed) $15.00

Offers a unique collection of data, calculation, procedures, and solutions for attacking problems associated with dynamics, vibration, wave motion, elasticity, shells and plates, plasticity, viscoelastic flow, behavior of materials, fluid flow, and aerodynamics.

SHOCK AND VIBRATION INSTRUMENTATION 1956 $5.00

This book places emphasis on applicable basic principles rather than problems of only passing interest.

CONTENTS: Evaluation of Mounts Isolating Nonrigid Machines From Nonrigid Foundations. Experimental Study of the Effects of Foundation Resilience on Vibration Isolation. Effect of Material and Slip Damping on Resonance Behavior. Shock and Vibration Environments. Mechanical Design for Random Vibration and Shock. Influence of Electrical and Mechanical Impedance on the Control and Performance of Servo-Vibration Machines. Shock Testing Machines and Procedures. Damaging Potential of Shock and Vibration. High Speed Computing Methods for Shock and Vibration Problems.

DESIGN DATA AND METHODS—APPLIED MECHANICS 1953 $4.00

Included in this collection of original and practical contributions are stress and deflection methods applied to circular and rectangular plates; analysis of circular beams; design data for plating; data on torsion, thermal stresses, stresses in pressure vessels, shrink-fitted assemblies, and thick-walled cylinders; and methods of treating and solving problems of vibration and of balancing rotating apparatus.

AVIATION

STRUCTURES FOR THERMAL FLIGHT 1953 $3.00

The problem areas herein covered are materials at elevated temperatures, cutaway airframe structures, factor of safety concepts, and elevated temperature testing techniques.

CONTENTS: Challenge of Progress. High Speed Problems of Large Airplanes. Aluminum Alloys for Elevated Temperature Service. Application of a New Structural Index to Compare Titanium Alloys With Other Materials in Airframe Structures. Optimum Stresses of Structural Elements at Elevated Temperatures. Thermostructural Efficiencies of Compression Elements and Materials. Weight Efficiency Analysis of Thin Wing Construction. Design Criteria for Heated Aircraft Structures. Some Structural Penalties Associated With Thermal Flight. Aircraft Structural Testing Techniques at Elevated Temperatures. Some NACA Research on the Effect of Transient Heating on Aircraft Structures. Utilization of Solar Furnaces in High Temperature Research.

THERMAL BARRIER SYMPOSIUM
(In July 1953 ASME Transactions) $1.50

Covers over-all problems which arise in selection and design of aircraft, problems associated with the various systems, aspects of structural design and analysis caused by aerodynamic heating and the specific weight parameters.

AUTOMATIC CONTROL

DYNAMICS OF AUTOMATIC CONTROLS 1948 $6.00

Covers the dynamic properties of controllers, the functional elements of a control, mathematical methods for handling control problems, components of the control loop and special control problems, effects of nonlinearities in the control loop, the on-off regulator, and the theory of the saturation-dependent pulsatile controller.

FREQUENCY RESPONSE 1953 $7.50

Features an unparalleled coverage of automatic control and servomechanism design based on frequency response. To the practicing engineer it brings data of the modern developments in analysis and practice. For the beginner it provides an introduction to typical methods of analysis and synthesis and examines field tests of representative industrial servo systems.

ATMOSPHERIC POLLUTION

SMOKE NEWS Published Bi-Monthly
(No discount allowed) $5.00 Annually

By direct reproductions of news items, announcements, photographs, and diagrams appearing in the daily press of the U. S. and Canada, this newsletter provides a broad coverage of activities in the air pollution field.

PROBLEMS AND CONTROL OF AIR POLLUTION 1955 $5.00

Presents some material on treatment and recovery of sulphur dioxide, industrial ideas on new developments and control, experiences in air pollution abroad, and research other information useful to those connected with the medical, biological, and meteorological aspects of air pollution.

INSTRUMENTS FOR THE STUDY OF ATMOSPHERIC POLLUTION 1953 $3.00

Lists over a hundred devices useful in studying air pollution together with the names and addresses of the manufacturers who can supply them.

GUIDE TO RESEARCH IN AIR POLLUTION
Third Edition 1954 $1.50

As a compilation of air pollution research of definite public and scientific interest, this Report will prove useful to those sponsoring research or seeking specific assistance. It lists sixty-eight organizations (colleges, universities, and research institutes) conducting research, along with a summary of the subjects engaging the attention of each.

RELIABLE ELECTRONICS FOR SMOKE REGULATION ORDINANCE 1949 $0.50

Shows how to develop an appropriate ordinance for communities to improve the cleanliness of the air.

CONTENTS: Creation, Organization, and Duties of Smoke Regulation Department. Establishment of Rules and Regulations. Installation and Operating Permits. Inspection. Fees. Emission Prohibited and Standard Measurements. Equipment Duplicate. Entrance to Premises. Opportunity of Appeals. Persons Liable. Prosecutions and Chimes. Co-ordination of Departments. General Provisions.

DESIGN ENGINEERING

DESIGN ENGINEERING—Training in Value Analysis, Selection of Engineering Materials, Manufacturing Trends, Research 1954 $3.50

There is a wealth of information based on actual experience in this book for those interested in the training of design engineers in value analysis, provisions for rewarding ideas for outstanding achievements, design and selection of engineering materials, and the effect of the trend toward administration.

METALS ENGINEERING-DESIGN 1953 $10.00

It provides criteria for facing the over-all problems of selection of materials, and takes up such specific items as high temperature considerations, elasticity, residual stresses, vibration, fatigue, shot peening, cold working, blending, flame strengthening, impact, corrosion, nondestructive testing, surface finish and mass production, and design procedures.

ENGINEERING TABLES 1956 $12.00

A collection of tables often wanted by engineers but not commonly found in handbooks covering:

Bar Stocks and Shafting. Conversion Factors. Formulas for Stress and Strain. Properties of Sections and Cylinders. Bearings. Bearing Load Analysis. Spur Gears. Helical and Herringbone Gears. Bevel Gears. Worm Gears. Cylindrical Fits. Standard Tapers. Keys and Keyseating. Bolts. Counterbores. Screw Threads. Studs. Screwdrive and Splines. Nuts. Pins. Seamings. Washers. Wrench Openings. Springs. Aircraft and Miscellaneous Tubing. Pressure Tubes. Pipe and Pipe Threads and Fittings. Electric Motors. Graphical Symbols. Welding. Gaskets. Hydraulic Standards and Symbols. O-Rings. Packings. Seals. Bibliography.

METALS PROTECTION 1954 $11.00

For each of the more than 200 steels in common industrial use (AISI, SAE, ASTM steels, cast copper alloys, aluminum alloys, zinc, magnesium, etc.), this book gives such information as its chemical composition limitations, heat-treatment and other characteristics, industrial uses, critical temperatures for forging, annealing, normalizing, and such mechanical properties as recrystallization temperature and hot working temperature, and a great deal of other pertinent information.

METALS: TEMPERATURE—CUTTING

EFFECT OF TEMPERATURE ON THE BRITTLE BEHAVIOR OF METALS With Particular Reference to Low Temperatures 1954 $7.00 $5.60*

CONTENTS: Evaluation of Brittle Failures in Steam and Engineering Structures. Concepts of Metal Behavior for Design Engineers. Metallurgical and Mechanical Factors. Mechanical Tendency Test Specimens and Reliability. Aspects of Current Research Including New Data on Transition, Distributed and Tempered Steels at High Strength Levels, and Ferrous Types of Cast Irons.

ELEVATED-TEMPERATURE PROPERTIES OF

Carbon Steels	1955	$3.75	$3.00*
Selected Wrought Alloys	1954	4.75	3.80*
Chromium Molybdenum Steels	1953	4.75	3.80*

Each of these reports is a graphical summary of the elevated temperature properties established. Each includes summary curves of tensile and yield strength, elongation and reduction of area, rupture and creep rates; also data sheets giving the chemical composition, processing data, heat-treatment, and other pertinent information about the steels included in the respective surveys.

*Price to ASME Members

MANUAL ON CUTTING OF METALS 1952 $10.00

Treats the mechanical characteristics and structures of the metals to be cut—irons and steels, high-nickel alloys, copper and its alloys, aluminum, and plastics—explains the influence of the composition and microstructure of each metal on the type of the cutting tool, chip formation and control, and surface finish; deals with cutting fluids and the cutting speeds for specific cutting conditions when turning a variety of metals; includes drawings of tool shapes; and has tables giving data on feeds and speeds.

TERMINOLOGY

AUTOMATIC CONTROL TERMINOLOGY
(ASME Standard No. 19D) 1954 $1.75

Terms defined herein apply primarily to the field of automatic control in industrial processes. Diagrams illustrate the terms of the definitions.

CONTENTS: Automatic Controllers. Basic Characteristics. Processes. Basic Elements and Characteristics. Characteristics of Automatic Control. Types of Automatic Controller Action. Adjustments of Automatic Controller Action. Elements and Characteristics of Automatic Controllers. Basic Terms. Block Diagrams, Symbols, and Automatic Control Combinations.

INDUSTRIAL INSTRUMENTS TERMINOLOGY
(ASME Standard No. 19C) 1950 $1.50

Lists and defines approximately 500 terms used by industrial and management engineers. Subjects range from elementary definitions to an entire series of computer production terms.

GLOSSARY OF TERMS IN NUCLEAR SCIENCE AND TECHNOLOGY 1955 $5.00

This glossary of terms clarifies today's nuclear language, contributes to the standardization of usage, and provides scientists and engineers with a sizable compendium of nuclear knowledge. Terms and definitions are alphabetically arranged and include those used in Physics, Reactor Theory, Reactor Engineering, Chemistry, Chemical Engineering, Biophysics, Radiobiology, Instrumentation, Isotope Separation, and Metallurgy.

10% Discount to ASME Members
except where stated "No discount allowed"

THE AMERICAN SOCIETY OF MECHANICAL ENGINEERS

29 W. 39th St., New York 18, N. Y.